GEOLOGICAL SURVEY OF CANADA
PAPER 90-4

GROUND PENETRATING RADAR

edited by

J.A. Pilon

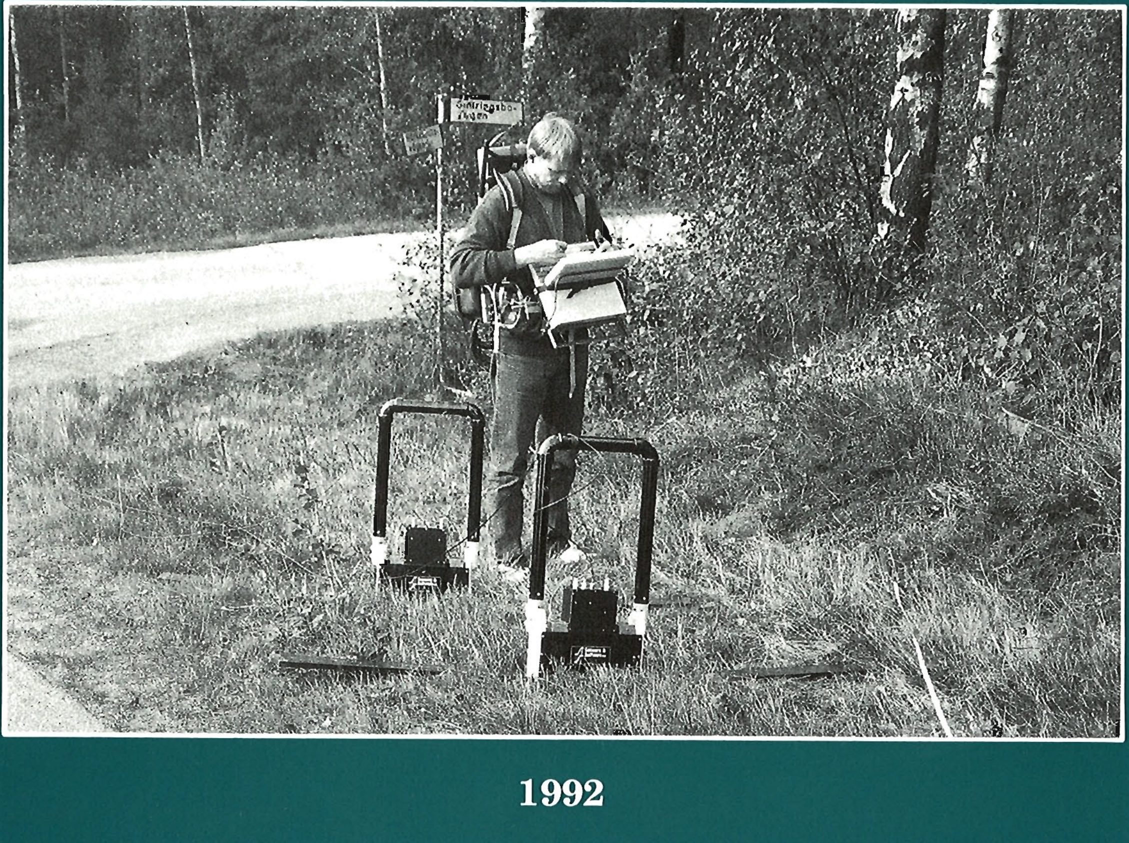

1992

Energy, Mines and
Resources Canada

Énergie, Mines et
Ressources Canada

Canada

THE ENERGY OF OUR RESOURCES

THE POWER OF OUR IDEAS

GEOLOGICAL SURVEY OF CANADA
PAPER 90-4

GROUND PENETRATING RADAR

J.A. Pilon

1992

Available in Canada through authorized
bookstore agents and other bookstores

or by mail from

Canada Communication Group — Publishing
Ottawa, Canada K1A 0S9

and from

Geological Survey of Canada offices:

601 Booth Street
Ottawa, Canada K1A 0E8

3303-33rd Street N.W.,
Calgary, Alberta T2L 2A7

100 West Pender Street
Vancouver, B.C. V6B 1R8

A deposit copy of this publication is also available for
reference in public libraries across Canada

Cat. No. M44-90/4E
ISBN 0-660-14538-3

Price subject to change without notice

Cover description

Ground Penetrating Radar survey in Sweden to determine depth to bedrock. (Photo courtesy Sensors and Software Inc.)

Original manuscript received: 1990 - 12
Final version approved for publication: 1991 - 09

CONTENTS

INTRODUCTORY REMARKS

At the Ground Penetrating Radar Workshop, an attempt was made to group the papers into various categories. In this volume the papers appear in alphabetical order by first author. These papers cover a wide range of topics related to ground penetrating radar design, application, and interpretation, and they constitute a substantial portion of the papers presented orally at the workshop.

The collection also provides a good overview of the state of the art in this field. It should be a useful introduction to the ground penetrating radar technique as well as an excellent reference.

The workshop was supported with funds provided by the Interdepartmental Panel on Energy Research and Development of Energy, Mines and Resources, Canada.

Finally, I would like to thank everyone who participated in the critical review of the manuscripts as they are too numerous to name individually.

J.A. Pilon
Editor

It was my pleasure, on behalf of the Geological Survey of Canada, to welcome participants to the Ground Penetrating Radar Workshop that was held in Ottawa 24-26 May 1988. The workshop was well attended, with some 13 countries being represented. This clearly shows the high level of international interest in this relatively new geophysical technique. This special publication of the Geological Survey of Canada will serve as a permanent record of many of the papers given during three days of presentations and lively discussion. It is hoped that the publication will serve to stimulate interest and further research and development of this most promising geophysical technique.

M.J. Berry
Director, Geophysics Division

Ground penetrating radar (GPR) is an electromagnetic technique useful for mapping layering in soils and rocks and for detecting underground objects due to changes in the electrical properties of materials. The frequencies employed are in the 10-1000 MHz range, which allows for higher resolution than other geophysical methods. The technique has been in existence for more than 15 years, but in the beginning little was known about propagation, penetration and the interaction of electromagnetic energy in earth materials. Consequently, trial and error methods were used, and experience was accumulated by various workers studying numerous applications under different conditions.

REMARQUES PRÉLIMINAIRES

À l'Atelier sur le géoradar, on a tenté de regrouper les exposés par sous-domaine. Dans le présent volume, les textes sont classés par ordre alphabétique des auteurs principaux. Ils touchent à une large gamme de sujets liés à la conception et à l'utilisation du géoradar ainsi qu'à l'interprétation des données qu'il permet de faire. De plus, ces textes correspondent pour la plupart aux exposés présentés à l'occasion de cet atelier.

Le présent document donne en outre un aperçu à jour du domaine. Il devrait non seulement servir d'introduction à la technique du géoradar, mais également constituer un excellent document de référence.

L'Atelier a reçu le soutien financier du Comité interministériel de la recherche et du développement du ministère de l'Énergie, des Mines et des Ressources.

Enfin, permettez-moi de remercier tous ceux qui ont participé à l'analyse critique des manuscrits, et qui sont trop nombreux pour être nommés individuellement.

J.A. Pilon
Rédacteur

Il m'a fait plaisir, au nom de la Commission géologique du Canada, de souhaiter la bienvenue aux participants de l'Atelier sur le géoradar qui a eu lieu à Ottawa du 24 au 26 mai 1988. Les participants ont été nombreux, provenant de quelque 13 pays différents. Cela montre le grand intérêt que suscite à l'échelle internationale cette technique géophysique relativement nouvelle. Cette publication spéciale de la Commission géologique du Canada permettra de conserver les nombreux exposés présentés durant les trois jours qu'a duré cet atelier très animé. Il est à espérer que cette publication stimulera l'intérêt et incitera à réaliser des travaux de recherche et de développement dans ce domaine géophysique des plus prometteurs.

M.J. Berry
Directeur, Division de la géophysique

Le géoradar est un instrument électromagnétique utile à la cartographie des couches de sol et de roche et à la détection des objets souterrains en fonction des changements observés au niveau des propriétés électriques des matériaux. Les fréquences utilisées se situant dans l'intervalle de 10 à 1000 MHz, la résolution obtenue est supérieure à celle des autres méthodes géophysiques. Cette technique existe depuis plus de 15 ans, mais à l'époque les connaissances sur la propagation, la pénétration et l'interaction de l'énergie électromagnétique dans le sol étaient limitées. Par conséquent, il a fallu procéder par tâtonnement et acquérir l'expérience par le biais de l'étude de nombreuses applications dans des conditions différentes.

Failure to understand the principles and limitations of a technique has been known to slow the acceptance and future development of a promising method. In order to assure that this did not happen, a workshop was held to bring together the accumulated experience of practitioners in the field. The Geological Survey of Canada had been investigating the method since 1974; therefore, it was thought appropriate that the GSC should host the workshop.

The GPR Workshop was held in Ottawa on 24-26 May 1988 with 143 registrants representing 13 countries. The workshop opened with a general overview followed by six sessions under the general headings of methodology, geology, engineering, environment, glaciology and interpretation. At the workshop 43 papers were given, 26 of which are incorporated in these proceedings. The general conclusions to the workshop were that the equipment was becoming more user-friendly and that interpretation software was being made more readily available. It was evident, however, that more research was required, especially on techniques for measuring the electrical properties of earth materials. With better information on electrical properties at GPR frequencies, advancements could be made more effectively in instrumentation and interpretative techniques. The workshop provided an excellent forum for the exchange of ideas and knowledge on the state-of-the-art for GPR, on a large number of current applications, and on many possible new applications.

L.S. Collett
Chairman
Ground Penetrating Radar Workshop

Le fait de ne pas connaître les principes et les limites d'une technique a bien entendu pour effet de ralentir l'adoption et le développement d'une méthode prometteuse. Afin d'éviter que cela ne se produise dans le cas du géoradar, un atelier a été organisé pour rassembler l'expérience accumulée par les praticiens du domaine. La Commission géologique du Canada ayant recours à cette méthode depuis 1974, il semblait tout indiqué qu'elle agisse en tant qu'hôte de l'atelier.

L'Atelier sur le géoradar a eu lieu à Ottawa du 24 au 26 mai 1988 et a attiré 143 participants de 13 pays différents. L'atelier a débuté par un survol du domaine suivi de six séances sur les sujets généraux suivants : méthodologie, géologie, ingénierie, environnement, glaciologie et interprétation des données. Des 43 exposés présentés à l'atelier, 26 sont inclus dans les présents comtes rendus. Selon les conclusions générales de l'atelier, l'équipement est de plus en plus facile à utiliser et le logiciel d'interprétation est en train de devenir plus aisément accessible. Cependant, il en est ressorti qu'il fallait poursuivre les recherches, en particulier sur les techniques de mesure des propriétés électriques des matériaux du sol. En obtenant de meilleures informations sur les propriétés électriques aux fréquences du géoradar, l'instrumentation et les techniques d'interprétation pourraient être perfectionnées plus efficacement. L'atelier a constitué une tribune qui s'est prêtée de façon admirable à l'échange d'idées et de connaissances sur le géoradar et sur un grand nombre de ses applications actuelles et possibles.

L.S. Collett
Président
Atelier sur le géoradar

ACKNOWLEDGMENTS

As technical program chairman I thank the following colleagues at the Geological Survey of Canada: L.S. Collett for chairing the workshop and for his support in organizing it and obtaining the necessary funds, A.S. Judge for discussions on the technical program, S.R. Dallimore and S.E. Pullan for their assistance in organizing the sessions and the support arrangements. Many thanks go as well to the secretarial support personnel, and to J. Kasper for her assistance in the editing process. In addition, special thanks to J.R. Rossiter of Canpolar Inc. for suggesting the idea of a Ground Penetrating Radar Workshop. I also thank the Interdepartmental Panel on Energy Research and Development for its funding support.

As the editor of this volume I wish to thank the reviewers of the scientific and technical reports: M. Allard of the Centre d'études nordiques, Québec City, Québec; S.K Anderson and R.W. Jacobel of St-Olaf College,

REMERCIEMENTS

En tant que président du programme technique je tiens à remercier mes collègues de la Commission géologique du Canada: L.S. Collett, président du colloque, pour son aide dans l'organisation des séances et pour avoir obtenu les fonds nécessaires, A.S. Judge pour ses commentaires concernant le programme technique, S.R. Dallimore et S.E. Pullan pour leur aide dans l'organisation générale et celle des séances. J'aimerais aussi remercier le personnel du secrétariat, et J. Kasper pour son aide dans la préparation éditoriale de ce volume. De plus, je tiens à remercier en particulier J.R. Rossiter de Canpolar Inc. qui a eu l'idée de tenir l'atelier sur les géoradars. Je remercie également le Comité interministériel de la recherche et du développement énergétique pour son soutien financier.

A titre de rédacteur des actes du colloque, je voudrais remercier les reviseurs des rapports scientifiques et techniques: M. Allard du Centre d'études nordiques, Québec (Québec); S.K Anderson et R.W. Jacobel du College St-Olaf, Northfield

Northfield, Minnesota; A.P. Annan of Sensors and Software Inc., Mississauga, Ontario; S. Arkone, S. Daly, A.J. Delaney, A. Kovaks and R.H. Wills of USA CRREL, Hanover, New Hampshire; G. Black of A-Cubed Inc., Mississauga, Ontario; J.L. Davis and J.R. Rossiter of Canpolar Inc., Toronto, Ontario; A.W. England of the University of Michigan, Ann Harbour, Michigan; T. Fenner and S.S. Smith III of G.S.S.I. Inc., Hudson, New Hampshire; J.M. Glover and H.V. Rees of Subsurface Geotechnical Services, London, England; F.L. Graf of the Philadelphia Electric Co., Philadelphia, Pennsylvania; A.L. Holloway of Atomic Energy of Canada Ltd., Pinewa, Manitoba; D.R. Inkster of Intera Technologies, Calgary, Alberta; K.C. Jezek and L.G. Thompson of the Byrd Polar Research Center, Columbus, Ohio; P.T. LaFlèche of NSERC, Ottawa, Ontario; S. Lee of the University of Toronto, Toronto, Ontario; D. Nobes of the University of Waterloo, Waterloo, Ontario; O. Olsson, Swedish Geological Co., Uppsala, Sweden; G.K.A. Oswald of Cambridge Consultants Ltd., Cambridge, England; J.E. Robinson of Syracuse University, Syracuse, New York; D. Roddy of Lakehead University, Thunder Bay, Ontario; B. Strongman of the Royal Candian Mounted Police, Edmonton, Alberta; R. Thierbach of the Federal Institute for Geoscience and Natural Resources, Hannover, Germany; J.P. Todoeschuck of the Defense Research Establishment Pacific, Victoria, British Columbia, and my colleagues at the Geological Survey of Canada, L.S. Collett, S.R. Dallimore, A.S. Judge, P. Keating, R.A. Klassen, G.J. Palacky, S.E. Pullan and P.B. Robertson, many of whom reviewed more than one paper for this edition.

J.A. Pilon

(Minnesota); A.P. Annan de Sensors and Software Inc., Mississauga (Ontario); S. Arkone, S. Daly, A.J. Delaney, A. Kovaks et R.H. Wills de USA CRREL, Hanover (New Hampshire); G. Black de A-Cubed Inc., Mississauga (Ontario); J.L. Davis et J.R. Rossiter de Canpolar Inc., Toronto (Ontario); A.W. England de l'Université de Michigan, Ann Harbour (Michigan); T. Fenner et S.S. Smith III de G.S.S.I. Inc., Hudson (New Hampshire); J.M. Glover et H.V. Rees de Subsurface Geotechnical Services, London (Angleterre); F.L. Graf du Philadelphia Electric Co., Philadelphia (Pennsylvania); A.L. Holloway d'Énergie atomique du Canada Ltée., Pinewa (Manitoba); D.R. Inkster de Intera Technologies Ltée, Calgary (Alberta); K.C. Jezek et L.G. Thompson du Byrd Polar Research Center, Columbus (Ohio); P.T. LaFlèche du CRSNG, Ottawa (Ontario); S. Lee de l'Université de Toronto, Toronto (Ontario); D. Nobes de l'Université de Waterloo, Waterloo (Ontario); O. Olsson du Swedish Geological Co., Uppsala (Suède); G.K.A. Oswald de Cambridge Consultants Ltée., Cambridge (Angleterre); J.E. Robinson de l'Université de Syracuse, Syracuse (New York); D. Roddy de l'Université de Lakehead, Thunder Bay (Ontario); B. Strongman de la Gendarmerie royale du Canada, Edmonton (Alberta); R. Thierbach du Federal Institute for Geoscience and Natural Resources, Hannover (Allemagne); J.P. Todoeschuck du Centre de Recherche pour la Défense Pacifique, Victoria (Colombie Britannique), et mes collègues de la Commission géologique du Canada, L.S. Collett, S.R. Dallimore, A.S. Judge, P. Keating, R.A. Klassen, G.J. Palacky, S.E. Pullan et P.B. Robertson, nombre d'entre eux ont examiné plus d'un manuscrit pour ce volume.

J.A. Pilon

Ground penetrating radar performance predictions

A.P. Annan[1] and L.T. Chua[1]

Annan, A.P. and Chua, L.T., 1992: Ground penetrating radar performance predictions; in Ground penetrating radar, ed. J. Pilon; Geological Survey of Canada, Paper 90-4, p. 5-13.

Abstract

The widespread use of ground penetrating radar (GPR) with a mixture of success and failure has led to a greater understanding of where GPR is likely to work and where it won't. The ability to quantitatively predict and emulate the response of simple targets has been needed for some time and is now easily achieved with simple PC programs. This paper describes some procedures for interactive radar modelling which can be used to define parameters for optimal system configuration prior to field survey work. The procedures for estimating radar range, for generating synthetic radargrams, and for calculating simple ray tracing travel time are outlined; examples of results are presented. The techniques have been developed from the necessity of understanding and explaining field observations and are now used prior to a survey to optimize survey parameters.

Résumé

L'utilisation répandue du géoradar qu'elle soit ou non couronnée de succès a permis de mieux déterminer où le géoradar peut donner de bons résultats. On ressentait depuis longtemps déjà le besoin de pouvoir prévoir quantitativement et d'émuler la réponse de cibles simples, activités qui sont maintenant réalisables à l'aide de simples programmes PC. Le présent article décrit quelques procédés de modélisation interactive des ondes radar qui peuvent servir à définir les paramètres de configuration optimale d'un système avant son utilisation sur le terrain. Les procédés d'estimation de la portée du radar, de production de radargrammes synthétiques et de calcul du parcours de l'onde en fonction de la durée du trajet sont présentés dans les grandes lignes; des exemples de résultats sont également donnés. Les techniques mises au point découlent de la nécessité de comprendre et d'expliquer les observations sur le terrain. Elles sont maintenant utilisées avant d'entreprendre un levé afin d'en optimiser les paramètres.

INTRODUCTION

Predicting performance of ground penetrating radar (GPR) is an important factor in deciding whether GPR surveys can be used effectively for particular applications. The best method of evaluating radar is to try it in the target environment; the second is to attempt to crudely emulate the response if enough basic information is available. Because some problems cannot be addressed by the use of GPR, the objective of this paper is to illustrate some simple modelling methods that can help predict the likelihood of success in a particular situation.

Over the years our ability to predict (usually rules-of-thumb) has developed from practical experience with real situations and real instrumentation. In this paper, we disucss three types of modelling that help quantify such predictions. The first model uses the radar range equation to predict whether a specific type of generic target can be detected at a specified range. The second model is the analog of the seismic method of generating synthetic seismograms from a borehole sonic log. In the radar case, synthetic "radargrams" are generated from an estimate of the attenuation and velocity (conductivity and dielectric constant) versus depth. The third model illustrates the use of simple ray tracing to estimate radar signal travel times.

Each section of this paper addresses one of the individual topics. No attempt is made to go into detailed theoretical analysis; we provide only a brief overview of how the analysis is approached.

---

[1] Sensors & Software Inc., 5566 Tomken Road, Mississauga, Ontario L4W 1P4

RADAR RANGE PREDICTION

In most cases, GPR is used to map surface features, which reflect or scatter energy back to the measurement system (Davis and Annan, 1989). The basic concept is illustrated in Figure 1. Annan and Davis (1977) have outlined the means of predicting range of detectability for a generic set of targets that might be encountered in a geologic environment. The procedure uses the conventional radar range equation combined with the appropriate parameters for the earth model to determine the return signal level from a generic target. Knowing the performance factor for a given radar system, a specific target can be detected if the return power exceeds the detection threshold of the radar receiver.

The means of predicting return power given a transmitter of a known power is illustrated in Figure 2. Power is generated in the transmitter electronics and is passed to the transmitting antenna with some energy loss. This energy loss is referred to as transmitter efficiency. The transmitting antenna then radiates the signal into the ground with the directionality of the antenna gain pattern. The energy propagates through the ground and is attenuated by electrical losses and by spherical spreading of the wave front. At the range of the target some of the energy is scattered by the target. The power radiated back towards the receiving system is dictated by the target cross-sectional area and backscatter gain. The return signal again suffers attenuation from spherical spreading and electrical absorption in the host medium. Finally, the signal acquired by the receiver depends on the receiver antenna pattern directionality and effective area. The receiving electronics detect the signal acquired by the receiving antenna reduced by the efficiency factor of the receiving antenna.

This model can be used, for example, to predict performance and to prepare nomograms indicating maximum range of a given target for a given environment. Figure 3 illustrates a typical radar range plot of a point-like target for varying system performance factors versus electrical attenuation or conductivity. A quick alternate approach, which we frequently use for analysing a problem, is a spread-sheet approach. Figure 4 shows the output of a spread-sheet program that tabulates all information in the radar range equation. The spreadsheet approach is extremely useful for doing "what if" analysis. In the program whose output is shown in Figure 4, the items listed under the heading "Model parameters" can be changed by the user at any time and the rest of the spread sheet values are automatically recomputed.

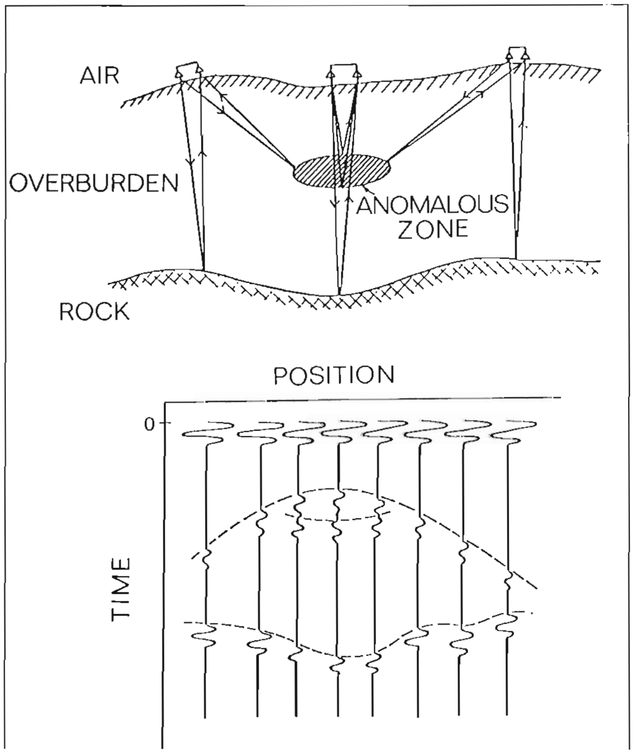

Figure 1. GPR concepts and schematic illustration of ground response.

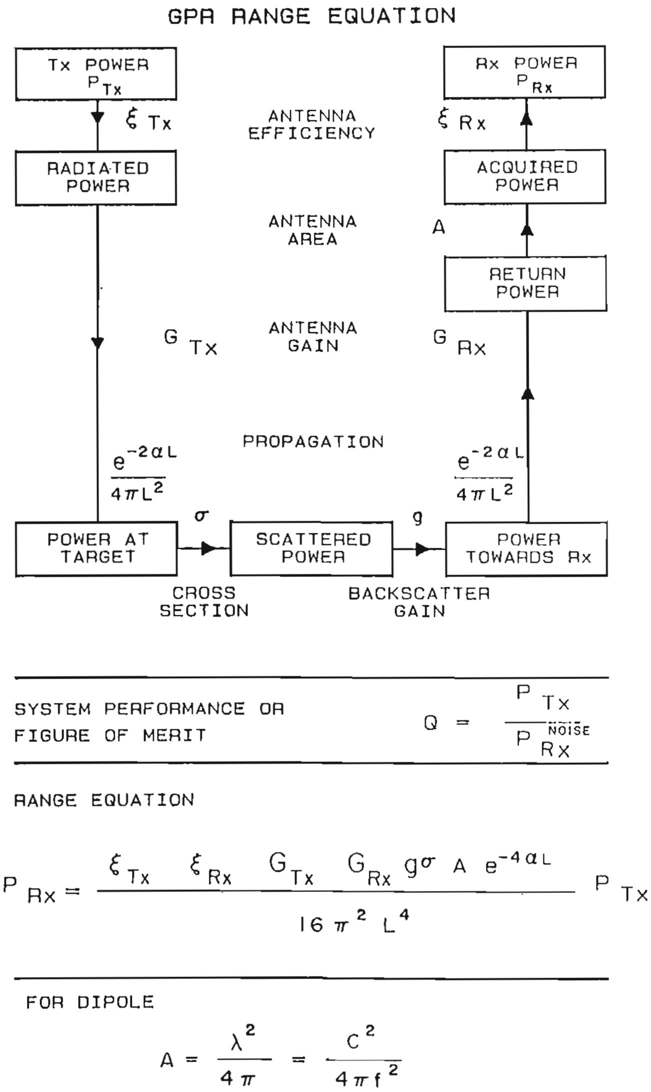

SYSTEM PERFORMANCE OR FIGURE OF MERIT

$$Q = \frac{P_{Tx}}{P_{Rx}^{NOISE}}$$

RANGE EQUATION

$$P_{Rx} = \frac{\xi_{Tx}\ \xi_{Rx}\ G_{Tx}\ G_{Rx}\ g\sigma\ A\ e^{-4\alpha L}}{16\pi^2 L^4}\ P_{Tx}$$

FOR DIPOLE

$$A = \frac{\lambda^2}{4\pi} = \frac{c^2}{4\pi f^2}$$

Figure 2. Flow diagram for predicting radar range.

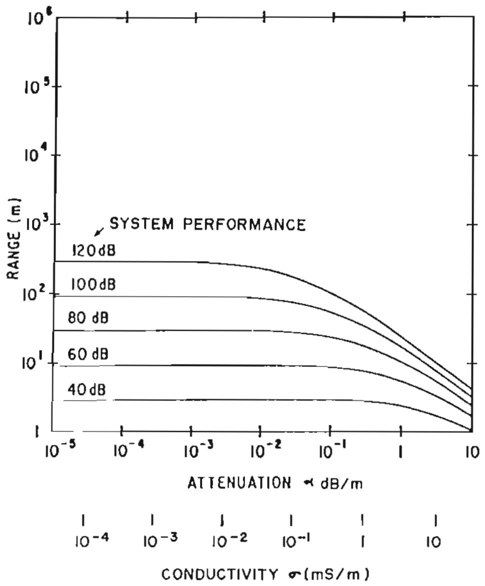

NOTE: CONDUCTIVITY ATTENUATION RELATIONSHIP BASED ON LOW LOSS ASSUMPTION.

$\alpha = 1.64\ \sigma/\sqrt{K}$ WHERE K = 16 IN THIS INSTANCE.

Figure 3. Radar range versus attenuation for performance factors for various systems and point targets.

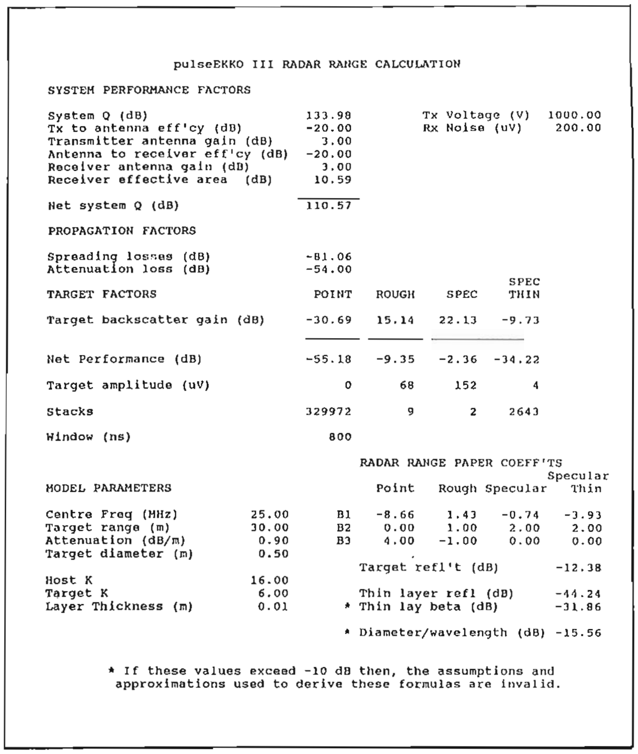

```
                    pulseEKKO III RADAR RANGE CALCULATION

SYSTEM PERFORMANCE FACTORS

System Q (dB)                     133.98          Tx Voltage (V)  1000.00
Tx to antenna eff'cy (dB)         -20.00          Rx Noise (uV)    200.00
Transmitter antenna gain (dB)       3.00
Antenna to receiver eff'cy (dB)   -20.00
Receiver antenna gain (dB)          3.00
Receiver effective area  (dB)      10.59
                                  ------
Net system Q (dB)                 110.57

PROPAGATION FACTORS

Spreading losses (dB)             -81.06
Attenuation loss (dB)             -54.00
                                                             SPEC
TARGET FACTORS                     POINT    ROUGH    SPEC    THIN

Target backscatter gain (dB)      -30.69    15.14   22.13   -9.73
                                  ------   ------   --------------
Net Performance (dB)              -55.18    -9.35   -2.36  -34.22

Target amplitude (uV)                  0       68     152       4

Stacks                            329972        9       2    2643

Window (ns)                          800

                                      RADAR RANGE PAPER COEFF'TS
                                                              Specular
MODEL PARAMETERS                        Point   Rough Specular   Thin

Centre Freq (MHz)          25.00      B1   -8.66    1.43   -0.74   -3.93
Target range (m)           30.00      B2    0.00    1.00    2.00    2.00
Attenuation (dB/m)          0.90      B3    4.00   -1.00    0.00    0.00
Target diameter (m)         0.50
                                        Target refl't (dB)         -12.38
Host K                     16.00
Target K                    6.00        Thin layer refl (dB)       -44.24
Layer Thickness (m)         0.01      * Thin lay beta (dB)         -31.86

                                      * Diameter/wavelength (dB) -15.56

         * If these values exceed -10 dB then, the assumptions and
          approximations used to derive these formulas are invalid.
```

Figure 4. Example output of radar range analysis set up on a spreadsheet.

The radar range equation generally oversimplifies real geological environments. The output is a good indicator of the likelihood of success if one understands the electrical properties of the environment and knows something about the characteristics of the target. As a general rule of thumb, if the return power for the ideal target is only equal to the system noise level then radar is unlikely to be effective for the problem. If the radar range equation gives a 10-20 dB margin for the target signal level compared to the system noise level then one has a fighting chance of success.

SYNTHETIC RADARGRAMS

In many instances GPR is used to map relatively flat lying strata in the geological section. The nature of the return record can be extremely complex if a number of strata are present. Also, if there are strong reflectors in the section, multiple events get mixed with primary returns. A synthetic radargram program is a powerful tool for assessing the type of response that we can expect in a given situation. The results are also beneficial in designing signal processing and time gain functions for presenting radar data.

The concept of a synthetic radargram is derived from the synthetic seismogram approach common in the petroleum industry (Treitel and Robinson, 1966; Wuenschel, 1960). Figure 5 shows a simple situation in layered earth. The particular model shown arose from an investigation of karstic features in limestone formations where the objective was to

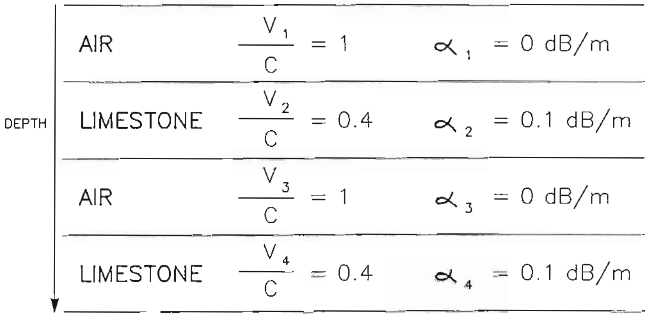

Figure 5. Layered earth model of an air filled bedding plane parting in a limestone sequence.

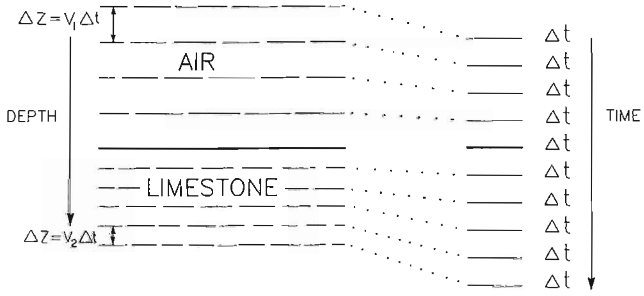

Figure 6. Translating space variation into equal time steps in a layered earth model.

discern whether observed radar signals were generated by large voids or by partings along bedding planes in the limestone.

To generate a synthetic radargram we employ the concept of the equal travel time, layered earth model commonly used in computing synthetic seismograms. The earth is subdivided into thin layers of equal travel-time thickness. Figure 6 illustrates layered earth sliced into equal travel time segments.

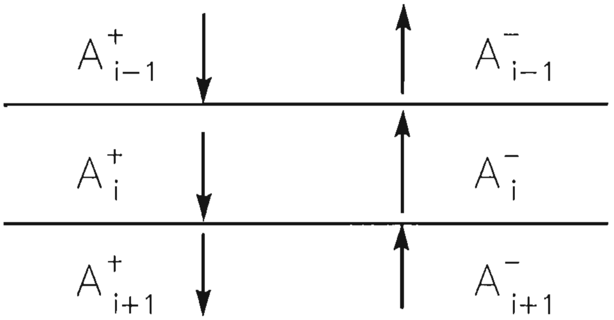

$$A^+_{i-1} = T_{i-1,i} \quad A^+_{i-1} + R_{i,i-1} A^-_i$$

$$A^-_i = T_{i+1,i} \quad A^-_{i+1} + R_{i,i+1} A^+_i$$

$$A^+_i = A^+_i \quad e^{-\alpha_i V_i \Delta t}$$

$$A^-_i = A^-_i \quad e^{-\alpha_i V_i \Delta t}$$

Figure 7. Reflection and transmission in the layered stack.

A plane wave is assumed to be incident at the top of the layered stack. In each equal travel time layer there is an upward and downward propagating wave. The amplitudes of these waves are determined by reflection and transmission of the incident signal at each interface as the incident wave propagates through the stack. The model results shown here were computed by simply time stepping through the response although more sophisticated algorithms might be applied. With the equal time step model, the time varying field propagates through one layer with each time step. Figure 7 illustrates how the amplitudes of the upward and downward propagating waves in each layer are coupled through the reflection and transmission coefficients at the layer interfaces.

Although a plane layered model with a plane wave incident is used in the calculations, an approximation of spherical spreading is achieved by reducing amplitude inversely with the cumulative travel time. When inverse time amplitude fall off is applied, the model response emulates attenuation as well as spreading loss effects. This model is not a perfect representation of the real world but indicates relative amplitudes and temporal shapes of reflection events that can be observed in real data from a stratified geological section.

Three examples of synthetic radargrams are presented. Figures 8 and 9 illustrate the response of a simple model as well as the application of a time varying gain to amplify the weaker events. The layered model represents the plausible field condition of air over ice over water over a soft gradational bottom sediment (typical of a northern Canadian lake in midwinter).

Figure 8 illustrates all aspects to the synthesis. On the right is the layered earth model with the velocity and attenuation shown versus depth. Next in from the right is the same layered earth in equal travel time layer format, which shows velocity and attenuation versus travel time. On the extreme left is the radar pulse incident on the layered earth. Next in from the left is the synthetic radargram, which consists of 10 replicas of the amplified ground response. The repeated plotting

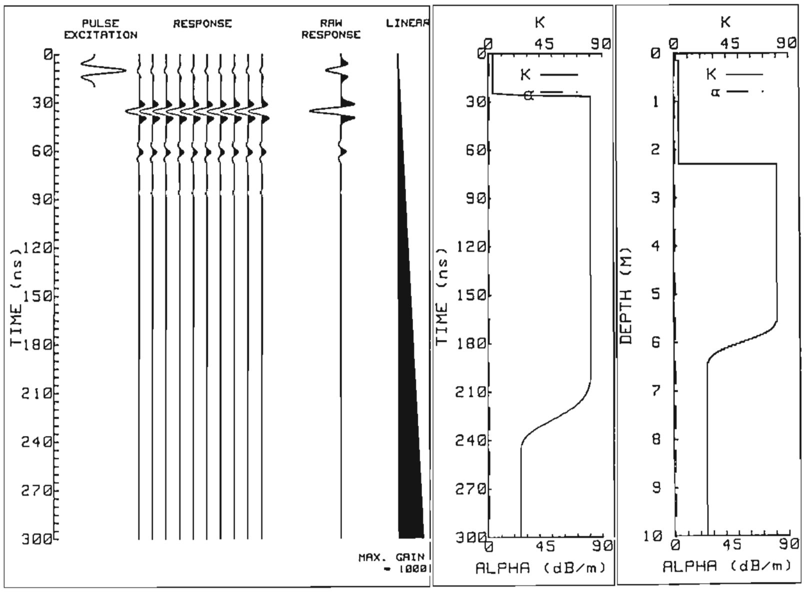

Figure 8. Example synthetic radargram for case of 2 m of ice over water over a gradational bottom.

presents the response in a manner similar to that in which field data are presented. In the middle of the page are the unamplified radar (raw) response record and the gain function applied to create the 10 traces emulating the section.

The synthetic radargram (Fig. 8) has a linearly increasing time gain function applied. In Figure 9 an automatic gain control (AGC) time gain function has been applied to the same data as shown in Figure 8. Two main features to note are the strength of the reflection between water and ice with the associated multiple reflection in the ice layer and the dispersion of the gradational water bottom reflection. Unfortunately these topics require more in depth discussion than we can provide in this brief overview. The important point to note is the potential usefulness of this type of modelling for quantitative interpretation.

Figure 10 shows the synthetic response computed to simulate the real responses obtained while traversing through an adit (tunnel) passing over two adits at lower levels in a potash mine (Annan et al., 1988). The synthetic response was computed to evaluate whether the reflections from both top and bottom of the tunnel could be detected. The raw synthetic data trace indicates that both interfaces should be detectable as distinct events. The application of AGC gain on the synthetic radargram amplifies the multiple reflections reverberating within the tunnel. The real radar data section has a quadratic time gain function applied and, if the tunnel events are examined carefully, we can distinguish reflections from both top and bottom of the tunnels. The radar section (Fig. 11) has a 20:1 vertical exaggeration; as a result the tunnels resemble point reflectors rather than a flat layered structure. In the middle of the centre tunnel, the plane layered model is a reasonable approximation.

Figure 12 shows a synthetic radargram used to model gradational boundaries representing a silty horizon and the capillary fringe above the water table. Gradational boundaries are frequent in real geological settings and the

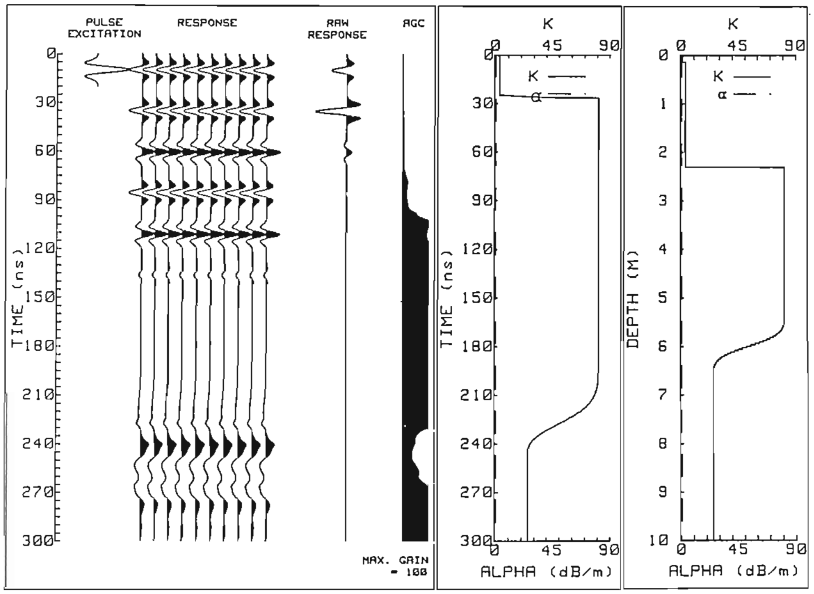

Figure 9. Automatic gain control (AGC) applied to same example as shown in Figure 8.

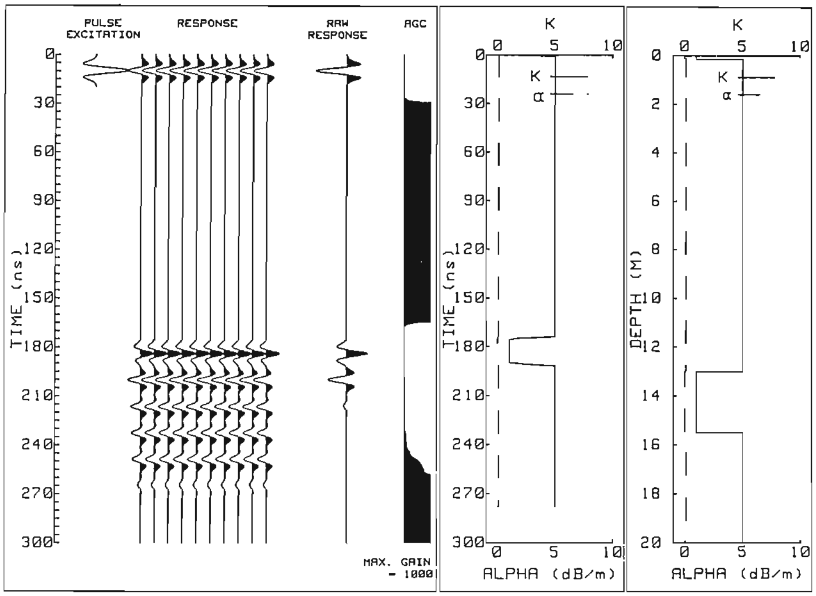

Figure 10. Example of synthetic radargram for the response of a wide air filled entry in a potash mine environment.

model in Figure 12 was based on data such as shown in Figure 13. One of the most gradational boundaries encountered is the water table. In general, capillary action smears out the water distribution in the ground so that the transition from unsaturated to saturated is quite broad typically being a metre or more in thickness. In fine grained soils, the transition zone can occur several metres thick; in very coarse grained soils (gravels and cobbles with no fines), the capillary fringe will be virtually nonexistent. The effect of a gradational boundary is to preferentially reflect the low frequency signals and to transmit the high frequency signals in a pulse.

In summary synthetic radargrams provide a very powerful tool for predicting what type of radar trace one is likely to observe in a given situation. The main problem at the current time is the lack of a suitable means to acquire reliable electrical property information from boreholes that will provide the input for the generation of the synthetic radargrams.

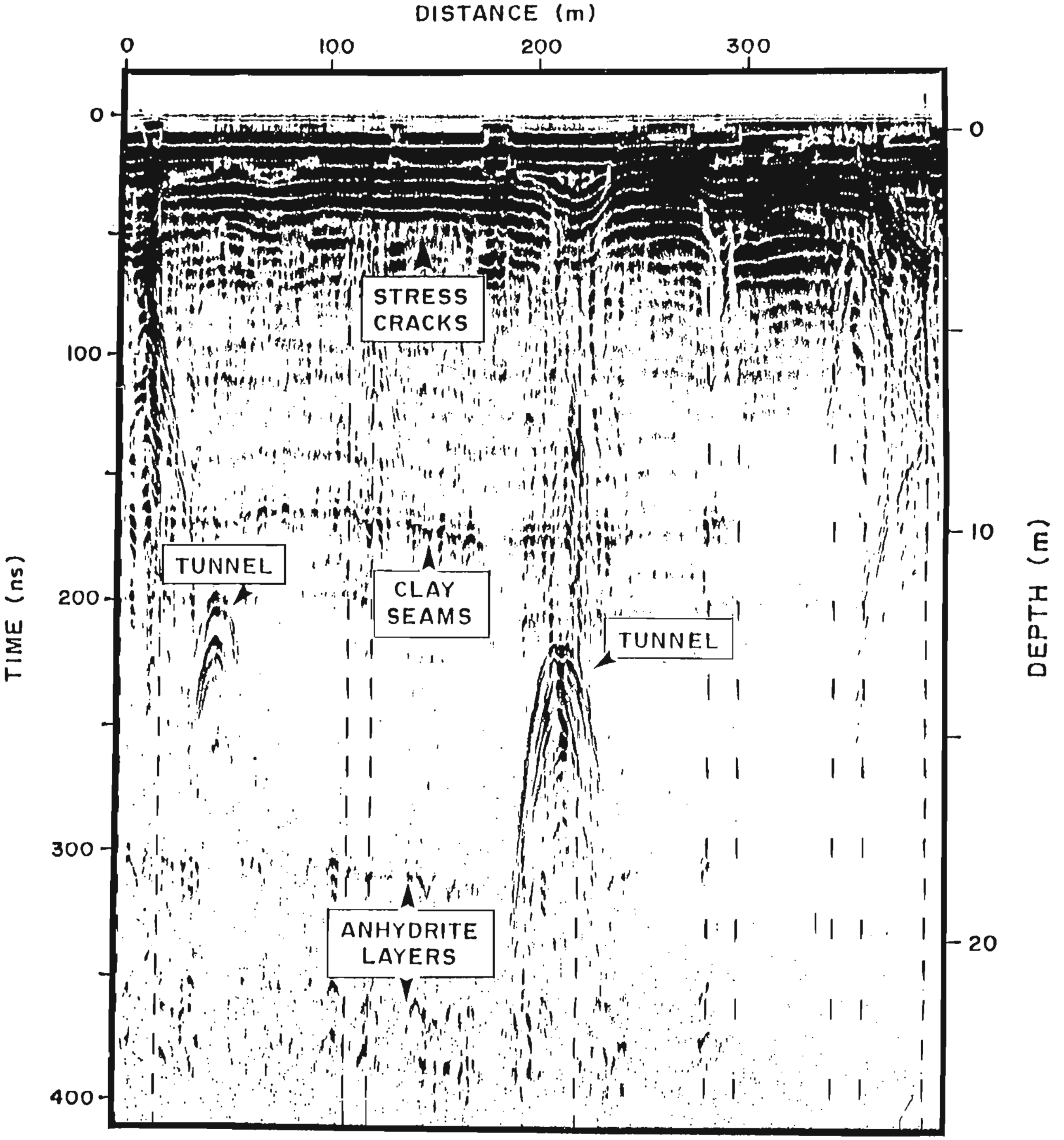

Figure 11. Example of a radar section over a tunnel under another entry in a potash mine.

SIMPLE TWO DIMENSIONAL RAY TRACING

Full modelling of wave propagation in complex geometrical structures is extremely time consuming on a computer. In addition formatting the problem is neither simple nor easily made general purpose. There are two modes of approaching such problems. One is to do a full finite difference or finite element wave propagation solution in two or three dimensions. The other is to use a ray tracing approach. In this paper we present a very simplified example of the use of the ray tracing method to determine radar arrival times. The model provides no information on amplitude, only on first arrivals. Figure 14 is a sketch of the simple geometry of a bistatic radar system traversing over a circular buried feature. This feature could be interpreted as a pipe if a two dimensional structure or as a buried barrel if a three dimensional structure. By simply permitting a distribution of waves to propagate out from the transmitting antenna and then following those that intersect the receiving antenna, we can derive first arrival times. This particular model was used to evaluate whether or not the diameter of a gas pipeline could be extracted from the radar profile data.

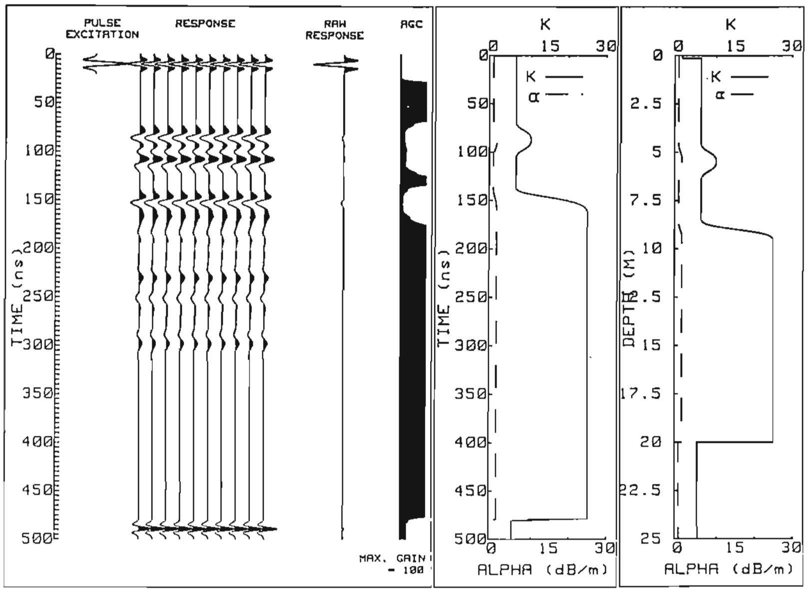

Figure 12. Example of a radargram derived for dry sand with a gradational water table overlying a sharp bedrock interface.

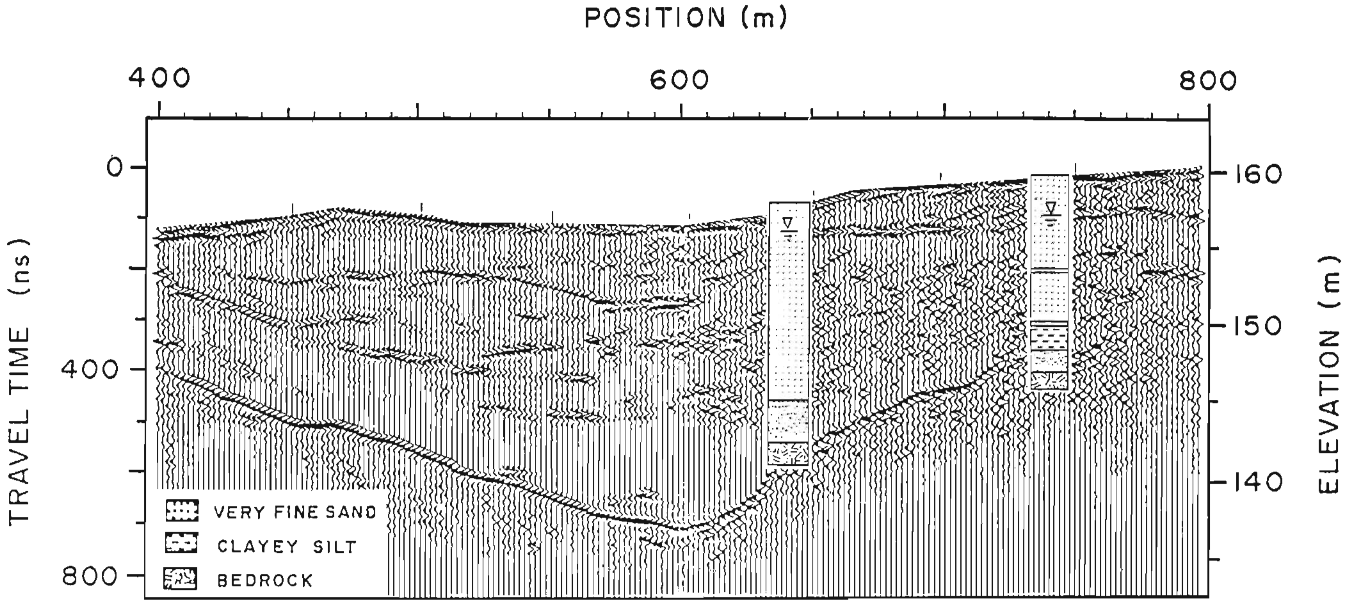

Figure 13. Example of a pulseEKKO III radar section in the environment simulated in Figure 12.

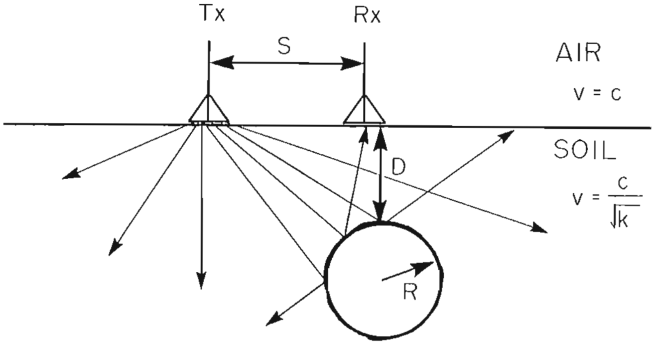

Figure 14. Schematic of a radar antenna system located over a circular or cylindrical object.

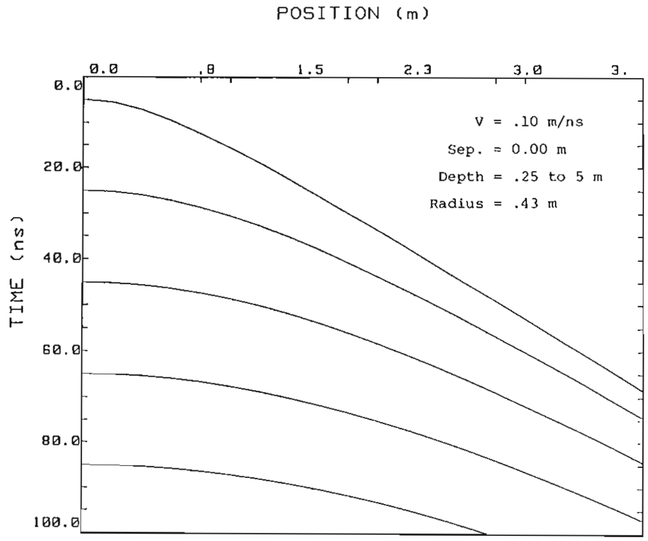

Figure 15. Illustration of the raypath travel times derived for a particular instance of the model shown in Figure 14.

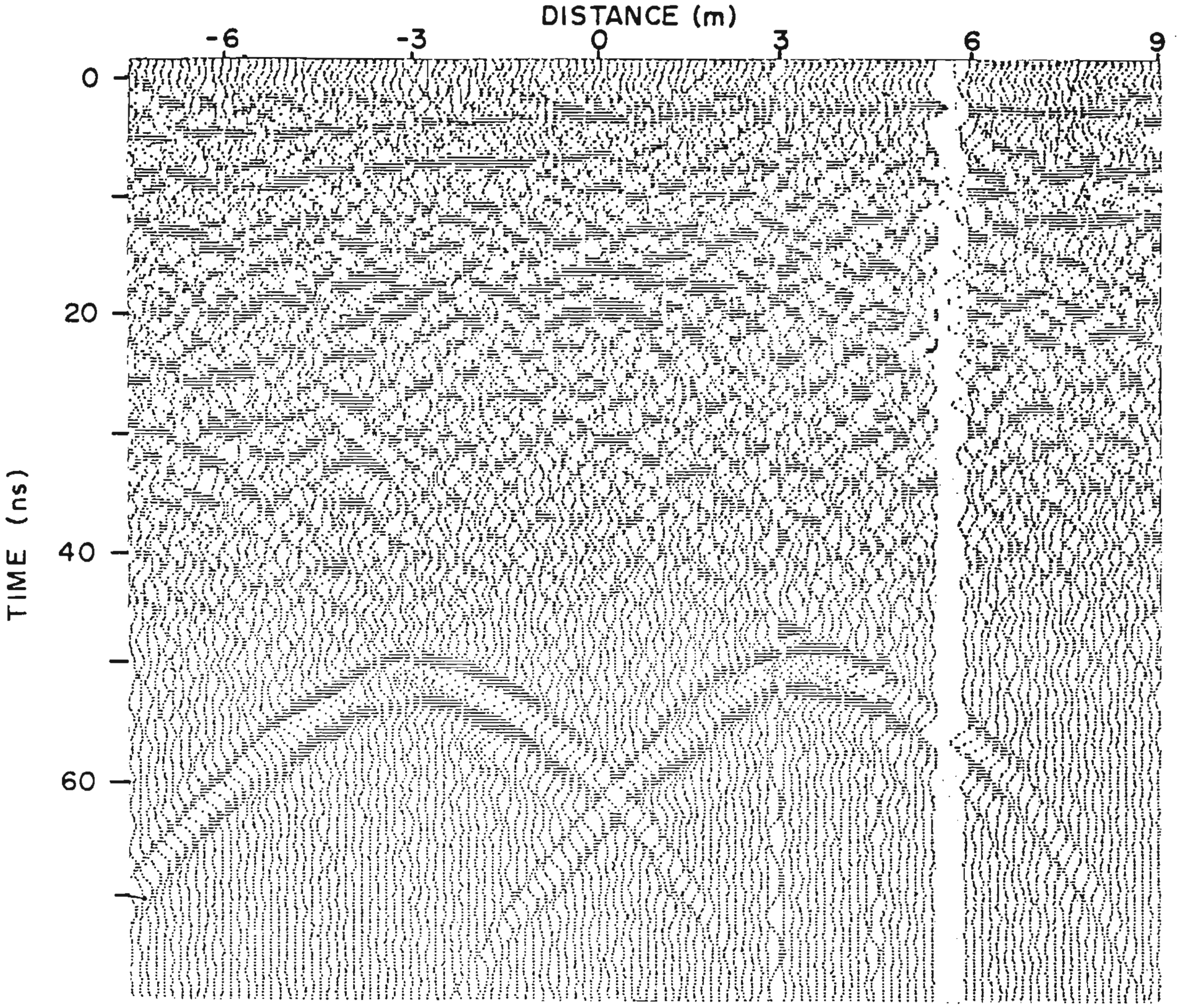

Figure 16. Example of a radar traverse over two identical culverts buried at a depth of 4 m.

Figure 15 exemplifies the type of model output that can be obtained. In general by carrying out this type of exercise we can evaluate the effect of antenna separation, depth of barrel, and pipe radius on the observed response. For example, a sensitivity analysis of the travel times with pipe radius can be used to discern when pipe radius can be detected. A real data set over two adjacent culverts is shown in Figure 16. For these data, we were unable to discern culvert diameter from the radar data with confidence but we could accurately pinpoint depth.

As already indicated, this model, although simplistic, is useful on some occasions. More sophisticated (and complex) models will have to be evolved as the need for more quantitative interpretation of radar data increases.

CONCLUSIONS

This paper has presented some simple models that facilitate the average GPR user to predict what kind of performance to expect in a given situation. Obviously there are numerous other forward models that can be investigated and added to this set of models. Whereas the simulation methods presented here do not answer every problem, they certainly provide insight as to what we can expect in many instances.

In conclusion, it is important that the development of such models continues. The major emphasis in the future should go into two and three-dimensional finite difference, finite element and ray tracing modelling to allow more complex structures to be evaluated. In particular, complicated geometries in layered media would be of considerable interest in many applications.

REFERENCES

Annan, A.P. and Davis, J.L.
1977: Radar range analysis for geological material; in Report of Activities, Part B, Geological Survey of Canada, Paper 77-1B, p. 117-124.
Annan, A.P., Davis, J.L., and Gendzwill, D.
1988: Radar sounding in potash mines, Saskatchewan, Canada, Geophysics, v. 53, p. 1556-1564.
Davis, J.L. and Annan, A.P.
1989: Ground penetrating radar for high resolution mapping of soil and rock stratigraphy, Geophysical Prospecting, v. 37, p. 531-551.
Treitel, S. and Robinson, E.A.
1966: Seismic wave propagation in layered media in terms of communication theory, Geophysics, v. 31, p. 17-32.
Wuenschel, P.C.
1960: Seismogram synthesis including multiples and transmission coefficients, Geophysics, v. 25, p. 106-129.

Design and development of a digital ground penetrating radar system

A.P. Annan[1] and J.L. Davis[2]

Annan, A.P. and Davis, J.L., 1992: Design and development of a digital ground penetrating radar system; in Ground penetrating radar, ed. J. Pilon; Geological Survey of Canada, Paper 90-4, p. 15-23.

Abstract

Extensive evaluation of the potential applications for ground penetrating radar (GPR) during the 1970s by the Geological Survey of Canada led to the conclusions that the expansion of the GPR method was limited by

- *instrument portability,*
- *instrument sensitivity, and*
- *inability to apply seismic-like processing.*

In 1981, A-Cubed Inc. embarked on a program to develop technology to put in place a GPR system that would overcome these limitations. A joint project between the Geological Survey of Canada and A-Cubed Inc. began in 1983 and led to the introduction of the pulseEKKO III system in 1986. In this paper, we present the design philosophy and principles underlying discrete measurement techniques accompanied by examples of field results.

Résumé

L'évaluation importante des applications potentielles du géoradar à laquelle s'est livrée la Commission géologique du Canada au cours des années 1970 a permis d'établir que l'adoption accrue des méthodes liées à l'utilisation du géoradar était limitée par :

- *la portabilité de l'instrument*
- *la sensibilité de l'instrument, et*
- *l'incapacité d'appliquer un traitement de type sismique.*

En 1981, la société A-Cubed Inc. a entrepris un programme technologique pour mettre en place un système géoradar qui permettrait de surmonter ces limites. Un projet mis en eouvre conjointement par la Commission géologique du Canada et A-Cubed Inc. en 1983 a mené à l'introduction du système pulseEKKO III en 1986. Dans le présent document, la philosophie et les principes de conception sous-jacents à certaines techniques de mesure sont présentés, appuyés par des résultats recueillis sur le terrain.

---

[1] Sensors & Software Inc., 5566 Tomken Road, Mississauga, Ontario L4W 1P4

[2] Formerly A-Cubed Inc., now at Canpolar Inc., 265 Rimrock Rd., Toronto, Ont. M3J 3C6

INTRODUCTION

The pulseEKKO III system developed by A-Cubed Inc. represents the culmination of a decade of effort in developing a precision instrument for ground penetrating radar (GPR) applications. Initial work in ground penetrating radar, which was carried out by the Geological Survey of Canada from 1974 to 1980 (Annan and Davis, 1976), was conducted in a wide variety of environments. The primary application was geological sounding to look for relatively deep structure. Structure that was near surface (1-3 m) was felt to be of little significance in the early stages of the work simply because such structure could be easily excavated. The objective was to develop a system that could penetrate to tens of metres in a favourable environment with 1-2 m resolution.

The initial conceptual work for the pulseEKKO III system evolved from use of a GSSI-SIR system (Morey, 1974) in a wide variety of geological settings. The weight, bulk, and power requirements of that system precluded the use of radar being viable in some applications. Quantitative interpretation was not usually possible given the data format. Considerable effort was expended to define an optimal configuration for a geological sounding radar system. A primary goal was to design the system to collect data digitally and thus to exploit existing seismic processing and computer technologies.

A team and the resources to achieve this objective were assembled in 1983. The pulseEKKO III system was subsequently developed by A-Cubed Inc. with the first prototype being delivered to the Geological Survey of Canada in 1986. This paper provides insight into the development of the system and design trade-offs.

DESIGN SPECIFICATIONS

As general goals, the radar system being developed had to provide the following capabilities:

1. It had to be lightweight, battery powered, and very portable.

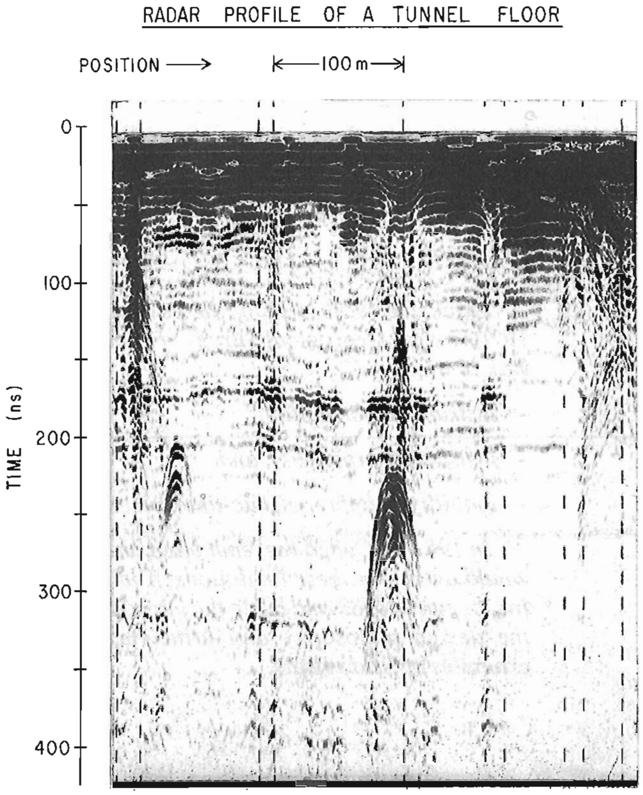

Figure 1. Example of continuous mode radar profiling section obtained in a potash mine.

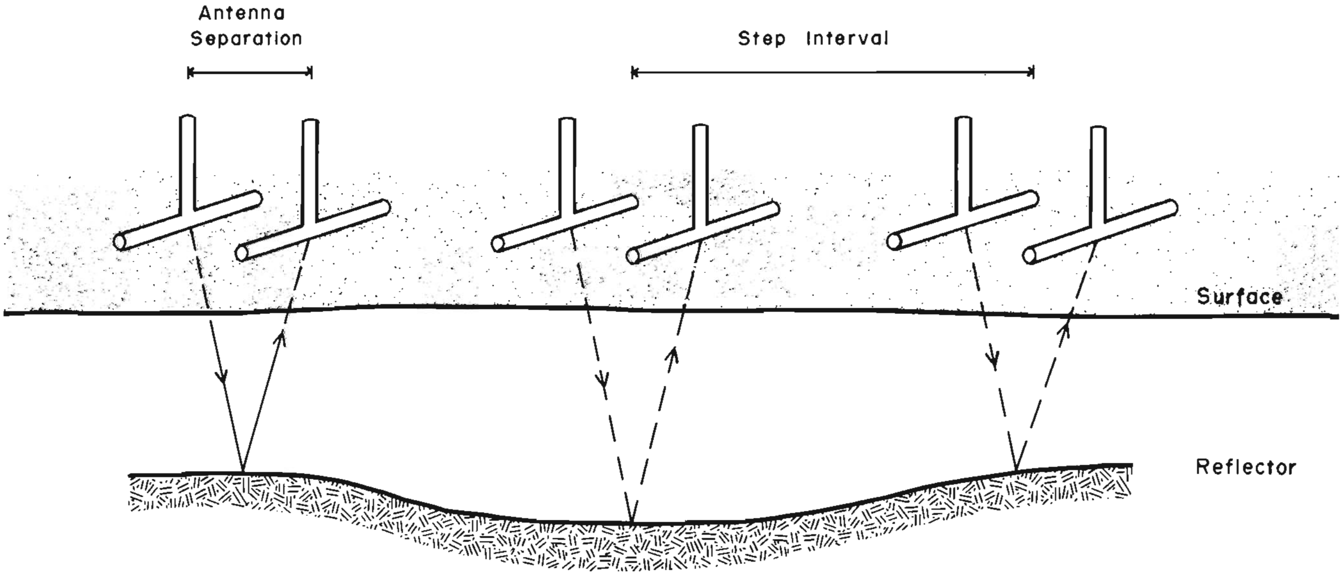

Figure 2. Step mode radar profiling.

2. It had to be user friendly to permit operation by unskilled personnel with a minimum of training.
3. It had to acquire digital data in a wide dynamic range to permit realistic use of seismic-style digital processing.
4. It had to achieve a performance factor or figure of merit of 130-180 dB depending on the operating frequency and bandwidth.
5. It had to be as free of intrinsic component artifacts as possible to allow sensible use of the available dynamic range.
6. It had to have the capability for calibrated amplitude measurement to provide the opportunity to determine quantitatively subsurface radar reflectivities.
7. It had to operate over as wide a frequency range as possible with 10-1000 MHz being the ultimate objective.

One fundamental factor that entered into the analysis was how should the radar be operated. The most successful type of GPR, in fact the only one really available at the time we began this work, was the GSSI-SIR. The SIR systems are continuous profilers, which have data acquisition tied into the data display time base and which require the system to be transported in a manner that is correlated with the display output. The primary display is a facsimile style, grey scale hardcopy. An excellent example record of this type acquired in a potash mine (Annan et al., 1988) is shown in Figure 1. Because the interface between the data acquisition and the display timebase lock had limited many of our geological sounding applications in arduous terrain, we had to eliminate this characteristic from the system for deep geological sounding in environments that are hard to access.

The ability to stack multiple records in the field is particularly important when there are external noise sources such as radio or TV transmissions in the local area. The reasons for stacking are many and are well known. To stack we need signals from the ground that are constant (time invariant), whereas external noise sources are incoherent (time varying). The simplest way to achieve this constancy is to measure with the antenna system in a static position rather than being constantly moved.

The concept of making measurements at a discrete point as opposed to continuously moving the antennas was not new as evidenced by many of the radio echo sounders developed for glacier sounding; it was felt to have many advantages. This mode of operation was a fundamental aspect of the design of the pulseEKKO III system. With this design concept in mind, a number of field tests were carried out using a modified SIR system (named the pulseEKKO I) to acquire data in various formats, which would allow us to assess this type of survey operation and to find how effective it would be.

The discrete step mode of operation is depicted in Figure 2. Figure 3 shows a sample of a pulseEKKO I record where, instead of moving continuously, the antennas were moved in discrete steps. This record looks very similar to the standard continuous profile record (such as shown in Fig. 1) except that the events appear to move in staircase-like steps rather than continuously. One thing that we noticed immediately was that the reflectors were much stronger and much more coherent than those observed with continuous profiling where the antenna coupling with the ground varied continuously.

We conducted a further experiment in very rough terrain where we made measurements at discrete intervals. The data were digitized and processed after the field survey (Davis et al., 1985b). An example data set is shown in Figure 4. The

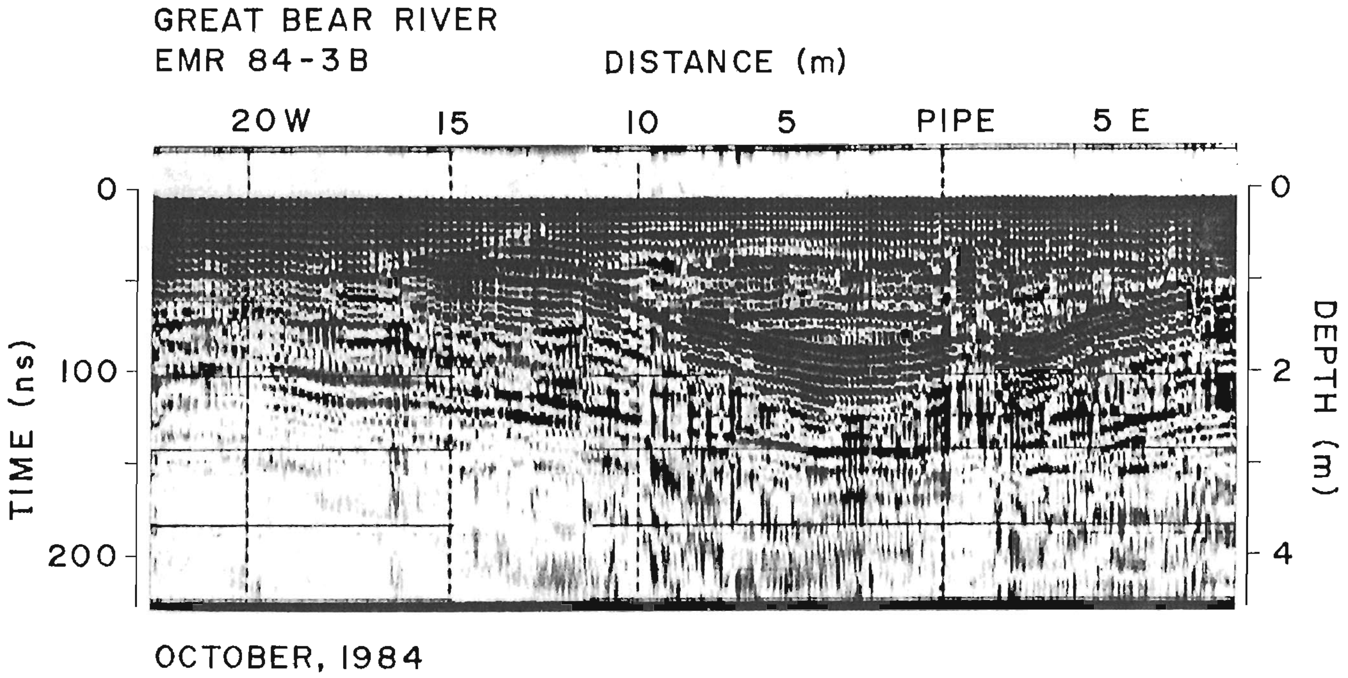

Figure 3. Example of pulseEKKO I discrete step profiling results.

data look rather jumbled; however, by applying topographic correction, the much more coherent section was obtained (Fig. 5). The geological section as inferred from geological mapping, radar, and seismic data are displayed in Figure 6. This example demonstrates one benefit of acquiring discrete step, digital data. Applying topographic corrections can transform a rather distorted image of the ground into one that is much more understandable.

With these design concepts in mind, we hardened the specifications for the pulseEKKO III system and began the development work.

SYSTEM IMPLEMENTATION

System implementation was carried out in two phases. In the first phase, the first totally digital radar (named the pulseEKKO II system (Davis et al., 1985a)) was designed and constructed. With the pulseEKKO I and II systems it was possible to acquire high frequency and low frequency data in digital form and to systematically evaluate the details necessary to implement pulseEKKO III in a second phase.

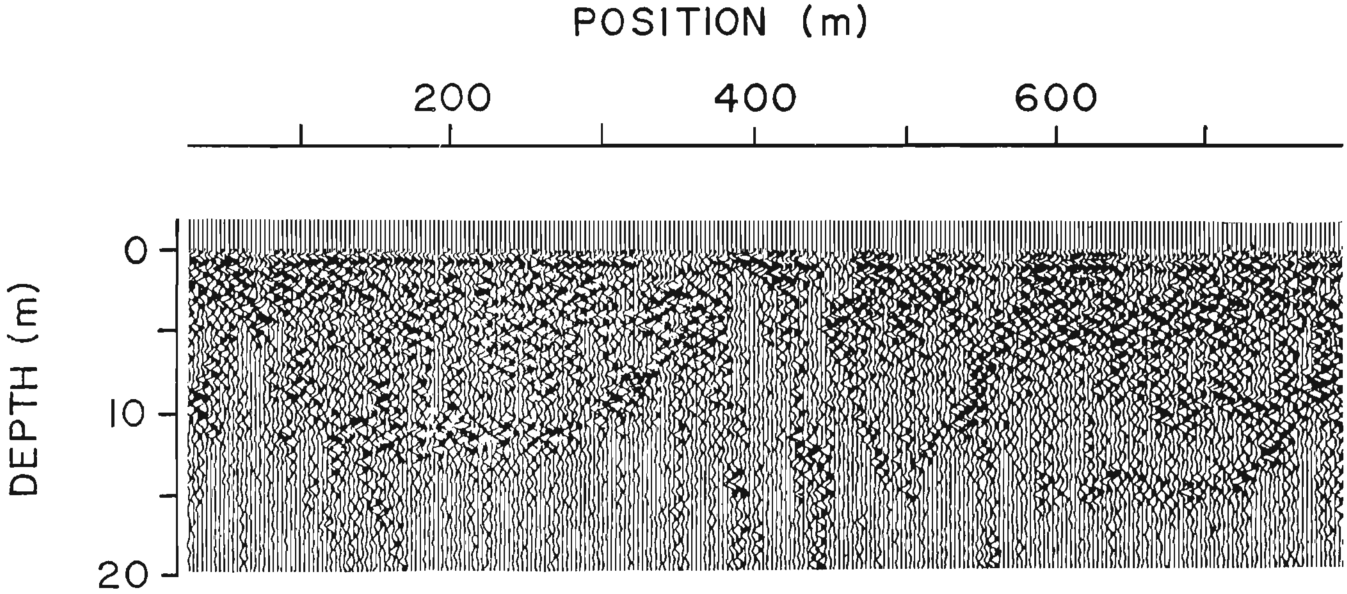

Figure 4. Example of digitized discrete step profiling results using variable area seismic-like display.

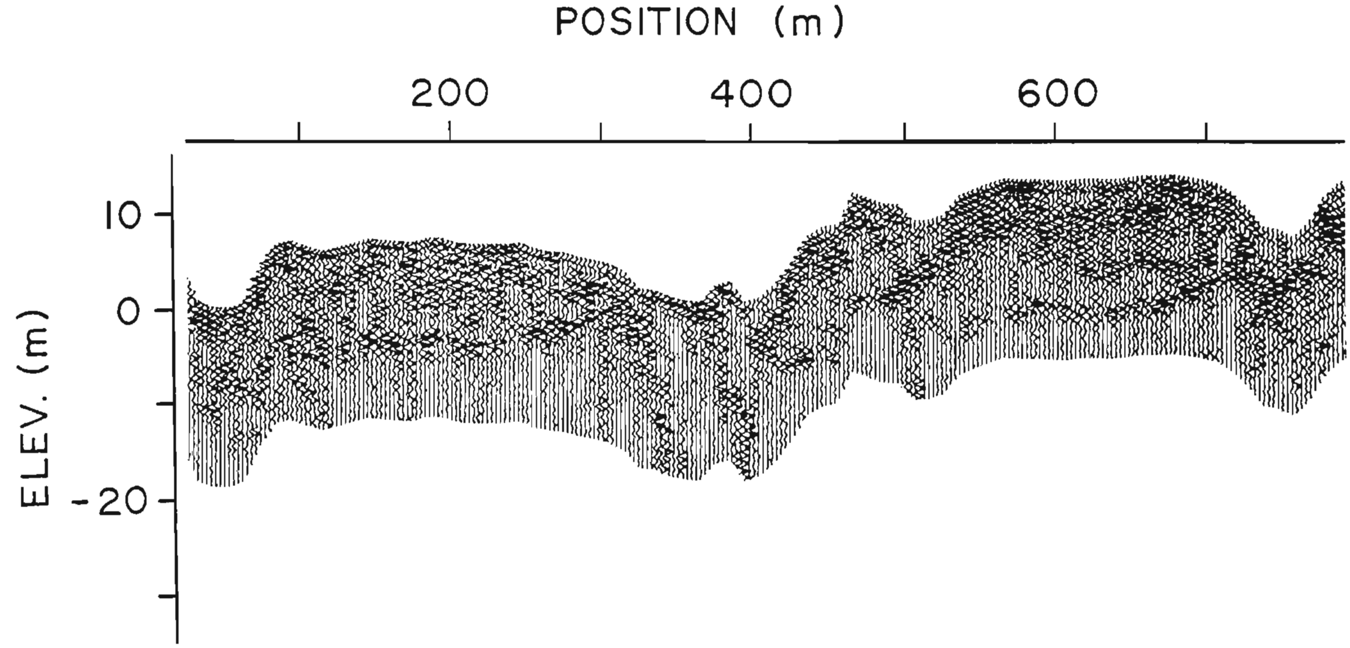

Figure 5. Data presented in Figure 4 compensated for topography.

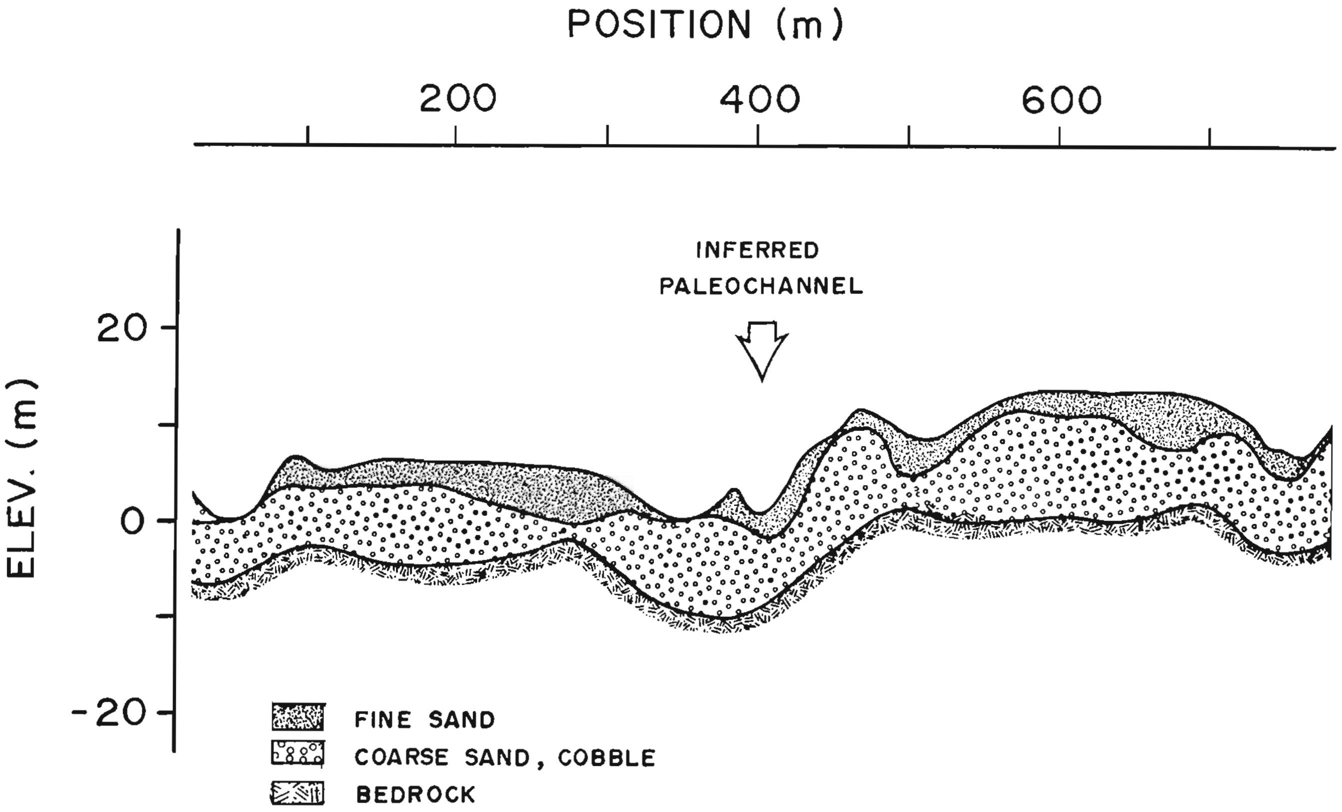

Figure 6. Geological interpretation of data shown in Figures 4 and 5 combined with seismic refraction survey information.

One major development effort was the design and construction of wide bandwidth, lightweight, portable antennas. Although we evaluated and tested many options for building directional antennas, in the end weight and portability became the deciding factor in system design.

To achieve good performance and penetration in most geological situations, operating frequencies had to be 100 MHz or lower. At these frequencies antennas become quite large, especially if a number of elements are included in the construction of the antenna in an attempt to make it directional. Because the design goal was a portable, lightweight system, such a large antenna structure was at odds with the whole design philosophy.

For GPR systems we found that when the antenna is placed in close proximity to the ground, the antenna characteristics change and most of the energy is transmitted into the ground. As a result, design focussed on the use of resistively loaded dipolar antennas that could be kept in very close proximity to the ground. Figure 7 shows how the radiation pattern of a small, electric dipole antenna varies as the electrical properties of the ground vary (Annan et al., 1975). The antenna pattern changes as ground electrical properties change with the peak in the pattern occurring at the critical angle of the air-earth interface.

The other key element of the system is the signal acquisition component or receiver. The state-of-the-art in this area is changing very rapidly. Several very high speed (flash) A/D convertors can sample at rates of up to several hundred MHz. These devices generally have limited dynamic range (i.e., 4-6 bit resolution). In the pulseEKKO II system, the unit employed had 8 bit resolution at 50 MHz sampling rate. At that time (in 1983) we decided that use of straight raw sampling was not fast enough for all requirements and was too power hungry for satisfactory operation in a battery powered, portable field instrument. We used synchronous sampling techniques in the pulseEKKO III system such as were used in the SIR system or any of the Tektronix or Hewlett-Packard sampling oscilloscopes.

Probably the most fundamental pulseEKKO development was the use of fibre optics for interconnecting all the components in the system. With the pulseEKKO III system, the transmitter and receiver are separate units and are interconnected into the console by fibre optics cables. Any wire cable in the vicinity of the radar can act as a parasitic antenna or radiator and will generate spurious ringing reflections. By using fibre optics, system artifacts are reduced greatly and the system performance is improved.

The resulting pulseEKKO III system with 100 MHz system antennas is shown in Figure 8. The transmitter and receiver modules, which are isolated by the fibre optics cables, contain their own battery power packs. The pulseEKKO III system is remarkably similar to the borehole radar system developed by the Swedish Geological Company

THEORETICAL

GEOMETRY

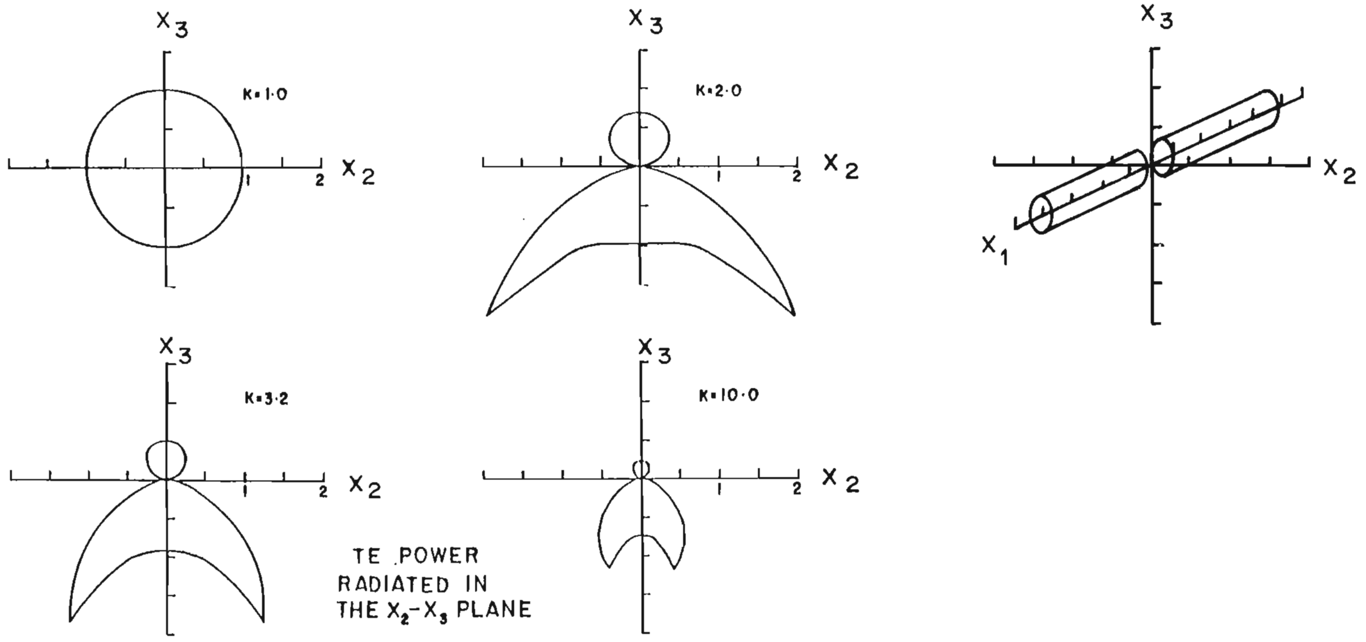

SCALE MODEL EXPERIMENT

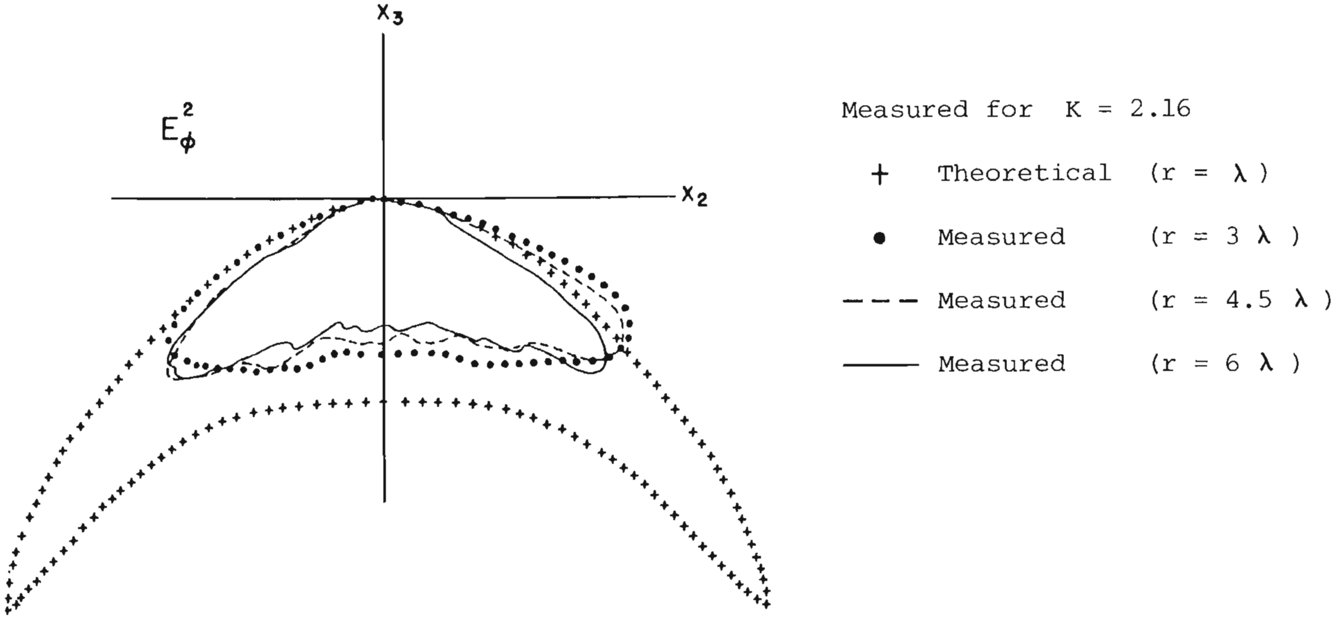

Figure 7. Dipole antenna pattern on soils of varying dieletric constant, K.

(Olsson et al., 1987). The specifications for the pulseEKKO III radar system now commercially available are summarized in Table 1.

EXAMPLE RESULTS

Many results from several case histories are presented in later papers in this proceedings. Here, one example of a set of data collected at a standard test site at Chalk River, Ontario, is presented. The geology at the site consists of fluvial and aeolian deposits of sand underlain by granitic bedrock. Figure 9 shows the system in profile mode operating along a road. Generally a crew of two is used, although in rough terrain a three person crew is beneficial.

The resulting data section is shown in Figure 10. Implicit with the pulseEKKO III system is use of computer processing. All data are recorded on digital tape in the field and are played back into a field computer. Radar reflection sections such as that shown in Figure 10 are the first stage in data analysis.

A computer facility such as that shown in Figure 11 indicates what is required to support a fully digital GPR operation. At this stage we can edit, process, generate filtered sections, and make topographic corrections. The whole spectrum of seismic processing concepts can be used. With the rapid evolution of computer technology, the sophistication of digital processing will change and expand in the near future. For the section presented in Figure 12, some enhancement processing and automatic gain control (AGC) have been applied to enhance the weak reflections and to make their display amplitude equal to the strong events. This type of processing is common in the seismic industry.

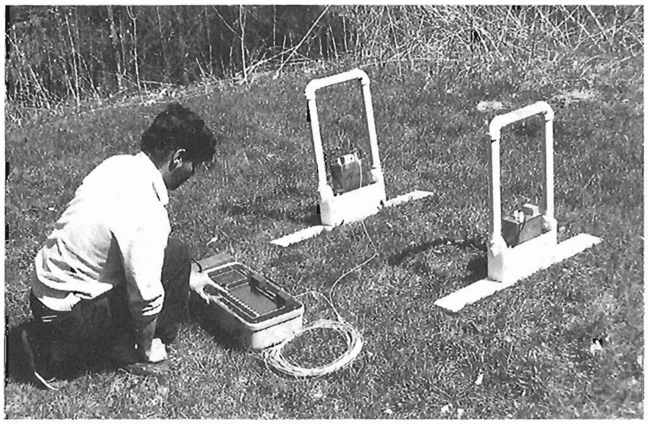

Figure 8. The first pulseEKKO III system.

Figure 9. The pulseEKKO III being used to profile along a road at a test site.

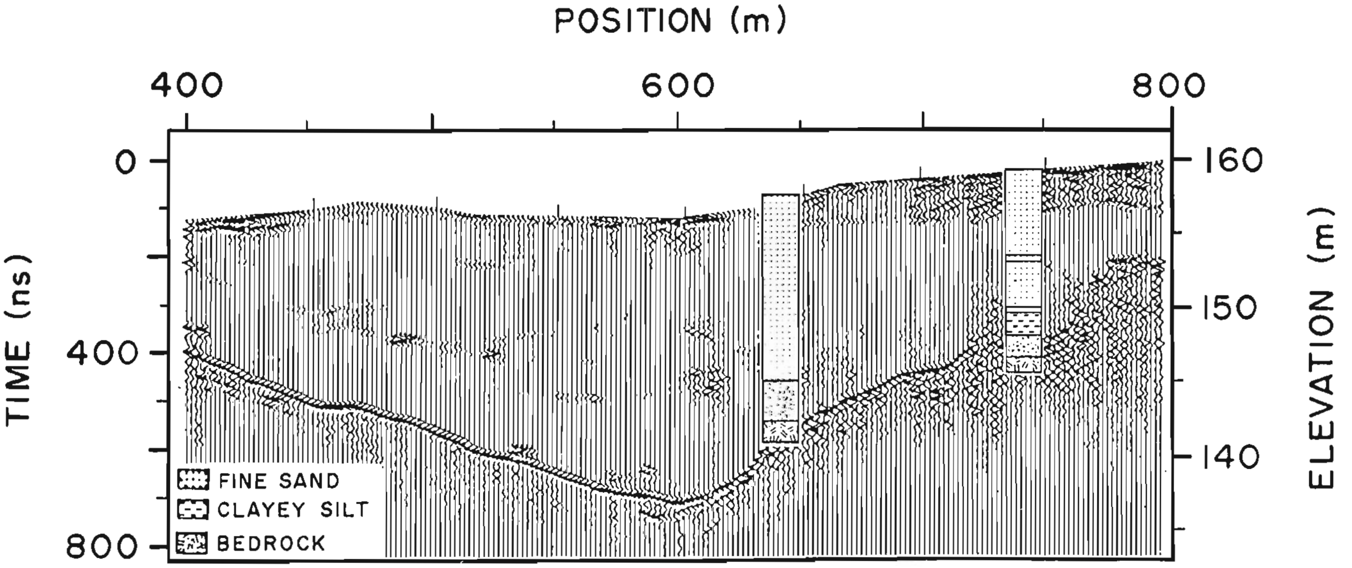

Figure 10. The pulseEKKO III data with topographic correction but without a large amount of time-gain applied.

The same data set processed to yield a colour image is shown in Figure 13. These figures show some different ways of displaying the same information. The important point is that, when we have 100 dB of dynamic range in data, several display techniques may be needed to see the various features in the data. In some situations, the signal being sought is considered to be a nuisance (geological noise is the term often applied) in another application.

Table 1. Specifications for pulseEKKO III system

RADAR PARAMETERS			
Centre Frequencies	50 MHz, 100 MHz, (200 MHz - optional extra)		
System Performance	155 dB		
Programmable Range Window	1-3200 ns		
Minimum Sampling Interval	800 ps		
Programmable Stacking	1-4096		
ANTENNAS			
	50 MHz	100 MHz	200 MHz
Size	10.5 x 184 x 0.8 cm	10.5 x 92 x 0.8 cm	10.5 x 46 x 0.8 cm
Weight	4 kg	3.2 kg	2.8 kg
TRANSMITTER ELECTRONICS			
Output Voltage	400 Volts (standard equipment) 1000 Volts (optional extra - for 50 and 100 MHz only)		
Maximum Repetition Rate	30 kHz		
Size	23 x 14 x 7 cm		
Weight	0.75 kg		
Power	12V (4 Amp-hour re-chargeable battery)		
RECEIVER ELECTRONICS			
Size	23 x 14 x 7 cm		
Weight	1.5 kg		
Power	12V (4 Amp-hour re-chargeable battery)		
CONTROL CONSOLE			
Size	47 x 27 x 23 cm		
Weight	10 kg (with lid)		
Power	12VDC (3 Amps)		
Recording	Digital Cassette		
Display	LCD Graphic (240 x 640 pixel)		
Data port	8 bit parallel I/O		
CABLES			
Control Console Power	1.5 m power cable		
Transmitter Trigger	20 m fiber optic cable		
Receiver Timing & Data	20 m fiber optic cable		
Computer Interface	1 m GPIO Interface cable		
			August, 1987

In many instances, since the pulseEKKO III system came into being, radar investigations have become clutter limited. The wealth of detailed subsurface information surpasses our ability to interpret and exploit in a timely fashion.

SUMMARY AND CONCLUSIONS

The first pulseEKKO III system was completed in the spring of 1986 and delivered to the Geological Survey of Canada at that time. Since then the prototype system has seen continuous field work for more than 2 years. It has been used in the Canadian Arctic, in mines, in wet conditions, and in desert areas and has been through the mill in terms of field

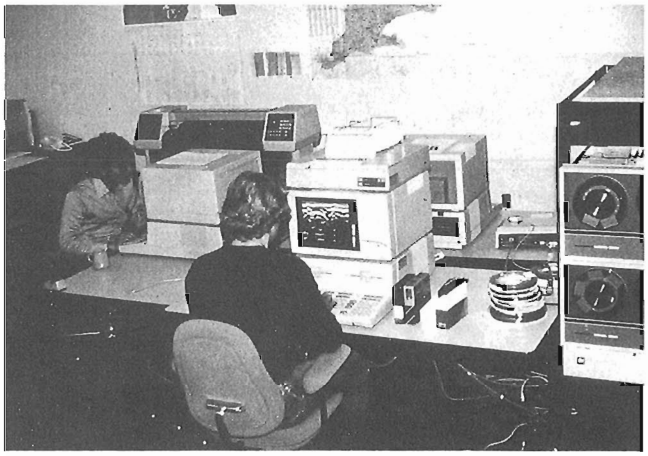

Figure 11. Computer processing facility for radar data analysis.

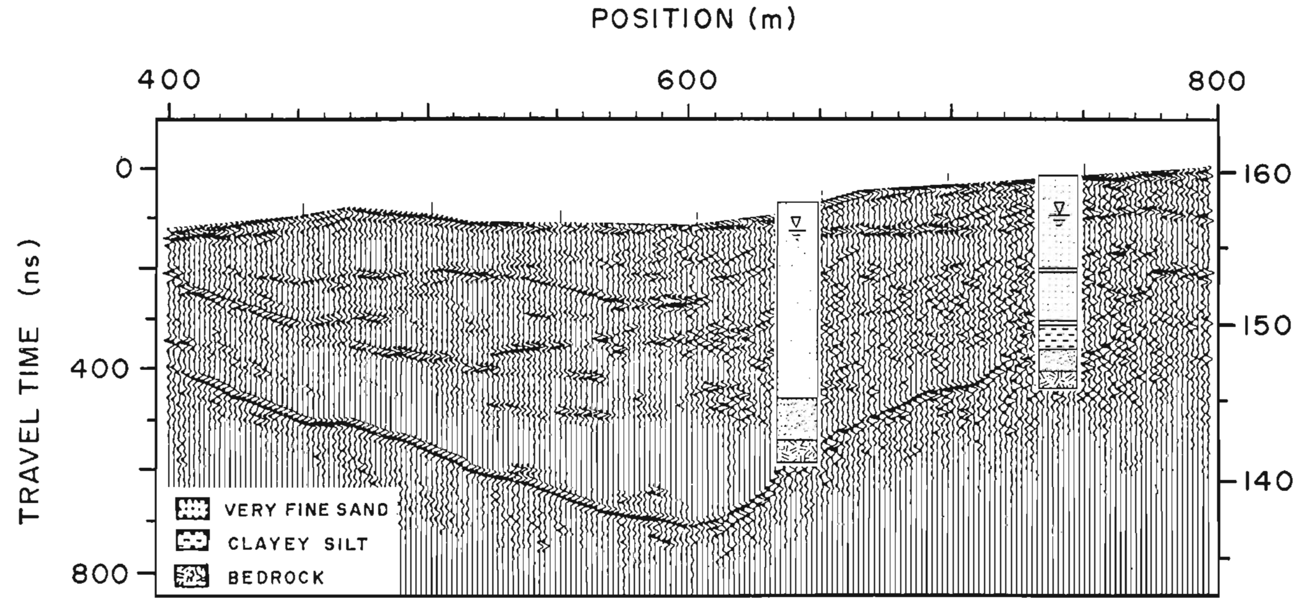

Figure 12. Example of the test site data shown in Figure 10 with AGC applied.

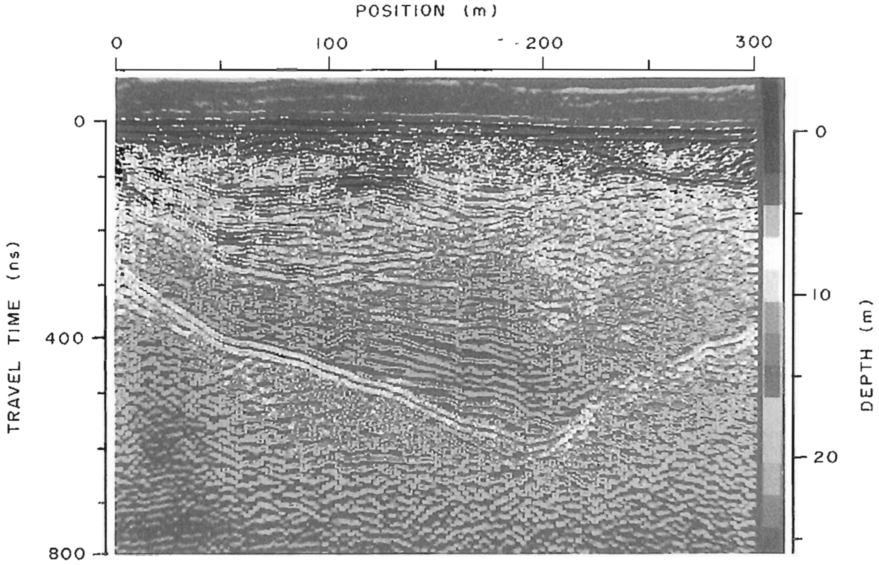

Figure 13.

Example of the test site data shown in Figure 10 or 12 using a colour display.

testing. Results are starting to come forth that demonstrate the benefits of this new generation of GPR system (Davis and Annan, 1992, Pilon et al., 1992).

The benefits of the pulseEKKO III system are many, but the more important are the following:

- high quality, artifact free data
- limits no longer instrumentation but rather ground clutter and attenuation factors
- simple-to-operate, portable system available
- reliable amplitude analysis becoming possible.

In summary, a new era in the GPR area is dawning and the method will see more rapid growth and expanded use as the advances of the seismic processing industry are adopted.

ACKNOWLEDGMENTS

The authors and A-Cubed Inc. would like to acknowledge the enthusiasm and support offered by the GSC personnel over the years of this project development.

REFERENCES

Annan, A.P. and Davis, J.L.
1976: Impulse radar soundings in permafrost; Radio Science, v. II, p. 383-394.

Annan, A.P., Davis, J.L., and Gendzwill, D.
1988: Radar sounding in potash mines, Saskatchewan, Canada; Geophysics, v. 53, p. 1556-1564.

Annan, A.P., Waller, W.M., Strangway, D.W., Rossiter, J.R., Redman, J.D., and Watts, R.D.
1975: The electromagnetic response of a low-loss, 2 layer dielectric Earth for horizontal electric dipole exitation; Geophysics, v. 40, no. 2, p. 286-298.

Davis, J.L. and Annan, A.P.
1992: Application of the pulseEKKO III ground penetrating radar system to mining, groundwater and geotechnical projects – selected case histories; in Ground penetrating radar, J.A. Pilon (ed.); Geological Survey of Canada, Paper 90-4.

Davis, J.L. and Annan, A.P.
1989: Ground penetrating radar for high-resolution mapping of soil and rock stratigraphy; Geophysical Prospecting, v. 37, p. 53-551.

Davis, J.L., Annan, A.P., Black, G., and Leggatt, C.D.
1985a: Geological sounding with low frequency radar (abstract); Extended Abstracts of the 55th Annual International Meeting of the Society of Exploration Geophysicists, Washington, D.C., October, 1985.

Davis, J.L., Annan, A.P., and Vaughan, C.J.
1985b: Placer exploration using radar and seismic methods; Canadian Institute of Mining Bulletin, v. 80, no. 898, p. 67-72.

Morey, R.M.
1974: Continuous subsurface profiling by impulse radar; Proceedings, Engineering Foundations Conference on Subsurface Explorations for Underground Excavations and Heavy Construction. Henniker, New Hampshire, p. 213-232.

Olsson, O., Falk, L., Forslund, O., Lundmark, L., and Sandberg, E.
1987: Crosshole investigations – results from borehole radar investigations; Stripa Project TR 87-11. Swedish Nuclear Fuel and Waste Management Co., Stockholm.

Pilon, J.A., Allard, M., and Seguin, M.K.
1992: Ground probing radar in the investigation of permafrost and subsurface characteristics of surficial deposits Kangiqsualujjuag, North Quebec; in Ground penetrating radar, J.A. Pilon (ed.); Geological Survey of Canada, Paper 90-4.

Pilon, J.A., Grieve, R.A.F., Sharpton, V., Coderre, J., and Kennedy, J.
1992: Reconnaissance ground penetrating radar survey of the interior of meteor crater, Arizona; in Ground penetrating radar, J.A. Pilon (ed.); Geological Survey of Canada, Paper 90-4.

Helicopter-borne alpine glacier surveys using short pulse radar

Steven A. Arcone[1], Allan J. Delaney[1], and Robert H. Wills[2]

Arcone, S.A., Delaney, A.J., and Wills, R.H., 1992: Helicopter-borne alpine glacier surveys using short pulse radar; in Ground penetrating radar, ed. J. Pilon; Geological Survey of Canada, Paper 90-4, p. 25-32.

Abstract

Helicopter-borne ground penetrating radar (GPR) surveys were performed in March 1986 on two small tributaries to the Yanert Glacier in the Alaska Range. The purpose was to find out if the UHF range could be used to investigate small, cold glaciers where fractures and crevasses might be minimal. The GPR used a GSSI model 3102 antenna unit rated at 8 W peak radiated power at a pulse centre frequency of approximately 500 MHz, which is considerably higher than that of conventional radio echo sounders. The glaciers were profiled for about 1 km along straight lines, starting at their termini where bedrock was exposed, and ending where the bottom returns were barely visible at more than 28 m depth. In one case, the analog graphic record revealed a linear bottom profile and predominantly homogeneous conditions within the ice sheet. Use of a geometric attenuation dependency correction of distance squared on the digitized records resulted in a calculated attenuation rate for absorption of near 0 dB/m for the peak value of the bottom returns, but about ± 3 dB/m for the total energy of the wavelet. The pulse centre frequency of the first bottom reflections shifted to only about 380 MHz on average; the incident pulse waveform was generally retained. Thus, the apparent homogeneity of the ice and smoothness of the bottom could permit far deeper penetration given more power. The high frequency range could provide greater resolution of the bottom topography than previously possible.

Résumé

En mars 1986, des levés par géoradar héliporté ont porté sur deux petits tributaires du glacier Yanert dans la chaîne de l'Alaska. L'objet de ce levé était de déterminer si le domaine des très hautes fréquences (UHF) peut servir à analyser les petits glaciers froids où les fractures et les crevasses peuvent être minimes. Le géoradar comportait un appareil à antenne GSSI de modèle 3102 dont la puissance nominale rayonnée était de 8 W en crête correspondant à une fréquence centrale d'impulsions d'environ 500 MHz, soit une fréquence considérablement plus élevée que dans le cas des échosondeurs ordinaires. Le profil des glaciers a été établi sur une distance de 1 km suivant des lignes droites, débutant à la partie frontale où le socle affleure et se terminant où les échos de fond sont à peine visibles à plus de 28 m de profondeur. Dans un cas, l'enregistrement graphique analogique a révélé un profil de fond linéaire et des conditions surtout homogènes au sein de la nappe glaciaire. L'utilisation d'une correction de la distance liée à l'atténuation géométrique, élevée au carré sur les enregistrements numérisés, a causé un taux d'atténuation calculé de l'absorption de près de 0 dB/m pour la valeur maximale des échos de fond, mais d'environ ±3 dB/m pour l'énergie totale de l'ondelette. La fréquence centrale d'impulsions des premières réflexions de fond n'est passée qu'à environ 380 MHz en moyenne; la forme de l'impulsion incidente a été généralement retenue. Par conséquent, l'homogénéité apparente du glacier et l'uniformité du fond pourraient permettre une pénétration beaucoup plus profonde si la puissance était plus grande. L'intervalle de haute fréquence pourrait donner une meilleure résolution de la topographie du fond que dans le passé.

---

[1] Department of the Army, Cold Regions Research and Engineering Laboratory, Corps of Engineers, 72 Lyme Road, Hanover, New Hampshire, U.S.A. 03755-1290

[2] Department of Physics and Astronomy, Dartmouth College, Hanover, New Hampshire, U.S.A. 03755, now at Skyline Engineering, Temple, New Hampshire, U.S.A. 03084

INTRODUCTION

Radio echo sounding of glaciers and ice sheets is usually performed at carrier frequencies ranging between 35 and 100 MHz. Transmitted pulse shapes generally consist of a burst of about 10-12 cycles of the carrier frequency. This range allows the use of high gain antennas, which, when used with a high power transmitter and an envelope detection scheme, can result in a system performance figure as high as 185 dB and an ability to sound ice sheets kilometres thick. The major drawback is the length of the pulse, which, for 10 cycles at 100 MHz, will extend only to about 17 m in ice. Attempts to increase this resolution with higher frequencies (e.g., 620 MHz: Goodman, 1975; Goodman et al., 1975; Clark and Goodman, 1975; and 840 MHz: Narod and Clarke, 1980) have met with difficulty because of increased scattering and absorption at the shorter wavelengths. An alternative approach is to use ground penetrating radar (GPR) at 100-500 MHz, which radiates an almost ideal doublet giving maximum resolution. However, GPR suffers from a much weaker performance figure, partly because of the low gain antennas necessary to form such pulses, and partly because of the inherent noise in the sampling process needed to reproduce the waveform. In this paper we discuss the results of using one such radar, operating at a centre frequency of about 500 MHz, for a survey of two small alpine glaciers in Alaska Range.

EQUIPMENT

Control unit

The radar system was controlled by a Xadar Electromagnetic Reflection Profiling System (Model 1316), which was mated to two different antenna packages manufactured by the GSSI Corporation. The Xadar unit triggers pulses at a pulse repetition frequency (PRF) of 50 kHz and compiles the received pulses into 8 scans per second. Before compilation, the received UHF waveforms are sampled and reproduced at audio frequency to allow recording on cassette magnetic tape (see Morey, 1974, or Annan and Davis, 1976, for more complete operating descriptions). A variety of time range gain (TRG) functions may be applied to the scans to suppress the higher amplitude early returns (especially the direct coupling between transmit and receive antennas) and to enhance the lower amplitude later returns. Generally, the system was operated in a designated EXP/2 mode, which gave an exponentially increasing gain over the first half of the scan and constant gain thereafter. An overall system gain was also used.

Each scan of return events (echoes) can be viewed at a variety of time ranges, which have been calibrated against time delays measured between antennas separated in air at a variety of spacings. The graphic records will show these time calibrations translated into ice thickness using the simple formula

$$d = ct/2\sqrt{\varepsilon_r} \qquad (1)$$

where t is time in ns, c is the velocity of wave propagation in air (0.3 m/ns, and ε_r is the relative dielectric constant, which is unity for air and 3.2 for ice (e.g., Glen and Paren, 1975). Corrections due to ice density are not considered. The factor of 2 in equation (1) accounts for the round trip of the echo.

All data presented were recorded in an analog mode, and the scans are displayed consecutively on electrosensitive chart paper on which darkness is proportional to signal amplitude. Examples of translations of scans into this graphic representation have been published extensively (e.g., Arcone et al., 1986). This method of display for strong signal returns is superior because continuity of events or banding from a single reflector is easy to recognize. The appearance of these bands indicates temporal coherency (i.e., retention of the phase integrity of the incident waveform) in the reflected waveforms.

The Xadar unit is also capable of recording in a digital mode whereby the waveforms received within each scan can be stacked and displayed. Use of this mode was unnecessary because of the signal strength received. It was not feasible in any case because fluctuations in the altitude of the helicopter during the stacking process (a 16-fold stack requires about 2 s to compile) would ruin the coherency of the desired returns.

Antennas

The antenna unit consists of both a transmit and a receive antenna shielded against back radiation and packaged in one housing. The GSSI Model 3102 is rated at 8W peak radiated power. (The manufacturer admits having arrived at this figure by calculation rather than measurement.) A typical radiated waveform in air is given in Figure 1 for which the approximate centre frequency is 500 MHz. The stronger oscillations of the 3102 waveform die out by about 6 ns giving a raw data resolution of minimum ice thickness of about 50 cm. Loading occurs when these (or any other) antennas

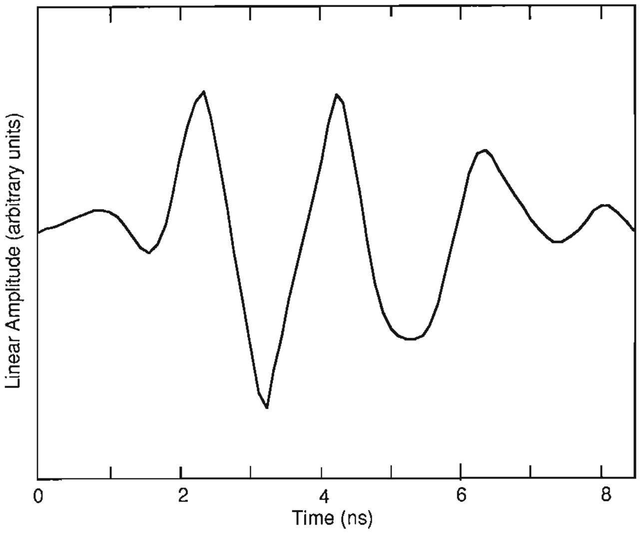

Figure 1. Transmitted wavelet of the GSSI model 3102 "500 MHz" antenna. The wavelet is actually a reflection from a water surface.

Table 1. Approximate area (W x L) of radar sensitivity at the base of ice sheets of different thicknesses using an antenna travelling at 7 m/s

Antenna altitude (m)	W x L below ice thickness (m)				
	10	20	30	40	50
2	10 x 11	16 x 17	23 x 24	30 x 31	37 x 38
4	12 x 13	19 x 20	26 x 27	33 x 34	40 x 41
6	15 x 16	22 x 23	29 x 30	36 x 37	42 x 43
8	18 x 19	25 x 26	32 x 33	38 x 39	45 x 46
10	21 x 22	28 x 29	34 x 35	41 x 42	48 x 49

are placed on the ground (or ice surface) for surface based profiling. This mode can lower the centre frequency of the pulse spectrum by as much as 50%. When ground electrical properties change, so does the loading and the transmitted waveform.

In an airborne mode, pulse width is minimal allowing maximum resolution within the raw data. The 3 dB beamwidth θ of the antenna unit is about 70° (two way power gain) in both principal planes and the basic pulse shape is maintained to ±70°, also in both planes (Arcone et al., 1986). The directive gain of these antennas is estimated to be no greater than 5 dB. The performance figure for an entire system from one manufacturer is estimated to be above 100 dB for the 3102, but, practically, in an airborne mode, 70 dB seems to be about the most attenuation the radar signals can experience before they are no longer detectable on the graphic display.

The value of θ can be used to estimate the lateral area of the ice bottom to which an antenna at height h over ice thickness d is sensitive. The width W (perpendicular to the flight direction) of this area is approximated using Snell's Law by

$$W = 2\,h\,\tan\left(\frac{\theta}{2}\right) + 2\,d\,\tan\left(\sin^{-1}\left[\frac{\sin(\theta/2)}{\sqrt{\varepsilon_{r_{ice}}}}\right]\right) \qquad (2)$$

The length L (parallel to the flight direction) of this area must account for the distance travelled during the compilation of one scan (0.125 s) so that

$$L = W + v/8 \qquad (3)$$

where v is aircraft velocity in m/s. Table 1 documents some values of W and L for various values of ice depth and antenna altitude at one value of v. Values of v less than that given marginally affect the results.

Helicopter mounting

A Bell 206B Jet Ranger helicopter was used for these studies. The antenna unit was mounted under two struts about 1.5 m from the body of the helicopter with antenna polarization perpendicular to the skid direction (Fig. 2). The radar operator sat in the back seat with the control unit. A second passenger was not permitted because of the high altitude of the glacier and the low speed required. At the low speeds used, average air speeds were calculated by timing the flight profiles between known distances, because the helicopter's air speed indicator was unusable. In these studies distances were derived from estimated air speeds because of the lack of any ground control.

The primary concern in operating the antenna near the helicopter was helicopter clutter. Consequently, the initial proving of the system was conducted over lakes (Arcone and Delaney, 1987), the constant ice thickness of which allowed us to separate clutter from desired signals. Despite the backshielding of the antennas, this clutter started at multiples of about 10 ns (round trip) but was of low enough amplitude as not to be significant. Of equal concern were internal events caused by mismatches between antennas (GSSI) and control unit (Xadar). Consequently, flight altitude and time range had to be adjusted to minimize the interferences of this coherent noise.

GLACIERS SURVEYED

The glaciers surveyed are two small tributaries to the north branch of Yanert Glacier, which is located on the west approach to Mt. Deborah in the Alaska Range. The glaciers are indicated by two arrows in Figure 3, which point in the

Figure 2. Bell 206B Jet Ranger with 3102 antenna unit mounted to the side.

direction of the flight lines. These glaciers were selected because they terminated upon bare and smooth bedrock with no terminal moraines (Fig. 4). Figure 4 shows the ice sheet gradually thickening away from the bedrock exposure, which allowed us to profile the glacier beginning at zero ice thickness. The smooth bedrock appearance suggests that these glaciers may be melted on the bottom and may move by sliding over the bedrock; hence we expected a smooth ice-bedrock interface. Interpretation complications arose from the ridged structure seen in the photographs as we could

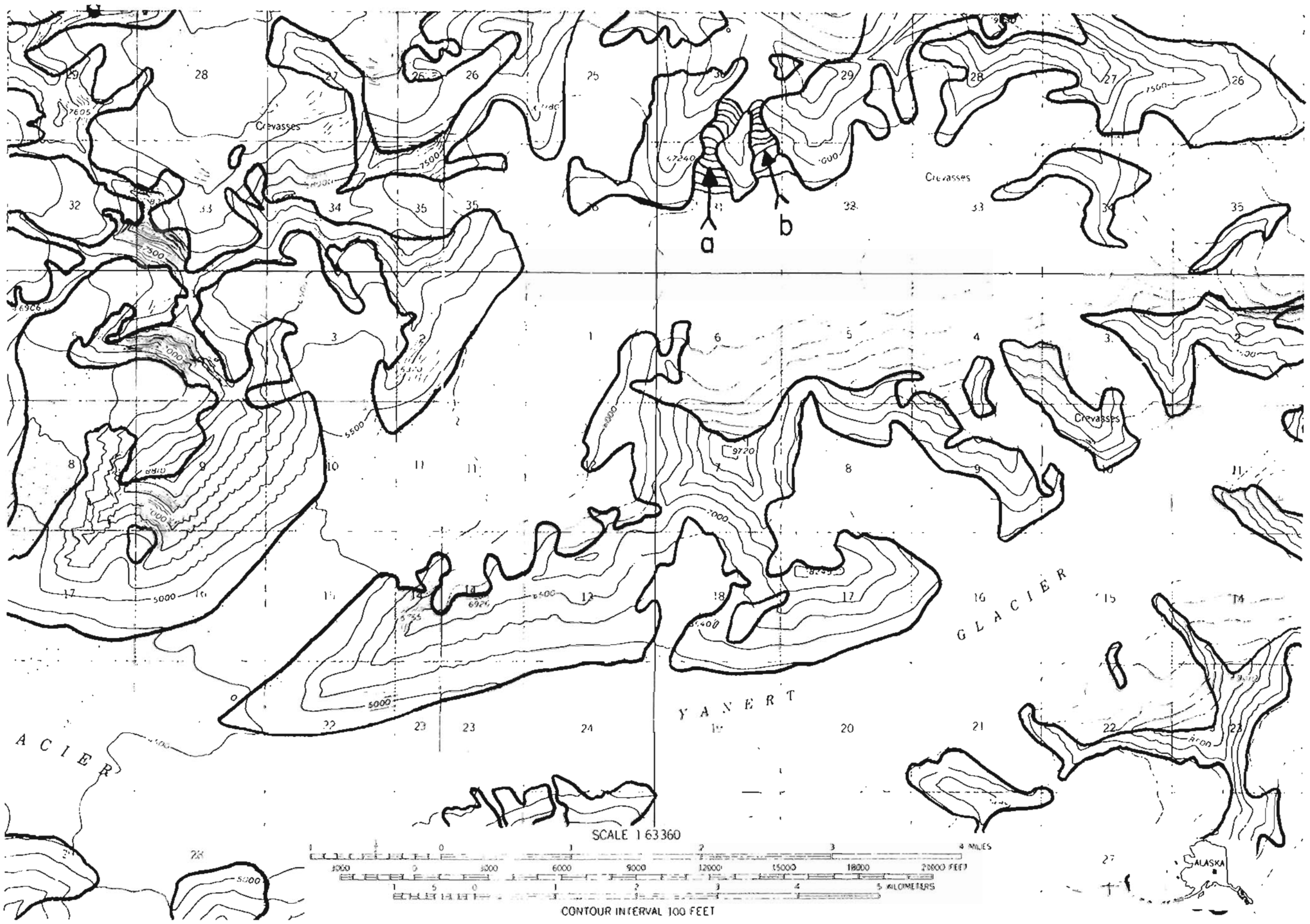

Figure 3. Topographic location map of the surveys a and b (dark arrows) at Yanert Glacier.

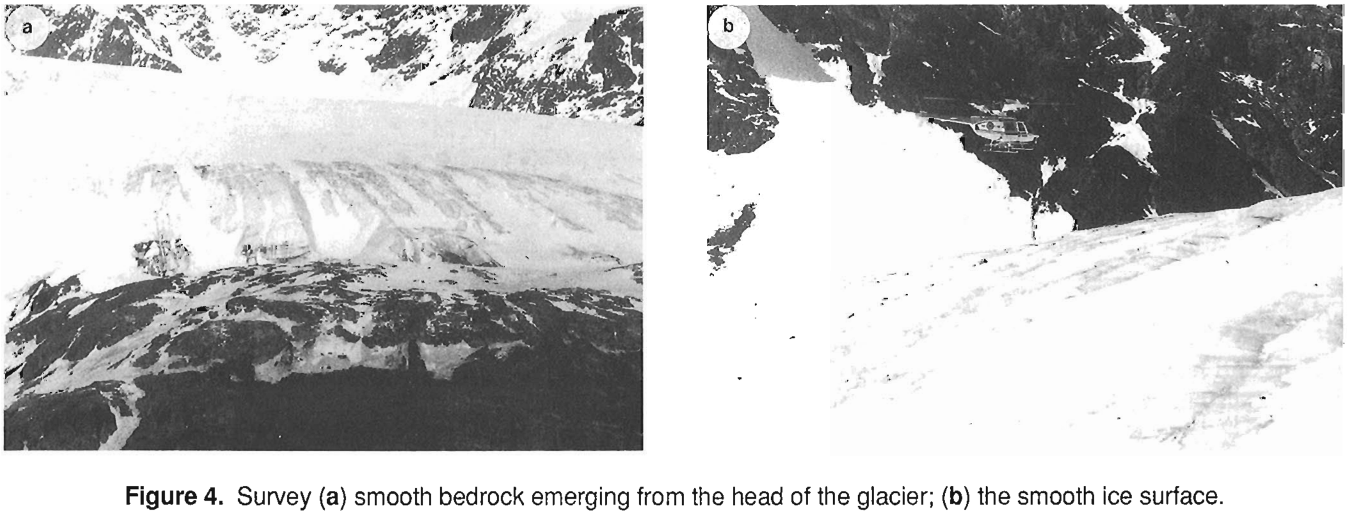

Figure 4. Survey (**a**) smooth bedrock emerging from the head of the glacier; (**b**) the smooth ice surface.

not be sure when the ice began under the snow fields at the glacier terminus. The radar records will reveal the snow-ice and ice-rock interfaces.

RESULTS

Figures 5 and 6 show the analog radar graphic records for profiles a and b. The vertical divisions are separated 44 ns, which corresponds to 3.7 m of ice. The horizontal dark bands are direct coupling between antennas, helicopter reflections, and internal system noise. The vertical lines are separated by about 1 min, which corresponds to about 400 m for an estimated air speed of 7 m/s. The rock surface was observed to disappear beneath the ice at the first 1 min demarcation in both figures. Figure 5 presents the more complicated case with a more obvious snow layer. Figure 6 shows a linear depth profile and some geologic noise caused by volume scattering. Of greatest interest are the frequency content and amplitude distributions of the bottom returns, which can provide information concerning the suitability of the radar for studying the propagation medium and the bottom surface. The graphic record suggests that these bottom returns are incoherent and noisy. However, when the scans of Figure 6 was displayed in analog form, much coherency was found. Consequently, some of the record (Fig. 6) were digitized (12.5 Ks/s) for analysis.

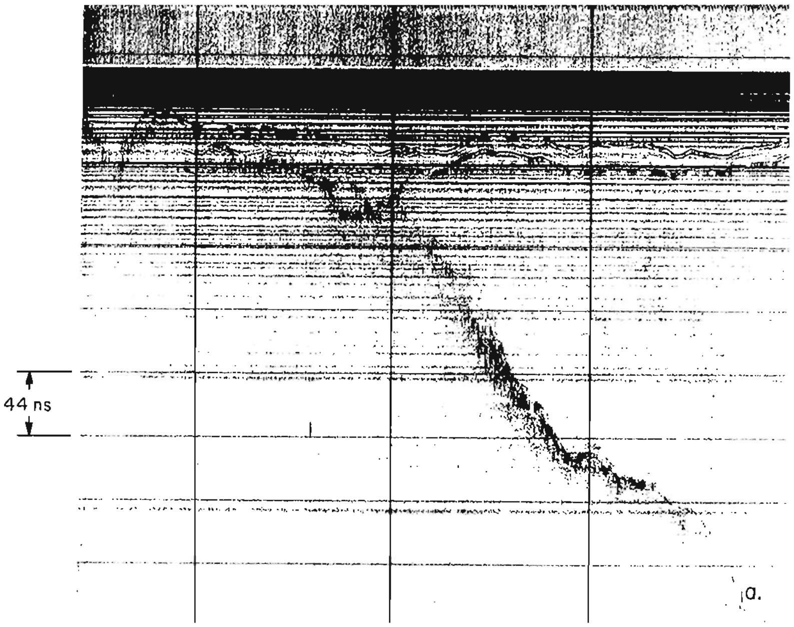

Figure 5. Analog radar record of Profile *a*.

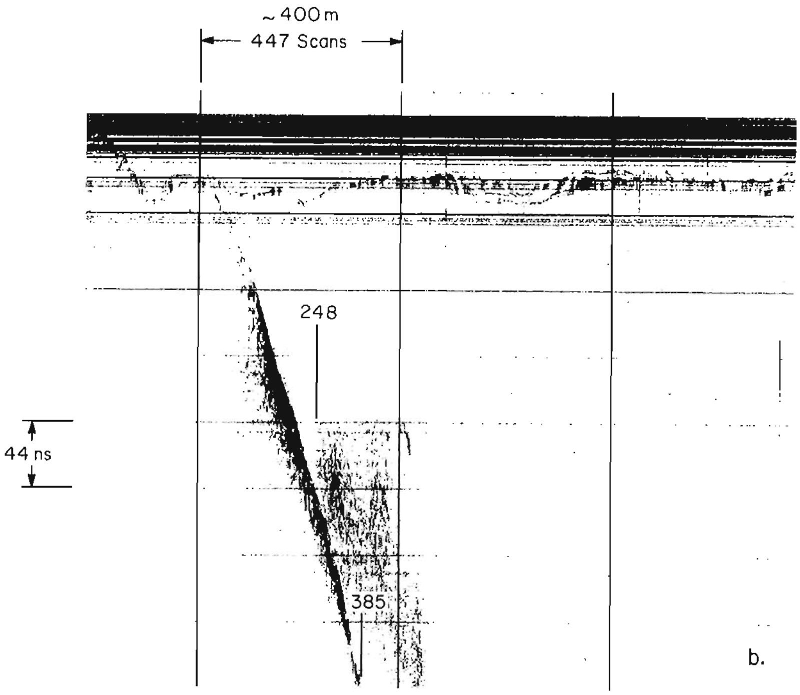

Figure 6. Analog radar record of Profile *b*.

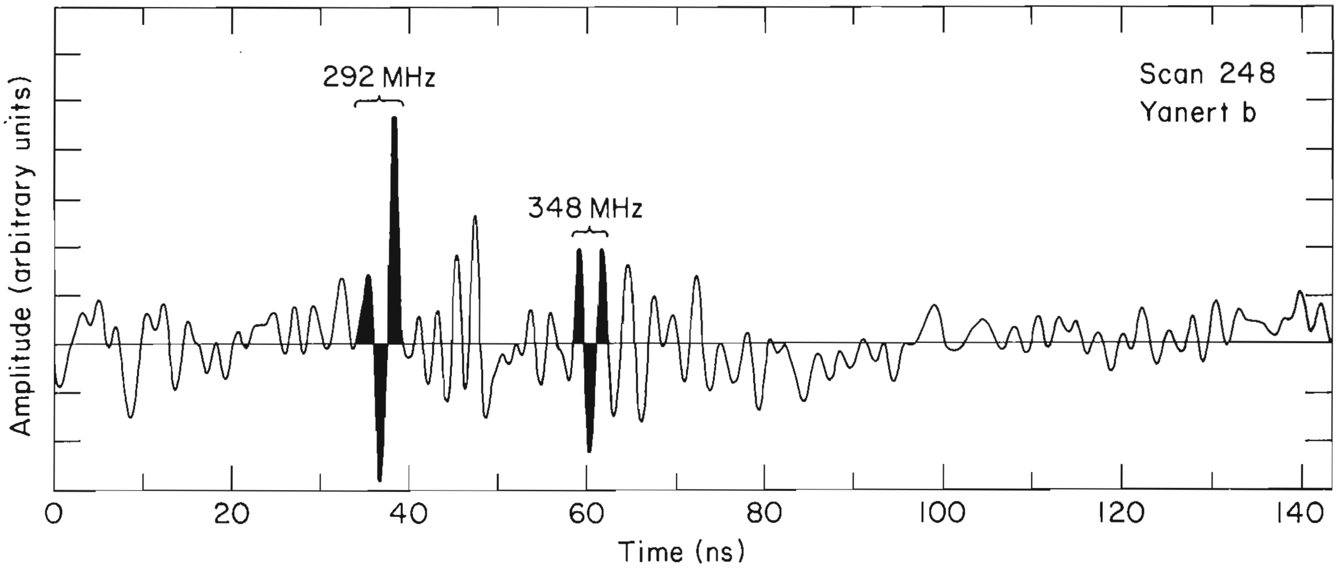

Figure 7. Analog recording of the bottom returns of scan 248 the position of which is shown in Figure 6.

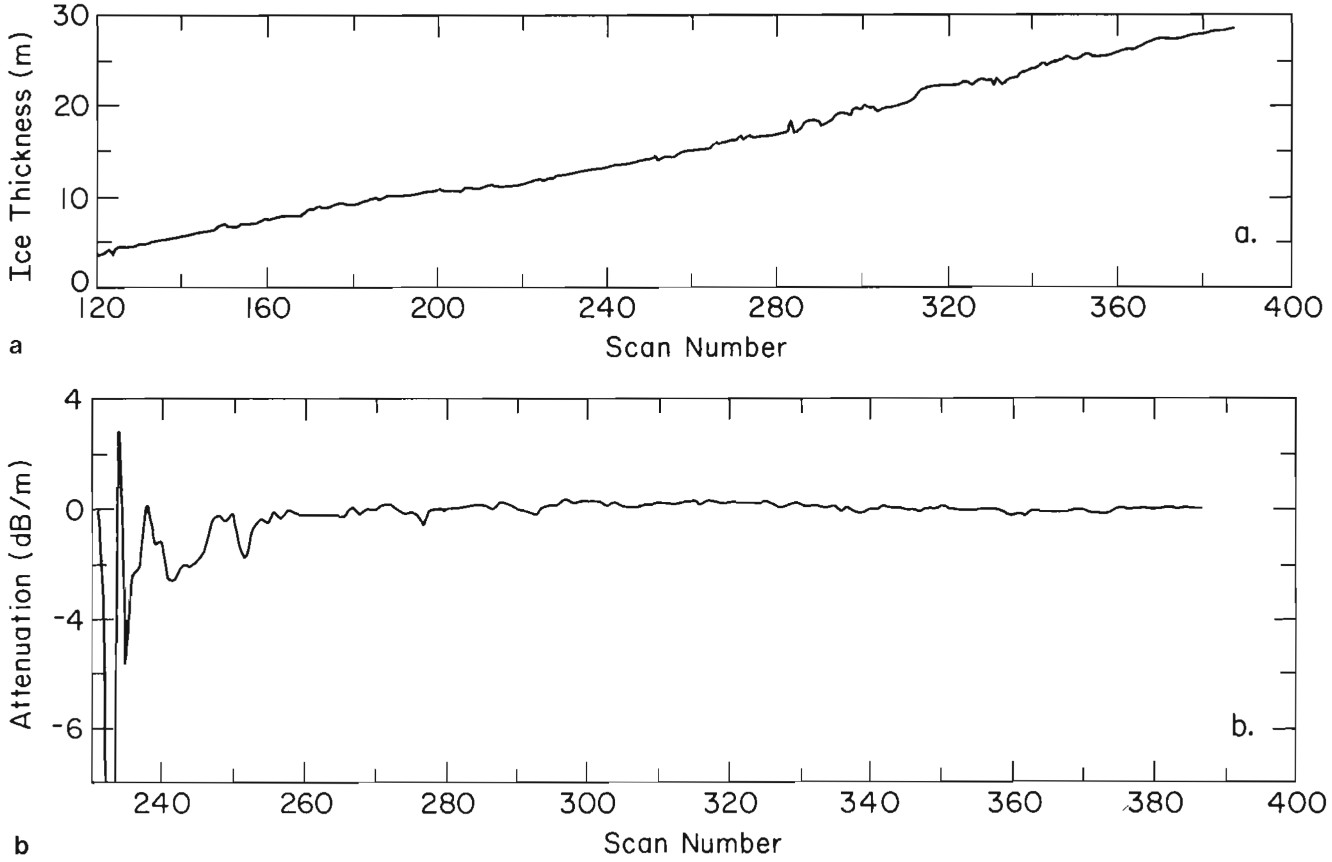

Figure 8. Depth (**a**) and peak value attenuation (**b**) plots for the bottom returns of Profile *b* beginning at 12.6 m ice depth. The scans analyzed are in a flat portion of the radar time range gain function.

Figure 7 gives part of the analog plot of the bottom returns of one scan (248 in Fig. 6). Two coherent wavelets are highlighted and the one of stronger amplitude is typical of those identified as the initial bottom return. The approximate maximum power frequencies of their spectra (Fig. 7) are calculated from their oscillation periods. The frequency values are lower than the transmitted frequency of the antennas as measured in water reflections (approximately 500 MHz). The loss of frequency content is examined later.

Figure 8a plots the ice thickness as a function of scan number for the glacier profile b (Fig. 6). Data for this figure were derived from measurements of the peak amplitudes from plots of the analog traces. The plot reveals a linear profile as was evident in Figure 6. The linearity permits an assumption of a geometric energy attenuation function of $1/r^2$, rather than a $1/r^4$ dependency characteristic of small targets. Using a $1/r^2$ correction factor, Figure 8b then plots the attenuation rate of the peak values of the bottom returns for each scan, arbitrarily using the particular scan at 12.6 m ice depth as a reference.Near this reference the rate shows large variations because of the small differences in ice depth relative to the reference. By about 8 m depth (scan 170) the relative change in ice depth is sufficiently great to reduce the signal attenuation rate to near 0 dB/m, which suggests that the ice is homogeneous and causes negligible signal attenuation due to conductive, dipolar, or scattering losses. However, this method of measuring signal absorption is not as meaningful as an analysis based on total energy content of the wavelets discussed next.

The results of Figure 8 are somewhat contradicted by those shown in Figure 9, which are based on an analysis of the digitized data. After digitization, we applied background removal by subtracting the average amplitude distribution across 100 scans from the amplitude distribution across each scan. Figure 9a then plots the attenuation rate in dB/m considering the total energy in the bottom return wavelets, which were windowed over an arbitrarily set time of 9 ns. The reference signal was the bottom return at approximately 8.5 m ice depth and the analysis considered total propagation distance from helicopter to ice bottom. The refractive gain experienced by the wavelet in passing from air to ice was not accounted for because this gain is experienced by all wavelets and the altitude fluctuations are relatively small. As in Figure 8, we applied a geometric spreading factor correction of $1/r^2$. The results show that after large fluctuations near the reference, the attenuation rate seems to fluctuate ±3 dB/m

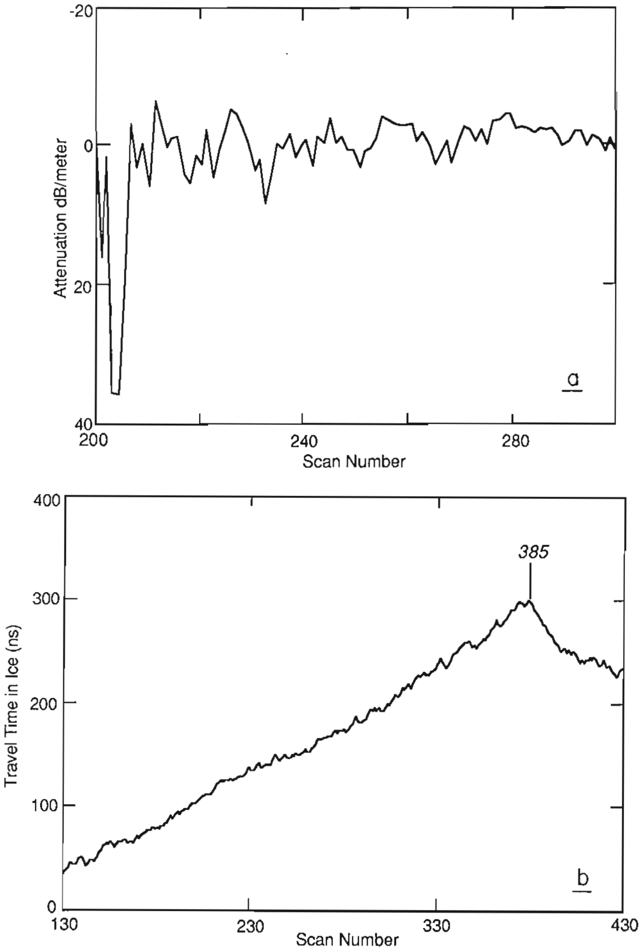

Figure 9. Total wavelet power attenuation (**a**) and ice depth (**b**) for a similar portion of the record analyzed in Figure 8.

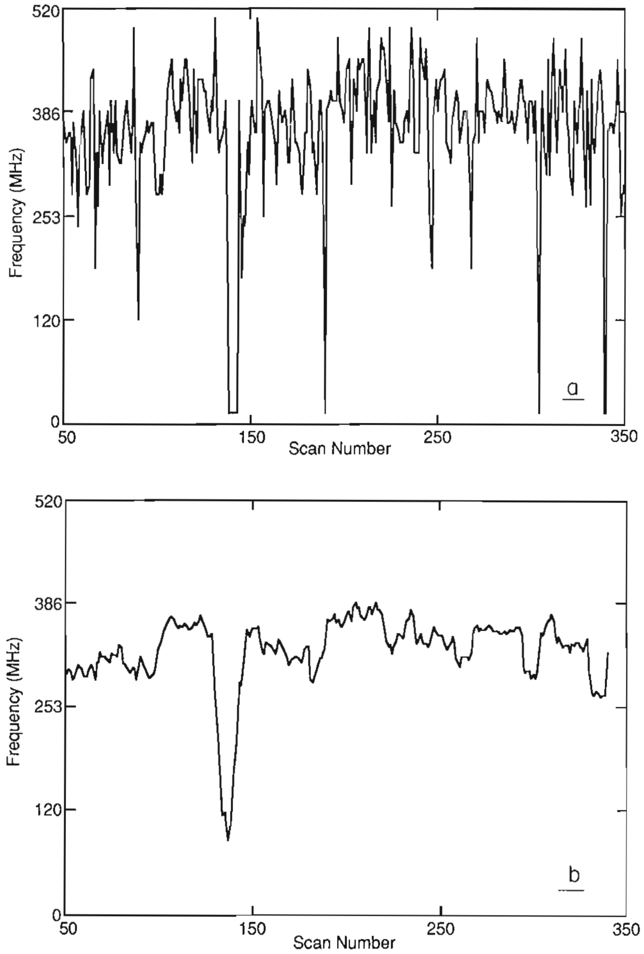

Figure 10. (**a**) Frequency of the strongest wavelet spectral component in the bottom returns for depths 1 to 25 m (300 scans). (**b**) 10 point smoothed version of (a).

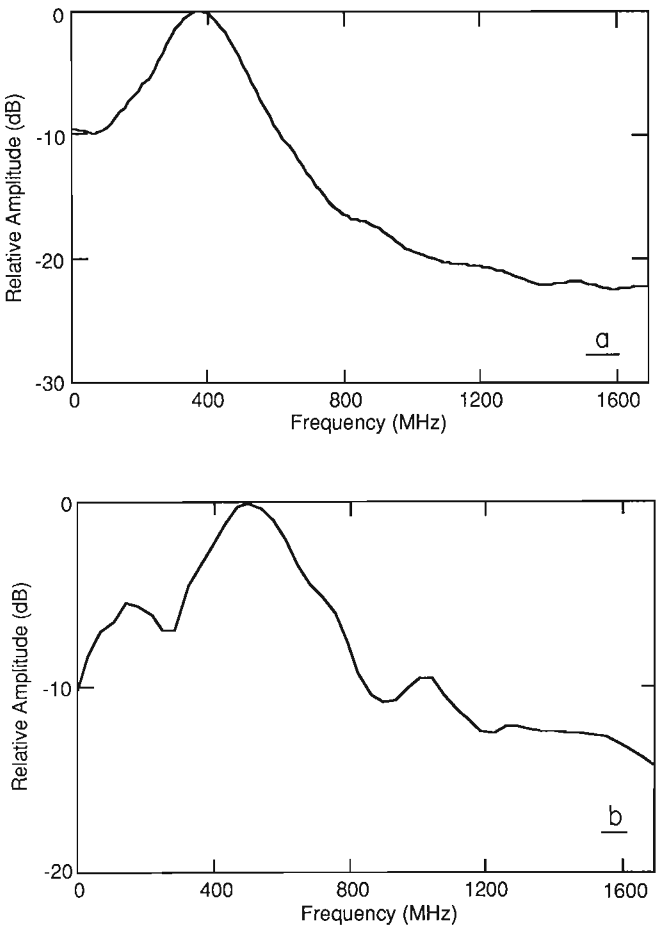

Figure 11. Comparison between the average frequency spectra of Profile *b* (**a**) and that of the incident wavelet in Figure 1 (**b**).

about 0, which is not evident in the data seen for the amplitude peaks in Figure 8. Goodman (1975) reviews past data and reports values between 2 and 5 dB/m at 300-500 MHz for glacier ice between -1 and -20°C.

Figure 9b shows the use of computer techniques to derive travel time and thus, ice depth. The digitized record excluding the first 30 ns, which contained only the direct coupling and helicopter reflections, was divided into two segments: one contained the ice surface reflections, the other the ice bottom reflections. After background removal, the amplitude values within each scan segment were squared and smoothed. The time delays between surface and bottom reflections were then determined by the time separation between the resulting peak values. These values were subsequently processed with a slew rate filter to suppress highly irregular values. Scan 385 marked on Figure 9b is the last scan containing a bottom return. The false decreasing values after scan 385 result from processed noise.

Figures 10 and 11 show some results of Fourier analysis performed on many of the scans. In Figure 10a are plotted the values of the strongest frequency components of 300 scans at depths between 1 and 25 m. Figure 10b is a smoothed version of Figure 10a and shows that the strongest frequency generally varies between 260 and 380 MHz and that there is no significant trend with depth. Figures 11a and b then compare the average power spectrum of the glacier bottom returns with that for reflections from a water surface. Figure 11 reveals that on the average, the strongest frequency of the transmitted wavelet spectrum has dropped from 495 to 380 MHz. The lack of any trend with depth suggests that this loss of frequency content results from bottom scattering, which in any case, is not severe. A centre frequency of 380 MHz would imply that the vertical scale of bottom roughness is less than about 10 cm (i.e., a quarter in situ wavelength) over the spot size of the radar beam (~500 m^2). It is not known if such a smooth ice-bedrock interface is characteristic of this type of glacier.

CONCLUSIONS

Helicopter-borne short pulse radar has been shown to be an effective means of profiling ice depth of shallow glaciers. The coherency of many of the bottom returns and lack of severe scattering in the body of the ice facilitated the depth interpretation. A performance figure improvement of only 10-20 dB would probably have permitted depth profiling to the head of these glaciers.

REFERENCES

Annan, A.P. and Davis, J.L.
1976: Impulse radar sounding in permafrost; Radio Science, v. 16, no. 5, p. 855-864.
Arcone, S.A. and Delaney, A.J.
1987: Airborne river-ice thickness profiling with helicopter-borne UHF short pulse radar; Journal of Glaciology, v. 33, no. 115, p. 330-340.
Arcone, S.A., Delaney, A.J., and Perham, R.E.
1986: Short-Pulse Radar investigation of fresh water ice sheet and brash ice. CRREL Report 86-6, U.S. Army Cold Regions Resesarch and Engineering Laboratory, Hanover, New Hampshire, 10 pages.
Clarke, G.K.C. and Goodman, R.H.
1975: Radio echo soundings and ice-temperature measurements in a surge-type glacier; Journal of Glaciology, v. 14, no. 70, p. 71-78.
Glen, J.W. and Paren, J.G.
1975: The electrical properties of snow and ice; Journal of Glaciology, v. 15, no. 73, p. 15-38.
Goodman, R.H.
1975: Radio echo sounding on temperate glaciers; Journal of Glaciology, v. 14, no. 70, p. 57-69.
Goodman, R.H., Clarke, G.K.C., Jarvis, G.T., Collins, S.G. and Metcalfe, I.R.
1975: Radio echo sounding on temperate glaciers; Journal of Glaciology, v. 14, no. 70, p. 57-69.
Morey, R.M.
1974: Continuous subsurface profiling by impulse radar; in Proceedings, Engineering Foundation Conference on Subsurface Exploration for Underground Excavation and Heavy Construction; American Society of Civil Engineers, New York, p. 213-232.
Narod, B.B. and Clarke, G.K.C.
1980: Airborne UHF radio echo sounding of three Yukon glaciers; Journal of Glaciology, v. 25, no. 91, p. 23-30.

Analysis of radar reflections from asphalt covered bridge deck structures

C. R. Carter[1], T. Chung[1], T. Masliwec[2], and D. G. Manning[2]

Carter, C.R., Chung, T., Masliwec, T., and Manning, D.G., 1992: Analysis of radar reflections from asphalt covered bridge deck structures; in Ground penetrating radar, ed. J. Pilon; Geological Survey of Canada, Paper 90-4, p. 33-40.

Abstract

The more than 9000 bridges in the province of Ontario represent a total investment of many billions of dollars. Unfortunately, because of heavy usage and the severe climate, different forms of deterioration take place, which can cause serious damage. Most of the bridge decks are asphalt covered, which poses a difficulty in detecting the faults because the damage occurs mainly in the concrete or the boundary between the concrete and the asphalt. These faults include debonding where the asphalt lifts off the concrete, scaling where the concrete degenerates into a gravelly matrix, and delamination where a shallow crack develops from the concrete surface down to the layer of reinforcement.

Previous studies have shown that impulse radar is capable of distinguishing between areas of good bridge deck and areas that suffer from one or more different forms of deterioration. One of the main problems in processing the reflected signals, however, is in distinguishing between the different asphalt structures that exist in different bridge decks. These include normal two-lift over concrete, normal two-lift over membrane over concrete, and three-lift over concrete.

In this paper, we present actual waveforms collected from bridge decks with these structures.

Résumé

Les ponts en Ontario, dénombrés à plus de 9000, représentent un investissement total de plusieurs milliards de dollars. Malheureusement, leur forte utilisation et un climat rigoureux engendrent différentes formes de détérioration qui peuvent les endommager gravement. La plupart des ponts sont recouverts d'asphalte rendant difficile la détection des fissures du fait que les dommages se produisent surtout dans le béton ou dans la limite entre le béton et l'asphalte. Ces fissures sont formées par le décollement de l'asphalte du béton, l'écaillement du béton en une matrice graveleuse et la délamination causée par une fissure peu profonde se formant dans la couche de renforcement à partir de la surface du béton.

Des études antérieures ont montré que le radar à impulsion peut faire la distinction entre les zones non endommagées d'un tablier de pont et celles qui ont subi une ou plusieurs formes de détérioration. L'un des principaux problèmes de traitement des signaux réfléchis, cependant, est de différencier les différentes structures d'asphalte que l'on retrouve dans différents tabliers de pont. Il s'agit notamment de deux couches ordinaires sur le béton, deux couches ordinaires sur la membrane déposée sur le béton et une couche triple sur le béton.

Dans le présent document, les formes d'ondes ont été enregistrées dans des tabliers de pont comportant ces structures.

---

[1] Communications Research Laboratory, McMaster University, Hamilton, Ontario L8S 4K1

[2] Ontario Ministry of Transportation and Communications, 1201 Wilson Avenue, Downsview, Ontario M3M 1J8

INTRODUCTION

Impulse radar has been used for a variety of applications such as locating geological structures, detecting underground pipes and cables, and, more recently, evaluating bridge decks. Testing has demonstrated the ability of the impulse radar signal to penetrate the asphalt and to assess a number of important features of the structure (Cantor and Kneeter, 1977, 1982; Alongi et al., 1982; Manning and Holt, 1983; Carter et al., 1986). First of these is the thickness of the asphalt, which is important because it provides a measure of the quantity of asphalt to be removed from a deck being resurfaced.The next factor is the cover over reinforcement, which is the depth of the reinforcing bars below the concrete surface.Another feature to be evaluated is the condition of the membrane, which is a tar based material covering the concrete, which helps prevent water from entering the concrete.Finally, we have the detection of faults in the concrete.

Most bridge decks are asphalt covered, which poses a difficulty in detecting the faults because the damage occurs mainly in the concrete or the boundary between concrete and asphalt. These faults include debonding where the asphalt lifts off the concrete, scaling where the concrete degenerates into a gravelly matrix, and delamination where a shallow crack develops from the concrete surface down to the layer of reinforcement. In all cases, the impulse radar signal reflects from the damaged area producing changes in the reflected waveform that differ from undamaged deck.

The use of impulse radar for the analysis of bridge decks in Ontario began in 1984 with a simple system housed in a van (Fig. 1) and called "Deck Assessment by Radar and Technology" (DART), comprising the radar, a fifth wheel for distance measurement and a multichannel instrumentation tape recorder for recording radar waveforms, radar sync, and fifth wheel pulses. The radar is a model PS-24 impulse radar purchased from Penetradar Corporation of Niagara Falls, New York. This radar has a pulse width of approximately 1 ns and a repetition rate of 5 million pulses per second. The radar is monostatic with the antenna design being based on the constant flare angle, variable width, open horn. The reflected signal is sampled much like in a sampling oscilloscope, using the sliding gate technique, and averaged producing an output voltage pulse waveform of approximately 1 ms in duration (Fig. 2). This waveform is obtained by positioning the antenna directly over a thin aluminum plate placed on the asphalt surface and obtaining the reflection. Peak A is a measure of the electric field at the asphalt surface and provides a calibration measurement for evaluating the dielectric constant of the asphalt, which is needed for the asphalt thickness measurement.

Figure 1. DART system and the van.

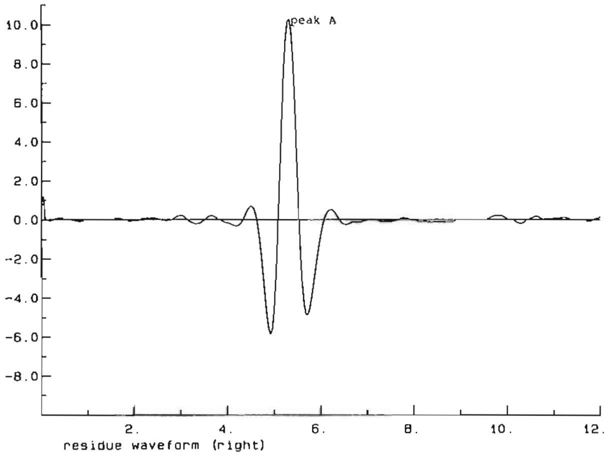

Figure 2. Impulse radar waveform.

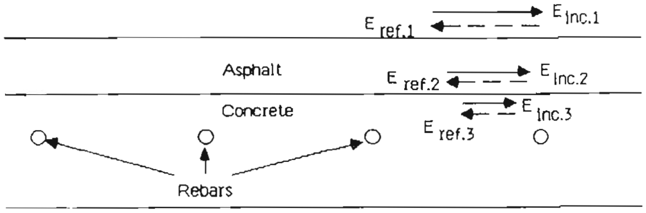

Figure 3. Transmission and reflection of the radar signal from the bridge deck structure.

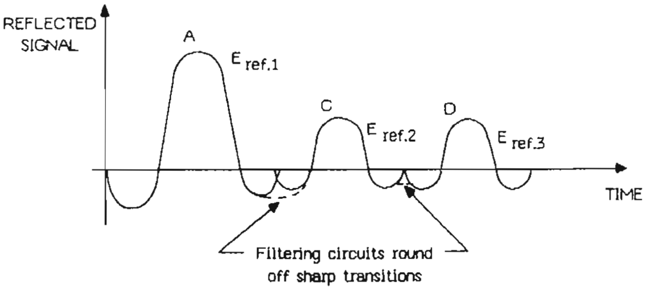

Figure 4. Signal received from good bridge deck structure.

WAVEFORM ANALYSIS

It is possible to gain some insight as to the type of waveforms to be expected by simply considering the transmission and reflection of waves from the various layers of asphalt, concrete and rebars. For example, consider the structure illustrated in Figure 3 of asphalt over concrete that contains rebars. The incident wave falling on the air-asphalt interface is partially reflected with a reflection coefficient of typically 0.33 (assuming an asphalt dielectric constant of 4) and partially transmitted with the corresponding transmission coefficient of 0.67. The wave proceeds through the asphalt, usually between 25 and 150 mm in thickness, to the asphalt-concrete interface where a second reflection takes place. Because the dielelectric constant of concrete is usually about 10, the reflection coefficient is 0.23 and the transmission coefficient is 0.77, which is quite high. Finally, the wave reflects off the rebars (normally 25-75 mm below the surface of the concrete).

In the resulting waveforms (Fig. 4) we see that the reflections from the air-asphalt interface, the asphalt-concrete interface, and the rebars all have the same orientation, namely, 180° out of phase with the incident electric field. Adding these three waveforms leads to the composite waveform shown, which has an initial peak at A from the air-asphalt interface, a second peak at C from the asphalt-concrete interface, and a third peak at D from the rebars. Note that the time delay from A to C is a measure of

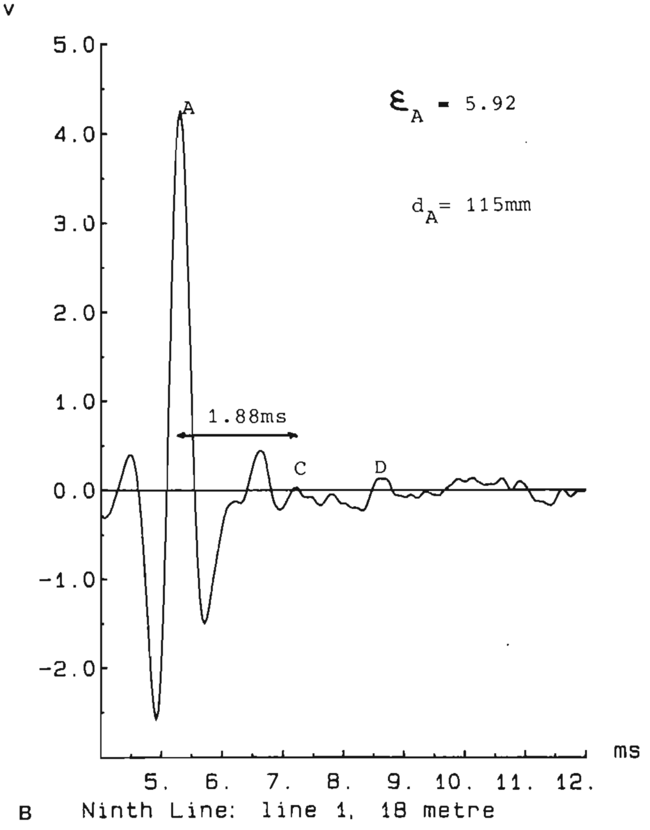

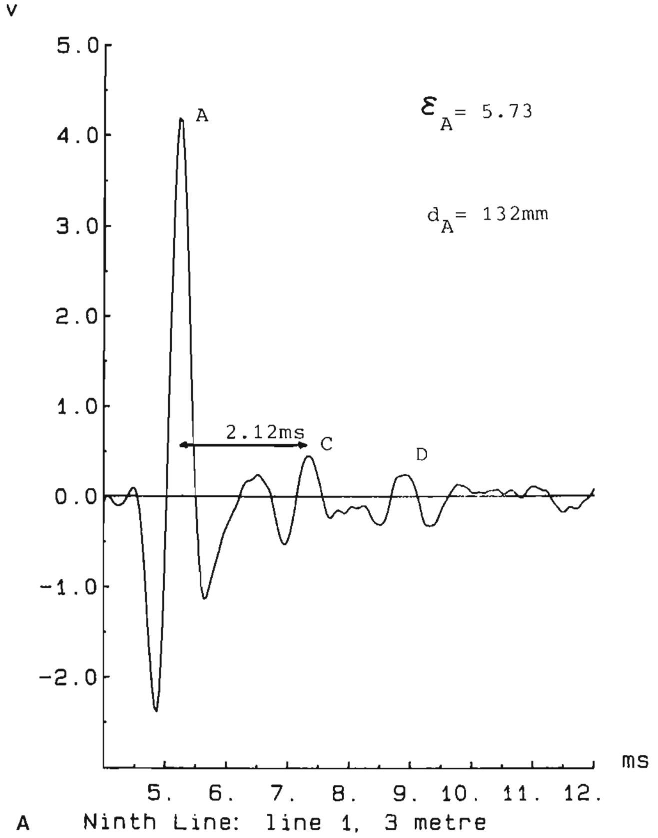

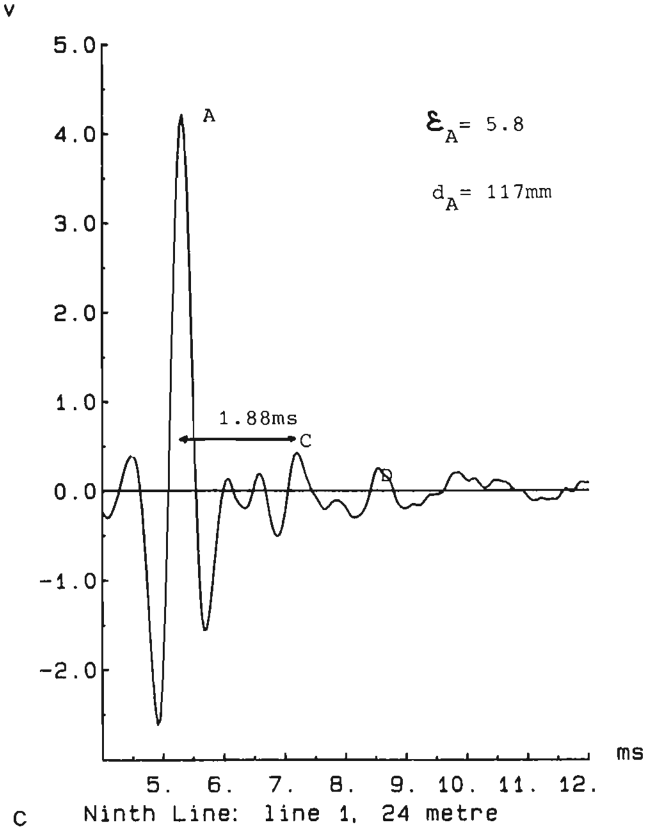

Figure 5. Ninth line bridge waveform from **A**. line 1 at 3 m; **B**. line 1 at 18 m; **C**. line 1 at 24 m.

the asphalt thickness and the time delay between C and D is a measure of the thickness of concrete over rebars. Although this explanation appears to be simplistic, it does apply to a number of cases found in actual practice as shown here.

FIELD EVALUATIONS

We evaluated in the field three bridge decks each having a different structure as follows: 1) Ninth Line bridge in Oakville, which is a relatively new deck in excellent condition having two layers of asphalt over rubber membrane and a well defined membrane-concrete interface; 2) Winston Churchill overpass across Highway 401 west of Toronto International Airport, which is a deck in poor condition with two layers of asphalt and little or no membrane material; and 3) Bloor Street Viaduct in Toronto, which is a deck showing some damage with three layers of asphalt and no membrane.

NINTH LINE DATA

A site visit to Ninth Line, Oakville, near 403 Highway was conducted in mid-May, 1987. Eight different lines were recorded. The bridge deck should be in good condition because it was built just several years ago. It is also known that beneath the asphalt surface lies a layer of waterproofing membrane. The purpose of processing Ninth Line data is to ensure that the expected signals from good deck are found in practice.

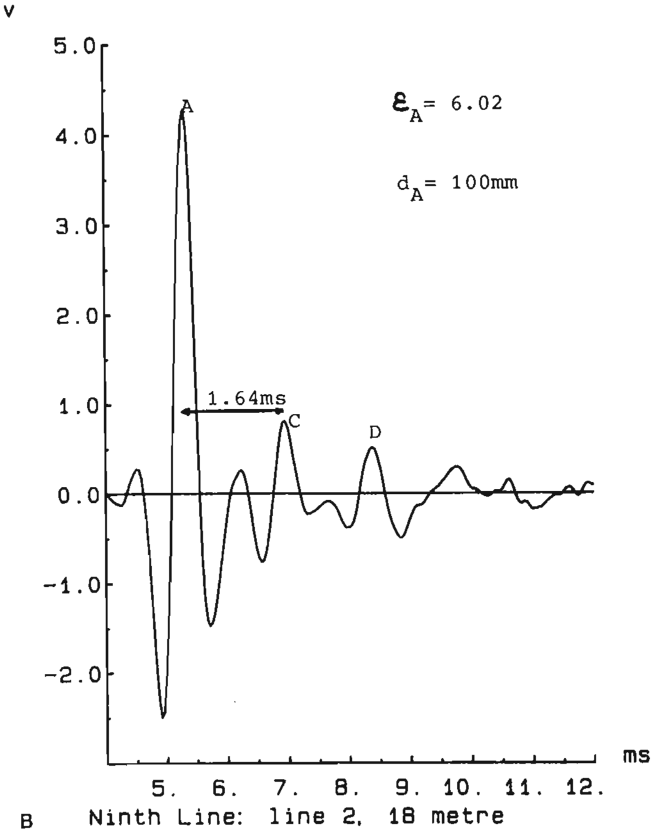

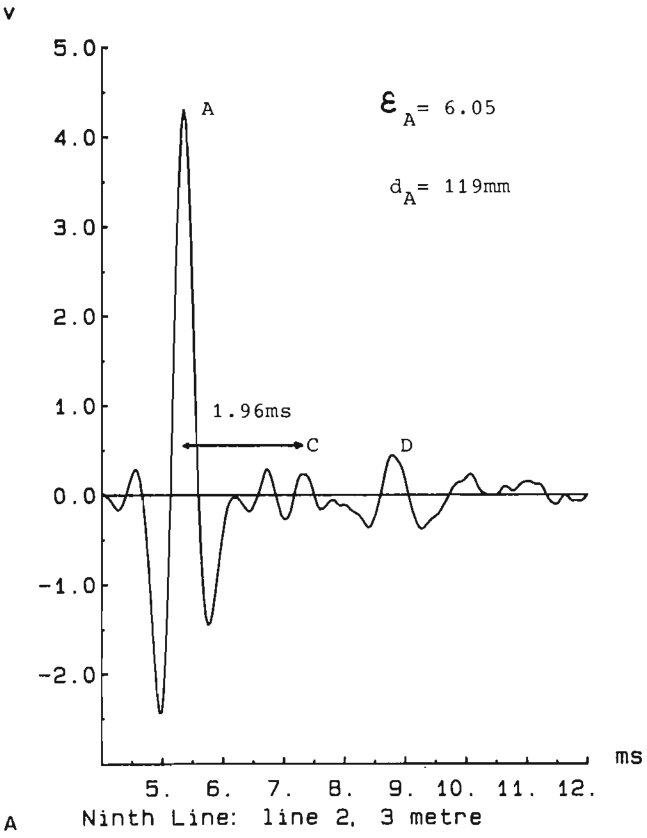

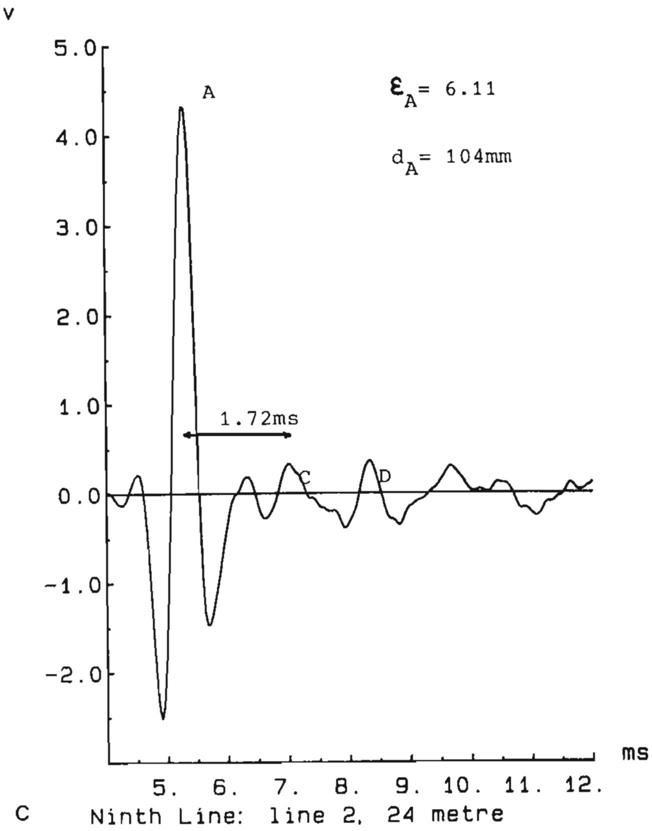

Figure 6. Ninth line bridge waveform from **A.** line 2 at 3 m; **B.** line 2 at 18 m; **C.** line 2 at 24 m.

Table 1. Actual asphalt thickness vs impulse radar results

	Line 1			Line 2		
Spot (m)	Survey (mm)	Radar (mm)	Error (%)	Survey (mm)	Radar (mm)	Error (%)
3	115	134	16.52	112	119	6.25
18	102	113	10.78	105	100	4.76
24	107	118	10.28	100	99	1.00

Table 2. Survey of concrete cover vs impulse radar results

	Line 1		Line 5		Line 8	
Spot (m)	Survey (mm)	Radar (mm)	Survey (mm)	Radar (mm)	Survey (mm)	Radar (mm)
1	82	66	120	62	72	58
3	80	80	82	104	64	78
6	90	81	87	103	63	72
9	82	91	88	108	80	68

Asphalt thickness

We measured the asphalt thickness (time delay between points A and C) at selected locations by piercing through the asphalt surface with a spike to the concrete surface. Three spots on each of lines 1 and 2 were chosen, and the measured thicknesses at the 3, 18, and 24 m locations are given in Table 1.

Sample waveforms from the impulse radar at these locations are now presented. First, however, it is necessary to calibrate the system using the flat plate reflection. The amplitude was found to be 9.95 V. Figures 5 and 6 provide waveforms corresponding to the 3, 18, and 24 m locations along lines 1 and 2, respectively. The peaks labelled A, C, and D are the interface boundaries of air-asphalt, asphalt-concrete, and concrete-rebars, respectively. The calculated asphalt thicknesses related to each of the waveforms are given in Table 1.

The comparison shows that the average error was about 12.5% for line 1 and about 4% for line 2 in measuring the asphalt thickness. A source of error that has not yet been eliminated is the difference in dielectric constant between the two layers of asphalt. Because the dielectric constant is determined only for the top layer, any change will affect the measurement of the thickness of the second layer.

Cover over reinforcement

A survey of the concrete cover measurement of Ninth Line has been obtained from Ministry of Transportation and Communications. The survey provided data for the centre line (line 5) and the two outside lines 1 m away from both barrier walls (lines 1 and 8). The measurements are given at 3 m intervals. Table 2 compares the survey results with the computer findings for the first 9 m of bridge deck.

On average, we found a 13% error existed in calculating the concrete cover for lines 1 and 8. However, the error increased to 25% for line 5.

Overall bridge deck conditions

The waveforms of Figure 5 and 6 are typical for most of the Ninth Line bridge deck. Effects of deterioration were found at only a few isolated places.

WINSTON CHURCHILL DATA

Data for the Winston Churchill overpass at Highway 401 were collected in the mid-May 1987. The bridge deck spans 76 m and the surface is strictly asphalt covered with no waterproofing membrane. Traffic travels north or south in a single lane each way. Visual inspection showed numerous locations where damaged asphalt and exposed concrete could be seen. Also in some areas, we noted rusted reinforcement bars.

We recorded three lines on the travelling portion of each lane and one line along the east curb.

Figure 7A provides a set of 20 consecutive waveforms spaced at 20 cm intervals along line 2 between 17 and 21 m; Figure 7B gives the average of the 20 waveforms. At the site, we noted that the asphalt and concrete cover over reinforcement are relatively thin. Identifying peaks A, C, and D in Figure 7B, we see that this observation correlates with impulse radar waveforms.

Asphalt thickness

Having obtained the value of the dielectric constant of asphalt, we estimated the thickness of asphalt by measuring the time delay between the reflection peaks at A and C. The averaged magnitude of surface echo from the waveforms was about 4.12 V and the metal plate reflection was 9.99 V. The dielectric constant of asphalt was found to be 5.77, which gave a calculated depth of asphalt of 60 mm. This result correlated well with the observed value of 55 mm.

Cover over reinforcement

The next positive peak (peak D) after the asphalt-concrete interface peak is believed to be the reflection from the rebars. Using a dielectric constant for concrete of 8, we deduced the cover over reinforcement to be 42 mm, which corresponds well with the observed value of 35 mm.

Overall bridge deck conditions

The asphalt surface of two areas was removed and it was found that the concrete was badly disintegrated, which indicates scaling. Figure 8 compares a normal reflection (A) with that from a scaled area (B) showing that the peak at C is far greater when scaling occurs. The remainder of the bridge was found to be in poor condition.

BLOOR STREET VIADUCT DATA

Data from Bloor Street Viaduct were collected in late-May, 1987. The bridge deck covers a total length of 447 m and has three driving lanes for each direction (east-west) of

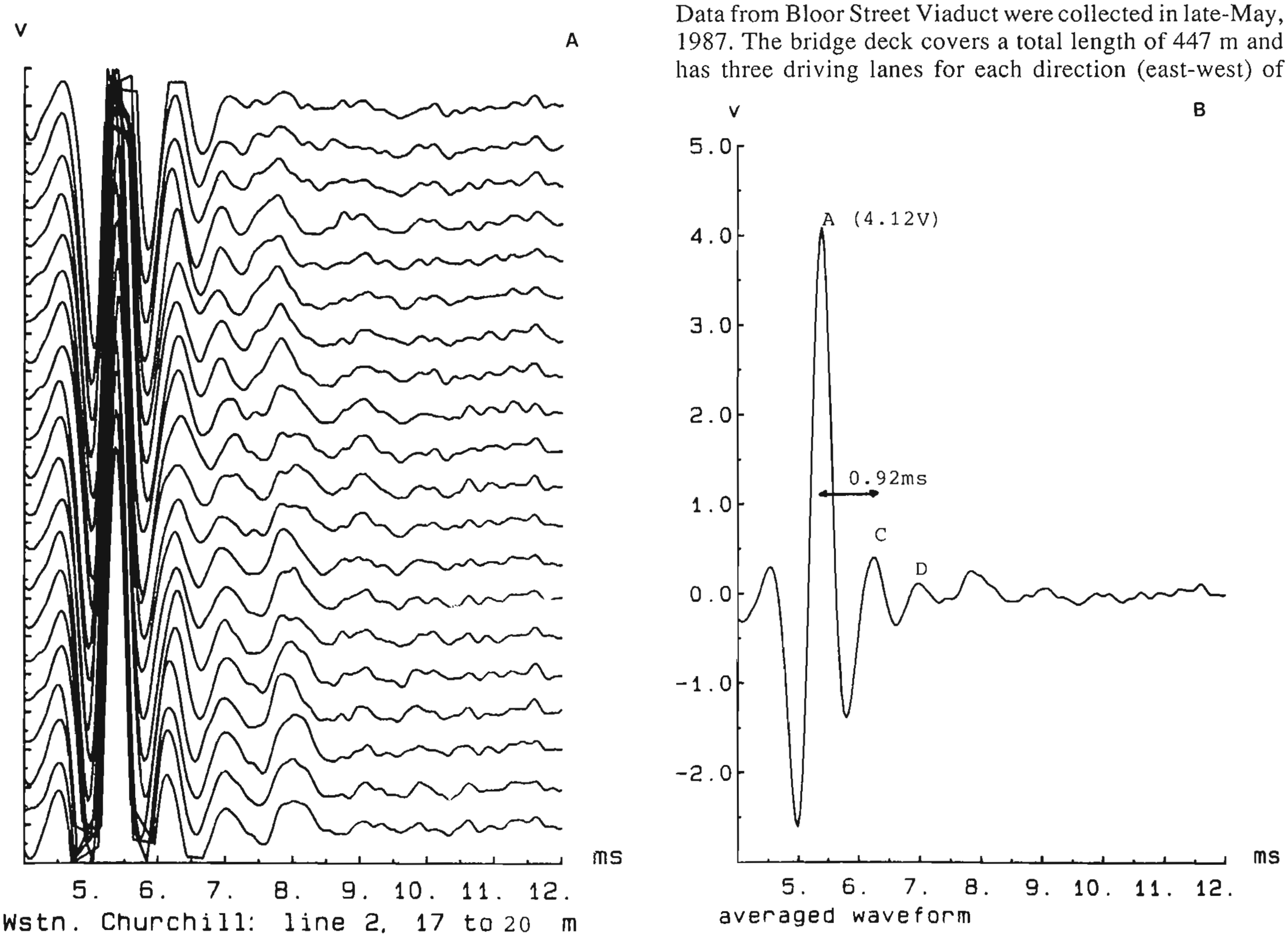

Figure 7. A. Waveform from Winston Churchill overpass line 2 between 17 and 20 m; **B.** Averaged waveform from 7A.

traffic. We recorded six lines on each side covering the two outermost lanes each way. We also noted that the bridge deck has numerous metal joints beneath the asphalt surface.

Asphalt thickness

A core sample (Fig. 9) was obtained from line 3 at about the 180 m location. The asphalt layer is actually composed of three different layers of material. The composition of the first layer is mainly tar and fine sand. The second layer contains tar, gravel, and stone. The bottom layer also contains tar, gravel, and stone but of a smaller size than the middle layer. The individual layers of asphalt from top to bottom have thicknesses of 26, 44, and 60 mm, respectively, with the overall thickness being 130 mm.

Figure 10 provides the radar signature from the core sample location. Except for the surface echo reflection, direct interpretation of the reflections, namely, peaks 1, 2, and 3, would be rather difficult unless it were known that three layers of asphalt exist. However, with the information we obtained from the core sample, we located the asphalt-concrete interface layer at peak 3. Using the time delay between peaks A and C, we obtained a measured value of 157 mm for an error of 20%.

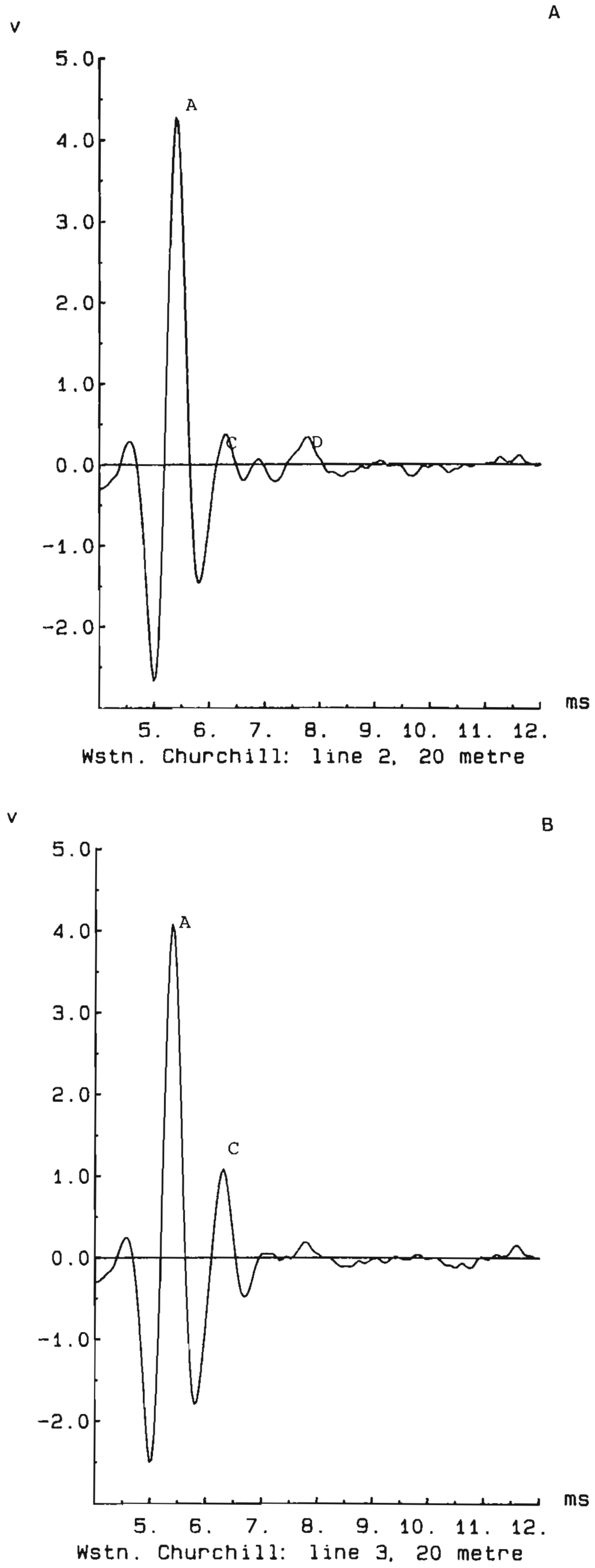

Figure 8. **A**. good structure; **B**. scaled structure.

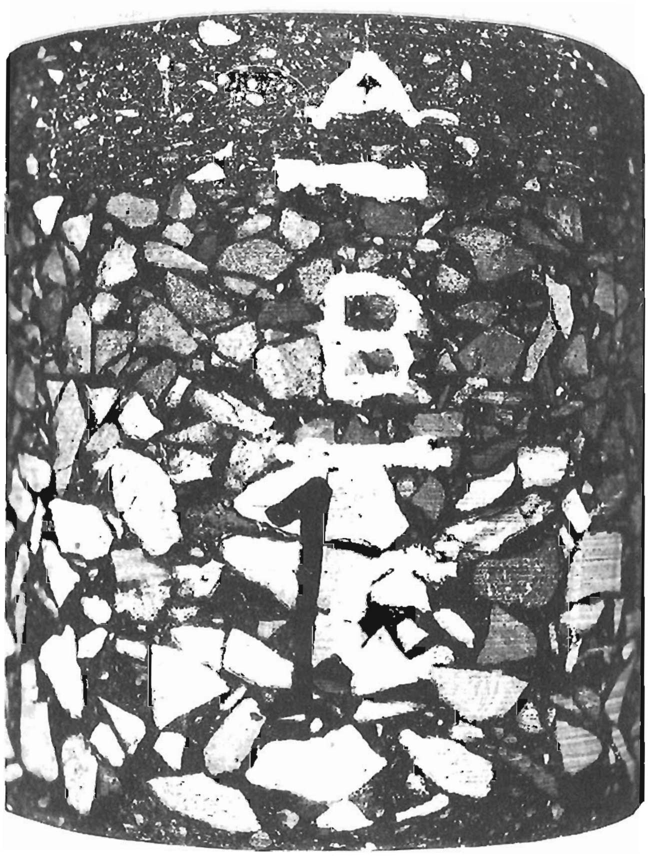

Figure 9. Asphalt core sample from Bloor Street Viaduct.

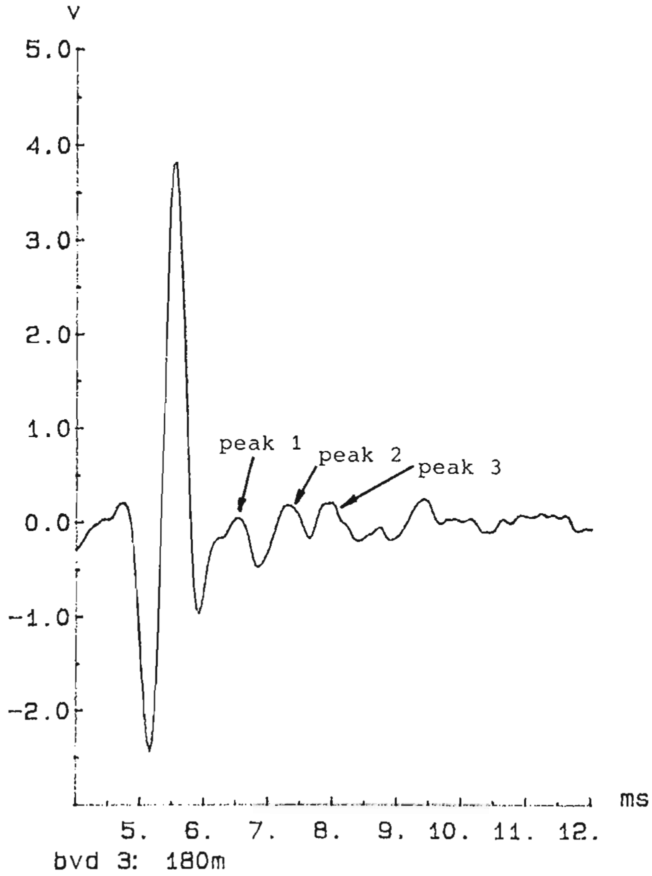

Figure 10. Radar signature from the core sample.

Cover over reinforcement

Having determined the asphalt-concrete interface peak, the next reflection we wanted to identify was the reflection from rebars. By referring to Figure 10, we noted a well defined characteristic (W) after the asphalt-concrete interface. We identified the rebar reflection at about 9.5 ms and estimated the concrete cover to be 78 mm.

CONCLUSIONS

Impulse radar has certain advantages over more conventional techniques in the evaluation of bridge decks. The main advantages are that the method is nondestructive and a large amount of data can be collected in a relatively short time. However, the interpretation of the waveforms requires a considerable amount of effort because there are many different types of bridge deck. Computer analysis appears to be reasonably accurate once the structure is known.

REFERENCES

Alongi, A.V. et al.
1982: Concrete evaluation by radar theoretical analysis; Transportation Research Record, v. 853, p. 31-37.

Cantor, T.R. and Kneeter, C.P.
1977: Radar and acoustic emission applied to the study of bridge decks, suspension cables and a masonary tunnel;Port Authority of New York and New Jersey, Engineering Department, Research and Development Division, Report No. 77-13.
1982: Radar as applied to evaluation of bridge decks; Transportation Research Record, v. 853, p. 37-42.

Carter, C.R., Chung, T., Holt, F.B., and Manning, D.G.
1986: An automated signal processing system for the signature analysis of radar waveforms from bridge decks; Canadian Electrical Engineering Journal, v. 2, no. 3, p. 128-137.

Manning, D.G. and Holt, F.B.
1983: Detecting deterioration in asphalt-covered bridge decks; Transportation Research Record, v. 899, p. 10-20.

Ground penetrating radar investigations of massive ground ice

S.R. Dallimore[1] and J.L. Davis[2]

Dallimore, S.R. and Davis, J.L., 1992: Ground penetrating radar investigations of massive ground ice; in Ground penetrating radar, ed. J. Pilon; Geological Survey of Canada, Paper 90-4, p. 41-48.

Abstract

A series of field trials have been carried out with newly developed ground penetrating radar systems to evaluate their use for mapping buried ground ice and near surface geology in continuous permafrost. In total, 17.5 line kilometres of surveys were conducted at three sites near Tuktoyaktuk, N.W.T. A modified Geophysical Survey System Inc. radar operating at 100 MHz (pulseEKKO I) was used for continuous near surface profiling, and a 30 MHz digital radar (pulseEKKO II) was used for detailed follow up surveys.

Correlating with subsurface data from geotechnical boreholes proved that the radar instruments used in the surveys were extremely useful for delineating massive ice and subsurface geology in a variety of terrains. In areas underlain by glaciofluvial sediments or with a thin cover of glacial till, continuous reflectors were consistently observed in the range of 100-200 ns (two-way travel time) for the pulseEKKO I and in the range of 200-400 ns for the pulseEKKO II. In areas of ideal signal penetration, reflections were observed to more than 800 ns. The two systems proved complimentary for interpreting subsurface information, enabling delineation of the upper and lower contact of thick massive ice bodies and geological contacts such as glaciofluvial channels. In areas of thick glacial till, the signal penetration was more limited and interpretation of data more difficult; however, continuous reflections to 500 ns were observed even with till thicknesses of 10 m.

Résumé

Une série d'essais sur le terrain ont été réalisés avec de nouveaux géoradars pour déterminer leur utilité à la cartographie de la glace dans le sol et de la géologie à faible profondeur dans le pergélisol continu. À trois endroits près de Tuktoyaktuk (T.N.-O.), on a effectué des levés sur 17,5 kilomètres linéaires au total. Un radar modifié de la Geophysical Survey System Inc. fonctionnant à 100 MHz (pulseEKKO I) a servi à produire des profils continus à faible profondeur, et un radar numérique de 30 MHz (pulseEkko II) pour effectuer des levés de suivi détaillés.

La corrélation des données radar avec les données de sondage géotechniques montre que les radars utilisés dans les levés ont été très utiles pour délimiter la glace massive et la géologie de subsurface dans divers types de terrains. Dans les zones reposant sur des sédiments fluvioglaciaires et recouvertes d'une mince couche de till, on a observé des réflecteurs continus dans l'intervalle de 100 à 200 ns (temps de parcours double) dans le cas du radar pulseEKKO I et dans l'intervalle de 200 à 400 ns dans le cas du radar pulseEKKO II. Dans les zones où la pénétration du signal est idéale, on a observé des réflexions à plus de 800 ns. Les deux systèmes s'avèrent complémentaires pour interpréter les données de subsurface; elles permettent de délimiter les contacts supérieur et inférieur des massifs de glace épais et les contacts géologiques comme les chenaux fluvioglaciaires. Dans les zones de till épais, la pénétration du signal a été plus limitée et l'interprétation des données plus difficile; cependant, des réflexions pouvant atteindre 500 ns ont été observées même lorsque le till mesurait 10 m d'épaisseur.

---

[1] Geological Survey of Canada, Terrain Sciences Division, 601 Booth Street, Ottawa, Ontario K1A 0E8

[2] Formerly A-Cubed Inc., 5566 Tomken Road, Mississauga, Ontario L4W 1P4 now at Canpolar Inc., 265 Rimrock Road, Toronto, Ontario M3J 3C6

INTRODUCTION

In many permafrost areas the presence of massive ground ice poses a significant geological hazard for development related activities such as pipeline construction or extraction of granular materials. Ground ice bodies vary substantially in sediment content and ice petrology depending on their origin and the extent of postdepositional deformation. Detailed drilling studies and mapping of ground ice bodies truncated by erosion have shown that they may have complex configurations with irregular upper and lower contacts. Because permafrost soils generally exhibit low electrical loss, the ground penetrating radar is potentially a practical tool for extending borehole information and establishing the character of ground ice bodies and associated sediments.

This paper presents the results of a series of field trials conducted to evaluate newly developed ground penetrating radar systems for mapping buried ground ice and near surface geology in continuous permafrost. Fieldwork was carried out in the Tuktoyaktuk coastal area of the Canadian Beaufort Sea (Fig. 1). The trials were conducted over a variety of terrains and landform to establish the utility of the radar technology at a field scale.

METHODOLOGY

Geological applications of ground penetrating radar have been well documented in the literature and are described in detail by others contributing to this volume. The radar technique is based on the measurement of the two-way travel time of a transmitted electromagnetic wavelet, which is reflected from various surfaces within the ground. The main consideration in permafrost materials is related to changes in electrical properties that occur at temperatures below freezing. In general, frozen soils are more resistive than unfrozen materials, with the actual velocity of propagation of an electromagnetic wavelet being effected substantially by the unfrozen water content (Annan and Davis, 1978; Patterson and Smith, 1981) and ice content (Kovacs and Morey, 1978, 1985). These properties are material and temperature dependant. Uncertainty in the velocity of wave propagation through in situ materials requires careful interpretation of radar data. Correlation with borehole data and determinations of the velocity structure in the ground with common depth point (CDP) soundings and wide angle reflection and refraction (WARR) soundings are essential.

Two radar systems with different system sensitivities and frequencies were used in the study to map near surface soils (Dallimore and Davis, 1987). The A-Cubed, pulseEKKO I radar, operating at a frequency of 100 MHz, was used for high resolution, continuous, near surface profiling. This extensively modified Geophysical Survey System Inc.

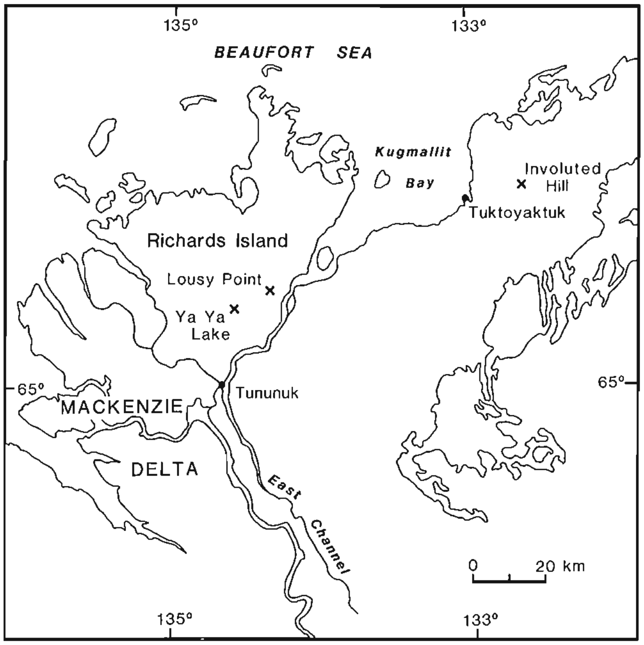

GSC

Figure 1. Location of ground probing radar surveys near Tuktoyaktuk.

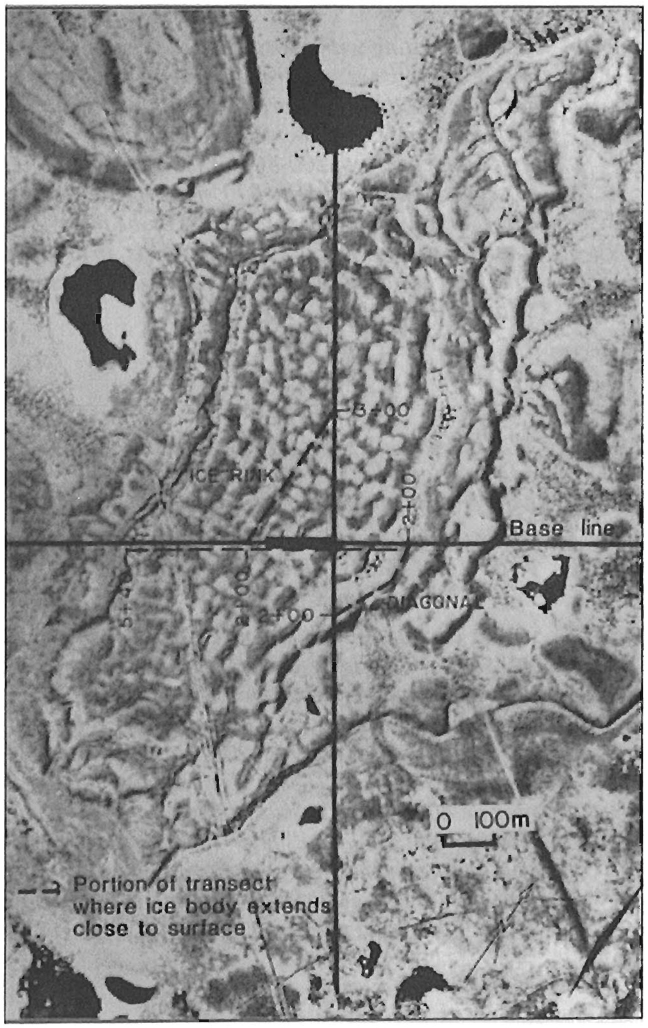

Figure 2. Involuted Hill test site showing location of radar surveys.

(GSSI) radar was towed slowly (4-6 km/h) on a toboggan behind a snowmobile. The pulseEKKO II radar was designed and constructed by A-Cubed Inc. to operate at the lower frequency of 30 MHz, with similar resolution to the pulseEKKO I system. The pulseEKKO II is a digital radar; it is operated to maximum advantage in a step mode where the signal to noise ratio is improved by averaging many traces at one location before moving to the next position. A step spacing of 4 m was used for most of the surveys reported in this paper.

FIELD WORK

In total, 12.5 km of pulseEKKO I profiling and 5.0 km of pulseEKKO II profiling were conducted along transects at two sites on Richards Island and one site near the village of Tuktoyaktuk on Tuktoyaktuk Peninsula (Fig. 1). The sites were chosen to test the radar equipment in winter field conditions and to establish the performance of the radar in different geological environments. The fieldwork was

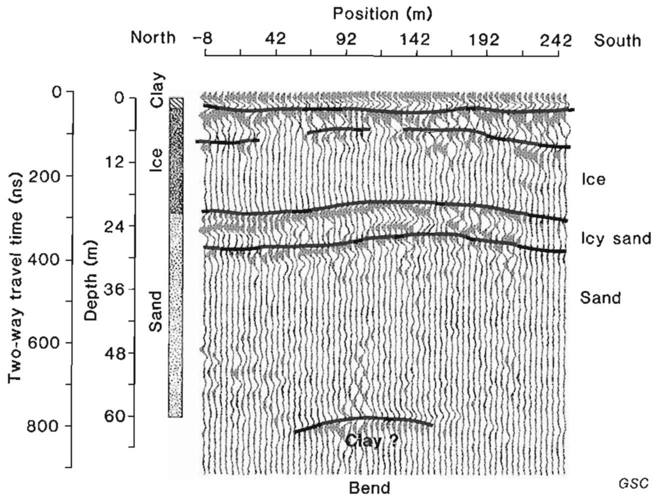

Figure 3. PulseEKKO II data along Involuted Hill diagonal showing radar penetration in areas of thin clay till cover.

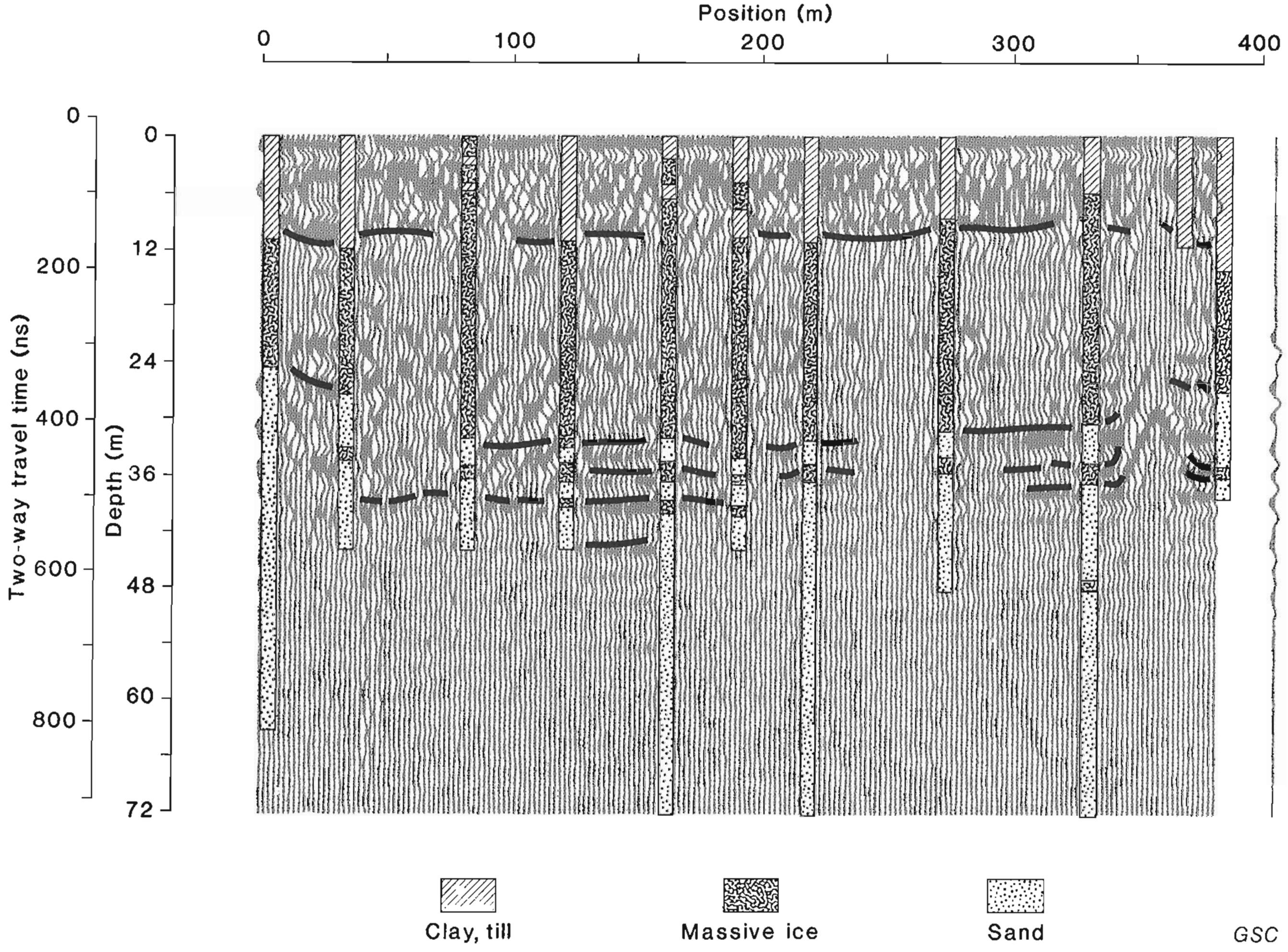

Figure 4. PulseEKKO II data along Involuted Hill main line showing radar penetration in areas of thick clay till cover.

conducted during late winter when snowcover over the tundra provided access for snowmobile transportation. A field drilling program was also carried out at the Richards Island sites to provide ground verification for the radar interpretations.

RESULTS

"Involuted Hill"

"Involuted Hill" (informal name) lies about 15 km northeast of Tuktoyaktuk (Fig. 1). The hill, considered typical of many of the uplands areas in this part of Tuktoyaktuk Peninsula, has a characteristic wrinkled appearance on aerial photographs (Mackay, 1963). The site was established as a test site for various geophysical and drilling investigations carried out during the early seventies by the Geological Survey of Canada. During that time more than 50 boreholes were drilled through the hill to establish the stratigraphy and provide ground verification for geophysical surveys (Annan, 1976; Davis et al., 1976). The drilling investigations established that the main part of the hill consists of a 2-15 m thick mantle of fine grained clay till over a 10-20 m thick body of massive ground ice. A thick unit of sand occurs beneath the ice. The clay till and the ice vary in thickness, with the ice extending close to the surface in some places.

Figure 5. Location of radar transects at Ya Ya Lake.

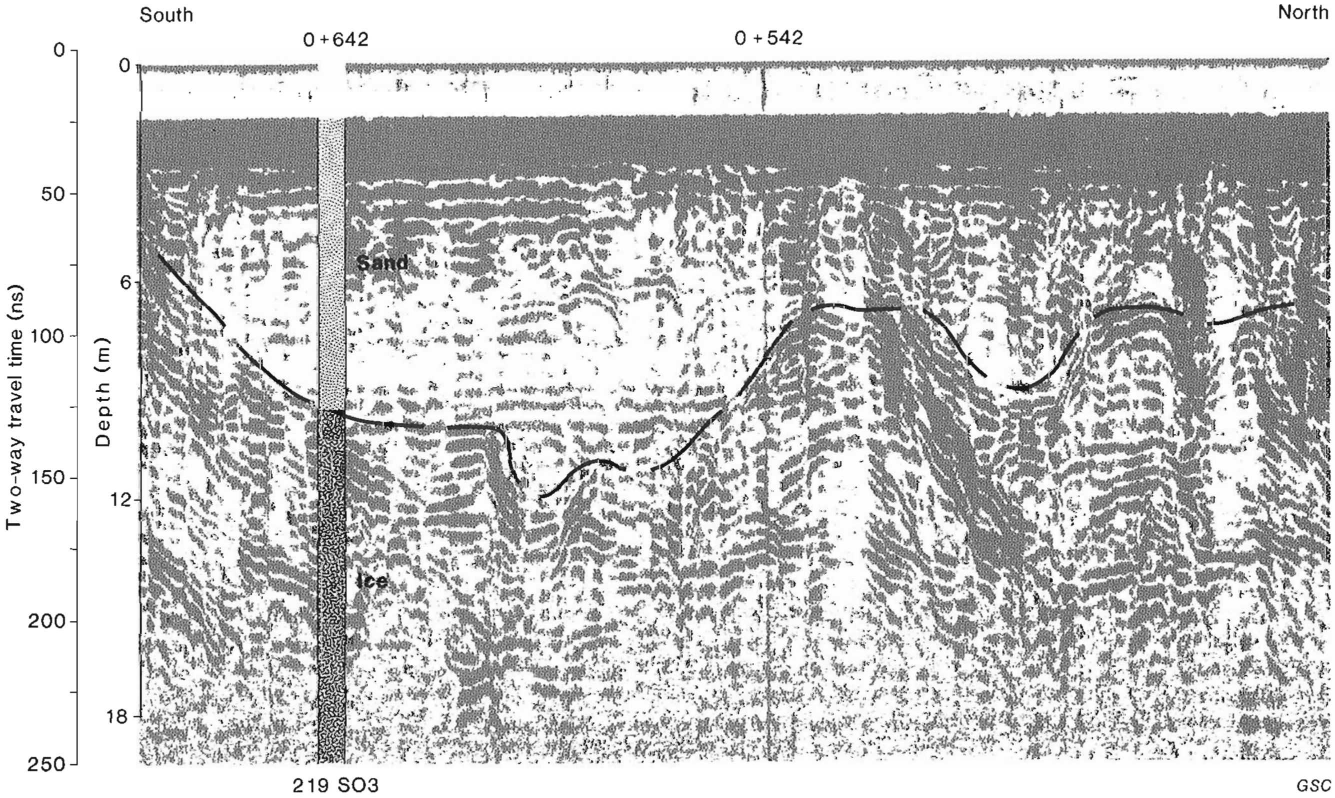

Figure 6. PulseEKKO I data along main transect at Ya Ya Lake showing near-surface channels in glaciofluvial sediments.

Ground penetrating radar studies carried out in the early seventies showed that signal penetration was very limited along the main transect where the clay till was more than a few metres thick (Davis et al., 1976). For the most part deep echoes (>100 ns) were only detected where the ice body came close to the surface and acted as a transparent window for radar transmission (Fig. 2). In these areas reflections were detected to about 300 ns two-way travel time. These deep reflections were interpreted as delineating the contact between the massive ice body and the sand.

The Involuted Hill site was revisited during the 1986 field work to compare the capabilities of the newer generation radars with those used previously. Soundings were run along the old base line and along areas of thin till cover where deeper reflections were detected during the early surveys. The pulseEKKO I radar showed similar depth penetration but substantially better resolution and less system noise than the early GSSI radar used in the original survey. However, as observed in the original survey signal penetration was restricted in the areas of thick till cover along the main line.

The pulseEKKO II radar detected deep reflections at nearly all locations where it was tested on the hill. In areas where the massive ice extended close to the surface, reflectors to 800 ns two-way travel time were found where the pulseEKKO I detected reflectors at a maximum of 400 ns travel time (Fig. 3). These data are displayed with a negative variable area shading and a time gain function applied with depth. The depth scale, which is also shown on the figure, has been estimated assuming a constant velocity of 0.14 m/ns. Correlation with borehole data suggests that the reflections shown in Figure 3 may represent the lower contact of the massive ice. A deep reflector at 800 ns may represent a lower clay encountered in a deep borehole drilled along the main line. The pulseEKKO II was measured to have 40 dB greater system performance than the pulseEKKO I.

In the less favourable terrain along the main transect, reflections detected at 550 ns indicate that radar signals were able to penetrate the thick clay till mantle. Figure 4 presents the radar and drilling data along a 400 m long portion of the main line. Correlation with the nine boreholes shown on the figure indicate that the radar is able to delineate the bottom of the till layer and the lower contact with the sand. The multiple reflections near the lower contact of the massive ice correlates with thin ice bands in the upper few metres of the sand.

"Ya Ya Lake"

The radar surveys near "Ya Ya Lake" (Fig. 1) on Richards Island were carried out over an ice-contact ridge composed of glaciofluvial sand and gravel. High quality granular resources in this area are rare. Extraction of gravel is often limited by ground ice, which occurs either as lenses within the gravel or as discrete bodies of ground ice at depth. This study was carried out in conjunction with a granular investigation being conducted by Indian and Northern Affairs (EBA Engineering Consultants Ltd., 1986) along two transects across the ridge (Fig. 5).

The results from the pulseEKKO I and the pulseEKKO II surveys suggest that radar is an ideal tool for investigating the stratigraphy of coarse grained sediments. Penetration with the pulseEKKO I was generally limited to the 100-200 ns range; however, this radar was very effective in detecting both near surface changes in geology and the upper contact of a massive ice body underlying a variable thickness of sand and gravel. Although drilling on the ridge was limited, it appears that the pulseEKKO 1 detected channel features in the ice (Fig. 6). These channels may be associated with coarser glaciofluvial sediments indicating that radar surveys may be useful in detailed delineation of granular resources.

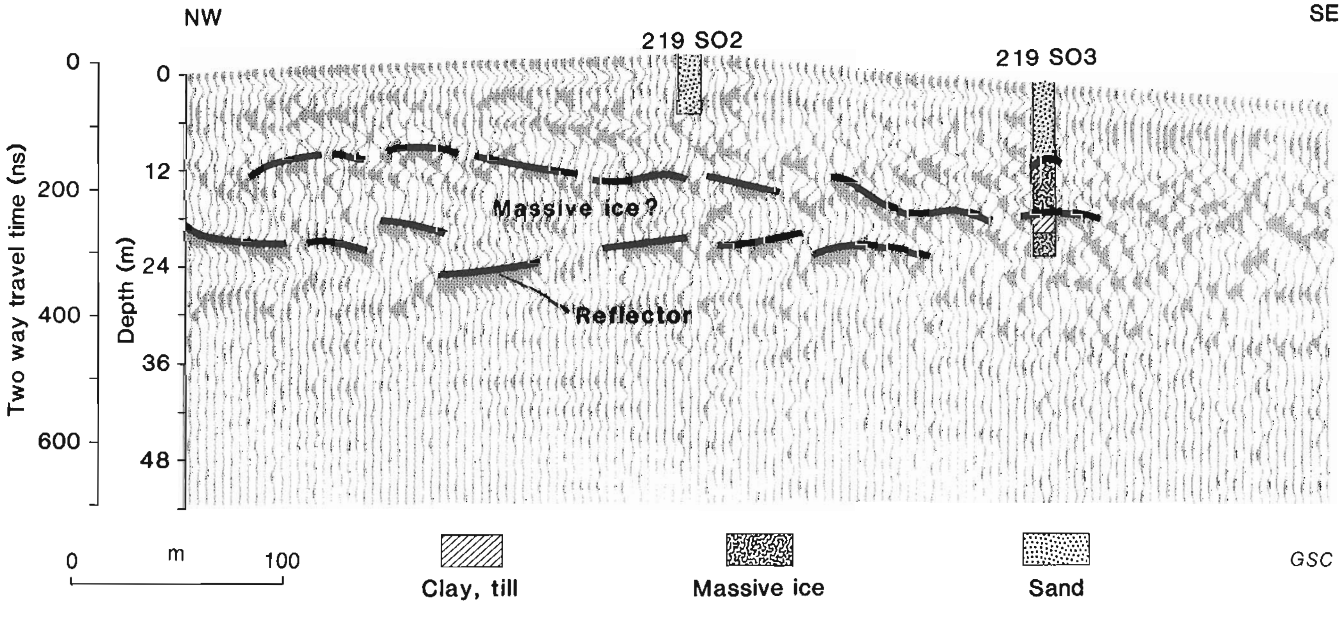

Figure 7. PulseEKKO II data along main transect at Ya Ya Lake.

The pulseEKKO II data suggest that the stratigraphy of the ridge is complex with numerous strong reflectors in the 200-450 ns range. Correlation with drill hole data suggest that some of this layering represents bands of clay till within the massive ice body that underlies the ridge (Fig. 7). Dallimore and Wolfe (1988) discussed the origin of the ice associated with the glaciofluvial deposit at Ya Ya Lake based on stratigraphic and isotopic data. They suggested that the ground ice is most likely of glacial origin. If their interpretation is correct the numerous reflectors within the ice body probably represent englacial and basal debris bands commonly found in active glacial ice.

"Lousy Point"

An 8 km long survey was conducted along a transect which started on the east channel of Mackenzie River near "Lousy Point" (Fig. 8). This transect is in the vicinity of the routes of several overland pipelines, which have been proposed to cross Richard's Island. The transect was chosen to cross a variety of terrain types to test the versatility of the ground penetrating radar systems in different surficial sediments. The transect began on the modern flood plain of Mackenzie River and then passed over an upland area underlain by glaciofluvial outwash material. Low areas along the transect are covered by variable thicknesses of glacial till and lacustrine sediments. The west part of the line crossed an upland area of glaciofluvial sediments. A gravity survey conducted by Rampton and Walcott (1974) suggested that much of the west part of the line is underlain by up to 25 m of massive ground ice.

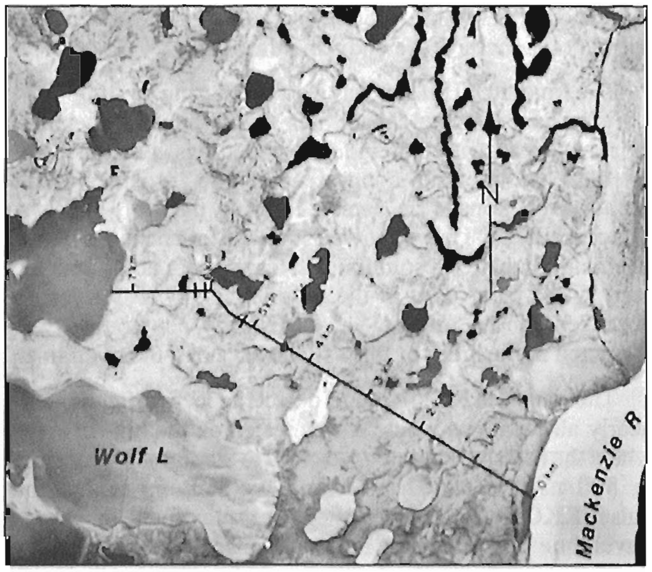

Figure 8. Location of radar transects at Lousy Point.

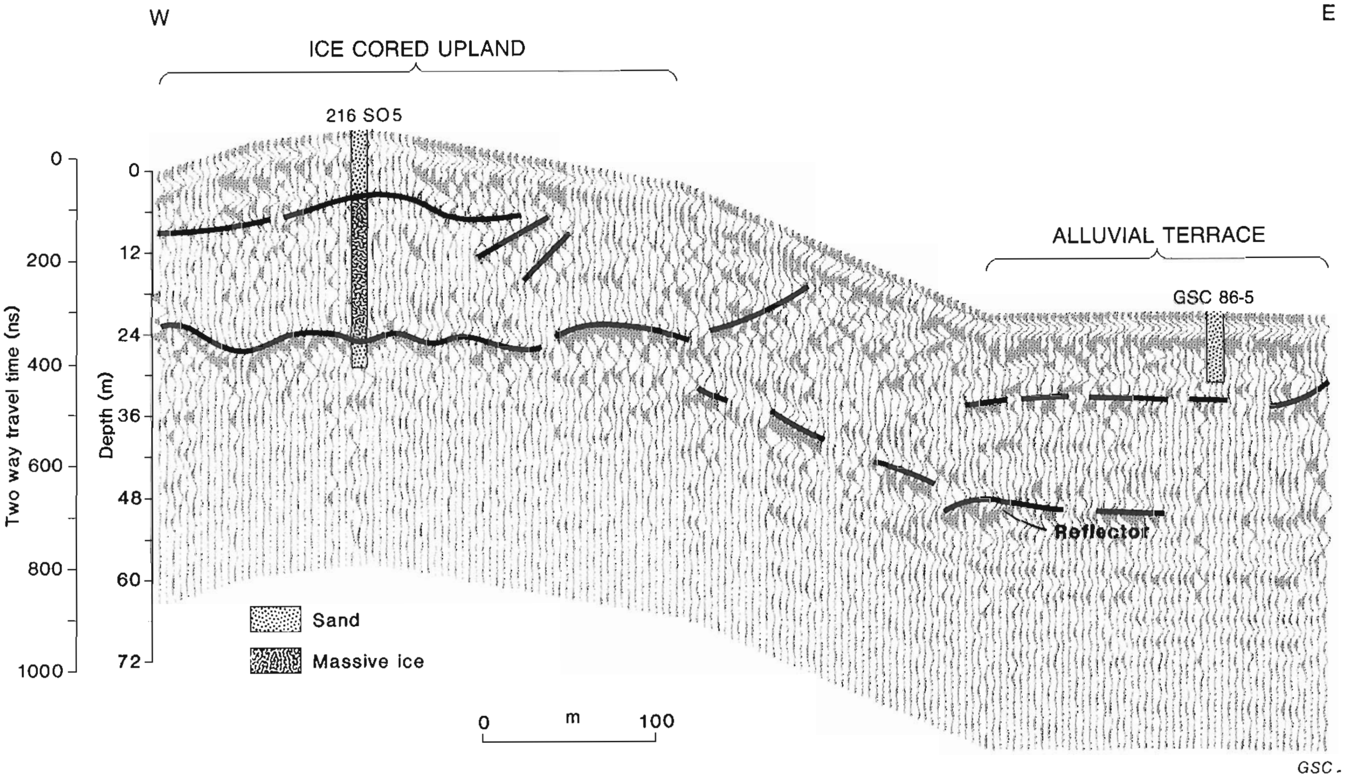

Figure 9. PulseEKKO II data at east end of Lousy Point line showing configuration of massive ice body.

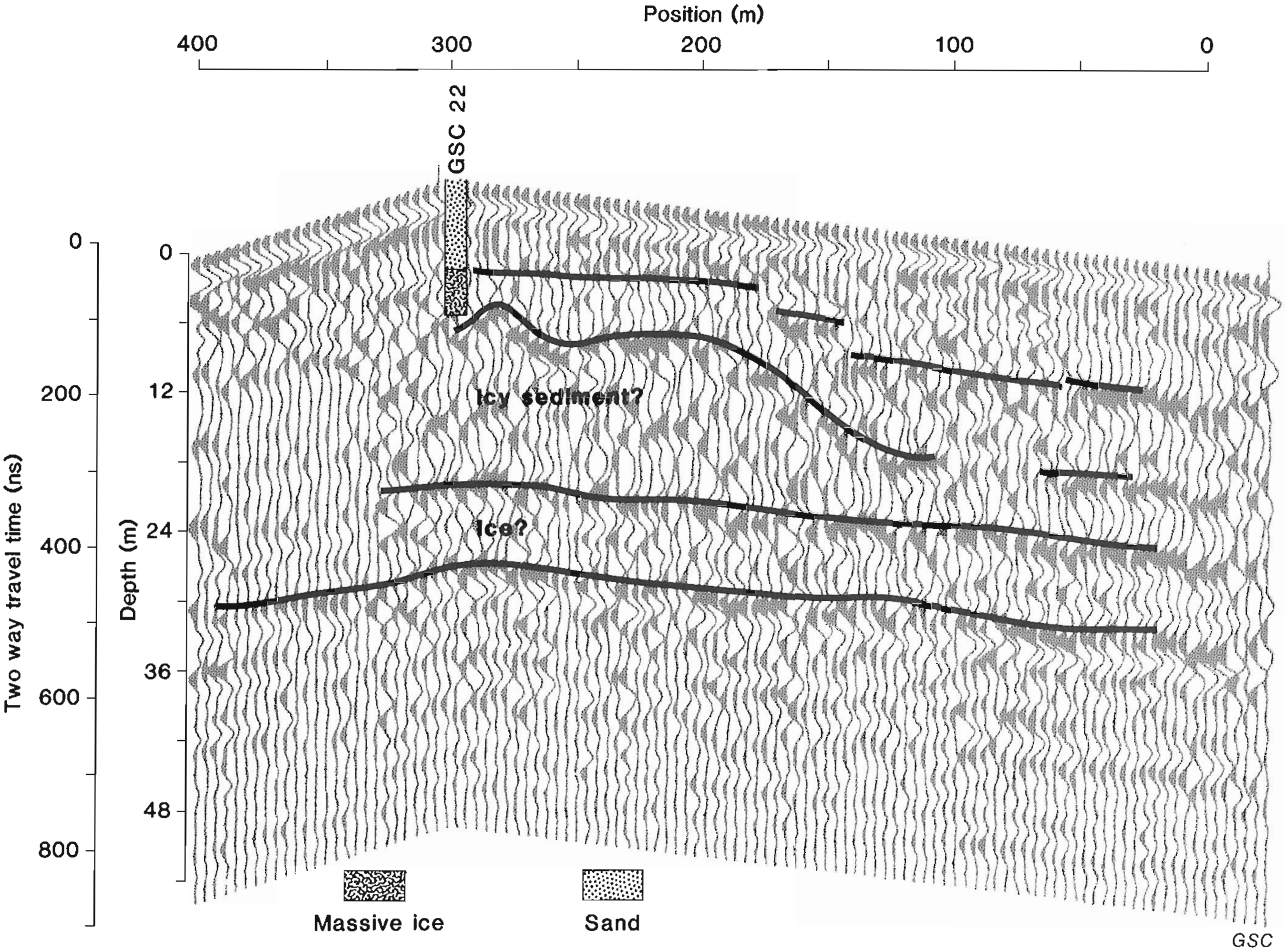

Figure 10. PulseEKKO data along west end of Low Point line.

Radar and drilling data confirm that many of the highland areas along the transect are underlain by substantial amounts of massive ground ice (Fig. 9). At the east end of the transect a 20 m thick ice body occurs beneath 9 m of stratified sand and silt. Radar profiling successfully delineated the morphology of the ice body; the pulseEKKO I wasmost useful for delineating the upper contact and the pulseEKKO II best delineated the lower contact with a basal sand. Unlike the data from Ya Ya Lake, the pulseEKKO II data suggested that the ice body was relatively clean with few internal reflectors being observed (Fig. 9). This result may be partially due to a different origin for the ice. Dallimore and Wolfe (1988) have suggested a segregated origin for this ice body.

Interpretation of radar data along the remaining part of the line is difficult because of limited data for ground verification. In general the radar systems were found to perform better in the upland areas where coarse sediments are common and where massive ice was encountered at depth. The utility of the radar systems in the low areas of lacustrine sediments and glacial till cover was limited. More drill data and further radar surveys would be required to fully evaluate their performance. The west portion of the radar transect, in the vicinity of the gravity surveys by Rampton and Walcott (1974), appears to also be underlain by massive ice. The nature of the radar data (Fig. 10) suggests that this ice is perhaps more like the ice at Ya Ya Lake with numerous internal reflectors possibly representing till bands within the ice.

DISCUSSION AND CONCLUSIONS

The studies carried out to date indicate that the ground penetrating radar technique is extremely valuable for detecting massive ground ice and mapping near-surface geology. The radar method is especially useful for correlating between boreholes or for determining the suitable drilling locations. Repeat surveys carried out at Involuted Hill indicate that advances in digital radar technology and in system performance have substantially improved depth penetration and resolution when compared to earlier radar system used in the mid-seventies. The successful completion of more than 17.5 km of rigorous field trials also demonstrates that the instruments are sufficiently robust and durable for extensive surveys such as might be conducted along the routes of proposed pipelines or highways.

The two radar systems used for the surveys described in this paper were found to be complimentary for field operations and interpretation of subsurface reflectors. The general pattern for operation used during the survey was to conduct a rapid survey of the entire transect with a 100 MHz continuous profiling radar (pulseEKKO I). This enabled a rapid assessment of the type of terrain expected along the survey line. At Lousy Point, for instance, the 8 km line was surveyed in about 6 h. These data were then reviewed to provide an overview of near-surface geology and the expected radar performance. Areas of particular interest were then chosen for detailed study and were resurveyed with the digital radar operating at a lower frequency of 30 MHz (pulseEKKO II). This survey proved to be the most valuable for delineating deeper ground ice bodies; however, in most instances it was necessary to review the pulseEKKO I data to improve the interpretation in the upper 10 m.

Correlation of radar data with borehole data and velocity soundings indicates that the velocity of prorogation of radar signals was in the range of 0.15-0.12 m/ns. In fact for practical purposes an assumed velocity of 0.14 m/ns was considered adequate for nearly all surficial materials. This was true for instance, at Involuted Hill, where over 10 m of clay till is present along the main line. The main reason for this relatively high velocity is most likely the extremely cold ground temperatures present in this region during March and April. Temperature records show that ground temperatures in the upper 10 m may vary from -7° to -18°C. It should be noted that depth penetration may be substantially reduced if surveys are conducted at other times of the year when a thawed layer may be present at the surface or ground temperatures are warmer.

ACKNOWLEDGMENTS

The authors would like to acknowledge the field assistance given by F.M. Nixon and J.G. Bisson. Funding for the field work was provided by the Panel for Energy Research and Development, and logistical support was given by the Polar Continental Shelf Project.

REFERENCES

Annan, A.P.
1976: Density of ice samples from Involuted Hill test site, District of Mackenzie; Geological Survey of Canada, Paper 76-1C, p. 91-95.

Annan, A.P. and Davis, J.L.
1978: High frequency electrical method for the detection of freeze-thaw interfaces; Proceedings, 3rd International Conference on Permafrost, Edmonton, Alberta, v. 1, p. 496-500.

Dallimore, S.R. and Davis, J.L.
1987: Ground probing radar investigations of massive ground ice and near surface geology in continuous permafrost; in Current Research, Part A, Geological Survey of Canada, Paper 87-1A, p. 913-918.

Dallimore, S.R. and Wolfe, S.A.
1988: Massive ground ice associated with glaciofluvial sediments, Richards Island, N.W.T., Canada; Proceedings, 5th International Conference on Permafrost, Trondheim, Norway.

Davis, J.L., Scott, W.J., Morey, R.M., and Annan, A.P.
1976: Impulse radar experiments on permafrost near Tuktoyaktuk, Northwest Territories; Canadian Journal of Earth Sciences, v. 13, p. 1584-1590.

EBA Engineering Consultants Ltd.
1986: Granular evolution Richards Island, N.W.T.; Contract report prepared for Indian and Northern Affairs Canada, Ottawa, Ontario.

Kovacs, A. and Morey, R.M.
1978: Remote detection of massive ice in permafrost along the Alyeska pipeline and the pump station feeder gas pipeline; Proceedings, ASCE Pipelines Division Specialty Conference, Pipelines in adverse environments, New Orleans, p. 268-279.
1985: Impulse radar sounding of frozen ground; Proceedings, Workshop on permafrosts geophysics, US Army Corps of Engineers, Cold Regions Research and Engineering Laboratory, Special Report, 85-5, p. 28-40.

Mackay, J.R.
1963: The Mackenzie Delta Area, Northwest Territories; Geological Survey of Canada, Miscellaneous Report 23, 202 p.

Patterson, D.E. and Smith, M.W.
1981: The measurement of unfrozen water content by time-domain reflectometry; Canadian Geotechnical Journal, v. 18, p. 131-144.

Rampton, V.N. and Walcott, R.I.
1974: Gravity profiles across ice-cored topography; Canadian Journal of Earth Sciences, v. 11, p. 110-121.

Applications of ground penetrating radar to mining, groundwater, and geotechnical projects: selected case histories

J.L. Davis[2] and A.P. Annan[1]

Davis, J.L. and Annan, A.P., 1992: Applications of ground penetrating radar to mining, groundwater, and geotechnical projects: selected case histories; in Ground penetrating radar, ed. J. Pilon; Geological Survey of Canada, Paper 90-4, p. 49-55.

Abstract

Ground penetrating radar is a technique that offers the capability of high resolution mapping of soil and rock conditions. The need for a better understanding of overburden conditions for activities such as geochemical sampling, geotechnical investigations, and placer exploration, as well as the factors controlling groundwater flow, has increased demand for techniques that can image the subsurface with higher resolution than previously possible.

The basic principles and practices involved in acquiring high quality radar data in the field are illustrated by selected case histories. One case history demonstrates how radar has mapped the bedrock to depths of 20 m and to delineate structure within overburden. Another example shows how the radar has been used to map not only bedrock under a lake but also changes of rock type to a depth of 50 m. Two case histories demonstrate how radar has been used to map fractures and changes of rock type to 40 m depth from inside mines. With the new instruments and field methods, the routine use of radar is becoming economically viable and the method will see greater use in the future.

Résumé

Le géoradar permet d'établir des cartes à haute résolution figurant les conditions du sol et des roches. La nécessité de mieux comprendre les conditions propres aux terrains de couverture dans le cadre de certaines activités comme l'échantillonnage géochimique, les analyses géotechniques et l'exploration des placers ainsi que l'étude des facteurs régissant l'écoulement de l'eau souterraine, a fait accroître la demande pour des techniques permettant de représenter graphiquement les couches profondes à une résolution plus grande qu'auparavant.

Les principes et usages de base mis en oeuvre pour acquérir des données radar de haute qualité sur le terrain sont illustrés par des cas choisis. Un cas sert à présenter la façon dont a été cartographiée le socle jusqu'à des profondeurs de 20 m et comment la structure dans le terrain de couverture a été délimitée. Un autre exemple illustre comment le radar a été utilisé pour cartographier non seulement le socle sous un lac, mais également les changements de type de roche jusqu'à une profondeur de 50 m. Deux autres cas sont donnés pour montrer comment le radar a servi à cartographier les fractures et les changements de lithologie jusqu'à une profondeur de 40 m à partir de l'intérieur de certaines mines. Avec l'apparition de nouveaux instruments et l'élaboration de nouvelles méthodes de terrain, l'utilisation courante du radar est en passe de devenir économiquement viable et ne fera que croître dans l'avnenir.

---

[1] Sensors & Software Inc., 5566 Tomken Road, Mississauga, Ontario L4W 1P4

[2] Formerly A-Cubed Inc., 5566 Tomken Road, Mississauga, Ont. L4W 1P4, now at Canpolar Inc., 265 Rimrock Road, Toronto, Ont. M3J 3C6

INTRODUCTION

Applications for the use of ground penetrating radar (GPR) are abundant. They include mineral and groundwater exploration, geotechnical and archaeological investigations, as well as rock mechanics and mine development requirements. Some specific examples include mapping bedrock depth, changes of rock type, fractures in bedrock, soil strata, and the water table in coarse grained soils.

The size and depth of features that can be detected with GPR are dictated by the GPR operating frequency and the geological setting. GPR operating at 500-1000 MHz have detected fractures of a few millimetres thick at ranges of several metres. GPR systems operating at 25-50 MHz can sound to depths in excess of 50 m in soils with low conductivity (less than 1 ms/m) such as sand, gravel, and rock, and in fresh water.

EQUIPMENT

Recent developments in GPR technology have increased the ability of the technique to sound to greater depths in geological materials. The newer radar systems, such as the pulseEKKO III (Annan and Davis, 1992) that we used in these case histories (Fig. 1), use state-of-the-art digital technology that allows use of sophisticated digital processing techniques. New instrumentation is portable and easy to use in the field and lends itself well to surveys in difficult field conditions. The radar unit (Fig. 1) digitizes the received signal in the receiver at the antenna. The signals are transferred by use of fibre optic cables, which greatly reduces "noise". The digital signal is transferred to the console where it is formatted for display on a graphics liquid crystal display (LCD) and stored on digital magnetic tape. The digital data are transferred to a desk top computer for processing and

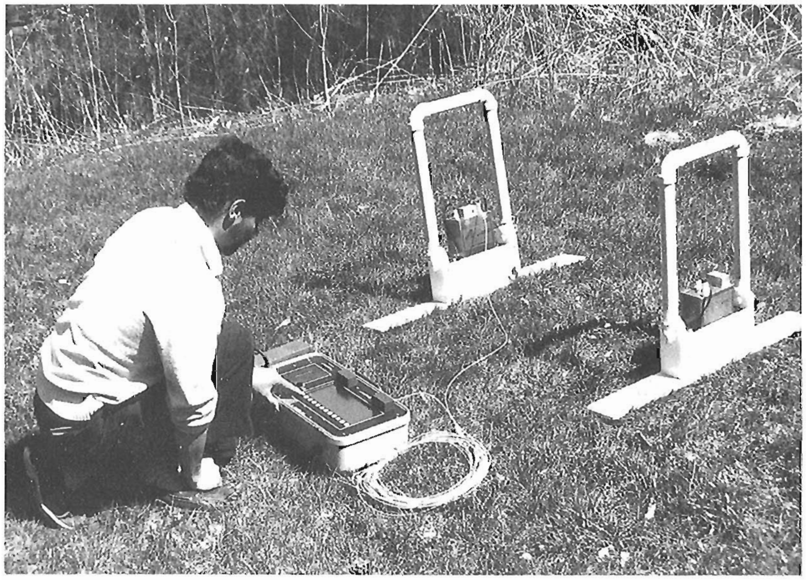

Figure 1. PulseEKKO III radar system with 100 MHz antenna.

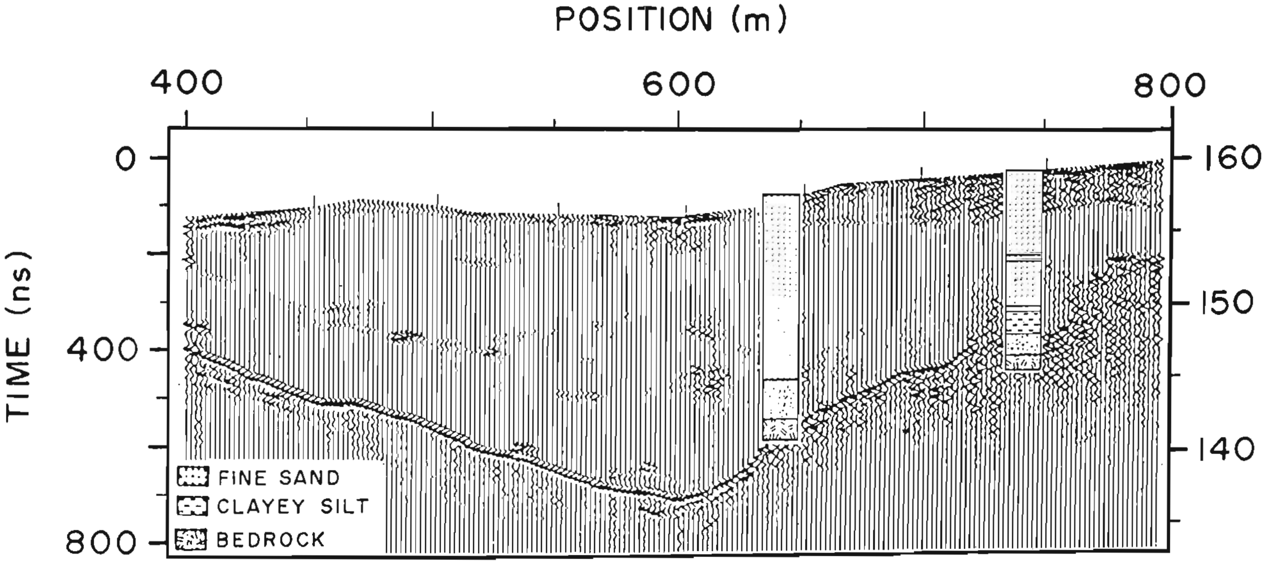

Figure 2. Radar record showing the bedrock topography under a fine sand overburden.

display in hard copy. Digital signal processing techniques commonly employed in the seismic industry are used to produce a high quality data display.

CASE HISTORIES

Five case histories are summarized to show how ground penetrating radar can be used to obtain detailed information of the bedrock topography, soil stratigraphy in the overburden even under a lake, and the extent of a contaminated groundwater plume. Two of the examples demonstrate that the GPR can detect and map features in the rock such as fractures and changes of geology from inside mines.

Soil stratigraphy and bedrock mapping

Figure 2 is a GPR record obtained using 100 MHz centre frequency antennas at 2 m station intervals on the surface at a site in eastern Ontario. The geological setting consists of water saturated fine sand over a granodiorite bedrock. The bedrock depth varies from 5 to 20 m along this 400 m profile. The surface topography was surveyed, and the data were compensated for the topographic variations along the survey line. Two boreholes nearby the survey line show that the radar data agree closely with bedrock depth on the borehole logs.

Figure 3 shows the same profile as Figure 2 but with a time varying gain applied. The weak reflections are caused by thin silt and clay layers as well as erosional unconformities

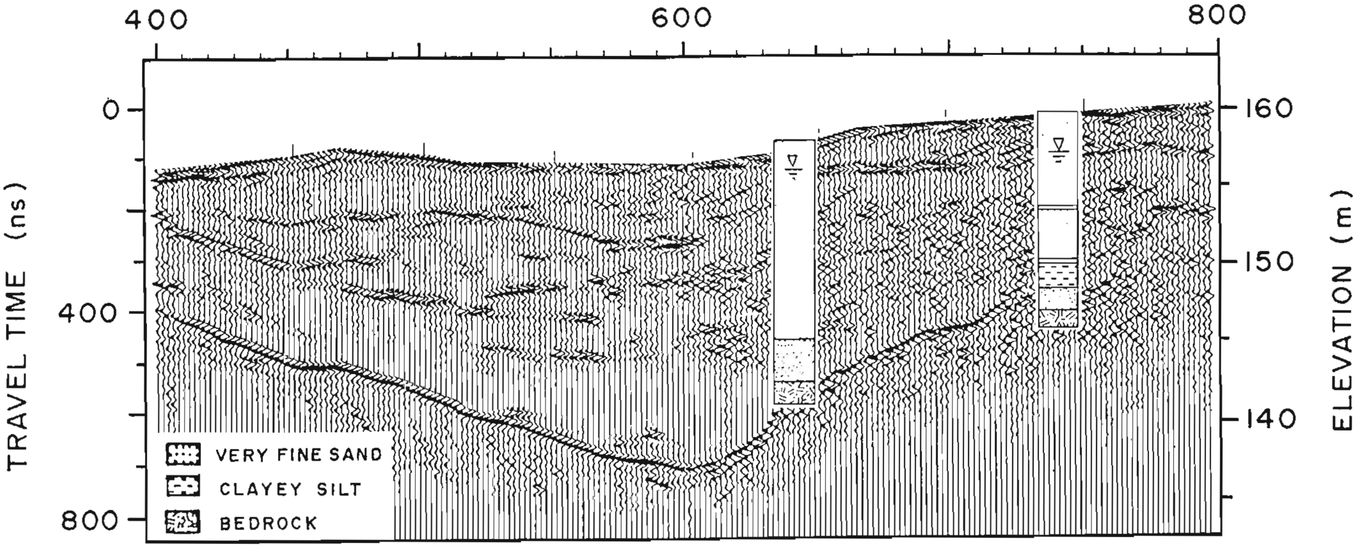

Figure 3. Same profile as Figure 2 but with additional gain applied. Reflections in the overburden are from silt and clay layers in the sand.

Figure 4. 13 MHz antennas in use on ice-covered lake.

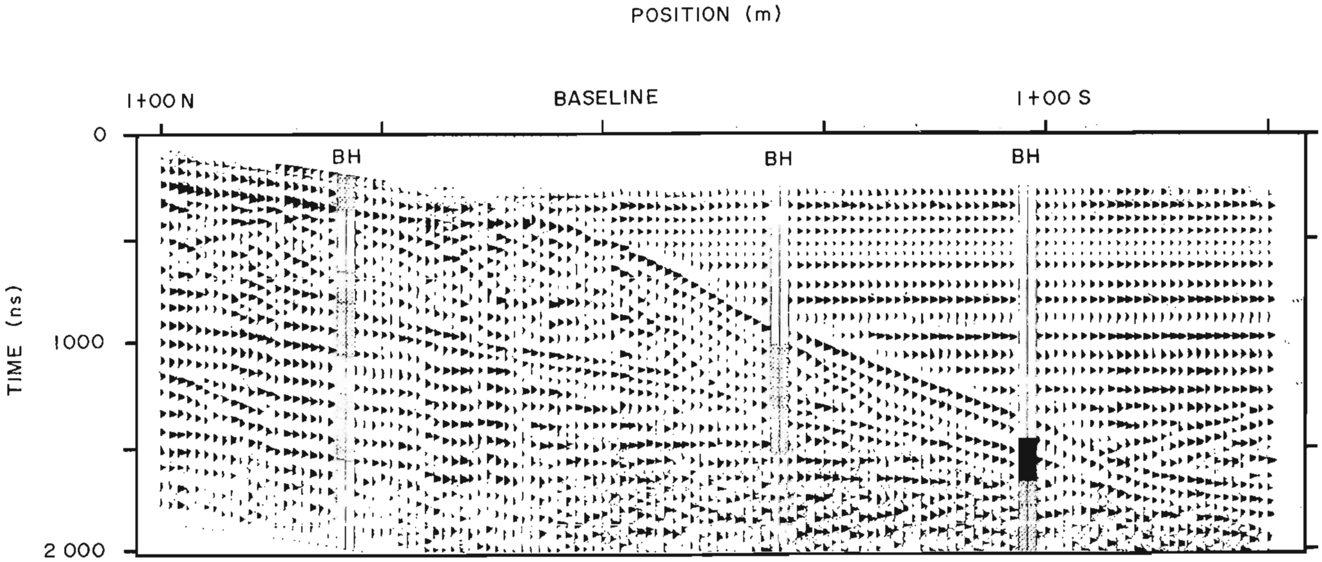

Figure 5. Radar record showing bedrock on shore and under a lake.

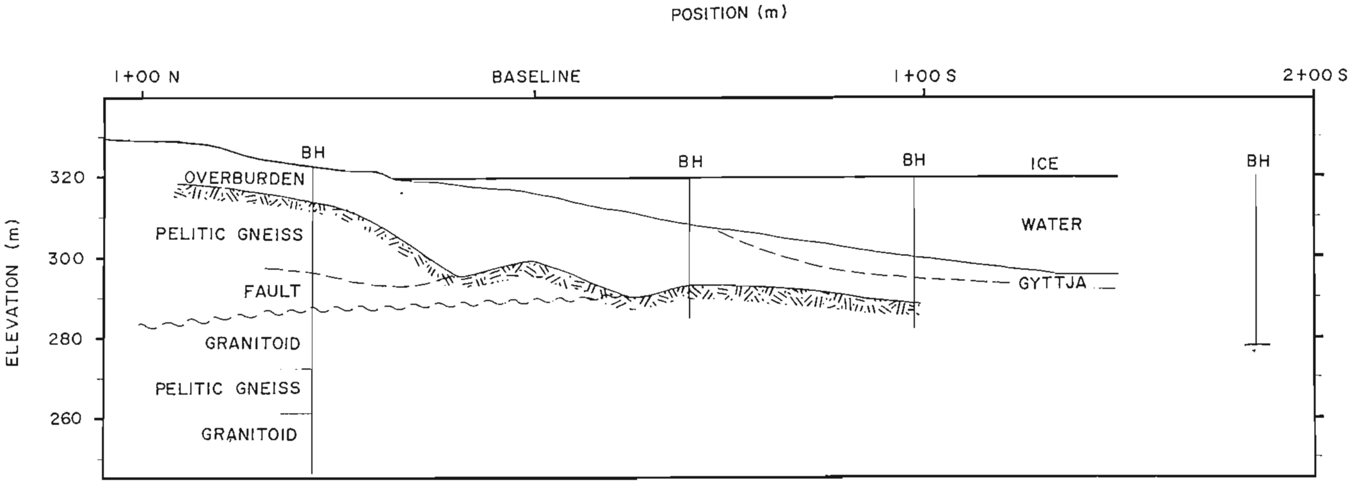

Figure 6. Interpreted geological section based on four borehole (BH) logs and the radar survey data shown in Figure 5.

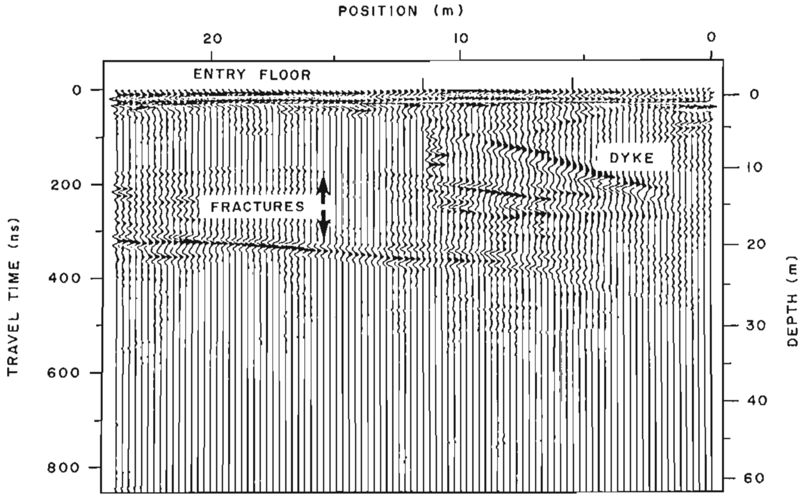

Figure 7. Radar record obtained in a tunnel in granite.

in the fine sand and overburden of eolian and fluvial origin. Because the data are in a form amenable to a wide variety of digital enhancement processing techniques, many other data presentations are possible.

Hydrogeologists have been studying the groundwater flow in this area for many years. A detailed knowledge of the bedrock topography and the soil strata are essential inputs for their groundwater flow model to predict the migration of contaminants. The radar has become an efficient method of extending the borehole information for detailed investigations in the area.

Bedrock mapping under a lake

In many instances knowledge of the bedrock topography under shallow lakes and rivers is required. Construction of dams, placer exploration, and mine engineering of crown pillars are typical examples. In this example, bedrock topographic relief under a lake had to be evaluated to determine the optimum location for a cofferdam to keep the lake water out of a planned open pit mine. The survey was carried out in the winter and the radar soundings were acquired from the ice covered lake surface (Fig. 4). A low operating frequency (12.5 MHz) was selected to minimize the

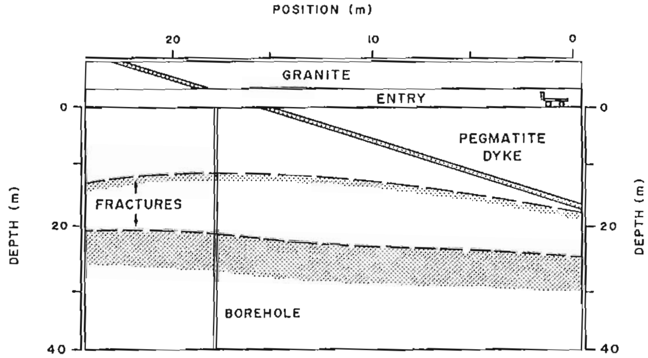

Figure 8. Geological section along the survey line in Figure 7.

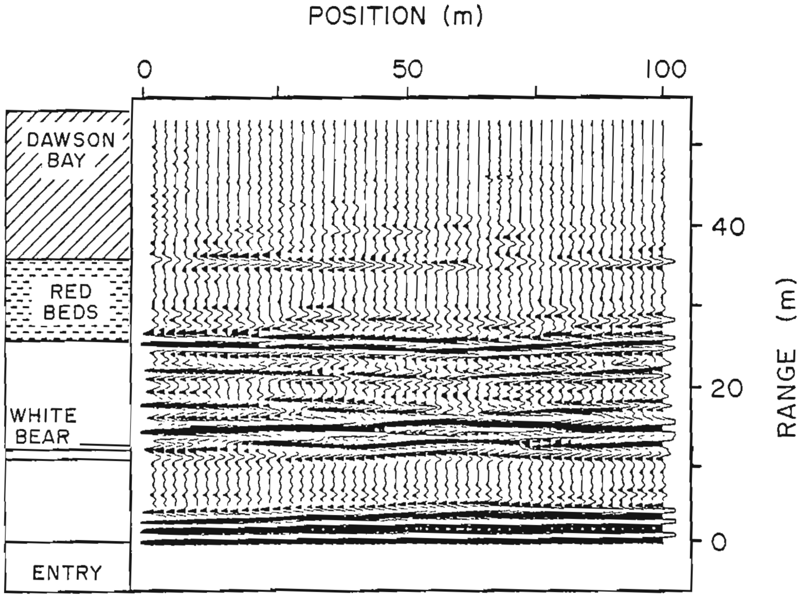

Figure 9. Geological section from potash mines in Saskatchewan beside a radar record obtained in the same mine.

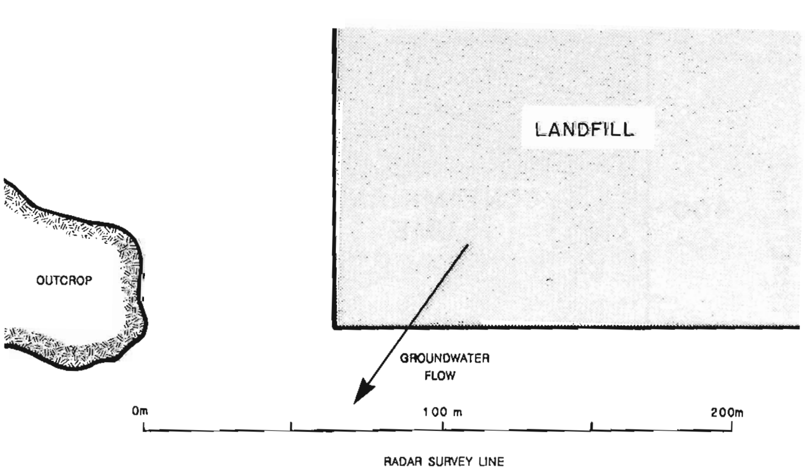

Figure 10. Schematic plan of a landfill site showing a downgradient radar survey line.

attenuation in the clayey muck at the bottom of the lake and to reduce scattering from small scale subbottom stratigraphy (Davis et al., 1985).

Radar data obtained at 2 m station intervals along a survey line extending 150 m from shore are presented in Figure 5. The data have been compensated for the surface topography on shore. There is good correlation with three boreholes drilled near the radar survey line. We have interpreted the section (Fig. 6) using radar signal velocities of 0.1 m/ns in the overburden, 0.12 m/ns in the bedrock, 0.033 m/ns in water, and 0.05 m/ns in the gyttja.

A 2 km by 15 m grid was surveyed at this site and a bedrock knob under the lake defined by the radar data is to provide a base for the proposed dam.

Fracture detection in igneous bedrock

The radar can be used in tunnels to detect and map features such as changes in geology, fractures, and voids around the tunnels. The radar record (Fig. 7) was obtained in a tunnel in a granite pluton located in southeastern Manitoba. Figure 8 shows a geological section along the radar survey line.

The radar data correlate well with the logs from the borehole drilled at position 18 m. A reflection is obtained from a dry fracture zone about 0.5 m thick and 12 m below the floor. A water bearing fracture zone occurs at 22 m depth and a reflection is also detected from this zone. A pegmatite dyke intersects the adit dipping at about 45 degrees. The reflection from the dyke shows up on the data very clearly.

This example gives a good indication of the sensitivity of the radar to geological features in hard rock environments. Reflections from fractures at 50 m range have been routinely mapped by GPR in granitic rock. Further examples of data from this site are presented by Holloway (1992).

Geological mapping in sedimentary rock

The thickness of salt above mining level in potash mines is an important in controlling mining operations (Annan et al., 1988). In Saskatchewan potash mines, this information is used to design the mine for maximum safe extraction of the potash in the salt which creeps and to assure that water does not enter the mine from the overlying saturated rocks. Figure 9 shows the geological section from a potash mine in southwest Saskatchewan beside the radar section obtained from inside the mine at the same location.

The reflections on the radar data correlate well with the known geology. A halite rich zone immediately above the entry generates a reflection at most masked by the transmit pulse. A sylvite rich zone about 1 m thick, called the White Bear, is located at 16 m. A further halite rich zone at a range of 22 m extends up to the Red Bed shales at 24 m above the entry. The radar data also show a reflection that correlates with the contact with the Dawson Bay limestones at a range of 35 m. Reflections from within the Dawson Bay formation are probably from the bedding planes in the limestone.

The GPR data mapped all the major stratigraphic horizons at the site and defined small scale variations that could not be mapped in any other manner. Mapping of the distance to the Red Beds above the mining horizon is important to the mine engineers because of the ever present concern about drilling into a water bearing formation. The radar also offers the potential of detecting anomalies such as brine pickets and solution collapse features prior to mining operations.

Leachate detection and mapping

Fresh, clean groundwater is becoming an increasingly valuable resource worldwide. In some areas careless disposal of wastes has greatly decreased the supply of potable water.

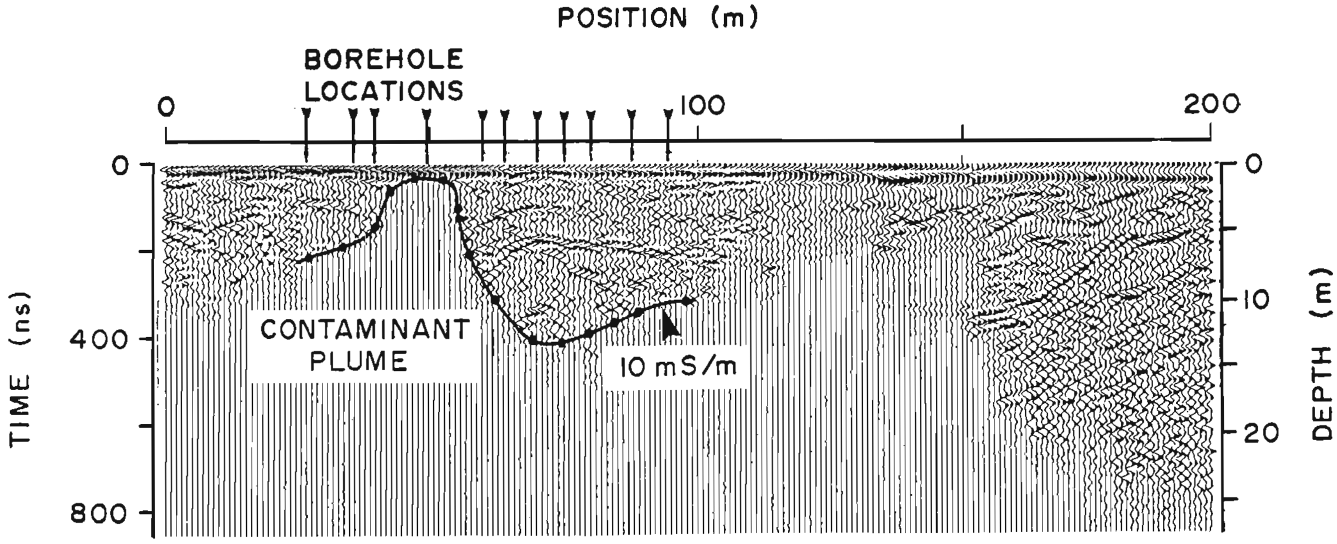

Figure 11. Radar record along the line shown on Figure 10. The area below the 10 ms/m line is interpreted to be in the contaminant plume.

Hydrogeologists frequently require methods to map the soil stratigraphy at waste disposal sites to assist in defining the extent of contamination emanating from the sites.

Figure 10 presents a schematic plan of a landfill site. Figure 11 presents the radar data along the survey line (Fig. 10), which is oriented orthogonal to the general groundwater flow direction. The soil is a fine sand of eolian and fluvial origins. The bedrock is about 20 m deep along most of this survey line but is only detected between stations 150-200 m. Most of the reflections on the data are from variations of grain size and density in the overburden. The zones where the radar reflections are weak or absent indicate the presence of contaminated leachate, which increases the electrical conductivity of the groundwater and strongly attenuates the radar signals.

The electrical conductivities of the groundwater have been measured at a number of boreholes along the survey line. The solid black line (Fig. 11) indicates the position below which the conductivity of the pore water is greater than 10 ms/m. Knowing that the soil type remains essentially the same along the line, the radar data indicate that the contaminant plume comes near the surface between 40 and 60 m as shown by the borehole data; it also extends between 110 and 150 m along the radar survey line at a depth of 6 m below the exiting surface. This type of information permits us to monitor the migration of contaminants in coarse grained soils. Radar data such as these are extremely useful for planning where to place monitoring wells around a waste impoundment site.

CONCLUSIONS

We have presented data from case histories representing a wide variety of geological settings and problems, from which we conclude the following:

- Radar can be used in a wide range of environments either on the surface or in mines.
- Radar technique provides high resolution soundings to a range of 50 m in resistive environments.
- Radar can be used to map overburden thickness, soil stratigraphy, changes of geology, fractures in bedrock, and leachate plumes in soils.
- Radar provides a powerful means for developing geological sections and tracing continuity in geological unit defined by limited borehole information.

As with any geophysical method, the GPR method is only effective in geological environments where electrical conductivity is low. The best environments exhibit conductivities less than 1 ms/m.

ACKNOWLEDGMENTS

The authors wish to acknowledge support received from the Geological Survey of Canada, DSS, and NRC PILP program for the development of the A-Cubed Inc. pulseEKKO III radar system. They especially wish to acknowledge the continuing enthusiastic encouragement and support of Len Collett and Jean Pilon of the Geological Survey of Canada. In addition, they thank those clients whose data are used for the case histories.

REFERENCES

Annan, A.P. and Davis, J.L.
1992: Design and development of a digital ground penetrating radar system; in Ground penetrating radar, J.A. Pilon (ed.); Geological Survey of Canada, Paper 90-4.

Annan, A.P., Davis, J.L., and Gendzwill, D.
1988: Radar sounding in potash mines, Saskatchewan, Canada; Geophysics, v. 53, p. 1556-1564.

Davis, J.L. and Annan, A.P.
1989: Ground penetrating radar for high-resolution mapping of soil and rock stratigraphy; Geophysical Prospecting, v. 37, p. 53 - 551.

Davis, J.L., Annan, A.P., Black, G., and Leggatt, C.D.
1985: Geological sounding with low frequency radar; in Extended abstracts, 55th Annual International Meeting of the Society of Exploration Geophysicists, Washington, D.C.

Holloway, A.L.
1992: Fracture mapping in granite rock using ground probing radar; in Ground penetrating radar, J.A. Pilon (ed.); Geological Survey of Canada, Paper 90-4.

The fractal dimension of diverse topographies and the effect of spatial windowing

A.W. England[1]
University of Michigan

England, A.W., 1992: The fractal dimension of diverse topographies and the effect of spatial windowing; in Ground penetrating radar, ed. J. Pilon; Geological Survey of Canada, Paper 90-4, p. 57-61.

Abstract

Scattering theories for radar backscatter from random, natural surfaces, e.g., from soil, rock, snow, ice, or from subsurface interfaces, must assume some statistical model of surface roughness. The fractal dimension (Df) may be an appropriate part of that statistical model. For example, the topographies of three diverse geological terrains – near Richmond, Virginia, near Brainerd, Minnesota, and west of Greeley, Colorado – show remarkable constancy among Df's for spatial wavelengths between 200 m and 90 km. However, Df varies with the method of estimating the power density spectrum. Spectra that are based upon raw elevation data yield Df's of 2.49 ± 0.02. If regional gradients are removed, Df's become 2.39 +0.08/-0.19. If amples are tapered by a Gaussian window, Df's become 2.21 +0.06/-0.09.

Résumé

Les théories sur la diffusion appliquées à la rétrodiffusion radar de surfaces naturelles prises au hasard, comme le sol, la roche, la neige, la glace ou les interfaces de subsurface, doivent reposer sur un certain modèle statistique de la rugosité de surface. La dimension fractale (D_f) peut être un élément approprié du modèle statistique. Par exemple, la topographie de trois terrains géologiques différents, soit près de Richmond (Virginie), près de Brainerd (Minnesota) et à l'ouest de Greeley (Colorado), fait preuve d'une constance remarquable entre les dimensions fractales D_f pour les longueurs d'onde spatiales variant entre 200 m et 90 km. Cependant, D_f varie selon la méthode d'estimation du spectre de puissance volumique. Les spectres qui sont basés sur des données d'altitude brutes donnent des D_f de 2,49 ± 0,02. Si l'on élimine les gradients régionaux, les D_f deviennent 2,39 + 0,08/-0,19. Lorsque les échantillons sont pondérés en fuseau par une fenêtre gaussienne, D_f devient 2,21 + 0,06/-0,09.

INTRODUCTION

Many radar scattering theories are based upon the variance spectrum and the correlation length of the scattering surface (e.g., Beckmann and Spizzichino, 1963). The implicit assumption in use of the correlation length is that elevation is normally distributed about a mean. This assumption may not be an appropriate for natural terrain – hilltops are generally not minor images of valleys. It is desirable, therefore, to find a more general statistical description of natural surfaces on which we might base a new scattering theory. Fractal dimension (D_f) may be part of such a description. In this paper, I examine the constancy of D_f as a function of scale for three diverse geological terrains, and for various methods of estimating the power density spectrum. Along the way, I also developed a rectangular prism method for measuring the D_f of topography. The method is analogous to the box method employed by Mandelbrot (1982) and others for measuring the D_f of 1-dimensional profiles. Huang and Turcotte (1989) reported a very similar study of D_f for the topography of Arizona. They found that D_f is relatively independent of the geological character of various Arizona terrains. Their measure of D_f differed somewhat from that derived here, but our conclusions are similar.

Fractal dimension, a term coined by Mandelbrot (1982), describes the irregularity of a line or surface if that line or surface is scaling. The method for measuring D_f is unspecified. Brown

---

[1] Department of Electrical Engineering and Computer Science, The University of Michigan, Ann Arbor, Michigan 48109 U.S.A.

and Scholz (1985), Aviles et al. (1987), Okubo and Aki (1987), and Barton and Larsen (1985), among others, have derived the fractal dimensions of profiles from the limited self-affinity of natural surfaces. Scaling can be either self-similar or self-affine. If the property f(x) is scaling, then f(bx)/b′ is invariant for a class of mutually dependent bases b and b′. If b′ = b, then f(x) is self-similar. If b′ is some other nonzero power of b, then f(x) is self-affine. The term "scaling" might refer to specific form or, more appropriately for our purposes, to statistical characteristics. That is, we are concerned with the statistical moments of elevation of a self-affine, two dimensional, rough surface.

The fractal dimension of a two dimensional surface ($2<D_f<3$) is intuitive in the sense that larger D_f's imply more volume filling topographies. The concept is complicated by the need to specify a reference roughness that has been called topothesy (Brown, 1987). The topothesy specifies the expected elevation at one wavelength, and D_f yields the slope of the power density spectrum of elevation at that wavelength. D_f will be couched in terms of variance because variance is a convenient parameter in scattering theory.

DEFINITION OF FRACTAL DIMENSION

A digital elevation model (DEM) is an N x N array of elevation measures at the intersections of a Cartesian grid. For b equally spaced subsamples in each cardinal direction of the N x N array, the sample interval, t, is N/b. If e_{kl} is the deviation from an elevation mean at each point in the array, then the variance V(b) is

$$V(b) = (1/b^2) \sum_{k=0}^{b-1} \sum_{l=0}^{b-1} e_{kl} e_{kl}^* \qquad (1)$$

where an * refers to the complex conjugate. The inverse discrete Fourier transform of e_{kl} is

$$e_{kl} = (1/b^2) \sum_{p=0}^{b-1} \sum_{q=0}^{b-1} E_{pq}(b)\, e^{(i2\pi/b)(pk+ql)} \qquad (2)$$

where $E_{qp}(b)$ are the Fourier coefficients for b x b samples. A substitution of equation 2 into equation 1 yields

$$V(b) = (1/b^4) \sum_{p=0}^{b-1} \sum_{q=0}^{b-1} E_{pq}(b)\, E_{pq}^*(b) \qquad (3)$$

It is readily shown that $E_{pq}(b) = b^2 E_{pq}(N) / N^2$ so that

$$V(b) = (1/N^2) \sum_{p=0}^{b-1} \sum_{q=0}^{b-1} G_{pq} \qquad (4)$$

where $G_{qp} = E_{pq}(N)\, E_{pq}^*(N) / N^2$. G_{pq} are the spectral components of a periodogram – an estimate of the power density spectrum. That is, the variance for b x b samples is the normalized power density spectrum summed over wavelengths from DC to the sample interval t.

If W(b) is the volume occupied by the expected deviation of the topography from its mean, then

$$W(b) = 2\, N^2\, V(b)^{1/2} \qquad (5)$$

The factor 2 occurs because the deviation can be + or -. Define the sample rectangular prism, v(b),

$$v(b) = 2 \left(\frac{N}{b}\right)^2 \frac{V(1)}{b}^{1/2} \qquad (6)$$

so that the number of sample prisms, L(b), that fit into W(b) is

$$L(b) = b^3 \frac{V(b)^{1/2}}{V(1)^{1/2}} \qquad (7)$$

The "box dimension" definition of D_f is

$$L(b) = b^{D_f} \qquad (8)$$

so that equations 7 and 8 yield

$$V(b) / V(1) = b^{2D_f - 6} \qquad (9)$$

If V(b) has an exponential dependence, $Cb^{-\beta}$, over the range of b, then D_f is $(3 - \beta/2)$. If V(b) can be approximated locally by an exponential function, a more useful solution can be obtained from the difference equation (b>>1)

$$V(b+1) - V(b) = V(1)\,(2D_f - 6)\, b^{2D_f - 7} \qquad (10)$$

Now V (b + 1) - V(b) = G(b), the power density at wavelength $2\pi b/N$. The G(b) often vary as $b^{-\alpha}$ (e.g., Sayles and Thomas, 1978; also note by Berry and Hannay, 1978) so that

$$V(b) + 1) - V(b) = -\, Cb^{-\alpha} \qquad (11)$$

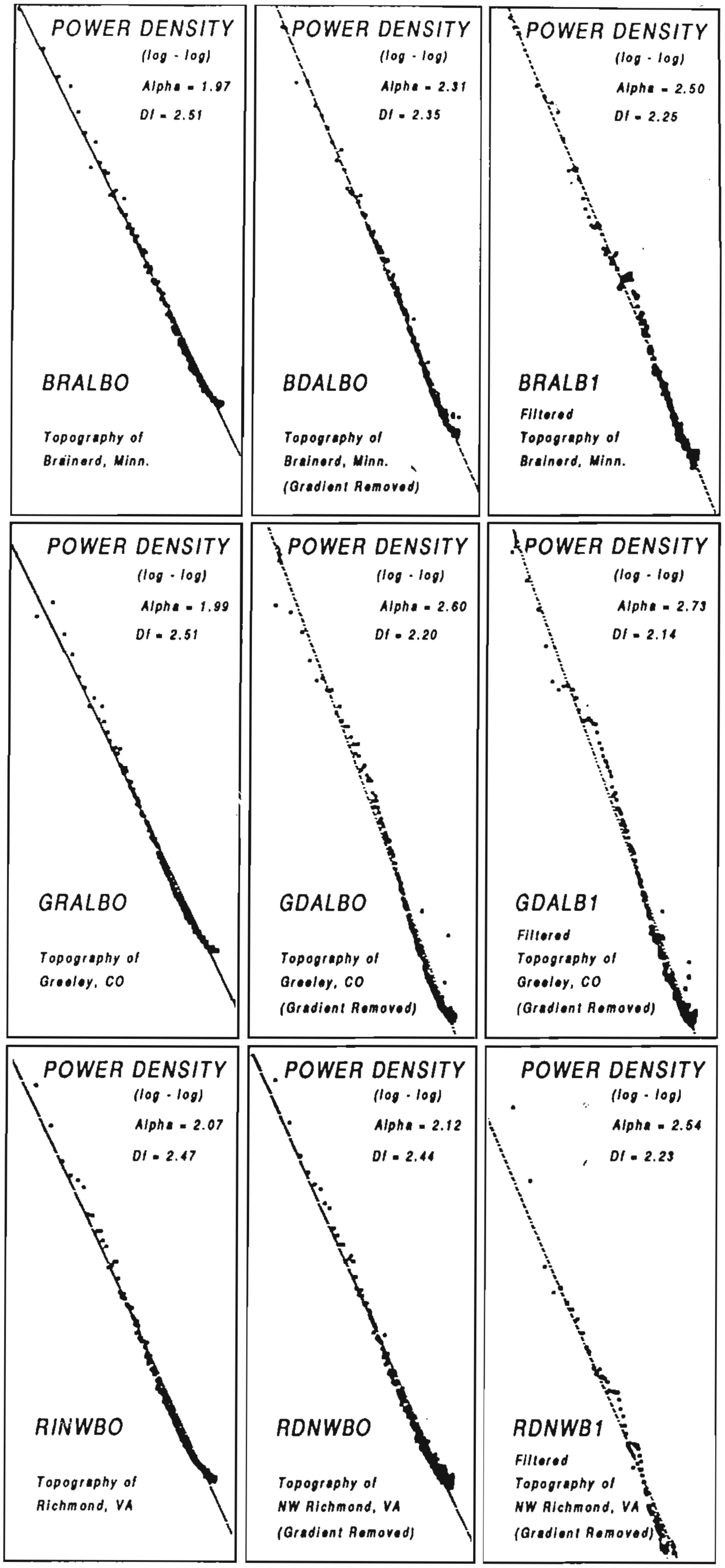

Figure 1. Power density spectra for 1° x 1° quad near Richmond, Virginia (Eastern Coastal Plain terrane), near Brainerd, Minnesota (Glacial terrane), and west of Greely, Colorado (Rocky Mountain terrane).

Table 1. Fractal dimensions for raw and windowed topography

1° x 1° DEMs:	Raw	Windowed*	Windowed**
Brainerd 2.51	2.27	2.25	
(grad removed)	2.35	2.25	2.27
NE quad	--	--	--
(grad removed)	2.47	--	--
NW quad	--	--	--
(grad removed)	2.47	--	--
Greeley 2.51	--	2.12	
(grad removed)	2.20	--	2.14
NE quad	--	--	--
(grad removed)	2.43	--	--
NW quad	--	--	--
(grad removed)	2.39	--	--
NW Richmond	2.47	--	--
(grad removed)	2.44	--	2.23

Width of Gaussian window: *1 sigma = N/4, **1 sigma = n/8
-- means that D_f was not computed

Equations 10 and 11 yield

$$D_f = 3.5 - \alpha/2 \qquad (12)$$

where α is the slope of the power density spectrum on a log-log plot.

D_f FOR THREE GEOLOGICAL TERRAINS

1:250,000 DEMs FOR 1° x 1° quads near Richmond, Virginia (Eastern Coastal Plain terrain), near Brainerd, Minnesota (glacial terrain), and west of Greeley, Colorado (Rocky Mountain terrain) were obtained from the U.S. Geological Survey. The sample interval was 90 m so that power density spectra were obtained for wavelengths over nearly 3 decades – from 0.18 to 92.2 km. Although these wavelengths are gross for radar scattering (they provide slope rather than roughness), the data do allow an inexpensive initial examination of the fractal behavior of diverse geological terrains.

The power density spectra (PDS) were estimated by four methods: (1) from raw elevation data, (2) from elevation data with regional gradients removed, (3) from elevation data multiplied by Gaussian windows, and (4) from a nonwrapped autocorrelation computation. One or more of these methods was applied to each 1° x 1° quad and to several quarter quads in a search for regional variability. The autocorrelation method was used sparingly because it required excessive computer time and appeared to add nothing new. For the Brainerd, Greeley, and Richmond quads. Figure 1 show the PDS for raw elevation data, for elevation data with regional gradients removed, and for elevation data with regional gradients removed and margins tapered by a Gaussian window. Alpha is the slope of the least squares, linear regression of PDS over the entire range of b. The fractal dimensions in Table 1 are based upon equation 12.

CONCLUSIONS

D_f varies with the method of estimating the power density spectrum. Spectra that are based upon raw elevation data yield D_f's of 2.49 ± 0.02. If regional gradients are removed, D_f's become $2.39 + 0.08/-0.19$. If samples are tapered by a Gaussian window, D_f's become $2.21 + 0.06/-0.09$. It is not clear which method yields the most reliable estimates of the slope of PDS. Fourier transforms of discrete sample sets have artifacts that would not appear if the sample sets were infinite. Conceptually, and through experience with 1-D PDS, removal of regional gradients significantly reduces these artifacts. Tapering data sets (making a finite data set approximate an infinite set whose boundary amplitudes are zero) is suspect because multiplication by a taper (a Gaussian window in this case) is a convolution in frequency space that distorts the spectral gradient, and D_f derives from the spectral gradient. However, that distortion is most severe at the highest spatial frequencies where the PDS is most in question. The PDS of a finite data set is uncertain because the discrete Fourier transform of N elements assumes an infinite, periodic data set of period N. If there is an unrealistic discontinuity between the N-1 and the 0 elements of the data set, then the quasiperiodic wraparound from the N-1 element back to the 0 element will contribute to an unrealistically high PDS at high spatial frequencies. Therefore, one should have most confidence in the PDS (and its consequent fractal dimension) for two dimensional data sets when the regional gradient has been removed, and when the marginal differences from an elevation mean have been removed by a spatial window such as a Gaussian taper.

The clustering of the D_f, whichever estimate is used, is impressive given the extreme differences in terrain among these data sets. This clustering further affirms, for example, the observations of Sayles and Thomas (1978) and the results of the fractal study of the Arizonan topography reported by Huang and Turcotte (1989). The spatial average of the two dimensional D_f of Arizona was reported as 2.09, which is about 6% smaller than the average of the windowed D_f for Brainerd, Greeley, and Richmond. Note that the variations in D_f among the extremely diverse terrains of Brainerd, Greeley, and Richmond are less than the 6% difference between averages. This difference between averages is probably caused by the difference in methods of measuring D_f, rather than by a true shift in D_f. However, like the Huang and Turcotte D_f, my D_f does not vary with the geological character of the terrain. That is, under this statistical description, variations in terrain type are reflected in the measure of topothesy or gain of the power density spectrum, not in the slope of the spectrum.

REFERENCES

Aviles, C., Scholz, C., and Boatwright, J.
1987: Fractal analysis applied to characteristic segments of the San Andreas Fault; Journal of Geophysical Research, v. 92, p. 331-334.
Barton, C. and Larsen, E.
1985: Fractal geometry of two-dimensional fracture networks at Yucca Mountain, southwestern Nevada; in Proceedings, International Symposium on Fundamental of Rock Joints, Bjorkliden, 15-20 September, p. 77-84.
Beckmann, P. and Spizzichino, A.
1963: The Scattering of Electromagnetic Waves from Rough Surfaces; Pergamon, New York, p. 80-96.
Berry, M. and Hannay, J.
1978: Topography of random surfaces; Nature, v. 273, p. 573.
Brown, S.
1987: A note on the description of surface roughness using fractal dimension; Geophysical Research Letters, v. 14, p. 1095-1098.
Brown, S. and Scholz, C.
1985: Broad bandwidth study of the topography of natural rock surfaces; Journal of Geophysical Research, 90, v. 12, p. 575-12, p. 582.
Huang, J. and Turcotte, D.
1989: Fractal mapping of digitized images: Application to the topography of Arizona and comparisons with synthetic images; Journal of Geophysical Research, v. 94, p. 7491-7495.
Mandelbrot, B.
1982: The Fractal Geometry of Nature; Freeman, San Francisco.
1985: Self-affine fractals and fractal dimension; Physica Scripta, v. 32, p. 257-260.
Okubo, P. and Aki, K.
1987: Fractal geometry in the San Andreas Fault System; Journal of Geophysical Research, v. 92, p. 345-355.
Sayles, R. and Thomas, T.
1978: Surface topography as a nonstationary random process; Nature, v. 271, p. 431-434.

Void detection using standing wave analysis

Jonathan M. Glover[1]

Glover, J.M., 1992: Void detection using standing wave analysis; in Ground penetrating radar, ed. J. Pilon; Geological Survey of Canada, Paper 90-4, p. 63-73.

Abstract

The detection of voids beneath concrete is one commercial application of the ground probing radar method. Specific uses include void detection beneath concrete roads and runways and behind concrete tunnel linings and pipes.

Thin layers of concrete can pose a problem to the ground probing radar method, because the reflection from the concrete base interferes with the radiating pulse to form a strong reverberation. This reverberation often masks the reflection from the base of the void and prevents a determination of void thickness.

A test site was constructed to simulate voids buried immediately beneath a thin layer of concrete. Seven cylindrical voids of varying diameter and thickness were dug into the clay base of the test site and were covered by 200 mm of dry sand to simulate a concrete layer. Data were collected using the GSSI-SIR 8 system with 900 and 1000 MHz antenna units. The magnitude spectra of the reflection waveforms were modelled using standard transmission line methods. The reverberations generated by the void targets were found to approximate standing waves.

A method of void detection and thickness estimation was derived, based on the measurements of the magnitude spectra. The method of depth estimation was difficult to use for voids with diameters of 0.25 m or less, because of waveguide effects generated by the clay walls of the voids. Similar waveguide behaviour is believed to effect more general applications of the ground probing radar method.

Résumé

La détection des vides au-dessous du béton est l'une des applications commerciales du géoradar. Parmi les applications spécifiques, on compte la détection des vides au-dessous des routes et des pistes d'atterrissage en béton et derrière les parois de tunnel et les tubes en béton.

Les minces couches de béton peuvent poser un problème pour l'emploi du géoradar étant donné que l'écho provenant de la base en béton interfère avec l'impulsion émise ce qui cause une forte réverbération. Cette réverbération masque souvent la réflexion de la base du vide et empêche de déterminer l'épaisseur du vide.

Un site d'essai a été construit pour simuler les vides enfouis juste au-dessous d'une mince couche de béton. Sept vides cylindriques de différents diamètres et épaisseurs ont été creusés dans la couche de base en argile du site d'essai et ils ont été recouverts de 200 mm de sable sec pour simuler une couche de béton. Les données ont été recueillies à l'aide du système GSSI-SIR 8 muni d'antennes de 900 et 1000 MHz. Les spectres d'intensité des échos ont été modélisés en utilisant des méthodes ordinaires par ligne de transport d'énergie. Les réverbérations produites par les vides cibles se rapprochent des ondes stationnaires.

Une méthode de détection des vides et d'estimation des épaisseurs, basée sur les mesures des spectres d'intensité, a ainsi été élaborée. La méthode d'estimation des profondeurs a été difficile à utiliser dans le cas de vides dont le diamètre ne dépasse pas 0,25 m en raison des effets des guides d'ondes produits par les parois en argile des vides. Les guides d'ondes pourraient avoir un comportement semblable dans des applications plus générales du géoradar.

---

[1] Subsurface Geotechnical Services, Unit 235, Stratford Workshops, Burford Road, London, UK E15 2SP

INTRODUCTION

The ground probing radar (GPR) technique uses UHF/VHF electromagnetic pulses to produce graphic sections of the near surface structure of the ground. One commercial application of GPR is the detection of voids beneath layers of concrete. Specific applications include void detection beneath concrete road bases, runways, and pavements (Clemena and McGhee, 1980; Steinway et al., 1981; Kovacs and Morey, 1983) and behind concrete tunnel linings and sewer pipe sections (Glover, unpublished report, 1981).

Voids are often identified as high amplitude reflections on the time-distance profiles, because the amplitude of concrete-void reflections are often greater than the background soil reflections. Figure 1 shows a typical response of air filled voids located behind a 100 mm thick concrete sewer pipe. The high amplitude reverberations produced by the void clearly identifies the width of the void; however, the strong reverberations generated by the inner surface of the void masks the reflection from the outer surface preventing a determination of void thickness. This reverberation is well developed where the concrete thickness is insufficient to produce a discrete reflection from the void in the time domain. This paper presents a method of detecting voids and determining their thickness, by analyzing similar reverberations in the frequency domain.

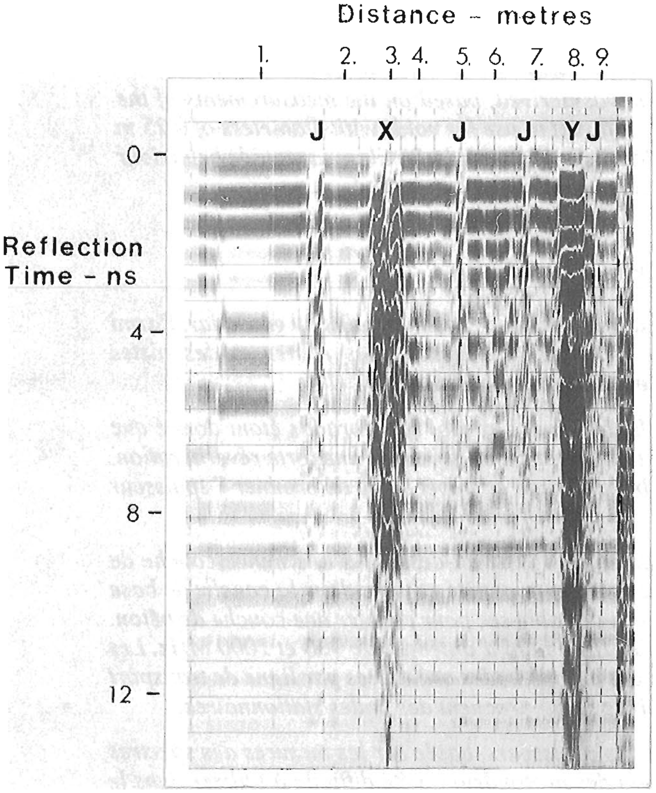

Figure 1. GPR profile through the roof of a concrete sewer pipe using the 900 MHz antenna unit. (X and Y are positions of air filled voids. J represents joints between the sections of concrete pipe.)

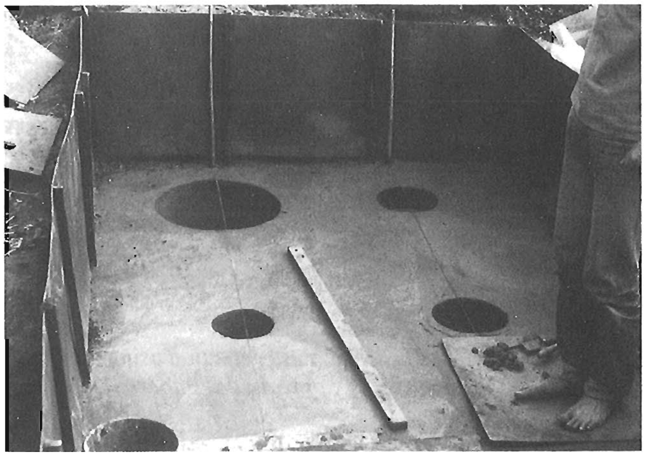

Figure 2. Cylindrical voids excavated into the clay base of the test site.

TEST SITE

A test site was constructed to simulate the conditions encountered in many void detection surveys. Figure 2 shows cylindrical void targets excavated into the clay base of the test site. A total of seven cylindrical voids of varying thickness and diameter were located in two lines on the test site base (Fig. 3). An aluminum sheet target was also placed on the clay interface as a reference target, with a known reflection coefficient of R = 1. The top surface of the voids were covered by styrene covers and then the clay layer was completely sealed using a polythene sheet. A layer of air dried sand of 200 mm thickness was poured onto the test site base to simulate a layer of concrete.

A monorail system was designed to allow the antenna units to be moved along the line of voids at a constant velocity. The system allowed changes to be made in ground clearance and orientation of the antenna units. Figures 4A and 4B shows the GSSI-SIR 8 system used to carry out the test site measurements. Performance tests on the system indicated that data showed no significant changes with time, soil, and temperature or relative humidity of the air, so it was valid to compare data sets obtained over a period of days. The filters and amplifiers in the control unit can cause significant phase and amplitude changes to the waveforms, so the system was set up to record both pre- and post-control module data.

QUALITATIVE INTERPRETATION

Figure 5 shows a typical 1 GHz profile of line 2. The two large diameter air voids produce typical void responses. Both reflections are characterized by high amplitude reverberations and phase changes relative to the sand-clay interface reflection, but the reflection from the base of the void is ambiguous. The reflections from the two smaller diameter voids show a slight phase change relative to the clay interface, but they do not show a well developed reverberation.

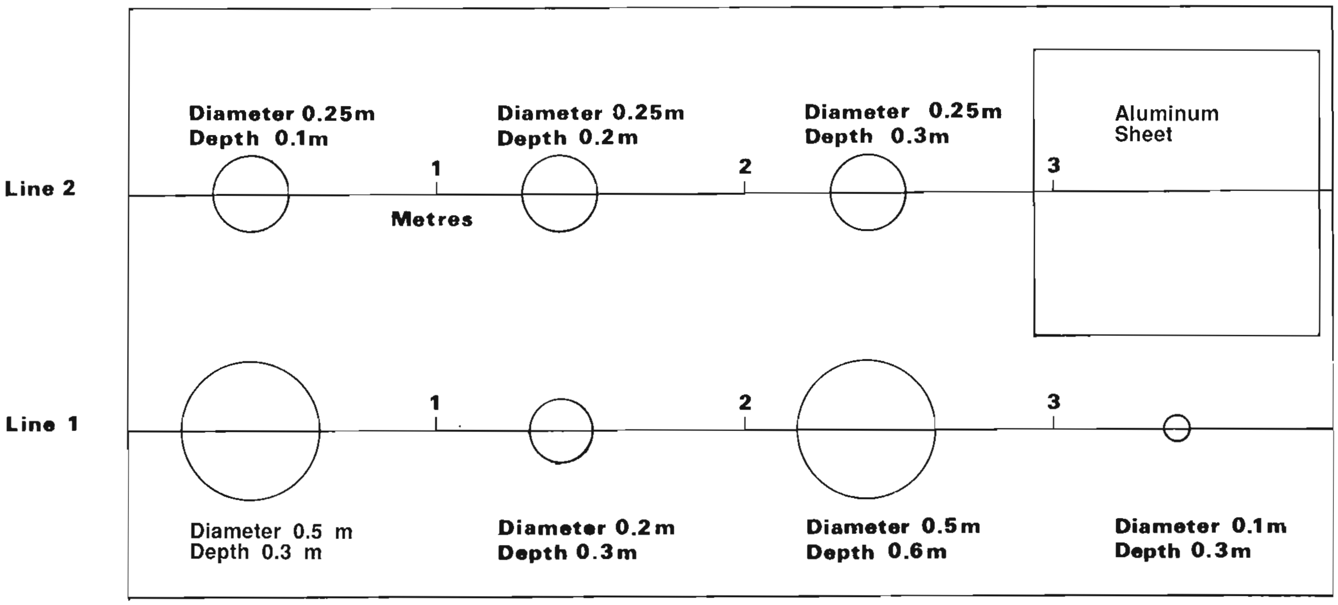

Figure 3. Plan of the test site. (The term "depth" refers to the vertical thickness of the voids, measured along the axial length of the cylindrical voids.)

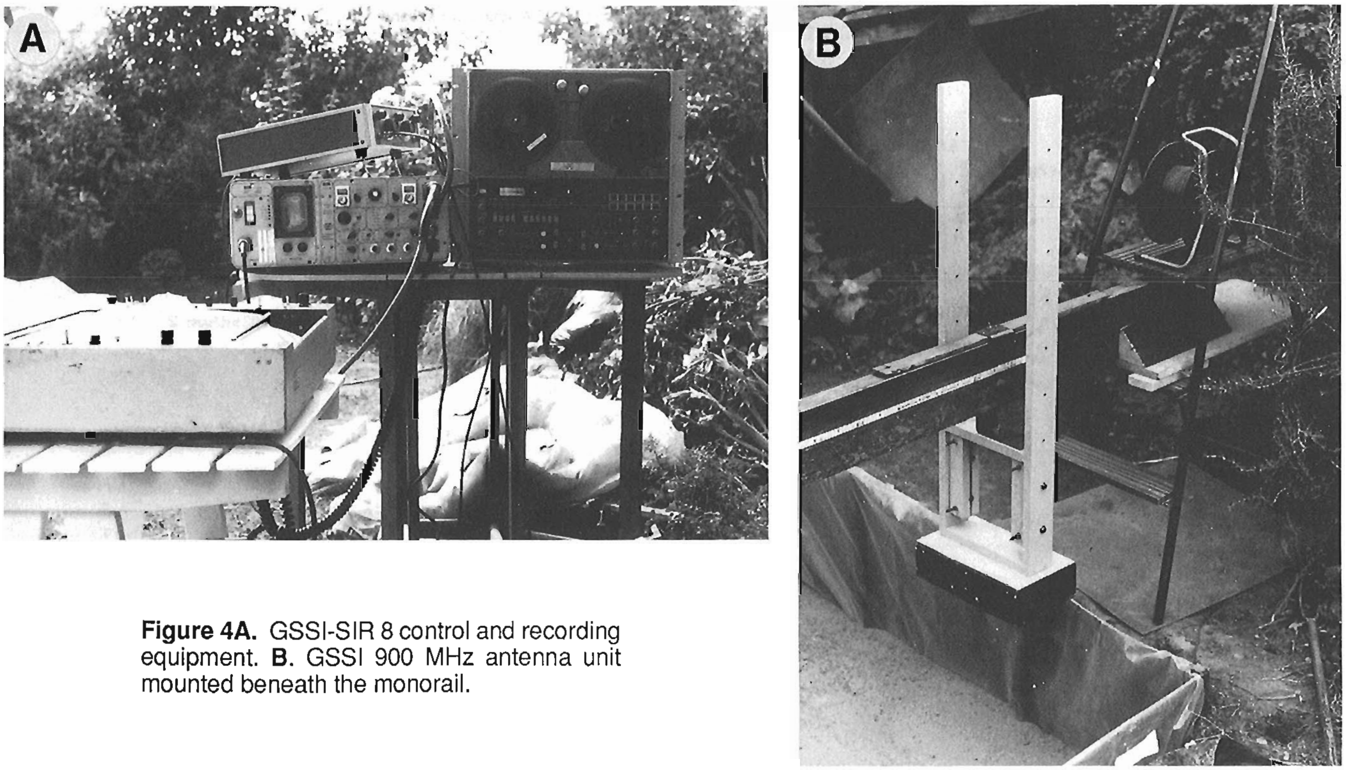

Figure 4A. GSSI-SIR 8 control and recording equipment. **B.** GSSI 900 MHz antenna unit mounted beneath the monorail.

METHOD OF PROCESSING

The GSSI antenna electronics contains a sampling head similar to that used by a high frequency sampling oscilloscope. This sampling process reconstructs the individual radar scans in analogue form over a much longer time base, usually of the order of a million times the original duration. This brings the waveform frequencies into the audio frequency range, which allows the use of normal cables and recording equipment. The low frequency representation of the high frequency waveforms are calibrated by time and frequency ratios as follows:

$$\text{Time ratio} = \frac{\text{Known time in nanoseconds}}{\text{Known time in seconds}} \qquad (1)$$

$$\text{Frequency ratio} = \frac{1}{\text{Time ratio}} \qquad (2)$$

The processing was carried out using the Princeton Applied Research Spectrum Analyzer model 4512 and some associated control and recording equipment. The spectrum analyzer digitizes specific waveforms and outputs the magnitude spectrum. Only the pre-control unit waveforms were processed, because the amplifiers within the control module introduced significant amplitude and phase distortion to the post control module waveforms.

The magnitude spectra are calibrated in terms of megahertz by multiplying the measured frequency points by the frequency ratio. The values for this experiment are given in Table 1.

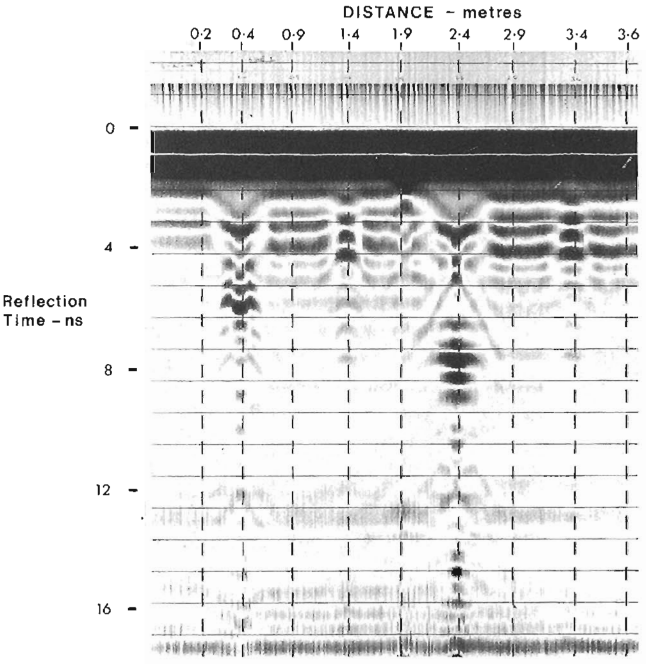

Figure 5. GPR profile along line 1, surveyed using the 1 GHz antenna at a ground clearance of 30 mm.

THEORY

The method of analysis assumed that the reverberations generated by the targets approximate to standing wave patterns. Standing waves are normally formed when a continuous frequency source is incident on a reflecting interface. The interference between the incident and reflected waves forms a space pattern of maxima and minima. In this

Table 1. Calibration of the frequency points of the magnitude spectra

Frequency ratio = 6 x 10^8

Sample point	Frequency nearest Hz	Frequency MHz range	Sample point	Frequency nearest Hz	Frequency MHz range
0	0	0			
1	6	36	18	116	692
2	13	78	19	122	732
3	19	114	20	129	774
4	26	156	21	135	810
5	32	192	22	141	846
6	39	234	23	148	888
7	45	270	24	154	924
8	51	306	25	161	966
9	58	348	26	167	1002
10	64	384	27	174	1044
11	71	426	28	180	1080
12	77	462	29	186	1116
13	84	504	30	193	1158
14	90	540	31	199	1194
15	96	576	32	206	1236
16	103	618	33	212	1272
17	109	654	34	219	1314

Scan rate 6.4 scans per second

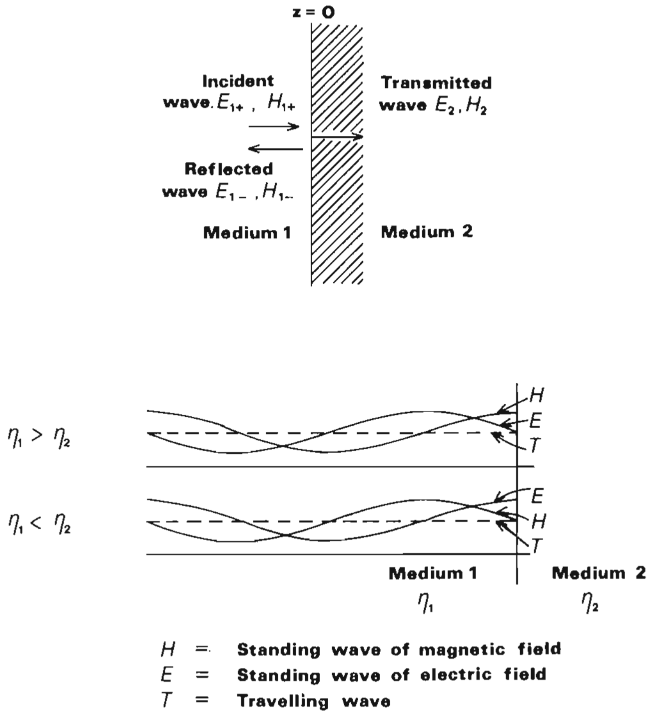

Figure 6. The formation of standing waves (after Ramo et al., 1965). Normal reflections from a planar interface for a single frequency, continuous wave.

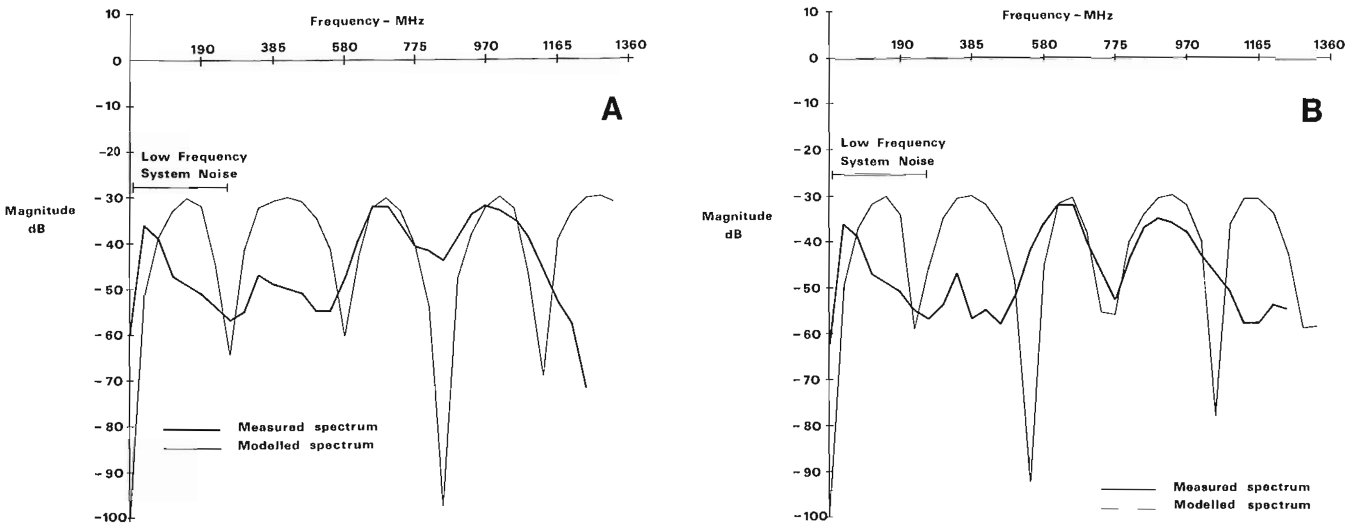

Figure 7. Comparison between the modelled and measured spectra (900 MHz antenna) for the aluminum sheet reflection, **A.** Ground clearance 180 mm. **B.** Ground clearance 230 mm.

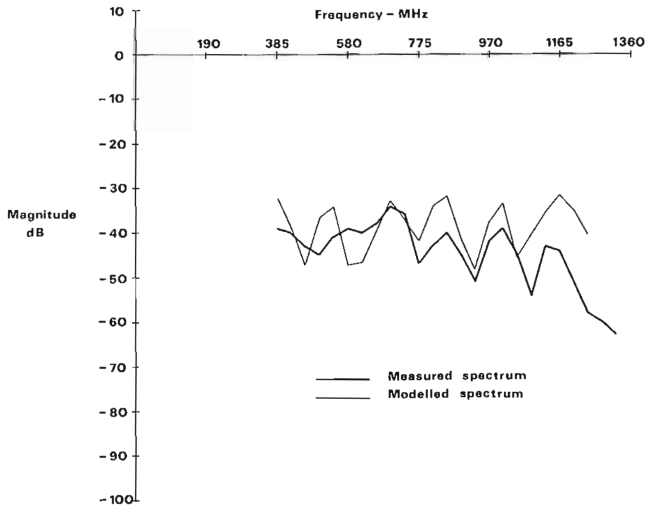

Figure 8. The modelled spectrum of the 0.6 m thickness void compared to the measured 1 GHZ spectrum (Ground clearance 30 mm).

case similar phenomena are caused by multiple reflections of a single transmitted pulse. Any interface lying close to the antenna generates a reverberation, but the nature of the reverberation varies depending on the dielectric properties of the materials concerned.

The amplitude of the standing wave at a particular position depends on the phase difference between the reflected and incident waves. Figure 6 shows that where the reflection coefficient is positive, an $\underline{E}$ field maximum occurs at the interface and subsequent maxima occur at even integer multiples of $\lambda/4$. The opposite applies to negative polarity reflections with maxima occurring at odd integer multiples of $\lambda/4$. The same criteria can be applied to several layers of material by considering the total number of wavelengths propagation between the source (antenna) and the terminating load (the base interface).

The magnitude spectra of the aluminum sheet waveforms were modelled using the Smith transmission line chart (Smith, 1944). Explanations of how the Smith transmission line chart are used are given in standard electromagnetic text books such as Ramo et al. (1965). The propagation velocities and impedances for the model were calculated from the dielectric constant values for the media. Dielectric constants for the sand and clay layers were calculated from measured volumetric water content values, using the empirical relationship derived by Topp et al. (1980). Figures 7A and B compare the measured and modelled magnitude spectra of the aluminum sheet at two different values of ground clearance respectively and Figure 8 compares the spectra for the 0.6 m thickness void. The overall agreement between the measured and modelled data indicated that the standing wave model was approximately correct. However, the modelling technique did not provide a direct way of identifying voids or measuring void thickness. A method was devised based on measurements of the frequency positions and relative amplitudes of the maxima and minima within the spectra.

The total number of wavelengths for propagation between the clay interface and the antenna is defined as follows:

$$\begin{array}{lclcl}\text{Total number} & = & \text{No. of wavelengths} & + & \text{No. of wavelengths} \\ \text{of wavelenghts} & & \text{in concrete (sand)} & & \text{in air (Ground clearance)}\end{array}$$

$$= f\left(\frac{Da}{c} + \frac{Dc}{Vc}\right) = f\,(T) \qquad (3)$$

where

Da is thickness of air between the antenna and the ground surface (ground clearance)

Dc is thickness of the concrete layer (sand)

f is frequency

Vc is velocity of the concrete layer (sand)

c is velocity of light in air (3×10^8 m/s).

By rearrangement

$$T = \frac{Da}{c} + \frac{Dc}{Vc} \tag{4}$$

The parameter T can be expanded to include an air void beneath the concrete slab:

$$T = \frac{Da}{c} + \frac{Dc}{Vc} + \frac{Dv}{c} \tag{5}$$

The positions of the received frequency domain maxima and minima occur at multiples of $\lambda/4$ from antenna to reflector, so the frequency positions at which they occur is given by:

$$F = \frac{N}{4T} \quad \text{(for N = 1,2,3, etc.)} \tag{6}$$

The frequency difference between adjacent maxima and minima is therefore defined as:

$$\Delta f = \frac{(N+2)}{4T} - \frac{N}{4T} = \frac{1}{2T}$$

Therefore

$$T = \frac{1}{2.\Delta f} \tag{7}$$

The polarity of the reflection coefficient of the load is given by:

$$F = N.\Delta f \quad \text{(where N = 1,2,3...)} \tag{8}$$

This equation identifies frequencies that are integer multiples of the frequency difference between the peaks and troughs. If the values of F are maxima then the load has a positive reflection coefficient and where the values of F are minima the load has a negative reflection coefficient.

The magnitude of the reflection coefficient of the terminating load of the standing wave controls the amplitudes of the maxima and minima values of electric field $\underline{E}$ at the position of the antenna. The layers between the load and the antenna can only modify the frequency positions at which these occur if losses within the propagation layers are assumed to be laterally constant. The ratio between the maxima and minima amplitudes is related to the reflection coefficient of the load by the following equation:

$$M_R = \frac{Amax}{Amin} = \frac{|R| + 1}{-|R| + 1} \tag{9}$$

$$\text{where } \underset{(dB)}{M_R} = \underset{(dB)}{Amax} - \underset{(dB)}{Amin} \tag{10}$$

and |R| is the absolute value of the reflection coefficient.

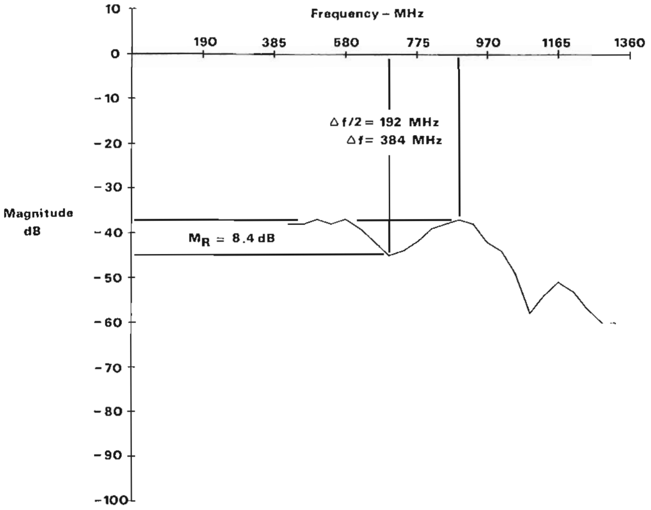

Figure 9. Measurement procedure, 1 GHz spectrum for the sand-clay interface. (Ground clearance 30 mm.)

CAVITY DETECTION AND DEPTH ESTIMATION METHOD

The first two stages of the method establish the background response of the concrete-soil reflections. This background response is then used to predict the various void responses. A concrete-soil waveform is analyzed in an area where the thickness of concrete is known. Figure 9 shows how the frequency difference Δf and magnitude ratio M_R were measured from the sand-clay interface magnitude spectrum, which simulated the concrete-soil interface in this experiment.

Measuring the velocity of concrete

By rearranging equations 4 and 7, the concrete velocity is obtained in terms of measured variables:

$$Vs = \frac{Dc}{\frac{1}{2.\Delta f} - \frac{Da}{c}} \tag{11}$$

Measuring the magnitude and polarity of background load reflection coefficient

The magnitude of the reflection coefficient is calculated from the magnitude ratio using a modified form of equation 9:

$$\text{antilog}_{10} \frac{(M_R)}{20} = \frac{+|R| + 1}{-|R| + 1}$$

where

$$MR\ (dB) = Amax\ (dB) - Amin\ (dB) \tag{12}$$

The polarity of the reflection coefficient is found by substituting Δf into equation 8. Maxima values of F indicate a positive reflection coefficient, whereas minima values of F indicate a negative reflection coefficient.

Measuring the velocity of the underlying soil

The reflection coefficient, $R_{1,2}$ is calculated using the following low loss reflection coefficient equation:

$$R_{1,2} = \frac{V_2 - V_1}{V_2 + V_1}$$

$$V_2 = V_1 \, (R_{1,2}+1)/(1-R_{1,2}) \qquad (13)$$

where V_1 and V_2 are the propagation velocities in media 1 and 2, respectively.

Predicting the max/min ratios of various void spectra

Load reflection coefficient values are calculated by substituting the "concrete" and "soil" velocities into equation 13. Table 2 lists the various void targets, their load reflection coefficients, and corresponding magnitude ratios for the test site conditions calculated from the background values using equation 9.

The finite depth air void corresponds to standing waves terminated by the base of the void (air-soil interface), whereas the "infinite" air layers are voids where the base of the void occurs at greater reflection times than the analyzed time window (= 17 ns).

Max/min ratios were also calculated for cavities completely and partially filled with water. The upper surface of the water layer will usually form the load for both types of water filled cavity because of the extremely low velocity in water, v = 0.033 m/ns, which means that only a small thickness is required to isolate the base of the cavity from the standing wave; i.e., the standing wave decays before the pulse propagates to the base of the void.

The values of max/min ratio given in Table 2 indicate that all the different types of void could be detected by setting threshold limits on either side of the background value. The test site conditions simulated saturated clay beneath concrete. Unsaturated soil would generally give much lower values of max/min ratio, so that all of the void reflections would have greater max/min values than background.

Table 2. Values of load reflection coefficient and magnitude ratio for the various types of void reflection

Target	Load reflection coefficient	Maximum to minimum ratio (M_R)	
		Calculated (dB)	Measured (dB)
Finite air void Load - air/clay	-0.653	13.6	14.3
Infinite air void Load - 'concrete'/air	+0.285	5.1	–
Infinite water void Load - 'concentre'/water	-0.67	14.1	–
Partially water filled void Load - air/water	-0.80	19.2	–
Background Load - 'concrete'/clay	-0.45	–	8.4

Cavity target identification and thickness estimation

Table 2 shows that the partially waterfilled void has the greatest max/min ratio of the four types of void target. This should uniquely identify this type of void in all conditions, because the air-water load has the largest value of reflection coefficient likely to be encountered in natural void systems. The other types of void reflection may not give max/min ratios that uniquely identify this type of void, but values of frequency difference should remove this ambiguity. The "infinite" air and water layers should both have Δf values that are identical to the background concrete-soil spectra, but the polarity of the load reflection coefficient, found through equation 8, would be positive for the air cavity and negative

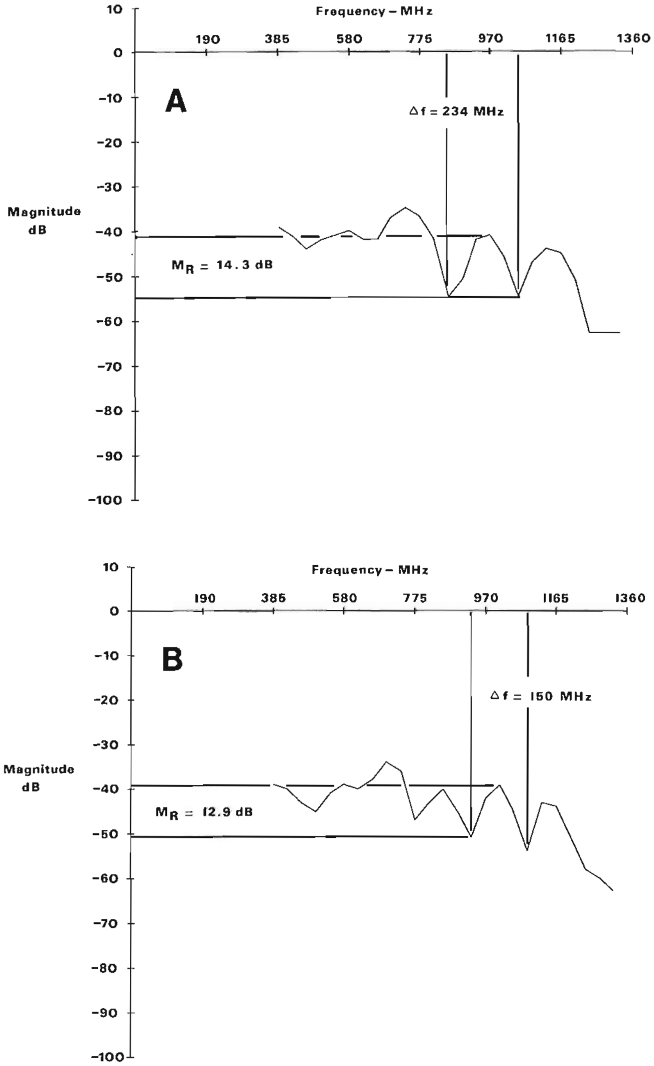

Figure 10. Measurement procedure, 1 GHz spectrum for **A.** the 0.3 m thickness, 0.5 m diameter void; **B.** the 0.6 m thickness, 0.5 m diameter void (Ground clearance 30 mm).

for the water filled cavity. Void spectra, which show a decrease in the values of Δf relative to the background level, indicate that the standing wave is being terminated by an interface below the concrete base. The thickness of this type of void can be calculated using a combined version of equations 5 and 7:

$$Dv = c\left(\frac{1}{2.\Delta f} - \frac{Ds}{Vs} - \frac{Da}{c}\right) \tag{14}$$

Figures 10A, B show the measuring procedure for the 0.3 and 0.6 m thickness, 0.5 m diameter voids. The thicknesses calculated using the above procedure were 0.28 and 0.64 m respectively. These values are within 7% of the known values.

APPLICATION OF CAVITY DETECTION METHOD

The method of cavity detection can only be applied where the base of the concrete is forming a standing wave reverberation. These reverberations can normally be identified by visual observation of the time-distance profiles.

As shown earlier the method of depth estimation could only be applied to the finite thickness voids and could not be applied to the infinite thickness air or water filled voids,

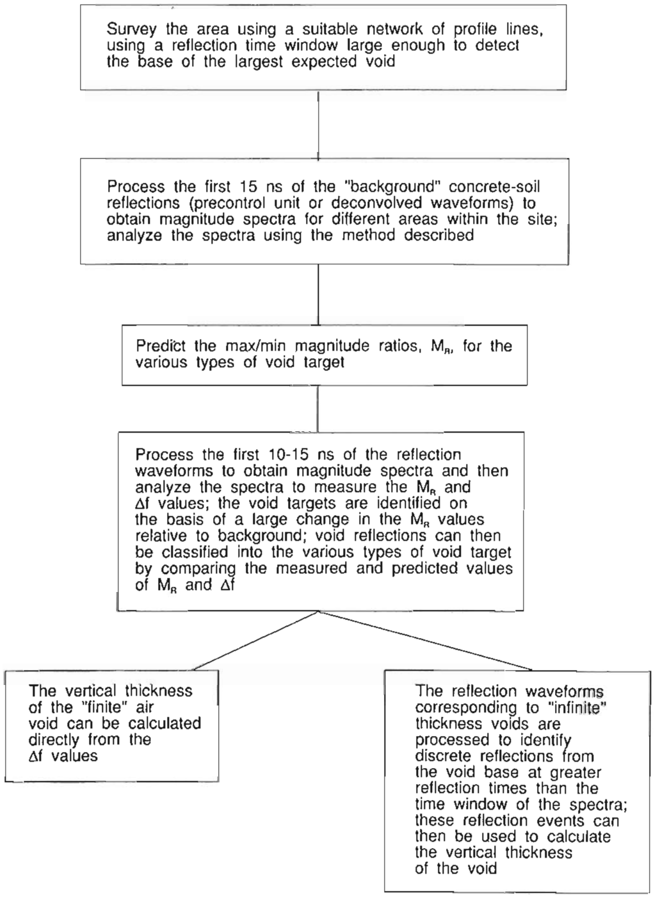

Survey the area using a suitable network of profile lines, using a reflection time window large enough to detect the base of the largest expected void

Process the first 15 ns of the "background" concrete-soil reflections (precontrol unit or deconvolved waveforms) to obtain magnitude spectra for different areas within the site; analyze the spectra using the method described

Predict the max/min magnitude ratios, M_R, for the various types of void target

Process the first 10-15 ns of the reflection waveforms to obtain magnitude spectra and then analyze the spectra to measure the M_R and Δf values; the void targets are identified on the basis of a large change in the M_R values relative to background; void reflections can then be classified into the various types of void target by comparing the measured and predicted values of M_R and Δf

The vertical thickness of the "finite" air void can be calculated directly from the Δf values

The reflection waveforms corresponding to "infinite" thickness voids are processed to identify discrete reflections from the void base at greater reflection times than the time window of the spectra; these reflection events can then be used to calculate the vertical thickness of the void

Figure 11. A new method of void detection using standing wave analysis.

Table 3. Standing wave analysis of two 0.25 m diameter voids, with vertical thicknesses of 0.1 and 0.2 m

Antenna (MHz)	Cavity thickness (m)	Frequency range	M_R (dB)	Δf	Load reflection coefficient	Load impedance (Ohms)
900	0.1	LOWER	15.7	384	-0.718	34.5
900	0.1	UPPER	14.1	384	+0.671	1066.1
900	0.2	LOWER	12.0	384	-0.600	52.6
900	0.2	UPPER	12.0	384	+0.600	837.0
1000	0.1	LOWER	14.0	384	+0.667	1050.8
1000	0.1	UPPER	12.0	300	-0.60	52.6
1000	0.2	LOWER	14.0	384	+0.667	1050.8
1000	0.2	UPPER	15.3	255	-0.710	35.6

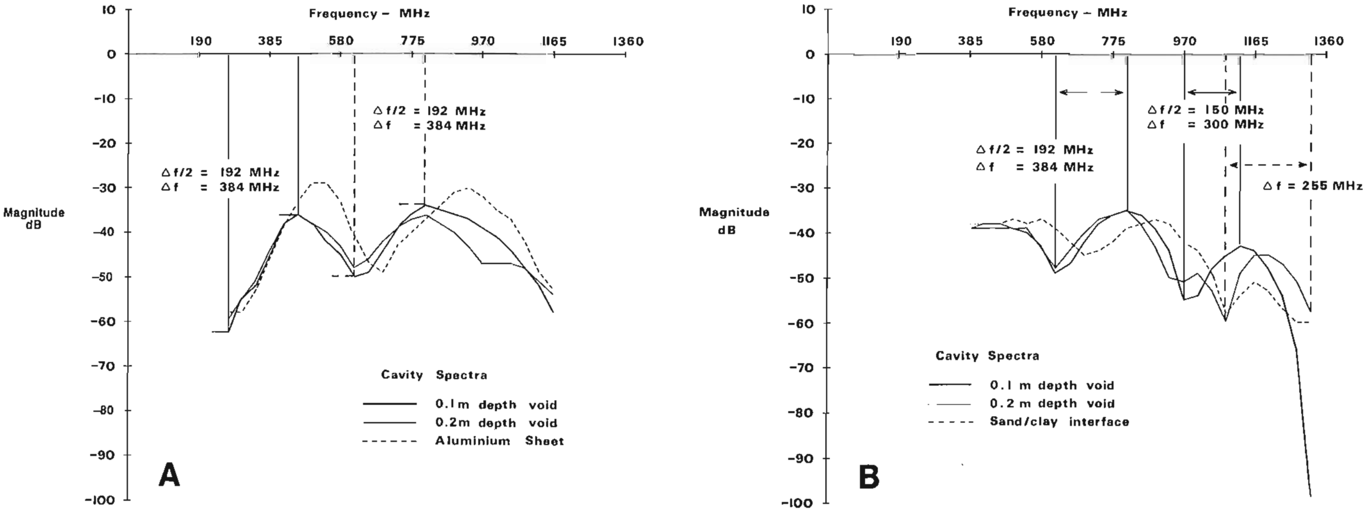

Figure 12A. 900 MHz spectra for 0.25 m diameter, 0.1 and 0.2 m thickness voids, compared to the aluminum sheet spectrum. **B.** 1 GHz spectra for 0.25 m diameter, 0.1 and 0.2 m thickness voids, compared to clay interface spectrum.

because the standing waves were terminated above the level of the cavity base. It should be possible to measure thickness of all void targets by using the revised procedure summarized in the block diagram (Fig. 11).

LIMITATIONS IMPOSED BY VOID DIAMETER

The test site data indicate that the method of depth estimation became more difficult to use as the diameter of the voids decreases. Figures 12A, B present the spectra for 0.25 m diameter voids of 0.1 and 0.2 m thickness, obtained using the 900 MHz and 1 GHz antenna units. A visual examination of the void spectra shows an assymetric distribution of maxima and minima as a function of frequency, across both antenna frequency ranges. The method of analysis was therefore applied in separate stages to the upper and lower parts of each spectrum curve. The positions at which Δf and M_R were measured are shown on Figures 12A and B. The analysis of the spectra is presented in Table 3, with the electrical characteristics of the load expressed in impedance. The load reflection coefficient is related to the load impedance through the following equation:

$$R_{1,2} = \frac{Z_2 - Z_1}{Z_2 + Z_1} \quad (15)$$

where

Z_1 is impedance of the 'concrete'

$$Z_1 = \frac{377.V_1}{c} \text{ (ohms)}$$

Z_2 is impedance of the load (ohms).

Both the lower and upper parts of the 900 MHz spectra have a Δf value identical to the clay interface, indicating that the standing wave is terminated by the top of the void. The impedance of the load increases dramatically between the lower and upper parts of the frequency range, causing a switch between the negative and positive polarity reflection coefficients. The reflection coefficients of the load are extremely high over both frequency ranges. Impedance was used to quantify the electrical properties of the load, instead of velocity, because the velocity values calculated for the load from the upper part of the frequency range were greater than the speed of the light. This clearly indicated that the terminating load to the standing wave was not behaving as a normal planar boundary between two materials.

The lower parts of the 1 GHz spectra overlap the upper part of 900 MHz spectra and show a similar type of behaviour, but above 960 MHz the two void spectra curves diverge to form different patterns of maxima and minima. Analysis of the spectra indicate that the air voids are now behaving in the predicted manner, with the load to the standing wave formed by the base of the void. The calculated void thicknesses of 0.117 and 0.206 m approximate to the true void thicknesses.

The electrical properties of standing waves produced by the 0.25 m diameter voids can be separated into three zones, by combining the data obtained from the two sets of spectra:

Zone 1 200-425 MHz

Terminating load formed by the top of the void; analysis indicates an anomalously low impedance value for the air void.

Transition

Zone 2 580-900 MHz

Terminating load still formed by the top of the void, but analysis indicates an anomalously high impedance value for the air void.

Transition

Zone 3 960-1360 MHz

Air void behaves in the predicted way, with the terminating load formed by the base of the void.

GUIDED WAVES IN VOIDS

It is normally assumed that the electromagnetic waves forming a GPR pulse propagate as a TEM mode, with both electric and magnetic field vectors orientated perpendicular to the direction of propagation; however, the analysis of the 0.25 m diameter void spectra indicated that the waves were propagating in a different way. It appears that the cylindrical air voids were acting as waveguides in the test site conditions.

Cylindrical waveguides are devices used in high frequency electronics, consisting of a dielectric medium surrounded by a cylindrical conductor. These devices cannot support the propagation of TEM waves because of the boundary conditions at the conductor surface. The $\underline{H}$ magnetic field must be parallel to the conducting surface, which is impossible for TEM waves propagating along the cylinder. However, two groups of electromagnetic waves, known as TE and TM waves, can propagate inside closed hollow conductors. The propagation of these waves is limited to frequencies above certain critical or cutoff frequencies. Both TE and TM waves can form in a number of different patterns (modes), but as the modes become more complicated the cutoff frequencies become higher so the lowest frequency, or dominant mode, tends to propagate most effectively. The cutoff frequencies for modes in cylindrical guides are directly proportional to the velocity of the medium filling the guide and inversely proportional to the radius of the guide. The dominant mode for a cylindrical waveguide is the $TE_{1,1}$. The cutoff frequency for the $TE_{1,1}$ mode is defined by the following equation:

$$Fc = \frac{V.0.293}{r}$$

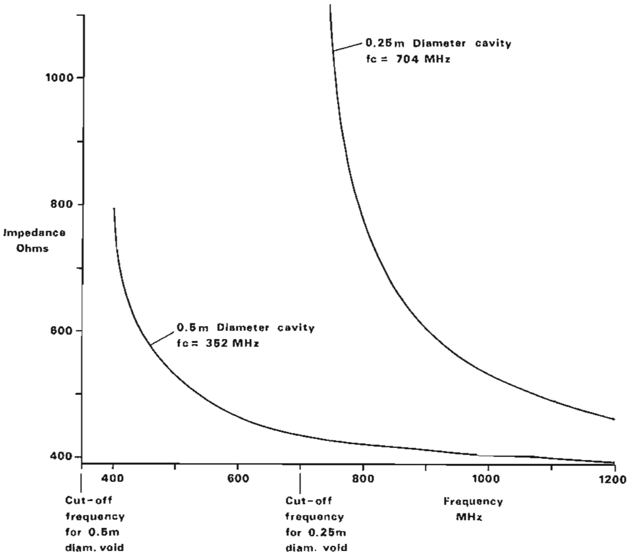

Figure 13. TE$_{1,1}$ wave impedance as a function of frequency, for cylindrical voids of 0.25 and 0.5 m diameter.

where

v is Velocity of medium enclosed by the guide

r is radius of the guide.

For a 0.25 m diameter air void Fc = 703 MHz, whereas for a 0.5 m void Fc = 352 MHz.

Below the cutoff frequency, the top of the guide forms an imaginary load impedance to incident waves. This results in a strong reactive reflection (negative polarity) of the wave energy back to the source, with no propagation of energy into the guide. This total reflection of energy is similar to the reflection generated by a sheet of metal.

Figure 13 shows the $TE_{1,1}$ wave impedance as a function of frequency above the cutoff frequency for perfect cylindrical waveguides of 0.25 and 0.5 m diameter. The impedance of the void is extremely high close to the cutoff frequency and then drops with increasing frequency towards the TEM wave impedance (377 ohms). Therefore, at frequencies well above the cutoff frequency the position of the maxima and minima within the spectra should approximate to the expected TEM pattern.

The combined frequency ranges for the 900 MHz and 1 GHz spectra extend well above and below the predicted cutoff frequency of the 0.25 m diameter air void. The frequency and high frequency responses of the 0.25 m diameter void (zones 1 and 3) agree with the wave guide model described above, but the central frequency range shows an anomalously high load impedance extending below the cutoff frequency and no evidence of wave propagation above cutoff frequency.

The anomalous behaviour in the vicinity of the cutoff frequency is probably caused by the finite conductivity of the clay guides. An imperfectly conducting guide causes two main variations to the waveguide properties: (1) The dispersion in phase and group velocities immediately above the cutoff frequency results in the severe attenuation of waves propagating within the guide. (2) The cutoff frequency no longer corresponds to a precise frequency point, but corresponds to a transitional frequency range between the two regions.

The high attenuation above cutoff frequency would prevent the $TE_{1,1}$ waves reaching the base of the void. The high impedance of the void in the vicinity of the cutoff would result in the top surface of the void forming a load with a positive reflection coefficient of unusually high magnitude as observed on the spectra.

The test site used cylindrical voids, because these provided a void of standard shape. Similar waveguide effects would occur in any shape of void, where an air or lowloss

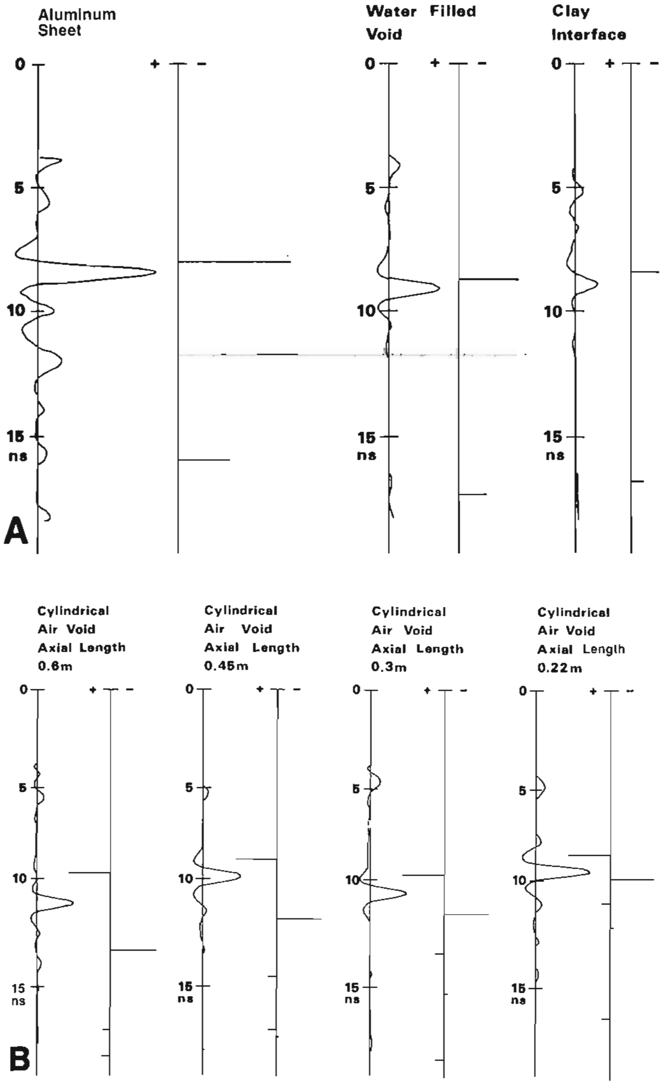

Figure 14. Comparison between the '900 MHz' waveforms and the predicted impulse response for **A.** the aluminum sheet, clay interface, and water filled voids; and **B.** the four air voids. (Unity amplitude was assumed equal to the amplitude of the aluminum sheet reflection).

dielectric is enclosed by a medium of fairly high conductivity such as clay. The shape of the guide effects the type and mode, of the dominant mode which propagates along the guide and varies parameters such as the cutoff frequency. The theory and properties of waveguides are explained in detail in electromagnetic textbooks such as Ramo et al. (1965).

An earlier experiment on the same test site was carried out using a 0.5 m thickness of wet sand to simulate a thicker layer of concrete. The sand layer was underlain by five cylindrical voids excavated into the clay base, all with diameters of 0.25 m. The thicker layer of sand provided sufficient time delay to isolate the void reflections from the transmitted pulse to produce discrete reflections. Figures 14A, B compare individual waveforms to their impulse responses, predicted from volumetric water content measurements using the relationship of Topp et al. (1980). The aluminum sheet, water filled void, and clay interface reflections (Fig. 14A) all show an approximate match to their predicted impulse response. However, the air voids reflections (Fig. 14B) all show a negative polarity reflection from the top of the void, where the impulse response predicted a positive polarity reflection. None of the void reflections show any evidence of the reflections predicted for the base of the void. These results suggest that the void targets are behaving as cylindrical waveguides, with the reflected pulses formed predominantly by frequencies below the cutoff frequency.

It is believed that waveguide effects may be a factor governing the general propagation of GPR pulses through the ground, particularly in clay rich soils. Waveguide propagation could be caused by any lowloss dielectric buried within a clay soil; such as voids, holes, or trenches backfilled with rubble fill, buried artifacts such as stone or brick walls, or concrete obstructions. The analysis of the void reflection has shown that waveguide behaviour can generate confusing reflections and can prevent the propagation of low frequency waves beneath the top of the wave guide structure.

CONCLUSIONS

Results from a test site experiment were used to develop a method of void detection and depth estimation based on standing wave analysis of GPR data. The method is applicable where voids have formed beneath thin layers of concrete and where the reflection from the base of the concrete slab interferes with the transmitted pulse to form a temporary standing wave pattern. The method of processing could also be applied to other applications that involve the detection of targets close to the antenna.

The method of depth estimation becomes more difficult to use as the area of the voids decreases, because of waveguide effects produced by the clay walls to the void. Similar waveguide behaviour may also influence the propagation of the radar pulses in more general applications of the GPR method.

ACKNOWLEDGMENTS

The author thanks Prof. D.J. Blundell, Royal Holloway and New Bedford College, University of London, for his supervision of this research project, which was funded by NERC CASE research grant. He also thanks his parents for allowing their garden to be used as a test site, and to Mr. D. Scott and Mr. A. Thomas for their assistance with this project.

REFERENCES

Clemena, L.C. and McGhee, K.H.
1980: Applicability of radar subsurface profiling in estimating sidewalk undermining; Transportatopm Research Records, v. 752, p. 21-28.
Kovacs, A. and Morey, R.M.
1983: Detection of cavities under concrete pavement; US Army CRREL Report 83-18, Hanover, New Hampshire.
Ramo, S., Whinnery, J.R., and Van Duzer, T.
1965: Fields and waves in communication electronics; Wiley, London.
Smith, P.H.
1944: A improved transmission-line calculator; Electronics, v. 17, p. 130.
Steinway, W.J., Echard, J.D., and Luke, C.M.
1981: Locating voids beneath pavement using pulsed electromagnetic waves; National Cooperative Highway Research Program, Report 237, Washington D.C.
Topp, G.C., Davis, J.L., and Annan, A.P.
1980: Electromagnetic determination of soil water content: Measurements in coaxial transmission lines; Water Resources Research, v. 16, no. 3, p. 574-582.

Radar investigations of firn structures and crevasses

Jonathan M. Glover[1] and Huw V. Rees[2]

Glover, J.M. and Rees, H.V., 1992: Radar investigations of firn structures and crevasses; in Ground penetrating radar, ed. J. Pilon; Geological Survey of Canada, Paper 90-4, p. 75-84.

Abstract

A ground probing radar survey investigated the near surface structure of part of the western margin of Greenland Ice Sheet, to detect buried crevasses, which pose a hazard to heavy transport movement across the ice.

The radar sections revealed that firn typically produced a sequence of reflections caused by thin ice layers within the compacted snow. Certain localized areas of the firn, however, showed a totally different structure, with few internal reflections apart from a weakly defined, angularly discordant layering. These areas were interpreted as isolated blocks of mature glacial ice buried within a firn sequence.

Two distinctly different crevasse responses were detected by the radar. The type 1 response was characterized by a reflection free zone adjacent to the crevasse walls, which was caused by secondary alteration of the firn forming the crevasse walls. This type of crevasse was generally buried at shallow depths, in relatively immature firn. The type 2 response was characterized by well developed, hyperbolic scattering events originating from the base of the snow bridge and the terminations of the firn layers against the crevasse wall. The type 2 response was either confined to the glacial ice or was buried at depth in mature firn, where secondary alteration was less likely to occur.

Résumé

Un levé par géoradar a été réalisé dans la structure à faible profondeur d'une partie de la marge occidentale de l'inlandsis groenlandais afin d'y détecter les crevasses enfouies qui représentent un danger pour le transport lourd sur la glace.

Les coupes radar ont révélé que le névé produisait en général une séquence de réflexions causées par les minces couches de glace présentes au sein de la neige compactée. Certaines zones du névé, cependant, ont revélé une structure totalement différente, ne produisant que quelques réflexions internes à l'exception d'une stratification angulairement discordante faiblement définie. Ces zones ont été interprétées comme des blocs isolés de glace mature enfouie au sein d'une séquence de névé.

Deux crevasses ont produit des réponses radar nettement différentes. La première était caractérisée par une zone sans réflexion près des parois de la crevasse, causée par une altération secondaire du névé formant les parois de la crevasse. Ce type de crevasse est généralement enfoui à faible profondeur, dans un névé relativement immature. Le deuxième type était caractérisé par des événements de diffusion hyperboliques bien formés prenant origine dans la base du pont de neige et dans les extrémités des couches de névé contre la paroi de la crevasse. La réponse du deuxième type de crevasse a été confinée soit dans la glace du glacier ou à grande profondeur dans un névé mature où une altération secondaire était moins susceptible de se produire.

---

[1] Subsurface Geotechnical Services, Unit 235, Stratford Workshops, Burford Road, London, UK E15 2SP

[2] Royal Holloway and Bedford New College, University of London, Surrey, UK TW20 OEX

INTRODUCTION

Subsurface radar has been used to detect crevasses at the western margin of Greenland Ice Sheet. The area of the subsurface radar survey grid covered an ice field laying between Wegner and South Lakes glaciers, close to the mining settlement of Maarmorlik. The area, lying at a latitude of 70°N and longitude of 55°W, has a surface elevation varying between about 1056 and 1111 m a.s.l. The ice thickness varies between about 170 and 300 m.

The survey covered the area of an exploration drilling grid north of the Maarmorlik lead-zinc ore body. Crevasses present a serious hazard to the movement of heavy drilling equipment and tractors across the ice (Fig. 1). The aim of the radar survey was to locate and delineate snow covered crevasses within the ice and to determine the depth of snow covering the crevasses (snow bridge thickness). This knowledge would allow safe roads to be marked out for the movement of equipment and personnel.

Ground probing radar (GPR) has been used for many years to measure the thickness of ice sheets and glaciers (e.g., Swithinbank, 1968; Robin et al., 1969). Radar systems used for this purpose were designed specifically for long range probing in low attenuation media; their low vertical and lateral resolution makes them inappropriate for crevasse detection. GPR has been used to investigate crevasses buried in Ross Ice Shelf, Antarctica, (Morey and Kovacs, 1982).

This paper describes the investigation of near surface firn structure of a subpolar ice field using a high resolution radar system. Another paper in this volume explains how the data can be enhanced by using digital processing techniques (Rees and Glover, 1992). The GPR technique has two main advantages over other methods of crevasse mapping, such as aerial reconnaissance and hand probing; 1) it can detect crevasses buried at depths of several metres, and 2) the technique is reasonably fast, with daily line kilometre rates of up to 810 km per day in good snow conditions. A similar survey had been carried out in the southern part of the exploration grid in the previous year (Morey, unpublished report, 1983). The first type of crevasse response described here was originally identified by Morey during that earlier investigation.

Figure 1. Exploration drilling rig operating on Greenland Ice Sheet.

Table 1. Typical density values for snow, firn, and ice (after Paterson, 1969)

Snow, ice type	Typical densities (g/cm^3)
"Wild snow" (new snow at low temperature in calm)	0.01–0.03
New snow (immediately after falling in calm)	0.05–0.07
Damp new snow	0.1–0.2
Settled snow	0.2–0.3
Depth hoar	0.2–0.3
Wind packed snow	0.35–0.4
Firn	0.4–0.85
Very wet snow and firn	0.7–0.8
Glacier ice	0.85–0.91

Table 2. Values of discrete vertical resolution, ground wavelength, and approximate lateral resolution for the firn medium

Frequency (MHz)	Discrete vertical resolution (m)	Ground wavelength (m)	Lateral resolution (m)
100	0.60	3.0	1.5
500	0.33	0.6	0.3

VELOCITY CALIBRATION AND RESOLUTION

Gudmandsen (1971) defines the relationship between the dielectric constant of ice and its density by the following equation:

$$\sqrt{K' = 1 + 0.85\rho} \qquad (1)$$

where ρ = density of the ice.

Table 1 shows the typical density range for firn, which is a mixture of compacted snow and ice that forms the top 10 m or so of many glaciers and ice sheets (Paterson, 1969). These values were used to calculate the range of dielectric constant using equation 1 as follows:

	ρ	K'	$V = C.K.^{1-1/2}$(m/ns)
Compacted snow	0.4	1.8	0.22
Ice	0.85	2.97	0.17

An intermediate estimate of 0.20 m/ns (K- = 2.25) was used to calibrate the time-distance profiles. The velocity of a firn sequence should decrease vertically as density increases with depth. Lateral changes would also be expected if the firn structure changed dramatically.

The two-way time window was set at 70 ns, allowing an estimated depth penetration of:

$$D = \frac{V.T}{2} = \frac{0.2 \times 70}{2} = 7.0 \text{ m}$$

Crevasses below this depth were unlikely to be a transportation hazard, even if 2-3 metres of snow was removed by excessive summer melting.

The Geophysical Survey Systems Inc. (GSSI) SIR 8 radar system was used for the survey operations. The radar system was used in combination with either the 100 MHz or 500 MHz centre frequency antenna units. Table 2 shows the values of discrete vertical resolution, wavelength, and approximate lateral resolution for both antennae based on the firn velocity value of 0.20 m/ns. The vertical resolution of both the antennae are greater than the ice layer thickness, so the ice layers generate a single composite reflection event formed by interference between the reflections from the upper and lower surfaces of the ice layer. The dielectric constant of the ice is greater than that of the surrounding snow, so the signs of the reflection coefficient of the upper and lower boundaries of the layer are negative and positive, respectively. Reasonably high amplitude composite reflections should be generated by layers with thicknesses of the order of $\lambda/4$. Where the layer thickness is less than $\lambda/4$, the composite reflection coefficient of the layer is directly proportional to the layer thickness, so the layer becomes effectively invisible to the radar where the ice layer thickness $<< \lambda/4$. Thus the higher resolution 500 MHz antenna would be more likely to detect the ice layers than the lower resolution 100 MHz antenna.

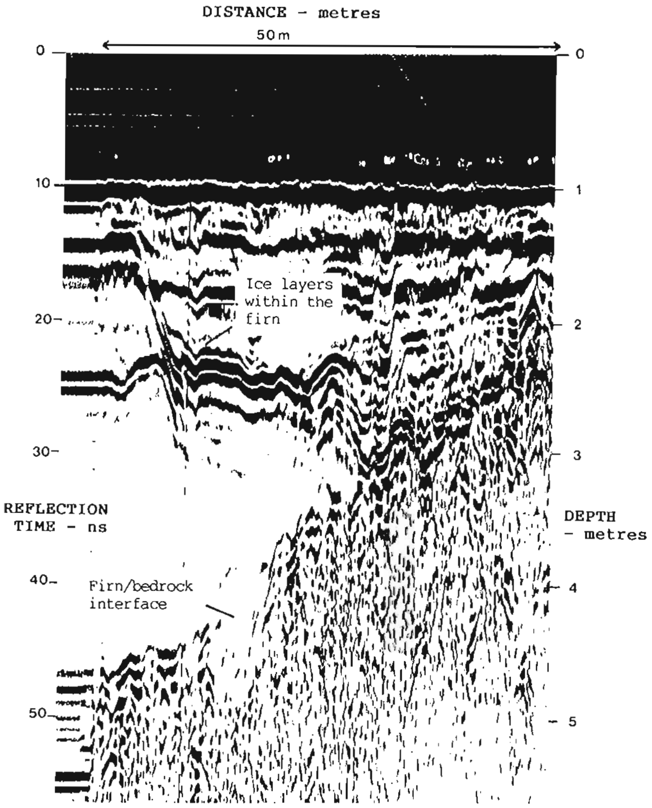

Figure 2. Test profile in the camp area, surveyed at 500 MHz.

Several test profiles were made in the camp area to test the resolution capability of the two antennae. Point probes revealed several ice layers within the compacted snow. The ice layers were estimated to be about 0.1 m thick separated by variable thicknesses of compacted snow. The total firn thickness varied between 2 and 4.5 m overlying bedrock. In Figure 2 a profile surveyed at 500 MHz shows reflection events corresponding to ice layers within the firn and the firn-bedrock interface. Figure 3 shows the same line profiled in the reverse direction at 100 MHz. The firn layers are poorly resolved and only the bedrock reflection event can be clearly correlated with Figure 2.

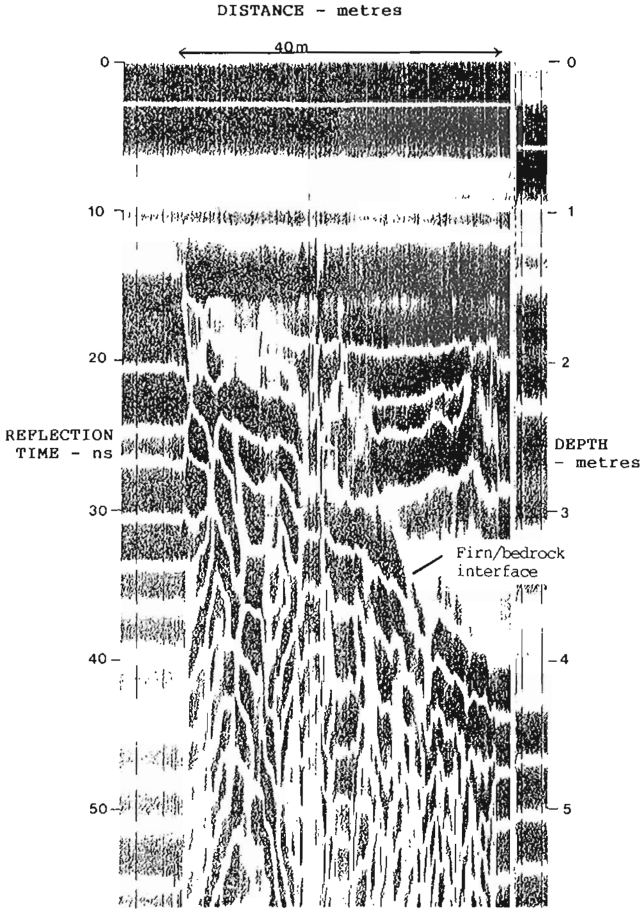

Figure 3. Test profile in the camp area, surveyed at 100 MHz.

Figure 4. Final towing arrangements used for the crevasse survey.

FIELD PROCEDURE

The GSSI equipment was towed along the survey lines using one or two skidoos depending on the snow conditions. The control and recording equipment were box-mounted on a sledge along with a small generator to provide power. Figure 4 shows the usual towing arrangement used for the survey. The skidoos towed the equipment at a speed of about 4 km/h. This fairly slow speed was necessary to provide sufficient data across the narrow crevasse targets.

The survey area was initially covered by a 500 m spacing square grid of profile lines, but additional lines were added where areal interpretation of the data was difficult. Position location was provided by a Topofil cotton thread chain between accurately surveyed grid points. Position markers were placed on the records at 50 m intervals. The Topofil chain showed an accuracy of about 3 m/km, but the position is only known to this accuracy at the marker positions. Intermediate positions can be interpolated between the markers, if a constant survey speed is assumed. The overall position location error was estimated to be 5 m.

RADAR INTERPRETATION OF UNDISTURBED FIRN

Firn consists of near horizontal layers of compacted snow separated by thin layers of ice. The ice layers are formed in early spring or late summer when percolating melt water from surface thaw is stopped by an impervious layer and subsequently refreezes as a result of heat losses to the subzero firn underneath. The alternating snow and ice layers, in the top 5 m or so, have markedly different densities. Below this level the density of the snow layers increases with compaction showing a nearly continuous transition from firn to ice with depth. The firn finally becomes glacier ice when the interconnecting air passages between grains are sealed off (density 0.8-0.85 g.cm^3). The increase in firn density with depth decreases the density contrast between the ice layers and surrounding firn. This results in a decreased reflection coefficient between the ice layers and firn, because the dielectric constant is directly dependent on density through equation 1.

Figure 5 shows a typical radar profile of the undisturbed firn. The thicker ice layers within the firn sequence are sufficiently electrically different from the firn to produce clear reflection events on the radar profile. These continuous reflections are produced by single ice layers and consist of combined reflections from the top and base of the ice layer. Measurements of the time delays between the reflection events and autocorrelation analysis indicated that most of the reflection events present on the profiles are primary reflection events and not multiple reflections. Below a depth of about 4 m, individual layers becomes less clearly defined, and the reflection events merge to form broader zones of overlapping reflection events. The higher concentrations of reflections are probably caused by a decreasing separation between the ice layers as the snow layers become compressed at depth.

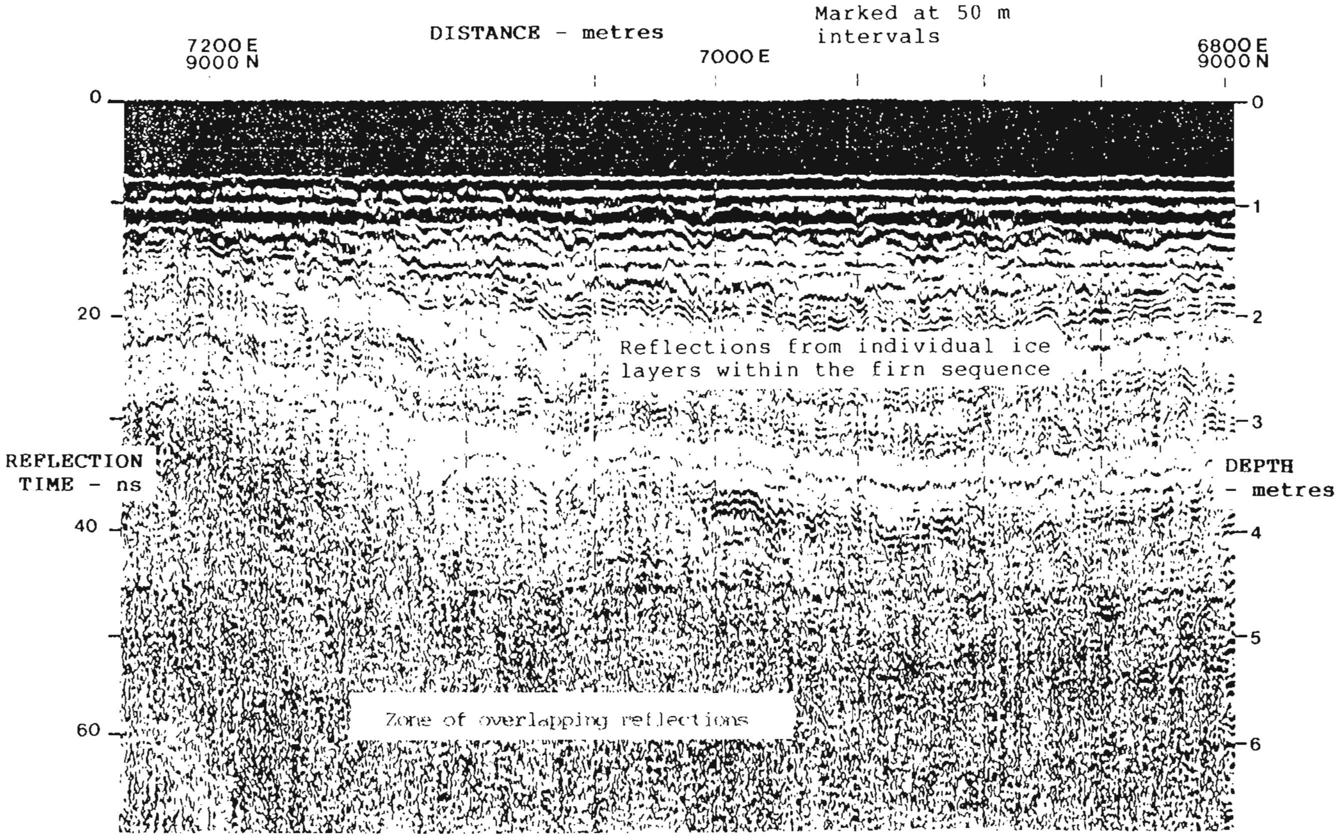

Figure 5. Typical profile of undisturbed firn.

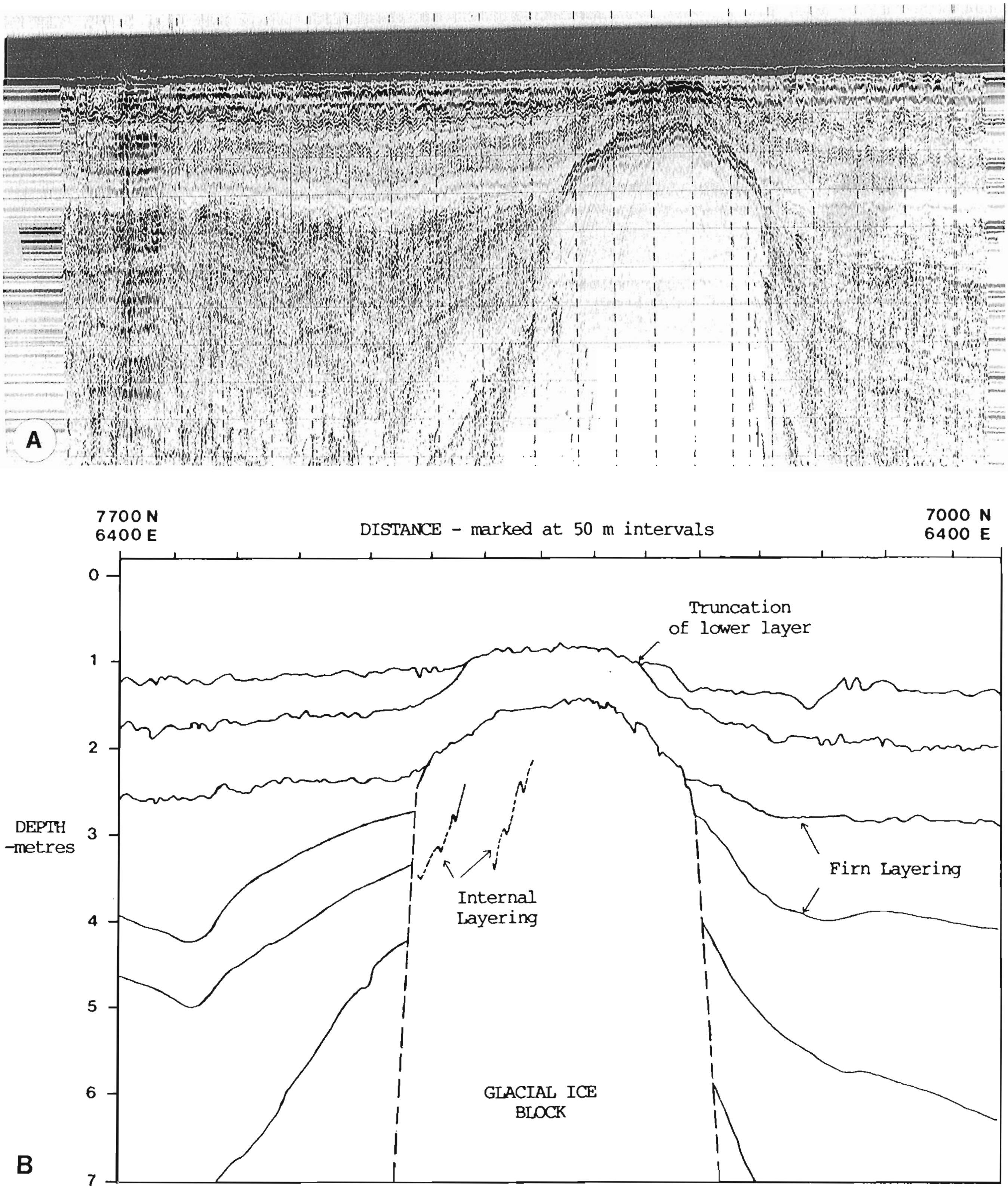

Figure 6A. Radar profile of Glacial ice block surrounded by a firn sequence. **B.** Interpretation of the glaical ice block.

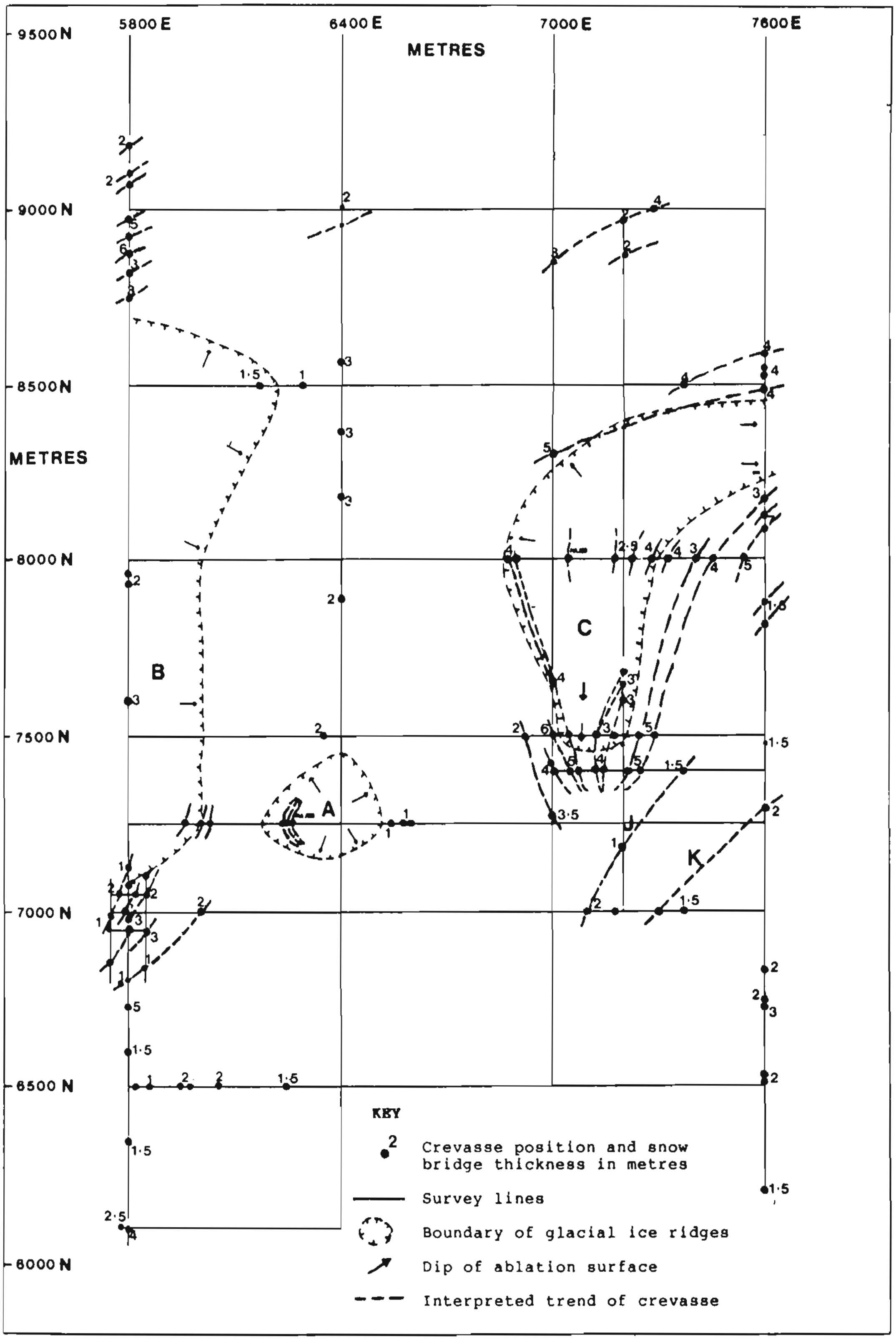

Figure 7. Plan of the crevasse distribution.

GLACIAL ICE BLOCKS

The time-distance profiles showed that certain areas of firn showed a totally different structure from that of undisturbed firn. These features are believed to be blocks of glacial ice or mature firn, which had at one time been buried at depth within the glacier. The boundary between glacial ice and surrounding firn is interpreted as an ablation surface. Subsequent accumulation has buried this old surface level within the firn sequence.

Figure 6A shows the radar profile of a glacial ice block surrounded by a firn sequence and its interpretation (Fig. 6B). The glacial ice shows a few weak internal reflections, which appear to form a relatively steeply dipping layered structure, angularly discordant to the adjacent firn layering. The weak nature of the internal reflections indicates a low dielectric contrast between the layers, which suggests an advanced stage of compaction. The angular discordance of the layering within the ice block to the surrounding firn suggests that the ice block layering predates the firn layering. The sides of the block are not detected as reflection events but can be recognized by the termination of the firn layers. The alignment of terminations suggests that the sides of the block are dipping at an angle of about 20-25 degrees from horizontal. The firn layers dip gently away from the ice block, forming an approximately symmetrical pattern of 'onlap' onto the block, with the dip decreasing towards the surface. This pattern resembles a typical sedimentary basin infill sequence. The top of the block is marked by a strong coherent reflection, which is consistent with the strong electrical contrast between shallow firn and an ice mass.

The radar profile (Fig. 6A) appears similar to diapiric structures measured in sedimentary rock sequences (e.g., salt domes) using seismic reflection techniques; however, this similarity is really caused by the vertical exaggeration of the depth scale on the radar profile. A diapiric structure is unlikely to form in firn, because the mechanical properties of firn-ice require a depth of burial of at least 30 m before plastic deformation should occur.

Figure 7 presents the final plan interpretation of the radar showing the location of crevasses and the positions of the ice blocks. The plan shows that the glacial ice blocks formed features with large areal dimensions and smoothly varying margins, compatible with an ablation surface. Exploration boreholes drilled at locations 80 m north and 200 m south of ice block A (Fig. 7), measured ice thicknesses of 180 and 250 m, respectively, so it seems highly unlikely that the blocks are bedrock.

Visual observation of neighbouring areas of ice showed isolated areas of blue ice surrounded by firn. These are probably the surface expressions of similar ice blocks, which have not been completely buried by firn.

RADAR INTERPRETATION OF CREVASSED AREAS

Snow bridges often form across the crevasse by secondary cornice (winddrift) deposition. Air temperature above freezing at the surface can cause the snow bridge, shallow firn, and ice of the crevasse walls to melt. This melt, water refreezes a few metres down the crevasse to form ice ledges, wall ice, and icicles. When temperatures above freezing are frequent the snow bridge can totally melt or collapse, leaving the crevasse exposed.

Meier et al. (1957) found variations in the firn structure in the vicinity of crevasse walls. They studied a relatively young, covered crevasse, which was about 1 m wide and covered by a thin snow bridge. The ice layers in the upper 5 m of firn became thinner close to the crevasse wall, whereas the snow between the ice layers became harder and more dense. Meier et al. (1957) suggested a two part explanation of this process. First, the melt water tends to escape over the edge of the ice layers and flows into the crevasse, reducing the thickness of the ice layers in the vicinity of the crevasse. Secondly, isotherms close to a crevasse are bent downwards, because the air in the crevasse heats at a faster rate than the surrounding firn, thereby impairing the refreezing process, which leads to ice layer formation. Conversely, daily temperature variations are greater at the crevasse wall than within the firn, so firnification of the snow is more thorough.

Type 1 crevasse response

Figure 8A and B shows an interpreted profile surveyed across a known snow covered crevasse. The crevasse had been exposed by melting during the previous summer and was known to be about 1 m wide and covered by 12 m of snow. These profiles were surveyed to check the interpretation of the data in a known situation. Figure 8 surveyed at 90 degrees to the crevasse orientation, clearly shows the ice layering within the firn sequence. The crevasse position corresponds to a short reflection, approximately the width of the crevasse, surrounded by a reflectionless zone. This reflectionless zone extends laterally for 4-5 m on either side of the crevasse position. The small reflector within the reflectionless zone probably corresponds to the base of the snow bridge and is located at a depth of 1.5 m.

The reflectionless zone is probably caused by a combination of secondary ice accumulation and modifications to the crevasse wall stratification similar to those described by Meier et al. (1957). Increased firnification of the snow layers or thinning of the ice layers would both reduce the reflection coefficient of the ice layers and so generate a reflectionless zone adjacent to the crevasse. However, it is difficult to explain how a gradual alteration of this type could generate such a sharp lateral boundary between the adjacent firn layer reflections and the reflectionless zone.

The firn layering adjacent to the reflectionless zone dips in an approximately symmetric manner away from the crevasse at an angle of about 2 degrees to the ground surface. The dipping layers revert to a nearly horizontal orientation at a distance of about 30 m from the crevasse. The ground surface along the test profile dipped gently downhill, and no marked changes in surface topography were associated with the crevasse. It is possible that the dip of the firn layers could be caused by lower firn compaction rates in the vicinity of the crevasse walls. The development of an alteration zone in the firn surrounding a crevasse and differential compaction of firn in the crevasse wall are likely to be time dependent processes. This interpretation could explain why the relatively young crevasses excavated by Meier et al. (1957) showed no definite change in dip of the firn layers in the vicinity of the crevasse and only a narrow (1 m wide) zone of altered firn. The position of the grid points in this area had been surveyed for several years and the relative displacement between yearly positions was only a few centimetres. With such slow flow rates the crevasses were likely to be relatively old.

Many of the potential crevasse targets identified in this survey area showed similar characteristics to this test case, but only a few showed a reflection from the base of the snow bridge. The reason why the crevasse itself is not detected could mean that the crevasse had closed leaving a relic alteration zone, or it could be due to the nature of the snowbridge. Meier et al. (1957) concluded that snow bridges, particularly old ones, are very irregular in thickness and the base itself consists of ice supporting large masses of icicles and hoarfrost deposits. This rough interface is likely to scatter incident radiation, rather than to reflect it coherently, so detection of the crevasse is less likely. Therefore, all of the reflectionless zones had to be marked as potential crevasse targets.

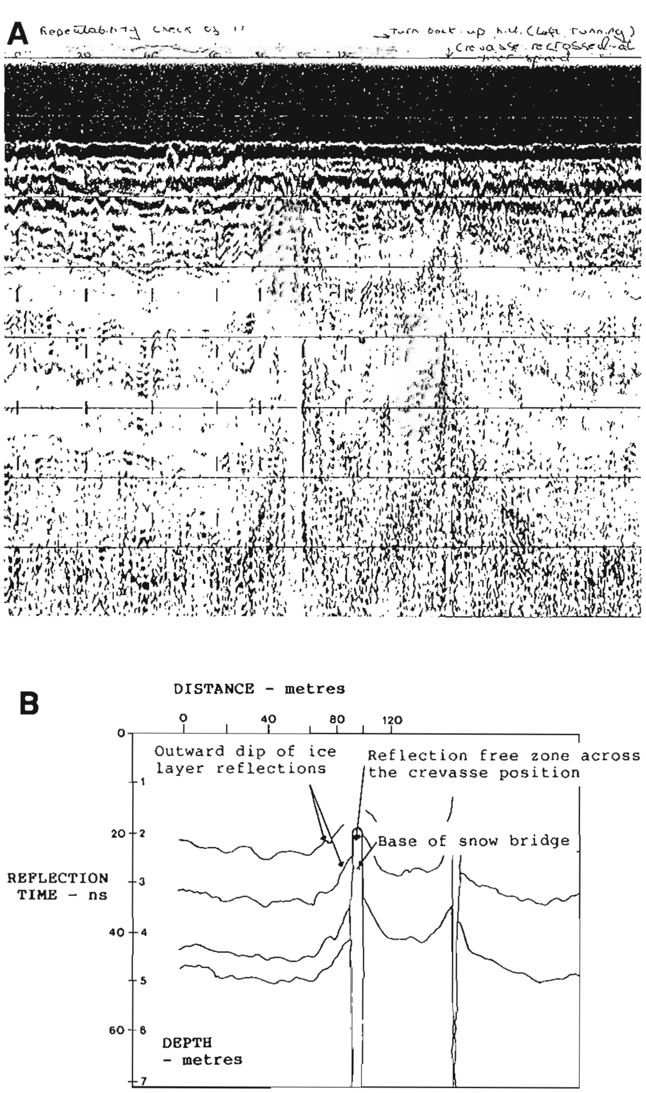

Figure 8. Type 1 crevasse **A.** profiled normal to the strike of the crevasse, and **B.** interpreted.

Type 2 crevasse response

A second type of crevasse pattern was recognized within areas interpreted as glacial ice and within adjacent areas of firn. The radar profile (Fig. 9A) contains several examples of this type of crevasse response. The common features are the marked hyperbolic scattering events, which are generated either by the base of the snow bridge or by the termination of firn layers against the crevasse wall. The top of the crevasse targets within the glacial ice mass are all located at the firn-ice interface and show no extension into the overlying firn. They are generally indicated by a sharp depression in the firn-ice interface. Some of these crevasse targets also show scattering events that originate from the crevasse walls. For example, the crevasse target at position A shows several edge scattering events, which appear to correspond to positions where internal layers of the glacial ice intersect the crevasse wall.

There are some clear differences between the radar profiles of the block of glacial ice (B) on the lefthand side of Figure 9B and the block in Figure 6B: 1) in Figure 9B the ice layers within the adjacent firn sequence terminate horizontally against the ice block, and 2) more internal layering is evident within the ice block. Once again the layering appears as weak reflection events, which are angularly discordant to the surrounding firn layers. To the east of position B the internal layers generally dip at about 1 degree to the east. One particular layer within the ice mass shows abrupt increases in reflection amplitude (bright spots). Some of these high amplitude segments correlate with crevasse positions and others are related to unknown internal features of the ice. The marked gap in the internal layering at position B is probably a major crevasse. There is certainly a major structural discontinuity within the glacial ice at this position indicated by the marked change in dip of the internal layering across this feature. However, the overlying firn shows no evidence of alteration and disruption. The terminations of the internal ice layers at position B show marked edge scattering events, in an analogous way to those of the predicted crevasse target at position A.

The firn adjacent to this area shows no concentration of reflections with depth and discrete ice layer reflections could be resolved over the whole depth range. This suggests a different accumulation-ablation history for this particular area. The crevasse target at position C (Fig. 9B) shows the typical characteristics of the type 2 crevasse response developed in firn; a slight lateral gap in the firn layer reflections combined with edge scattering from the reflection terminations and localized distortion of the dip of the firn layering. The edge scattering interferes with the firn layer reflections to form a complicated reflection response.

Both variations of the type 2 response showed no development of a reflectionless zone around the crevasse, which suggests that the alteration processes described previously are not occurring. The secondary alteration is unlikely to develop within the glacial ice, because the crevasse walls are already in an advanced state of firnification. The type 2 crevasses within the firn are generally covered by a thick layer of firn cover (35 m). If this formed soon after the crevasses opened then the crevasse wall would be insulated from the diurnal variations in air temperature and meltwater, both of which form the alteration zone. This would also explain why the crevasse itself is detected, because the absence of secondary ice accumulation should leave the crevasse top and walls smooth, resulting in a more coherent reflection of the pulse energy.

When the type 2 crevasse responses were first recognized there was no direct evidence that they were produced by crevasses. However, on the last day of the survey the type 2 crevasse response in ice was confirmed when the skidoo and sledge dropped sharply over the crevasse target at position 62°50′E 72°50′N, as the snow bridge covering the crevasse partially collapsed.

FURTHER INTERPRETATION OF TIME-DISTANCE PROFILES

Once the crevasses could be recognized on the radar profiles, their positions and depths were plotted onto the plan diagram presented in Figure 7. The positions of the glacial ice block boundaries were also marked onto this diagram. Where possible, the crevasse trends have been interpreted by connecting the crevasse intersections between adjacent survey lines.

The GPR survey was carried out before the drilling program had started. The main road routes to the proposed borehole position were covered by a small part of the total radar grid. The comprehensive coverage provided by the square 500 m grid of profiles allowed a plan interpretation of the crevasse trends across the exploration area. Thus new roadways could to be planned if the borehole positions were modified during the drilling program. The basic grid was usually sufficient to interpret the crevasse trends, but additional lines had to be surveyed in critical areas to increase control on the interpretation. Note that the crevasse location

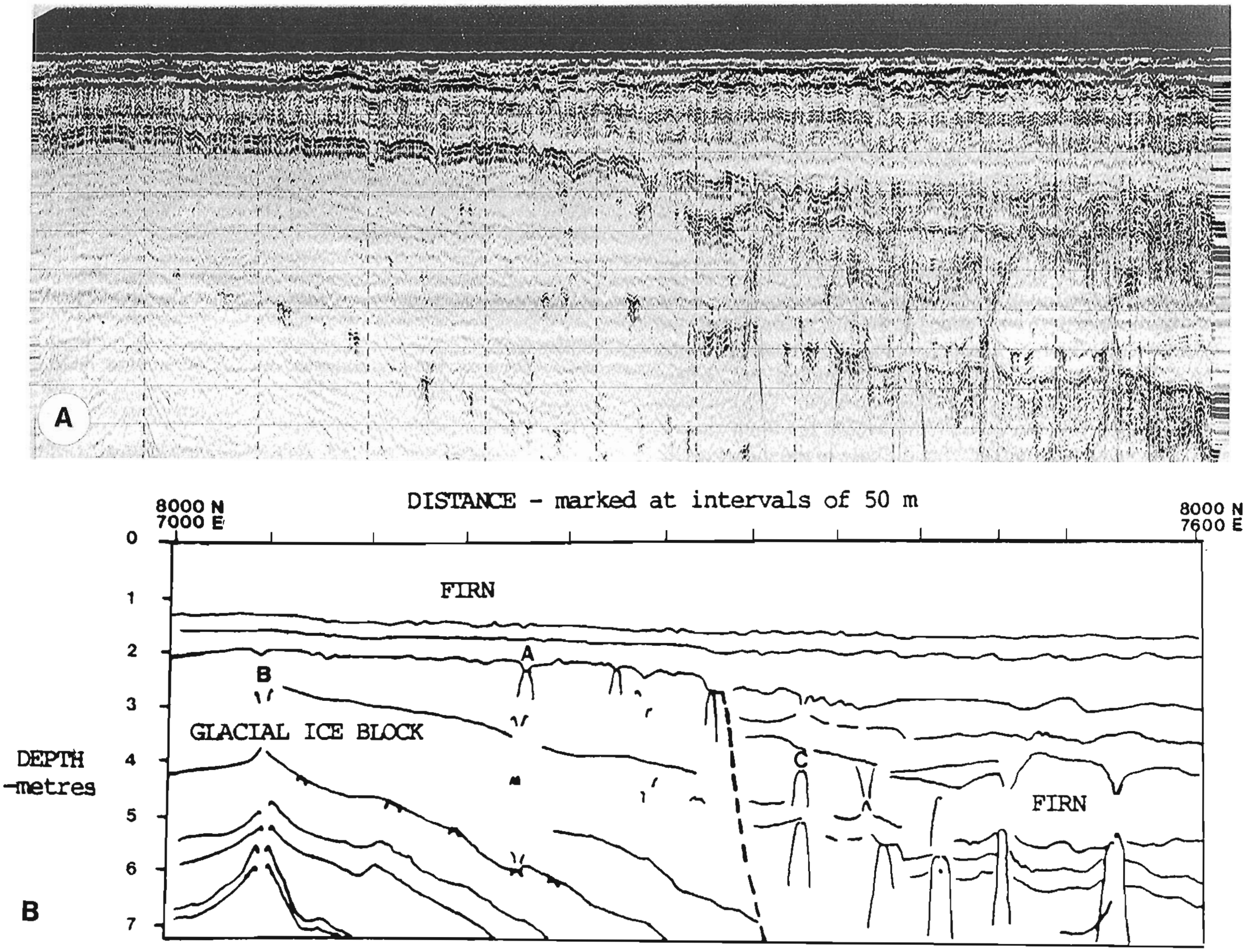

Figure 9A. Radar profile across the margin of a glacial ice block presenting several examples of the type 2 crevasse response, **B.** interpetation.

is only certain on the survey lines. The interpolation of point locations is an based on the assumption that the crevasses are continuous between survey lines and follow the most direct route. The areas surveyed in detail showed that this was generally the case, but some crevasses did show marked changes of direction over short distances and others started and finished over distances as small as 20-30 m.

CONCLUSIONS

The primary objective of the radar survey was to locate and map the position of crevasses within the exploration drilling area in as short a time as possible. Unfortunately the commercial nature of the project did not allow time to check the GPR results by boreholes or pit excavations. Thus certain parts of the radar interpretation have to be based on indirect evidence rather than direct ground confirmation. This approach is not entirely satisfactory, but the authors felt that it was important to present the data to at least demonstrate the potential for high resolution radar profiling of firn.

The crevasses were represented by two distinctly different responses on the time-distance profiles. Both types of crevasse response were proved by direct ground evidence.

The type 1 crevasse response was characterized by a well developed, reflection free zone adjacent to the crevasse walls. This reflection free zone was explained by a reduction in the reflection coefficient of the ice layers within the firn, resulting from secondary alteration of the crevasse wall. This type of crevasse was generally buried at shallow depth in relatively immature firn.

The type 2 crevasse response was characterized by hyperbolic scattering events originating from the base of the snow bridge and the terminations of the firn layers against the crevasse wall. The type 2 response was either confined to the glacial ice, or was buried at depth in mature firn, where secondary alteration was less likely to occur. The crevasse responses detected in sea ice in McMurdo Ice Shelf show a similar hyperbolic response from the base of the snow bridge; (Morey and Kovacs, 1982) but no reflections from the crevasse wall.

The nature of the crevasse response appears to depend on the amount of secondary alteration to the crevasse wall. New crevasses forming in immature firn are probably give a type 2 response and then gradually change to a type 1 response, provided the snow bridge melts periodically. Crevasses forming in mature firn or glacial ice would probably maintain a type 2 response.

The firn layering in the vicinity of both types of crevasse response appeared to dip away from the crevasse position over distances of up to 30 m. This outward dip of the layering, below the level of the snow bridge, may be caused by reduced firn compaction rates in the vicinity of the free surface of the crevasse wall.

The GPR profiles also provided detailed information of the internal structure of the firn. Several unusual blocks of material were located within the firn. These blocks have been tentatively interpreted as mature glacial ice surrounded by immature firn, based on indirect sources of evidence.

We conclude that the GPR method could be used effectively to locate and map buried crevasses. The main disadvantage of the method is the obvious danger of moving across crevassed areas. Skidoos are a relatively safe mode of transport provided there is a reasonable snow cover of at least 1 m across the crevasses. It is therefore essential to carry out such surveys before the first summer melt occurs. Crevasses with a very thin snow cover can normally be recognized by aerial reconnaissance or surface observation (Fowler, 1963).

The continuous profiles of firn structure may also provide information that can be used for research purposes. The detection of ice layers within the firn suggests that the radar technique can be used to correlate firn stratigraphy over large areas and may be particularly useful for studying and dating relict ablation surfaces.

ACKNOWLEDGMENTS

The authors are grateful to Professor D.J. Blundell, Royal Holloway and New Bedford college, University of London, for his supervision of this research project, which was funded by NERC CASE research grants. We also wish to thank Cominco Europe Ltd. for allowing these data to be used for research purposes and Mr. R. Nicols, Cominco, for his assistance with this project.

REFERENCES

Fowler, G.W.
1963: Crevasses: Part 1 Formation and detection; Bulletin U.S. Antarctic Projects Office, v. 3, p. 14-18.

Gudmandsen, P.
1971: Electromagnetic probing of ice; Chapter 9 in Electromagnetic Probing in Geophysics, J.R. Wait, (ed.); Golem Press, p. 321-350.

Meier, M.R., Conel, J.E., Melbourne, W.G., Pings, C.J., and Walker, P.T.
1957: Preliminary study of crevasse formation; U.S. Army Snow, Ice and Permafrost Research Establishment, Report 38, 61 p., Wilmette, Illinois.

Morey, R.M. and Kovacs, A.
1982: The effects of conductivity on high-resolution impulse radar sounding, Ross Ice Shelf, Antarctica; U.S. Army CRREL Report 82-42, Hanover, New Hampshire.

Paterson, W.S.B.
1969: The Physics of Glaciers; Pergamon Press, Oxford, 250 p.

Rees, H.V. and Glover, J.M.
1992: Digital enhancement of ground probing radar data; in Ground penetrating radar, J.A. Pilon (ed.); Geological Survey of Canada, Paper 90-4.

Robin, G.Q., Evans, S., and Bailey, J.T.
1969: Interpretation of radio echo sounding in polar ice sheets; Royal Society of London, Philosophical Transactions, v. 265A, no. 1166, p. 437-505.

Swithinbank, C.W.M.
1968: Radio echo sounding of Antarctic glaciers from light aircraft; Union Géodésique et Géophysique Internationale, Association Internationale des sciences Hydrographique, Assemblée générale Berne, 25 Sept. 7 Oct. 1967, p. 405-414.

Fracture mapping in granite rock using ground probing radar

Arthur L. Holloway[1]

Holloway, A.L., 1992: Fracture mapping in granite rock using ground probing radar; in *Ground penetrating radar, ed. J. Pilon; Geological Survey of Canada, Paper 90-4, p. 85-100.*

Abstract

Because of its high resistivity (3000-10 000 Ω-m in intact rock), granite is an excellent medium for propagation of electromagnetic energy at the radar range of frequencies. Both surface and downhole antennas have been used at frequencies between 20 and 900 MHz to delineate fracture zones in the porphyritic granite of the Lac du Bonnet batholith in eastern Manitoba.

A major fracture zone was clearly detected in the granite at a distance of 30 m below the 240 m level of the underground research laboratory using a radar frequency of 120 MHz and verified by drilling. Diagrams that show details of the fracture patterns and the excellent correlation between intersecting profiles are presented.

Conventionally, fracture zones in granite rocks have been mapped where they intersect ground surface by airphoto analysis and by geophysical magnetic and electromagnetic methods. Determining the dips of these features has been problematic, and often a high degree of uncertainty is associated with the analysis, particularly if the features are considered to be of low to intermediate dip. The dips of such features can be determined by radar surveys carried out on outcrops below which these fracture zones occur. A case study presents an accurate prediction of a borehole intersection of a fracture zone that was made on the basis of the fracture orientation determined by radar. The near surface imaging of these features, as determined by radar, is considered far more precise than with other geophysical techniques.

Résumé

En raison de sa forte résistivité (3000 à 10 000 Ω-m dans la roche intacte), le granite constitue unt excellent milieu de propagation de l'énergie électromagnétique dans le domaine des fréquences radar. Pour délimiter les zones de fracture dans le granite porphyritique du batholite de Lac du Bonnet dans l'est du Manitoba, on a utilisé deux antennes, l'une à la surface et l'autre en fond de trou, à des fréquences variant entre 20 et 900 MHz.

À une distance de 30 m au-dessous du niveau de 240 m du laboratoire de recherche souterrain, on a détecté une importante zone de fracture dans le granite en utilisant une fréquence radar de 120 MHz, que l'on a confirmée par un forage. Des diagrammes montrant la configuration détaillée des fractures et l'excellente corrélation entre les profils concourants sont présentés.

Dans le passé, les zones de fracture dans les roches granitiques ont été cartographiées, là où elles recoupent la surface du sol, à l'aide de photographies aériennes et de méthodes magnétiques et électromagnétiques. La détermination du pendage de ces zones était problématique, et souvent une grande incertitude était associée à l'analyse, en particulier dans le cas de zones de pendage faible à intermédiaire. Ces pendages peuvent être déterminés à l'aide de levés radar des affleurements au-dessous desquels reposent ces zones de fracture. Une étude de cas, dans laquelle est prévue avec précision l'intersection d'un trou de sondage avec une zone de fracture en se basant sur l'orientation des fractures déterminée par radar, est présentée. La représentation graphique de ces zones gisant à faible profondeur, telles que déterminées à l'aide du radar, est considérée beaucoup plus précise que celle établie à l'aide de tout autre technique géophysique.

---

[1] Atomic Energy of Canada Ltd., Whiteshell Nuclear Research Establishment, Pinawa, Manitoba R0E 1L0

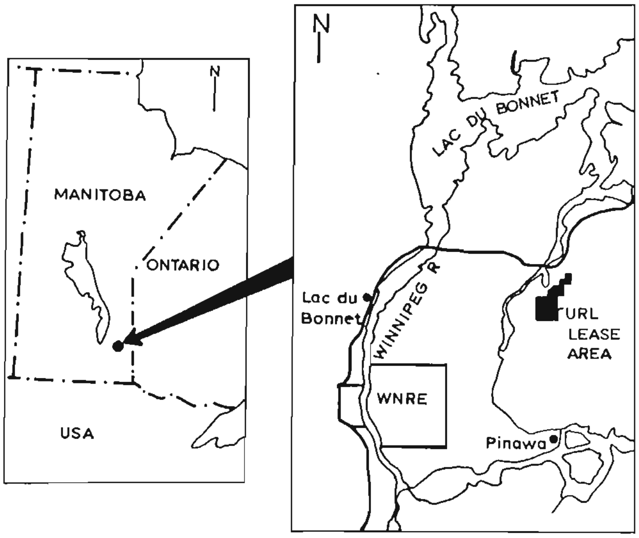

Figure 1. Location of the Whiteshell research area, including the URL.

INTRODUCTION

As part of the Canadian Nuclear Fuel Waste Management Program, Atomic Energy of Canada Limited (AECL) is investigating plutonic rocks of Canadian Shield to determine their suitability as a disposal medium. The research and development program, currently in the concept assessment phase (Dormuth and Nuttall, 1987), is described in detail by Whitaker (1987). Field methods have been developed at four research areas on Canadian Shield. Currently the main focus of the field work is the Whiteshell research area, located in eastern Manitoba (Fig. 1) on the Lac du Bonnet batholith.

Investigations are underway from both the surface and underground to characterize the rockmass of the Whiteshell research area in terms of its geological, hydrogeological, geochemical, and geotechnical properties. One major component of the research deals with the development of methods to characterize the hydrogeological conditions within plutonic rockmasses, because this work will provide the primary control on the movement of any radionuclides that might be released from a disposal vault.

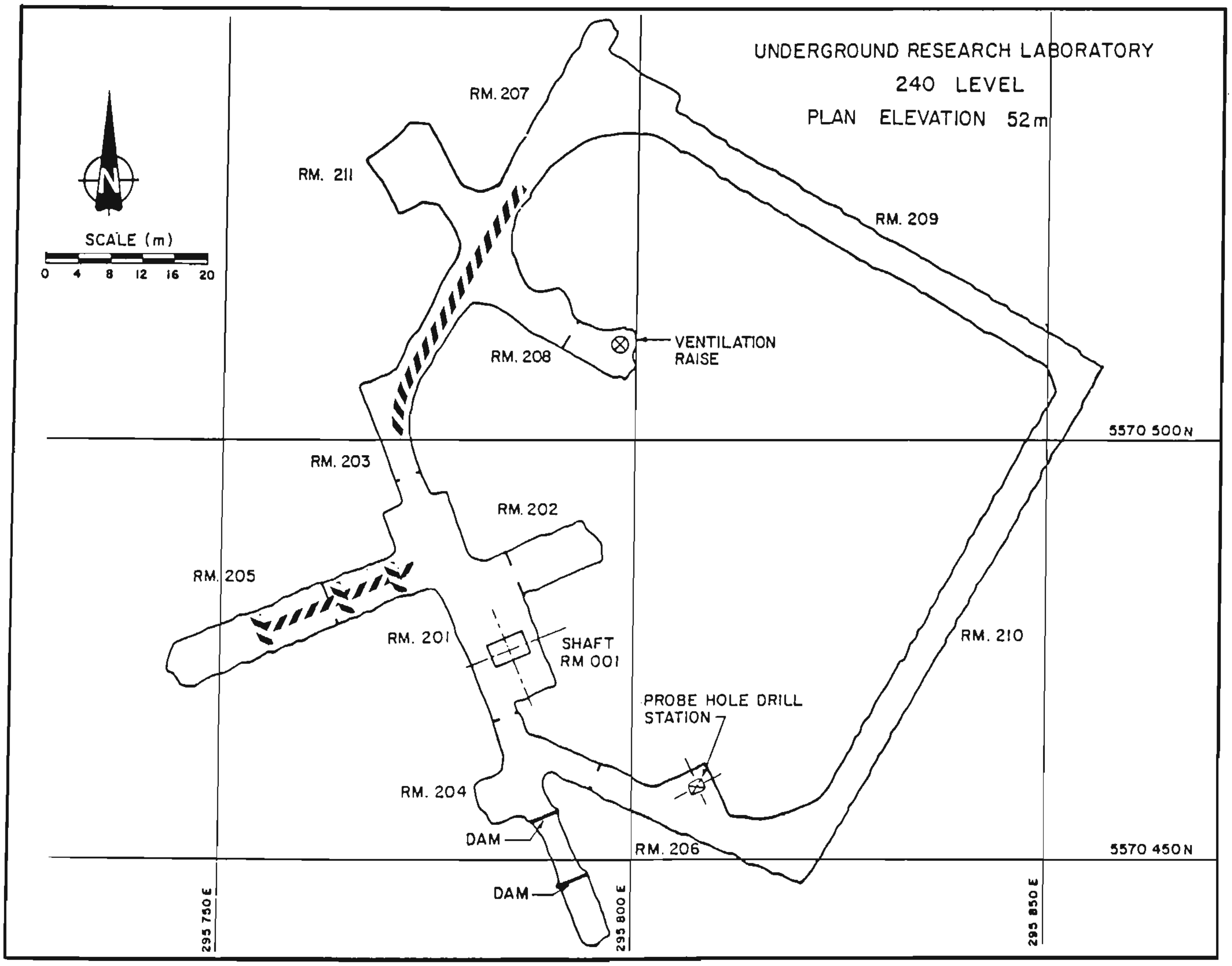

Figure 2. Layout of the 240 level and the location of the radar surveys.

As part of this research, AECL is constructing an underground research laboratory (URL) to a depth of 435 m within the Lac du Bonnet granite to conduct various full scale in situ experiments. The purpose of this facility and the long term experiments to be conducted within it are described by Simmons (1986). Experiments are also being performed during the construction phase, and new underground methods are being developed to characterize the rockmass.

The radar reflection survey method has been used in the underground excavations of the URL facility, and also from the ground surface at two of the study areas in the surrounding Whiteshell research area to detect major fracture zones in the granite rock. These studies demonstrate that the radar method shows great promises as a high resolution, nondestructive, geophysical technique that can locate and orientate fracture zones up to 50 m away from the profiling surface in granite rock.

The method has been used to probe below rock outcrops and adjacent to underground excavations. Processing techniques have been developed to determine the true orientations of dipping planar reflectors, and these orientations have been successfully correlated to fracture zones identified in drill core. In some cases, fracture geometry has been successfully extrapolated from the radar survey data to distances greater than 100 m, and subsequent drilling has shown these extrapolations to be accurate.

RADAR REFLECTION PROFILING AT THE UNDERGROUND RESEARCH LABORATORY

Radar reflection surveying using surface-style antennas has been performed at the URL since excavation of the shaft was begun in 1984. Fractures have been mapped behind the shaft walls, and under the floor and behind the walls of the underground levels.

Initial shaft survey

A Geophysical Survey Systems Inc. (GSSI) System 7 radar was used for shaft-wall profiling at a frequency of 500 MHz, providing a probing range of 5 m. A series of horizontal surveys around the walls of the shaft were carried out every 2.5 m (Holloway et al., 1986), and vertical fractures within 5 m of the shaft walls were detected. A method of plotting the reflectors on a structure contour plot was developed, and the results were confirmed by cored boreholes and geological mapping.

Surveys on the 240 level

Radar reflection surveys were carried out on the 240 m level in 1986 November and 1987 July, by A-Cubed Inc. now operating as Multiview Geoservices Inc., a consulting

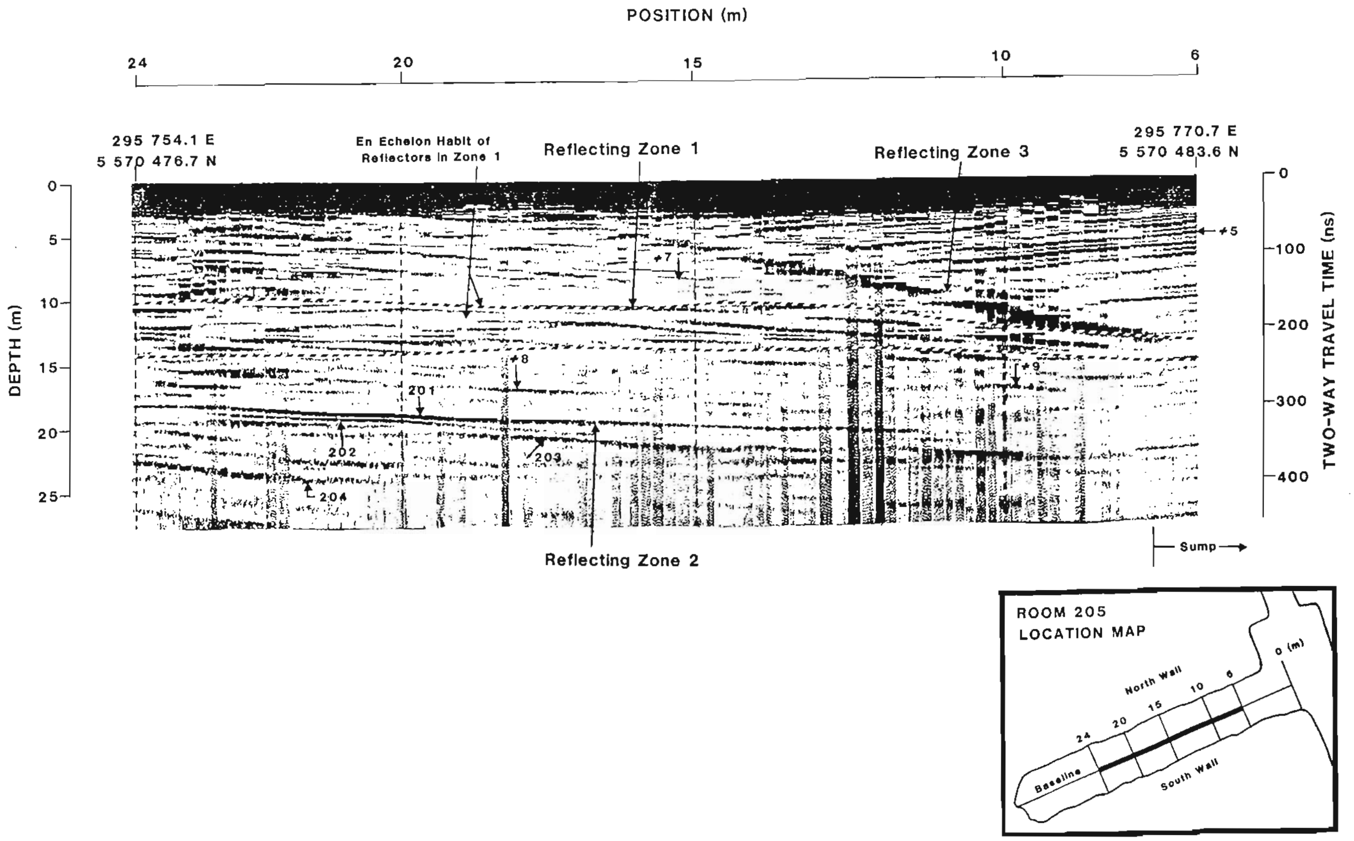

Figure 3. pulseEKKO I radargram for the base line in room 205, URL.

geophysical company from Mississauga, Ont. The object of the surveys was 1) to determine the location and orientation of fracture zones in the proximity of the 240 m level of the URL, and 2) to evaluate the suitability of the radar systems developed by A-Cubed Inc. for characterization of granite rock within an underground environment.

Two systems were used: the pulseEKKO I (pEI), a modified version of an older GSSI radar system, and the pulseEKKO III (pEIII), a digital radar system developed by A-Cubed, now manufactured by Sensors & Software Inc. Both systems used fibre optic cable for signal transmission to increase the signal to noise ratio. Good working conditions on the 240 m level and a compact A-Cubed antenna design enabled profiling at the 120 MHz frequency. The layout of the 240 m level and the location of the radar surveys discussed here are shown in Figure 2.

All four lines on the floor in room 205 of the 240 m level were profiled with the analog pEI system, whereas only the base line was profiled with the pEIII. The steel tracks for guiding mine carts had been removed prior to radar surveying.

pulseEKKO I survey: data presentation

The antennas used in these surveys had a frequency of 120 MHz, with a receiver-transmitter spacing of 2 m. Continuous readings were taken, with movement of the antennas pausing momentarily every 0.2 m. Figures 3-5 present the raw analog radargrams from the long axis of the floor of room 205 and the perpendicular tie lines that intersect the main line at 20 and 10 m, respectively.

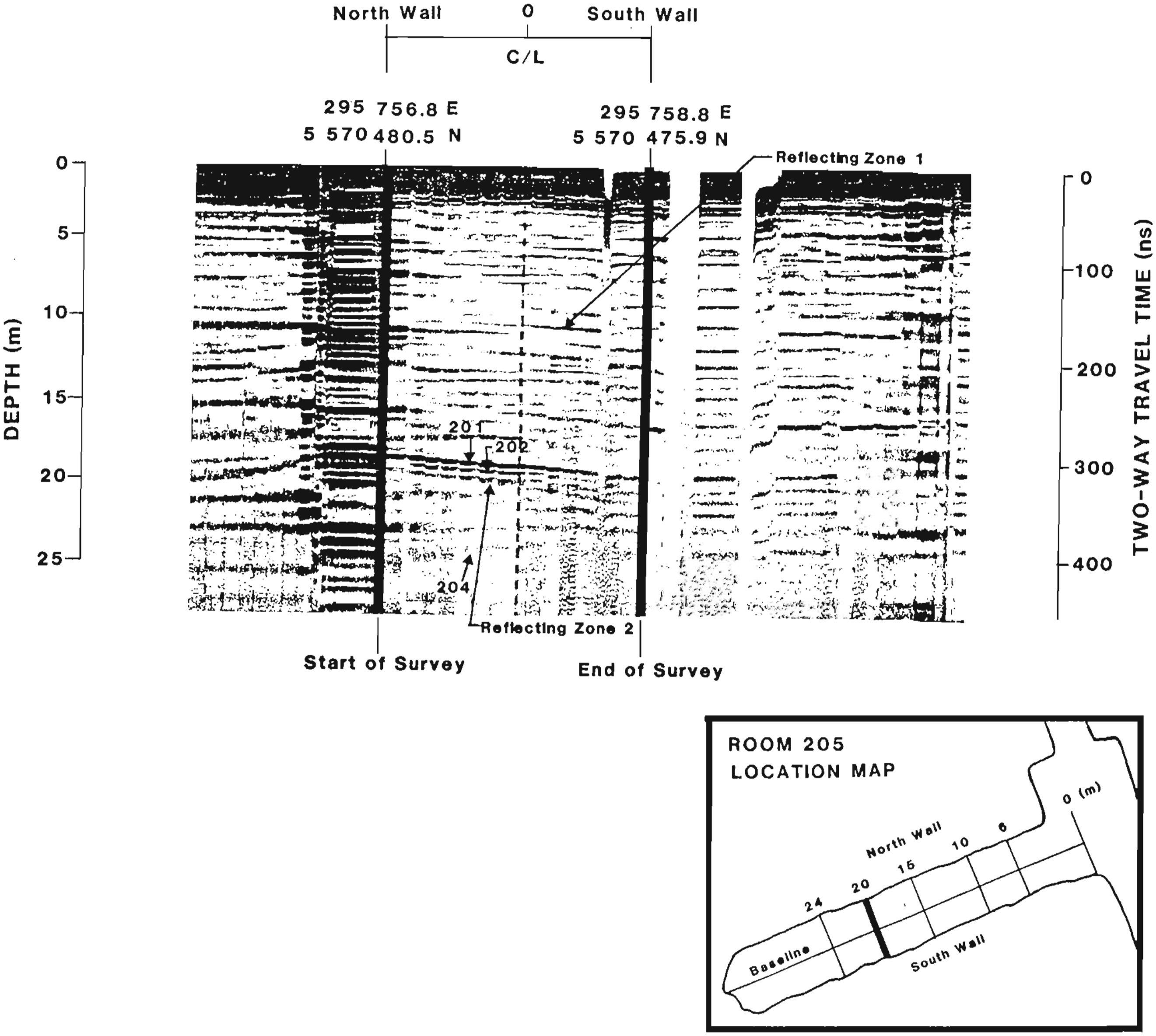

Figure 4. pulseEKKO I radargram for the tie line at 20 m in room 205, URL.

On each of these figures, the horizontal axis represents the antenna position in metres along the survey line, and the vertical axis represents the distance below the floor. The distance axis assumes a velocity of 120 m/μs, which was determined both by WARR (wide angle reflection and refraction) surveys performed by A-Cubed Inc. and by separate surveys by AECL personnel (Holloway et al., 1986).

The annotated positions on the profiles and subsequent interpretations with dip correction applied refer to the midpoint of the transmitter-receiver antenna pair. The dip correction technique, used by AECL and its role in radar reflection data interpretation are outlined in Appendix A.

Three principal groups of reflectors, labelled zones 1-3, are visible in the data from the main profile (Fig. 3). These and other reflectors have also been identified in the radargrams for the tie lines and have been labelled consistently.

Reflecting zone 1 consists of a series of shallow dipping to subhorizontal reflectors that can be detected on all survey lines. Individual, discrete reflectors within this zone can be identified on the radargrams, each generally less than 10 m long, spaced less than 1 m apart, and often in an en echelon pattern. Examples of this en echelon habit are indicated in Figure 3.

Reflecting zone 2 lies below zone 1, is subparallel to it, and contains the strongest shallow dipping reflectors seen in this series of radargrams. The style of the individual reflectors in this zone is similar to those in the upper zone, but they persist over greater distances. The most prominent reflector in this zone (201) provides a good reference for the top of the zone. The darkness intensity of the reflector on the radargrams is related to the reflector strength. The bottom of the zone is more difficult to define, with progressively weaker reflectors gradually merging with the background noise. Three other significant subreflectors have been identified in this zone and labelled on the radargrams as 202, 203, and 204.

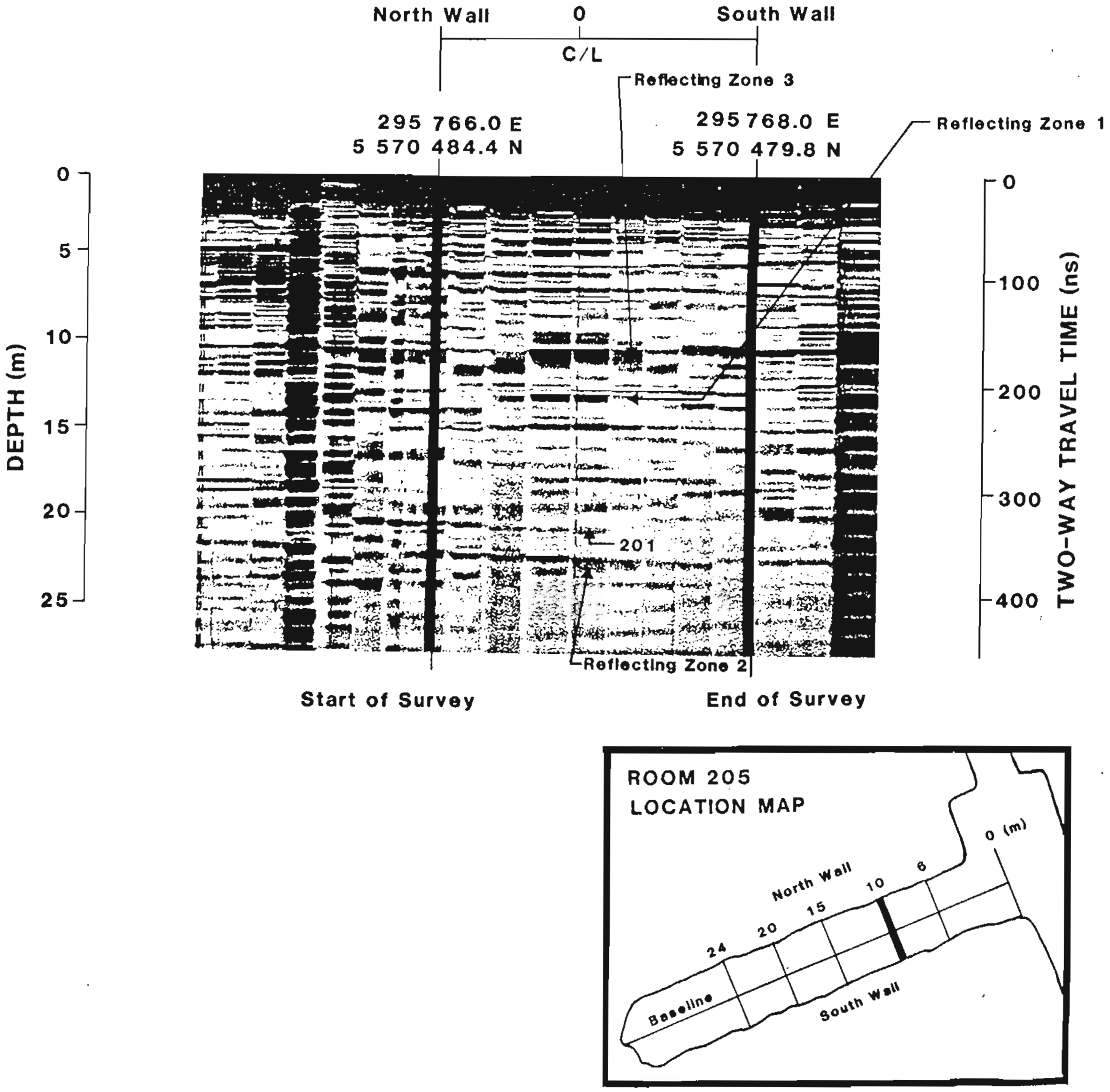

Figure 5. pulseEKKO I radargram for the tie line at 10 m in room 205, URL.

The style of reflecting zone 3 is markedly different than that of the first two zones. It consists of a continuous reflector with an uncorrected dip of about 45 degrees, whose width and intensity increase with depth. This zone was also detected on the 10 m tie line, where it appears to be subhorizontal.

The series of tightly spaced, slightly dipping reflectors, labelled #5 on the extreme right of Figure 3 are most likely caused by reverberations between the antennas and a series of slightly dipping, waterfilled boreholes that were drilled under the floor of room 205.

The tie lines cover a distance of only 5 m, so accurately determining the apparent dips of the reflectors is difficult. Errors in the apparent dip lead to inaccuracies in calculating the true orientation of the reflecting zone. Most of the reflectors correlate with excellent accuracy between the surveys, despite the fact that all four were run completely independantly.

Figure 6 shows how well the data from the base line and the tie lines correlate, combining the north half of the 20 m tie line with the 20-to 10 m section of the baseline and the south half of the 10 m tie line. At the 20 m and 10 m positions, denoted by heavy vertical lines in Figure 6, the antenna midpoints were in exactly the same position along both surveys, and all genuine reflectors should be repeated at the same position on both. The strong correlation of even small, weak reflectors is quite apparent and provides an excellent test of the repeatability of the data.

Before comparing the main reflectors with the information available from cored boreholes drilled in the immediate area, dip corrections were applied to the radar data, to determine the correct depths to the planar reflectors under the survey lines. The positions and orientations of zones 1 and 2 were not greatly affected by this procedure because of their shallow dips. The steep dip of zone 3, however, caused it to be substantially altered. The true orientations of the planes are as follows:

Reflecting zone 1: 093/15 (dip to right)
zone 2: 020/15
zone 3: 335/90

Reflector interpretation

Cored borehole HC14 was drilled in room 205 within the plane of the main profile line. The borehole has an azimuth of 068 degrees, a plunge of 70 degrees, and a borehole length of 43.3 m. A plot of the number of fractures encountered per metre in borehole HC14 is shown in Figure 7, as is the interpreted geology below room 205 (Everitt et al., AECL unpublished memo). Fracture zone 2 (FZ2), a major fracture

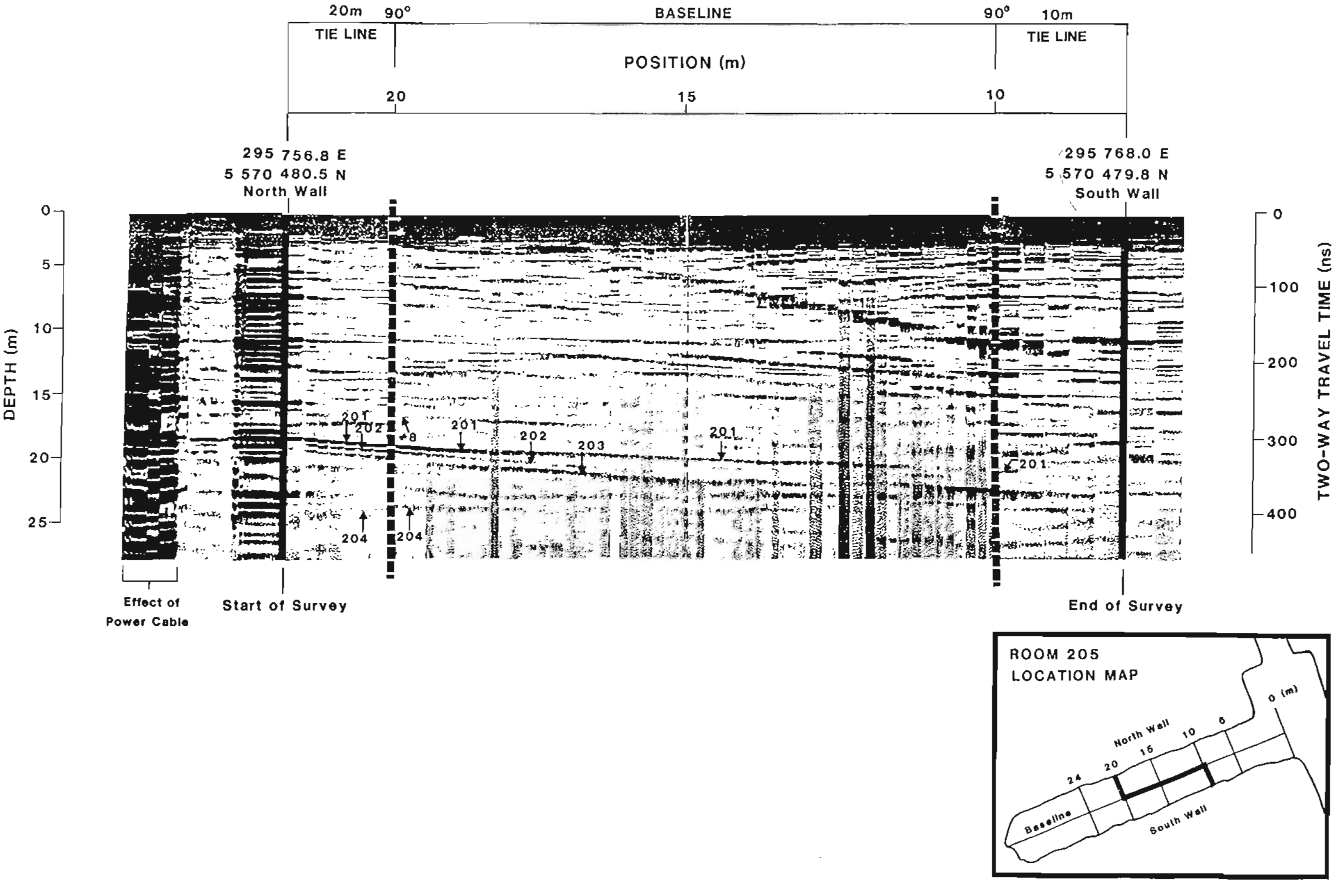

Figure 6. pulseEKKO I radargram fence diagram showing the correlation of reflectors in Room 205, URL between the base line and tie lines.

zone that has been intersected by drilling through much of the URL lease area, and an upper splay of the same zone were detected between 20 and 30 m and 13 and 15 m, respectively, in this borehole.

In Figure 8 the corelog information from HC14 has been superimposed on the radargram of the main profile: the reflecting zones correspond closely to the zones of major fracturing.

The orientation of Fracture zone 2 was determined by radar to be 020/15, and compares closely with the orientation of the top of the zone as determined independantly by geological mapping of borehole data (Fig. 9).

Because of its orientation, reflecting zone 3 was not intersected by borehole HC14 or any other boreholes drilled from the 240 level, nor was anything that could be interpreted as its extension. There are several geological and geophysical indications that this reflector represents neither a fracture zone nor a discrete fracture. It is significant that geological mapping does not indicate the presence of such a fracture in the floor or walls of room 205 at its projected intersection point. The reflector is quite different in character than the two reflecting zones that can be correlated to fractures; these take the form of a series of discrete segments, often appearing en echelon in habit. By contrast, reflector 3 is a continuous, strongly reflecting, broad band. Although it appears to be traceable over a relatively long distance in the raw radargram, after the dip correction its detectable length is ony a few metres. The dip of this feature has been calculated to be between 70 and 90 degrees. Several possible interpretations could account for this reflection. It has a similar orientation to a pegmatite dike, but it is unlikely that such a unique, strong reflection would result from a feature that is so common and is so similar in mineralogy to the granite. A more reasonable explanation is that the feature is the result of reflections off steel stressmeters located in the shallow boreholes underlying room 205 (Spinney, 1990). The steel would reflect much of

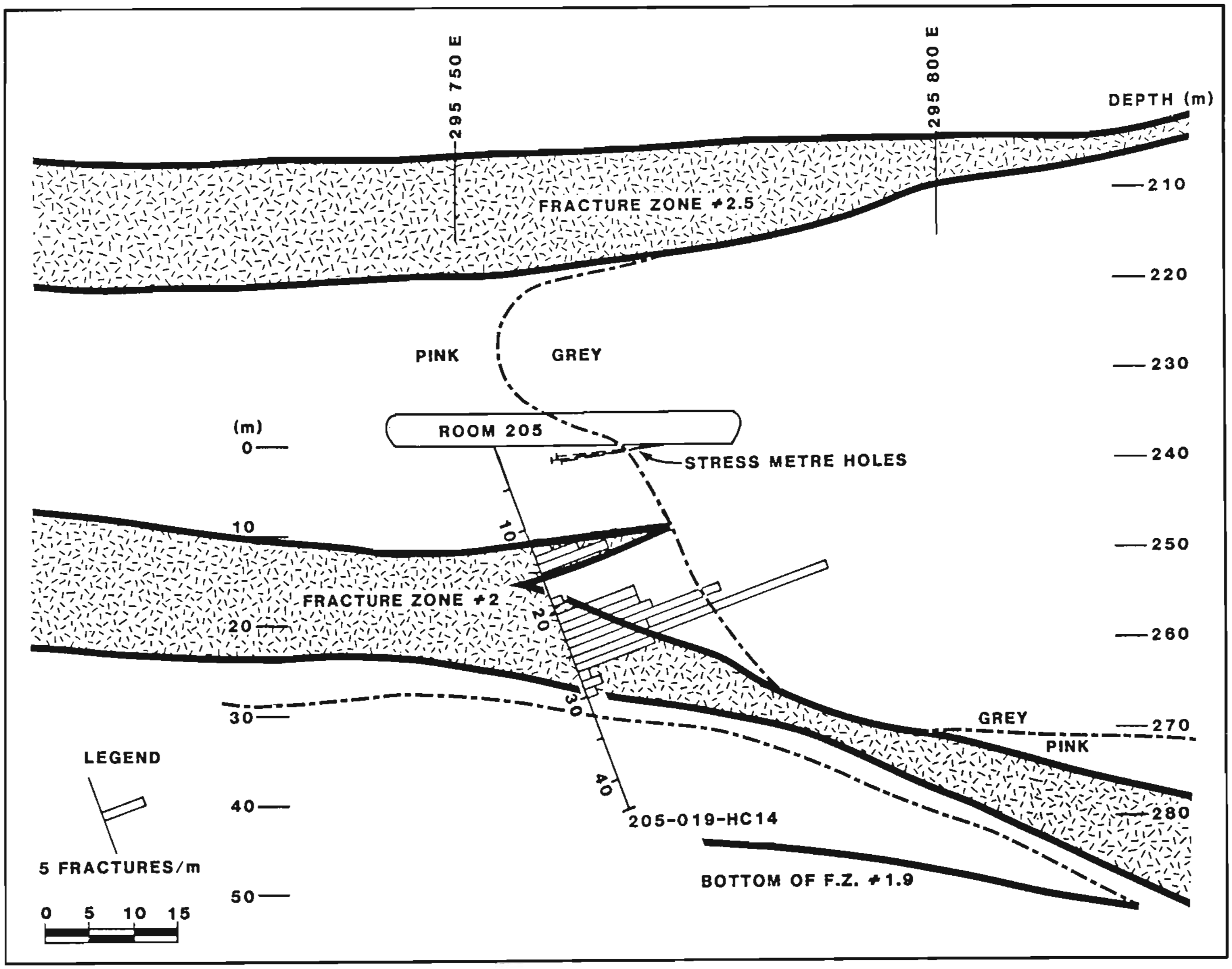

Figure 7. Geological cross-section through the plane of room 205, URL including borehole HC 14 (from Everett et al., AECL unpublished memo).

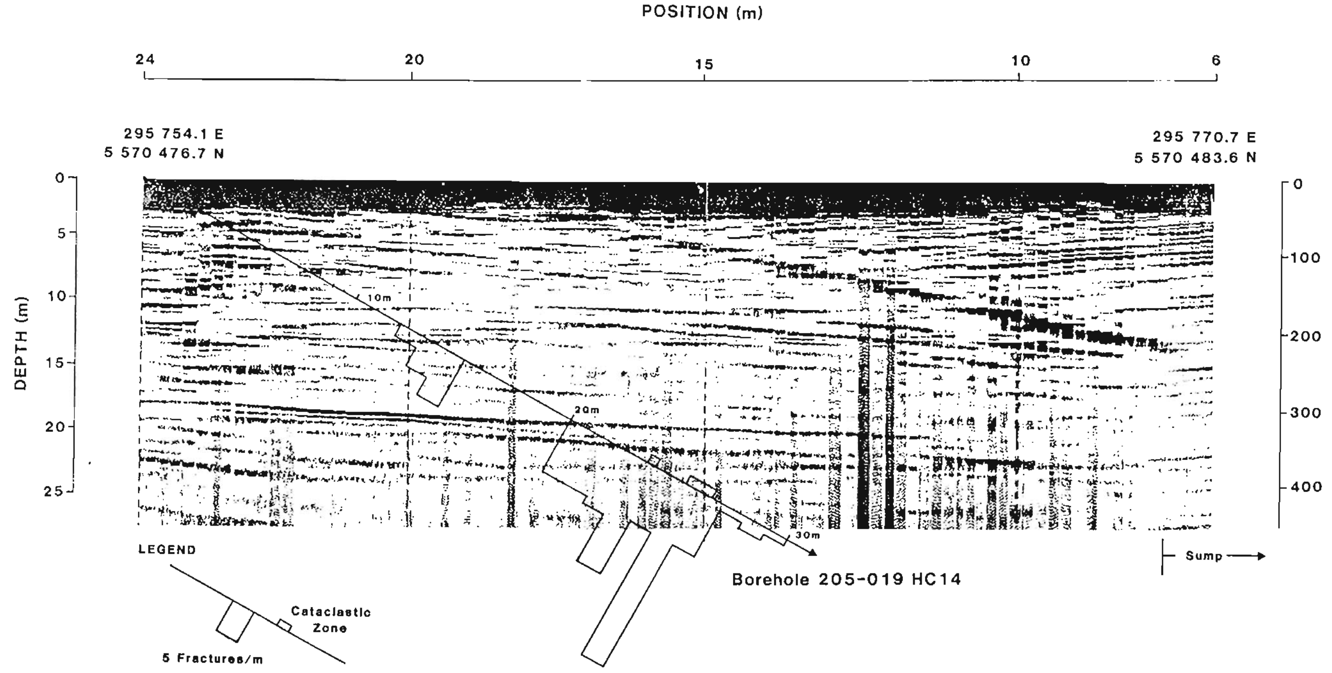

Figure 8. pulseEKKO I radargram from baseline, room 205 survey with fracture log of borehole HC14 superimposed.

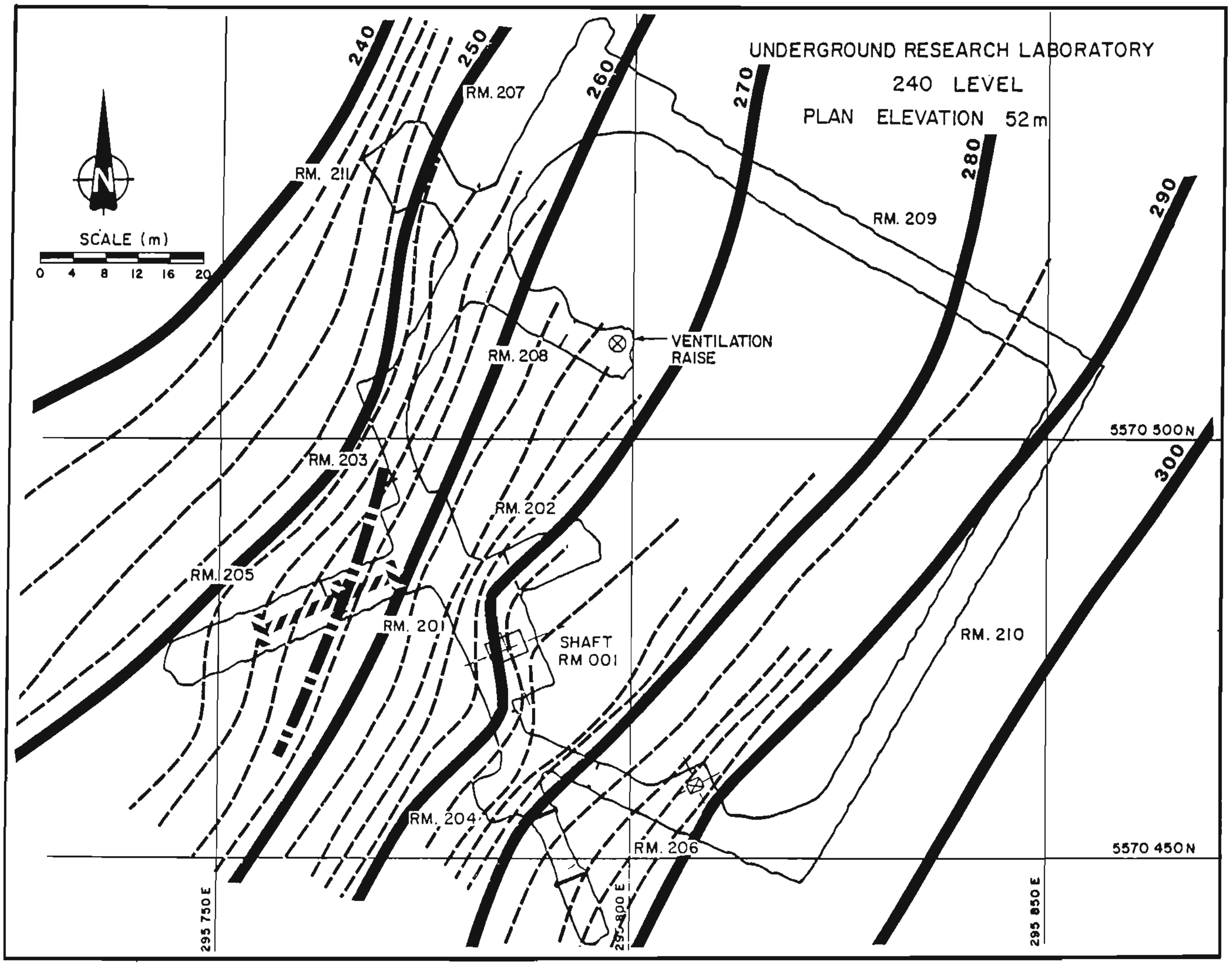

Figure 9. Structure contours in the 240 level area of the URL to the top of FZ2 based on geological mapping and core logging. Strike of radar reflector 201 has been superimposed for comparison.

the radar energy and would be viewed as a point source. Whatever the cause of reflector 3, its steep dip indicates either a subvertical feature, or a point reflector. The lack of mapped fractures in the area, and the unique geophysical character suggest that it was caused by the stressmeters.

pulseEKKO III digital data presentation

Only the main profile line in room 205 was surveyed with this system, using 120 MHz antennas with a transmitter-receiver spacing of 2 m. The digital capability allows many types of data processing to be performed, including a variety of noise suppression techniques and spectral analysis.

The radargrams for this digital system are plotted as a series of wiggle traces in a variable area format. All positive amplitudes (deflections to the right) are shaded.

Instead of continuous profiling, as was done with the pEI system, a discrete reading was taken every 0.2 m. About 15 seconds were required to complete each reading because of stacking and other processing done in real time. At each reading location the data were stacked 512 times.

Figure 10 shows the pEIII radargram for the main profile of room 205. Apart from the three reflecting zones in the upper 25 m section seen in the pEI survey, two deeper zones, subparallel to reflecting zone 1 can be seen. These depths have not been probed by boreholes to date, so the reflectors cannot be confirmed as fractures, but their similarity to the upper reflectors in style and orientation make this possibility quite likely. Figure 7 indicates the geologically extrapolated location of FZ 1.9, which corresponds closely to the position of reflecting zone 5. To date no fracturing has been predicted by geological mapping for the area adjacent to reflecting

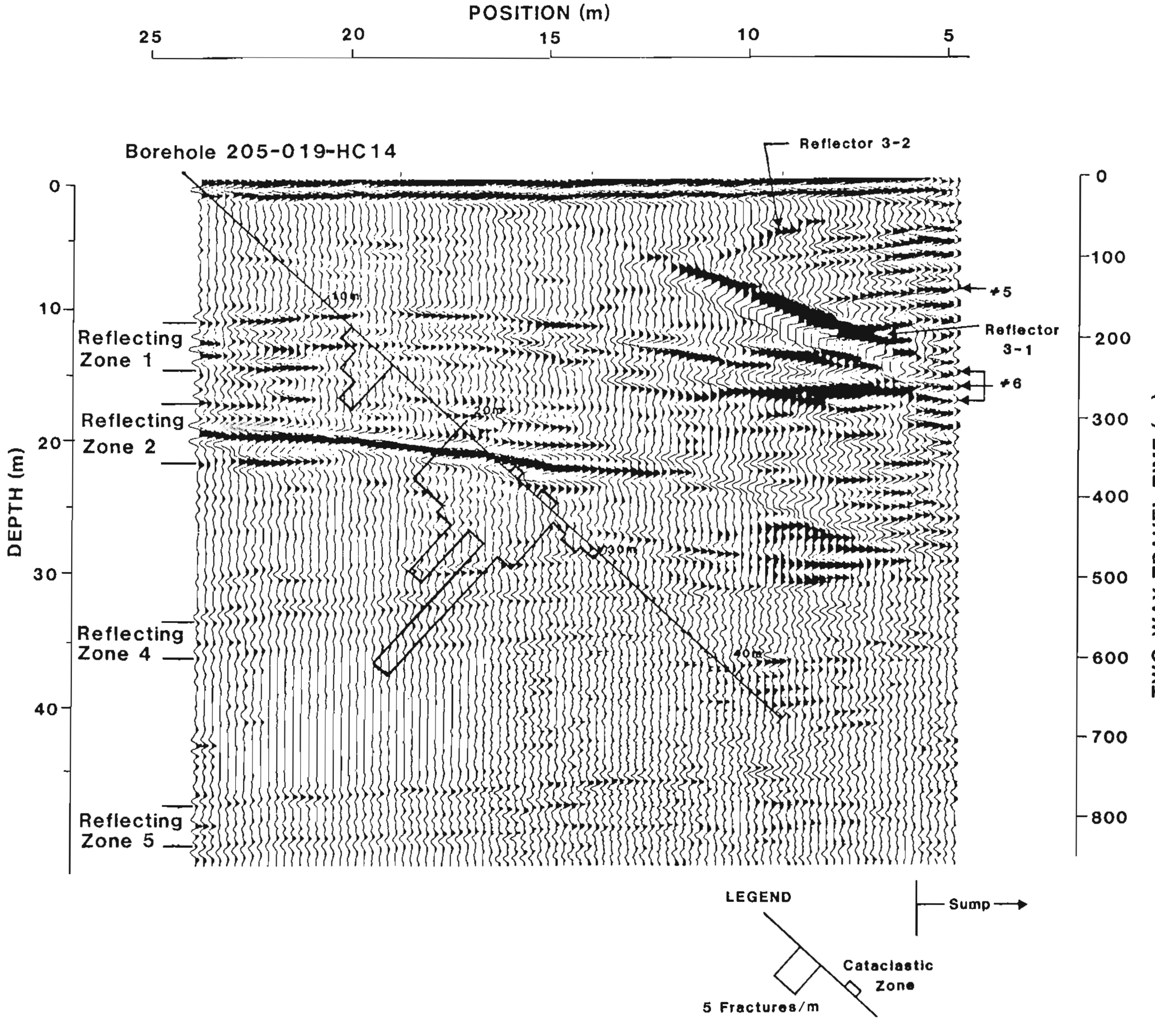

Figure 10. pulseEKKO III radargram for the base line in room 205, URL.

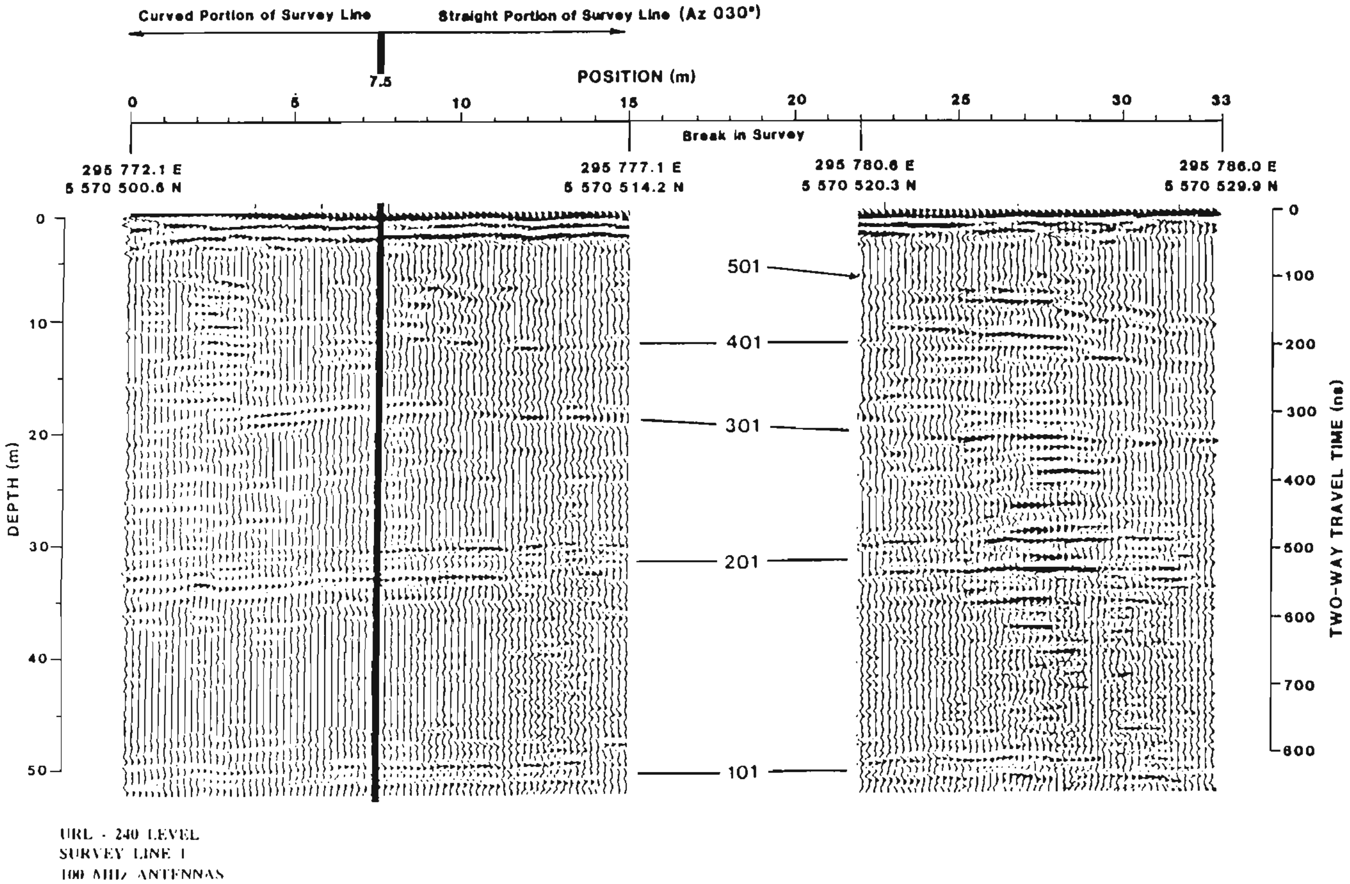

Figure 11. pulseEKKO III radargram for survey in room 207, URL.

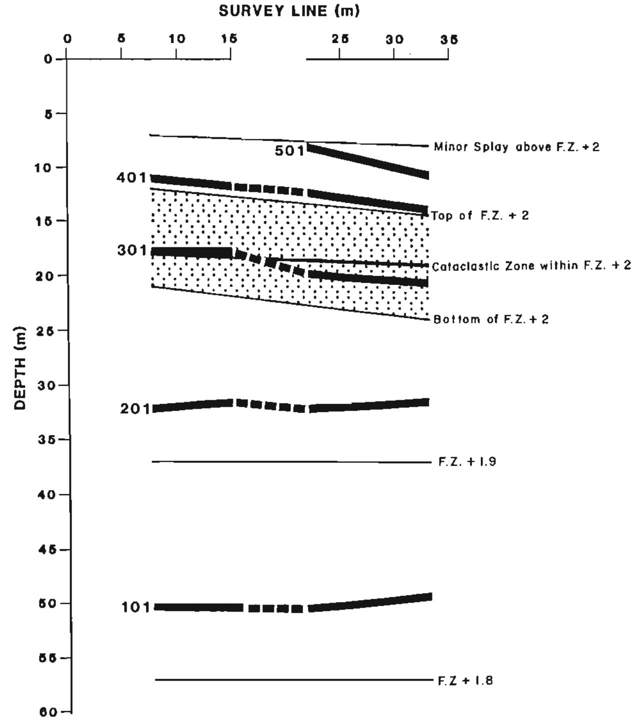

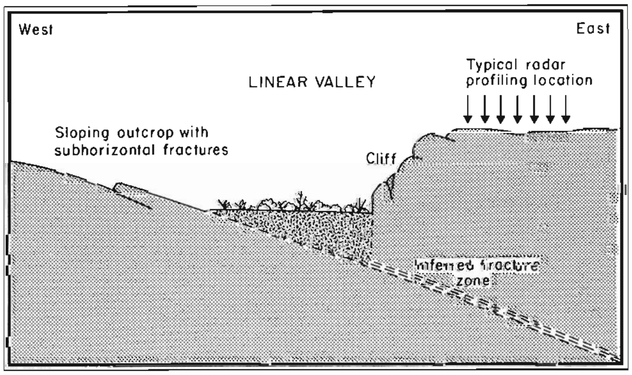

Figure 12. Geological cross-section through the straight portion of the radar survey in room 207, with positions of the major radar reflectors identified in Figure 11 superimposed for

Figure 13. Schematic cross-section showing fracture and topographic characteristics of curvilinear valleys in the Whiteshell research area (after Stone and Kamineni, 1988).

zone 4. The apparent dip of both these lower reflecting zones suggests that they will merge with the base of FZ2 to the right of Figure 10, which is consistent with the geological interpretation of splays below FZ 2.

pulseEKKO III, surveying in room 207

The floor of room 207 (Fig. 2) was surveyed with the pEIII system by A-Cubed Inc. personnel in 1986 November, and the raw data are presented in Figure 11. Because of the layout of the underground level, the radargram is divided into a curved portion of the survey line, to the left of the 7.5 m mark, and a straight portion.

The five main reflecting zones identified in Figure 11 have been superimposed upon a cross-section of the geology below the profile line in Figure 12. Once again, all significant fracturing to a depth of 50 m has been detected by the radar survey. A dip correction would have had only a minimal impact because of the subhorizontal nature of the reflectors.

The survey could be run only in one direction because of the underground room layout and the presence of steel tracks in the tunnel; thus the true orientation of the reflectors cannot be determined solely from the radar survey in this case.

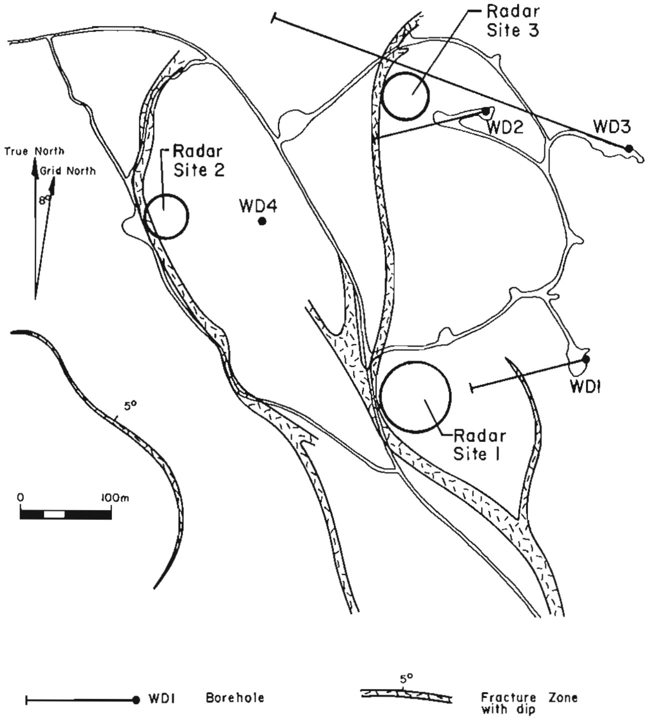

Figure 14. Location of surface radar profiling locations in relation to the gross structural geology, and the boreholes used in confirming radar reflector orientation extrapolations (after Ejeckam et al., 1990).

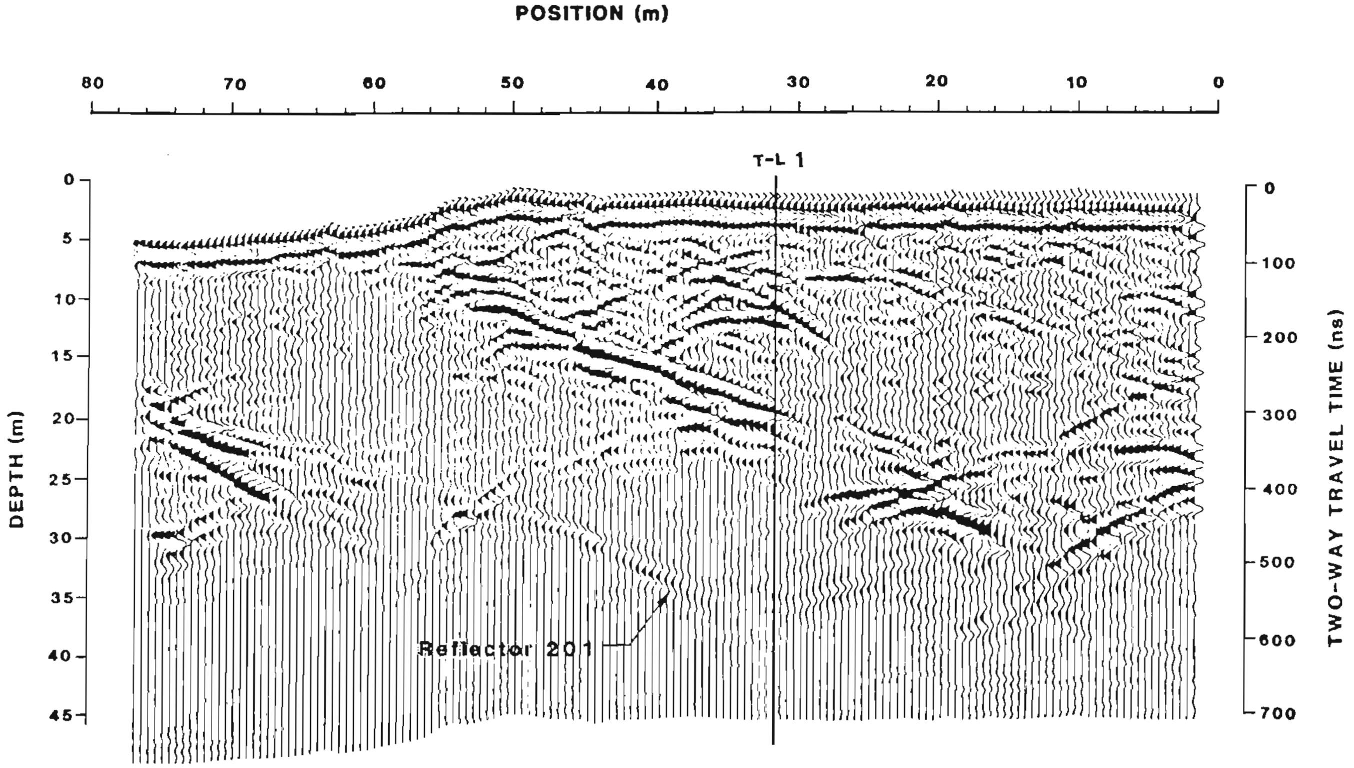

Figure 15. pulseEKKO III radargram for the base line of Site 1, permit area D, Whiteshell research area.

FRACTURE MAPPING FROM THE SURFACE

In granitic terrain, shallow to intermediate dipping fracture zones express themselves on the ground surface as asymmetrical linear valleys, partially filled with surficial deposits as shown in Figure 13. The footwall of such a feature is often a dip slope, whereas the hanging wall is a steep cliff with relief exceeding 10 m in some places. The surface traces of these features have been identified by geological mapping, airphoto analysis, and surface geophysics. It is difficult to accurately determine the dip using these techniques because the actual point of intersection is usually covered by glacial deposits and other surficial material.

These fracture zones are often important hydrogeological features and knowledge of their location and orientation is needed to develop an understanding of groundwater flow through the rockmass.

Radar reflection profiling on the hanging wall has been used successfully at two study areas in the Whiteshell research area to determine the location and orientation of a number of shallow to intermediate dipping fracture zones that come to the surface.

Figure 14 summarizes the geology of area D, located 5 km northeast of URL.The surface traces of the linears have been shaded. Three locations in D were chosen for radar profiling on the hanging wall of these features to determine the orientations of possible fracturing below. To keep the target within the probing range of the radar system, sites were chosen that were of low to moderate relief and were close to the updip edge of the expected fracture. The locations are labelled on Figure 14.

Predictions of the borehole length to intersection of fracture zones were made for boreholes WD1 and WD4 based upon radar surveys at sites 1 and 2 before drilling began. Site 3 was surveyed after borehole WD2 was drilled.

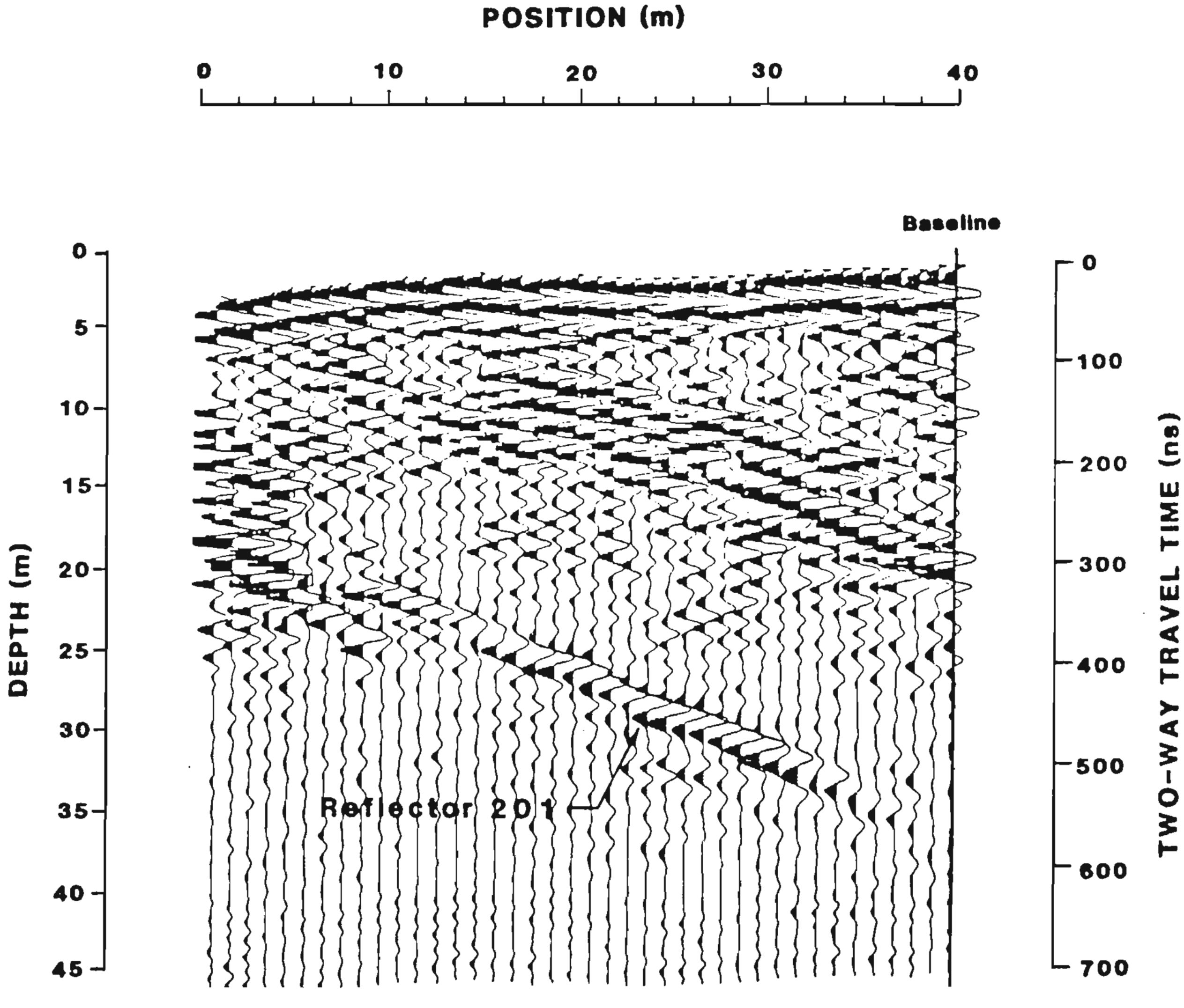

Figure 16. pulseEKKO III radargram for tie line 1 of Site 1, permit area D, Whiteshell research area.

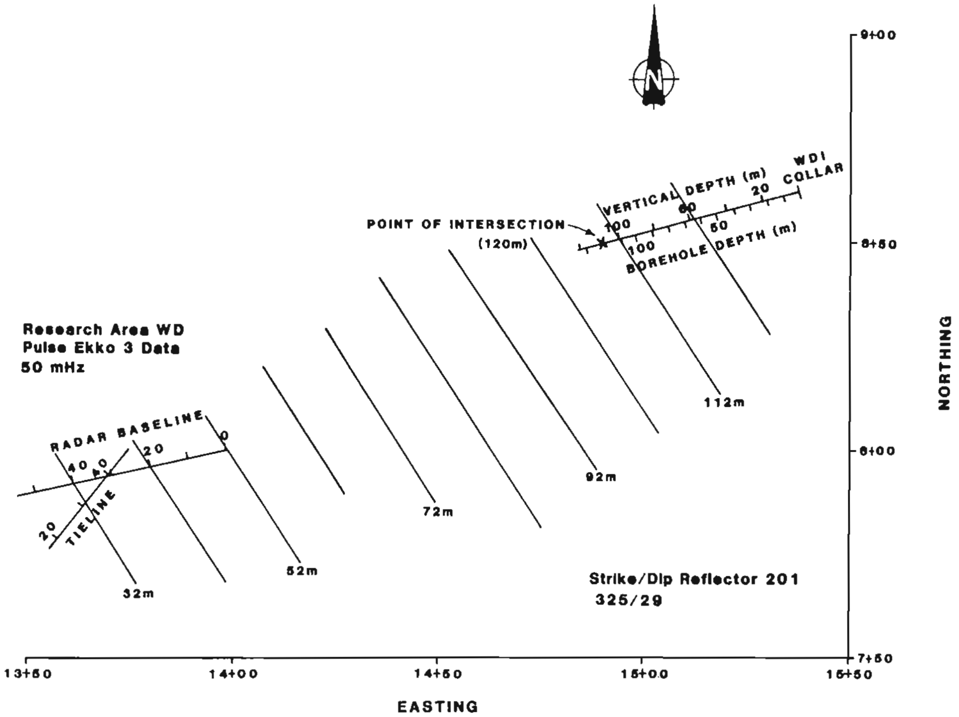

Figure 17. Structure contours of dipping reflector 201 extrapolated to intersect borehole WD1, permit area D, Whiteshell research area.

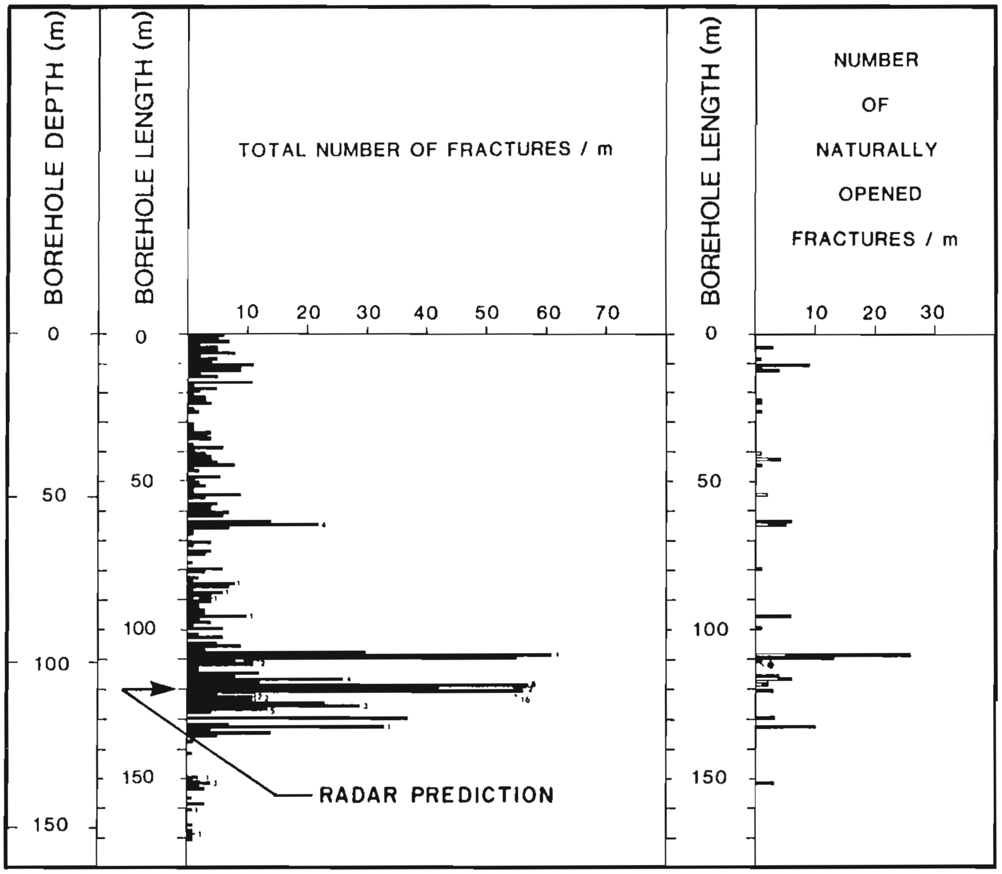

Figure 18. Fracture log of WD1, collared after radar prediction, showing agreement between radar data and actual fracture log (after Ejeckam et al., 1990).

At each radar site, intersecting profiles were laid out on the granite outcrops and surveyed with the radar system. The results from the baseline and tie line 1 from site 1 are shown in figures 15 and 16, respectively. The data seen in the figures have had topographic corrections applied to them. The lowermost dipping reflector, 201, results from the low dipping fracture zone. The upper, subparallel reflector appears to be a related, minor splay, but this has not been confirmed to date by any borehole data.

Reflector 201 was determined to have a strike of 325 degrees and a corrected dip of 29 degrees. Structure contours determined for the dipping planar reflector are shown in Figure 17 These were extrapolated to the point of intersection with proposed borehole WD1, with a predicted intersection at a borehole length of 120 m. In Figure 18 the fracture log (fractures logged per metre) of borehole WD1 shows that a major fracture zone occurred very close to the location predicted from the radar survey. Even though the radar data were extrapolated over distances greater than 100 m, the predicted intersection of the fracture zone was accurate to within 10 m. The orientation of the main reflectors observed on the survey from the other areas shown in Figure 14 were extrapolated to adjacent boreholes with equal success.

CONCLUSIONS

The radar profiling completed underground at the URL facility and from rock outcrop on the ground surface at the Whiteshell research area has shown that the method is a quick and reliable technique to determine zones of significant fracturing within 30 m of the profiling surface in the Lac du Bonnet granite. In some locations, this range can be increased to 50 m, but this is dependent upon site-specific conditions such as the intensity of fracturing in the upper sections. Too much shallow fracturing reflects much of the energy, which decreases the effective probing distance.

In working underground, surveying difficulties can arise from the often hostile environment; metal is commonly abundant, which can cause ringing in the radar records, and often there is only limited room for profiling. Interpretation may also be complicated by the existance of guided wave modes in drifts and tunnels.

Work on the rock outcrops at surface can be disrupted by areas of high relief, which make accurate profiling difficult, and by areas with a highly conductive glacial overburden veneer, which can drastically reduce the probing range of the system at any radar frequency. Fracture mapping using radar reflection techniques will continue to be used in the geoscientific research of the Canadian Nuclear Fuel Waste Management Program.

REFERENCES

Dormuth, K.W. and Nuttall, K.
1987: The Canadian Nuclear Fuel Waste Management Program; Radioactive Waste Management and the Nuclear Fuel Cycle, 1987, v. 8 (2-3), p. 93-104.

Ejeckam, R.B., Stone, D., and Kamineni, D.C.
1990: Surface and subsurface geology of Permit Area D, Lac du Bonnet Batholith, Manitoba; AECL Technical Record TR 490.

Everitt, R.A., Kamineni, D.C., Stone, D., Read, R.S., and Chernis, P.J.
Recent developments in the geological characterization of fracture zone #2; unpublished AECL memorandum.

Holloway, A.L., Soonawala, N.M., and Collett, L.S.
1986: Three dimensional fracture mapping in granite excavations using ground probing radar; Institute of Mining and Metallurgy Bulletin, v. 79, p. 54.

Regan, D.M.
1973: Structural Geology, An Introduction To Geometrical Techniques (2nd Edition): New York, John Wiley and Sons, 208 p.

Simmons, G.R.
1986: Atomic Energy of Canada Limited's Underground Research Laboratory for nuclear waste management; in Proceedings, Geothermal Energy Development and Advanced Technology International Symposium, Tohoku University, Sendai, Japan, 1986. (Also issued as AECL-9283).

Spinney, M.H.
1990: An in situ test of vibrating wire stressmeters in granitic rock; AECL report number AECL-10112.

Stone, D. and Kamineni, D.C.
1988: Recognition of low-intermediate dip fracture zones at surface: An example from Permit Area D, Lac du Bonnet Batholith; AECL Technical Record TR 465.

Telford, W.M., Geldart, L.P., Sheriff, R.E., and Keys, D.A.
1982: Applied Geophysics. Cambridge, Cambridge University Press, 860 p.

Whitaker, S.H.
1987: Geoscience research for the Canadian Nuclear Fuel Waste Management program; Radioactive Waste Management and the Nuclear Fuel Cycle, 1987, v. 8 (2-3), p. 145-196.

APPENDIX A

Dip correction technique

A dip correction procedure is used by AECL to provide geometrical corrections to planar radar reflection data so that the correct distances to, and orientations of, dipping planar reflectors can be determined.

Radar energy propagates outwards from a transmit antenna into a medium in a conical form. Part of this energy is reflected because of electrical discontinuities in the rock, such as water-filled fractures, and is subsequently detected at the receiver antenna. Where transmitter and receiver antennas are adjacent to one another, as is commonly the case in radar profiling, reflections detected at the receiver follow travel paths that strike the reflecting interface at normal incidence, such as raypath 1 in Figure A-1. Energy travelling in other directions is reflected and refracted away from the antennas in accordance with Snell's Law, such as along raypaths 2 and 3.

Radar systems measure the time taken for a ray to travel from the transmitter through a medium and arrive at the receiver but cannot detect the direction of travel. The data are plotted in two dimensions assumping that all energy comes from vertically below the antenna position, which is true only for the special case of the reflecting feature being planar and parallel to the surface being profiled. In the example shown in Figure A-2, a reflection profile observed along profile line YX receives reflections from the dipping planar interface YZ. In this two dimensional example, the profile line YX is in the direction of the dip of reflector YZ. Typical antenna points a to d receive reflections along the corresponding normals labelled a" to d".

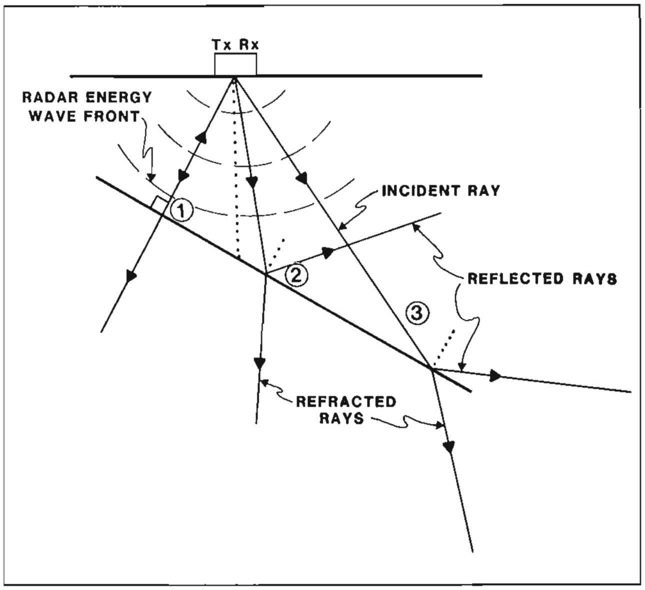

Figure A-1. Typical waves coming from a radar receiver, and their reflected and refracted counterparts and encountering a dipping planar radar reflector

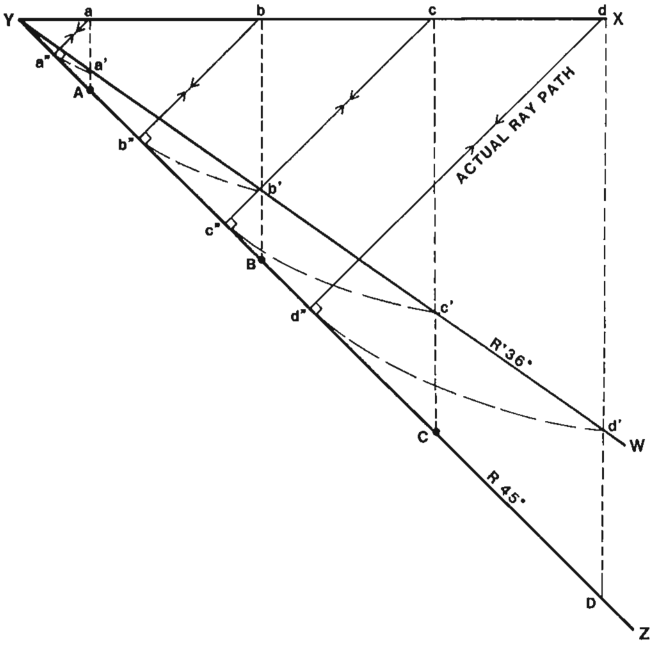

Figure A-2. Two dimensional dip correction procedure for a planar reflector with a to d typical radar survey points, a″ to d″ the actual point of reflection; and a′ to d′ the apparent points of reflection. The example shows how an apparent (or uncorrected) dip of 36 degrees is produced on a radargram by a planar feature such as a fracture zone that dips at 45 degrees.

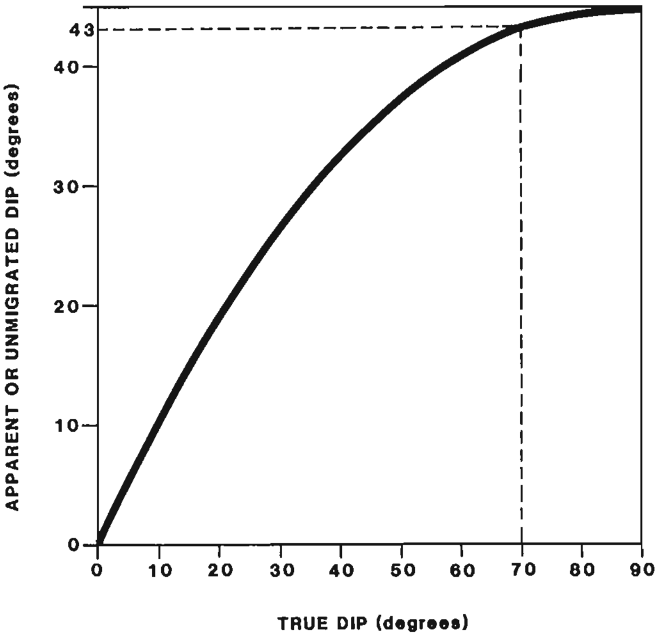

Figure A-3. A plot of true corrected dip versus uncorrected dip for a two dimensional case showing how the dip correction becomes more significant as the dip angles increase.

In uncorrected radar data, the reflecting point is plotted directly underneath the antenna position such as at a, b etc. and thus the actual distance to the reflector is underestimated. The uncorrected data generated from this example would thus determine the dip of this feature to be 36 degrees, when the correct or true dip is 45 degrees. As true dip increases, the discrepancy between unmigrated dip and true dip also increases (Fig. A-3).

A trigonometric correction is applied, which moves the apparent point of reflection (such as point a in Figure A-2) to its actual point of reflection, position a", enabling the correct orientation to be determined.

The orientation of the targets are generally unknown prior to radar reflection surveying; therefore, the profile lines are usually at some angle other than along the direction of dip. A three dimensional correction is required to determine the true orientations of planar reflectors in this case. In this procedure, the true depth of the reflector, immediately below the midpoint of the antennas is determined by extrapolating along both strike and dip, from the apparent point of reflection. The trigonometric calculations are more complex than for the two dimensional case but are still relatively simple.

A computer program has been developed by AECL that will correct suitable reflection data in three dimensions if the reflector is picked from at least two lines. The corrected dips of the reflector along the various profile lines are apparent dips only. The strike and true dip of the feature can be calculated based on the concept discussed by Regan (1973) of two apparent dips determining the orientation of a plane. If the reflector is detected in only one profile line, the program assumes that the profile line is along the dip direction, and corrects the data in two dimensions.

The data to be input into this program to compute the true orientations of the radar reflectors are determined by measuring the apparent angles the planar reflectors make with the profiling surface on the radargrams themselves and entering the appropriate values. A plot of the true orientations is from the values calculated available as output.

A microprocessor based ice-radar system for surface profiling

R.W. Jacobel[1], S.K. Anderson[1] and D.F. Rioux[1]

Jacobel, R.W., Anderson, S.K., and Rioux, D.F., 1992: A microprocessor based ice-radar system for surface profiling; in Ground penetrating radar, ed. J. Pilon; Geological Survey of Canada, Paper 90-4, p. 101-105.

Abstract

We have built a radio-echo sounder which uses a low-frequency, broadband impulse transmitter and a microprocessor based digital recording system. The unit is mounted on skis, and power is delivered by a small generator and batteries. The receiver uses a portable, digital storage oscilloscope, which passes data via a microprocessor unit to a cassette tape for offline analysis on a personal computer. Though originally intended primarily for studies on temperate ice, the sounder has been tested in Antarctica during the 1987-88 field season. The system performed well there and in field tests and subsequent studies on South Cascade Glacier, Washington, and a number of interesting results were obtained. An oblique incidence profile where transmitter-receiver separation varied was used to study the dielectric permittivity of the ice and to locate internal layers at shallow depths. The sounder was also deployed in conjunction with hot water drilling experiments attempting to create cavities at known locations within the ice. Waveforms from different transmitter-receiver orientations around the borehole were combined in the offline analysis to produce a more directional, synthetic aperture emphasizing returns from the borehole region.

Résumé

Un radio-échosondeur a été construit avec un émetteur à impulsion à large bande et faible fréquence et un système d'enregistrement numérique exploité à l'aide d'un microprocesseur. Il est monté sur des skis et l'électricité est produite par un petit générateur et des piles. Le récepteur comporte un oscilloscope à mémoire numérique portatif qui passe les données par l'entremise d'un microprocesseur à une bande en cassette aux fins d'analyse en différé sur un ordinateur personnel. Bien que d'abord prévu pour effectuer des études de la glace tempérée, l'échosondeur a subi des essais dans l'Antarctique durant la saison de 1987-1988. Le système a bien fonctionné et l'on a obtenu un certain nombre de résultats intéressants dans des essais de terrain et des études ultérieures sur le glacier South Cascade (Washington). Pour étudier la permittivité diélectrique de la glace et localiser les couches internes à faible profondeur, on a utilisé un profil d'incidence oblique indiquant les endroits où s'observanit une variation de la séparation émetteur-récepteur. L'échosondeur a également été utilisé dans des expériences de forage à l'eau chaude visant à créer des cavités à des endroits connus au sein du glacier. Les formes d'onde provenant de différentes orientations émetteur-récepteur autour du trou de sondage ont été combinées dans l'analyse en différé pour produire une ouverture synthétique plus directionnelle en mettant l'accent sur les échos provenant de la région du trou de sondage.

---

[1] Department of Physics, St. Olaf College, Northfield, Minnesota, U.S.A. 55057

INTRODUCTION

Although radar systems of various design have been used in sounding ice for more than 20 years, only recently has the digital recording of the echo waveforms been feasible. The principal difficulty has been the need for 1) high speed digitizers to achieve bandwidths on the order of 100 MHz to accurately record the waveforms, and 2) the speed to repeat the process rapidly while storing the data, as required in profiling applications. The advantages of digital recording over earlier analog methods occur both in the acquisition of data and in offline processing. Digitally recorded waveforms can be "stacked" in time to reduce incoherent noise and thus to enhance a signal. Signals from different points in space may also be combined to produce a synthetic aperture, thereby narrowing the radar beamwidth. In offline processing, waveforms can be easily filtered, power spectra can be produced, and a host of postprocessing techniques widely used in geophysical analysis can be applied. For example, methods of predictive deconvolution, which allow the removal of effects due to imperfect input waveforms, can be applied. Statistical techniques such as principal moment analysis can be employed to enhance subtle echo differences such as one might expect over changing bed conditions (F.H.M. Jones, unpublished report, 1987).

Because of the specialized requirements of these radar systems, a number of groups have developed receiving and recording equipment specifically for this purpose. We have instead chosen to adapt commercially available electronics to our needs and so have designed a system that could be fairly easily duplicated by others. The unit was built for under $10 000 and weighs less than 32 kg. It is mounted on skis and intended for stationary as well as small scale profiling applications.

RADAR TRANSMITTER

With minor modifications, the radar transmitter is similar to the one described by Watts and England (1976), and Watts and Wright (1981). Two pulser units were built along with separate triggering circuits, which allow "free running" trigger rates to vary between 0.1 and 10 KHz. The transmitter may also be triggered by pulses from an odometer wheel, linked to the transmitter by a fibrer optic coupling, which typically would be used when profiling. The system also operates in a "wake up mode" where waveforms may be recorded at a fixed location at preset time intervals without an operator being present. A block diagram overview of the system (Fig. 1) depicts the receiver, data acquisition system, and control features. Details of the transmitter can be found in the references above.

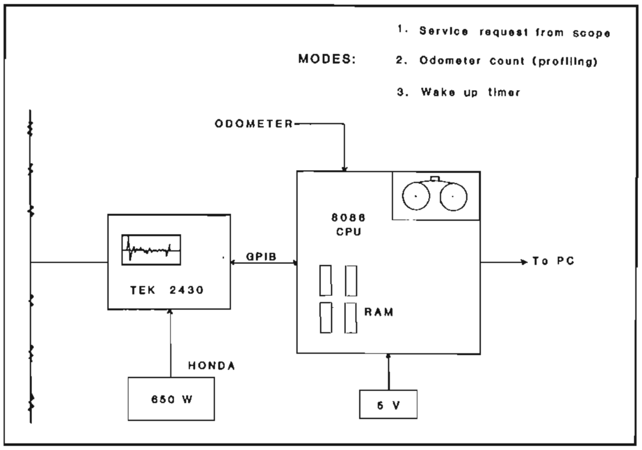

Figure 1. Block diagram of the radar recording system.

The centre frequency of the transmitted impulse is determined by the length of the attached dipole antenna and may be varied by simply changing the length of these wires (Watts and England, 1976). The broadband characteristics of the waveform result from the impulse created by the transmitter; they are a positive feature of the system design in that information about internal scattering sources is contained in the power spectrum of the returned energy (Jacobel and Raymond, 1984; Jacobel and Anderson, 1987). A negative feature of low frequency impulse radars is the lack of directionality of the antennas. We devoted considerable time to this problem in an attempt to build antennas that would better direct energy into a well defined region of the ice, but our efforts were without success. We built antennas in conical spiral pattern mounted on a fabric form, which collapsed to a flat disk for ease of transport. These antennas indeed improved the directionality of the radar but produced unacceptable ringing of the impulse waveform even when heavily damped with resistive loading. We believe this arises from electromagnetic coupling between turns of the spiral and is an unavoidable consequence of the impulse waveform. Our subsequent attempts to gain more directionality from the radar focused on postrecording techniques as described in the section entitled "Performance tests and results".

RECEIVER AND DIGITAL RECORDING SYSTEM

The radar receiver is a Tektronix 2430 portable digital storage oscilloscope. This instrument we feel represents the best optimization of a number of competing requirements, among them: bandwidth, power consumption, cost, weight, and reliability. The oscilloscope uses a 100 megasample per second digitizer and will automatically switch into a sampling mode for sweep speeds requiring higher digitizing rates. The vertical amplifier has an analog bandwidth of 150 MHz, more than adequate even for the highest frequencies present in the echo waveform. Each waveform is digitized into 1024 points, and stacking to eliminate noise is available in an averaging mode that can be varied from 2 to 256 waveforms.

The digital scope has a triggering feature, which makes it ideal for radar application. Signals fed to the input are continuously digitized, whether or not a trigger is received. The scope is set to trigger in a particular bin (for example, bin 128 of 1024) when the voltage exceeds a selected threshold level. When this condition is fulfilled, the digitizer is latched and the waveform is displayed and stored in memory. Thus, information is present about the waveform that actually preceded the trigger. Gone are the problems, typical in analogue scopes, of capturing the first arrival of the airwave and uncertainties about timing relative to it. The scope may simply be set to trigger on a stable part of the airwave, and the complete waveform, including time before the trigger, is recorded and saved (Fig. 2).

Power consumption of the scope is significant, however, and necessitated designing the system to be ski-mounted instead of movable in a backpack. The oscilloscope requires up to 180 W, although during typical operation 120 W is more common. Nevertheless, this power is more than can be easily supplied by batteries; as a result we have employed a 650 W Honda generator for the power source. The scope and the generator each weigh about 16 kg. The latter provides remarkably clean and quiet power. Any electrical noise is eliminated by using the scope's averaging mode when acquiring waveforms.

The 2430 communicates set-up and waveform information over a standardized interface, the General Purpose Interface Bus (GPIB or IEEE-488); it may be linked to a number of microprocessor devices that can receive

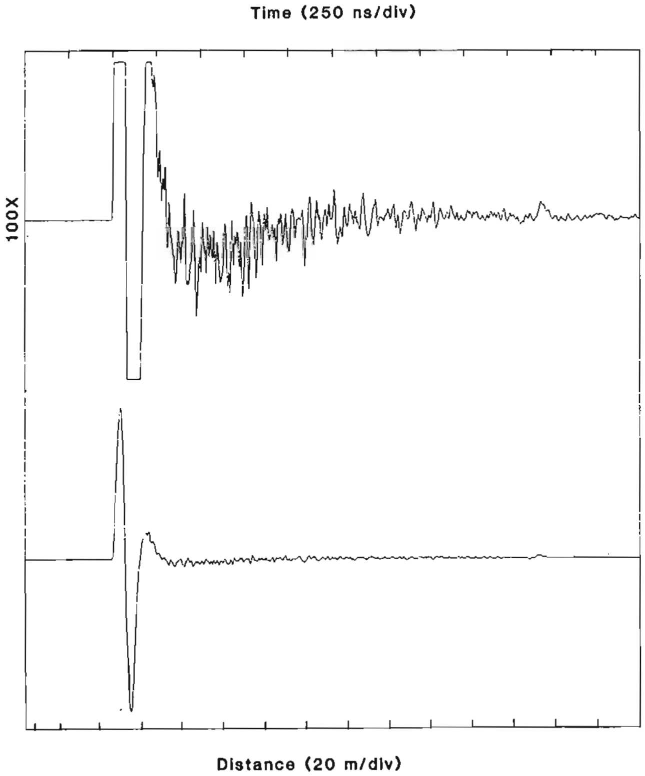

Figure 2. Digitally recorded incident waveform on two amplitude scales. Note that portions of the waveform occurring prior to the trigger (on the rising edge of the first arrival or airwave) are recorded as well.

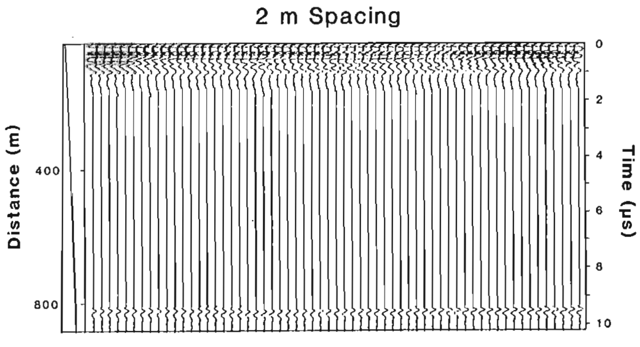

Figure 3. Radar profile of a portion of ice stream B, Siple Coast West Antarctica. Radar centre frequency is 2 MHz and waveforms are recorded at 2 m intervals. The nearly flat bed at 800 m depth is clearly seen as are nearsurface crevasses, a characteristic feature of ice streams.

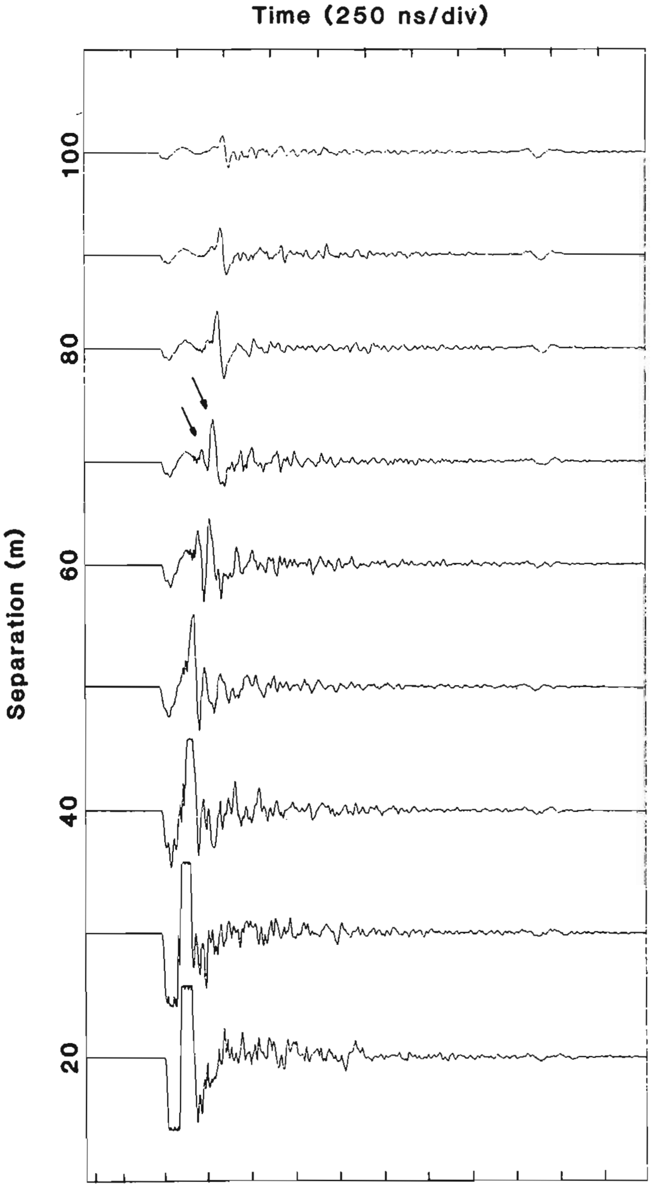

Figure 4. Oblique incidence profile showing the direct arrival (airwave) decreasing in amplitude as separation is increased. Also present are two echoes (arrows) from internal layers seen most clearly at separations beyond 60 m.

parallel information in this format. The 2430 has two advantages over more specialized time base and digitizing systems: 1) it uses standard commercial technology, and 2) it has ease of compatibility with recording devices. To accomplish the task of delivering digitized waveforms to tape, we chose an Intel 8086 microprocessor design kit, which is supported by 4K of RAM, 8K of ROM, a keypad/LED display interface, RS-232 serial communications, and standard 8255A I/O chips all supplied by the manufacturer on a single board. Essentially, we have elected to use commercial technology for the more difficult job of waveform acquisition (the Tektronix 2430 oscilloscope) and to handle the data transfer and storage with a dedicated microprocessor and interfacing designed in house.

The digitized waveform data are sent over the GPIB on command and are stored in RAM until the entire waveform has been collected. Typical transfer times are 0.3-0.4 s depending on the command issued. From RAM the waveform is written to tape via a Braemar CM 600 Mini-Dek digital cassette recorder. The CM 600 operates at 300 baud, which is significantly slower than the GPIB. Thus writing a single waveform to tape takes about 3 s and the total collection/write time is therefore about 3.5 s. This factor limits the speed of operation in profiling. For example, in dense sample profiling, with one waveform recorded each metre, surface speed is limited to about 0.25 m/s. Speeds of up to 6 m/s are possible for less dense profiling; we found this to work quite acceptably, for example, when the system was towed behind a snowmobile. Position information is obtained with an odometer wheel-shaft encoder arrangement, and pulse count corresponding to distance travelled is recorded on tape along with the waveform.

To retrieve the records from tape for processing and analysis, tapes are read offline on a cassette deck and are transferred to a personal computer over the RS-232 line. In our field trials, this has been accomplished at a base camp within hours of acquiring the data. Much of the data manipulation and waveform processing can be done on the PC so that, for example, stacked A-scope or Z-scope displays can be produced in the field. In this way decisions can be made immediately that may influence subsequent work.

PERFORMANCE TESTS AND RESULTS

The system was tested and deployed in several experiments on South Cascade Glacier, Washington, during the summer of 1986, and on ice stream B in West Antarctica during the 1987-88 field season. Figure 3 shows the results of a profile about 1 km in length made on ice stream B employing antennas with a centre frequency of 2 MHz. The nearly flat bed at 800 m depth in this part of the ice stream is clearly seen in the profile as are nearsurface crevasses, which are a characteristic feature of the ice stream.

Figure 4 shows the results of an oblique incidence profile done on South Cascade Glacier in which transmitter-receiver distance was systematically increased from 20 to 100 m. Such a profile is useful for identifying shallow layers that are not otherwise observed in fixed transmitter-receiver profiling because the echo is often obscured by the airwave arrival (Jezek et al., 1978). Echoes from two such layers are evident at the larger separations in this profile (arrows) and were used to determine the dielectric properties of the ice, as well as the layer depth.

In an effort to gain more directionality from the antennas to study changes within the ice in the region of a borehole, we made recordings with transmitter and receiver located in turn at intervals around a circle with the borehole at the centre. In our data processing these waveforms were easily combined, producing a "synthetic aperture" that enhances reflectors common to all views, and reducing those that are not. For example, the strength of the bedrock echo is enhanced relative to the noise, and so presumably are echoes from internal targets beneath the drill site.

Figure 5 shows waveforms recorded at a drill site on South Cascade Glacier over 4 days. Each waveform is actually the sum of four records made around the hole as described above. Waveforms are multiplied by the scaling function shown at the bottom of the figure, which corrects for attenuation losses and also has the effect of suppressing (and distorting) the direct (airwave) arrival. The purpose of this experiment was to look for changes occurring as a result of drilling. The waveform marked 7/30 was recorded at the site prior to

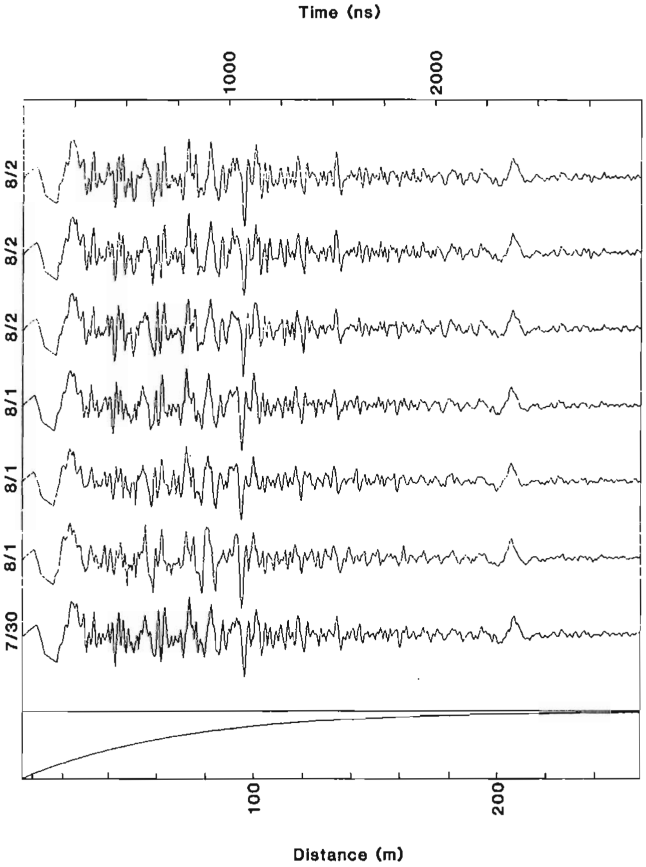

Figure 5. Synthetic aperture waveforms made by combining data from pairs of transmitter-receiver locations taken in turn around a borehole location. Change of the waveform in time are <u>not</u> evident as the hole was drilled, enlarged, and salt added.

drilling. On 7/31 a borehole was drilled that reached the bed at a depth of 200 m, which is in agreement with the radar results. The borehole did not connect at the bed during the time covered by the figure, and water levels in the hole remained roughly constant at about 30 m below the surface.

Subsequent waveforms were recorded after additional drilling to enlarge portions of the borehole and after salt injections. No obvious changes in the waveform are evident. Further processing of the data, using principal component analysis to emphasize differences present in the waveforms, also produced negative results. Evidently, the radar is not highly sensitive to regions with small changes in the dielectric, or at least not to those having this geometry.

ACKNOWLEDGMENTS

Development of this radar system was carried out in the Physics Department of St. Olaf College and was supported by a number of people who deserve recognition. The authors wish to acknowledge the essential contribution of Dr. Duane Olson who supervised the work in interfacing and microprocessor development. We appreciate the technical support of Mike Sjulstad, Don Spitzack, and members of the St. Olaf academic computer staff. We thank Francis Jones of the Department of Geophysics and Astronomy, University of British Columbia, for valuable discussions about the principal component analysis, and Dr. David Wright of the U.S. Geoloical Survey for helpful advice about the radar transmitter. We wish to thank the staff of the Project Office Glaciology, U.S. Geological Survey, for their hospitality and use of the research facilities on South Cascade Glacier, Washington. In particular, we appreciate the ideas and efforts of Andrew G. Fountain in collaborating on the drilling experimet and for his advice and discussions about the analysis. Finally, we wish to thank the National Science Foundation for its support of the project with grant number DPP-8406672 to St. Olaf College.

REFERENCES

Jacobel, R.W. and Anderson, S.A.
1987: Interpretation of radio-echo returns from internal water bodies in Variegated Glacier, Alaska; Journal of Glaciology, v. 33, no. 115, p. 319-323.

Jacobel, R.W. and Raymond, C.F.
1984: Radio echo-sounding studies of englacial water movement in Variegated Glacier, Alaska; Journal of Glaciology, v. 30, no. 104, p. 22-29.

Jezek, K.C., Clough, J.W., Bentley, C.R., and Shabtaie, S.
1978: Dielectric permittivity of glacier ice measured in situ by radar wide-angle reflection; Journal of Glaciology, v. 21, no. 85, p. 315-329.

Watts, R.D. and England, A.W.
1976: Radio-echo sounding of temperate glaciers: ice properties and sounder design criteria; Journal of Glaciology, v. 17, p. 39-48.

Watts, R.D. and Wright, D.L.
1981: Systems for measuring thickness of temperate and polar ice from the ground or from the air; Journal of Glaciology, v. 27, no. 97, p. 459-469.

Impulse radar studies of interface roughness

Kenneth C. Jezek[1], Steven A. Arcone[2], Steven Daly[2],
and Robert H. Wills[3]

Jezek, K.C., Arcone, S.A., Daly, S., and Wills, R.H., 1992: Impulse radar studies of interface roughness; in Ground penetrating radar, ed. J. Pilon; Geological Survey of Canada, Paper 90-4, p. 107-115.

Abstract

Recent progress by several investigators has led to improved methods for estimating interface roughness via wave scattering measurements. These techniques, already tested on sonar data, are based on a union of scalar scattering theory derived from the Helmholtz-Kirchoff integral with statistical representations of measured echo amplitude variations as have been employed to describe phenomena such as laser speckle. The usefulness of these methods has been in their ability to identify successfully parameters common to both the probabilistic and scattering formulations, which are also related to interface characteristics – such as the root mean square roughness, correlation function, and Fresnel reflection coefficient.

In this paper, we discuss the application of this approach with its possible advantages and limitations to impulse radar data. We begin by modelling echo amplitude variations via a parameter gamma defined by previous investigators as the ratio of the coherently to incoherently scattered energy. In our case, gamma is inversely proportional to the square of the wave number, the square of the root mean square (r.m.s.) roughness and integral of the surface correlation function. We evaluate gamma for a set of typical system and surface parameters and then use it to calculate probability density functions of echo amplitude. Using our model results as a guide, we go on to an examination of impulse radar data collected over a brash ice jam that formed in a river channel.

Résumé

Plusieurs chercheurs ont réalisé récemment des progrès qui ont conduit à l'amélioration des méthodes d'estimation de la rugosité de l'interface en recourant à des mesures de diffusion des ondes. Ces techniques, dont les résultats ont déjà été comparés aux données sonar, sont basées sur l'union de la théorie de diffusion scalaire dérivée de l'intégrale de Helmholtz-Kirchoff avec des représentations statistiques des variations mesurées de l'amplitude de l'écho telles qu'utilisées pour décrire certains phénomènes comme les tavelures laser. L'utilité de ces méthodes réside dans leur capacité à déterminer les paramètres communs aux formules probabilistes et de diffusion, qui sont également liés aux caractéristiques d'interface, comme la rugosité moyenne quadratique, la fonction de corrélation et le coefficient de réflexion de Fresnel.

Dans le présent article, l'application de cette approche ainsi que de ses avantages et limites possibles relativement aux données recueillies par radar à impulsion sont abordés. Les variations d'amplitude des échos sont d'abord modélisées au moyen d'un paramètre gamma que des chercheurs antérieurs ont défini comme le rapport de la diffusion cohérente à la diffusion incohérente de l'énergie. Dans le cas présent, le gamma est inversement proportionnel au carré du nombre d'ondes, au carré de la rugosité moyenne quadratique et à l'intégrale de la fonction de corrélation de surface. Le gamma est évalué pour une série de paramètres typiques du système et de la surface pour ensuite servir au calcul des fonctions de densité de probabilité de l'amplitude de l'écho. En utilisant les résultats du modèle comme guide, les données recueillies par radar à impulsion au-dessus d'un embâcle formé dans un chenal fluviatil suite à la débâcle des glaces sont alors analysées.

---

[1] Byrd Polar Research Center, The Ohio State University, 125 South Oval Mall, Columbus, Ohio 43210-1308

[2] Department of the Army, Cold Regions Research and Engineering Laboratory, Corps of Engineers, 72 Lyme Road, Hanover, New Hampshire, U.S.A. 03755-1290

[3] Department of Physics and Astronomy, Dartmouth College, Hanover, New Hampshire, U.S.A. 03755, now at Skyline Engineering, Temple, New Hampshire, U.S.A. 03084

INTRODUCTION

The objective of this paper is to present a comparison between an analysis of impulse radar data collected over a rough surface and a stochastic theory of wave scattering. The theory we use was developed by Stanton (1984) to describe fluctuations in the peak amplitude of the envelope of long sonar pings collected over the sea floor. The approach was later adapted by Stanton and others (1986) to study acoustic scattering from the underside of sea ice. In the following sections, we briefly describe the theory and then use it to model echo amplitude variations incorporating typical inpulse radar and prescribed surface roughness parameters. Based on the intuition obtained from the modelling exercise, we go on to describe a preliminary analysis of radar data collected over brash ice.

THEORY

We are presently involved in a direct application of the approach described by Stanton (1984) for modelling fluctuations in the amplitude of the envelop of sonar echoes reflected from the sea floor. The theory is twofold involving first a formulation developed by Eckart (1953; outlined by Clay and Medwin, 1977, ch. 10) of scattering from a rough surface. Key assumptions in the theory include: surface scattering only; normal incidence; and uniform and small roughness ($4k^2\sigma^2 < 1$ where $k = 2\pi$/wavelength is the wave number and σ is the r.m.s. surface roughness). Moreover, at this stage in our research, we ignore polarization effects and dielectric roughness (the latter as might occur when blocks of ice are floating in regions of open water).

Based on the above assumptions, Eckart showed that the mean of the peak envelop amplitude of the coherently reflected signal $< E >$ is

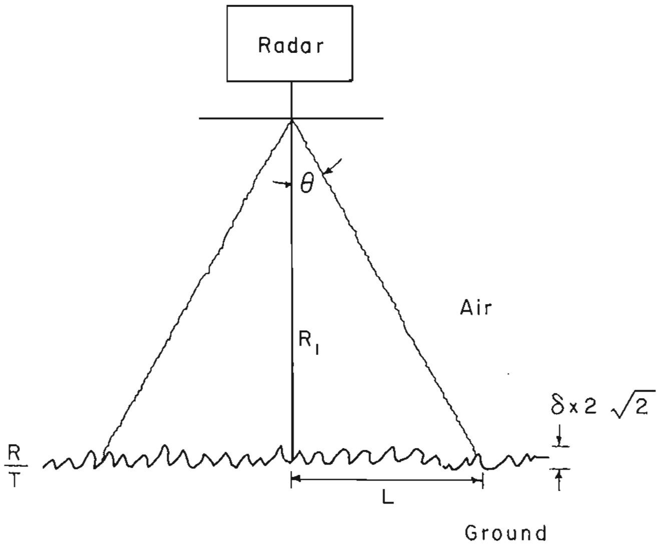

Figure 1. Experimental geometry for an impulse radar collecting data over a rough surface.

$$< E > = E_0 \, e^{-2k^2\sigma^2} \tag{1}$$

where E is the peak amplitude corresponding to the zero roughness case. Equation 1 indicates that the smaller the product of the wave number and the r.m.s. roughness the greater the coherent signal level.

Experimentally, $< E >$ is difficult to measure accurately. A more robust parameter is the second moment of the signal about the mean because it does not require information about the phase of the signal. Using Eckart's procedure, Clay and Medwin computed the mean squared signal ($< E^2 >$), which, for normal incidence and a monostatic array, is given by

$$< E^2 > = \frac{k^2B^2R^2L^2}{8\pi R_1^4} \iint_{surface} e^{-a(\xi^2+\eta^2)} \, e^{-4k^2\sigma^2[1-C(\xi,\eta)]} \, d\xi d\eta \tag{2}$$

where

B = proportional to source power

R = the Fresnel reflection coefficient

$a = (k^2L^2/2R^2)\,(1 + R^2/k^2L^4)$

x = x -x′

h = y - y′

C = two-dimensional correlation function of the surface, and L and R are defined in Figure 1. R_1 is the height of the source and receiver above the surface.

Stanton (1984) evaluated the integral in equation 2 by expanding the second exponential for small $4k^2\sigma^2$. The first term of the expansion turns out simply to be the square of the coherent signal. The second term is the mean square scattered signal $< s^2 >$. Ignoring higher order terms the integral reduces to the form

$$< E^2 > = < E >^2 + < s^2 > \tag{3}$$

To acquire experimentally the statistical measures required in equation 3, data are collected by sampling the amplitude of the echo envelop scattered from independent patches of the rough surface and compiling those samples into normalized histograms or probability density functions (PDFs). A reasonable model for describing the normalized histograms is the Rice PDF. Rice (1954) derived this PDF for the envelope of a sine wave plus noise. In our case the sine wave translates into a constant vector representing the coherent signal, and the noise translates into a random vector representing the specular signal. Under the assumption that the average separation between scatterers is less than the area subtended by the incident beam, Stanton went on to describe the sum of the coherently reflected signal and the scattered via the Rice PDF. Defining

$$\gamma = \frac{< E >^2}{< s^2 >}, \tag{4}$$

the Rice PDF is given by

$$\omega(e) = \frac{2(1+\gamma)}{<e^2>} \exp\left\{ \frac{-(1+\gamma)e^2 + \gamma <e^2>}{<e^2>} \; I_o(\xi') \right\} \qquad (5)$$

where $e = (E\,E^*)^{1/2}$

$$\xi^{-1} = \frac{2e\,[\gamma(1+\gamma)]^{1/2}}{<e^2>^{1/2}} \qquad (6)$$

and I_o is the modified Bessel function.

Hence, a relationship between the shape of the PDF and the properties of the rough surface as incorporated into the scattering theory can be established through the parameter γ. From the derived expressions for $< E >^2$ and $< s^2 >$, Stanton showed that

$$\gamma^{-1} = \frac{4k^2\,\sigma^2 a}{\pi} \iint C\,d\xi d\eta \qquad (6a)$$

In the modelling section of this paper, we use a sample correlation function reported by Clay and Leong (1974) and found useful for modelling ripple-like features. In that case

$$\iint C d\xi d\eta = \frac{2}{3}\; l_1 l_2\,, \qquad (6b)$$

and

$$l_1 = 30\,\sigma^{1.25} \qquad (6c)$$

where l, and σ are in metres. We assume $l_1 \approx l_2$.

MODELLING

To develop some intuition for the relationship between radar frequency and surface roughness, we used equations 5 and 6a-c to construct several sample PDFs. Figure 2 shows several calculated curves. At frequencies below 300 MHz

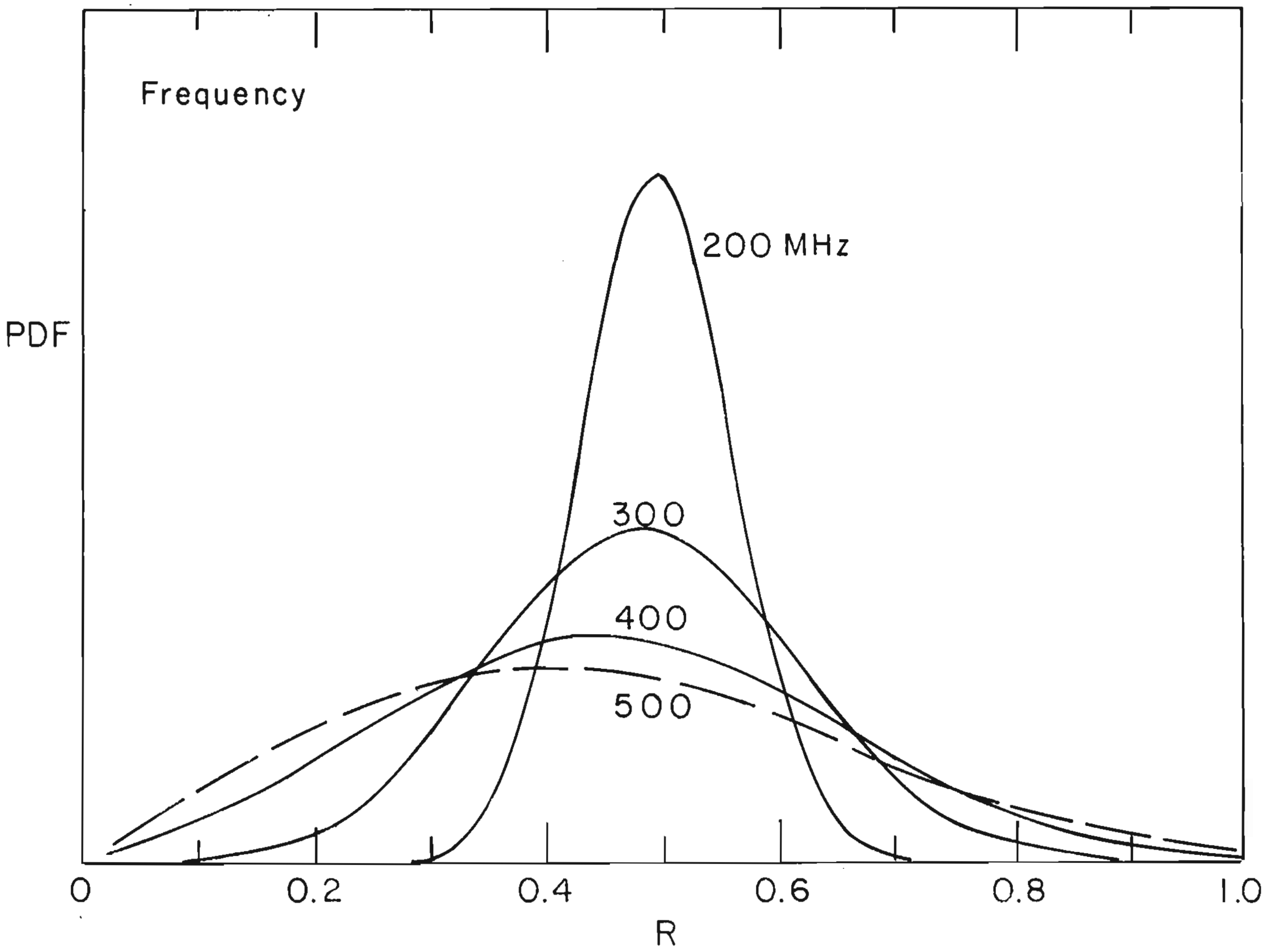

Figure 2. PDFs for a radar having a half beamwidth of 45° and 10 m above a surface with a peak to peak roughness of 10 cm. The mean normalized signal was chosen to be 0.5 (if normalization is to a perfect conductor then this is simply the reflection coefficient). The vertical axis is arbitrary and units are chosen to ensure the area under each curve is unity. The curves are parametric in frequency.

(wavelength = 100 cm), the PDFs are nearly Gaussian as would be expected when the coherent return dominates the measured signal. Above 300 MHz, the PDF takes the skewed shape of the Rayleigh distribution for which the scattered component dominates the measured signal.

Figure 3 shows PDFs calculated assuming 10 cm peak to peak roughness and a 200 MHz signal. As beamwidth decreases, the PDF narrows; for all beamwidths the PDF remains Gaussian.

Finally, Figure 4 shows various PDFs calculated at a fixed frequency but for different roughnesses. The skewness of the curves increases with the roughness.

BRASH ICE EXPERIMENT

Impulse radar data were collected over a brash ice jam that formed in South Channel north of Seaway Island in Lake St. Clair near Detroit, Michigan (Daly and Arcone, 1989). This channel helps drain St. Clair River where the jam originally formed. The ice consisted of broken pieces ranging up to 1 m in diameter, about 5-10 cm thick and tightly jammed to depths ranging up to 1.7 m. Figure 5 shows part of this jam and reveals that most pieces were lying horizontally. The afternoon air temperature had been above freezing for several days and the water temperature was between 0 and 1°C so that the pieces were not lying above a frozen matrix. The original data (Daly and Arcone, 1989) showed about 18% of the radar echoes to have been reflected from water. Consequently, the assumption of no dielectric roughness is not consistent throughout the jam but it is a good approximation for the entire jam. Figure 6 is a frequency analysis of the projected horizontal equivalent diameters and was developed from an overhead photograph. The mean equivalent diameter and also, standard deviation, are 15.5 cm.

The impulse radar equipment was a Xadar Electromagnetic Reflection Profiling System control unit that ran a GSSI Model 3102 "500 MHz" antenna mounted off the skids of a helicopter. The helicopter flew at 6-10 m altitude. The control unit compiles scans at the rate of 8/s so that, at the helicopter speed of ~10 m/s and a radar 3 dB beamwidth of ~70° (Arcone et al., 1986), every ninth scan was compiled

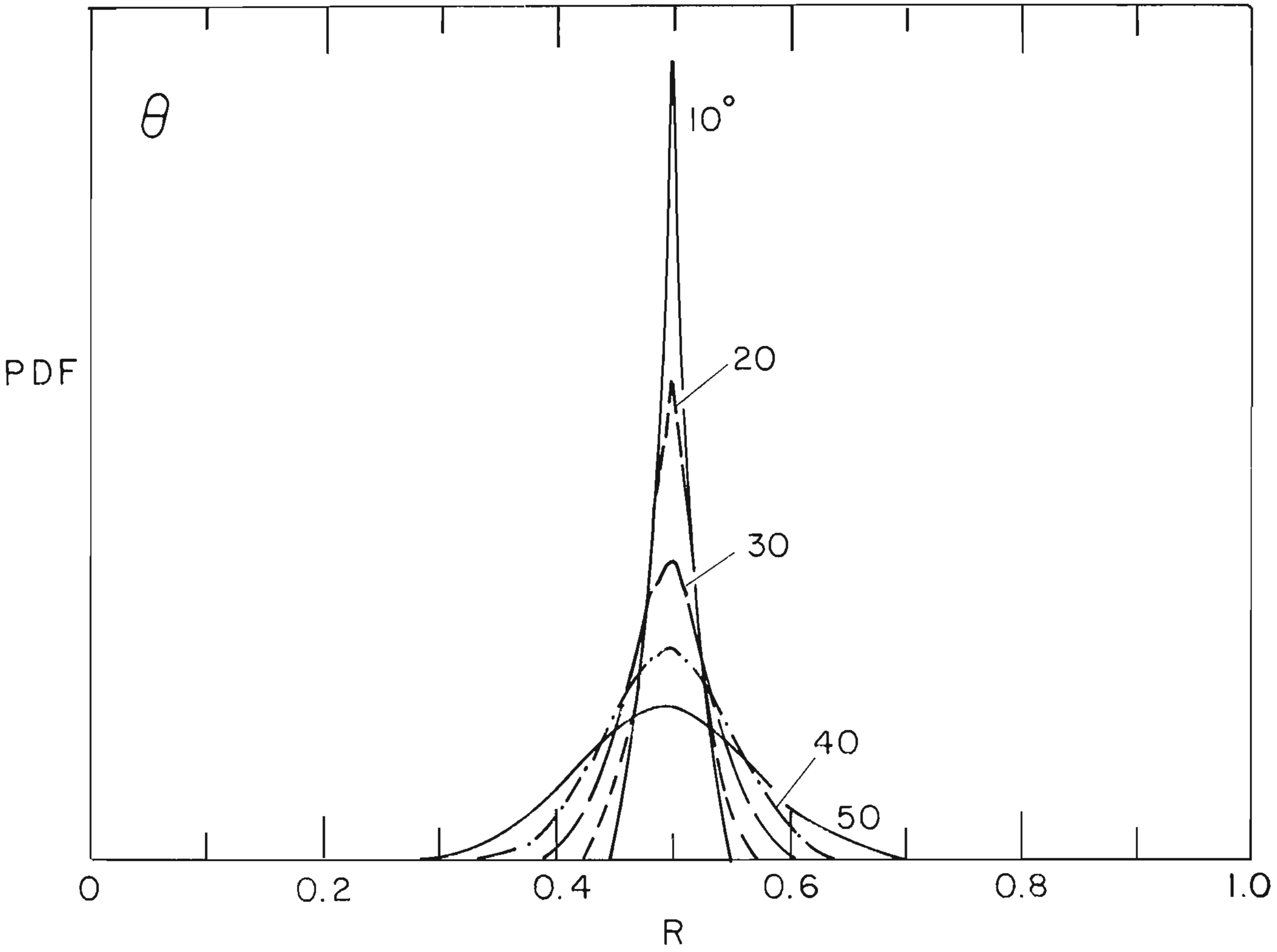

Figure 3. PDFs for a radar operating at 200 MHz 10 m above a surface with 10 cm peak to peak roughness. Curves are parametric in beamwidth.

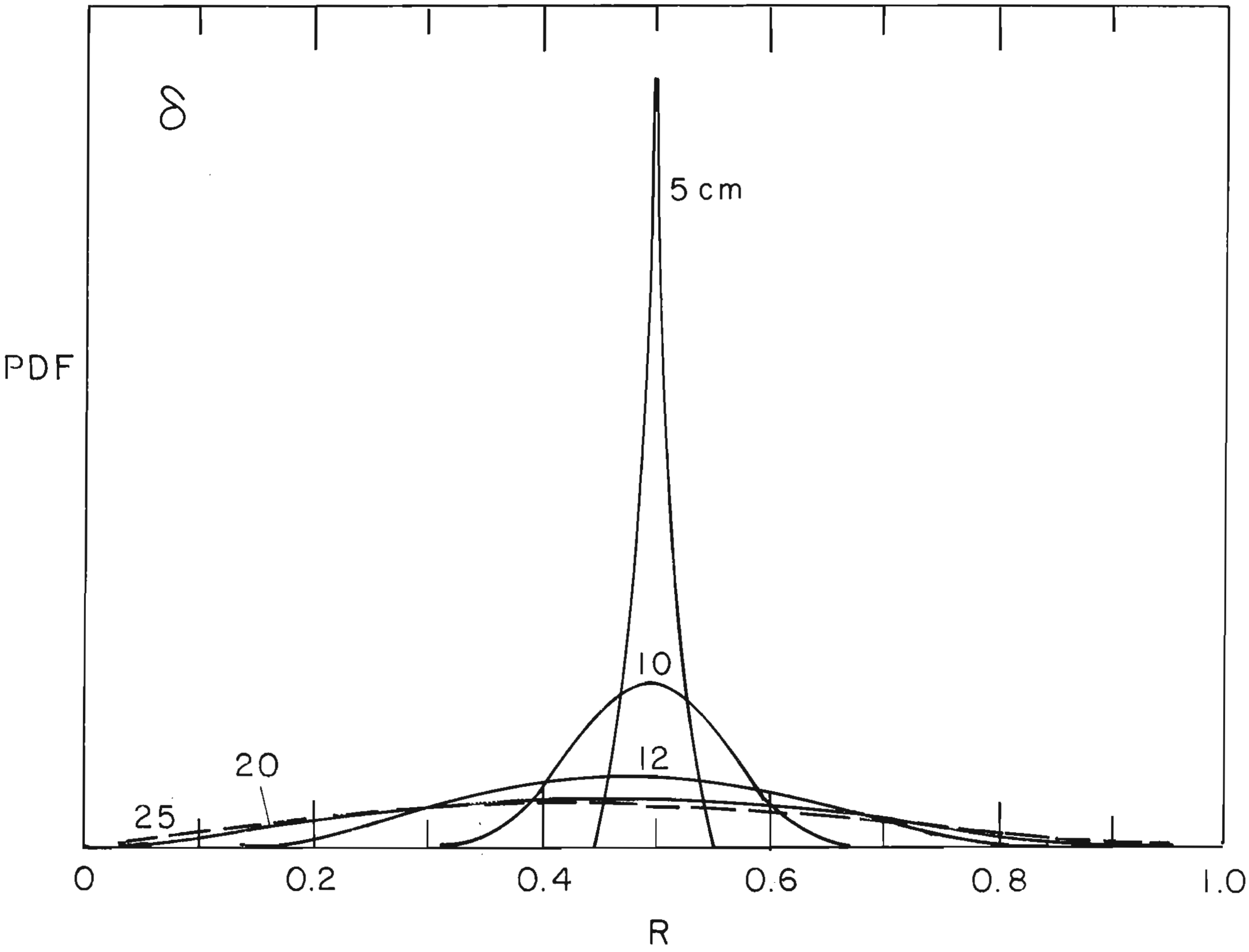

Figure 4. PDFs for a radar operating at 200 MHz having a 45° half beamwidth and 10 m above the surface. Curves are parametric in surface roughness.

Figure 5. Photograph of the ice jam on South Channel north of Seaway Island near Detroit, Michigan, taken 25 February 1987.

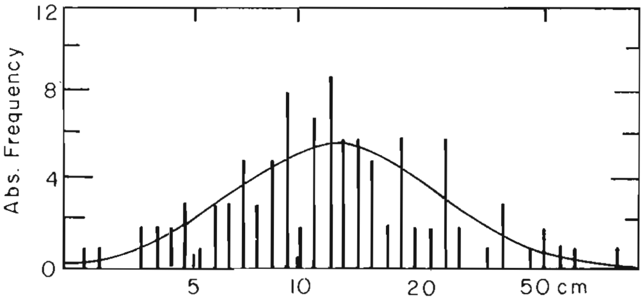

Figure 6. Frequency distribution of the diameters of equivalent area circles for ice pieces contained in a photograph of a 2.6 x 1.4 m area taken from the bow of a ship.

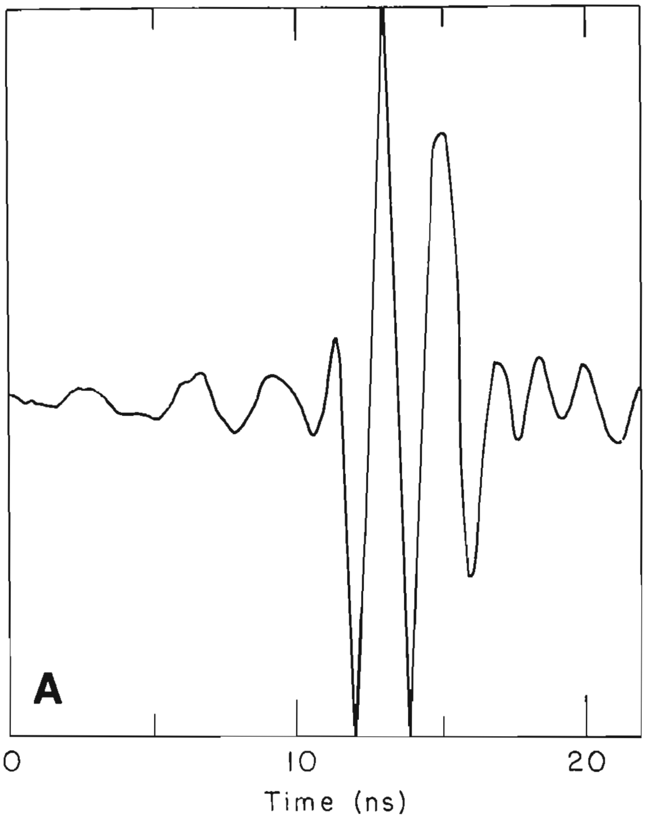

Figure 7A. Waveform and **B.** Fourier amplitude spectra (solid line) of the transmitted waveform. The dashed curve is the average Fourier amplitude spectrum for 193 returns from the brash ice. Both curves are normalized to O dB peak value.

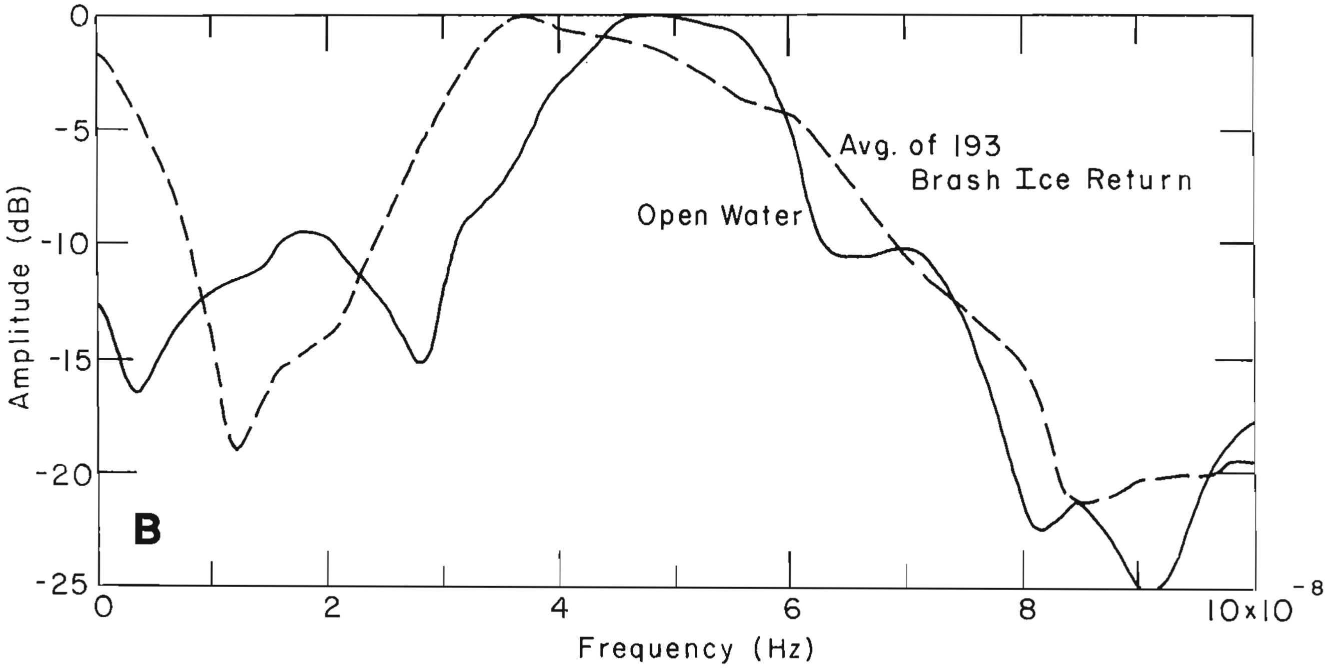

above a different section of ice. The time range gain function of the control unit was operated in an exponential mode such that exponentially increasing gain was applied over the first half of the scans. All brash ice reflection data were recorded over the second half of the scans where uniform gain was applied.

The transmitted pulse shape and its associated amplitude spectrum are shown in Figure 7. This pulse shape was obtained over open water. The spectrum reveals a 3 dB bandwidth extending from 400 to 500 MHz. Also shown is the average Fourier amplitude spectrum for 193 returns (each of which illuminated a statistically independent patch on the ice) over the brash ice, a few waveforms of which are shown in Figure 8. This comparison of transmitted and received Fourier spectra is discussed later.

Because the impulse radar waveform has a wide bandwidth, we followed a suggestion by Stanton to divide the Fourier transform amplitudes of the 193 returns into discrete frequency bins each of which was then compiled into histograms. After normalization, each histogram was fitted with the Rice PDF (Fig. 9) using the parameter values summarized in Table 1. Data at frequencies below 200 MHz are not considered reliable because the frequency content of the transmitted signal in that band is less than 10 dB of the flat portion of the transmitted power spectrum.

Table 1. Two parameters are used to fit the Rice PDF to the measured data. Gamma is described in the test. The second parameter, $< e^2 >$, is the mean of the distribution

FFT bin #	Frequency (GHz)	$< e^2 >$ ($*10^6$)	Gamma
2	0.07	7	3
3	0.13	1	5
4	0.20	2.25	2.25
5	0.27	7	1
6	0.33	36	1
7	0.40	42	0.3
8	0.46	45	0.0
9	0.53	45	0.0
10	0.60	25	0.0
11	0.66	9	1
12	0.73	4	1
13	0.80	3	1.7

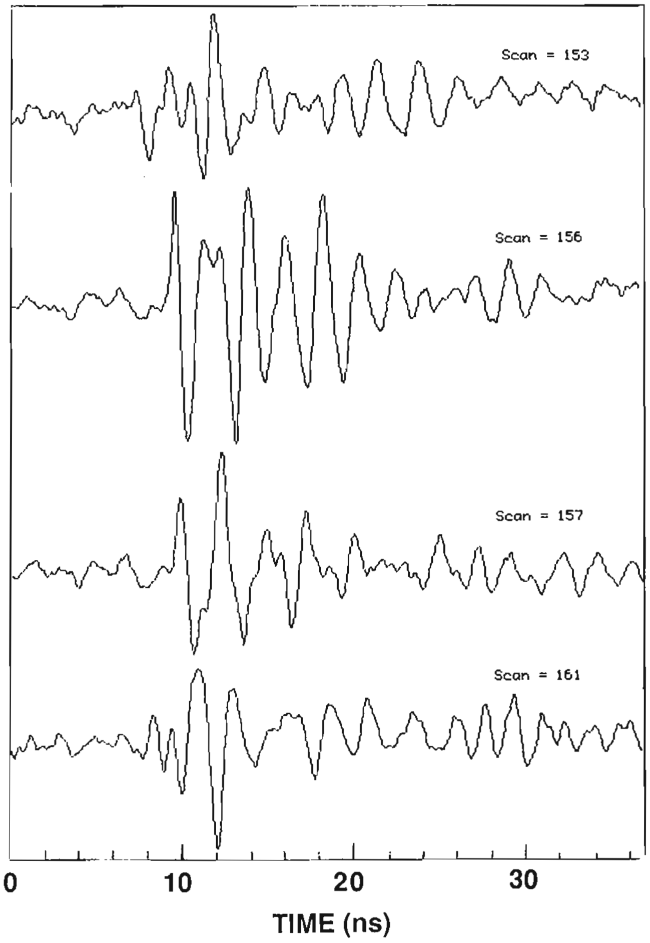

Figure 8. Selected waveforms of the brash ice returns.

The shapes of the PDFs between 200 and 600 MHz vary, as would be expected based on the previous discussion. The value of γ generally decreases as frequency increases. Because the curves change from Gaussian to Rayleigh distributions we can estimate the r.m.s. roughness by noting that when $\gamma > 1$ the coherent component dominates. By equations 1 and 3

$$< E >^2 = E^2_o \, e^{-4k^2\sigma^2}$$

Defining the transition frequency as occurring when

$$4k^2\sigma^2 \approx 1$$

we find that for 200 MHz

$$\sigma \cong 12 \text{ cm.}$$

We have no direct measure of this quantity, but judging from Figure 5 and the fact that the slabs, which ranged up to 8 cm thick, were generally at a slight tilt, $\sigma = 12$ cm is certainly a plausible estimate. Daly and Arcone (1989) arrive at an average freeboard height of 9.1 cm using direct reduction of radar echo delay times for this same data set.

Above 600 MHz the data behave in an unexpected fashion. The PDFs become more Gaussian, an observation for which we have no firm explanation. If the effect is real then we offer the following tentative suggestions. A first explanation is that the individual ice pieces are resonant somewhere above 600 MHz and that such resonance enhances the coherent addition of the backscattered energy. The most plausible resonant frequency must be that associated with a typical effective diameter; 15.5 cm. The equivalent frequency of a half wave dipole dielectric

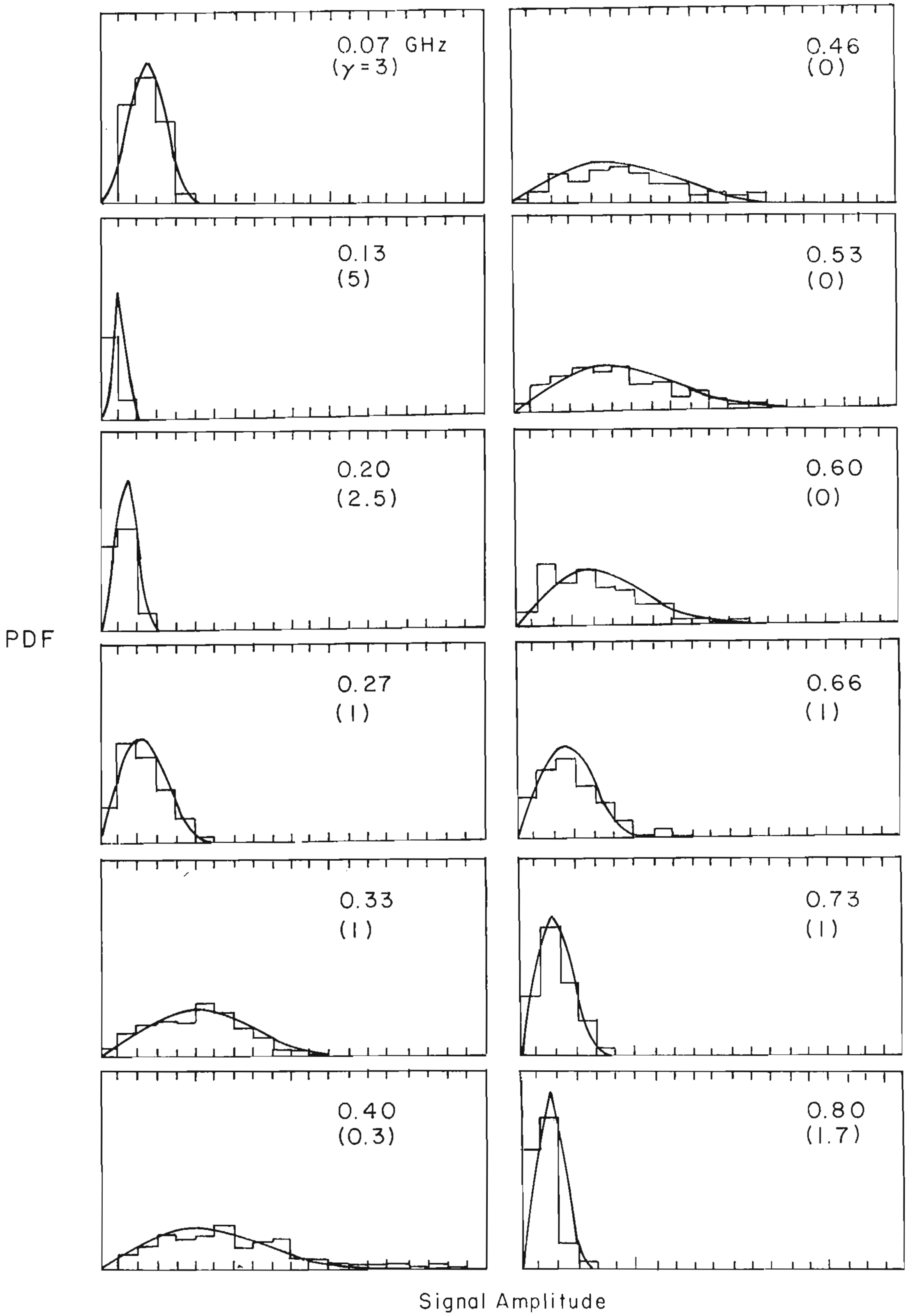

Figure 9. PDFs of echo amplitude for discrete frequencies recorded in pulses scattered from brash ice. The horizontal axis is a system measure of echo amplitude; the data have not been normalized to a reference surface. The vertical axis is in arbitrary units chosen such that the area under each curve is unity. The horizontal bars represent the form of the measured histograms; the solid curves are Rice PDF fits to the data selected by choosing the parameter gamma and the mean value of the curve.

(n = 1.79) disk is then 540 MHz, which is in the right frequency range. A second explanation is that the thickness of the ice slabs (which were predominantly horizontal; see Fig. 5) caused constructive interference and thus, reinforcement of the coherent energy backscattered from the main areas of the slabs. Slab thicknesses were typically 5-8 cm for which the corresponding range in resonant frequencies for constructive interference between top and bottom reflections is 530-840 MHz. Conceptually, we would then think of the ice covered channel behaving as a "shattered mirror" of finite thickness.

It is not likely that above 700 MHz we are looking at only noise statistics. The average Fourier amplitude spectrum of the 193 brash ice returns (given previously in Fig. 7 for comparison with the incident pulse spectrum) shows that the dominant frequency has shifted from the 470-500 MHz range down to 370 MHz and that all frequencies up to 800 MHz are within 15 dB of the peak. Typical peak reflection amplitudes were 2.9-9.4 dB less than that of the open water reference, which, in itself, represented a propagation loss of about 42 dB. Adding up all these values gives a total decrease at 800 MHz of less than 70 dB down from peak amplitude at 500 MHz, which is within the performance figure of the radar. The strong asymmetry of the brash ice spectrum (in that the power above 400 MHz does not decrease with increasing frequency as rapidly as it does with decreasing frequency below 350 MHz) also suggests relatively stronger backscatter occurring around 600-800 MHz.

CONCLUSIONS

The results presented here suggest that the approach developed by Stanton for analyzing acoustic echo data may have application for interpreting surface statistics from impulse radar data as well. We are encouraged by the fact that the measured PDFs can be fit with the Rice PDF and that using the scattering parameter γ, we can compute a reasonable surface roughness for brash ice. Many issues remain, especially issues relating to the signal and electronic noise components of the echo frequency spectrum, polarization effects and resonance phenomena.

REFERENCES

Arcone, S.A., Delaney, A.J., and Perham, R.
1986: Short-pulse radar investigations of freshwater ice sheets and brash ice; CRREL Report 86-6, U.S. Army Cold Regions Research and Engineering Laboratory, Hanover, NH.

Clay, C.S. and Leong, W.K.
1974: Acoustic estimates of topography and roughness spectrum on the sea floor southwest of the Iberian Penninsula; in Physics of Sound, ed. L. Hampton; Plenum Press, New York.

Clay, C.S. and Medwin, H.
1977: Acoustical Oceanography: Principles and Applications; Wiley Interscience; New York, ch. 10 and app. 10.

Daly, S.F. and Arcone, S.A.
1989: Airborne radar survey of a brash ice jam in the St. Clair River; CRREL Report 89-2, U.S. Army Cold Regions Research and Engineering Laboratory, Hanover, NH.

Eckart, C.
1953: The scattering of sound from the sea surface; Journal of the Acoustical Society of America, v. 25, p. 566-570.

Rice, S.O.
1954: Mathematical analysis of random noise; in Selected Papers on Noise and Stochastic Processes, ed. N. Wax; Dover Press, New York, p. 133-194.

Stanton, T.K.
1984: Sonar estimates of sea floor microroughness; Journal of the Acoustical Society of America, v. 75, p. 809-818.

Stanton, T.K., Jezek, K.C., and Gow, A.J.
1986: Acoustical reflection and scattering from the underside of laboratory grown sea ice: measurements and prediction; Journal of the Acoustical Society of America, v. 80, p. 1486-1494.

Estimating sea ice thickness from impulse radar sounding time of flight data

Austin Kovacs[1] and Rexford M. Morey[2]

Kovacs, A. and Morey, R.M., 1992: Estimating sea ice thickness from impulse radar sounding time of flight data; in Ground penetrating radar, ed. J. Pilon; Geological Survey of Canada, Paper 90-4, p. 117-124.

Abstract

Two floes of second year sea ice were probed using "impulse" radar sounding and direct drilling methods. The resulting two-way time of flight of the impulse radar electromagnetic wavelet, travelling from the surface to the ice "bottom" and back to the surface, was compared with snow and ice thickness data obtained from a drillhole. From this comparison, simple relationships are presented to estimate the thickness of sea ice, between about 1 to 8 m thick, with or without a snow cover. Relations are also presented that show the bulk or apparent dielectric constant of the ice floes versus ice thickness, again with or without the snow cover. The data revealed that the apparent dielectric constant of the sea ice decreased with increasing ice thickness from a value of about 7 for ice 1 m thick to about 3.5 for ice 6 m thick.

Résumé

Deux masses flottantes de glace de mer de deuxième année ont été sondées par radar à impulsion et forage direct. Le temps de parcoursdouble de l'ondelette électromagnétique produite par un radar à impulsion, se déplaçant de la surface vers le "fond" de la glace pour retourner à la surface, a été comparé aux données recueillies par forage sur l'épaisseur de la neige et de la glace. À partir de cette comparaison, des relations simples sont présentées pour déterminer l'épaisseur de la glace de mer, mesurant entre environ 1 et 8 m, qu'elle soit recouverte ou non de neige. Les relations entre la constante diélectrique apparente des masses de glace flottante et l'épaisseur de la glace recouverte ou non de neige sont également présentées. Les données ont révélé que la constante diélectrique apparente de la glace de mer diminue avec l'augmentation de l'épaisseur de la glace, passant d'une valeur d'environ 7 pour la glace de 1 m d'épaisseur à environ 3,5 pour la glace de 6 m d'épaisseur.

INTRODUCTION

The remote measurement of sea ice thickness using impulse radar has been actively pursued for some time. However, sea ice is a complex, lossy dielectric consisting of pure ice, liquid brine, and air; these properties vary with ice thickness, temperature, and time. Knowledge of the bulk dielectric constant (E) of sea ice therefore forms the basis for the measurement of its thickness because the velocity of the impulse radar electromagnetic (EM) wavelet in the ice is directly related to E.

If one knows the bulk dielectric constant of the sea ice (at the radar sounding frequency) then the velocity of the EM wavelet in the ice can be determined; and if the transit time of the wavelet from the surface to the ice bottom and back is measured by an impulse radar system, then the ice thickness can be estimated. Unfortunately, the dielectric constant of the sea ice is generally not known and some representative value is assumed, which can lead to a poor estimate of the EM wavelet velocity and therefore ice thickness determination.

---

[1] Department of the Army, Cold Regions Research and Engineering Laboratory, Corps of Engineers, 72 Lyme Road, Hanover, New Hampshire, U.S.A. 03755-1290

[2] Consultant, 17 Sunland Drive, Hudson, New Hampshire

In this report we present the results of more than 225 drillhole measurements to determine sea ice thickness and snow depth. These measurements were correlated with impulse radar sounding data to develop simple relations between the impulse radar EM wavelet two-way travel time and the snow plus sea ice thickness and the sea ice thickness.

FIELD MEASUREMENTS

Two floes of second year sea ice were studied to determine their snow and ice thickness variation and the two-way time of flight of an impulse radar EM wavelet travelling from the surface to the ice bottom and back to the surface. The measurements included impulse radar profiles made on the surface and from a helicopter. A Geophysical Survey

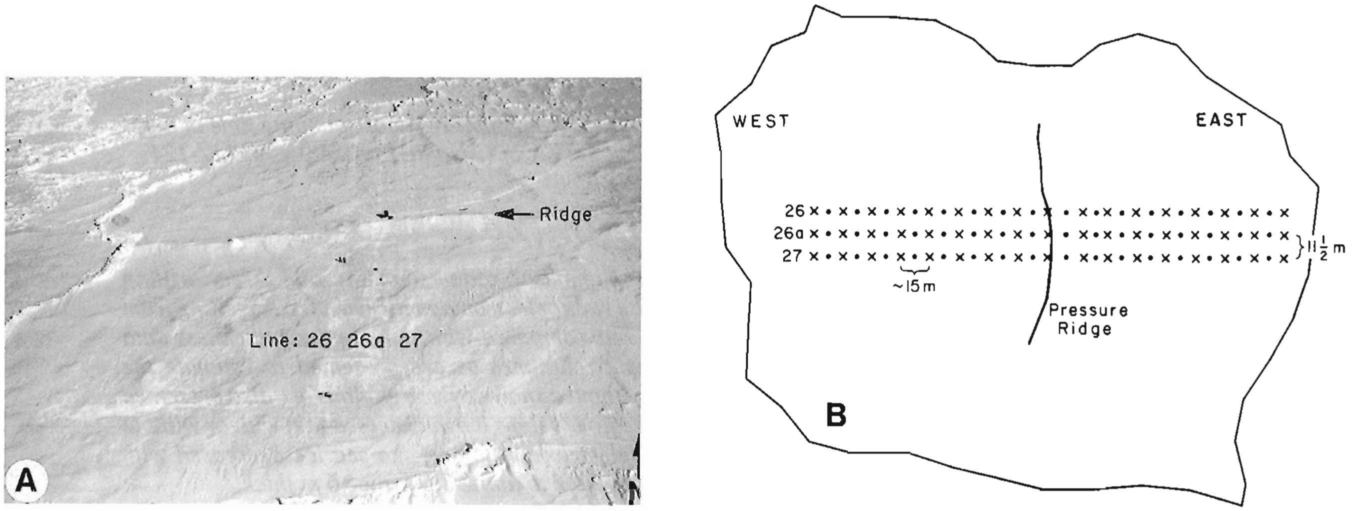

Figure 1A. Aerial view of ice floe studied in 1985; **B.** and the survey tracks along which radar sounding were made in 1985.

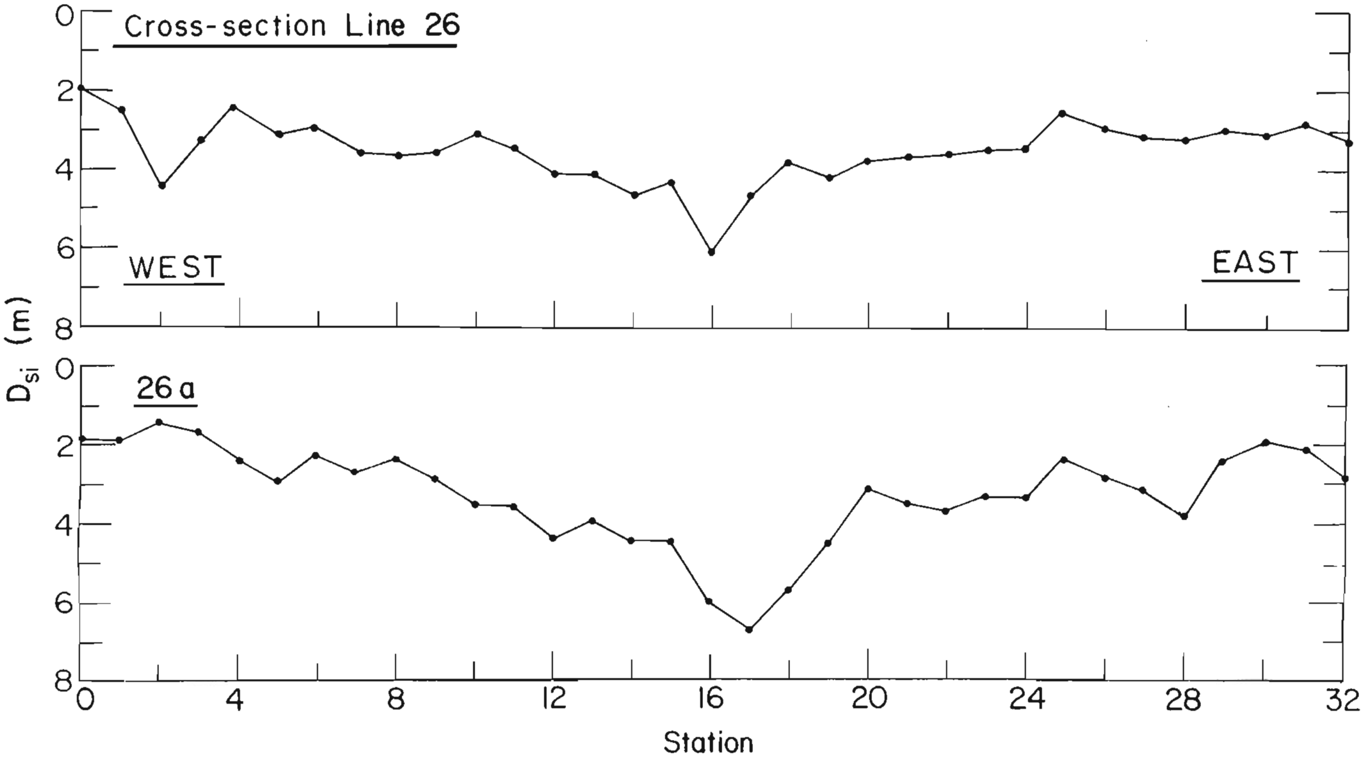

Figure 2. Radar sounding profiles taken in 1985 with the 80 MHz antenna along lines 26 (top) and 26a (bottom).

Systems, Inc., impulse radar system was used. On one sea ice floe the company's designated 80 MHz antenna was used, and on the second floe their designated 120 MHz antenna was used. The actual free-space centre frequencies of the broadband wavelet spectra transmitted by these antennas are about 50% higher than their designated values; but they decrease as a result of antenna loading effects associated with antenna-surface coupling. Because ice and snow surface conditions varied across the floes, the centre frequency of the wavelet spectra also varied. This variation was not determined. Therefore, in this report, sounding results are referenced to the manufacturers designated antenna frequency.

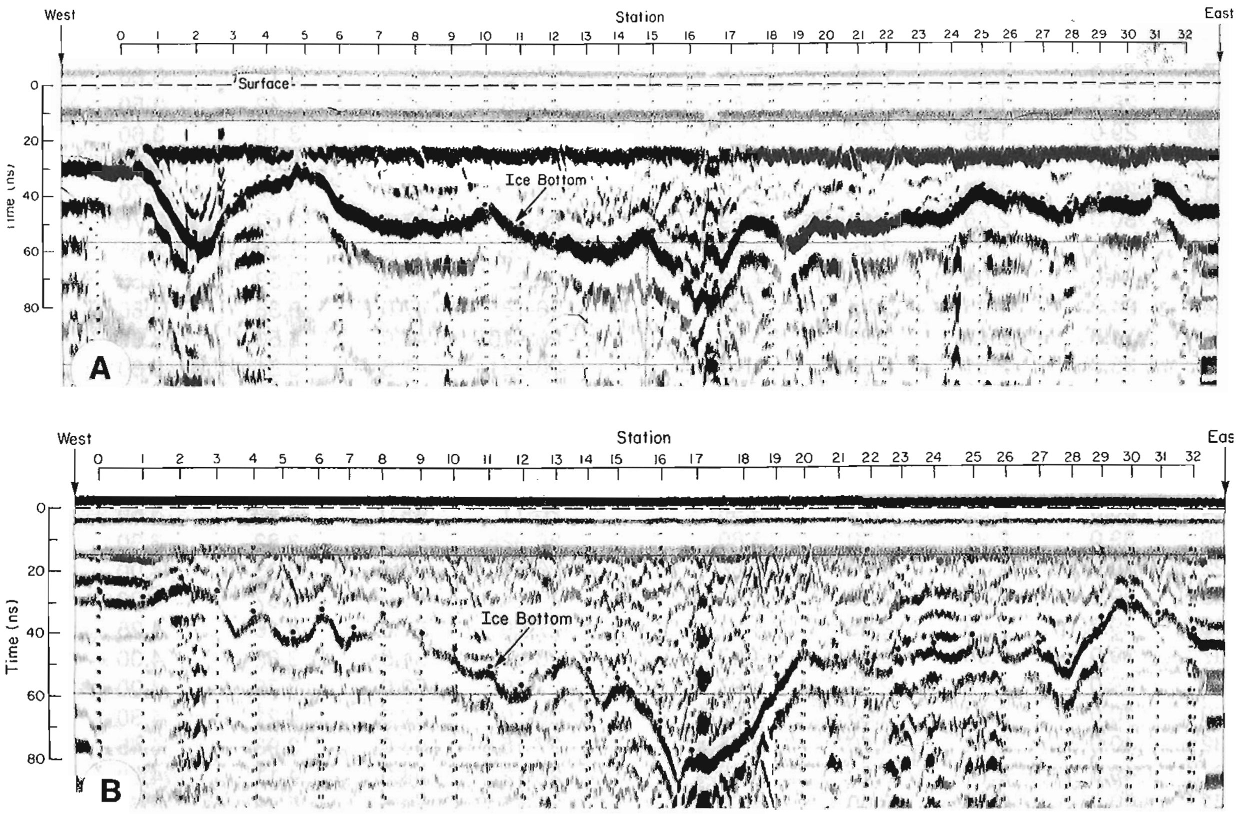

Figure 3. Snow and ice thickness, D_{si}, **A.** line tracks 26 and **B.** line 26a profiled in 1985 with the 80 MHz antenna.

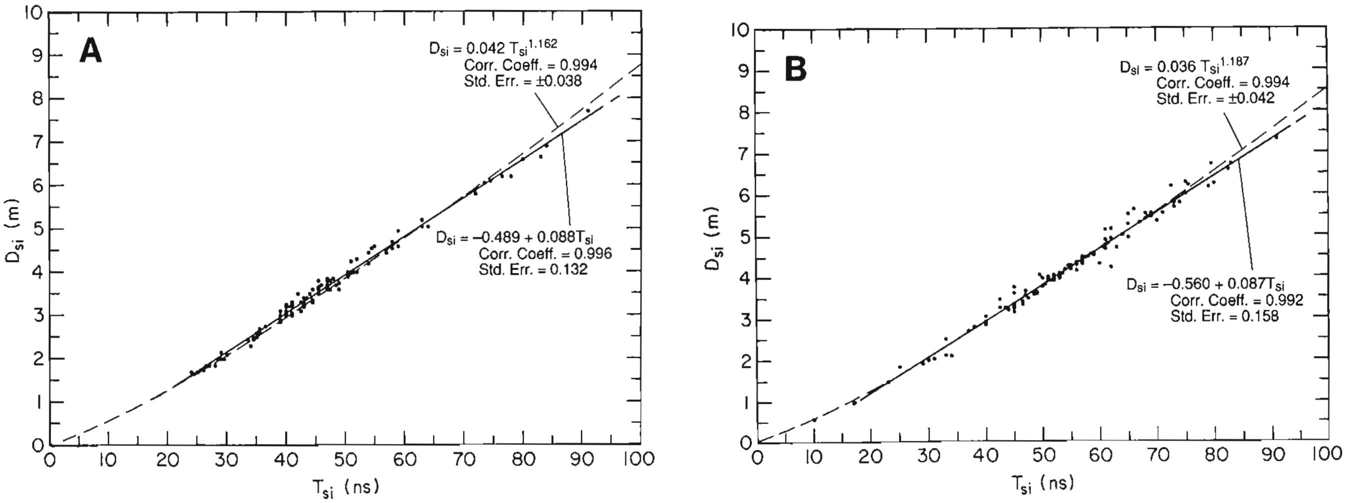

Figure 4. Snow and ice thickness, D_{si}, versus two-way EM wavelet flight time, T_{si}, in snow and ice for **A.** 1985 data obtained with the 80 MHz antenna; **B.** 1987 data obtained with the 120 MHz antenna.

Table 1. Radar and thickness information from the 80-MHz antenna for the ice floe studies in 1985

Sta. no.	Time in S&I (ns)	Ice thick (m)	S&I thick (m)	S&I App. diel. cosnt., E_{asi}	Sta. no.	Time in S&I (ns)	Ice thick (m)	S&I thick (m)	S&I App. diel. const., E_{asi}
27-2	25.0	1.60	1.70	4.87	26-a26	44.5	3.25	3.30	4.09
27-3	26.0	1.70	1.75	4.97	27-0	44.5	3.40	3.60	3.44
27-4	26.5	1.75	1.85	4.62	27-30	45.5	3.41	3.50	3.80
26-a3	27.0	1.58	1.85	4.79	27-11	45.5	3.57	3.65	3.50
26-a0	28.0	1.78	1.85	5.15	27-28	45.5	3.71	3.80	3.23
26-0	28.5	1.91	2.00	4.57	27-26	45.5	3.42	3.50	3.80
26-a30	29.0	1.95	2.00	4.73	26-a23	45.5	3.13	3.60	3.59
27-7	29.0	1.97	2.15	4.09	26-22	46.0	3.63	3.70	3.48
26-a1	29.5	1.88	2.00	4.90	26-7	47.0	3.52	3.70	3.63
26-5	30.0	2.06	2.10	4.59	26-21	47.0	3.62	3.70	3.63
26-4	33.5	2.27	2.45	4.21	27-20	47.0	3.30	3.85	3.35
26-a31	34.0	2.06	2.30	4.92	26-9	47.0	3.58	3.65	3.73
26-a4	34.5	2.25	2.45	4.46	26-18	47.0	3.38	3.80	3.44
26-a6	34.5	2.12	2.50	4.28	26-a10	47.0	3.50	3.60	3.84
26-a8	35.0	2.31	2.50	4.41	26-a21	47.5	3.51	3.60	3.92
26-25	35.0	2.34	2.60	4.08	26-20	47.5	3.77	3.80	3.52
26-a29	35.5	2.43	2.65	4.04	27-21	48.0	3.79	3.85	3.50
26-1	35.5	2.50	2.60	4.19	26-8	48.5	3.63	3.70	3.87
27-25	35.5	2.31	2.70	3.89	26-a22	49.0	3.67	3.75	3.84
27-24	36.5	2.55	2.75	3.96	26-11	49.0	3.40	3.60	4.17
26-26	39.0	2.94	3.00	3.80	26-a28	50.5	3.82	3.90	3.77
27-22	39.0	2.76	3.10	3.56	26-a13	50.5	3.93	4.00	3.59
26-a32	39.0	2.81	2.90	4.07	27-14	51.0	3.87	4.00	3.66
27-13	39.0	2.73	2.85	4.21	27-29	51.0	4.16	4.25	3.24
26-a7	39.0	2.50	2.90	4.07	26-a11	51.5	3.62	4.00	3.73
26-31	39.0	2.79	2.90	4.07	27-19	52.0	3.76	4.00	3.80
26-29	40.0	2.94	3.05	3.87	26-19	52.0	4.21	4.30	3.29
27-32	40.0	2.72	3.10	3.75	27-15.5	54.0	3.93	4.45	3.31
26-6	40.0	2.71	3.10	3.75	26-12	54.0	4.11	4.20	3.72
27-31	40.0	2.85	3.00	4.00	26-15	54.5	4.12	4.55	3.23
26-30	40.0	3.07	3.25	3.41	26-a14	55.0	4.32	4.60	3.22
27-27	40.0	2.77	3.20	3.52	26-a12	57.0	4.37	4.45	3.69
26-a25	40.5	2.71	3.20	3.60	26-14	58.0	4.64	4.70	3.43
26-a9	41.0	2.75	3.00	4.20	26-a15	58.0	4.20	4.70	3.43
27-10	41.0	3.14	3.20	3.69	26-2	58.0	4.43	4.55	3.66
26-27	41.0	3.13	3.25	3.58	26-17	59.0	4.55	4.95	3.20
26-a5	41.0	2.97	3.05	4.07	26-a19	59.0	4.51	4.60	3.70
26-32	41.0	3.23	3.30	3.47	26-a14.5	63.0	4.80	5.20	3.30
26-3	42.0	3.02	3.50	3.24	27-18	63.0	4.84	5.05	3.50
27-12	42.5	2.97	3.10	4.23	26-a15.5	64.0	4.59	5.05	3.61
27-9	42.5	3.23	3.30	3.73	26-a18	72.0	5.59	5.80	3.47
27-23	43.0	3.19	3.30	3.82	26-a16	73.5	5.95	6.05	3.32
26-28	43.0	3.18	3.25	3.94	26-16	74.5	6.06	6.10	3.36
26-10	43.0	2.98	3.20	4.06	27-17	76.5	5.99	6.20	3.43
26-a27	43.0	3.07	3.30	3.82	27-17.5	78.0	6.05	6.20	3.56
26-a24	43.0	2.99	3.40	3.60	26-a17.5	80.0	6.29	6.60	3.31
27-8	43.5	3.30	3.40	3.68	27-16.5	83.0	6.35	6.65	3.51
26-24	44.0	3.41	3.50	3.56	26-a17	84.0	6.61	6.90	3.33
26-23	44.0	3.45	3.50	3.56	26-a16.5	91.0	7.65	7.70	3.14
26-a20	44.5	3.07	3.35	3.97					

Table 2. Radar and thickness information from the 120-MHz antenna for the ice floe studies in 1987

Sta. no.	Time in S&I (ns)	Ice thick. (m)	S&I thick. (m)	App. diel. const. I, E_{asl}	App. diel. const. I, E_{ai}	Sta. no.	Time in S&I (ns)	Ice thick. (m)	S&I thick. (m)	App. diel. const. S&I, E_{asl}	App. diel. const. I, E_{ai}
lead	10.0	0.55	0.55	7.44	7.44	E-32	55.0	4.01	4.20	3.86	4.23
lead	17.0	0.95	0.95	7.20	7.20	C-25	55.0	4.12	4.27	3.73	4.01
lead	23.0	1.45	1.45	5.66	5.66	E-38	55.0	4.19	4.22	3.82	3.88
C-47	25.0	1.60	1.82	4.24	5.49	E-33	55.0	4.21	4.28	3.85	3.84
C-59	29.0	1.75	1.90	5.24	6.18	G-11	55.0	4.16	4.25	3.77	3.93
C-60	30.0	1.78	1.98	5.16	6.39	E-30	56.0	4.07	4.15	4.10	4.26
I-22	31.0	2.01	2.02	5.30	5.35	I-39	56.0	4.27	4.35	3.73	3.87
I-23	33.0	2.06	2.11	5.50	5.77	I-31	56.0	4.03	4.29	3.83	4.34
C-46	33.0	2.20	2.50	3.92	5.06	C-21	57.0	4.29	4.31	3.94	3.97
I-24	34.0	2.05	2.09	5.96	6.19	C-33	57.0	4.30	4.35	3.73	3.95
C-64	37.0	2.46	2.70	4.22	5.09	E-23	57.0	4.26	4.42	3.74	4.03
C-52	38.0	2.75	2.80	4.14	4.30	E-21	57.0	4.30	4.32	3.92	3.95
G-11	40.0	2.45	3.05	3.87	6.00	C-22	57.0	4.29	4.48	3.71	3.97
C-54	40.0	2.60	2.85	4.43	5.32	C-20	57.5	4.30	4.46	3.74	4.02
G-20	40.0	2.90	2.92	4.22	4.28	G-35	58.0	4.42	4.49	3.75	3.87
C-63	40.0	2.83	2.85	4.43	4.50	I-38	58.5	4.48	4.55	3.72	3.84
C-50	42.5	3.10	3.26	3.82	4.23	I-35	59.0	4.55	4.57	3.75	3.78
C-49	42.5	3.23	3.46	3.40	3.90	I-13	59.0	4.50	4.52	3.83	3.87
C-44	43.5	3.16	3.26	4.00	4.26	I-17	60.0	4.11	4.31	4.36	4.80
C-57	44.0	3.18	3.20	4.25	4.31	C-34	60.5	4.68	4.71	3.71	3.76
C-55	45.0	3.22	3.25	4.31	4.39	E-22	61.0	4.66	4.67	3.84	3.86
G-25	45.0	3.05	3.15	4.10	4.90	C-37	61.0	4.70	4.76	3.70	3.79
C-45	45.0	3.30	3.33	4.39	4.18	C-38	61.0	4.97	5.13	3.18	3.39
E-25	45.0	3.62	3.76	3.22	3.48	C-24	61.0	4.70	4.88	3.57	3.79
C-53	45.0	3.31	3.34	4.08	4.16	C-10	61.0	4.63	4.76	3.70	3.91
E-29	45.0	3.57	3.61	3.50	3.58	I-40	61.5	4.78	4.80	3.69	3.72
C-56	46.5	3.35	3.40	4.21	4.34	C-40	62.0	4.90	4.92	3.57	3.60
C-65	46.5	3.27	3.33	4.39	4.55	G-39	62.0	5.06	5.15	3.26	3.38
C-43	47.0	3.51	3.56	3.92	4.03	E-38	62.0	4.19	4.22	4.86	4.93
G-33	47.0	3.35	3.55	3.94	4.43	G-38	63.0	4.68	4.70	4.04	4.08
I-18	47.0	3.50	3.66	3.71	4.06	C-19	64.0	4.98	5.00	3.69	3.72
G-26	47.5	3.35	3.48	4.19	4.52	I-36	64.0	4.94	5.01	3.67	3.78
G-21	48.5	3.46	3.58	4.13	4.42	C-9	65.0	5.06	5.26	3.44	3.71
E-26	49.0	3.51	3.59	4.19	4.38	C-4	65.0	5.05	5.50	3.14	3.72
E-19	49.0	3.37	3.63	4.10	4.76	I-41	65.0	4.91	4.94	3.90	3.94
I-12	49.5	3.70	4.05	3.36	4.03	E-40	66.0	5.60	5.62	3.10	3.12
G-17	50.0	3.55	3.78	3.94	4.46	C-7	67.0	5.08	5.30	3.60	3.91
G-18	50.0	3.75	3.77	3.96	4.00	C-18	68.0	5.49	5.52	3.41	3.45
G-19	50.0	3.95	3.97	3.57	3.60	I-37	68.0	5.37	5.39	3.58	3.61
E-27	50.5	3.79	3.82	3.93	4.00	C-23	68.5	5.44	5.44	3.57	3.57
I-31	51.0	3.76	4.00	3.66	4.14	C-17	69.0	5.41	5.44	3.62	3.66
G-34	51.0	3.88	3.92	3.81	3.89	C-15	69.0	5.32	5.51	3.53	3.78
C-31	51.5	3.85	3.91	3.90	4.03	C-16	69.0	5.51	5.52	3.52	3.53
C-28	52.0	3.83	4.04	3.73	4.15	C-8	69.0	5.44	5.46	3.59	3.62
E-24	52.0	3.82	3.93	3.94	4.17	G-41	70.0	5.30	5.33	3.88	3.92
G-20	52.0	3.90	3.92	3.96	4.00	C-6	71.0	5.50	5.53	3.71	3.75
G-28	52.0	3.89	3.91	3.98	4.02	C-11	72.5	6.16	6.18	3.10	3.12
C-30	52.0	3.93	3.95	4.05	3.94	C-14	73.0	5.66	5.67	3.73	3.74
I-32	52.0	3.97	4.00	3.96	3.86	E-36	73.0	5.75	5.78	3.59	3.63
E-20	52.0	3.89	3.92	3.96	4.02	G-12	74.0	5.76	5.77	3.70	3.71
C-29	53.0	3.93	3.97	4.01	4.09	C-1	75.0	6.19	6.27	3.22	3.30
C-27	53.0	3.83	3.98	3.84	4.31	C-35	75.0	5.96	5.99	3.34	3.56
C-26	53.0	3.90	4.03	3.96	4.16	C-36	75.5	6.15	6.20	3.34	3.39
C-42	53.0	4.07	4.09	3.78	3.82	C-13	79.0	6.15	6.16	3.70	3.71
C-41	53.5	4.04	4.08	3.87	3.95	E-11	79.5	6.64	6.71	3.16	3.22
C-32	54.0	3.93	4.18	3.76	4.25	C-39	80.0	6.22	6.24	3.70	3.72
E-18	54.5	4.17	4.27	3.66	3.84	E-13	82.5	6.44	6.58	3.54	3.69
E-31	55.0	3.69	4.18	3.90	5.00	C-12	83.0	6.52	6.72	3.43	3.65
						E-12	91.0	7.15	7.32	3.48	3.64

The first ice floe, located north of Prudhoe Bay, Alaska, was studied during the first week of May 1985, when air temperatures were between 15 and 20°C. On this floe, three parallel lines, about 240 m long and 11.5 m apart, were established. Along each line, radar sounding profiles and tape measured snow, D_s, and ice, D_i, thicknesses were made. The center of the lines crossed over a small pressure ridge (Fig. 1A). Ice thickness was determined by use of an electric drill powering a 5 cm diameter continuous-auger flight system. With a generator, this system, with ten 1 m long stainless steel auger flights, weighed about 60 kg. On average, ice was drilled at about 70 m/h. This time included drilling, tape measurement of ice thickness, and relocation of equipment to the next drill site. These sites were spaced about 7.5 m apart along each of the three lines (Fig. 1B).

The second ice floe was studied in late April 1987, when air temperatures were also between 15 and 20°C. This floe was located northwest of Prudhoe Bay. On this floe, radar sounding and snow and ice thickness measurements were made at random locations. Ice thickness measurements were made using a tape lowered through holes bored in the ice by a hotwater drilling system. This system weighed about 240 kg and consisted of a small oil-fired boiler, a high-pressure pump, a generator, and a hose reel with 60 m of hose. The drill probe consisted of a hollow, 1 m long, 2.5 cm diameter brass rod with a tapered end. Water exited at the probe tip through a hole about 63 mm in diameter. Heated sea water was used as the drilling fluid. With 55 m of hose resting on the ice, the temperature of the water at the probe tip was about 45°C. In a 4 h period, with air temperatures at 18°C, the hotwater drill we used melted holes through ice having an average thickness of 4.9 m at an average rate of 1.75 m/min. This rate included the short time required to move the hose and probe from one site to the next and to measure the snow and ice thickness. Each site was 5 m from the previous one. As with the mechanical auger flight system, the hotwater drilling was a two person operation.

RESULTS

In 1985, radar profiles along each of the three lines shown in Figure 1 were made by dragging the 80 MHz antenna on the surface. The graphic records of the two-way EM wavelet travel times obtained along lines 26 and 26a are presented in Figure 2. Only one voltage polarity was printed to highlight the reflection from the ice bottom and to aid in picking the two-way time of travel, T_{si}, of the transmitted EM wavelet from the antenna on the surface, through the snow, to the bottom of the ice, and then back to the antenna. Because the antenna was pulled along the surface, the travel time includes the wavelet propagation time through the snowcover, where it existed, as well as in the ice. Cross-sections of the snow and ice thickness measured along lines 26 and 26a are presented in Figure 3. Figures 2 and 3 reveal similar profile variations.

The EM wavelet travel time (ns) in the snow and ice (S&I) at each station is listed, in ascending order, in Table 1. Also listed are the ice and the snow plus ice thicknesses (m), and the calculated apparent dielectric constants for the combined snow plus ice thickness, E_{asi}, at each station. E_{asi} was

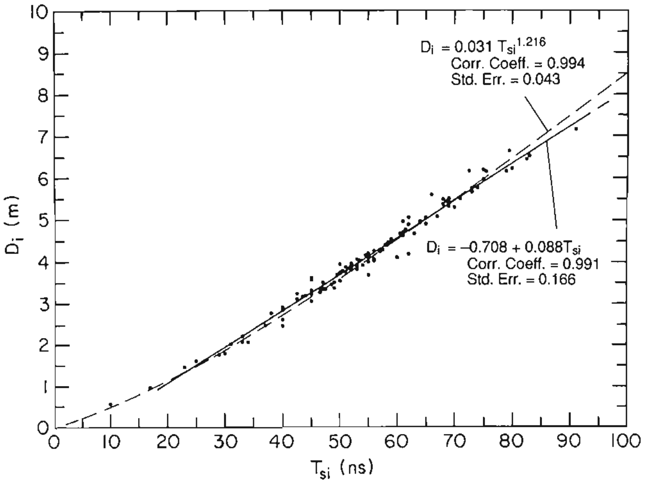

Figure 5. Ice thickness, D_i, versus two-way EM wavelet flight time, T_{si}, in snow and ice for 1987 data obtained with the 120 MHz antenna.

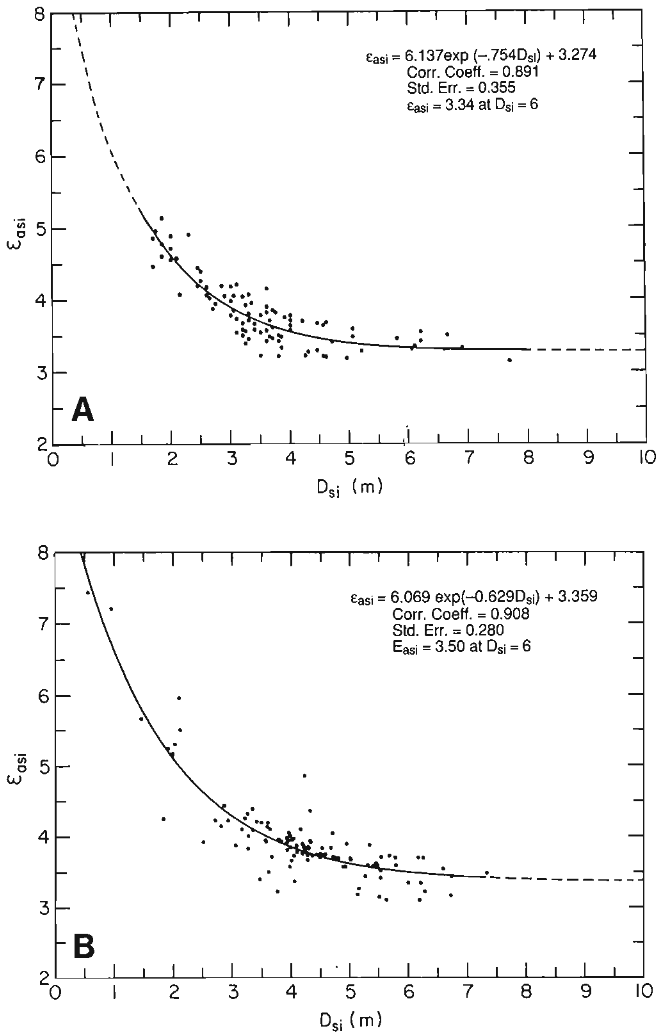

Figure 6. Apparent dielectric constant of snow and ice, E_{asi}, versus snow and ice thickness, D_{si}, for **A.** the 1985 data obtained with the 80 MHz antenna; **B.** the 1987 data obtained with the 120 MHz antenna.

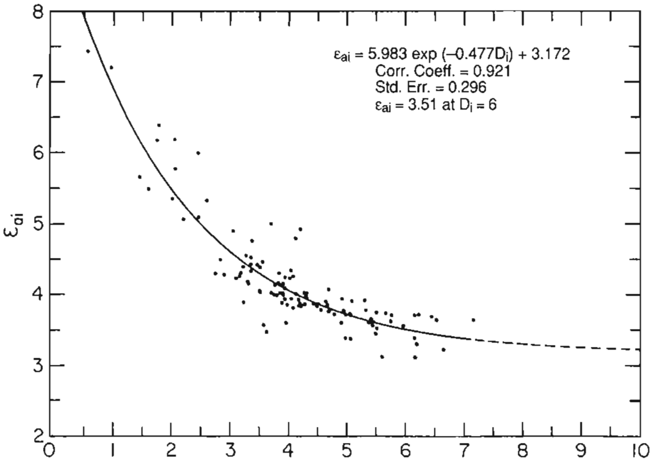

Figure 7. Relative apparent dielectric constant for ice, E_{ai}, versus ice thickness, D_i, for 1987 data obtained with the 120 MHz antenna.

determined from $E_{asi} = (T_{si}\ '\ C/2\ D_{si})^2$, where $C = 0.3$ m/ns and D_{si} is the snow-ice thickness. E_{asi} represents a bulk electrical property that controls the effective speed at which the EM wavelet travels in the medium.

A similar presentation of the data collected in 1987 with the 120-MHz antenna is given in Table 2. The ice thickness at each station is also listed in Table 2 along with the relative apparent dielectric constant of the ice, E_{ai}, as determined by $E_{ai} = (T_{si}\ '\ C/2\ D_i)^2$.

In most ground based or airborne radar sounding surveys of sea ice thickness, the goal is to estimate the ice thickness from the EM wavelet two-way travel times. The snow cover is generally not of interest but is frequently present on winter ice. To aid in the above goal, plots of D_{si} versus T_{si} are shown in Figure 4 for the 1985 and 1987 data, respectively. There may be a slight bias in the data of less than 1 ns. This bias would be caused by system timing inaccuracies. Another reason for a time bias is that the EM wavelet was not reflected from the ice-water boundary, the tape measured interface depth, but from a moist zone interface about 5 cm above the ice bottom (Kovacs et al., 1987). Linear and power regression curves were fitted to the data. Both curves have nearly identical correlation coefficients. The power curve is more realistic because it shows that the time is zero when the thickness is zero. Also, the linear curve indicates that the ratio D_{si}/T_{si} is a constant, which implies that the bulk dielectric constant, E_{asi}, is a constant independent of sea ice thickness. Younger, thinner sea ice has a higher dielectric constant, E_{ai}, than older, thicker sea ice because there is proportionately more brine versus depth in thinner sea ice, which retards EM wavelet propagation (Kovacs et al,. 1987). Therefore, D_{si}/T_{si} cannot be a constant. However, the reason for including the straight line curves is that they represent simple equations for estimating the thickness of winter sea ice from the measured EM wavelet two-way travel time in ice between about 1 and 8 m thick. In addition, use of the linear curves provides thinner and therefore more conservative estimates for ice between about 1 and 2 m thick, a range of practical concern for certain over-ice travel.

The slope of the linear regression line passing through the data in figures 4 and 5 is the same, but there is a slight vertical offset. Statistically this offset is not significant, because the line for one data set falls well within the standard deviation of the other. Nevertheless, the offset is related to differences in snow cover thickness (averaging 20 cm in 1985 versus 11 cm in 1987) and, to a lesser extent, to antenna frequency and timing variations between antennas and to ice floe property variations.

For the situation where only sea ice thickness is desired, we stripped out the snow thickness and provide the relation between D_i and T_{si} for the 1987 data (Fig. 5). This relation may be useful for estimating the relative thickness of cold winter sea ice between about 1 and 8 m thick.

Plots of E_{asi} as a function of D_{si} for the 1985 and 1987 data are given in Figure 6. A similar plot of E_{ai} versus D_i for the 1987 data is shown in Figure 7. These plots clearly show that E_{asi} and E_{ai} increase rapidly with decreasing ice thickness. This result is expected because the brine content is higher in the thinner ice; it is this conductive liquid fraction that greatly affects the electromagnetic properties of sea ice (Kovacs et al., 1987). As sea ice grows thicker and ages, more brine drains out of the ice. The result is that the bulk dielectric constant of the thicker ice seems to reach a relative constant value, as can be inferred from the data in Figure 6. This trend is in agreement with the model results of Kovacs et al. (1987).

Our attempt to profile the snow-ice thickness from the air at the 1985 field site was not successful. An attempt by Exxon Corporation to profile the same floe, using a radar system developed for them by Cambridge Consultants, Ltd., Cambridge, England, was also not successful (G.F. Gehrig, Exxon, personal communication). We believe the ice was too lossy to allow the 80 MHz antenna's transmitted EM wavelet to penetrate, to and be reflected from, the bottom of this type of sea ice. This was so even when the helicopter-mounted antenna was flown as low as 5 m above the surface. No airborne radar profiling was undertaken during the 1987 field study.

DISCUSSION

The data presented here allowed us to develop relationships for estimating snow plus sea ice thickness and ice thickness from just the measured two-way time of flight of an EM wavelet, in about the 100 to 200 MHz frequency band, travelling from the surface to the ice bottom and back to the surface. Knowledge of the bulk dielectric constant or the EM wavelet velocity in the snow and ice is not needed. The simple linear relationships seem to be good for ice thickness from about 1-8 m. Another relationship presented is that found between E_{ai} and D_i. This relation shows that thin winter sea ice has a higher E_{ai} than thick ice. This result is reasonable because the dielectric constant of pure ice, at the frequencies of interest, is about 3.15, but for sea ice the bulk dielectric constant is higher (because of its brine content) and varies with brine volume. However, as sea ice grows thicker or ages there is less brine in the ice because of brine drainage processes. This drainage freshens the ice, which reduces its bulk dielectric constant.

ACKNOWLEDGMENTS

Funding for this study was provided by the U.S. Department of Navy, Naval Ocean Research and Development Activity, under contract no. N6845286MP6003, program element 63704. The field assistance of R. Roberts of USACRREL and the helpful review comments by Drs. S.R. Dallimore and H.V. Rees are also acknowledged and appreciated.

REFERENCES

Kovacs, A., Morey, R.M., and Cox, G.F.N.
1987: Modeling the electromagnetic property trends in sea ice, Part I; Cold Regions Science and Technology, v. 14, p. 207-235.

An expert system for automated interpretation of ground penetrating radar data

S. Lee[1], E. Milios[2], R. Greiner[2], and J. Rossiter[3]

Lee, S., Milios, E., Greiner, R., and Rossiter, J., 1992: An expert system for automated interpretation of ground penetrating radar data; in *Ground penetrating radar, ed. J. Pilon; Geological Survey of Canada, Paper 90-4, p. 125-131.*

Abstract

One of the major limitations to the use of impulse radar for many applications is the requirement of expert personnel to satisfactorily interpret the data. Although numerical processing, such as stacking, deconvolution, and filtering, can be helpful, the results usually still require expert assessment before they can be used. We have developed a preliminary automated system for interpreting airborne inpulse radar signals for ice thickness profiling.

We have adopted an integrated approach that includes numeric computation in the form of deconvolution filtering with rule-based classification of signal features at multiple levels. Noise reduction and deconvolution techniques are used to enhance the radar signals for better resolution of overlapping events. Motivated by human perceptual (visual) knowledge, a hierarchy of data structures is constructed as representations of signal characteristics at various levels of abstraction. Classification rules, based on the protocols collected from an expert, physical constraints on the helicopter motion and the nature of the radar signals are used to produce the current signal interpretation. A prototype system has been implemented on the Symbolics Lisp Machine and tested on real data.

Résumé

L'une des principales limites à l'utilisation du radar à impulsion dans de nombreuses applications est la nécessité de recourir à un personnel spécialisé capable d'interpréter de façon satisfaisante les données. Même si le traitement numérique, comme la sommation, la déconvolution et le filtrage, peut être utile, les résultats doivent néanmoins être évalués par un expert avant d'être utilisés. Un système automatisé préliminaire a été conçu pour interpréter les signaux d'un radar à impulsion aéroporté et produire des profils d'épaisseur de la glace.

Une approche intégrée faisant appel au calcul numérique sous la forme d'un filtrage de déconvolution ayant recours à une classification à base de règles des formes de signaux à des niveaux multiples a été adoptée. Les techniques de réduction du bruit et de déconvolution servent à améliorer les signaux radar et ainsi obtenir une meilleure résolution des événements chevauchants. En se fondant sur les connaissances de la perception humaine (visuelle), on a construit une hiérarchie des structures de données pour représenter les caractéristiques des signaux à différents niveaux d'abstraction. Les règles de classification, basées sur les protocoles établis par un expert, les contraintes physiques sur le déplacement de l'hélicoptère et la nature des signaux radar sont utilisés pour interpréter les signaux. Un système prototype a été appliqué à la Symbolics Lisp Machine et mis à l'essai sur des données réelles.

---

[1] Dept. of Elec. Eng., University of Toronto, Ont., Canada M5S 1A4 (currently with SPAR Aerospace Ltd.)

[2] Dept. of Computer Science, University of Toronto, Ont., Canada M5S 1A4

[3] Canpolar Inc., 265 Rimrock Road, Unity, Toronto, Ont., Canada M3J 3C6

INTRODUCTION

Measuring the thickness of river or sea ice over large distances is important in polar regions for the study of ice dynamics, the tactical planning of transportation routes, and the location of underice oil entrapment for Arctic petroleum exploration. Because of the enormous size of the ice cover over water, traditional methods for surface measurement have gradually given way to impulse radar sounding from the air using either helicopters or small fixed wing aircraft. Ice thickness can be calculated from radar impulse travel time between top and bottom reflections, given the speed of radar signal through the ice. In practice, each radar return signal is put side by side to form a signal image, which is then analyzed for an interpretation of the ice thickness distribution, types, and other structural information. The performance objective is to correctly recognize scenes that can be reliably determined from visual interpretation of the data by the human expert.

Among numerous ways of remotely determining the properties of floating ice, radar sounding appears to have better potential to give a continuous profile of ice thickness along a given track for relatively nonsaline ice types. Impulse radar (Rossiter, 1980) differs from more conventional types of subsurface radar in that instead of transmitting many cycles of a particular frequency, a broadband monocycle pulse is transmitted. The advantage of impulse radar is that relatively low frequencies can be used, giving the ability of penetrating lossy materials, while retaining adequate time resolution for accurate depth estimates. The main disadvantage is that it is not possible to focus the antenna radiation pattern, which is similar to that of a half-wave dipole. Therefore, to achieve reasonable spatial resolution and to receive a strong enough return signal, measurements must be made on or near the surface.

The method is based upon the physical principle that, when an electromagnetic wave is incident upon an interface where a change in electrical properties occurs, a reflection occurs.In the impulse radar system under discussion, an extremely short electromagnetic pulse is generated by the radar device mounted under a low flying helicopter, and is radiated downwards towards the ice. Primary reflections or echoes from the top and bottom of the ice are received. The time separation between the top and bottom echoes represents the travel time from the top ice surface to the bottom interface and back. Once the speed of propagation within the ice is known, either from a knowledge of the electrical properties (speed $= \frac{c}{\sqrt{\varepsilon}}$, where ε is the ice dielectric constant) or from direct mechanical calibration by measurement of ice thickness, then the travel time can be converted directly to ice thickness. The subsurface is assumed to be consistent, homogeneous, and isotropic, and parallel layers and secondary reflections are negligible.

A signal image, $I[i,j]$, is formed by putting consecutive traces side by side ($I[i, j] \triangle y_i[j]$). In the signal image, the x-axis represents horizontal displacement, the y-axis represents vertical depth from the impulse radar, while intensity values are proportional to the strength of return radar echoes. Such an image can be interpreted as depicting the ice layer's substructure along a vertical cross-sectional plane. Each trace $y_i[n]$ (i is the trace index and n represents depth) will consist of an ice surface reflection followed by an ice-bottom reflection for the case of ice, or just an air-water reflection from open water where there is no ice.

SYSTEM OVERVIEW

We break down the interpretation task into three steps as follows: image processing to enhance the radar image for visual clarity; construction of a hierarchy of signal abstractions corresponding to the signal structures the

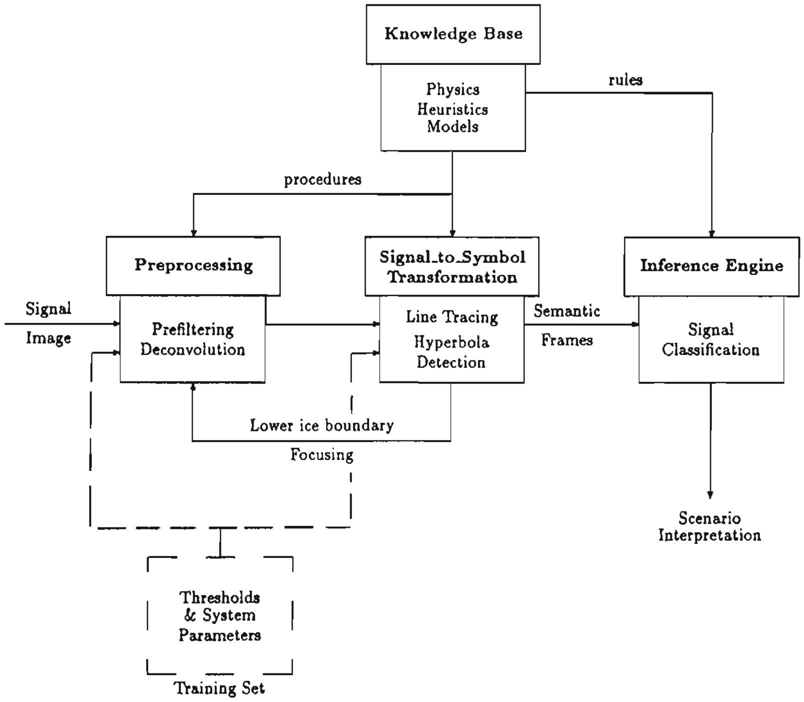

Figure 1.

Overall system architecture.

human expert visually concentrates on; and interpretation using classification rules. The overall architecture of the impulse radar signal interpretation system is shown in Figure 1.

PREPROCESSING AND DECONVOLUTION

Several radar traces are stacked (averaged) to reduce jitter noise, and the amount of subsequent processing is also alleviated. A Gaussian kernel $N(0,\sigma)$, defined as $\text{Gauss}_{N(0,\sigma)}(i,j) = \frac{1}{2\pi\sigma^2}\exp(-\frac{i^2+j^2}{2\sigma^2})$, is convolved with the signal image to smooth out sharp changes. It is a two dimensional, low pass, filtering operation.

The probing waveform of our impulse radar system is not a true impulse, but a wavelet (triplet) of very short duration. The echoes from various (lossy) interfaces will appear as time-shifted and distorted versions of this probing wavelet. Visual identification of these interface boundaries is particularly difficult when distances between interfaces are small, causing wavelets from different interfaces to merge together. The idea of deconvolution is to remove the effect of the probing wavelet by collapsing each "replica" of the probing wavelet to an impulse at the appropriate position and with the appropriate amplitude and phase. The resulting simplified waveform will then be a sequence of impulses where various reflecting interfaces can be identified more easily. In ice thickness profiling applications, the signal at the receiver at a particular position can be represented as

$$y(n) = x(n) * h(n) + u(n) \tag{1}$$

where $u(n)$ is the measurement noise, $x(n)$ is a sequence associated with the basic signature wavelet, and $h(n)$ is the reflection coefficient sequence corresponding to various "stratigraphic" events.

To implement deconvolution, an average wavelet selected from a region of strong reflections, such as those obtained from open water, was taken as the signature wavelet.

Based on preliminary analyses and experimental testing of several simple deconvolution filters, Riad compensator (Riad, 1980), defined in equation 2, is best suited to our problem with its flexibility and low computational cost:

$$H(\Omega) = \frac{Y(\Omega)}{X(\Omega)} \cdot \frac{1}{1+\frac{\alpha}{X(\Omega)^2}} \tag{2}$$

The filter parameter α is usually optimized using heuristic criteria.

SIGNAL ABSTRACTION

Using perceptual (visual) knowledge, a hierarchy of data structures is constructed as representating signal characteristics at various levels of abstraction (Chandrasekaran, 1986; Milios and Nawab, 1989). Instead of doing the classification by a one-step (direct), discriminant, function-like mapping, intermediate symbols are constructed, which are then used as attributes to a higher level classification process. Symbols at each level are produced by a classification process using the symbols from the previous level as attributes. Each such computational process is much more tractable. We define five levels of abstraction (Fig. 2), based on protocols collected from an expert.

The base level or level 0 abstraction is simply the deconvolved image itself, which is a two dimensional array of intensity values (with position on the x-axis, depth on the y-axis, and intensity on the z-axis). We will regard the image as a collection of POINTs. The level 1 abstraction consists of peaks of each trace (i.e., a slice of the deconvolved image for a specific x). Peaks in the deconvolved image correspond to radar reflections caused by layer interfaces in the real world. Peaks of a radar trace correspond to local maxima, therefore they are located at zero crossings of the first difference of the trace. We define a PEAK to denote a local maximum and its associated features.

At each trace, peaks that are potential reflection interfaces must be chosen. The essential attributes that characterize a peak are strength, the normalized intensity of the peak, and symmetry, the symmetry of the peak shape. Histogram statistics of the strength and symmetry attributes of peaks selected from a region of open water

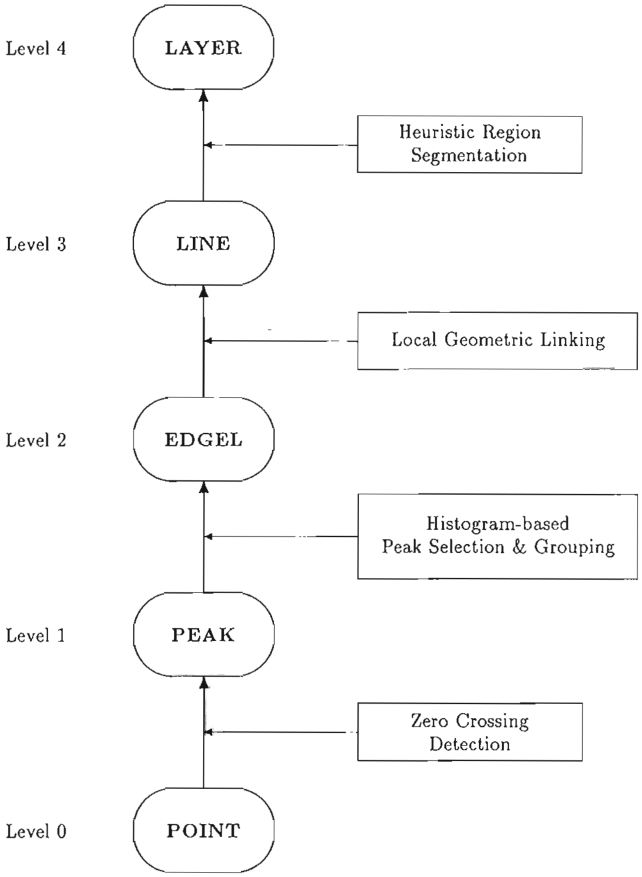

Figure 2 The five levels of signal abstraction associated with the signal image, together with the grouping operations for computing them.

have been used to guide the separation of those candidate peaks from noise peaks. Open water region statistics were used because the deconvolution signature wavelet was derived from such region and such statistics are reliable and easy to interpret. Guided by these histograms, strong and symmetrical peaks are selected as candidate peaks for interfaces.

The level 2 abstraction is aimed to create more global structures based on contextual information. A sequence of neighbouring peaks with similar characteristics are linked together. Sequences of peaks are referred to as EDGELs. Similarity requirements for peak linking are simple but very conservative. Only peaks in the immediate neighbourhood are considered. Edgels are incrementally built from peaks. A peak is joined to an edgel if the following two conditions are satisfied: (1) small pixel distance between two candidate peaks; and (2) similar peak intensity values. The resulting edgels are the "islands of reliability".

The basic edge elements, serving as seeds for region growing, are then extended at level 3 abstraction to fill small gaps to form LINEs. Each line is a list of edgels and artificial joints (connecting two adjacent edgels). The local geometrical constraints for forming lines from edgels (McKeown and Pane, 1985), based on visual grouping criteria, include the following: similar edgel average intensity, close physical proximity, tolerance for overlap, similar orientations, and smooth connection.

The highest level or level 4 abstraction is a LAYER, which is essentially an interval together with its constituent lines. The top reflecting line from the top of the ice is strong and consistent, so that the problem is to identify the bottom boundary lines for various ice floes. Picking the longest and strongest line below the top line as the bottom-boundary line is the heuristic used to partition lines into layers. These high level symbolic structures, layers, constitute the data base on which our rule-based deduction system makes inferences.

RULE-BASED CLASSIFICATION

Complex symbolic structures built up from the lower levels are fed into a rule based interpreter, which is a form of production rule system (Charniak and McDermott, 1985). Domain knowledge for characterizing and classifying ice is derived from the domain expert and is encoded in typical IF-THEN rules to run in the forward chaining mode. Figure 3 shows a glossary for ice interpretation. Rule examples are shown in Figure 4; the symbol x denotes a variable.

IMPLEMENTATION AND RESULTS

The system was tested with several data sets from two different field trips. Figure 5 shows the results of the program on a data set containing mainly open water with some damp

Term	Meaning	Sketch
Floe	Large ice piece	
Rubble	Small ice piece	
Thick/Thin/Very-thin	Ice thickness classification	
Damp/Lossy	Undetectable ice bottom at melting/sub-zero temperatures	
Open water	Strong and clear reflection attributed to water region	
Smooth/Rough bottom	Bottom roughness classification	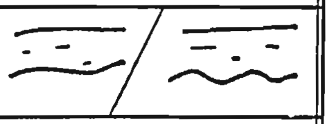
Sharp features at bottom	Hyperbola(e) detected at ice bottom	

Figure 3. Glossary for ice interpretation.

ice. The program identified the different vertical layers and characterized them as shown.Detailed data sets and results can be found in (Lee et al., 1989).

The system was implemented in Lisp on a Symbolics Lisp machine. The signal processing portion was built using two software packages: SPLICE (formerly KBSP), a signal processing environment suitable for one dimensional signal processing (Dove et al., 1984; Myers, 1986), and ImageCalc, a two dimensional, image processing package (Quam, 1984). Signal abstraction was implemented using the Flavors object oriented facility of Lisp. The rule based classification was carried out in MRS (Russell, 1985), a logic programming environment with a meta-level facility for controlling the inference strategy. As mentioned previously, we used a forward-chaining strategy.

```
IF              $x is an interval
       AND
                $x does not have a detectable
                bottom boundary
       AND
                $x does not have scattered
                bottom reflection
THEN            $x is WATER
IF              $x is an interval
       AND
                it cannot be proved that
                $x is water
THEN            $x is ICE
IF              $x is ice
       AND      $x has a detectable bottom
                boundary
THEN            $x is ICE-LAYER
IF              $x is ice
       AND
                $x does not have a detectable
                bottom boundary
THEN            $x is VERY-DAMP
IF              $x is ice-layer
       AND
                length of $x is greater than
                a length-threshold
THEN            $x is FLOE
IF              $x is ice-layer
       AND
                bottom undulation of $x is greater than
                a roughness-threshold
THEN            $x has a ROUGH bottom
IF              $x is ice-layer
       AND
                thickness of $x is greater than
                a thickness-threshold
THEN            $x is THICK
IF              $x is ice-layer
       AND
                $x has hyperbolae detected in its
                bottom boundary
THEN            $x has some SHARP-POINTED features
                in its bottom
```

Figure 4. A subset of the IF-THEN rules associated with the ice classes of Figure 3. $x denotes a variable bound to a vertical layer.

DISCUSSION

In this paper we described an effort to automate the visual interpretation of impulse radar data obtained for the purpose of measuring the thickness and properties of lake and river ice. Our approach includes three major components as follows:

– signal processing to enhance the signal image and transform it to a simpler form that facilitates subsequent automatic interpretation.

– representation of the signal data at multiple levels of abstraction, defined to reflect the signal aspects that are deemed important for interpretation by the expert. Computation of such representation involves classification and grouping at successive levels, following the paradigm presented by Milios and Nawab (1989).

```
Region at (interval 0 51) is 63.75 m long
Interpretation: Very thin and damp floe, with 0.28 m in
  thickness and smooth ice bottom.
There are also some sharp features at the bottom.

Region at (interval 52 61) is 11.25 m long
Interpretation: Open water.

Region at (interval 62 83) is 26.25 m long
Interpretation: Very thin and damp floe, with 0.32 m in
  thickness and smooth ice bottom.

Region at (interval 84 96) is 15.0 m long
Interpretation: Open water.

Region at (interval 97 126) is 36.25 m long
Interpretation: Thin floe, with 0.41 m in thickness and
  smooth ice bottom.

Region at (interval 127 226) is 123.75 m long
Interpretation: Open water.

Region at (interval 227 248) is 26.25 m long
Interpretation: Very thin and damp floe, with 0.34 m in
  thickness and smooth ice bottom.

Region at (interval 249 255) is 7.5 m long
Interpretation: Open water.
```

Figure 5. Results on a data set containing mainly open water with some damp ice. "Region at (interval i j)" indicates a vertical layer between traces i and j. Knowledge of parameters of the impulse radar system allows us to convert the difference i - j into horizontal distance in metres, giving the width of the vertical layer found, and vertical travel time into ice thickness and depth. Below each such vertical layer specification the pseudo-english interpretation that the system generated is provided.

- rule based classification to assign semantic meaning to entities at the highest level of abstraction, namely vertical layers corresponding to physical regions with uniform ice properties.

We worked closely in cooperation with our expert (J. Rossiter), who participated in the project in several ways. The original design of the system was motivated by the analysis of protocols collected, while the expert was analyzing data sets new to him. During the development of the system the expert helped decide on the appropriate setting of the thresholds necessary for classification. Thresholds at the peak level were set by a formal histogramming technique, whereas thresholds for the classification of layers were set based on consideration of the physics and the geometry of the impulse radar process. The expert's final contribution was to provide a fairly varied collection of data sets that allowed extensive testing of the system and to evaluate the results.

The good aspects of our approach are the following:

- We produced an integrated system that starts with raw signals and produces semantic intepretations.
- By using the notion of signal abstraction, we had explicit representation of the signal entities relevant to the interpretation.
- As a result, the expert could understand the operation of the system and how it reached its conclusions.
- Our prototype system constitutes a feasibility demonstration of the approach in a specific application.

During the development of our system, we encountered the following difficulties:

- Success of the deconvolution process depends on accurate knowledge of the wavelet. Because the wavelet is subject to distortions during propagation, using its mathematical form obtained from the physics of the impulse radar was not considered appropriate by the expert. Instead, the wavelet was determined experimentally from open water regions. Although the deconvolved signal was much better for intepretation than the original, it did contain phantom layers that had to be removed by an ad hoc method, exploiting the fact that their location was predictable.
- Setting the thresholds associated with the classification at all levels using histogramming requires ground verification, which is not easy to obtain with certainty. Our threshold setting was a result of a mixture of experimentation, histogramming, and the use of physical arguments.
- Our system is a bottom-up system and employs neither feedback from the interpretation back to the signal processing, nor the computation of signal abstractions. Our original intention was to study feedback issues, but just building the bottom-up system proved to be a fairly challenging task.
- Linking up peaks into edges is fairly simplistic in our system. To compensate for the naivity of our method, we were conservative and chose to stick to the principle of least commitment, to avoid having to backtrack. Researchers in the geophysical data interpretation area have recently come up with more sophisticated line tracing methods, which are worth considering in future systems (Cheng and Lu, 1988) and which might enable us to go directly from peaks to lines, without the intermediate edge level.

Ground verification of the available data sets is an important issue. In this study we relied solely on the expert's experience for ground verification, which was sufficient for the scope of a feasibility study. For the development of an operational system, more accurate (and more expensive) methods of verifying data on the ground are necessary, such as correlating impulse radar data with aerial photographs, synthetic aperture radar data, and surface measurements.

In summary, the contribution of this work is in demonstrating on real data a framework for computationally extracting the appropriate signal features from the numeric signal and relating them to signal interpretations. The framework is modular from a software engineering viewpoint and is designed so that its components are reusable in implementing extensions, such as feedback.

More work is needed before we can claim that we have a system that is comparable to the expert in terms of performance. Issues that remain are the use of feedback, to improve the performance of the signal processing part of the system, and the tracing and characterizing of more complicated entities in the signal image, such as hyperbolic echoes. Feedback should be extended to include an interface with the impulse radar instrument itself, allowing the interpreting system to adjust the instrument's setting to improve the quality of the received data.

ACKNOWLEDGMENTS

The first author was supported through an NSERC postgraduate scholarship. The second and third authors and the computing facilities used in this research were supported by an NSERC strategic grant to the Department of Computer Science, University of Toronto. The impulse radar data was kindly provided by the Alberta Remote Sensing Centre (86-0830).

REFERENCES

Chandrasekaran, B.
1986: From numbers to symbols to knowledge structures: Pattern recognition and artificial intelligence perspectives on the classification task; in E.S. Gelsema and L.N. Kanal, ed. Pattern Recognition in Practice II, Elsevier Science Publishers, North Holland, p. 547-559.

Charniak, E. and McDermott, D.
1985: Introduction to Artificial Intelligence. Addison-Wesley Publishing Co., Inc., Reading, Massachusetts, 701 p.

Cheng, Y. and Lu, S.Y.
1988: The binary consistency checking scheme and its applications to seismic horizon detection; in Proceedings, IEEE Computer Society Conference on Computer Vision and Pattern Recognition, v. 11, no. 4, p. 463-468.

Dove, W., Myers, C., and Milios, E.
1984: An object-oriented signal processing environment: The knowledge-based signal processing package; Technical Report 502, Research Laboratory of Electronics, MIT.

Russell, S.
1985: The complete guide to MRS. Technical Report KSL-85-12, Stanford University, 80 p.

Lee, R., Milios, E., Greiner, R., Rossiter, J., and Venetsanopoulos, A.
1989: On the machine analysis of radar signals for ice profiling; Signal Processing, December 1989, p. 371-386.

McKeown, D.M. and Pane, J.F.
1985: Alignment and connection of fragmented linear features in aerial imagery; in Proceedings, IEEE Computer Society Conference on Computer Vision and Pattern Recognition, San Francisco, CA, p. 55-61.

Milios, E. and Nawab, H.
1989: Signal abstractions in signal processing software; IEEE Transactions on Acoustics, Speech and Signal Processing, v. 37, no. 6, p. 913-928.

Myers, Cory
1986: Numeric and symbolic representation and manipulation of signals; PhD thesis, MIT, 234 p.

Quam, Lynn
1984: The image calc vision system intruction manual. SRI International, 80 p.

Riad, S.M.
1980: Optical fiber impulse response evaluation using frequency domain optimal compensation deconvolution; in Proceedings, FOC '80, International Fiber Optic and Communication Exposition (San Francisco, CA), p. 210-213.

Rossiter, J.R.
1980: Review of impulse radar sounding of sea ice; in Proceedings, International Workshop on the Remote Estimation of Sea Ice Thickness, St. John's, September 25-26, 1979, C-CORE, 1980, p. 77-107.

Application of ground penetrating radar to a study of peat stratigraphy: preliminary results

D.C. Nobes[1] and B.G. Warner[2]

Nobes, D.C. and Warner, B.G., 1992: Application of ground penetrating radar to a study of peat stratigraphy: preliminary results; in Ground penetrating radar, ed. J. Pilon; Geological Survey of Canada, Paper 90-4, p. 133-138.

Abstract

Previous studies on the utility of ground penetrating radar (GPR) for peat inventories have met with mixed results. In our current study of the correlation of stratigraphy and physical properties of peat with the GPR response, the first site selected was Ellice Swamp, near Stratford, Ontario. A suite of 17 cores were obtained at a spacing of about 100 m. Each core was analyzed for stratigraphy, wet bulk density, water content, organic matter content, and humification at 10 cm intervals. Cross-sections compiled for each of these parameters were compared with the GPR profile. The GPR data were taken at 1 m intervals across the same transect in Ellice Swamp. Preliminary processing of the GPR data reveal some important insights on the utility of GPR in peatland inventories. The base of the peat yields a strong, clear reflection event. The character of the event is simpler where limnic peat and gyttja are lacking above the basal silty clay. Where limnic peat and gyttja are present, the event is more complex. The surface aerobic zone has a number of small events that are obscured in some places by the multiples from the thin snow and ice cover. The GPR response shows a marked transition between the surface aerobic and the underlying anaerobic zones. The anaerobic peat layers contain relatively few internal reflectors and appear to be relatively homogeneous and transparent to GPR.

Résumé

Les études antérieures portant sur l'utilité du géoradar pour inventorier les tourbières ont donné des résultats partagés. Dans la présente étude de la corrélation de la stratigraphie et des propriétés physiques de la tourbe avec la réponse du géoradar, le premier endroit choisi a été le marécage Ellice, près de Stratford (Ontario). On a prélevé une série de 17 carottes selon un espacement d'environ 100 m. Dans chaque carotte, on a analysé la stratigraphie, la masse volumique apparente humide, la teneur en eau, la teneur en matières organiques et l'humidification à des intervalles de 10 cm. Les coupes compilées pour chacun de ces paramètres ont été comparées au profil établi par géoradar. Les données géoradar ont été recueillies à des intervalles de 1 m le long du même transect traversant le marécage Ellice. Le traitement préliminaire des données géoradar donnent quelques indices importants sur l'utilité du géoradar pour inventorier les tourbières. La base de la tourbe produit une réflexion forte et nette. Cette réflexion est plus simple lorsque l'argile silteuse basale n'est pas recouverte de tourbe lacustre ni de gyttja. Lorsque la tourbe lacustre et le gyttja sont présents, l'événement est plus complexe. La zone aérobie en surface donne un certain nombre de petits événements qui sont obscurcis par endroits par les multiples que produit une mince couche de neige et de glace. La réponse du géoradar indique une transition marquée entre les zones aérobies superficielles et anaérobies souterraines. Les couches de tourbe anaérobies contiennent relativement peu de réflecteurs internes et elles semblent être relativement homogènes et transparentes aux signaux émis par le géoradar.

---

[1] Department of Geology, University of Canterbury, Private Bag 4800, Christchurch, New Zealand. Formerly at the Department of Earth Sciences, University of Waterloo, Waterloo, Ont.

2 Department of Geography and Quaternary Science Institute, University of Waterloo, Waterloo, Ontario N2L 3G1

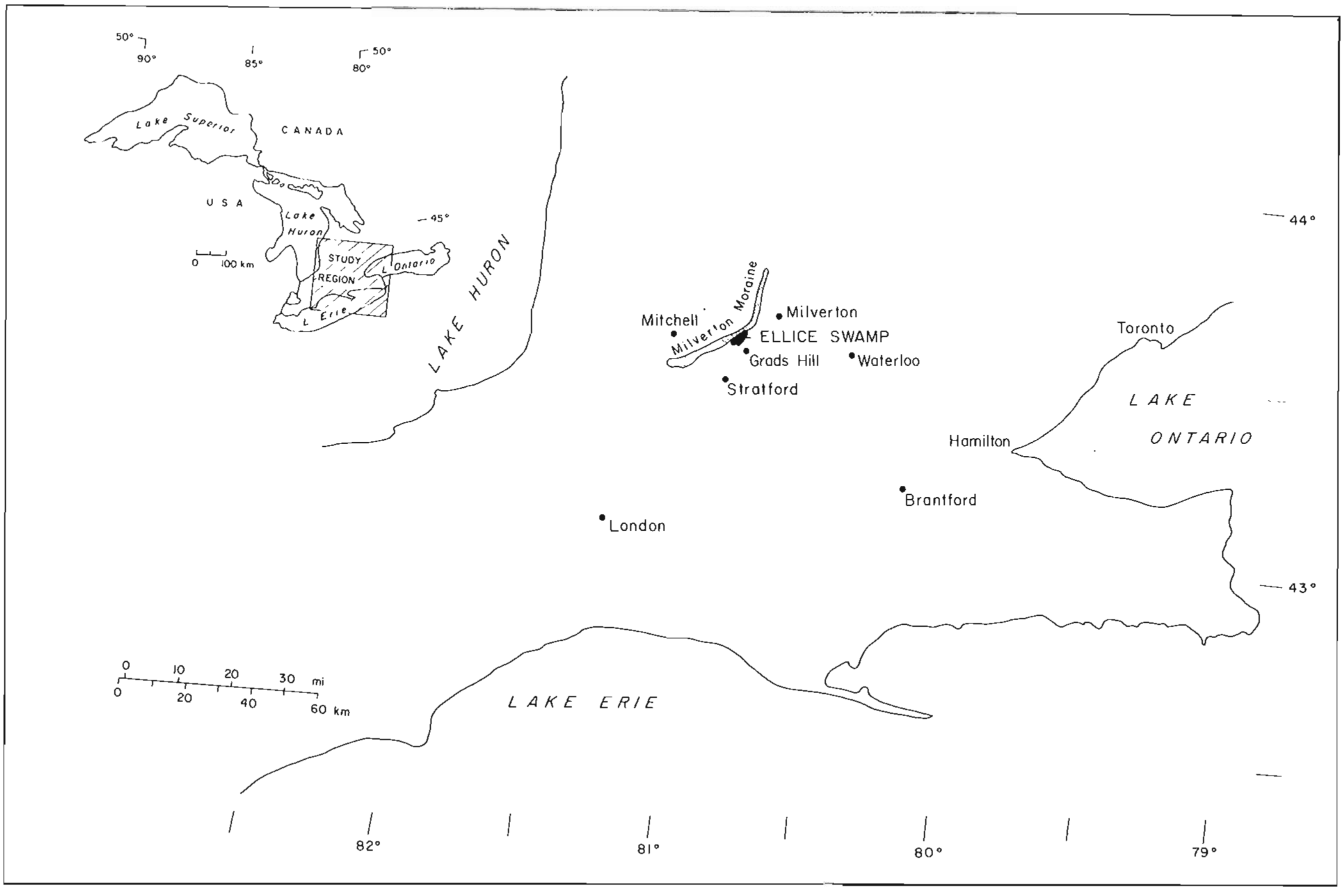

Figure 1. Location of Ellice Swamp, near Stratford, Ontario.

Figure 2. Aerial photograph of Ellice Swamp. The position of the cutline used for the core and GPR profiles is marked (arrows).

INTRODUCTION

Peatlands, common in northern latitudes, constitute a potentially important economic resource. Canada has the second largest peat reserves in the world (Zoltai and Pollett, 1983). Ontario alone ranks third, with an estimated 26 million hectares of peatlands (Korpijaakko, 1981). Peat inventories are normally conducted by extensive mapping and coring programs that are time consuming. A simple and relatively fast method for mapping peat stratigraphy and estimating peat volumes would aid in peat inventories. We have begun a systematic study to test the utility of ground penetrating radar (GPR) in mapping the areal and stratigraphic extent of peatlands, with the goal of establishing GPR as a simple and effective tool for peat inventories.

Previous studies on the correlation of the GPR response and the peat physical properties have been inconclusive. Some studies found a strong correlation between the permittivity (the dielectric coefficient) and the volume and energy content of the peat (Tolonen et al., 1982; Tiuri et al., 1983, 1984). On the other hand, Ulriksen (1982) found no correlation between the permittivity and the energy content. All researchers noted a correlation with bulk density, which is strongly dependent on the water content. Because GPR responds to changes in the permittivity, then the peat properties could, in principle, be mapped using GPR.

The purpose of our study was to conduct an intensive field program to compare the GPR response with the results of detailed physical analyses of peat cores. Work on the raw GPR field data study is not yet complete, but preliminary results are most encouraging. The GPR section accurately reflects peat stratigraphy, in particular the transition from the surface aerobic to the underlying anaerobic zone; also the basal peat-mineral transition is readily apparent. Further analysis is required, and this work will be extended to other sites and peatland types in the future.

SITE DESCRIPTION AND STUDY METHODOLOGY

The first site selected for the study was Ellice Swamp, near Stratford in southern Ontario (Fig. 1). The bog has developed on the eastern flank of Milverton Moraine (Karrow, 1971). Shortly after deglaciation, drainage was impeded, which led to local ponding during which lacustrine silts and clay were deposited. Silty gyttja, gyttja, and limnic peat represent open-water deposits prior to onset of peatland development. Moss peat with abundant *Scorpidium scorpioides* and sedge remains form the main body of the peat. Overlying this peat, a distinct near surface layer is represented by a well decomposed, amorphous, black detrital peat with abundant wood. Finally, modern *Sphagnum* peat forms a thin layer about 30-50 cm thick at the surface with black spruce and tamarack cover.

The bog is situated on a height of land between the north branches of the Thames and Nith Rivers. Black Creek flows through the bog and drains northward to Nith River. Two artificial drainage ditches form the present western and eastern boundaries of the bog. The vegetation of the modern bog reflects disturbance by artificial drainage, frequent fires, peat mining activities, recreational sports trails, and red pine plantations. A Canadian National Rail line runs northwards through the bog.

The core and GPR profiles were taken along a cutline running northwest through Ellice Swamp (Fig. 2). The GPR profiles were obtained using the A-Cubed (now Sensors and Software) pulseEKKO III with a nominal signal frequency of 100 kHz. Cores were taken at 100 m intervals; additional cores were taken concurrently with the GPR profile. The stratigraphy of each of the 17 peat cores was recorded. Subsamples, taken every 10 cm along each core were analyzed for wet bulk density, water content, degree of humification, and organic matter content. Cross-sections were compiled for each physical parameter.

The GPR data were gathered at 1 m intervals across the bog, using a common offset technique. The GPR transmitter and receiver antennae were maintained at a constant separation of 40 cm, as the system was stepped across the bog. To date, preliminary filtering of the raw radar records has removed some of the response caused by the snow and ice that covered the bog at the time of the GPR survey. The 20-30 cm thick ice layer caused the GPR signal to reflect numerous times within the ice layer, giving rise to a number of multiples. These multiples appear as banded "events" across the GPR section, which at times obscure the reflected arrivals from the peat. An overall GPR section was constructed by averaging five GPR records to yield an average record every 5 m for the length of the bog. The net presentation thus consists of almost 300 records, rather than almost 1500 raw GPR records. This leads to some loss of detail, but the noise is reduced by averaging adjacent records.

RESULTS AND DISCUSSION

The cross-sections for water content, humification, organic matter content, and wet bulk density are shown in Figures 3A-D. Some correlation exists between the individual parameters, especially humification and organic matter content, and bulk density and stratigraphy (Fig. 4A). The most direct correlation between the preliminary GPR section and the peat properties can be made with the peat stratigraphy and the peat bulk density. The GPR appears to be responding primarily to density changes associated with stratigraphic variations. The GPR section and stratigraphy are shown for comparison in Figures 4A, B. A number of important features can be identified.

The basal silty clay gives rise to a strong clear reflective event on the GPR profile (event "A"). The silty clay is commonly overlain by a thin layer of limnic detritus, limnic peat and gyttja. Where the layer of detritus is present, the reflection from the basal clay is more complex (event "B"); where the detritus is absent, the basal reflection is simpler in character (event "C"). Finally, the transition from the aerobic to the anaerobic zone is well delineated (event "D"). The aerobic zone contains a number of small events. The

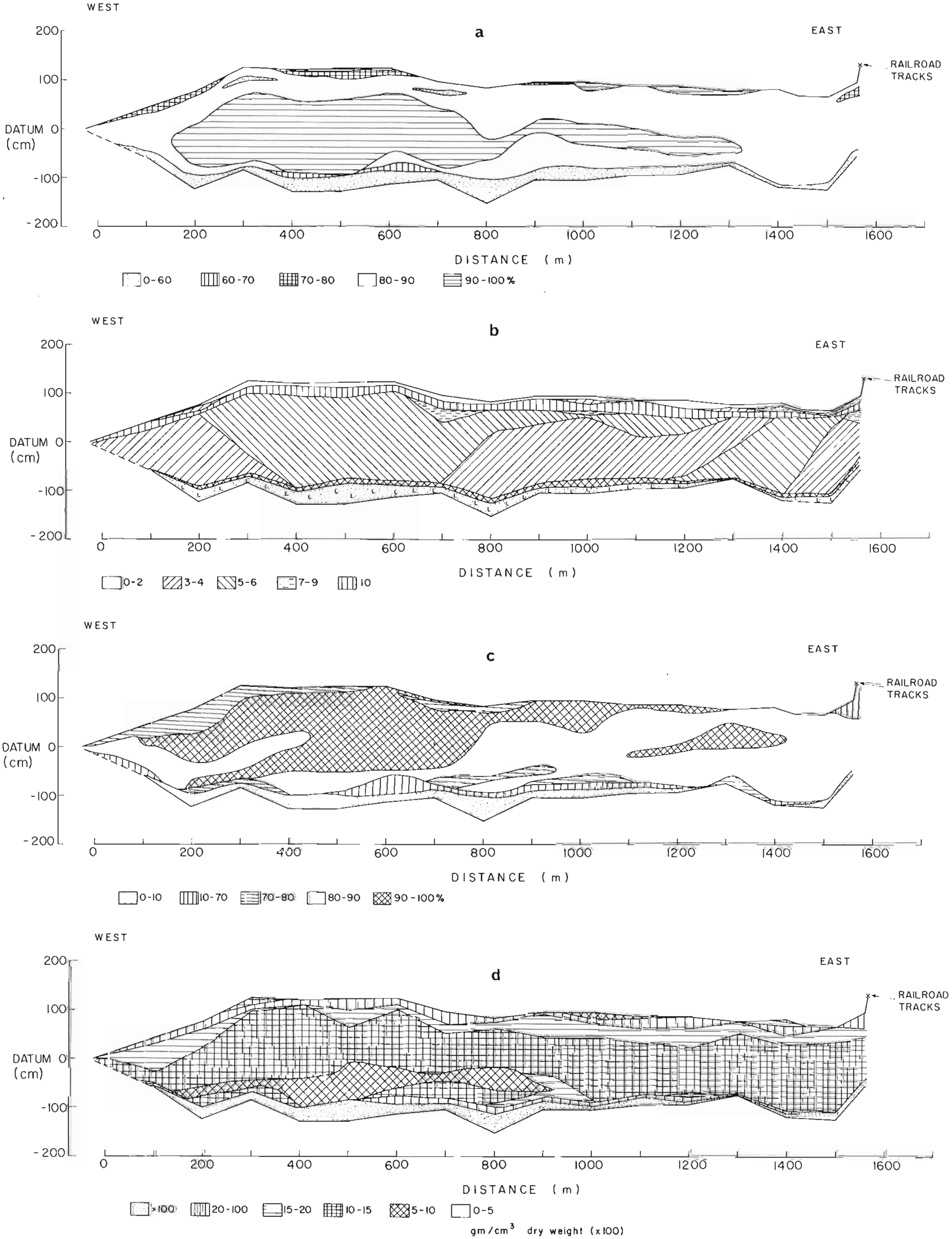

Figure 3. Cross-sections for **A.** percent moisture content from core analyses; **B.** degree of humification; **C.** percent organic matter content; and **D.** wet bulk density.

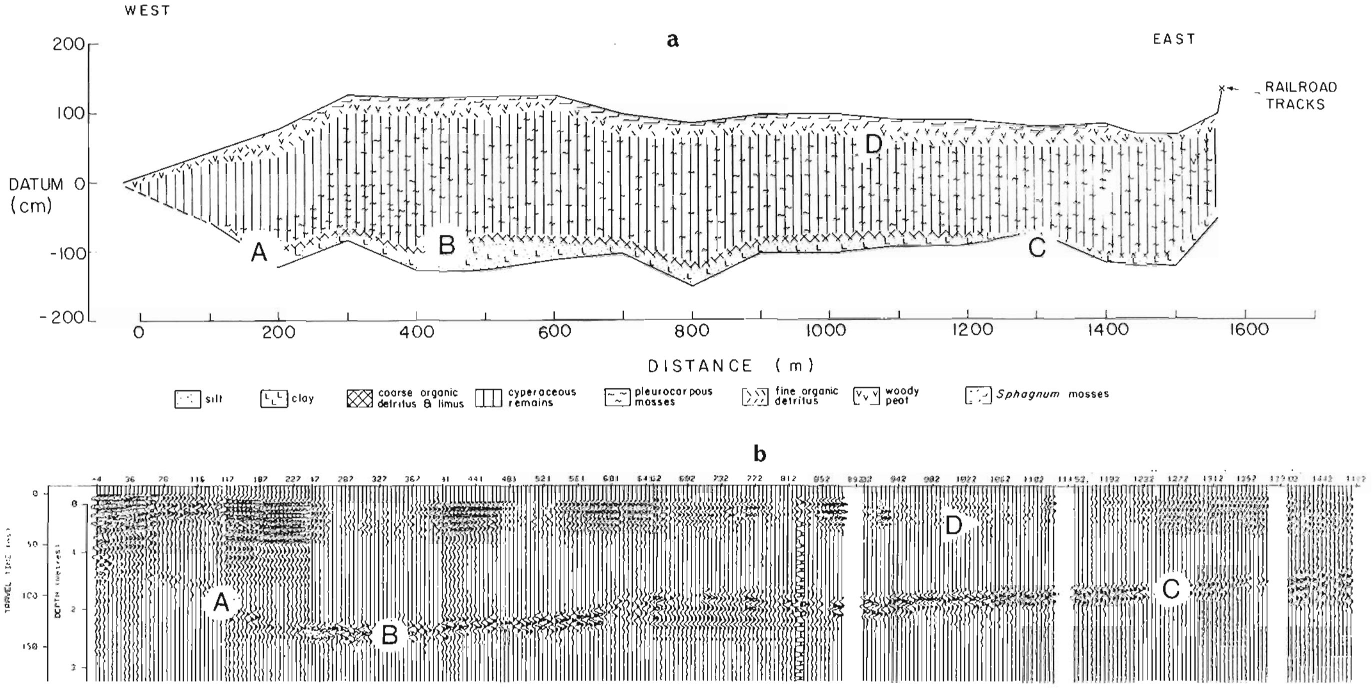

Figure 4. Comparison of the stratigraphy (**A**) and the GPR response (**B**) along the Ellice Swamp cutline. The major features are event "a", the transition from the peat to the underlying silty clay; event "b", the more complex reflection which occurs where limnic peat and gyttja are present; event "c", the simpler event where the limnic detritus is absent; and event "d", the transition from the surface aerobic to the underlying anaerobic zone.

underlying anaerobic zone appears to be relatively transparent to GPR signals, and we do not note any events within the anaerobic zone.

CONCLUSIONS

This study represents one of the first serious attempts to compare the physical properties of the peat with the GPR response by compiling cross-sections for each parameter for a single site in southern Ontario. We believe that it would be premature to speculate on wide-ranging applications of the technique. Our tests to date demonstrate great promise for GPR as a tool in assessing both the spatial and vertical extent of peat.However, the real applicability of GPR in peat inventories must await further testing in a much larger suite of peatland types throughout Ontario.

Peatlands are complex ecosystems that vary stratigraphically and areally. Peat has numerous characteristics that depend upon the botanical composition and state of decomposition. These factors in turn can control a variety of other peat parameters. Hence, we cannot assume that GPR will be a viable tool in all peatland types, because a whole spectrum of peat-forming systems exist that differ topographically, hydrologically, and morphologically. However, the real applicability of GPR in peat inventories has been addressed by additional testing both in Ellice Swamp (Warner et al., 1990) and elsewhere (Theimer, 1990).

ACKNOWLEDGMENTS

Our thanks go to R. Balloch, J. Easton, D. Gorling, R. Greenly, K. Hanf, H. Kubiw, and G. Schneider for field and laboratory assistance. Drafting was done by N. Bahar. We acknowledge the support of the Ontario Geological Research Fund.

REFERENCES

Karrow, P.F.
1971: Quaternary geology of the Stratford-Conestoga area, Ontario; Geological Survey of Canada, Paper 70-34.

Korpijaakko, E.
1981: A preliminary estimate of Ontario's peat resources; in Proceedings, Symposium on Peat, Thunder Bay, Ontario, p. 321-330.

Theimer, B.D.
1990: Principles of bog characterization using ground penetrating radar; M.Sc. Thesis, University of Waterloo, Waterloo, Ont.

Tiuri, M., Toikka, M., Marttilla, I., and Tolonen, K.
1983: The use of radio wave probe and subsurface interface radar in peat resource inventory; aProceedings, Symposium on Remote Sensing in Peat and Terrain Resource Surveys, Aberdeen, Scotland, p. 131-143.

Tiuri, M., Toikka, M., Tolonen, K., and Rummukainen, A.
1984: Capability of new radiowave moisture probe in peat resource inventory; Proceedings, 7th International Peat Congress, Dublin, Ireland, p. 517-525.

Tolonen, K., Tiuri, M., Toikka, M., and Saarilahti, M.
1982: Radiowave probe in assessing the yield of peat and energy in peat deposits in Finland; Suo, v. 33, p. 105-112.

Ulriksen, C.P.F.
1982: Application of Impulse Radar to Civil Engineering; Ph.D. Thesis, Lund University of Technology, Sweden.

Warner, B.G., Nobes, D.C., and Theimer, B.D.
1990: An application of ground penetrating radar to peat stratigraphy of Ellice Swamp, southwestern Ontario; Canadian Journal of Earth Sciences, v. 27, p. 932-938.

Zoltai, S.C. and Pollett, F.C.
1983: Wetlands in Canada: their classification, distribution, and use; in Ecosystems of the World, v. 4B, Mires: Swamp, Bog, Fen, and Moor, A.J.P. Grove (ed), Elsevier Publ. Co., Amsterdam, p. 245-268.

Fracture characterization in crystalline rock by borehole radar

Olle Olsson[1], Per Anderson[2], Seje Carlsten[2], Lars Falk[3], Börje Niva[4], and Eric Sandberg[3]

Olsson, O., Anderson, P., Carlsten, S., Falk, L., Niva, B., and Sandberg, E., 1992: Fracture characterization in crystalline rock by borehole radar; in *Ground penetrating radar, ed. J. Pilon; Geological Survey of Canada, Paper 90-4, p. 139-150.*

Abstract

A new, short pulse, borehole radar system (RAMAC) has been developed within the framework of the International Stripa Project for characterizing fracture zones within a rock mass. The RAMAC system has now been in operation for 7 years. During that time measurements have been performed corresponding to a measured borehole length of more than 100 km. The bulk of these measurements have been performed in granites and gneisses.

Examples are given of results from radar measurements at different sites, using the RAMAC system in three different configurations: single hole reflection mode, crosshole reflection mode, and crosshole tomography mode. Techniques for interpretation of data from the three measurement modes have been developed. If data from all three sets are analyzed together, a consistent three dimensional model of a site can normally be constructed.

The RAMAC system operates at centre frequencies in the interval 20-60 MHz. At those frequencies, single hole reflection ranges of 50-150 m are normally obtained in gneissic and granitic rocks. Crosshole ranges have in some cases been in excess of 300 m. Large probing ranges in combination with a resolution on the order of a few metres makes the borehole radar a unique instrument for investigations of fracture zones in crystalline rock.

Résumé

Dans le cadre de l'International Stripa Project, on a mis au point un nouveau système radar à impulsions courtes pour trou de sondage (RAMAC) afin de caractériser les zones de fracture au sein d'un massif rocheux. Le système RAMAC est exploité depuis maintenant sept ans. Durant cette période, des mesures ont été prises sur plus de 100 km de trous de sondage. La plupart des trous ont été forés dans du granite ou du gneiss.

Les résultats obtenus à différents endroits, en utilisant le système RAMAC selon trois configurations différentes (mode de réflexion en puits unique, mode de réflexion de puits à puits et mode de tomographie de puits à puits) sont présentés. Pour interpréter les données recueillies selon les trois modes de mesure, on a mis au point différentes techniques. Si les données des trois séries sont analysées ensemble, il est habituellement possible de construire un modèle tridimensionnel cohérent d'un endroit donné.

Le système RAMAC fonctionne aux fréquences centrales dans l'intervalle de 20 à 60 MHz. À ces fréquences, on obtient habituellement des distances de réflexion en puits unique de 50 à 150 m dans les roches gneissiques et granitiques. Les distances de puits à puits ont dépassé dans certains cas 300 m. Les grandes distances de sondage combinées à une résolution de quelques mètres font du radar de sondage un instrument exceptionnel pour l'analyse des zones de fracture en milieu de roche cristalline.

---

[1] ABEM AB, Stockholm, Sweden. Current address: Conterra AB, Box 493, S-751 06 Uppsala, Sweden

[2] Geosigma, Box 894, S-751 08 Uppsala, Sweden

[3] ABEM AB, Uppsala, Sweden

[4] ABEM AB, Skolgatan 11, S-930 70 Malå, Sweden

INTRODUCTION

Development of a new borehole radar system was initiated to improve the possibilities for describing groundwater flow through fractured crystalline rock. Accurate descriptions of the groundwater flow regime are required in connection with the disposal of high level nuclear waste. Potential nuclide transport paths need to be identified through nondestructive testing. For this purpose, borehole radar was considered a potential method and the development of a new borehole radar system was included as a part of the International Stripa Project.

The development of the borehole radar system started in 1983 and a prototype system was first operated during autumn 1984. Further development led to a system (RAMAC) designed for field work on a production basis. This system has been in operation regularly since mid 1985. The total measured volume comprises about 100 000 traces (1988), which corresponds to a measured borehole length of about 100 km if measurements are taken every metre. Borehole radar surveys with this system have so far mainly been performed in granites and gneisses.

THE RAMAC SYSTEM

The RAMAC system (Fig. 1) is a short pulse radar system that consists of five parts as follows;

- a microcomputer with one 5 inch floppy disc and a 20 MByte hard disc for controlling measurements, data storage, data presentation, and signal analysis
- a control unit for timing control, storage, and stacking of single radar measurements
- a borehole transmitter for generating short radar pulses
- a borehole receiver for detecting and digitizating radar pulses
- a motor-driven cable winch with a specially designed optical borehole cable for communicating between borehole probes and control unit.

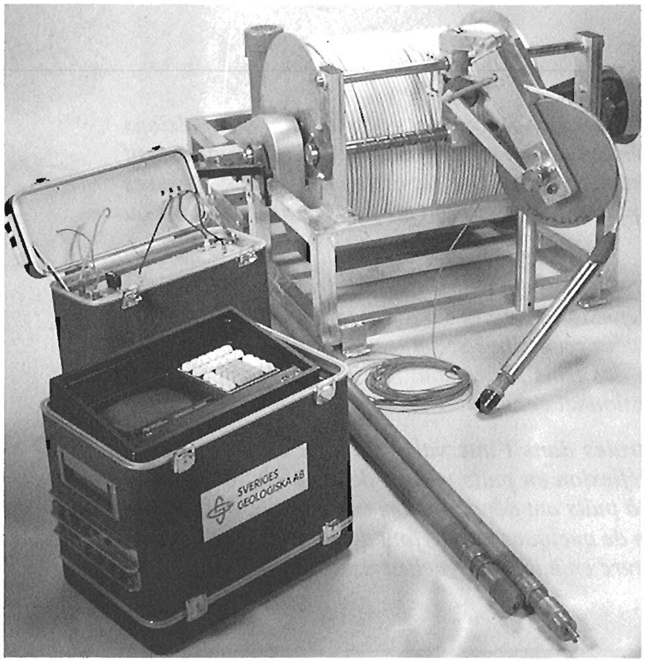

Figure 1. The RAMAC borehole radar system.

The RAMAC system works in principle in the following manner: a short current pulse is fed to the transmitter antenna, which generates a radar pulse that propagates through the rock. The pulse is made as short as possible to obtain high resolution. The pulse is received by the same type of antenna, is amplified, and is registered as a function of time. The recording of the signal is similar to that of a sampling oscilloscope, i.e., for each pulse from the transmitter only one sample of the received electric signal is taken at a specific time. When the next pulse is generated, the new sample taken is displaced slightly in time. Thus, after a number of samples a replica of the entire signal is recorded. The sampling frequency and the length and position of the sampled time interval can be set by the operator. Optical fibres are used to transmit the trigger signals from the computer to the borehole probes and for transmission of data from the receiver to the control unit. The optical fibres have no electrical conductivity and will not support waves propagating along the borehole. Another advantage of optical fibres is that they can not pick up electrical noise, so that, as the signal is digitized downhole, the signal will not deteriorate along the cable. The quality of the results will thus be independent of cable length.

There is no direct connection between transmitter and receiver. Both probes are instead connected directly to the control unit and the transmitter and the receiver can be put into the same as well as into separate holes. In other words, the radar may be used both for single hole and crosshole measurements. The system also provides absolute timing of the transmitted pulses and a calibrated gain in the receiver, which makes it possible to measure travel time and amplitude of the radar pulses in a crosshole measurement; hence provide data for a tomographic analysis. The absolute time depends on the length of the optical fibers and is hence a quantity which has to be obtained through calibration for a given set of optical fibers. Block diagrams of the control unit, transmitter, and receiver are shown in Figure 2, and the technical specifications of the system are given in Table 1.

MEASUREMENT CONFIGURATIONS

Single hole measurements

In single hole measurements the transmitter and receiver are located in the same borehole. The transmitter and receiver are kept at a fixed separation by fibreglass rods. The transmitter-receiver array is moved along the borehole and measurements are made at fixed intervals. The measurement at each position takes about 30 seconds including the movement to the next measuring position. The separation of measurement points is normally 0.5 or 1 m.

The transmitter-receiver separation is made as small as possible to obtain good resolution close to the borehole. To avoid saturation of the receiver amplifier there is a minimum separation allowed depending on the attenuation of the rock. Typical separations in crystalline rock are 5-15 m.

Crosshole measurements

In a crosshole measurement the transmitter and receiver are placed in separate boreholes. The transmitter may also be kept at a fixed position on the ground while the receiver is moved in a borehole. This measurement configuration, with the transmitter on the ground, is termed vertical radar profiling (VRP). The recorded signal may be analyzed both for the travel time and amplitude of the first arrival and for the occurrence of later arrivals such as reflections.

The separation of measurement points in crosshole tomographic surveys is normally 4-5 m for both transmitter and receiver. For crosshole reflection surveys the moving probe is normally moved in increments of 1 m to avoid spatial aliasing, whereas the separation of measurement points for the fixed probe is significantly larger.

PROCESSING AND INTERPRETATION OF RADAR DATA

Single hole reflection data

Interpretation procedure

The principle of single hole reflection measurements is depicted in Figure 3. The transmitter and receiver are lowered or pushed into the same hole while the distance between them is kept constant. The result is displayed in the form of a diagram where the position of the probes is shown along one axis (horizontal axis in Fig. 3) and the propagation distance along the other axis. The amplitude of the received signal is shown in a grey scale where black corresponds to large positive signals, white to large negative signals, and grey to small signals.

The distance to a reflecting object is determined by measuring the difference in arrival time between the direct and the reflected pulse. The basic assumption is that the speed of propagation is the same everywhere, an assumption that is

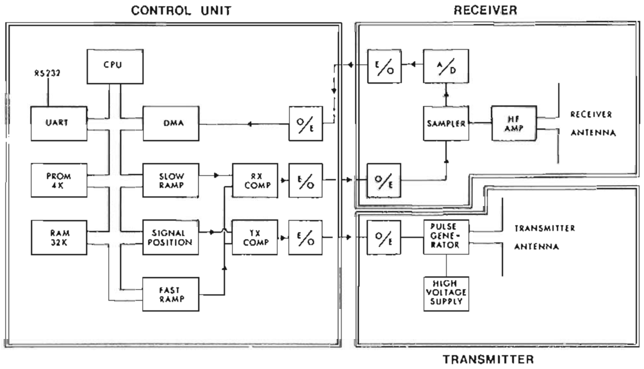

Figure 2. Block diagram of the borehole radar system.

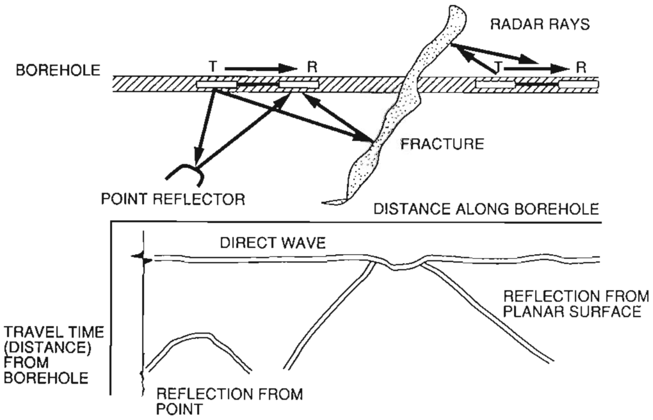

Figure 3. The principle of the borehole reflection radar and the characteristic patterns generated by plane and point reflectors.

Table 1. Technical specifications of the borehole radar system

Item	Specification
General	
Frequency range	10-80 MHz
Performance factor	150 dB
Sampling time accuracy	1 ns
Maximum optical fibre length	1000 m
Maximum operating pressure	100 Bar
Outer diameter of transmitter-receiver	48 mm
Minimum borehole diameter	56 mm
Transmitter	
Peak power	500 W
Operating time	10 h
Length	5.4 m
Weight	18 kG
Receiver	
Bandwidth	10-200 MHz
A/D converter	16 bit
Least significant bit at antenna terminals	1 µV
Data transmission rate	1.2 MB
Operating time	10 h
Length	5.4 m
Weight	18 kg
Control unit	
Microprocessor	RCA 1806
Clock frequency	5 MHz
Pulse repetition frequency	43.1 kHz
Sampling frequency	30-1000 MHz
No. of samples	256-4096
No. of stacks	1-32767
Time window	0-11 µs

normally valid in a homogeneous media such as granite. The two basic patterns are point reflectors and plane reflectors (Fig. 3).

From the radar reflection measurements the angle of intersection between the borehole and a fracture plane and also the point of intersection can be determined with the aid of a theoretically computed nomogram (Olsson, Falk et al., 1987). The information contained in the radar images is cylindrically symmetric because dipole antennas have been used because of the small borehole diameter. One degree of freedom still remains as the fracture plane can be rotated on a conical surface without any effect on the radar image. Consequently one can not obtain the complete orientation of a fracture plane from measurements in a single borehole. The orientation can, however, be determined by combining results from two or more boreholes.

A technique has been developed for determining the orientation of a fracture zone if radar data from several adjacent holes are available. A computer program calculates the possible orientations of a fracture plane when its angle of intersection with a borehole has been determined. The program can also calculate the possible orientations of a fracture plane defined by two intersection points with boreholes. The possible orientations of a plane are plotted using the Wulff projection. Points where the curves intersect are candidates for the correct orientation of the plane (Olsson, Falk et al., 1987). The Wulff projection technique has also been extended to include analysis of reflections observed in crosshole measurements.

Data processing

In many cases reflections from fracture zones and other inhomogeneities in the rock mass are not readily observed in the original radar data. To enhance reflections digital bandpass and deconvolution filters are applied.

A suitable filter to remove ringing is the moving average filter. The filter is constructed so that the average is formed from a number of traces adjacent to the trace to be filtered and the average is subtracted from the centre trace. The same is done for all traces along the borehole. With this type of filter, features on the radar signals that are similar for several adjacent traces will be removed, including the direct pulse as well as structures nearly parallel to the borehole. The width of the filter, i.e., the number of traces included in the average, is chosen close to one wavelength.

A time variable gain is normally applied to the data before plotting to enhance the small signals received at late times.

Analysis of crosshole radar data

Tomographic analysis

The general idea behind tomographic reconstruction is that information about the properties of the interior of a region can be obtained through measurements at the boundary. In general the transmitter and receiver probes are located at the boundary of the area and each ray connecting transmitter and receiver can in principle be considered to represent the average of a measured property of the rock along the ray. To estimate this property at a given point several rays need to pass close to the same point and need to have different directions and hence different information content. The requirement that several rays should intersect the same point leads to the constraint that the source and receiver positions and hence the boreholes have to be confined to the same plane.

In a borehole radar crosshole measurement, data can be extracted on the travel time and the amplitude of the direct wave between transmitter and receiver, i.e., the first arrival. For the tomographic analysis it is assumed that the travel time can be constructed as the line integral of the slowness along each ray. The amplitudes can not be obtained from a line integral directly but the problem can be linearized by taking the logarithm of the data. The logarithm of the amplitudes can then be subject to tomographic inversion.

The problem is then analyzed. The plane between the boreholes is divided into a number of cells and the line integral is calculated as a sum where the contribution from each cell is considered in proportion to the length of the ray within each cell (Fig. 4). A matrix equation of the following form is then used on the data:

$$d_i = \sum_{j=1}^{M} G_{ij} b_j \tag{1}$$

where d_i represents the date for ray 'i', G_{ij} the length of ray 'i' in cell 'j', and b_j the attenuation of slowness of cell 'j'. The equation system has to be solved with iterative methods because of its size. We have in our work used the conjugate gradient method (Ivansson, 1984, 1986) as we found it most efficient.

The radar velocity (or slowness) has small variations around a certain average value. We have found it useful to put the crosshole data in such a form that these variations are studied rather than the absolute values of these properties. The concept has also been adopted for the amplitude data. In this context we define the terms "residual travel time" and "residual amplitude". These residual data correspond to the measured data after we subtract the expected data value

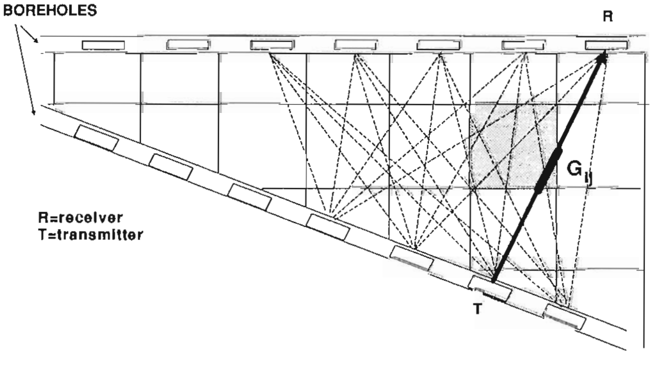

Figure 4. Generalized crosshole tomography geometry decomposed into cells and showing an example of a ray pattern.

which would have been obtained in the homogeneous medium with properties close to those of the investigated rock.

The residual travel time, t_r, is defined as the measured travel time, t_m, minus the estimated travel time for a homogeneous medium with a constant velocity, v_0. The residual travel time then becomes

$$t_r = t_{m-r/v0} \tag{2}$$

where r is the distance between transmitter and receiver.

The residual amplitude is defined as the quotient (expressed in dB) of the received amplitude, E_m, and the estimated amplitude in a homogeneous medium with constant attenuation α_0. The residual amplitude, d_r, thus becomes

$$d_r = -20\log_{10}\frac{E_0\exp(-\alpha_0 r)\,a(\theta_1)\,a(\theta_2)}{E_m \qquad r} \tag{3}$$

where E_0 represents a reference level corresponding to the ratio of transmitted power to received sensitivity, and $a(\theta)$ describes the antenna radiation pattern. Using the base 10 logarithm and multiplying by 20, the residual amplitudes become represented in dB.

With this conversion into residual data it is possible to look at small variations from large average values. The residual data are also suitable for detecting systematic errors in the data and can be used to calibrate of system parameters such as zero time and performance factor.

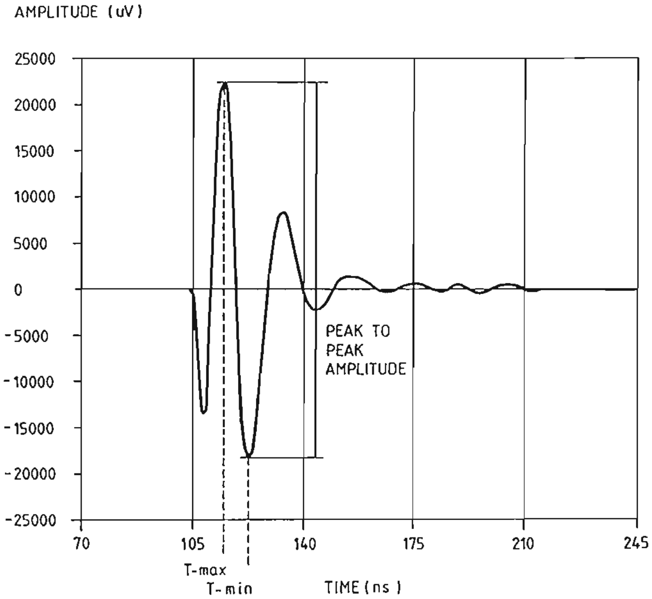

Figure 5. Radar signal obtained from a crosshole measurement. The data identified by the automatic routine for extracting of travel times and amplitudes are indicated.

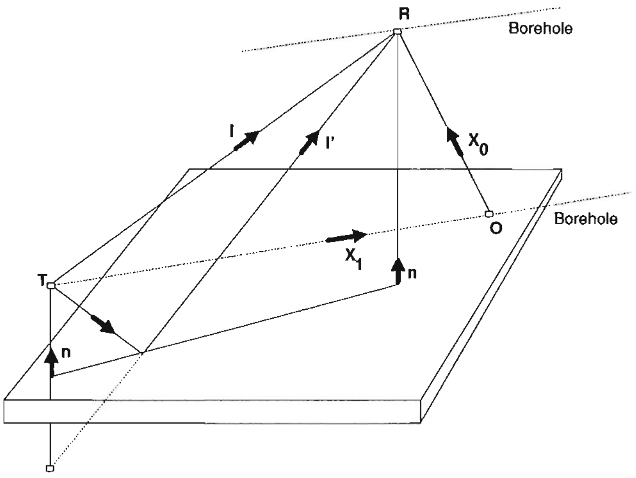

Figure 6. Principal ray paths in a bistatic radar configuration where the ray is reflected in a plane. T = transmitter, R = receiver, I = direct wave, I' = reflected ray, x_0 = location vector of receiver, x_1 = location vector of transmitter, n = normal vector to plane.

A typical example of a radar signal recorded from a crosshole measurement is shown (Fig. 5). From this signal trace we extract the time of first arrival and the magnitude of the signal.

A tomographic survey normally includes many rays. Thus it is important to use some automatic procedure for extracting the data from the recorded traces; manual treatment of each ray would be extremely time consuming and hence costly. For the radar data we have adopted a simple approach, which has already proven to be reasonably efficient. We devised an algorithm that picks out the maximum and minimum for each trace and the time instances at which these events occur. The travel time is then defined as the time to the maximum or minimum of the pulse, and the amplitude is defined as the difference between the maximum and minimum, i.e., peak-to-peak amplitude. This travel time definition leads to an offset error that has to be corrected for so that the travel time is zero for rays with zero length.

The basic step in preparing data for tomographic inversion is to combine coordinate data for the picked travel times and amplitudes. The accuracy required in source and receiver coordinates is of the same order as the distance travelled by the radar waves during a sampling interval (about 2 ns). The sampling interval normally corresponds to a propagation distance of 0.2-0.5 m.

After the travel time and amplitude data have been combined with the coordinates of the source and receiver points the residual data are calculated using equations 2 and 3. At this stage, the coordinate system is rotated to put the source and receiver points into one of the coordinate planes.

The tomographic data are subject to a number of errors such as; errors in time and amplitude picking, constant offset errors in time and gain, and coordinate errors. Both the stochastic and systematic errors, which may exist in the data set, must be recognized. The errors must be understood, quantified, and corrected before a tomographic inversion is attempted. A good way to reveal errors is to plot the residual data as a function of the length of the rays. From these plots an offset and a slowness or attenuation correction is determined by fitting a straight line to the data. A grey scale pixel plot is then made of the average slowness or attenuation for all rays. In this plot each ray corresponds to a pixel and individual rays containing errors (e.g., due to errors in time and amplitude picking) can be identified. Rays containing errors are removed from the data set before tomographic inversion.

The data correction and quality checking procedure is described in detail (Olsson, Falk et al., 1987).

Tomographic inversion is then made with the iterative conjugated gradient (CG) method described by Ivansson (1986). The inversion is normally made with rectangular basis functions, i.e., the velocity of each cell is assumed to be constant within that cell. A cell size of about 3 m is normally used.

Crosshole reflection analysis

When the transmitter and receiver are positioned in different boreholes, reflected pulses are observed some time after the directly propagated pulse has arrived. Only the direct pulse is used in the tomographic analysis, so the crosshole reflections provide additional independent information about the fracture zones. This method has provided complementary information on the orientation of the fracture zones identified in the single hole reflection data and the tomograms.

It is particularly convenient that crosshole reflections in principle can determine a complete orientation of the fracture zone, because of the additional freedom provided by a bistatic radar configuration. The analysis is, however, more complicated than for single hole measurements. The method of analysis is presented here in some detail.

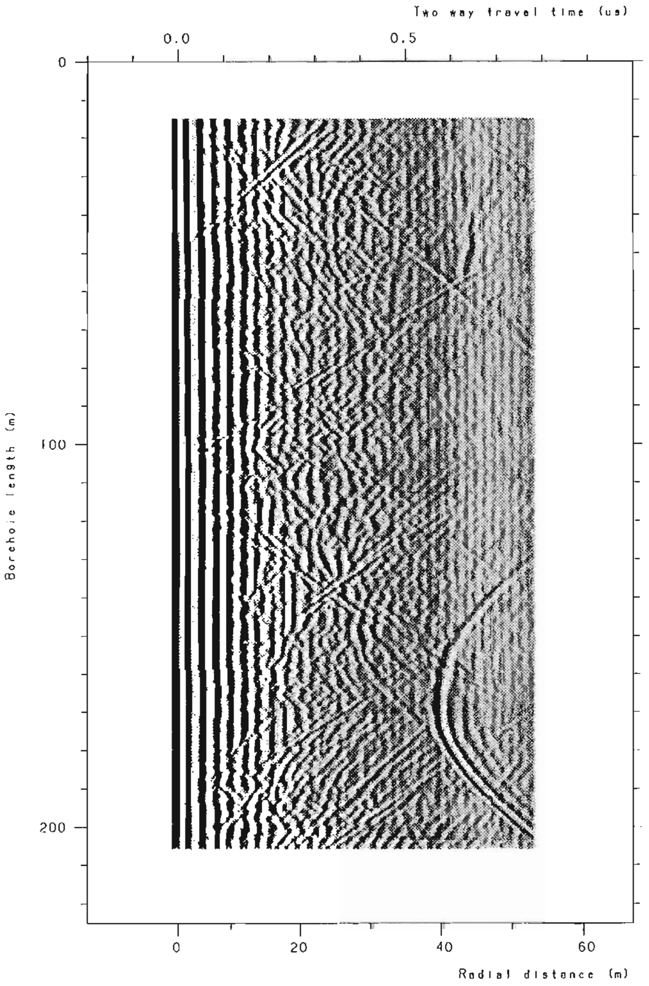

Figure 7. Radar reflection map of unfiltered data from borehole F4 at Stripa Mine. (Centre frequency of 60 MHz.)

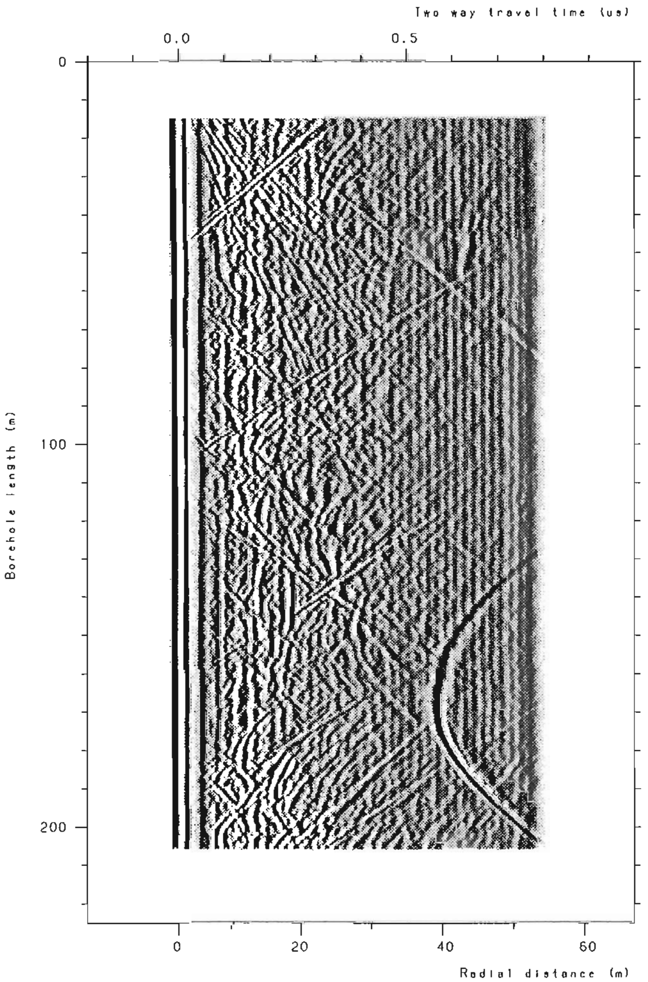

Figure 8. Radar reflection map of deconvolution filtered data from borehole F4 at Stripa Mine. (Centre frequency at 60 MHz.)

The bistatic radar configuration is defined in Figure 6. The receiver and transmitter are in known positions described by the vectors x_0 and x_l. The distance l propagated by the direct pulse and the distance l′ propagated by the reflected pulse are then conveniently combined into the expression

$$l'^2 = l^2 + 4\,(x_0\,n)\,(x_l\,n) \qquad (4)$$

where n is the unit normal vector of a plane causing the reflection. The formula is valid as long as the origin is in the reflecting plane. One such point can be determined from the radar picture, because l = l′ when the antenna passes that point where the fracture plane intersects the borehole. Using this point as an origin we can then analyze the reflection.

The reflection curves are digitized and analyzed using in a special program. Equation 4 is used to plot the possible orientation of a zone in a Wulff diagram, for every reflection identified with the zone. Performing the same procedure for several different crosshole measurements we obtain a number of curves all intersecting each other near some point corresponding to the correct orientation. This procedure is very similar to the one used for analysis of single hole reflection data.

In principle all quantities in equation 4 can be obtained from the measured data, so the two independent components of the unit vector n can be determined from a minimum of two separate measurements. Compare this with the special case of the single hole measurement where the receiver and the transmitter are moved along the same borehole. The angle between the fracture plane and the borehole can then be determined immediately, but no more information about orientation of the plane is available because of the axial symmetry of the single hole configuration.

THE STRIPA MINE

The Stripa Mine is an old Swedish iron mine, which is now operated as a research facility for geological problems related to the final disposal of high level radioactive waste. The experiments are performed in a granitic intrusion adjacent to the leptite containing the iron ore (Carlsten, 1985). A special test site (Crosshole Site) was prepared for the development

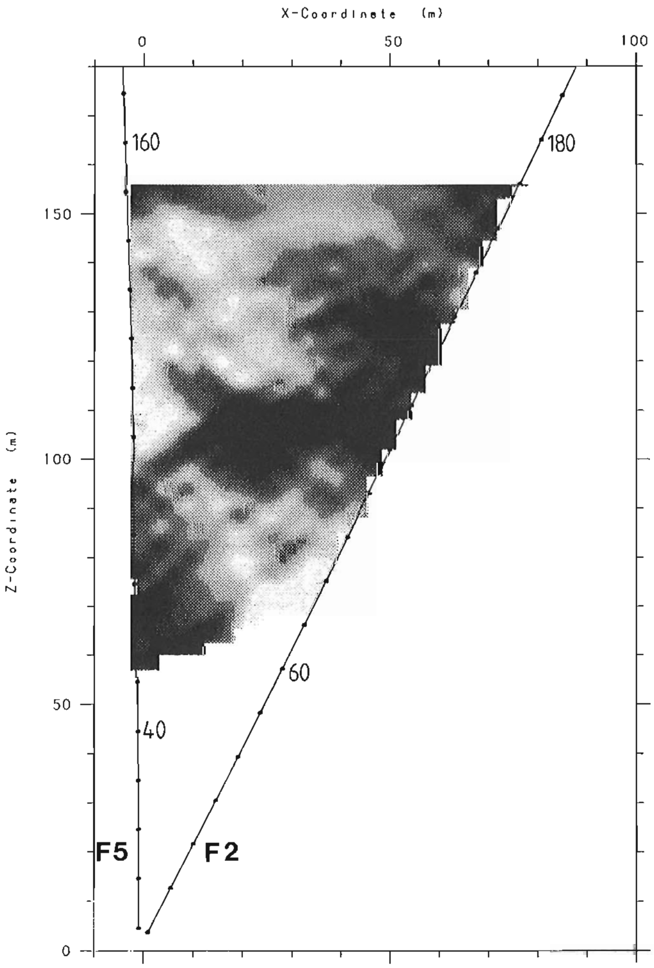

Figure 9. Residual slowness tomogram for the borehole section F5-F2. (Centre frequency of 60 MHz.)

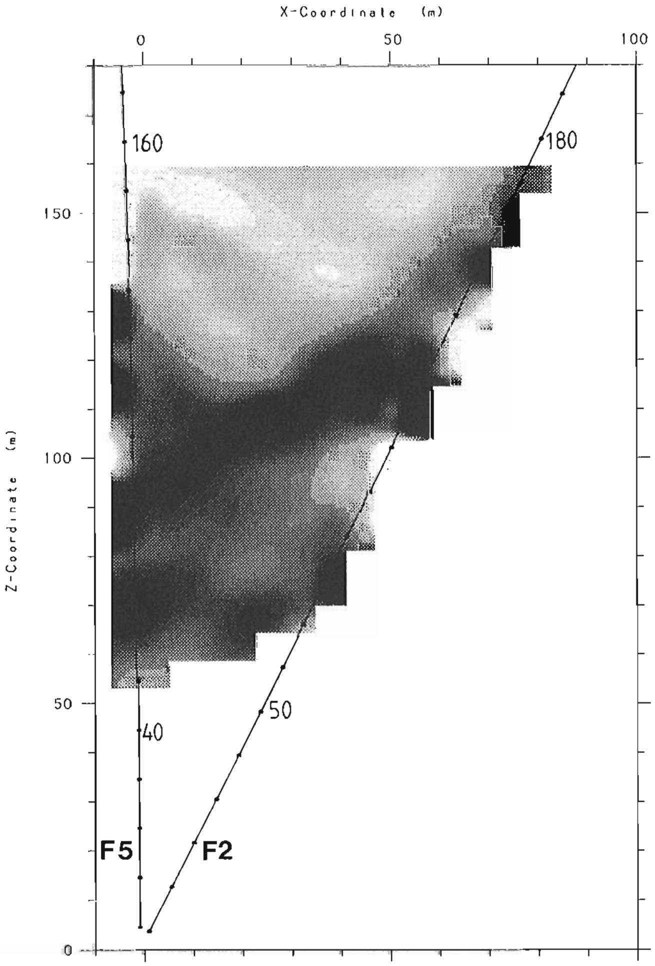

Figure 10. Residual attenuation tomogram for the borehole section F5-F2. (Centre frequency of 60 MHz.)

of radar, seismic, and hydraulic crosshole testing techniques (Olsson, Black, Cosma et al., 1987). Six boreholes were drilled from the end of a drift in a fanlike fashion. The boreholes outline a tilted pyramid with a height and base of about 200 m. All boreholes start from the top of the pyramid.

Single hole reflection surveys

Single hole reflection measurements have been performed in all boreholes at two different centre frequencies, 20 and 60 MHz. Figure 7 shows the raw data collected in borehole F4 at the higher frequency. Measurements were made with a fixed transmitter-receiver separation of 7.5 m and measurements were taken with 0.5 m increments along the borehole. The radar range actually exceeded the 55 m shown in Figure 7. The range obtained at the centre frequency 20 MHz was about 100 m (Olsson, Falk et al., 1987). Figure 8 shows the same data after deconvolution filtering has effectively reduced ringing and provided a radar map with clearly identifiable reflectors, most notable in the early returns.

The reflections intersecting the borehole at 55 and 110 m correspond to fracture zones. These zones consist of brecciated and mylonitized rock and have widths ranging from 1 to 8 m. It has been shown that the bulk of the groundwater flow at this site takes place in these fracture zones (Olsson, Black et al., 1987).

The reflections that seem to intersect the borehole near its beginning are caused by the other boreholes at the site. These boreholes are 76 mm in diameter and are filled with groundwater with a resistivity of about 100 m. This result demonstrates the great sensitivity of the radar method and its capability to identify small objects with relatively small contrast in properties.

The reflection shaped as a hyperbola seen at a borehole depth of about 170 m and its axis at a distance of 40 m from the borehole is caused by an air filled drift extending in a direction nearly perpendicular to that of the borehole.

Crosshole tomography surveys

Crosshole tomography surveys were performed in more than 10 sections between the boreholes at the Crosshole Site at centre frequencies of both 20 and 60 MHz. For most sections, measurement points were 4 m apart resulting in a regular ray pattern covering the plane defined by each pair of boreholes. The number of rays included in each section was 1000-1300.

Tomographic inversion was made of both travel times and amplitudes. Because of the large number of rays involved, the fairly simple approach described above was adopted for extracting travel times and amplitudes.

Slowness and attenuation tomograms obtained for the borehole section F5-F2 are shown in Figures 9 and 10, respectively. Darker colours correspond to increased slowness and attenuation which both are indicate of increased fracturing. The dark area in the centre of the tomographic sections corresponds to the fracture zone seen to intersect borehole F4 at a depth of about 110 m in the single hole reflection measurements (Fig. 8). The general appearance of the slowness and attenuation tomograms are quite similar but there are some differences with respect to the details. These differences are considered to be real physical effects even though minor discrepancies can be caused by data errors. Characteristic differences between structures appearing in slowness and attenuation tomograms have been observed for other borehole sections measured at Stripa (Olsson, Eriksson et al., 1988).

The tomograms map the variation in electric properties across the measured plane. To a first approximation, increased attenuation and slowness is associated with increases in fracturing. In these maps, fracture zones appear irregular both with respect to geometry (width and linearity) and contrast in properties. These variations have also been observed where the boreholes intersect these zones. The width of the zone in the centre of Figures 9 and 10 varies from 1 to 8 m at the seven borehole intersections.

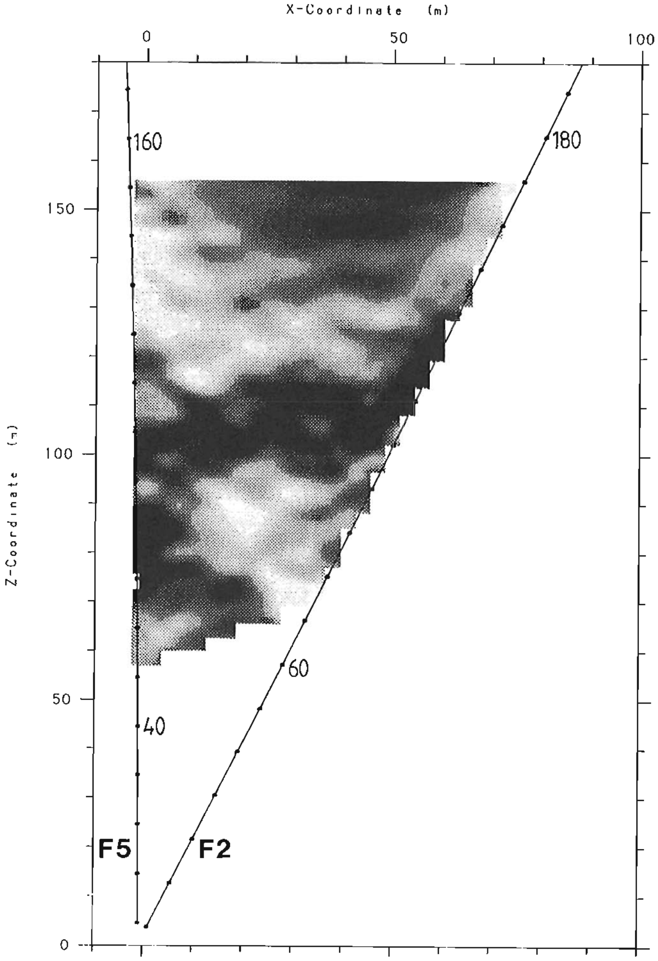

Figure 11. Tomographic map showing increase in radar attenuation for borehole section F5-F2 obtained by taking the difference between data measured after and prior to salt injection. (Centre frequency of 60 MHz.)

A large number of tomographic sections have been measured at the Crosshole Site. One important aspect of the results is that there is agreement in the location of anomalous features where different sections intersect, i.e., along boreholes and along lines in space between boreholes. This repeatability gives confidence that the anomalies depicted by the tomographic technique are real and are correctly positioned in space. The results of seismic tomography at the Crosshole Site are in excellent agreement with the radar results, which gives us more confidence in both methods (Olsson, Black et al., 1987).

Borehole radar tomography can also be used to show the actual transport paths of groundwater, by applying differential tomographic techniques. Regular tomography, as already described, can locate fracture zones, which are potential groundwater flow paths, but no direct information is given of the actual flow or potential for flow. Using an existing tomographic survey as a reference, we can inject water, which changes the electric properties; we then repeat the measurements. Analysis of the difference between two such measurements should then indicate the location of the injected water. A simple way to change the properties of the water is to add a saline tracer to increase the conductivity. Increased conductivity causes increased attenuation of the radar waves and a tomographic analysis of the differences between measurements after and prior to saline injection will indicate the distribution of the tracer. The results from such an experiment performed at Stripa is shown in Figure 11.

Saline water with a salinity of 0.5% was injected at a rate of 0.8 L/min in the fracture zone seen (Figs. 9 and 10) from borehole F3, which is located about midway between F5 and F2 but somewhat out of the plane. The tracer does not distribute evenly across the fracture zone, instead it is concentrated to two locations; one about midway between F5 and F2 and one close to F2. Comparing the magnitudes of the attenuation anomalies shows that the saline tracer has caused an increase in attenuation of about 20%. The experiment includes 11 borehole sections, which is intended to give a three dimensional view of the flow system at this site (the analysis is currently in progress).

This experiment demonstrates the ability of the radar technique to actually show the groundwater transport paths through rock. The radar is a unique instrument for this type of application and will in the future provide new insights to hydrogeologists working with groundwater transport in fractured rock. The difference technique can, for example, also be useful in mapping results of grouting activities made for reinforcement purposes.

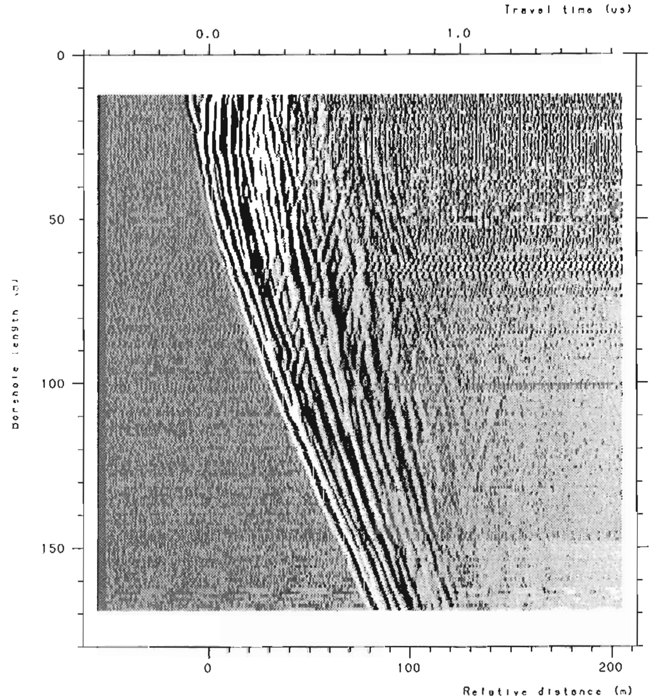

Figure 12. Radar reflection map obtained from VRP survey in borehole Kl 6 at the Klipperås site. (Centre frequency of 20 MHz.)

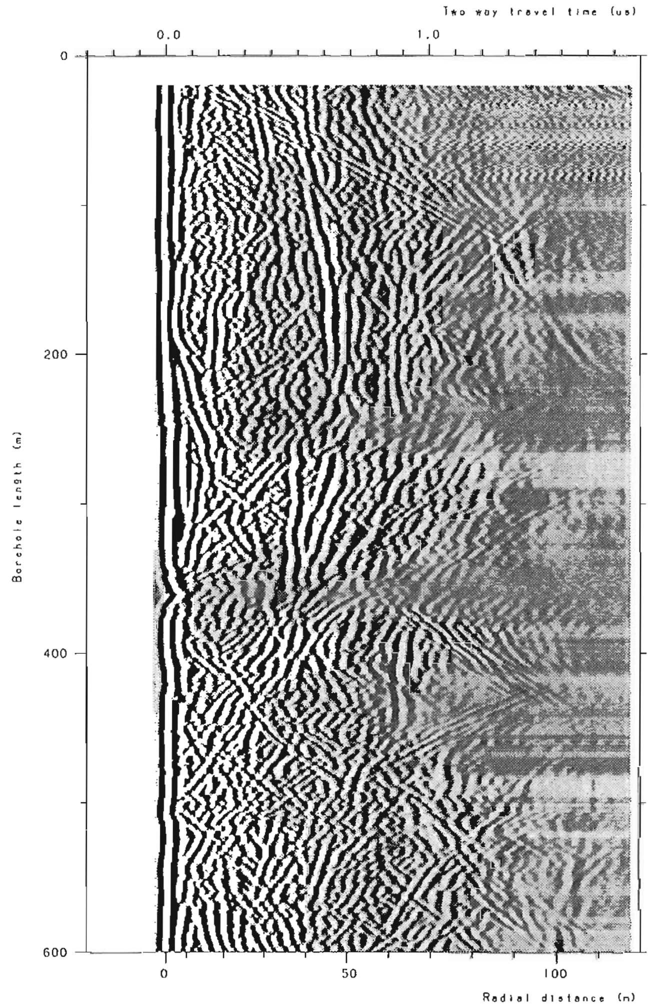

Figure 13. Radar reflection map from borehole Kl 6 at the Klipperås study site. (Centre frequency of 20 MHz.)

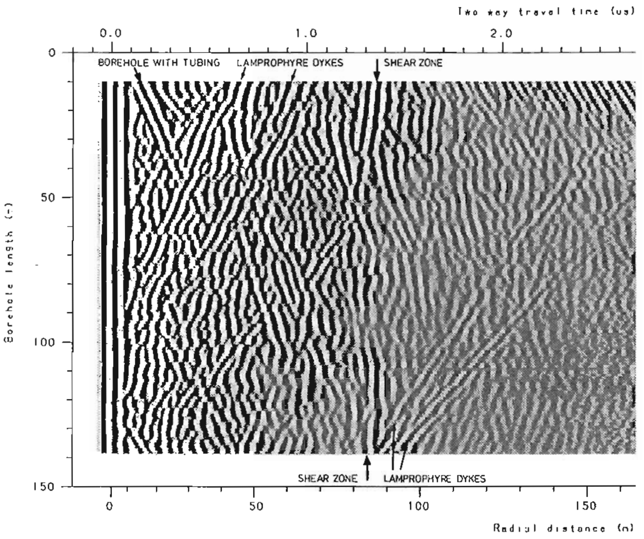

Figure 14. Radar reflection map from a single hole reflection measurement in borehole BO US 85.003 at Grimsel Rock Laboratory. (Centre frequency of 20 MHz.)

KLIPPERÅS

The Klipperås site is located in southeastern Sweden. This study site is part of the Swedish program for final disposal of radioactive waste in crystalline rock. The rock type at the site is granite intersected by numerous basic dikes. Fourteen deep cored boreholes have been drilled to investigate the geological conditions at depth.

Borehole radar measurements were made to provide additional data on the geometry of geological features such as fracture zones and dikes (Carlsten et al., 1987). Reflection measurements at two frequencies, 20 and 60 MHz, were made in most of the cored boreholes. The distance between the boreholes was in general too large (>300 m) to make crosshole measurements meaningful. Surface to borehole or vertical radar profiling (VRP) measurements were made to get radar velocity calibrations and to provide data with which to orient specific features. During a VRP measurement the transmitter is located on the ground surface some distance (40-50 m) away from the borehole, while the receiver is moved along the borehole and measurements are taken at regular intervals, normally 1 m. One example of a result from a VRP survey is shown in Figure 12.

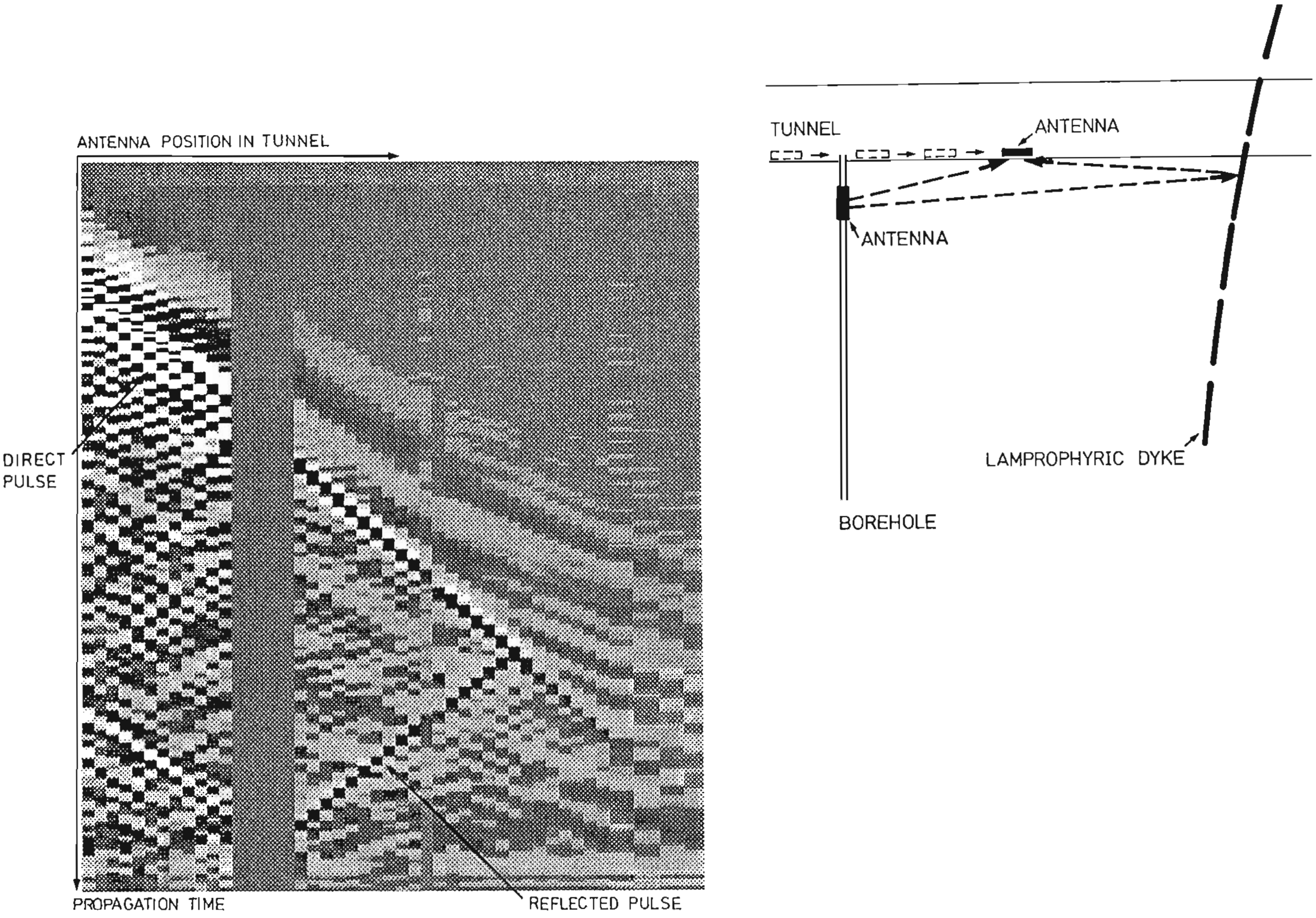

Figure 15. Radar reflection map obtained from a tunnel to borehole measurement at Grimsel Rock Laboratory. (Centre frequency of 20 MHz.)

Figure 13 shows the results from a single hole reflection survey with the centre frequency 20 MHz in borehole Kl 6. The radar range at this site is 120-130 m. A number of reflectors nearly parallel to the borehole can be seen in the radar reflection map. These structures correspond to greenstone dikes, which are steeply dipping and strike east. Borehole Kl 6 is directed east and has a dip of 60°. This borehole intersects a major fracture zone at a depth of 360 m (reflectors 2 and 3). Here we can observe a delay of the direct pulse propagating along the borehole because of a significant decrease in radar velocity in the zone. The reflection that intersects the borehole at the beginning is caused by the ground surface.

Radar measurements were made in 10 boreholes at the Klipperås site. The results from these boreholes clearly indicated the anisotropy of the rock structure. Inclined boreholes towards the north exhibit a characteristic pattern of almost exclusively parallel structures, which intersect the boreholes almost perpendicularly. Inclined boreholes directed towards the east or west shows a pattern of reflectors nearly parallel to the boreholes as exemplified by borehole Kl 6 (Fig. 13). This result indicates that the major structures at the site are vertical and strike east. The radar results agree well with the structural model of the site, which had been constructed earlier without access to the radar results. This model was in some aspects incomplete and the radar results filled these gaps and gave greater confidence to the three dimensional tectonic model of the site.

THE GRIMSEL ROCK LABORATORY

Grimsel Rock Laboratory is situated in a granitic rock body in Swiss Alps. This underground research facility is operated as a joint venture between Switzerland and the Federal Republic of Germany (NAGRA, 1985).

An example of a result from a single hole reflection survey in borehole BO US 85.003 is shown in Figure 14. The 150 m long borehole has a dip of 15° and is drilled from a tunnel. Most of the reflections seen in this radar map are caused by lamprophyre dikes that intersect the granite. These dikes have a low resistivity and act as very good reflectors. In this radar map we can follow reflections to a radial distance of 150 m from the borehole. Some reflections are also caused by fracture zones but those reflections generally have a smaller magnitude than those caused by lamprophyres. A lamprophyre connected to a shear zone can be seen at a distance of about 90 m extending in a direction nearly parallel to the borehole.

The borehole radar experiments at Grimsel Rock Laboratory have also comprised a comprehensive crosshole tomography program which have included repeated radar surveys accompanied by injection of saline tracers (Niva and Olsson, 1987, 1988a, 1988b). As a part of this program, tests were also made to study if the borehole radar system could be operated in the reflection mode from tunnels. Measurements where the receiver was located in a radial hole a short distance away from the tunnel while the transmitter was moved along the tunnel and measurements made every 2.5 m proved quite successful. Results from such a measurement are shown in Figure 15. We can follow the delayed arrival of the direct pulse as the transmitter is moved along the tunnel. The gap in the data is caused by a connecting tunnel which also causes reflections which can be observed in the data. A strong reflection caused by a lamprophyre-shear zone, which intersects the tunnel, is readily identified in the radar map. This same zone was observed in the single hole reflection measurements at a distance of 90 m (Fig. 14). If we consider this measurement as being performed in connection with the excavation of the tunnel and that the transmitter is moved along with the tunnel front, this result implies that this zone could have been detected 50 m in advance.

CONCLUSION

Considerable experience now exists operating the RAMAC borehole radar system in crystalline rock environments. The system has proven its capability of characterizing fracture systems and other inhomogeneities present in crystalline rock. The system is flexible and can be operated in both single hole and crosshole configurations. Crosshole configurations include borehole to surface and borehole to tunnel surveys.

The RAMAC system operates with centre frequencies in the interval 20-60 MHz, corresponding to wavelengths of 6-2 m. At those frequencies single hole reflection ranges of 50-150 m have regularly been obtained in granitic and gneissic rock. Crosshole ranges have in some cases exceeded 300 m. A maximum practical distance between boreholes for crosshsole surveys in granite is about 200 m. Large probing ranges combined with a resolution on the order of a few metres makes the borehole radar a unique instrument for investigating fracture zones in crystalline rock. This borehole radar technique can also be used to map the actual flow paths of groundwater by measuring the difference in radar attenuation before and after a saline traceris injected.

ACKNOWLEDGMENT

The authors would like to express their gratitude to the International Stripa Project, The Swedish Nuclear Fuel and Waste Management Co (SKB), and NAGRA Switzerland who have funded the experiments presented in this paper.

REFERENCES

Carlsten, S.
1985: Hydrogeological and hydrochemical investigations in boreholes – Compilation of geological data; Stripa Project IR 85-04, SKB, Stockholm, Sweden.

Carlsten, S., Olsson, O., Sehlstedt, S., and Stenberg, L.
1987: Radar measurements performed at the Klipperås study site; SKB TR 87-01, SKB, Stockholm, Sweden.

Ivanson, S.
1984: Crosshole investigations – Tomography and its application to crosshole seismic measurements; Stripa Project IR 84-08, SKB, Stockholm, Sweden.
1986: Seismic borehole tomography – Theory and computational methods; Proceedings, IEEE, 74, p. 328-338.

NAGRA (Nationale Genossenschaft fuer die Laqerung radioaktiver Abfaelle)
1985: Grimsel Test Site – Overview and test programs; NAGRA NTB 85-46, NAGRA, Baden, Switzerland.
Niva, B., and Olsson, O.
1987: Radar crosshole tomography at the Grimsel Rock Laboratory – Results from phase 1; NAGRA, Baden, Switzerland.
1988a: Radar crosshole tomography at the Grimsel Rock Laboratory – Results from phase 2; NAGRA, Baden, Switzerland.
1988b: Radar crosshole tomography at the Grimsel Rock Laboratory – Results from phase 3; NAGRA, Baden, Switzerland.
Olsson, O., Black, J., Cosma, C., and Pihl, J.
1987: Crosshole investigations – Final report; Stripa Project TR 87-16, SKB, Stockholm, Sweden.
Olsson, O., Eriksson, J., Falk, L., and Sandberg, E.
1988: Site characterization and validation – Borehole radar investigations, stage I; Stripa Project IR 88-03, SKB, Stockholm, Sweden.
Olsson, O., Falk, L., Forslund, O., Lundmark, L., and Sandberg, E.
1987: Crosshole investigations – Results from borehole radar investigations; Stripa Project TR 87-11, SKB, Stockholm, Sweden.

Radar design for geophysical sounding

G.K.A. Oswald[1]
Cambridge Consultants Limited

Oswald, G.K.A., 1992: Radar design for geophysical sounding; in Ground penetrating radar, ed. J. Pilon; Geological Survey of Canada, Paper 90-4, p. 151-164.

Abstract

Broadband radar has been developed and used as a tool for shallow geophysical sounding by diverse groups since the mid-1970s. This paper contends that successful application is most probable with specially adapted equipment, whose design takes into account operational requirements and a conservative assessment of local conditions. Experience suggests that impulse radars operating in a time domain are as effective as those using continuous wave or synthesized waveforms. Airborne, surface, and borehole deployment systems are described, and results are illustrated.

Résumé

Depuis le milieu des années 1970, la radar à large bande a été mis au point et utilisé par divers groupes comme un outil de sondage géophysique à faible profondeur. Dans le présent article, on soutient qu'il est plus probable que l'application soit concluante si l'on utilise un équipement spécialement adapté dont la conception tiendra compte des exigences opérationnelles et reposera sur une évaluation conservatrice des conditions locales. L'expérience indique que les radars à impulsion fonctionnant dans un domaine temporel sont aussi efficaces que ceux qui utilisent l'onde entretenue ou des formes d'onde synthétisées. Les systèmes aéroportés et les systèmes installés à la surface du sol ou dans des puits sont décrits et leurs résultats illustrés.

HISTORICAL INTRODUCTION

Materials, features, and objects buried in the ground are difficult to find. The lack of ability to locate them is a basic constraint in many industrial activities, and much effort is applied trying to achieve effective through-the-earth sensing.

Radar systems for subsurface inspection have been under investigation for at least 25 years. For at least half of that time they have been used commercially for shallow probing of rocks, soils, and other materials. Many different systems have been applied to various requirements, but intense activity during the mid-1970s was followed by some disillusion with a technique that promised much but in many situations delivered an unacceptably low success rate.

Most recently, several groups including at least five in United Kingdom have become involved in this technique, looking for and in many cases solving problems facing designers. The Geophysics Group at Cambridge Consultants Limited (CCL) has worked successfully in this field for more than 5 years, and its activities are now part of the Radio Applications Group. Our business is to develop instrumentation on our clients' behalf, and we have followed a conservative development policy to minimize their risks.

We have avoided any attempt to build "general purpose" instruments for soil inspection. Although this technique generally is vulnerable to misapplication, there are many situations where appropriately designed equipment can be expected to yield results that are cost effective. We have investigated various applications and have developed purpose-built instruments, where the application was feasible and where suitable terms could be agreed.

CCL's involvement in the design of geophysical radar systems has stemmed from previous research by staff members performed while at the Scott Polar Research Institute in Cambridge. Work at the institute concentrated on penetrating polar ice sheets using air- and surface-borne pulsed radar systems (Robin et al., 1969; Oswald and Robin, 1973).

---

[1] Cambridge Consultants Limited, Science Park, Milton Road, Cambridge CB4 4DW England

This work extended over several years and showed that, besides measuring the depth of ice cover up to more than 4000 m, the radar returns could be used to distinguish between different basal interfaces. However, polar ice of this kind is a benign material, exhibiting very low losses; thus the technical challenge shifted to more demanding materials.

While probing of shallow surface layers was under development elsewhere (Moffatt, 1973; Morey, 1974), very low frequency, broadband systems were advanced by Ferrari and others in Cambridge for use on temperate ice in Iceland and later on glaciers in Karakoram (Ferrari et al., 1976). Shallow soil-probing radar systems were investigated by Evans, Theodorou, and Gorman in Cambridge (summarized by Theodorou, 1979) whose work set the scene for some of the later developments at CCL. Coal seam probing was investigated by Cook (1975) and others. In the United Kingdom, work has continued at CCL and SPRI, at Queen Mary College, London, at British Gas, at ERA Technology, and at other institutions.

Measurement of ice thickness has been a major aim at CCL, partly for historical reasons, but also because it has received much attention as a tool in arctic offshore oil and gas exploration activities. However, techniques developed successfully for this application are relevant to ice. More recently ice related research and development has dwindled and attention has shifted to other applications of the technology. CCL's work was described by Oswald (1988) in a special issue of Institute of Electrical Engineers.

There are wide geographical variations in priorities for development of ground sounding techniques. Unfortunately some of the largest markets for these techniques involve the most difficult targets and ground conditions, particularly in United Kingdom. We believe that the use of radar will advance most rapidly by combining technical improvements and conservative predictions of performance, and by minimizing its misapplication.

EARLY DESIGN DECISIONS

As an inspection method for solids, radar techniques are attractive because the impedance contrasts are relatively low – particularly in comparison with acoustic methods. However, the system designs are unconventional in radar terms.

Broadband, relatively low frequency systems are used for inspection of solids because electromagnetic attenuation increases with frequency in terrestrial materials, and because high range resolution is always required in these applications. The main system characteristics are derived by a trade-off between penetration, resolution, antenna size, and operational requirements and must be based on a firm understanding both of the types of target to be detected and the materials in which they are buried.

A ground penetrating radar systems can generally be divided into two major functional units: the data gathering system and the processing and display system. This separation is useful because quite different requirements govern the design of the two parts, and the interface between them is particularly simple, consisting only of stored data with well defined characteristics. The first part we call the "radar system", and the second the "display system".

The ultimate requirement of the radar system is that it generates stored data of sufficient quality and quantity, under well defined conditions, for any subsequent processing and analysis by the user.

The fundamental design decision for the radar system concerns the range of frequencies to be used; it is usually determined by the characteristics of the medium and a trade-off between the resolution and penetration required.

The second choice concerns the modulation scheme to be used, and from it will flow many of the more detailed aspects of the system design. This scheme will have important consequences not only for the design of the radar front-end, but also for the design of antennas and digital control and processing systems.

Other decisions involve the details of antenna and mechanical design; of data conversion and storage; of control and operational facilities such as navigation, time, and event indexing; and of the display or output format.

Once data have been gathered and stored (digital storage is important to benefit from postprocessing) it is transferred for display. In some applications on-the-spot interpretation is important, where the system is being used to guide excavators, in which case at least a basic display system must be incorporated in the field equipment.

The display system can otherwise be isolated from the radar system itself, allowing less complexity of the part of the system deployed in the field and in its own environmental specification. It accepts as its input raw data from the radar system and must provide as its output a display suitable for the user to interpret. A sophisticated system may achieve some automated interpretation, particularly if the characteristics of the wanted target are known; however, in most cases we need to make use of the powerful image processing capacity of the human eye.

Increasingly sophisticated signal- and image-processing techniques are being applied, particularly where some characteristic of the target is known and can be automatically selected or enhanced. However, it remains true that whatever processing and display facilities are to be used, their effectiveness depends on the quality of the data fed to them.

DESIGN CONSTRAINTS

In a technical study performed by CCL in 1981, the physical limiting factors and design criteria were listed. Operational requirements also greatly affect the design of the system. In what follows the reader may be assisted by reference to the block diagram of a generic geophysical radar system (Fig. 1).

Physical limiting factors

Attenuation of propagating wave in the ground as a result of dielectric and conduction losses

This universal physical effect influences the entire design of these radar systems.

Clutter from external reflectors near or above ground surface

External clutter must be considered in the layout of the system and the arrangement of the antennas, which restricts the environment in which radar sensing can be undertaken.

Filtering of radiated signal by heterogeneous ground

Variations in the medium modify the apparent backscatter impulse response of real targets and limit the effectiveness of detection enhancement by matched filter processing.

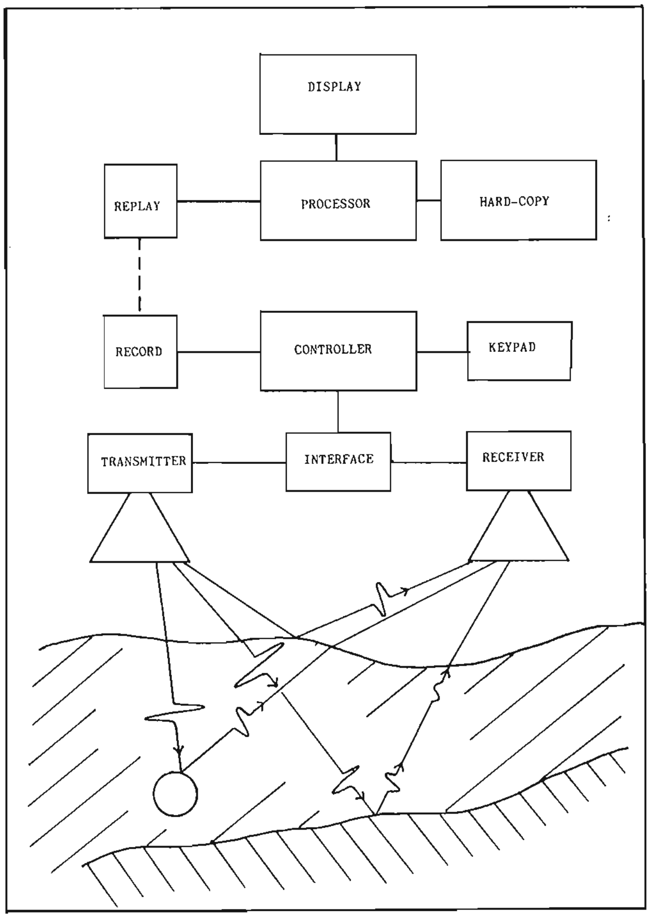

Figure 1. A generic, ground probing radar system configuration.

Design criteria

Dynamic range of receiving electronics

This limits the ability of the system either to respond to weak target reflections, or to provide a linear response to strong signals at short range. Though precise linearity is seldom required, it is frequently necessary to detect weak targets superimposed on strong returns such as clutter.

Dynamic range of display system

In the absence of automated analysis, the radar returns must eventually be displayed for interpretation, and though the eye is an excellent signal processor it functions best with good "linear" information as raw material. Nonlinear representations such as false-colour images need careful design and handling.

System generated clutter

Static clutter (generated, for example, by an aircraft or vehicle structure) can be removed by simple signal processing, subject to the limitations of mechanical and thermal stability (described below). In contrast with conventional, focused radar systems, the broadband, broadbeam output of a ground penetrating radar is hard to isolate completely from such structures.

Reverberation in transmitting and receiving electronics and antennas with their support structures

Reverberation directly limits performance. The rate of decay of each target return must be greater than the rate of attenuation in the ground for deeper targets to be distinguished.

Multiple reflections and scattering between ground surface or targets and antennas and other system components

This item has implications for the antenna design, positioning, and polarization, each of which may be used to minimize the effect.

Mechanical instability of radar probe

Mechanical instability determines the extent to which simple processing can be used to remove system clutter; in practice the antennas and their support structure, cabling, and so on, are not perfectly rigid and the associated clutter will change in proportion.

Thermal instability of radar frontend

In addition to mechanical instability the frequencies, delays, gains, power levels, noise figures, and other electronic values used in the system up to the point of digitization will change to a finite extent with time and temperature.

Instability or nonrepeatability of analogue controls

The quantitative accuracy (and therefore accessibility for digital processing) of recorded data, acquired by radar systems with continuously variable, unrecorded controls, is seriously limited.

Shortterm "jitter" of radar frontend

Jitter (timing instability) and phase instability contribute signal related noise, which dominates random amplitude disturbances where high signal slew rates occur.

Thermal noise in receiving system

Finally there is a noise "floor", which can be lowered by standard techniques of averaging and filtering but which places a practical limit on the penetration that can be achieved with a given range of frequencies.

The relative effects of some of these items are illustrated, for the case of ice thickness measurement (Fig. 2), where the thermal noise floor includes noise arising from random short-term timing jitter. Figures for attenuation in sea ice are taken from Vant (1976), whereas other signals are estimated from first principles and observed behaviour. Experience in the field has in general confirmed these estimates.

Operational requirements

The design of a ground penetrating radar system must reflect its intended mode of use. The requirement specification must answer the following questions:

1) Will the system be deployed either as a self-propelled ground vehicle; or as a towed, hauled, or portable sensor, above or below ground, on board an aircraft or helicopter, or in some other special form (such as in a borehole)? This will determine the acceptable size, weight, material characteristics, and environmental specification of the various system modules and will influence the design of interfaces between them.
2) How fast must it cover the ground? This will determine frontend and data transmission and storage characteristics.
3) Is is it necessary to obtain a rapid assessment of the signal quality?
4) Is it necessary to have full image processing and display on site? The answers to questions 3 and 4 will determine not only the level of online processing and realtime data communications required, but also the processing and display facilities that must be provided in the field as opposed to "at base".

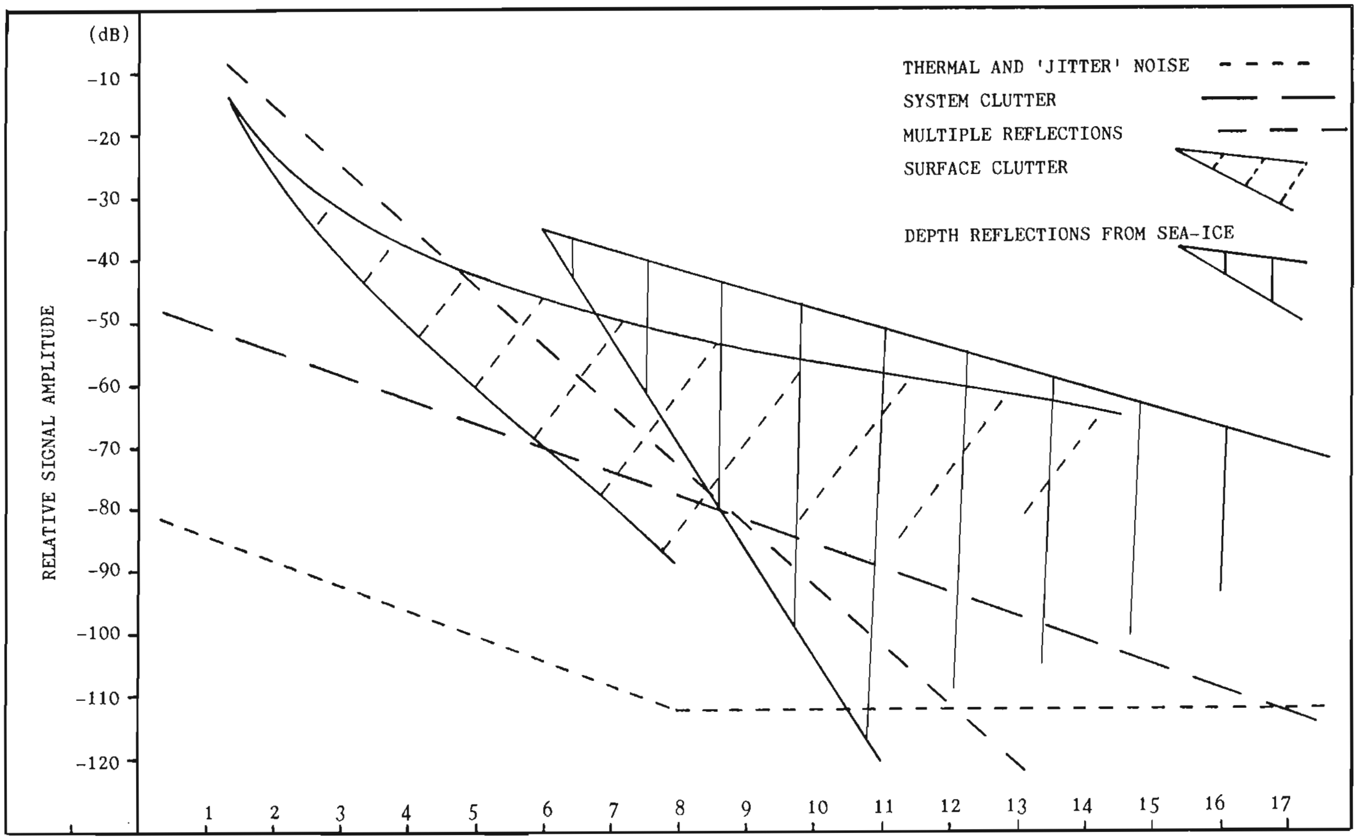

Figure 2. Illustration of relative signal strengths for various sources and targets.

It is almost always important to be able to determine the quality of data generated by radar system on the spot or within a short time of making the survey, so that it may be repeated if necessary without wasting logistical resources. However, it may be desirable to perform final processing, display, and analysis offsite.

Figure 3. Measuring ice floe thickness in flight over Alaskan Beaufort Sea.

5) Can the control, data conversion, and recording systems be located close to the two antennas and Radio Frequency (RF) electronics? This will influence the partitioning of the electronic system, and the environmental specification of critical components.

6) What power supplies will be available? What conditioning will they need?

7) What qualifications are required for use of the system under the particular conditions (for example, does it need to be intrinsically safe, or to be approved for airborne use)? This may have strong implications on cost and timescales.

8) What environmental conditions must the field equipment withstand? For example, a system for use on a helicopter in the Arctic must be capable of withstanding vibration, high wind loading on external components, and extreme cold. Use in a mine requires protection against water and dust or mud and implies restrictions on the materials and power sources used. Use on the surface may require strong protection against handling abuse.

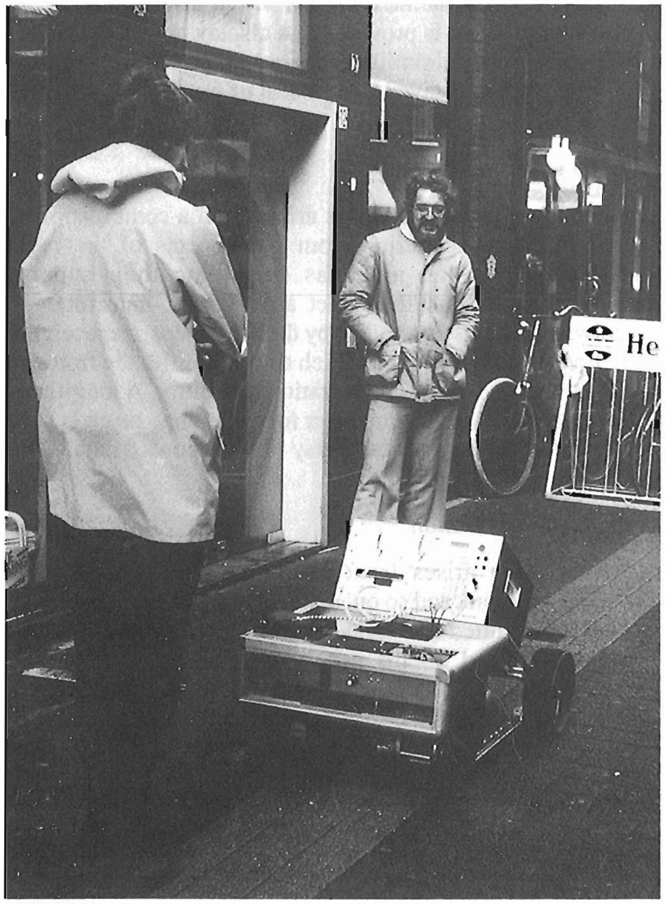

Figure 4. CCL ground probing radar cart in operation.

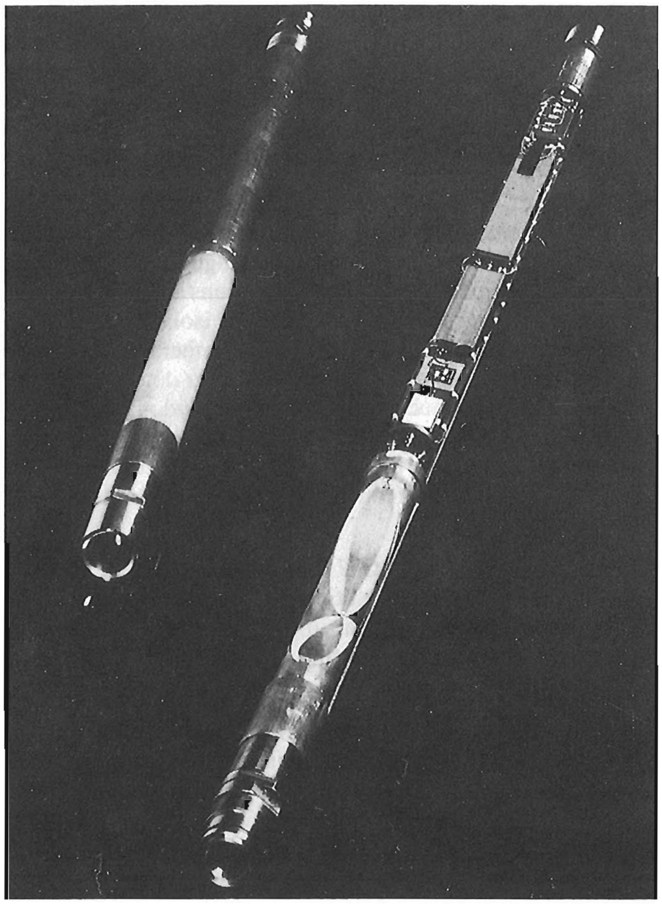

Figure 5. Impulse radar system for deployment in a borehole.

CCL IMPULSE RADAR SYSTEM DESIGNS

We have designed and constructed impulse radar systems for a variety of geophysical applications. These include

- a helicopter mounted system for measuring sea ice thickness
- a trolley mounted system for surface inspection and service location
- a system for sensing mineral seam boundaries from a borehole.

These systems are at various stages of development (Fig. 3, 4, 5); most of our field experience to date has involved the helicopter mounted system.

Impulse radar compared with broadband continuous wave systems

Broadband radar systems may be implemented in several different ways, which can be divided into those that use the broadband characteristics of a transient impulse to generate the necessary spectrum and phase relationships in the radiated field, and those that use continuous wave (CW) or quasi CW techniques.

Conceptually, many of the advantages lie on the side of CW techniques. These include a high transmitter duty cycle, and precise control over the characteristics of the radiated signal and over its processing in reception. In principle these modulation schemes help the designer to overcome problems of broadband noise, imperfections in antenna response, and inconveniences in the response of the propagation medium.

However, we have concluded that the expected benefits of CW schemes, though large in concept, are difficult to realize in practice. The major challenges in constructing successful equipment for these applications arise not from the laboratory characteristics measured in isolation, but from their performance in the imperfect environment in which they are put to work. In practice, the ability to detect targets of interest is limited much less severely by random noise or by isolated imperfections of the antennas and electronics than by the presence of other, unwanted targets or disturbances that are real and cannot be reduced by the standard techniques of noise reduction.

For example, though CW schemes in principle allow, for example, phase compensation for dispersive broadband antennas, proximity to varying propagation media will disturb the response of the antenna and render the compensation invalid.

Adaptive systems can be contemplated but involve sophisticated online signal analysis, coupled with extensive predictive knowledge of the behaviour of the antenna. Though sophisticated organization and control is available, selecting an optimum arrangement is a serious exercise in itself. In implementing these systems there is also, of course, a cost penalty.

As a result we have, to date, worked with systems based on the radiation of transient impulses into the medium under inspection, and employing conventional sampling techniques on reception.

General characteristics of the impulse radar system

Dynamic range of receiving electronics

The receiver employs a broadband RF amplifier, sampler, and signal averaging circuits, which together yield a dynamic range of typically 96 dB rising to 120 dB for some systems. A 16 bit A/D conversion has normally been used after the averaging process, and raw data are recorded on digital tape.

The "System performance" figure-of-merit used to describe some systems is of little practical value in most cases. It can be calculated for these systems as ranging from 126 dB to 166 dB, which represents the ratio of transmitter output power to minimum detectable signal at the receiver input. Very high repetition rates are used with receiver filtering to achieve very low effective noise levels.

Dynamic range of display

A fibre optic oscillographic recorder is used to give hard-copy, grey-scale plots of the radar output and offers up to about 25 dB dynamic range for visual inspection. Digital gain compensation is provided as a display option. Real time video display with similar dynamic range is also used for airborne work and saves a great deal of paper.

System generated clutter

Static clutter in these systems arises from a combination of reflections and scattering from components of the radar system outside the antennas (including their support structure), and from the direct arrival from transmitter to receiver. Clutter is minimized by the use of separate receiving and transmitting antennas, which also simplifies the frontend engineering and allows polarization flexibility. A long-time-constant, high-pass, digital filter for each range beam is used to remove these signals on replay of the recorded data.

Impulse reverberation

Reverberation arises from the impulse response of the antennas, feeders, and so on, resulting in a finite ringing 'tail' to any transmitted and reflected signal. Ring-down rates of between 10 and 20 dB can be achieved during a time corresponding to the period of the nominal bipolar output pulse, depending on the medium and matching conditions.

Multiple reflections and external clutter

This item covers clutter signals whose propagation involves reflection or scattering at the ground or ice surface, or transmission through its upper layers. They cannot be removed in the same simple way as static clutter, nor do they involve the target itself for which some selective processing can be applied.

Scattering from irregularities at the surface, including various ice ridges and blocks, boulders, curbs, vehicles, buildings, and pedestrians, constitutes a serious constraint. An antenna is required that is effectively shielded from surficial features. The type of antenna developed by CCL for surface and airborne use provides a large measure of shielding. Clutter from the surrounding structure of a helicopter platform is largely restricted to the skids. When working on the ground, our experience shows that external targets have not been a problem. Irregularities do, however, disturb the matching of the antennas into the surface, and some surface preparation is likely always to improve the stability of the whole system. Where significant ground clearance exists, as with the helicopter system, cracks, faults, surface rubble, and vehicle reflections can mask target reflections.

Mechanical instability

The helicopter-borne system is attached rigidly to hard points on the aircraft, and vibration has not been a problem with the system except under fault conditions. However, clutter variations because of the rotating helicopter blades have occasionally caused problems.

CCL's surface based radar system is assembled as a rigid, self propelled cart. Ground clearance variations beneath the antennas are the only significant mechanical source of clutter instability, though minor effects have been attributed to the motor power conductors or supports.

Thermal instability

Variations in sample delay are the most critical source of thermal instability. The electronics determining the delay provide a degree of temperature compensation, and substantial metalwork provides a high thermal mass. It is advisable to operate transmitting and receiving electronics continously to avoid thermal transients on start up. Choice of critical components can be important, and we have moved away from the use of avalanche devices, which are generally thermally stressed.

Instability and nonrepeatability in analogue processing

Data in CCL impulse radar systems is recorded digitally after undergoing only linear, time invariant processing. The range window selected for sampling and conversion is recorded with the data, which are therefore quantitative and repeatable. Subsequent processing is performed digitally. Instability or indeterminacy in analogue processing components is, therefore, eliminated.

Jitter

Timing accuracy is of prime importance in an impulse radar system. Short-term errors (jitter) amount to about 20 ps rms, though more recent designs (using hour delay- and pulse-generating elements) show a significant improvement on this figure. The figure of 20 ps relates to systems employing avalanche devices as the transmitting and sampler pulse-generating elements. Pulse initiation is a chaotic process, which, though naturally temperature dependent, cannot be described in purely thermal terms.

Thermal noise

By using a linear RF amplifier at the receiver front end, an effective noise figure of 4-6 dB can be achieved.

Operational characteristics

The systems developed at CCL are shown in Table 1.

Table 1. Systems developed at CCL

	Ice penetrating radar	Surface radar	Borehole radar
Platform	Helicopter-mounted	Self propelled	Self contained
Quality assessment	Real time	In the field (Experimental)	Offline
Field processing	No	No	Required for operational use
Control and recording	Inboard	Onboard	Internal control External recording
Power supplies	Aircraft DC	Battery	Safe battery
Special qualifications	Aircraft approval	None	Mine regulations
Environment	Vibration, temperature	Dust, mud	Water

Antenna designs

The antenna design used to date in CCL impulse radar systems evolved, with fairly radical changes, from the tapered impedance travelling-wave antenna developed by Evans, Theodorou, and Gorman (Theodorou, 1979); it was initially proved using small-scale physical models with correspondingly short drive pulses.

The range of frequencies required for the first full-scale system extended from the high tens to the low hundreds of Megahertz; a one-sixth scale antenna model was used initially; further development for the airborne system took place at a later stage using one-fifth scale antennas attached to a one-fifth scale model of a helicopter.

Though the technique can lead to uncertainties as a result of imperfect modelling, it can offer enormous benefits in terms of time and cost because real trials may involve flying helicopters or large solid test beds; costs can run into hundreds of pounds (dollars) per hour and the range of available experiments is extremely limited.

We were trying to achieve an antenna that could be used close to large metal structures, that would radiate energy at frequencies whose wavelengths are comparable with or larger than features of the structure, that (in the case of an airborne system) would be unaffected by the helicopter rotors and by vibration, and that would provide the necessary signal bandwidth to achieve resolution of a fraction of a metre.

We have in each case used separate transmitting and receiving antennas, to minimize system clutter and the complexity of the front-end electronics. In practice, the use of separate antennas also allows greater flexibility in operating the system.

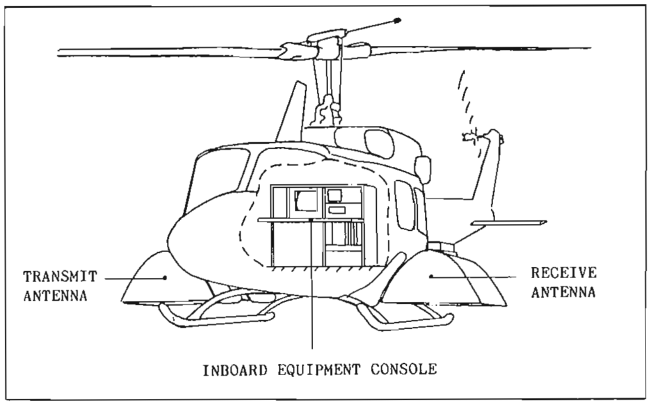

Figure 7. Helicopter system arrangement.

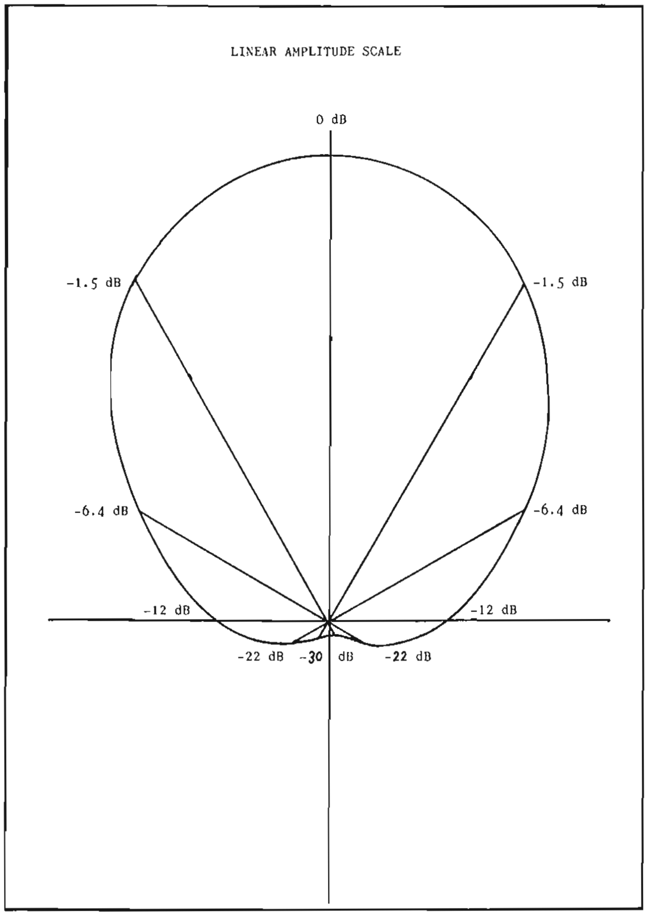

Figure 6. Azimuth polar plot (H-Plane) for an STL antenna.

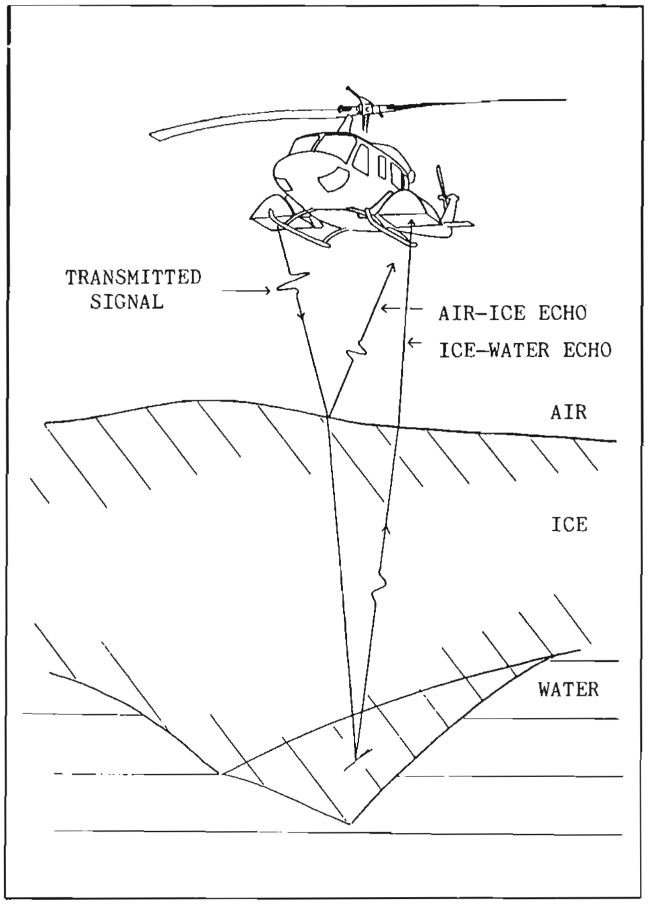

Figure 8. Helicopter mode of operation.

We have used the label "sectored transmission-line" for the family of antenna designs of which these are a member; they achieve a broad bandwidth and high backwards isolation at the expense of some efficiency and operate with pulses whose length is large compared with the maximum dimension of the antenna.

A tubular version of this antenna design has been implemented for use in boreholes, as described later.

A polar diagram for one version of this antenna is shown in Figure 6.

Impulse radar for measuring sea ice thickness

There is a requirement in the offshore resources industry in the Arctic for extensive surveys of the thickness of the sea ice cover. Numerous attempts have been made with broadband radar by various American and Canadian companies and establishments (Kovacs and Morey, 1979; Rossiter, 1979). These efforts have indicated that the objective can be achieved for some types of ice but have not yet yielded industry accepted equipment for the task.

Development of an impulse radar system for this purpose began in 1983 based on the requirement stipulating operation from a helicopter and the ability to measure the thickness of both first- and multi-year ice.

The program has been performed under conditions where timescales were unyielding and testing was only possible under severe constraints. The success of the program and the system probably owes as much to the overall development philosophy and contractual relationships as to particular items of the technical solution.

The Arctic offshore industry operates with obvious seasonal fluctuations, and the ice that forms the greatest hazard is encountered during a more or less reliable period of late winter and early spring. The summers of 1983, 1984, and 1985 were spent considering the approach for the following season, the autumn getting contracts under way, and the winter feverishly working to meet the spring deadline; the ice waits for no-one.

The spring of 1984 saw the first deployment of a system employing antennas of a novel design and electronics whose design owed more to the need for repeatability and quantitative accuracy than to experimental flexibility. Subsequent seasons demonstrated the operation of further modifications and facilities.

In this case, the system requirement specified the use of a helicopter as the radar platform. A diagram of the arrangement of the system is shown in Figure 7; its mode of operation illustrated in Figure 8.

Under these conditions the requirement for structural reliability, electromagnetic compatibility (EMC), and aerodynamic acceptability is practically if not logically prior to that for the equipment to work. The antennas were subjected to severe in-site stress tests to prove survivability, and following additional EMC and flight tests, administrative approval was obtained.

Testing facilities for the full-scale system at Cambridge were barely adequate – in fact they indicated that, though small-scale model results were acceptable, the pulse shape might be degraded at full scale. However, the antenna design has the advantage of several degrees of freedom in which its characteristics can be "trimmed". We took advantage of this feature and proceeded with field trials, where a very acceptable pulse shape was obtained with the system mounted on the helicopter.

The system has been outlined by Paulley et al. (1987). Figure 3 shows the system in operation in 1986. The scale of one antenna can be seen, and it is clear that it is approaching the limits of aerodynamic modification of the aircraft. RF electronics are located close to the antennas to minimize the effect of cable reflections, losses, or movement.

Two examples of floe profiles obtained with this equipment are shown in Figure 9A, B. The plot shows a vertical slice of the floe. The upper, sharply defined line represents the ice-air interface; the lower, thicker line represents the ice-water interface. Higher frequencies in the upper surface reflection are attenuated as a proportion of the lower reflection, as a result of increasing dielectric absorption with frequency. The pulse shape is not ideal because there is some structure trailing each first arrival; however, it provides a good basis for immediate interpretation and can be improved by digital matched filtering. Figure 10A, B shows a profile of much thinner first year ice. Using a reference waveform obtained from a known, extended, totally reflecting surface (sea water), we have applied a digital matched filter to obtain clear upper and lower surface reflections (Fig. 10A) from ice less than 2 m thick.

Three experimental trials were carried out during successive arctic spring seasons in 1984, 1985, and 1986. In 1985 we experienced some difficulties with new equipment. When second year ice floes were selected as targets, the interpretation of results required expert attention and at that stage would not have been acceptable in commercial operation. However, the results obtained in that year compared favourably with those obtained over the same ice by Kovacs (1987) using an electromagnetic induction sensor. On inspection the impulse radar provided measurements at 70% of the positions where drill comparisons were obtained, and showed much of the detailed ice profile. The mean ice thickness measured by drilling was 3.66 m, whereas the average of the radar readings was 3.78 m. Spot measurements showed an rms deviation of about 25%, though positioning errors combined with the relatively steep slopes of the second year floe probably account for half of the measurement errors. Kovacs' induction measurements also deviate by about 25% rms but show none of the detail evident from the drilled and radar data.

Having made this point, note that both instruments were under development, and that limitations must be expected. We believe that induction sensors may be preferred both for measurement of thin or warm ice, and for average measurements over wide areas. However, for detailed inspection of thick, consolidated ice floes, radar should be the preferred method.

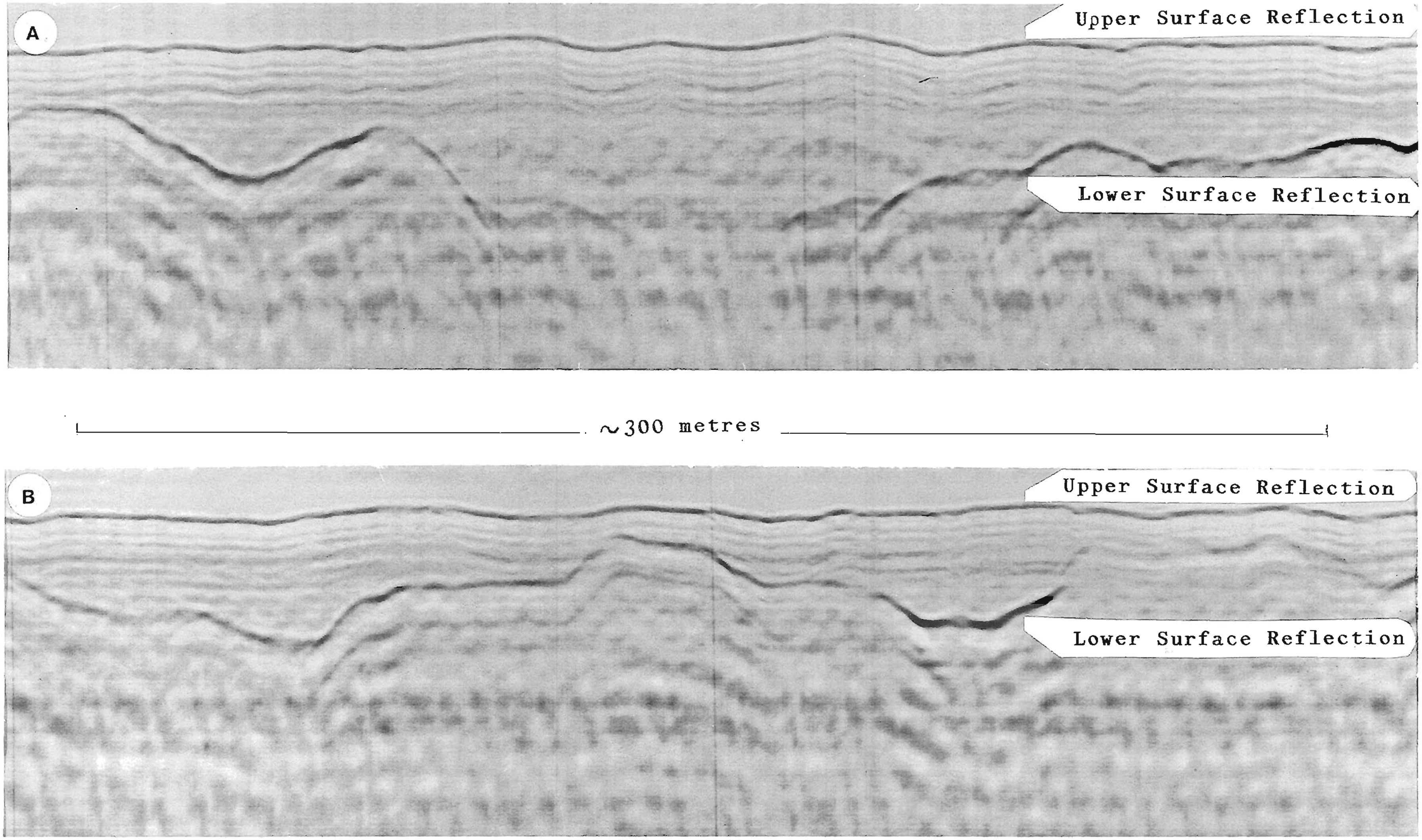

Figure 9A. A multiyear ice keel deeper than 11 m; **B**. An irregular, multiyear floe profile showing block sttructure.

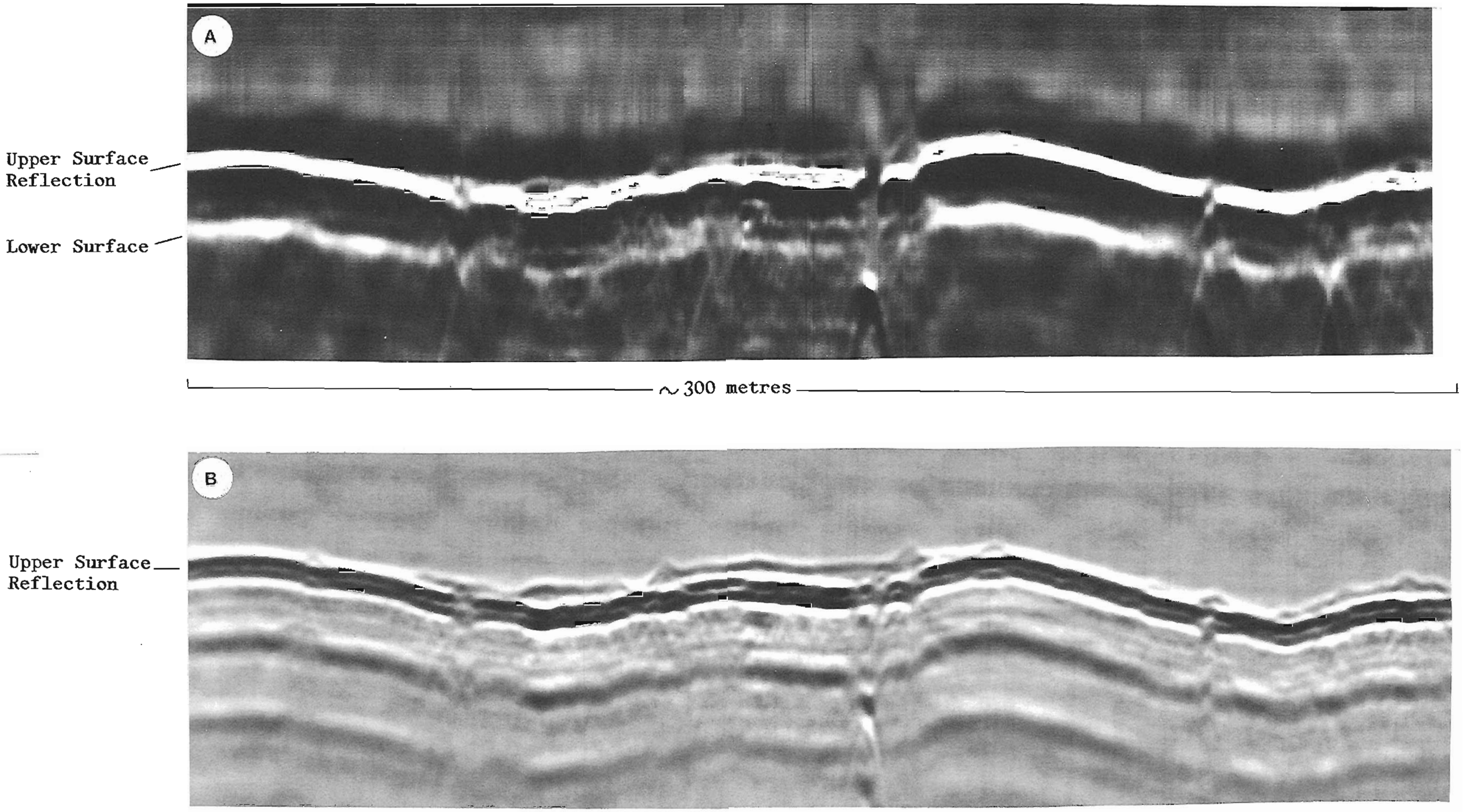

Figure 10A. Annual ice profile after matched filtering;the lower surface reflection is resolved (thickness is 1.0-1.2 m). **B**. The same data unfiltered. The lower surface is obscured by signal artifact.

Problems encountered in 1985 were overcome before successful trials were carried out in 1986, providing clear and easily interpreted profiles of multiyear floes, with measurement accuracy of 0.3 m (rms). The system is now available for use in offshore investigations.

The radar system elements have now been developed to the point where it can be offered for commercial data-gathering operations.

Impulse radar probe for surface inspection

In the surface based system (Fig. 4), the radar system output is digitized and recorded on the probe cart. There is no physical connection to the outside world; the data acquisition and display processes are completely decoupled, processing and display being performed only on replay of the digital tapes generated by the radar system.

The cart incorporates a minimum integrated electronics system to provide repeatable, self-documenting data recording on board a mechanically stable, self-propelled antenna platform.

We have implemented an antenna design that allows radiation with a smooth phase response over a 10:1 frequency range, with a high front-to-back ratio, which allows it to be used close to metal components of the cart and electronics package and isolates it effectively from external targets such as buildings, vehicles, and pedestrians.

The system is designed as a testbed for experiments with different targets, materials, antennas and pulse shapes. Its features are

- constant speed, self-propelled
- annotated digital tape records
- compact 6U rack includes tape recorder, 16-bit VME bus processor, interfaces (IEEE-488), controls, and power supplies
- 100-1000 MHz operating frequency range
- 1 MHz pulse repetition rate
- dynamic range: 96 dB
- scan rate: 10 Hz
- tape capacity: >90 min.

The cart travels in a straight line until stopped by the operator; disturbance of the record by the operator's presence is minimal. The tape can be addressed in blocks, and a new block is entered as the start address for each run together with range window selection. Data can either be replayed directly from the cart onto a grey-scale recorder, or be transferred via IEEE-488 interface to computer compatible nine track tape.

The radar cart is used to improve the data gathering part of the process for different targets and materials. Different display processes have been seen as secondary to generating good raw data and are very much dependent on the ultimate

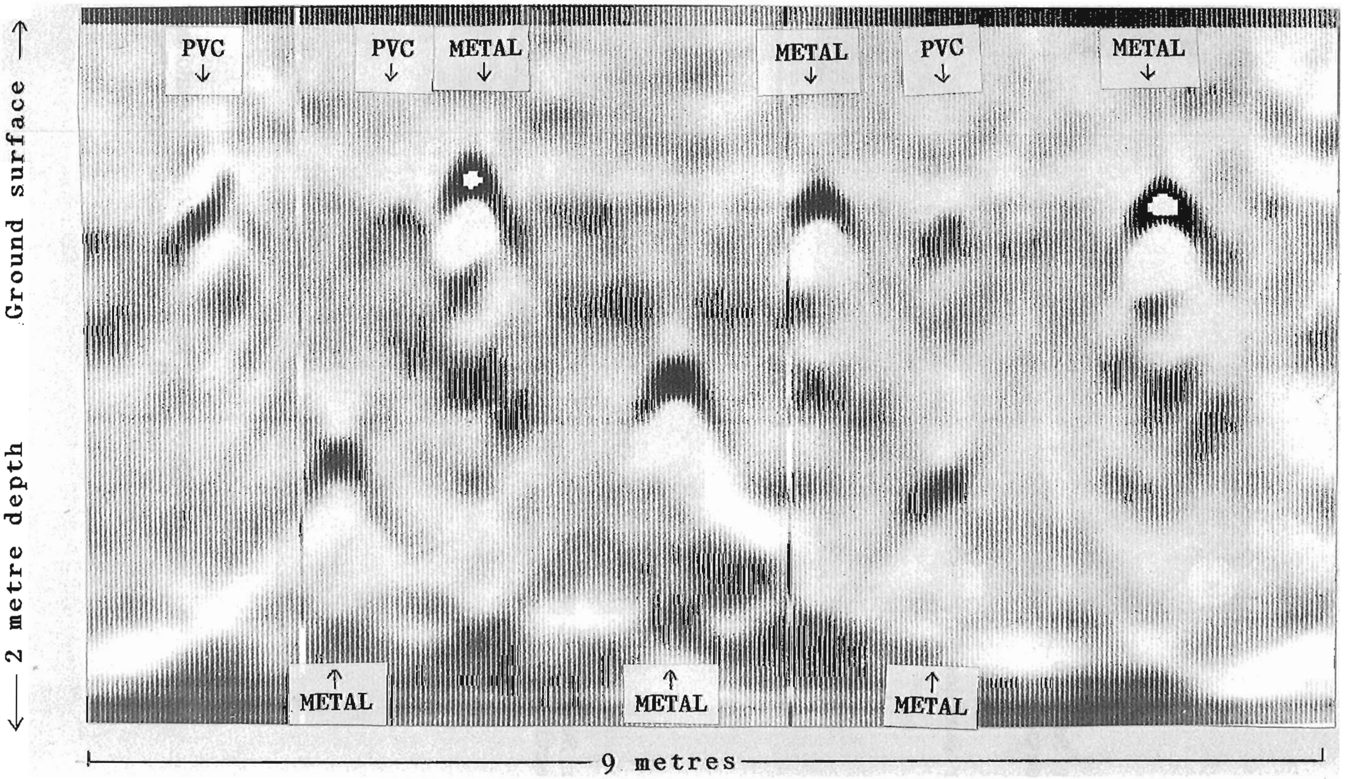

Figure 11. Unprocessed returns from metal and plastic pipes buried in sand (partial record).

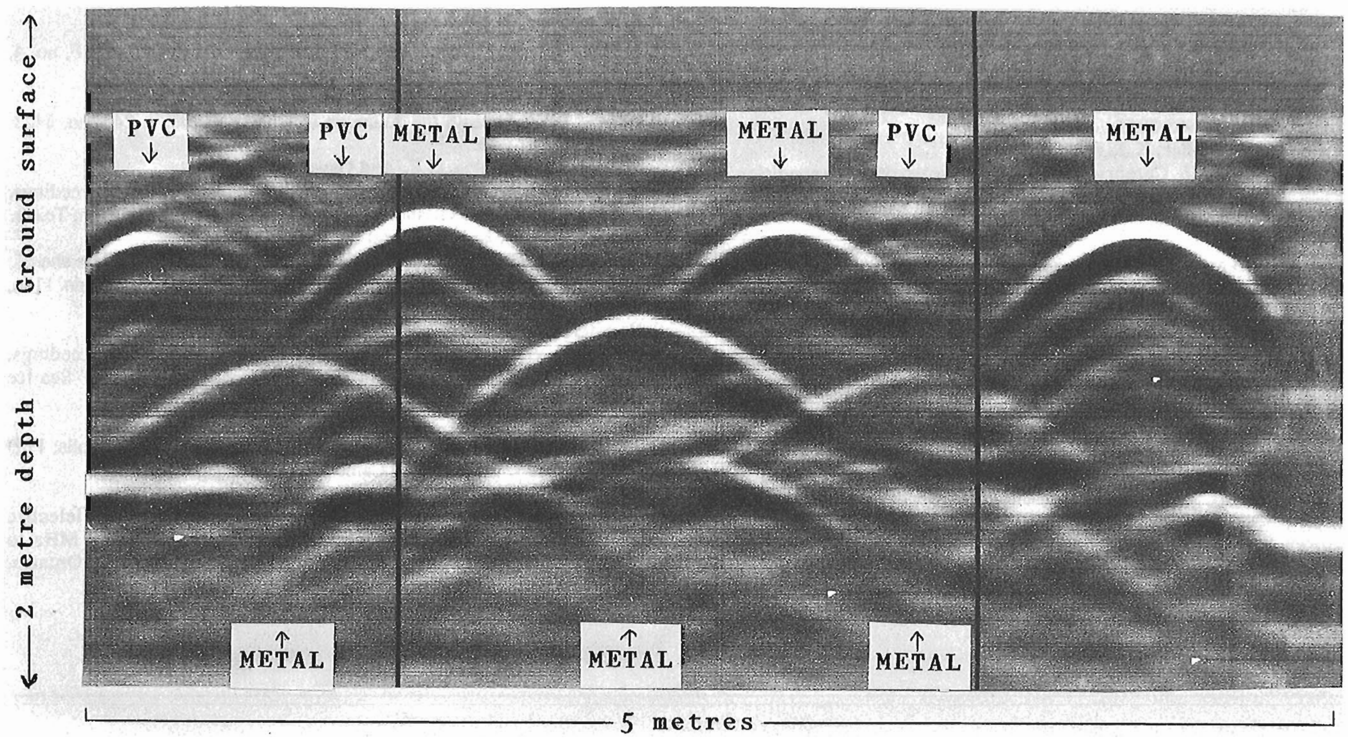

Figure 12. Pipe positions after hyperbolic migration.

purposes of the user; however, this is now a more active target for development. Pulse compression and migration processes have been implemented, and target-selective analysis is under consideration.

An example of a plot showing pipes buried in sand is shown in Figure 11. After migration processing to narrow the effective beamwidth, the plot in Figure 12 is obtained, showing the pipe positions. These were known metal and plastic targets buried in sand at depths of up to 1.5 m, and positional errors were of the order of 5 cm. We emphasize that this is a benign medium, used for comparative tests.

Borehole system for mineral seam sensing

CCL has worked with the sponsorship of British Coal in developing a radar system for use in a borehole. We have once again adopted the approach of testing the antenna concept in the form of a small-scale model before proceeding to full-scale development. Separate transmitting and receiving antennas are used, and again they can be described by the term "sectored transmission-line" antennas. For the borehole they are folded within a 70-mm diameter tube, for attachment to a standard drilling pipe, and radiate over a band from 50 to 500 MHz. Each antenna provides a front-to-back ratio greater than 14 dB, giving discrimination of over 28 dB for the pair in reflection mode. The beam pattern varies in detail with the transmission medium but gives good directional information.

Signal generation and reception are carried out by miniaturized electronics within the antenna tube. The system (Fig. 5) can operate as a self-contained system requiring only a single 12 volt power input and returning synchronous high resolution LF analogue output data to the surface. Trials in coal are being conducted by British Coal.

CONCLUSIONS

Radar sounding of soils, rocks, and ice is an extremely promising technique, which is developing rapidly and showing increasing commercial benefits.

However, each set of conditions under which it is proposed to be used, must be assessed and the scale of development and application must be suited to the level of confidence arising from this assessment. It is not appropriate to attempt to design a standard system and hope to apply it indiscriminately with an acceptable rate of success.

Each of the systems built by CCL to date has been designed to derive maximum information about the limitations and potential performance of broadband radar under various conditions. In each case to date the answer has been that the technique can be highly cost effective, if appropriate equipment is used under the correct conditions; with the wrong equipment or under bad conditions it is an expensive method that provides no information.

REFERENCES

Cook, J.C.
1975: Radar transparencies of mine and tunnel rocks; Geophysics, v. 40, no. 5, p. 865-885.

Ferrari, R.L., Miller, K.J., and Owen, G.
1976: The 1976 Cambridge-Reykjavik universities expedition to Vatnajokull, Iceland. Cambridge University Engineering Department Special Report 5.

Kovacs, A.
1987: Airborne electromagnetic sounding of sea ice thickness and sub-ice bathymetry; CRREL Report 87-23. US Army Cold Regions Research and Engineering Laboratory, Hanover, N.H., 47 p.

Kovacs, A. and Morey, R.M.
1979: Investigations of sea ice anisotrophy, electromagnetic properties, strength and under-ice current orientation;Proceedings, International Workshop on the Remote Estimation of Sea-Ice Thickness, St. Johns, Newfoundland, p. 109-153.

Moffatt, D.L.
1973: Subsurface applications of periodic electromagnetic video pulse signals; Proceedings, Thru-the-Earth Electromagnetic Workshop, Colorado School of Mines, Golden, 15-17 Aug.

Morey, R.M.
1974: Continuous subsurface profiling by impulse radar; Proceedings, Engineering Foundation Conference on Subsurface Exploration of Underground Excavation and Heavy Construction, Heuniker, N.H., p. 213-232.

Oswald, G.K.A.
1988: Geophysical radar design; Proceedings, IEE, v. 135, pt. F, no. 4, p. 371-379.

Oswald, G.K.A. and Robin, G. de Q.
1973: Lakes beneath the Antarctic ice sheet; Nature, v. 245, no. 5423, p. 251-254.

Paulley, T.A., Gehrig, G.F., and Oswald, G.K.A.
1987: Measurement of arctic sea ice using impulse radar; Proceedings, 19th Annual Offshore Technology Conference, Houston, Texas.

Robin, G. de Q., Evans, S., and Bailey, J.T.
1969: Interpretation of radio echo sounding in polar ice sheets; Philosophical Transaction of the Royal Society A, v. 265, no. 1166, p. 437-505.

Rossiter, J.R.
1979: Review of impulse radar sounding of sea ice; Proceedings, International Workshop on the Remote Estimation of Sea-Ice Thickness. St. Johns, Newfoundland, p. 77-107.

Theodorou, E.A.
1979: The design of a radar sounding system for rocks and soils; PhD Thesis, University of Cambridge, Cambridge, UK.

Vant, M.R.
1976: A combined empirical and theoretical study of the dielectric properties of sea ice over the frequency range 100 MHz to 4 GHz; PhD Thesis, Carleton University, Ottawa, Ontario, 438 p.

Ground probing radar in the investigation of permafrost and subsurface characteristics of surficial deposits in Kangiqsualujjuaq, northern Quebec

J.A. Pilon[1], M. Allard[2], and M.K. Séguin[2]

Pilon, J.A., Allard, M., and Séguin, M.K., 1992: Ground probing radar in the investigation of permafrost and subsurface characteristics of surficial deposits in Kangiqsualujjuaq, northern Quebec; *in* *Ground penetrating radar, ed. J. Pilon; Geological Survey of Canada, Paper 90-4, p. 165-175.*

Abstract

Four geomorphological units were probed with ground penetrating radar (GPR) to investigate the internal structure and composition of surficial deposits near Kangiqsualujjuaq on the east coast of Ungava Bay. The results obtained in the field have furnished information on the active layer, details of the internal stratigraphy, as well as the location of the base of ice-bearing permafrost. These results illustrate that GPR is a useful geophysical tool for the study of surficial deposits in areas of permafrost.

Résumé

Quatre unités géomorphologiques ont été sondées à l'aide d'un géoradar pour en étudier la structure interne et la composition des dépôts de surface près de Kangiqsualujjuaq sur la côte est de la baie d'Ungava. Les résultats obtenus sur le terrain ont donné des renseignements sur le mollisol et des détails sur la stratigraphie interne et la profondeur de la base du pergélisol contenant de la glace. Ces résultats illustrent le fait que le géoradar constitue un outil géophysique utile à l'étude des dépôts de surface dans les zones pergélisolées.

INTRODUCTION

In the Canadian Arctic, detailed studies of permafrost and structure of surficial deposits are limited by the lack of both cores from boreholes and natural sections. In the last decade geophysical methods have increasingly been used to investigate surficial deposits (Séguin and Allard, 1987; Scott et al., 1978). Recently, the availability of a high power, multifrequency, digital ground probing radar (GPR) system to the Geological Survey of Canada has significantly increased our ability to profile and investigate the internal makeup of surficial deposits (LaFlèche et al., 1987). In this paper we present the results of four GPR surveys conducted over different Quaternary substrates during the summer of 1986 in Kangiqsualujjuaq on the east coast of Ungava Bay in northern Québec. At this location, staff of the Centre d'Etudes Nordiques of Université Laval have conducted detailed studies of permafrost since 1984 (Allard and Séguin, 1987; Fournier et al., 1987; Gahé et al., 1987; Séguin and Allard, 1987). Through these activities, a variety of Quaternary geological deposits have been instrumented with multithermistor cables to study permafrost characteristics and investigated by varied geophysical methods comprising electrical resistivity, induced polarization, self-potential and electromagnetic surveys (Gahé et al., 1987). In addition, both natural and artificial sections through the deposits are also available; the Kangiqsualujjuaq region thus constituted an ideal test site for the GPR because of the substantial body of knowledge available to help with the interpretation of the radar survey results.

---

[1] Geological Survey of Canada, 601 Booth Street, Ottawa, Ontario, Canada, K1A 0E8
[2] Université Laval, Centre d'Etudes Nordiques, Québec, Canada, G1K 7P4

REGIONAL SETTING

The Kangiqsualujjuaq region (Fig. 1) is situated on the treeline; black spruce and tamarac occur in sheltered valleys south and up to 40 km northeast of the village. The regional treeline appears to be maintained a few kilometres inland because of the climatic influence of Ungava Bay (Payette, 1983). The climate of the region is characterized by low daily thermal amplitude in summer and large daily thermal amplitude in winter with the frost season carrying well into June (Thériault, 1983). The average annual temperature is estimated at -5.3°C; that of January at -22°C and that of July at 9°C (Fournier et al., 1987). The annual total precipitation is estimated to be between 350 and 400 mm, of which 40-45% occurs as snow (Wilson, 1971). Prevailing winds measured at the Centre d'Études Nordiques weather station in Kangiqsualujjuaq are predominantly west-southwest.

The surficial materials are influenced by the history of glacial, periglacial, and marine events and comprise the following major classes: (1) bedrock, usually exposed on moderate to steep slopes below marine limit at about 100 m above mean sea level (asl); (2) till, mantling plateaus and slopes, where it has been subject to modification by solifluction or wave washing, or both; (3) sands and gravels of glaciofluvial and deltaic origin; (4) silty clays of marine origin on valley floors below 100 m asl; (5) sands and gravels forming raised beaches; (6) organic deposits forming peat plateaus, palsas, and peat hummocks; (7) intertidal mud flats strewn with boulders.

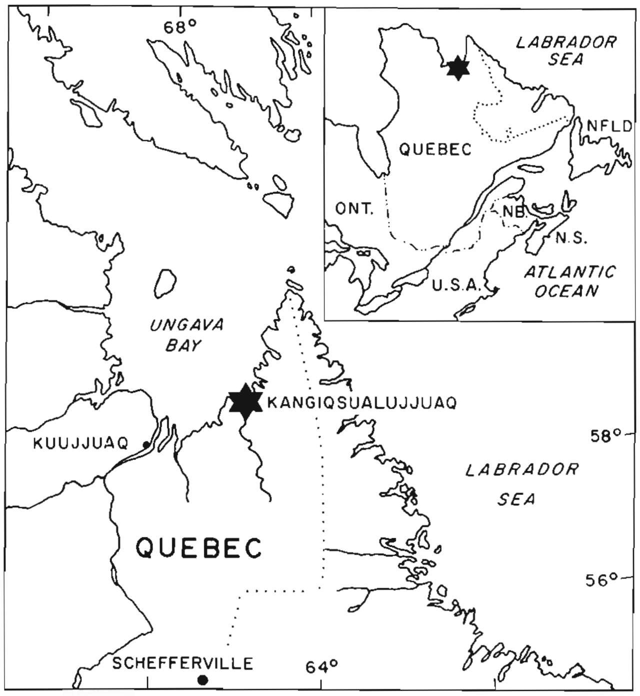

Figure 1. Site location of Kangiqsualujjuaq, northern Québec.

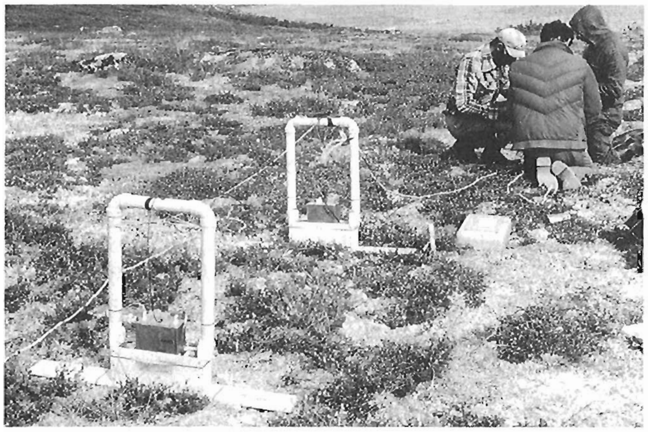

Figure 2. The pulse EKKO III ground probing radar system, on the marine terrace in Kangiqsualujjuaq. The system consists of transmitter and receiver antenna packages and a central control unit. The various units are connected by fibre optic cables.

Figure 3. Photograph of a section at site 1 showing thick, bouldery till overlain by 1 m of fluvial sands, above an unconformity; the radar profile was made on top of this terrace.

Table 1. Typical dielectric constant, electrical conductivity, velocity and attenuation observed in common geologic material (f ≈ 100 MHz) (after Annan, 1983)

Material	K	$\sigma(mS.m^{-1})$	$v(m.ns^{-1})$	$\alpha(dB.m^{-1})$
Air	1	0	0.3	0
Distilled Water	80	0.01	0.033	$2x10^{-3}$
Fresh Water	80	0.5	0.033	0.1
Sea Water	80	3000	0.01	10^3
Dry Sand	3-5	0.01	0.15	0.01
Fresh Water Saturated Sand	20-30	0.1-1.0	0.06	0.3
Limestone	4-8	0.5-2.0	0.12	0.7
Shales	5-15	1-100	0.09	5
Silts	5-30	1-100	0.07	6
Clays	5-40	2-1000	0.06	15
Granite	4-6	.01-1	0.13	0.07
Dry Salt	5-6	.01-1	0.13	0.06
Ice	3-4	0.01	0.16	0.01

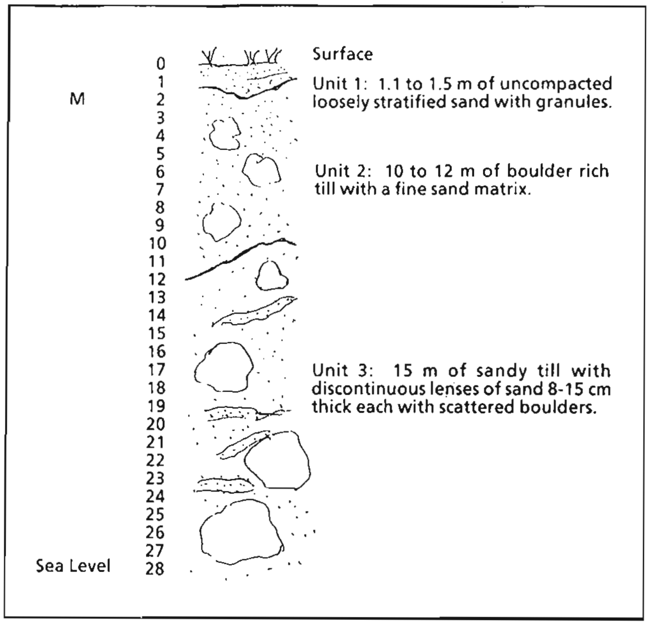

Figure 4. Stratigraphy at site 1, a fluvial terrace cut in a thick, bouldery till deposit as measured in the cliff face.

The study sites discussed in this paper were selected to represent these surficial deposits and include till, wave reworked glaciofluvial deposits, marine clay silt, and peat.

METHOD

Ground probing radar is a relatively new geophysical tool. The first commercial model became available in the mid 1970s. GPR operates on the same principle as conventional radars in that a short pulse of electromagnetic energy is emitted by a transmitter antenna, reflects off a distant electrical boundary, and the reflection is picked up by a receiver antenna. The time taken for the pulse to travel from the transmitter to the receiver antenna via the reflector is measured (Davis and Annan, 1989), and the distance to a reflector can be calculated when the propagation speed of the pulse in the material is known. The propagation velocity can be measured in situ by conducting a common mid point (CMP) or a wide angle reflection and refraction survey. In air, the pulse travels at the speed of light (0.3 m/ns). In the subsurface, the pulse travels slower dependent upon the electrical properties of the material traversed. Table 1 presents typical dielectric constants, electrical conductivities, velocities of propagation, and attenuation factors observed in common geological materials for a frequency of 100 MHz.

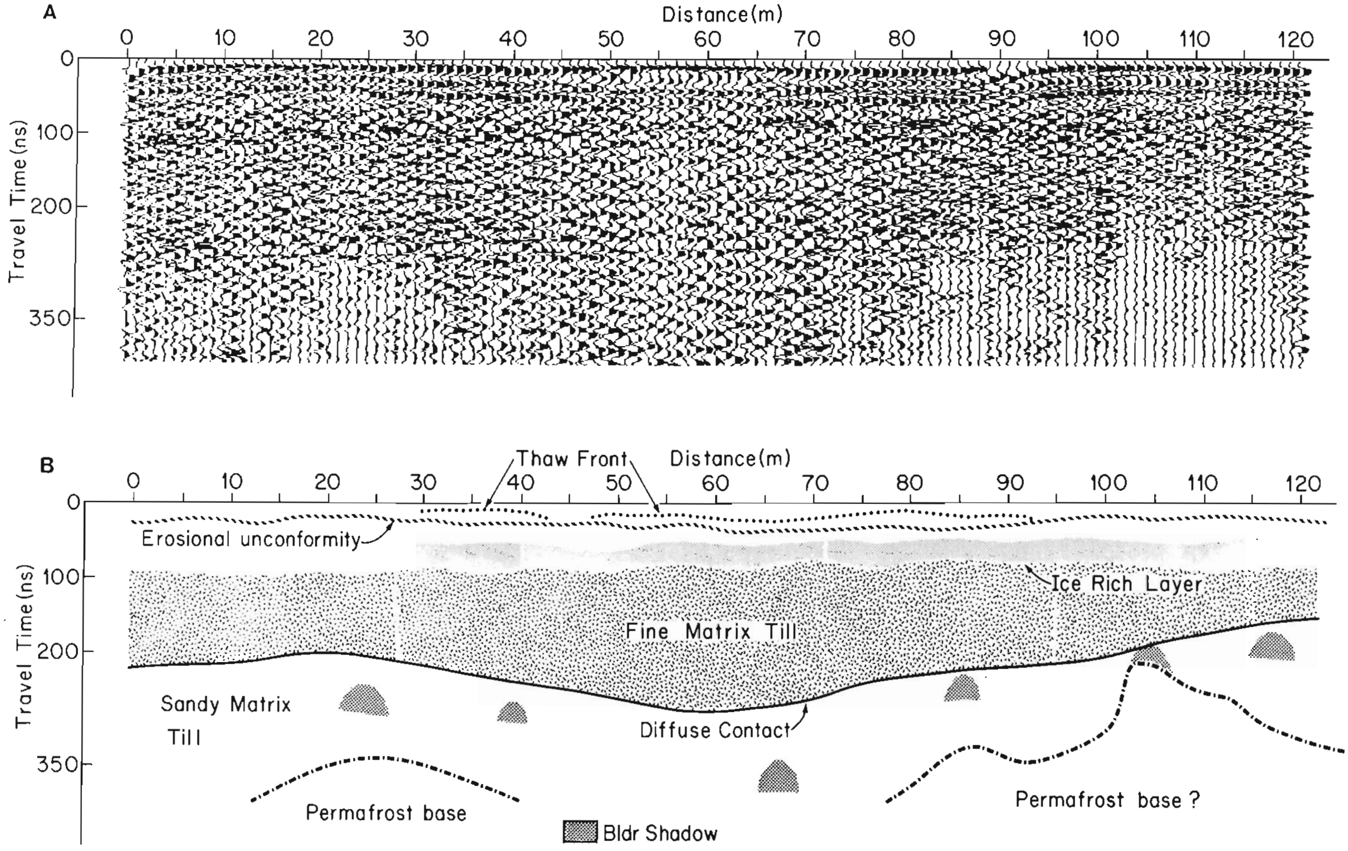

Figure 5A. The 100 MHz ground probing radar profile obtained at site 1 in Kangiqsualujjuaq; **B.** The summary interpretation diagram of the same profile.

Reflectors detected with a GPR system are caused by dielectric contrast in the subsurface materials. Common causes of subsurface reflections are material interfaces (overburden-rock, sand-clay, and so on), water table limits, boundaries between frozen and unfrozen water, and ice lenses. A large dielectric contrast exists between water and most geological materials (Table 1). As such, the presence or absence of water controls to a large degree the subsurface propagation characteristics of the radar pulse (see contrast between dry and freshwater saturated sand; Table 1). Thus the ability of a material to retain water within its pore space is an important factor in the determination of its bulk electrical properties. The depth to which a radar pulse will effectively penetrate depends on the electromagnetic absorption characteristics of the subsurface (see Table 1). The pulseEKKO III system used in this study (Fig. 2) is a fully digital, ground probing radar system with a system performance of 150 dB, which incorporates signal stacking and digital data processing (LaFlèche et al., 1987).

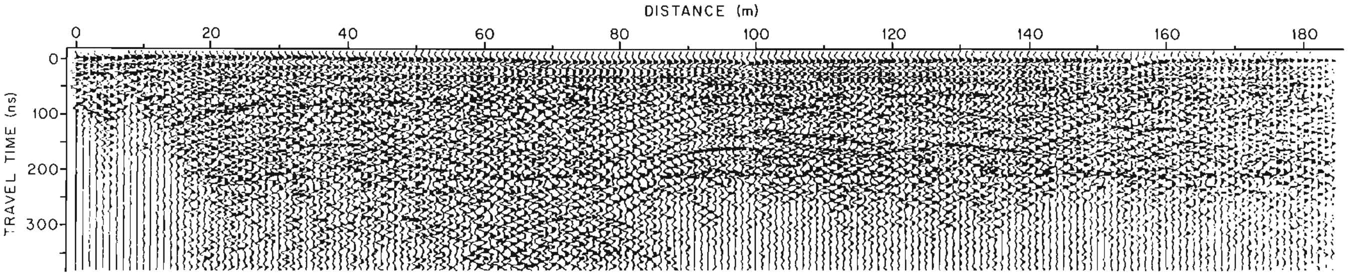

Figure 6. Ground probing radar survey results obtained at site 2, a sandy marine terrace.

Figure 7.

Photographic view of the large borrow pit 200 m southeast of the radar survey line at site 2 in Kangiqsualujjuaq; steeply dipping gravel beds can be seen in the centre of the picture.

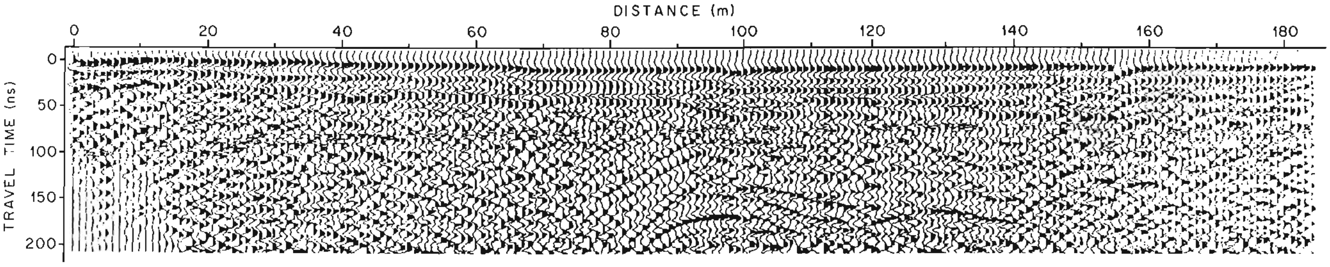

Figure 8. Enlargement of the first 200 ns of radar data in site 2; note the strong reflectors indicating the unconformity around 50-60 ns.

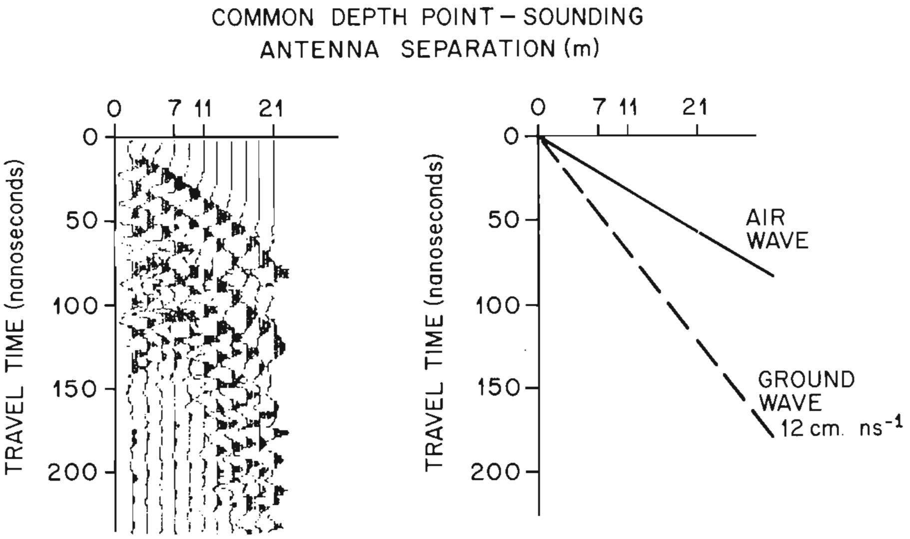

Figure 9.

CMP survey obtained on the marine terrace to determine the ground wave propagation speed at site 2 in Kangiqsualujjuaq.

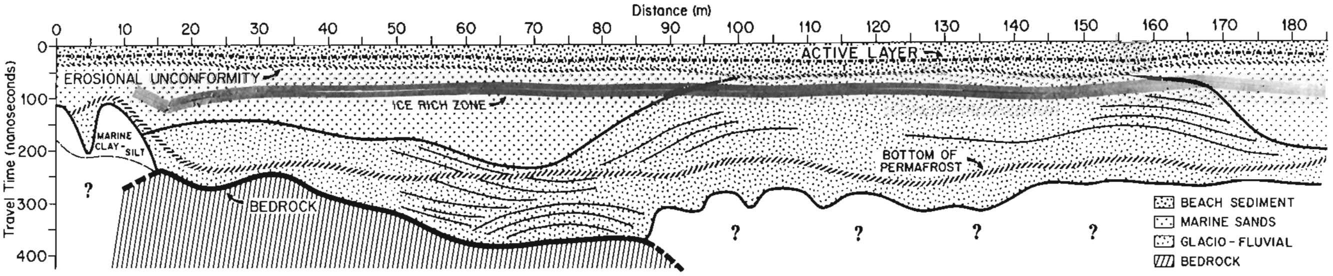

Figure 10. Interpretation sketch of the radar results obtained at site 2.

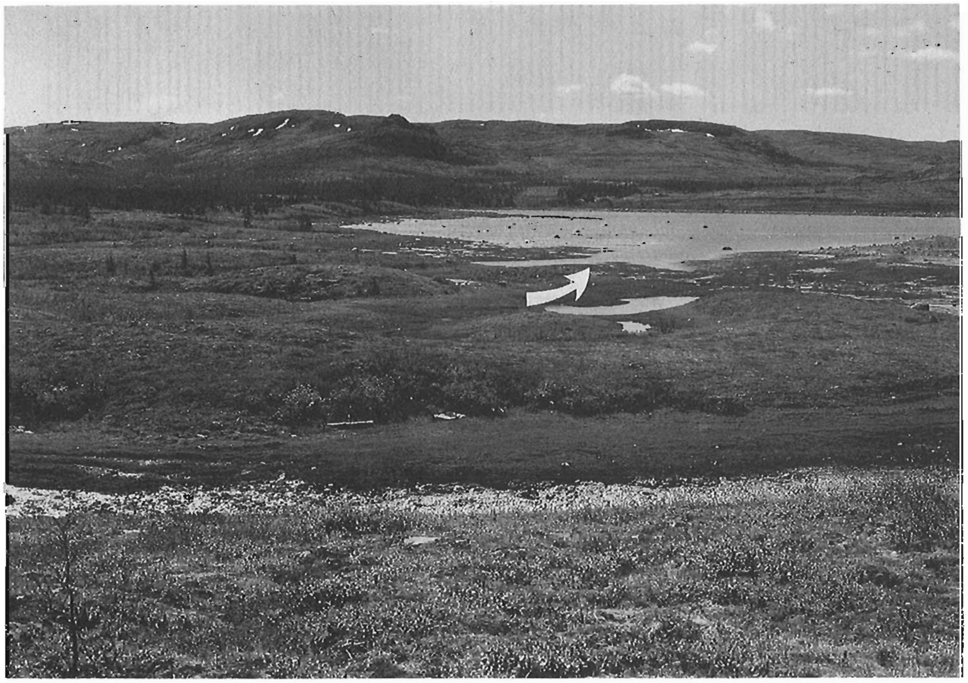

Figure 11.

Permafrost mounds in clay-silt near the shoreline; near ground is the surface of site 3A. (Arrow points at site 3B.)

SITE INVESTIGATIONS

The Kangiqsualujjuaq site 1 is a fluvial terrace cut in a thick, bouldery till deposit (Fig. 3). The stratigraphy is well known from the numerous sections along George River (Fig. 4). The contact between units 1 and 2 is sharp with a boulder lag, whereas the contact between units 2 and 3 is gradual and diffuse. The GPR survey at site 1 was conducted at a frequency of 100 MHz, along a 121 m transect parallel to the cliff face some 25-30 m inland. A CMP survey carried out at this site yielded a ground wave propagation speed of 12 cm/ns.

As can be seen on the radar profile (Fig. 5A) and its summary interpretation diagram (Fig. 5B), the contact between units 1 and 2 appears at about 30 ns (±1.5 m) and can be traced for the full length of the transect (Fig. 5A, B). At the time of survey, in August, the initial radar reflector corresponds roughly to the thaw depth. In part of the radar profile, however, between points 30, 45, 50, and 92, a separation indicates divergence of the stratigraphic and thermal contacts. At a depth of about 80 ns (±5 m) an undulating and irregular reflector most likely indicates an ice rich zone in the upper permafrost layer. Between survey points 75 and 120 the diffuse contact between the upper finer till and the lower sandier till is visible at about 200 ns (±12 m). A faint irregular reflector around 350 ns (about 21 m) is tentatively interpreted as the permafrost base. The latter compares favourably with the results of an induced polarization survey carried out on the same line (Gahé, 1988). Large boulders of 2-4 m in diameter, as observed in the geological section, are apparent in the profile at depth as point reflectors shadowing what lies underneath (Fig. 5A, B).

Site 2 is a sandy marine terrace at about 20 m asl composed of glaciofluvial deposits. A 50 m wide section in a large and deep borrow pit 200 m southeast of the transect line lies parallel to the survey axis and contains an erosional contact between wave reworked sand and gravel, and truncated glaciofluvial structures near the surface. The radar survey results discussed here are those obtained at a frequency of 100 MHz along a 185 m traverse using a 2 m antenna separation and an interval between survey points of 1 m (Fig. 6). The borrow pit allows some direct observation of the geological setting (Fig. 7). Beginning at 38 m along the transect, the axis of the radar survey follows a conspicuous beach ridge, which can be clearly seen in Figure 6.

Figure 8 shows an enlargement of the first 200 ns of radar data along this transect. Figure 9 is a CMP survey along this profile indicating that the ground wave propagation speed in this material is 12 cm/ns. Bedrock topography beneath the

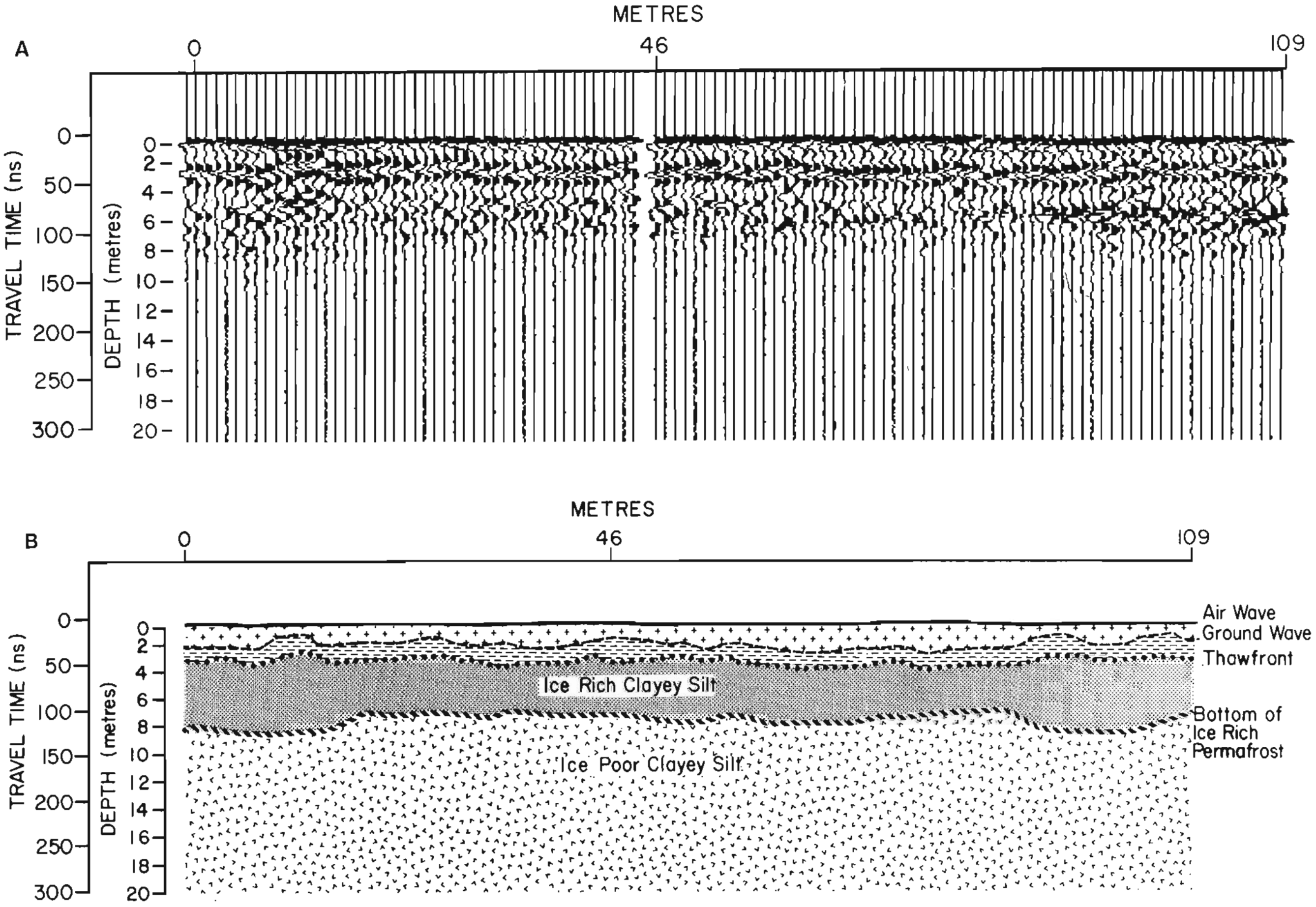

Figure 12A. Ground probing radar profile collected at site 3A in Kangiqsualujjuaq; **B.** Interpretation of the ground probing radar profile at site 3A.

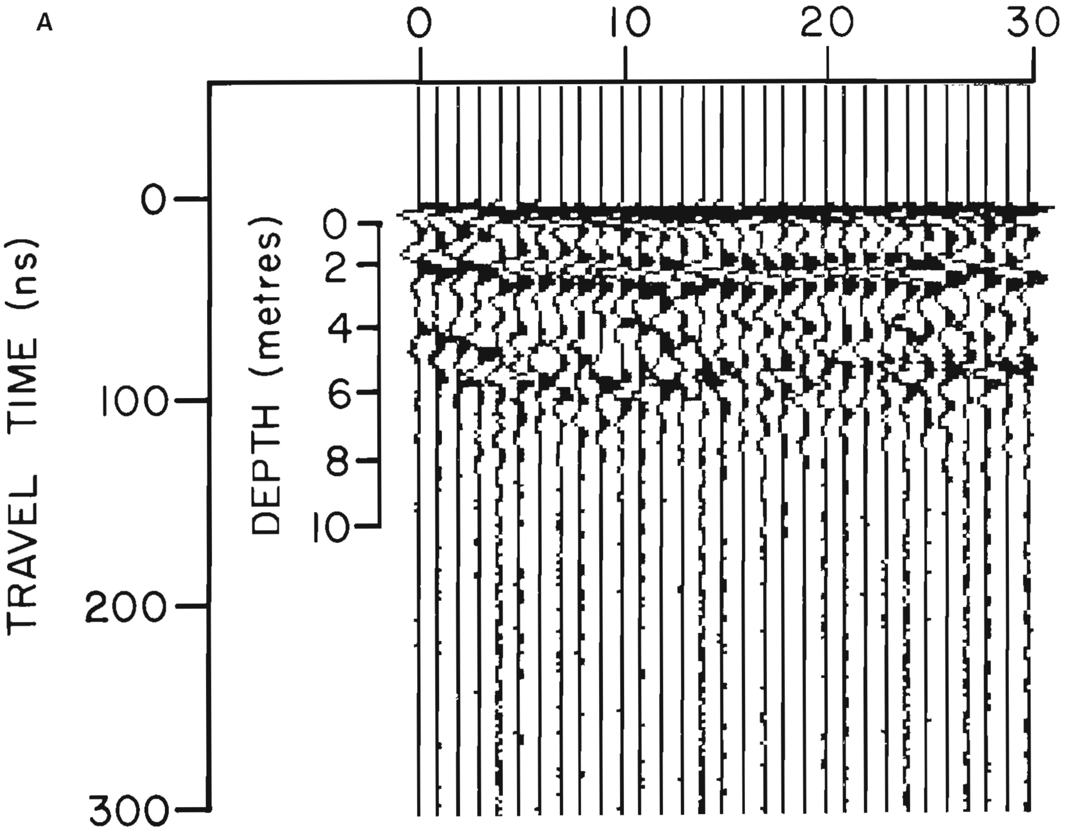

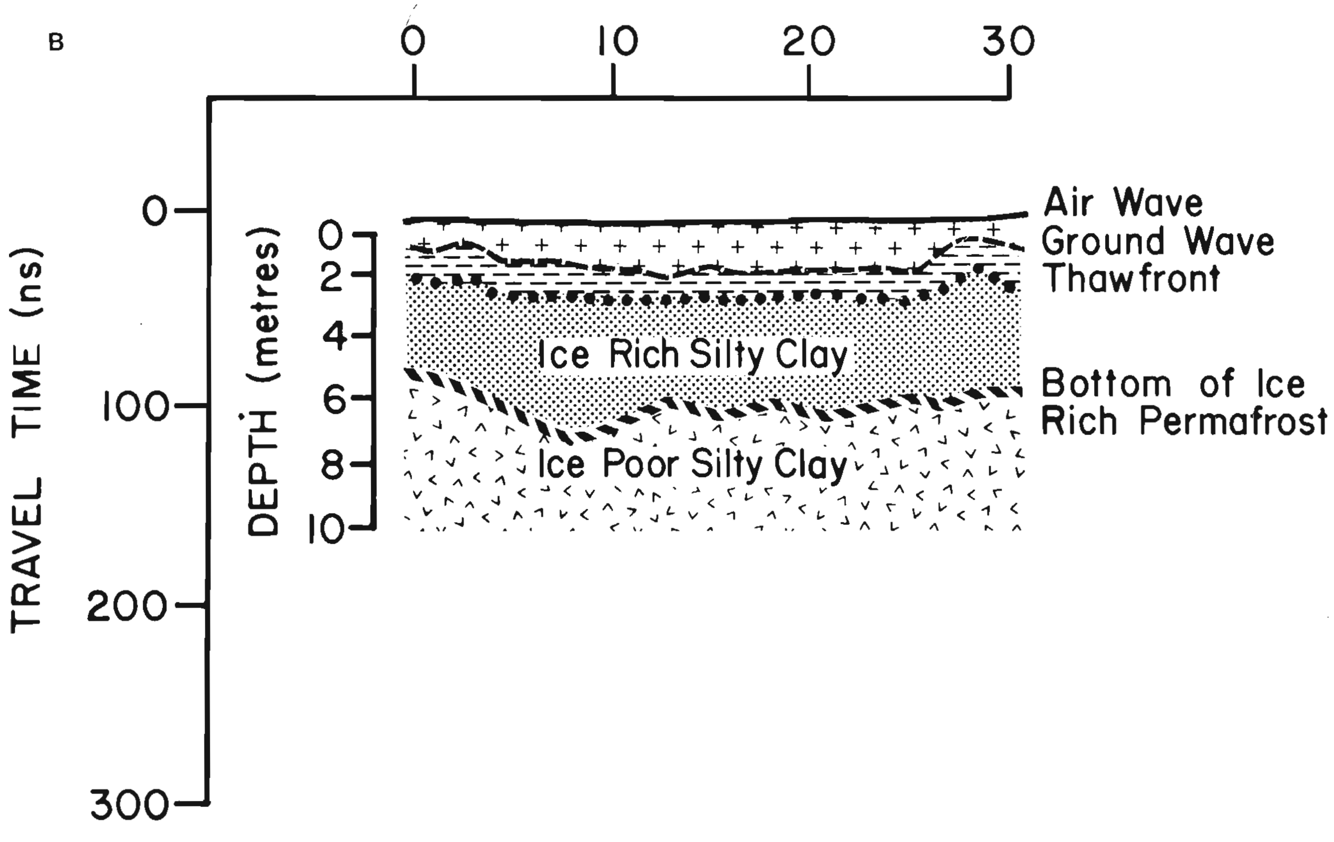

Figure 13.

A. Ground probing radar profile gathered at site 3B in Kangiqsualujjuaq; **B.** Interpretation of the ground probing radar profile at site 3B.

Figure 14. Aerial photograph of Kangiqsualujjuaq bay and surrounding areas. (Sites 3A, 3B and 4 are indicated.)

surficial deposits is irregular and is typical of the stoss and lee topography found in this region as a result of glacial sculpturing. Using the propagation speeds obtained from the CMP survey, Figure 10 shows the interpretation sketch of the results. Between stations 15 and 60, we calculate that bedrock lies on the average beneath 19 m of surficial deposits and reaches 24 m between survey points 60 and 90. The attenuation around 100 ns observed between stations 0 and 15 is caused by a clayey substrate, which masks the underlying material. Elsewhere (90-185 m) along the transect the cause of attenuation beneath the coarse stratified sediments is uncertain. It could be a fine sediment of unexplained origin, or saline groundwater under the permafrost. The bulk of the unconsolidated deposits consists of stratified glaciofluvial gravelly material and postglacial marine sands and silts with ice rafted boulders. There is a dome-like structure within the glaciofluvial gravel beds interpreted as a buried esker (Fig. 6, 8). The near surface erosional unconformity, created by wave washing during emergence (Fig. 8, 10), occurs between 1.5 and 3 m below the surface. Reworked marine sediments above the unconformity comprise coarse sand and fine gravel.

A

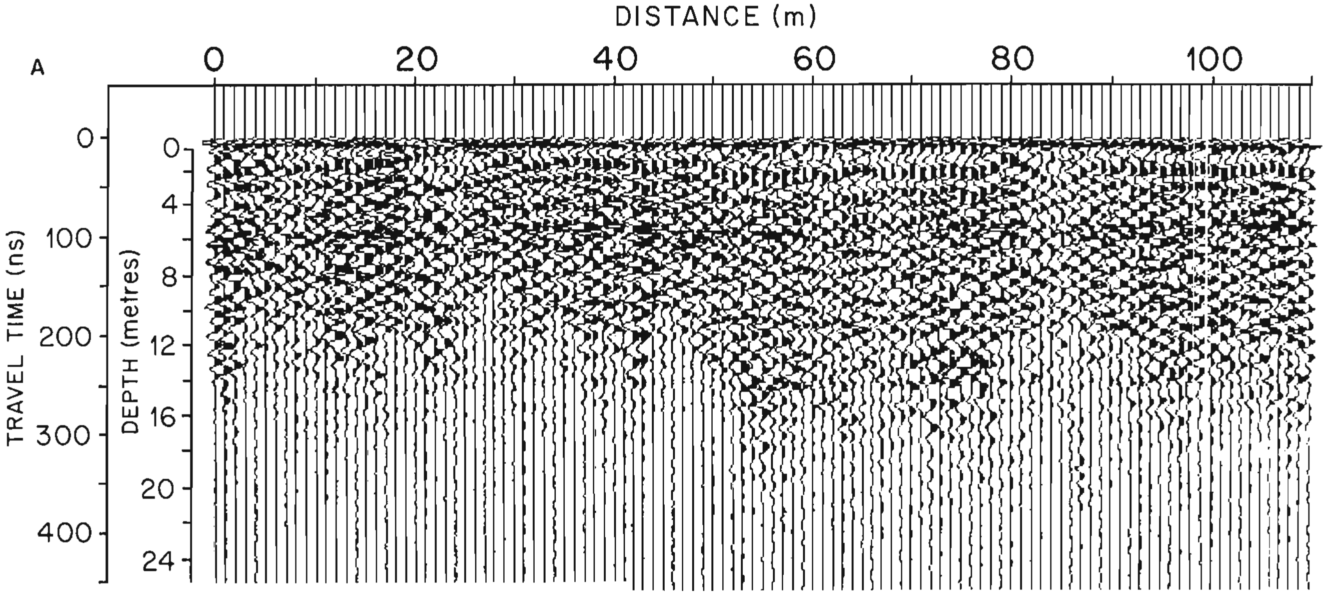

PALSAS KANGIQSUALUJJUAQ

B

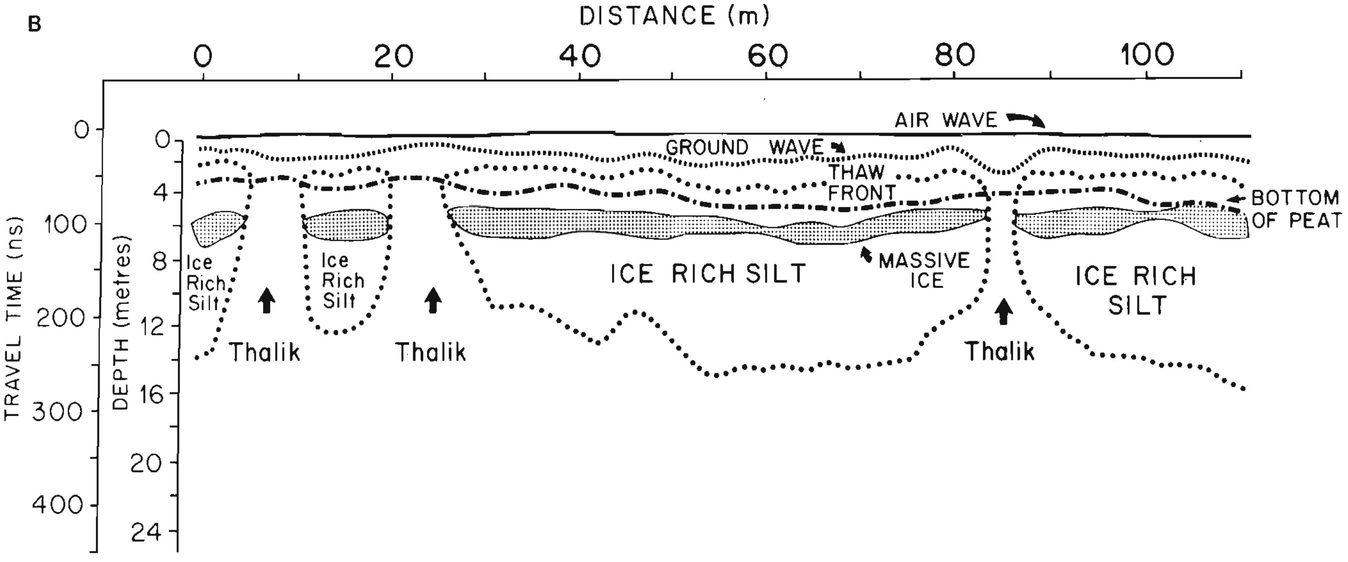

PALSAS KANGIQSUALUJJUAQ LINE 2A

Figure 15A. 100 MHz radar profile of site 4; B. Interpretation of the ground probing radar profile at site 4 in Kangiqsualujjuaq.

The first reflector beneath the surface is the thaw front varying in depth between 1.5 and 2 m (±50 ns), as confirmed by two thermistor cables along the transect (Bouchard, 1988). An important reflector zone at about 100 ns on (Fig. 6, 8) is interpreted as an ice rich zone corresponding with the coldest permafrost layer observed at about 6 m. An undulating but continuous reflector, which occurs between 200 and 260 ns (12.5 to 15.5 m), cuts stratigraphy and is interpreted to mark the base of permafrost that has been measured with electrical resistivity and induced polarization methods (Séguin and Allard, 1987) to be at about the same depth.

Site 3 consists of two permafrost mounds in marine clay-silt close to the shoreline (Fig. 11): 3A is 2-10 m asl and 3B is less than 5 m asl. Figures 12A and 13A show radar profiles collected on these frost mounds. The clay-silt material is 13-28 m thick as observed in boreholes (Allard et al., 1988). The permafrost thickness, as measured with thermistor cables in the boreholes, is 15 m at site 3A and 9 m at site 3B, which is adjacent to the shoreline. The radar profiles show that radar returns were obtained from the ice rich layers in the upper 3-4 m of the permafrost. Below the ice rich zones, the signal fades away in the saline cryotic clays, as expected from the attenuation coefficients for these materials given in Table 1. Figures 12B and 13B show the interpretation of these two profiles.

Site 4 is a peat plateau located near a lake at 36 m above sea level (Fig. 14). The radar transect, which has been previously used for other geophysical surveys (Gahé and Séguin, 1985; Gahé et al., 1987; Gahé, 1988) cuts across an uneven section of the peat plateau along an axis running southwest. The surface peat varies from a few decimetres to a maximum of 1.1 m in thickness. The peat overlies postglacial marine clays and clay-silt containing ice rafted boulders; a boulder pavement lies at the stratigraphic contact between the peat and the clayey silt. A drillhole in the centre of the plateau a few metres from the survey line revealed a thickness of 24 m of clayey-silt. The near surface layer of the permafrost zone beneath the peat has numerous thick ice lenses adding up to a volumetric ice content of 70% (Gahé et al, 1987). The thickness of frozen ground and the abruptly attenuated radar signal are evident in the unfrozen marine clay sediments in the subpermafrost (Fig. 15A, B). The more massive ice lenses near the surface appear as abundant multilayered reflectors between 50 and 100 ns (4-8 m). From the radar profile, permafrost is interpreted to be thicker beneath the peat mounds and thinner beneath the depressions, and the ice content is lower below the depressions in the peat plateau (e.g., sample points 22-23; 85-86; Fig. 15A, B). The strong reflector around 75 ns represents a thick ice lens. The CMP survey at this site yielded a propagation speed of 8 cm/ns, from which we calculate a maximum permafrost depth of 13 m, which compares favourably with the result of other geophysical surveys along this profile Gahé et al., (1987).

CONCLUSION

As illustrated by the results of the field test conducted in the Kangiqsualujjuaq area, ground probing radar (GPR) is an excellent geophysical tool for the study of permafrost. GPR has been used successfully to determine the thickness of the thawed zone and of the active layer, to detail the internal stratigraphy of the surficial deposits, and to detect the base of icebearing permafrost. Like all geophysical systems, GPR cannot be used universally and has certain limits imposed on it by the electrical characteristics of fine grained surficial materials, which limit the propagation of a VHF electromagnetic signal. GPR operates most successfully in granular materials, as illustrated by the resolution of sedimentary structures and stratigraphic details at site 2. Even in clayey silts, a material much less favourable for the propagation of the VHF signal, significant geotechnical information can be retrieved on radar profiles, as illustrated at sites 3 and 4 (e.g. the near surface concentration of ground ice). We find that GPR works best in materials less suitable to other geophysical survey systems (e.g., seismic refraction survey method). It is even possible to obtain a general view of the fabric of till layers (site 1). GPR is an important complement to the modern arrays of geophysical methods available to study the internal makeup and permafrost characteristics of unconsolidated materials.

ACKNOWLEDGMENTS

The authors wish to express their gratitude to field assistants: Christian Bouchard, Richard Fortier, Richard Levesque, Jacqueline Bouchard, and Johanne Plourde. They also wish to thank the Inuit community of Kangiqsualujjuaq for their welcome and to Mr. Jean-Guy St-Aubin for his help with recharging and the loan of batteries to power the system. This paper is the result of a collaboration between the Centre d'Études Nordiques of Université Laval and the Geological Survey of Canada. Thank you also to Mrs. J. Barr for typing the manuscript, to A. Rafeek, L. Campbell, and G. MacLeod of the Geophysics Division for drafting the illustrations, and to Richard Delaunais for the photographic work.

REFERENCES

Allard, M. et Séguin, M.K.
1987: Le pergélisol au Québec Nordique: Bilan et perspectives; Géographie physique et Quaternaire, v. XLI, no. 1, p. 141-152.

Allard, M., Séguin, M.K., and Pelletier, Y.
1988: Shoreline permafrost in Kangiqsualujjuaq Bay, Ungava, Québec; Proceedings, Fifth International Permafrost Conference, Trondheim, Norway, v. 1, p. 113-122.

Annan, A.P.
1983: General state-of-the-art review of ground probing radar; A-Cubed Inc. Report to Earth Physics Branch, Energy, Mines and Resources, March, 1983, 89 p. + Annexes.

Bouchard, C.
1988: Le régime thermique du pergélisol dans un sol sableux à Kangiqsualujjuaq, Québec Nordique; Univ. Laval, Dept. Géographie, Mémoire de Baccalauréat.

Davis, J.L. and Annan, A.P.
1989: Ground penetrating radar for high-resolution mapping of soil and rock stratigraphy; Geophysical Prospecting, v. 37, p. 531-551.

Fournier, A., Allard, M., et Séguin, M.K.
1987: Typologie morpho-génétique des marelles du marais litteral de la Baie de Kangiqsualujjuaq, estuaire du George, Québec Nordique; Géographie physique et Quaternaire, v. XLI, no. 1, p. 47-64.

Gahé, E.

1988: Géomorphologie cryogène et géophysique dans la région de Kangiqsualujjuaq; Université Laval, Dept. de Géographie, Thèse de doctorat, 210 p.

Gahé, E. et Séguin, M.K.

1985: Géophysique du pergélisol à Kangiqsualujjuaq, Québec Nordique; Annales de l'ACFAS, p. 52-53.

Gahé, E., Allard, M., et Séguin, M.K.

1987: Géophysique et dynamique Holocene de plateaux palsiques à Kangiqsualujjuaq, Québec Nordique; Géographie physique et Quaternaire, v. XLI, no. 1, p. 33-46.

Gahé, E., Allard, M., Séguin, M.K., and Fortier, R.

1988: Measurements of active layer and permafrost parameters with electrical resistivity, self-potential and inducted polarization; Proceedings, Fifth International Permafrost Conference, Trondheim, Norway, v. 1, p. 148-158.

LaFlèche, P.T., Judge, A.S., and Pilon, J.A.

1987: Ground probing radar in the investigation of the competency of frozen tailings pond dams; in Current Research, Part A, Geological Survey of Canada, Paper 87-1A, p. 191-197.

Payette, S.

1983: The forest tundra and present tree-lines of the northern Quebec-Labrador peninsula; in Tree-line ecology, S. Payette and P. Morisset (ed.); Proceedings, Northern Quebec Tree-line Conference, Nordicana, v. 47, p. 3-24.

Scott, W.J., Sellmann, P.V., and Hunter, J.A.

1978: Geophysics in the study of permafrost; Proceedings, Third International Conference on Permafrost, v. 2, p. 93-115.

Séguin, M.K. and Allard, M.

1987: La géophysique appliquée au pergélisol du Québec Nordique: historique et développements récents; Géographie physique et Quaternaire, v. XLI, no. 1, p. 127-140.

Thériault, M.

1983: Une typologie des régimes climatiques du Québec; Univ. Laval, Ph.D. Thesis, unpublished.

Wilson, C.

1971: Le climat du Québec, Atlas climatique du Canada, 1re partie; Ottawa, Service de météorologie.

Reconnaissance ground penetrating radar survey of the interior of Meteor Crater, Arizona

J.A. Pilon[1], R.A.F. Grieve[2], V. Sharpton[3], J. Coderre[2], and J. Kennedy[3]

Pilon, J.A., Grieve, R.A.F., Sharpton, V., Coderre, J., and Kennedy, J., 1992: Reconnaissance ground penetrating radar survey of the interior of Meteor Crater, Arizona; in *Ground penetrating radar, ed. J. Pilon; Geological Survey of Canada, Paper 90-4, p. 177-186.*

Abstract

A ground penetrating radar survey (GPR) has been conducted inside Meteor Crater, Arizona. Meteor Crater, 1.2 km in diameter, was selected to assess the usefulness of GPR to determine subsurface structure and stratigraphy of impact craters because of its good state of preservation and the availability of good ground verification data from various drill holes and shafts. Four transects were conducted on the crater floor with a pulseEKKO III system using the following experimental conditions: frequency 50 MHz, antenna separation 2 m, time window 1024 ns, and sample interval of 800 ps. Two common depth point surveys were conducted to determine the speed of propagation of the radar pulse. The data were processed using various filters developed for seismic data processing. Maximum depth of penetration of the radar pulse was about 80 m, with the most prominent reflector being the water table at 60-65 m. Various other reflectors, representing the interface between the interior breccia lens and the overlying fall back breccia and between postimpact sedimentary deposits, were also identified. It was also possible to identify the crater wall at depth and what may be listric faulting in the autochthonous target rocks of the wall. The test survey is judged to be highly successful and extends the essentially one-dimensional data obtained from drilling to a two-dimensional map of the subsurface. The Meteor Crater experience will be essential for interpretating future surveys, where drilling data are not available, to constrain the depth and nature of various lithological boundaries within other impact craters.

Résumé

Un levé par géoradar a été réalisé à l'intérieur du cratère Meteor en Arizona. Ce cratère de 1,2 km de diamètre a été choisi en vue d'évaluer l'utilité du géoradar à déterminer la structure et la stratigraphie de subsurface des cratères d'impact étant donné son état de conservation satisfaisant et la disponibilité de bonnes données de vérification au sol recueillies dans divers trous de sondage et puits. Quatre transects ont été réalisés sur le fond du cratère à l'aide d'un système pulseEKKO III dans les conditions expérimentales suivantes : fréquence de 50 MHz, séparation d'antenne de 2 m, fenêtre temporelle de 1024 ns et intervalle d'échantillonnage de 800 ps. Deux levés de points-miroirs ordinaires ont été menés pour déterminer la vitesse de propagation de l'impulsion radar. Les données ont été traitées en utilisant divers filtres conçus pour le traitement des données sismiques. La profondeur de pénétration maximale de l'impulsion radar a été d'environ 80 m et le réflecteur le plus important a été la nappe phréatique située à 60-65 m. Divers autres réflecteurs, représentant l'interface entre la lentille de brèche intérieure et la brèche de retombée sus-jacente et entre les dépôts sédimentaires postérieurs à l'impact, ont également été identifiés. Il a été en outre possible de déterminer la paroi du cratère en profondeur et les failles probablement listriques se formant dans les roches autochtones cibles de la paroi. Le levé d'essai est considéré très concluant et il permet d'utiliser les données de forage essentiellement unidimensionnelles pour établir des cartes bidimensionnelles des roches de subsurface. L'expérience réalisée au cratère Meteor jouera un rôle essentiel dans l'interprétation des levés futurs où les données de forage ne seront pas disponibles, en précisant la profondeur et la nature des différentes limites lithologiques au sein d'autres cratères d'impact.

---

[1] Geological Survey of Canada, Terrain Sciences Division, 601 Booth Street, Ottawa, Ontario K1A 0E8
[2] Geological Survey of Canada, Geophysics Division, 1 Observatory Crescent, Ottawa, Ontario K1A 0Y3
[3] Lunar and Planetary Institute, 3600 Bay Area Blvd., Houston, Texas, U.S.A. 77058

INTRODUCTION

Current knowledge of hypervelocity impact cratering, which is now recognized as an important geological process in the early evolution of the terrestrial planets and their satellites, has drawn heavily on the results of laboratory experiments and field studies at terrestrial impact structures. Meteor Crater is a relatively young (~50 000 a old), well preserved impact crater in northern Arizona, which has been extensively studied. It is often cited as the canonical example of terrestrial, simple, bowl shaped craters, which occur on earth up to ~4 km in diameter. The preservation and existing literature make Meteor Crater an ideal test site to assess the capabilities of ground penetrating radar (GPR) in determining the internal structure of hypervelocity impact craters.

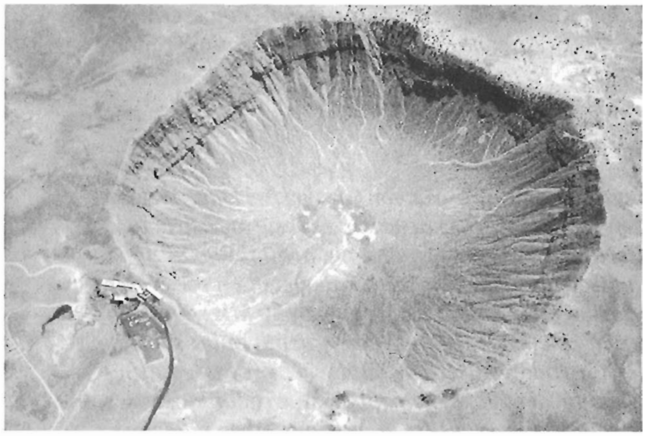

Figure 1. Aerial photograph of Meteor Crater, Arizona.

This paper presents part of the results of a reconnaissance GPR survey conducted at Meteor Crater in the fall of 1987. The GPR survey was designed to acquire information on the subsurface nature of the crater and the surrounding ejecta blanket. Five GPR transects were conducted, four of which were carried out on the interior floor of the crater. They included three complete north-south transects and a partial east-west transect, connecting the three north-south surveys. This paper is concerned with defining the internal structure of the crater and, therefore, does not discuss the transect on the north side of the crater, across the ejecta blanket from its edge to the crater rim.

GEOLOGICAL SETTING

Meteor Crater is located in north-central Arizona at 35°02′N, 111°01′W, in the Canyon Diablo region of the southern part of Colorado Plateau. The arid climate and the thin, sparse soil contribute to extensive exposures of bedrock on an essentially flat, low relief erosional surface. In the crater region, the plateau is underlain by about 1200 m of nearly flat lying Palaeozoic and Mesozoic strata overlying the crystalline Precambrian basement.

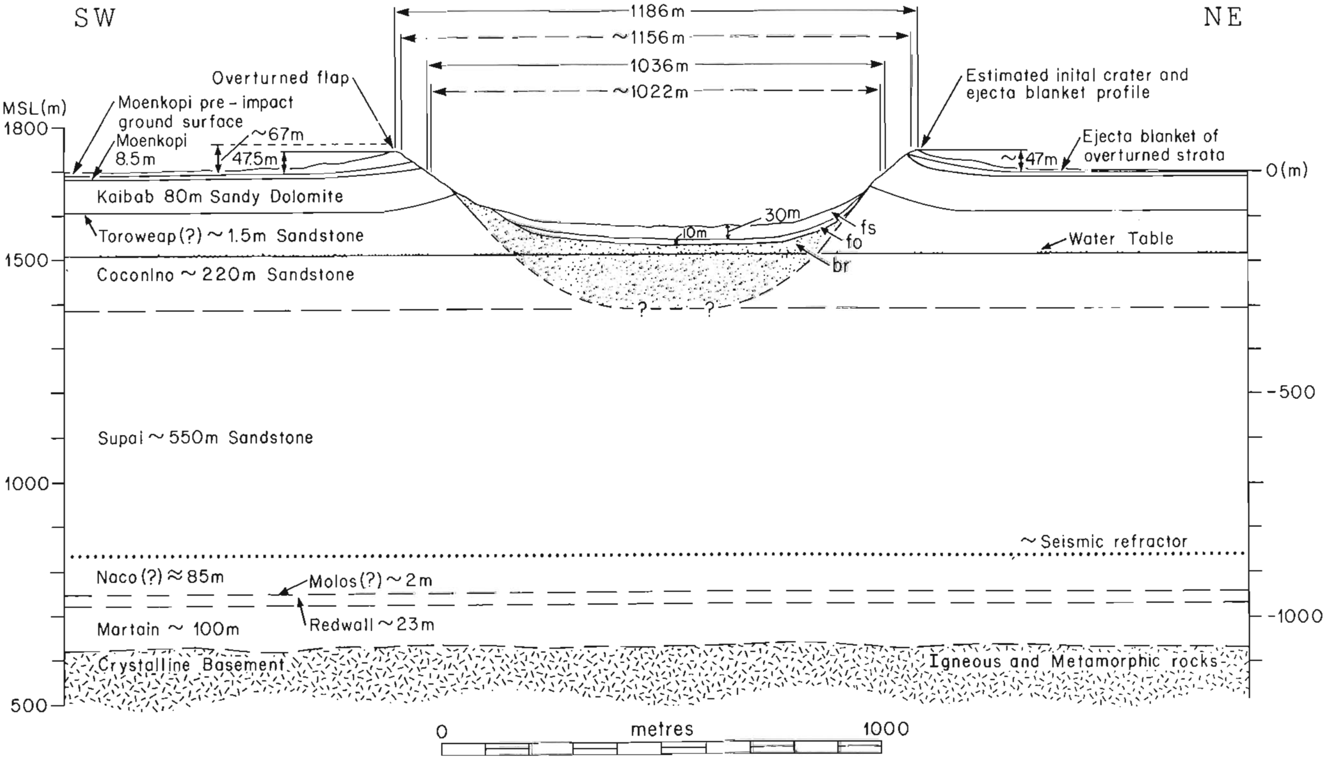

Figure 2. Geological cross-section of Meteor Crater, after Roddy (1978). Section is based on the interpretation of drill hole data. fs = filling sediments, fo = fallout, br = breccia lens.

The geology of Meteor Crater has been described in detail by Shoemaker (1960, 1963, 1974) and its characteristics summarized by Roddy et al. (1975) and Roddy (1978), among others (as well as in other extensive literature pertaining to Meteor Crater). Meteor Crater is a roughly circular feature with slightly squarish sides (Fig. 1). Its rim has an average diameter of 1186 m. In cross-section, the crater has the form of a shallow bowl with an average depth of 167 m from rim crest to floor (Roddy et al., 1975). Figure 2, after Roddy (1978), is a geological cross-section, summarizing the stratigraphy, the present water table, the preerosion and posterosion crater dimensions, and related aspects. The short-dashed information lines on Figure 2, associated with the rim crest and apparent diameters, rim crest depth, and rim height, are estimated preerosion initial values. All other crater dimensions are present posterosion values. The wide-spaced dotted line is an interpreted transitional zone between the breccia lens and enclosing fractured autochthonous target rock (Ackermann et al., 1975). The subsurface relations are based largely on the interpretation of drillhole data. Sources of the information shown in the cross-section are given in Roddy (1978).

The target material intersected by the crater consists mainly of a series of sandstones and dolomites. The upward sequence (Fig. 2) is as follows: the Supai Formation consists of interbedded, red and yellow, fine grained argillaceous sandstone and subordinate siltstones: The Coconino Sandstone consists of white, crossbedded, fine grained, unusually clean sandstone: It is overlain conformably by the thin (2.7 m) Toroweap formation, consisting of white to yellowish- or reddish-brown, calcareous, medium to coarse grained, sandstone interbedded with dolomite. The Kaibab Formation consists of fossiliferous marine sandy dolomite, dolomitic limestone, and minor calcareous sandstone, resting conformably on the Toroweap: The uppermost unit, the Moenkopi Formation, consists of pale to reddish-brown, very fine grained sandstone, resting unconformably on the Kaibab.

These lithologies offer particularly low attenuation coefficients, ranging from 0.01 to 0.7 mS/m (milli Siemens per metre), for electromagnetic radiation at frequencies around 100 MHz (Pilon et al., 1992), which ensure good GPR signal penetration.

These characteristics, combined with the deep water table about 231 m below the Colorado Plateau surface and some 60-64 m below the bottom of the crater, depending on the season (E. Shoemaker, personal communication, 1987), make for an ideal test site to assess the capabilities of GPR to detect the internal stratigraphy and structure found inside the crater.

METHOD

Ground probing radar is a relatively new geophysical tool. The first commercial model became available in the mid 1970s. GPR operates on the same principles as conventional radars in that a short pulse of electromagnetic energy is emitted by a transmitter antenna, reflects off a distant electrical boundary and the reflection is picked up by a receiver antenna. The time is measured for the pulse to travel from the transmitter to the receiver antenna via the reflector (Annan, 1983). The depth to a reflector can be calculated when the propagation speed of the pulse in the material is known. This propagation velocity can be measured in situ by conducting a common depth point (CDP) or a wide angle reflection and refraction (WARR) survey. In air, the pulse travels at the speed of light, 0.3 m/ns (metres per nanosecond). In the subsurface, the pulse travels at a velocity that is dependent upon the electrical properties of the material traversed. This velocity will be some appreciable fraction of the speed of light.

The overall depth to which a radar pulse will penetrate effectively depends on the electromagnetic absorption characteristics of the subsurface. Reflectors detected with a GPR system are caused by dielectric contrasts in the subsurface materials. Common causes of subsurface reflections are material interfaces (such as overburden-rock, or sand-clay), water table limits, boundaries between frozen and unfrozen water, and so on. A large dielectric contrast exists between water and most geological materials. As such, the presence or absence of water controls to a large degree the subsurface propagation characteristics of the radar pulse. Thus, the ability of a material to retain water within its pore space is an important factor in the determination of its bulk electrical properties.

The pulseEKKO III GPR system, deployed inside Meteor Crater, is shown in Figure 3. It is a fully digital GPR system, with a system performance of 150 dB. It incorporates signal stacking and digital data processing (LaFlèche et al., 1987). For the experimental surveys conducted inside Meteor Crater, radar reflection profiling was carried out with the following configuration: the centre frequency of the antennas was 50 MHz, the antenna separation was 2 m; the station interval between sampling points was 2 m; a time window of 1024 ns and a sample interval time of 800 ps (picoseconds) yielded 1280 points per trace. Each trace is the sum of 512 stacks. In total, 1.8 km of line, with ~900 traces were acquired at Meteor Crater.

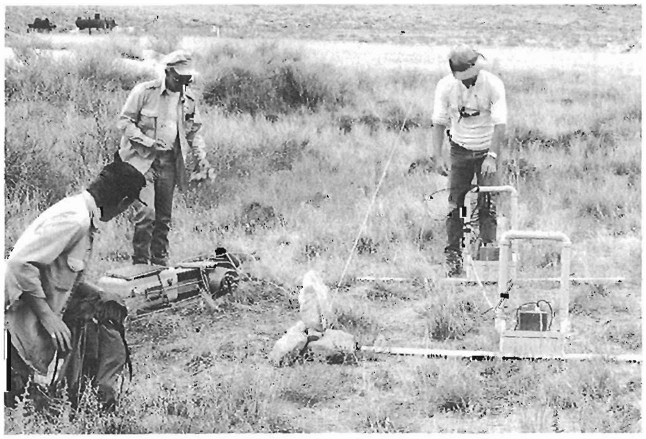

Figure 3. PulseEKKO III GPR system set up at Meteor Crater on line 4; Note the large steel boiler in the background (see text).

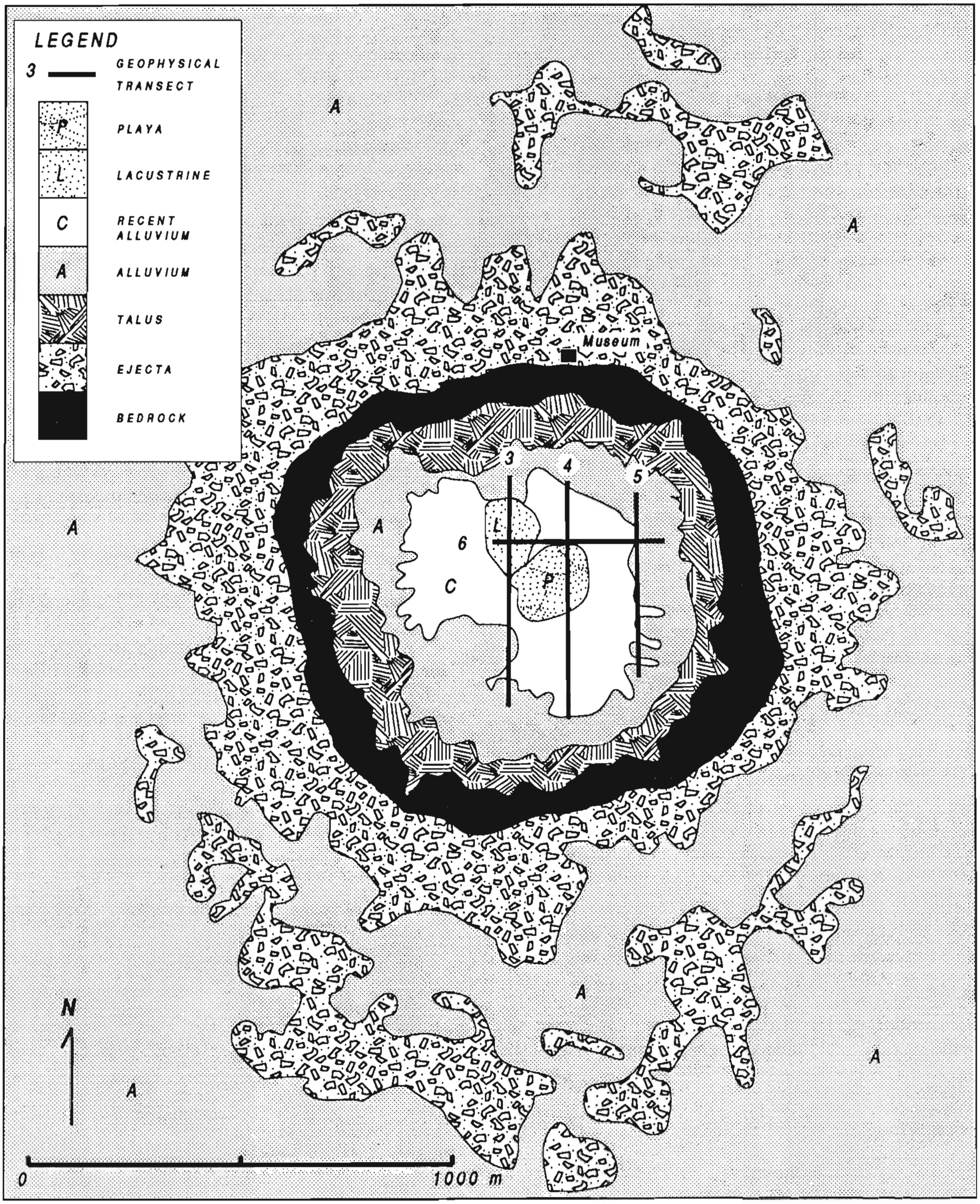

Figure 4. Location map of the GPR transects on the floor of Meteor Crater; geology after Shoemaker (1974).

The digital data were recorded on magnetic tape cassettes. The data were subsequently formatted in the SEG "Y" seismic data format. The formatted data were then processed through the Veritas Aurora seismic analysis program at the Geological Survey of Canada. The following processing routines were applied to the raw radar data: 1) gain was applied with an automatic gain control (AGC); 2) the signal in each trace was subjected to a bandpass filter test to retain only the information contained between 25 and 70 MHz; 3) a predictive deconvolution was performed to rid the data of multiple returns; and 4) the radar data for each survey transect were processed through a nine trace, moving window, coherency filter to enhance the coherent returns and to further diminish remaining incoherent and cultural noises (e.g., VHF radiocommunications).

RESULTS

The results presented are those obtained along the three north-south continuous GPR transects across the interior floor of the crater (Fig. 4). Besides these transects, we carried out two CDPs to measure an average speed of propagation for the radar signal in the floor of the crater. The CDP soundings inside the crater were measured to a separation of 20 m between receiver and transmitter in 0.5 m increments. These surveys yielded propagation speeds of 16.2 cm/ns (Fig. 5) and of 17.3 cm/ns, respectively. The slight differences in the speed of propagation obtained can be attributed to minor variations in the lithologies and the associated water content in the materials on the floor of the crater. In our analysis, we used a propagation speed of 16 cm/ns. The calculated depths obtained with this speed correspond well with known features in the crater subsurface as determined from drilling data. The delay time observed at the beginning of the CDP (Fig. 5) is the time required for the signal to travel along the fibre optic links between the control console, the transmitter, and the receiver.

Figures 6A, 7A, and 8A present the processed GPR data obtained along transects 3, 4, and 5 across the floor of the crater (Fig. 4) and Figures 6B, 7B, and 8B show the interpretation of the data from these transects. All three transects show a number of common prominent features (Fig. 6A, 7A, 8A). The most notable is the almost continuous echo obtained around 750 ns, which represents the surface of the water table. The strength of this return is the result of the large dielectric contrast between unsaturated and saturated breccia, which is mostly made up of blocks of Coconino sandstone (Shoemaker, 1974). The dielectric contrast of this material should be similar to that found between dry sand (k = 3 5) and freshwater saturated sand (k = 20 ~ 30) (Annan, 1983). Because this dielectric contrast is constant at this boundary, the varying signal intensity observed for this boundary on the profiles is mainly the result of variations in the antenna-ground coupling on the rough surface, which is covered with boulders and small gullies on the crater floor. This roughness is responsible for significant variations in the amount of electromagnetic energy transferred in the ground and thus of the intensity of the returns.

The next dielectric boundary, as we proceed towards the surface, appears as a discontinuous subhorizontal undulating reflector between 510 ~ 550 ns. On transect 3 (Fig. 6A), it appears as a relatively strong almost continuous reflector between stations 40 and 160, 180 and 240, and as a fainter undulating reflector between stations 340 and 514. On transect 4 (Fig. 7A), it is a relatively faint discontinuous reflector between stations 0 and 60 and a stronger reflector between stations 80 and 120. It becomes sporadic until station 380, where it becomes relatively continuous until station 480. On transect 5 (Fig. 8A), it appears as a fairly strong continuous return around 510 ns, between stations 80 and 180. It reappears as a fainter more discontinuous reflector between stations 260 and 320 and, again, as a stronger reflector between stations 370 and 390. Below this reflector, the density of large point reflectors, which appear on the radar profiles as downward pointing parabolic returns, is much higher than above. This change leads us to interpret this relatively irregular dielectric boundary as the top of the breccia lens, with the parabolic reflectors representing large imbedded blocks in the breccia. This is particularly evident on lines 3 and 4 (Fig. 6A, 7A), that are the more central lines. Some credence to this interpretation is given by the fact that 510 550 ns corresponds to a depth of ~40 m (Fig. 6A, 7A, 8A), which is about the depth to the top of the breccia lens as given in Figure 2, after Roddy (1978).

The next relatively prominent electrical boundary on the profiles appears rather discontinuously at a depth between 460 ~ 500 ns. On transect 3 (Fig. 6A), it shows clearly between stations 100-160, 200 and 240, more faintly between stations 300 and 320, and 340 and 360 and, finally, as a strong reflector between stations 390 and 500. On transect 4 (Fig. 7A), it is very discontinuous and weak around 450 ns. On transect 5 (Fig. 8A), it is more prominent at around 450-470 ns. It shows clearly between stations 110 and 120, 160 and 170, 180 and 210, 220 and 240, and 320 to 380. This faint and irregular dielectric boundary quite likely represents the top of the fallback ejecta layer, composed of fragments derived from all the formations excavated by the crater, including strongly shocked rocks and oxidized meteoritic

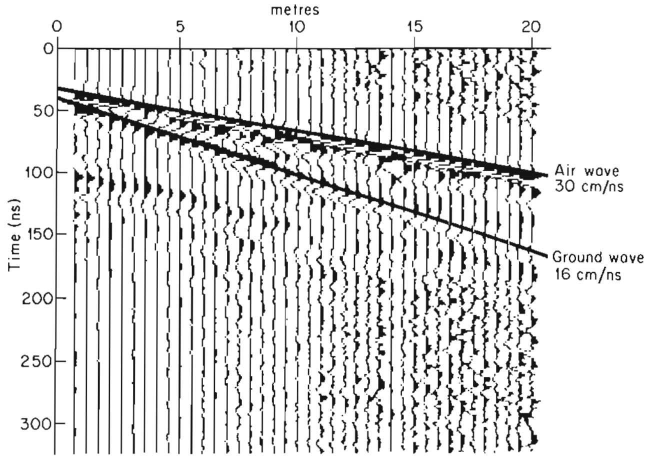

Figure 5. Results of the 50 MHz CDP sounding on the floor of Meteor Crater.

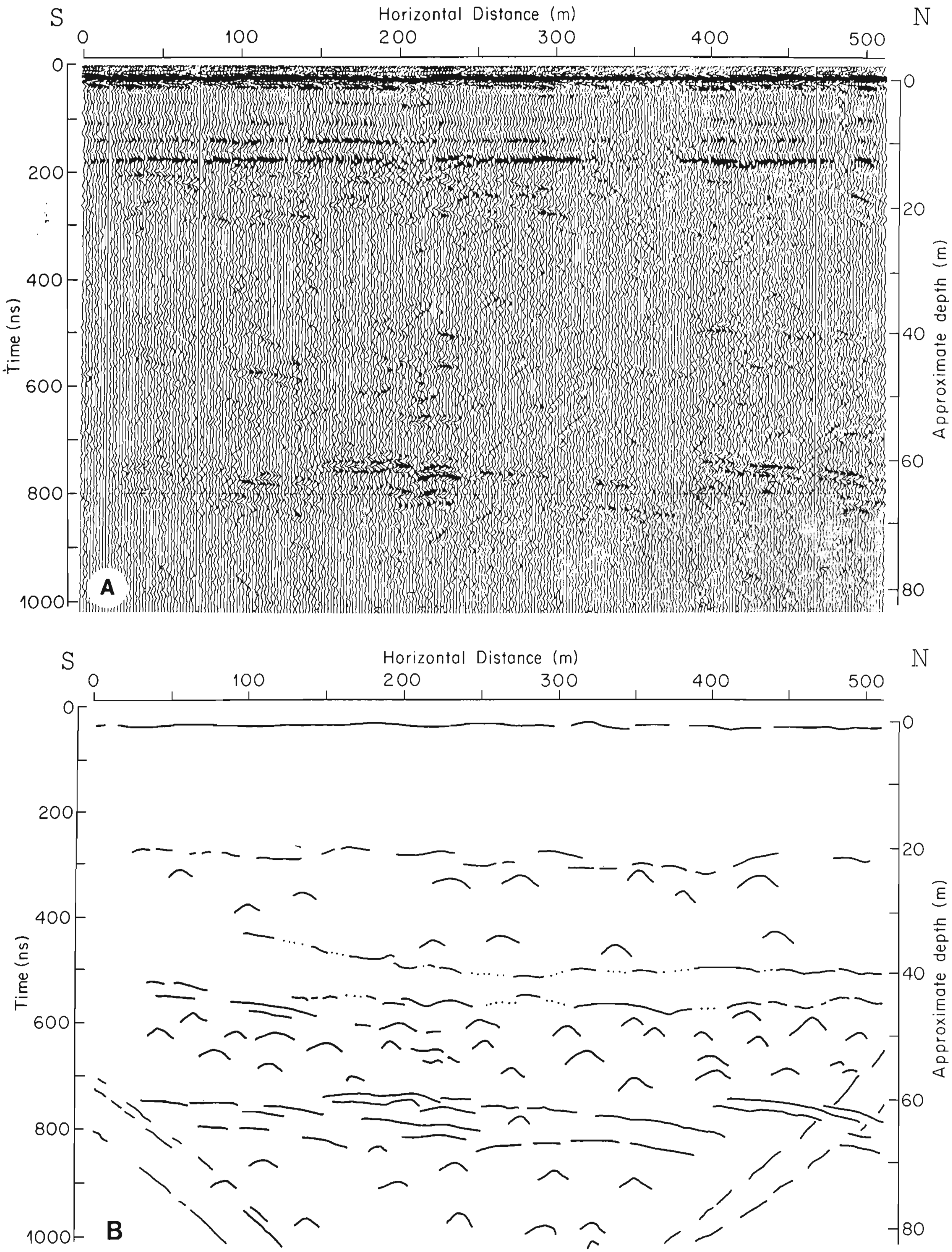

Figure 6. GPR results obtained along transect 3, about in the centre of the crater: **A.** processed radar data; **B.** line interpretation of radar data.

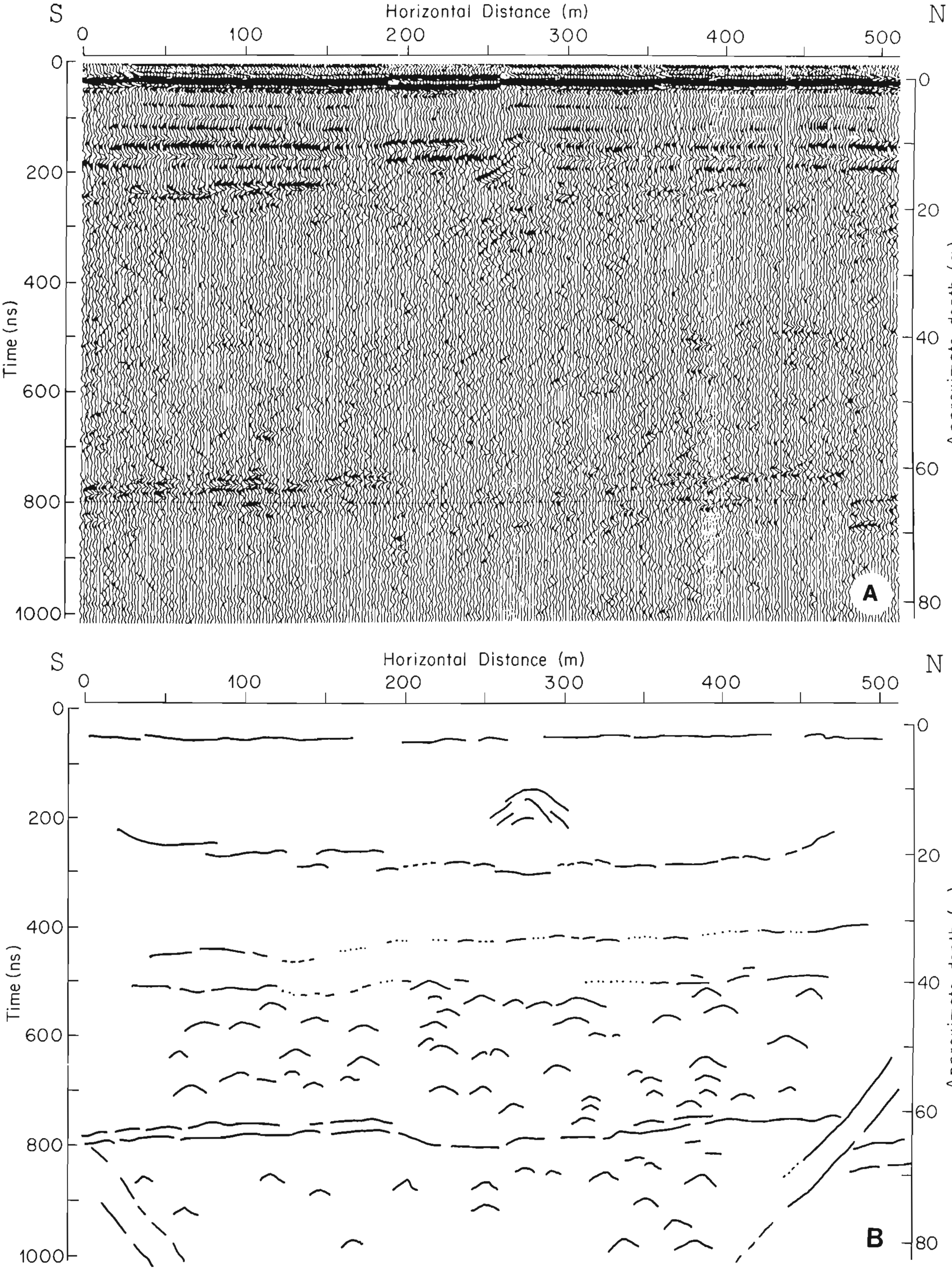

Figure 7. GPR results obtained along transect 4, 100 m east of the centre of the crater. **A.** and **B.** as in Figure 6.

material (Shoemaker, 1974). Why it shows very clearly in some places (e.g., transect 3, stations 390 to 500 (Fig. 5)) and not in others may result from variations in composition or higher concentrations of highly shocked rock and other debris, or both.

The next prominent dielectric boundary is located between 260 and 290 ns. It is fairly strong and consistent on the three radar transects. On transect 3 (Fig 6A,B), it is fairly continuous and horizontal between stations 20 and 50, 70, and 140. It is still continuous but more undulating until station 320 and fainter until stations 440 and 460. On transect 4 (Fig. 7A,B), it is relatively continuous between stations 30 and 140, 160 and 200, 240 and 280, and 300 and 420 and seems to disappear near station 480. On transect 5 (Fig. 8A,B), it is quite strong between stations 110 and 140, 160 and 180, and 220 and 280. This dielectric boundary probably marks the gradation between the Pleistocene alluvium on the floor and the upper lacrustrine beds filling the crater.

The final dielectric boundary found in the crater floor is very continuous on all three transects and is the first return below the ground wave at the top of the profiles, at about 50 ns (Fig. 6, 7, 8). It denotes the contact between the Pleistocene sediments (in places the lacustrine beds) and the Holocene alluvium and playa beds at the surface. The thickness of the holocene averages about 1.6 m throughout the crater floor (Shoemaker, 1974). A wedge of Pleistocene talus mantles the lowest part of the crater wall between points 20 and 80 at the beginning of transect 5 (Fig. 8A,B). This area is the only one in the crater where we began the radar transect high on the talus slope, some 10 ~ 12 m above the crater floor. This position may have affected the speed of propagation, as seen in the inward dip of the radar reflectors up to about station 80 (Fig. 8A,B).

An example of the care that must be taken when interpreting radar data is shown by the strong parabolic reflector observable on line 4 (Fig. 6A) near station 275 at about 125 ns. This very prominent echo is not caused by a

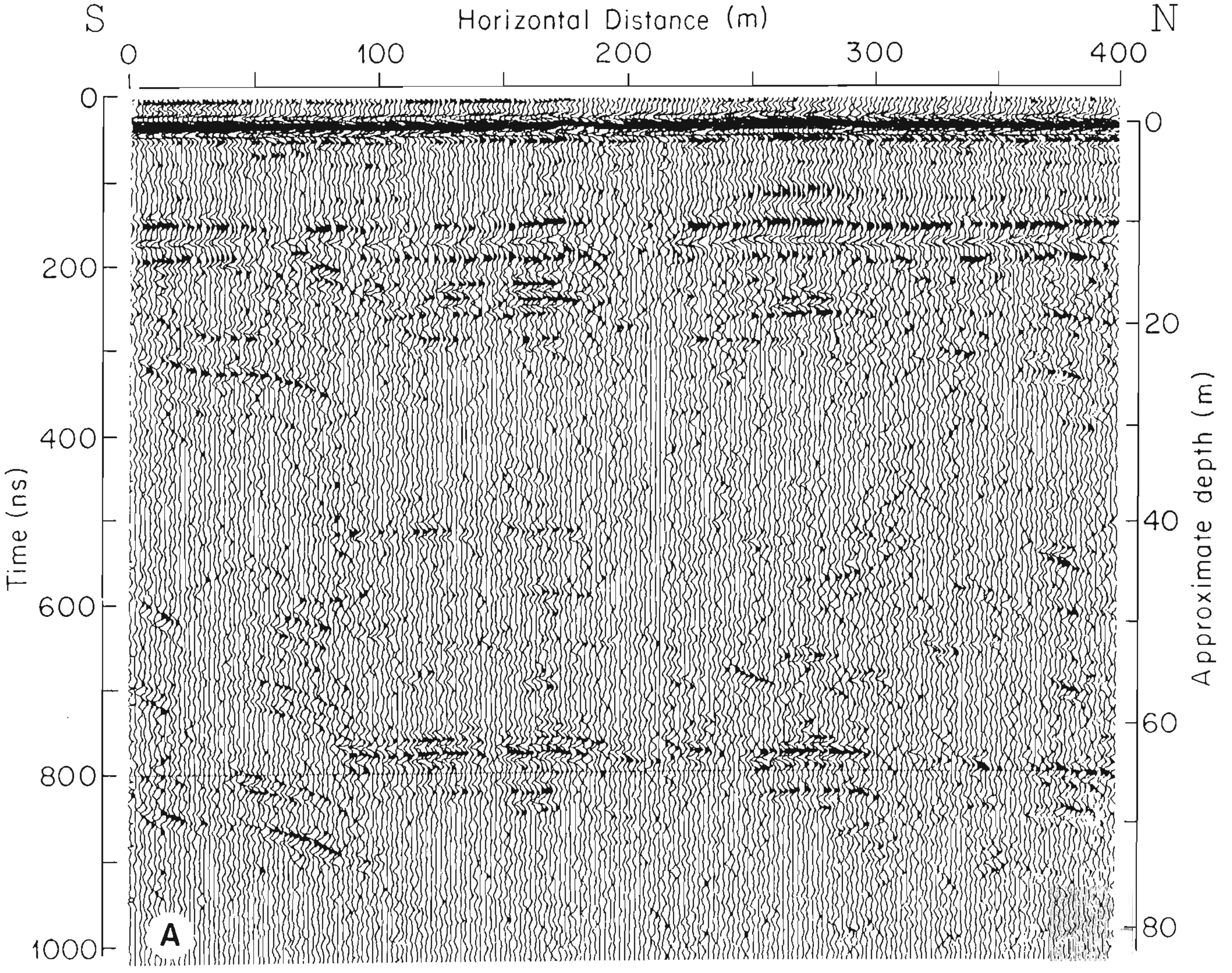

Figure 8. GPR results obtained along transect 5, 200 m east of the centre of the crater. **A.** and **B.** as in Figure 6.

subsurface geological feature. It is an artifact caused by sidelobe reflections off a large steel boiler on the crater floor (Fig. 3). The boiler was used for power during drilling and excavation endeavours at the turn of the century. Similarly, the horizontal returns at 100, 150, and 250 ns on all traces are also artifacts. They are multiples of the ground wave, which had been removed by the deconvolution filter but reappeared with the application of the coherency filter.

In addition to this stratigraphic information on the crater fill, some details of the autochthonous target rocks are also available in the radar transects. This detail is particularly evident at the beginning of transect 5 as faint, discontinuous, diagonal, inward dipping reflectors bounding either side of the apparent step discontinuity in the water table between points 75 and 85 (Fig. 8A,B). The innermost reflector originates around 270 ns and extends down to the bottom of the profile. The outer one begins at about 300 ns and also extends down to the bottom of the profile (Figure 8A,B). The innermost one represents probably the crater wall between target rocks and breccia, the outermost one a listric fault within the target rocks. The distortions and discontinuity in the echos, at what must be the horizontal water table level, result from different speeds of propagation for the radar signal in the autochthonous target rocks on one side and the allochthonous, disturbed rock fragments of breccia infilling the crater on the other side. Some of that distortion is also attributable to the topographic elevation difference, which was not corrected for in the radar profile processing. A similar feature can also be seen at the north end of transect 4 around station 490 (Fig. 7A,B). In this case, the weak, diagonal reflector is much more continuous. Another diagonal reflector appears at depth, at the other end of the same traverse, around the intersection of 900 ns and station 40. Because we lack other evidence, such as marked propagation speed differences, we hesitate to interpret these as crater boundaries. Similar features can also be seen at depth at either end of transect 3 (Fig. 6A,B).

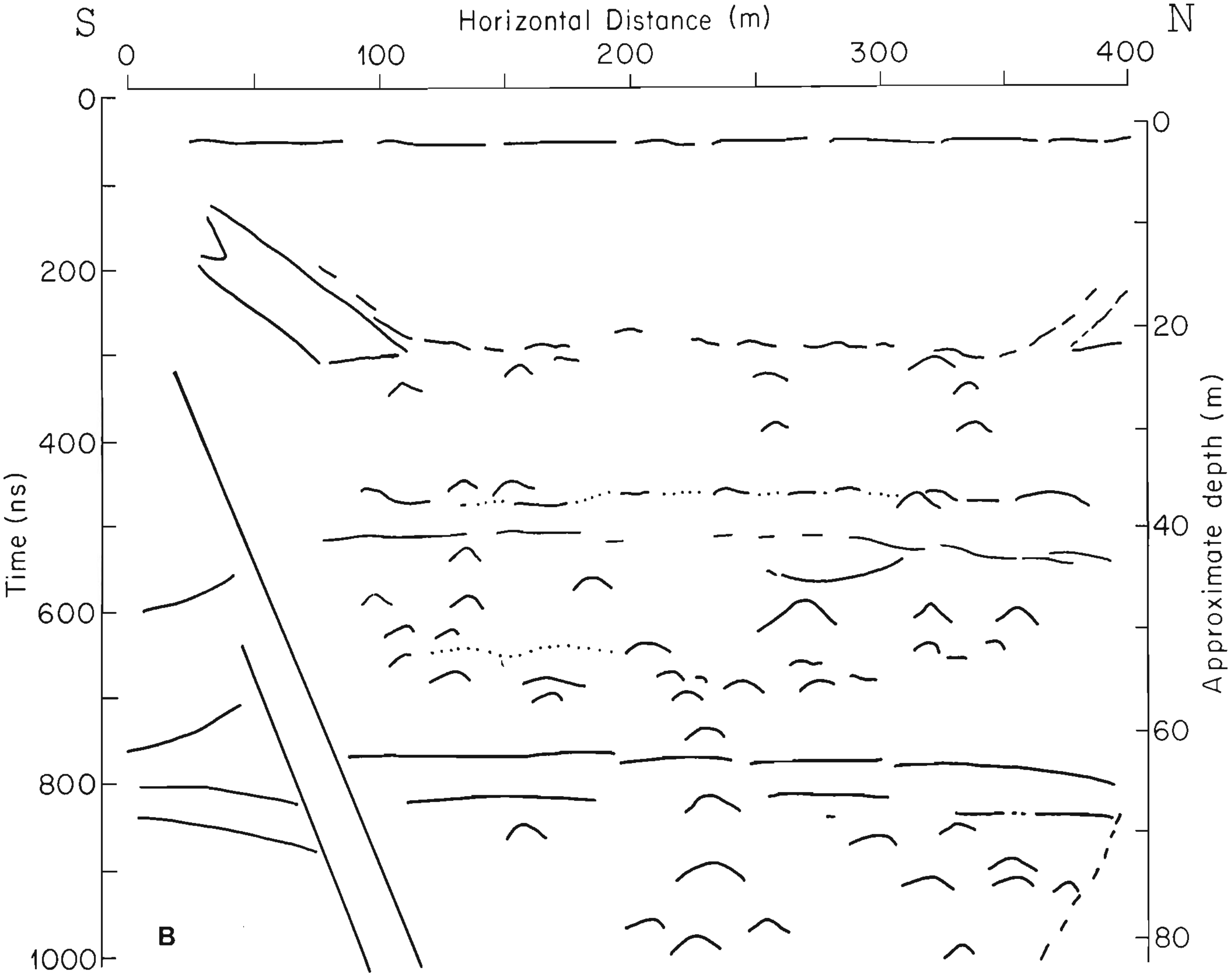

Figure 8. (cont.)

SUMMARY AND CONCLUSIONS

The results of the reconnaissance GPR survey of the interior of Meteor Crater show clearly the utility of GPR for detecting subsurface internal structures. As can be clearly seen on the radar cross-sections, a number of dielectric reflectors were identified at depth. The ability to conduct CDP surveys and thus calculate the propagation speed of the electromagnetic signal allowed the creation of a depth scale for these reflectors. The depth of some of the observed reflectors corresponds to lithological boundaries known from previous data from drilling and shaft excavation. These data, however, are one dimensional whereas the radar profiles are two dimensional. They, thus, provide significant new information on the internal structure of impact craters, such as the variability in the thickness of the various strata detected. The next step in the study of Meteor Crater, using GPR, is to undertake a more detailed survey with closer spaced orthogonal lines to obtain a true three-dimensional image of the subsurface.

The successful interpretation of the Meteor Crater radar data resulted, in a large part, from the availability of preexisting data on the subsurface structure. This situation begs the question of the ease of detailed interpretation of radar data at other structures, where such information is unavailable. Future plans include radar surveys at other small impact structures to answer this question. The experience gained with the well constrained Meteor Crater survey will help significantly with the interpretation of the survey results at these other impact structures.

Lastly, it is important to note the capability of state-of-the-art, high powered, digital GPR systems to detect features such as the water table in arid conditions, even if they are at substantial depth from the surface (≅65 m). This capability of GPR systems had not been demonstrated before and may have considerable utility in planning irrigation schemes in semidesert environments.

ACKNOWLEDGMENTS

We would like to thank the Barringer Crater Company for a grant towards the field work and the staff at Meteor Crater for assistance. The efforts of J. Rupert (GSC) in reformatting the data are also appreciated, as well as those of V. Allen (GSC) in setting up an interface between the various computing systems used. We also thank Dr. Bernt Milkereit for the data processing on Aurora, Mrs. M. Ford (GSC) for typing the manuscript, A. Rafeek (GSC) for the drafting, and R. Delaunais (GSC) for the photographic work. This paper constitutes Geological Survey of Canada Contribution 17289 and Lunar and Planetary Institute Contribution No. 710. The Lunar and Planetary Institute is operated by the Universities Space Research Association under Contract No. NASW-4066 with the National Aeronautics and Space Administration.

REFERENCES

Ackermann, H.D., Godson, R.H., and Watkins, J.S.
1975: A seismic refraction technique used for subsurface investigations at Meteor Crater, Arizona; Journal Geophysics Research v. 80, p. 765-775.

Annan, A.P.
1983: General state-of-the-art review of ground probing radar; A-Cubed Inc. Report to Earth Physics Branch, Energy, Mines and Resources, March, 1983, 89 p. + Annexes.

Laflèche, P.T., Judge, A.S., and Pilon, J.A.
1987: Ground probing radar in the investigation of the competency of frozen tailings pond dams; in Current Research, Part A, Geological Survey of Canada, Paper 87-1A, p. 191-197.

Pilon, J.A., Allard, M., and Séguin, M.
1992: Ground probing radar in the investigation of permafrost and subsurface characteristics of surficial deposits in Kangiqsualujjuaq Northern Quebec; in Ground penetrating radar, J.A. Pilon (ed.); Geological Survey of Canada, Paper 90-4.

Roddy, D.J.
1978: Pre-impact geologic conditions, physical properties, energy calculations, meteorite and initial crater dimensions and orientations of joints, faults and walls at Meteor Crater, Arizona; Proceedings, Lunar Planetary Science Conference 9th, p. 3891-3930.

Roddy, D.J., Boyce, J.M., Colton, G.W., and Dial, A.L.
1975: Meteor Crater Arizona, rim drilling with thickness, structural uplift, diameter, depth, volume, and mass-balance calculations; Proceedings, Lunar Science Conference 6th, p. 2621-2644.

Shoemaker, E.M.
1960: Penetration mechanics of high velocity meteorites, illustrated by Meteor Crater, Arizona; in Structures of the Earth's Crust and Deformation of Rocks, International Geological Congress, Copenhagen, XXI Session, pt. 18, p. 418-434.
1963: Impact mechanics at Meteor Crater, Arizona; in The Moon, Meteorites, and Comets, B.M. Middlehurst and G.P. Kuiper (eds.) p. 301-336. University of Chicago Press, Chicago.
1974: Synopsis of the geology of Meteor Crater; in Guidebook to the Geology of Meteor Crater, p. 1-11, 37 Annual Meeting Meteoritic Society.

Digital enhancement of ground probing radar data

Huw V. Rees[1] and Jonathan M. Glover[2]

Rees, H.V. and Glover, J.M., 1992: Digital enhancement of ground probing radar data; in Ground penetrating radar, ed. J. Pilon; Geological Survey of Canada, Paper 90-4, p. 187-192.

Abstract

Digital signal processing techniques were applied to ground probing radar (GPR) data. The data set was taken from a high resolution profile of shallow firn containing a buried crevasse, located on the western margin of the Greenland ice field. The aim of the processing was to improve the resolution of the reflection events on the radar profile.

Techniques commonly used for seismic reflection data were applied to the data. Spiking (deconvolution) filters were not successful, because the assumptions inherent to the method do not apply to GPR data. However, processes such as minimum entropy deconvolution (MED), based on wavelet estimation, can be used to enhance firn reflections without degrading the crevasse response.

Other types of processing also enhanced the GPR data. Direct Current (DC) drifts superimposed on the reflection waveforms were reduced by applying a drift correction process, which subtracts the drift function from the waveforms. Matched filters were also used to improve the signal-to-noise ratio. The wavelet estimate on which the matched filter was based was calculated by log spectral averaging.

Résumé

Des techniques de traitement numérique des signaux ont été appliquées aux données recueillies par géoradar. L'ensemble de données provient d'un profil à haute résolution d'un névé peu profond contenant une crevasse enfouie, située dans la marge occidentale de l'inlandsis groenlandais. Le traitement visait à améliorer la résolution des phénomènes de réflexion sur le profil radar.

Les techniques généralement utilisées pour les données de sismique réflexion ont été appliquées à ces données. Les filtres de déconvolution contractante n'ont pas donné des résultats satisfaisants du fait que les hypothèses inhérentes à la méthode ne s'appliquent pas aux données radar. Cependant, les procédés comme la déconvolution à minimum d'entropie, basés sur l'estimation du signal, peuvent être utilisés pour améliorer les réflexions dans le névé sans détériorer la réponse de la crevasse.

D'autres types de traitement ont également permis d'améliorer les données recueillies par géoradar. Les variations du courant continu superposées aux échos ont été réduites en appliquant un procédé de correction des variations qui consiste à soustraire la fonction de variation des formes d'onde. Des filtres accordés ont également été utilisés pour améliorer le rapport signal sur bruit. Le signal sur lequel a été basé le filtre accordé a été calculé à l'aide de la moyenne spectrale logarithmique.

---

[1] Royal Holloway and Bedford New college, University of London, Surrey, UK TW2O 0EX

[2] Subsurface Geotechnical Services, Unit 235, Startford Workshops, Burford Road, London, UK E15 2SP

INTRODUCTION

A high resolution GPR survey of the western margin of the Greenland ice sheet produced continuous profiles of near surface firn structure (Glover and Rees, 1992). This paper describes attempts to enhance the quality of the data using digital signal processing techniques. A number of different processes were applied to one particular section of profile, (Fig. 1). This record was chosen because it contains a crevasse response and numerous reflection events from ice layering within the firn. The aim was to increase the resolution of reflection events and enhance the crevasse response, as well as evaluating the suitability of each process for inclusion in a real time system. The initial processing was applied using a seismic processing package because of the apparent similarity between these data and seismic reflection data.

ANALOGUE-DIGITAL CONVERSION

Field data were recorded on an FM magnetic tape recorder at a rate of 6.4 traces per second. The analogue signals were sampled by a 12 bit analogue-to-digital converter and stored on a VAX 11/780. Digital samples were taken every 0.25 ms with 560 samples taken per trace. Analogue-to-digital conversion was triggered by the feed through pulse with a delay applied so that sampling began at the appropriate position on the start of the next trace.

GRAPHICAL PRESENTATION OF THE DATA

The digital data were displayed in two forms. The first was the variable area wiggle-line format commonly used for presenting seismic data (see Figs. 1, 3, 4). The second used a 32 level grey-shade pixel format produced by a line printer (see Figs. 5, 6), similar to that used by McMechan (1983) to display seismic data.

DATA PROCESSING

Data preparation

An individual trace from this data is illustrated in Figure 2. This signal has two distinctive zones; a high amplitude region at the beginning of the trace corresponding to the feed through pulse, and a lower amplitude region, which occupies the rest of the signal. The low amplitude region contains the reflected data. A mute was applied to the beginning of each trace, so that the processed data were not corrupted by the presence of the feed through pulse. Automatic gain control (AGC) was applied to the data before any filtering was attempted, to equalize the signal energy over the record. There were difficulties associated with this process, because in areas where there were no reflection events the AGC overamplified noise. These areas included the upper part of the record and the crevasse response.

Spiking filter

The first process applied to the data was the spiking (deconvolution) filter. The aim of this filter is to remove the convolutional component of the signal resulting from the wavelet and to yield the reflection coefficient series. There was no prior knowledge of the source wavelet so the filter coefficients were obtained by solving the Wiener equation, where the autocorrelation of the wavelet is assumed to be a scaled version of the autocorrelation of the trace. The cross correlation between the wavelet and the desired output is a zero delay, unit spike.

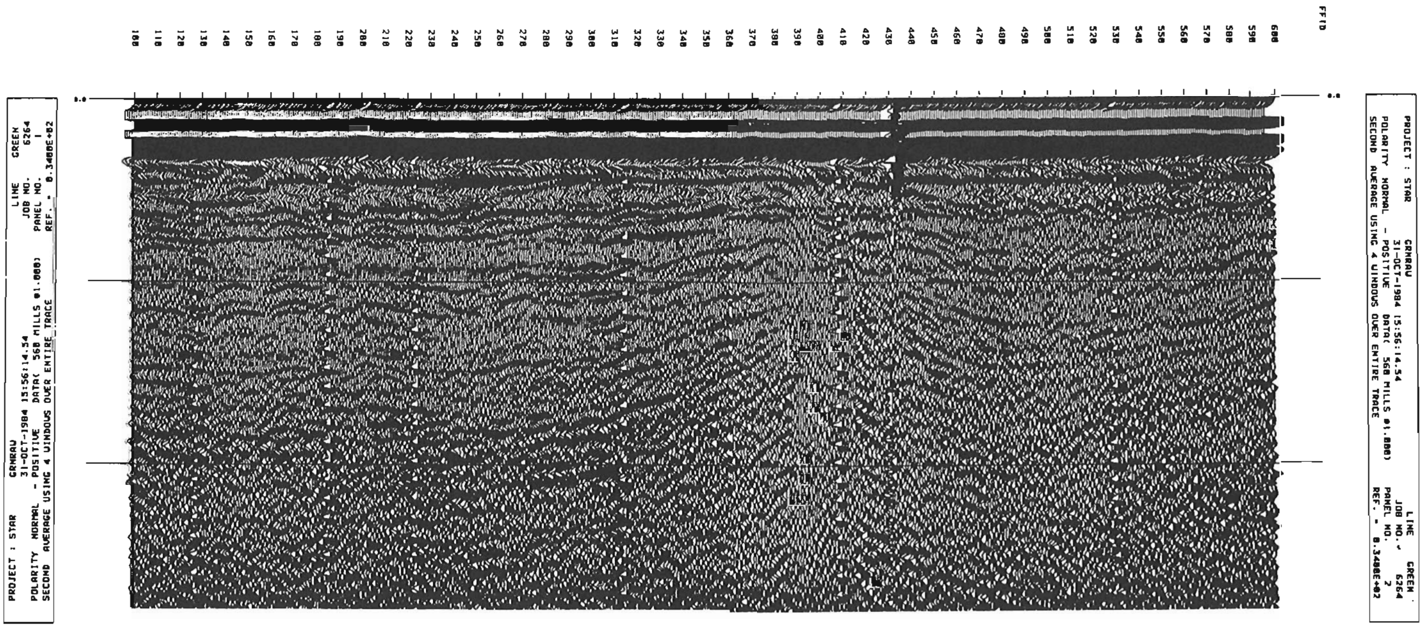

Figure 1. Unprocessed profiles across a type 1 crevasse response, presented using variable area, wiggle line format.

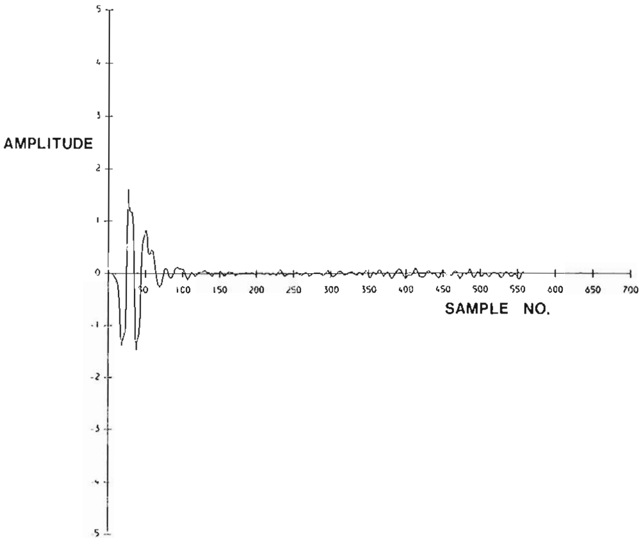

Figure 2. An individual trace from Figure 1.

Each trace in the record was considered independently, resulting in a separate filter being applied to each one. The length of the filter was always 101 samples. The processed data are shown in Figure 3. In general, the resolution of individual reflection events has been reduced and the crevasse is no longer a distinctive feature of the record. The processing has not improved the quality of the data and is therefore unsatisfactory.

In applying this process, we must assume the following: 1) the source wavelet is minimum phase, and 2) the reflection coefficient series is a white noise series, which implies that the autocorrelation function of the trace is the same as the source wavelet, except for a constant scale difference.

The major concern is that the first assumption does not apply to ground probing radar data. Cepstral analysis (Otis and Smith, 1977) of the data indicated that the wavelet is not minimum phase. The second assumption may also be invalid, because the data do not contain as many reflections as normal seismic data. The parts of the waveform where no reflections are present would not approximate to a white noise series of reflection coefficients.

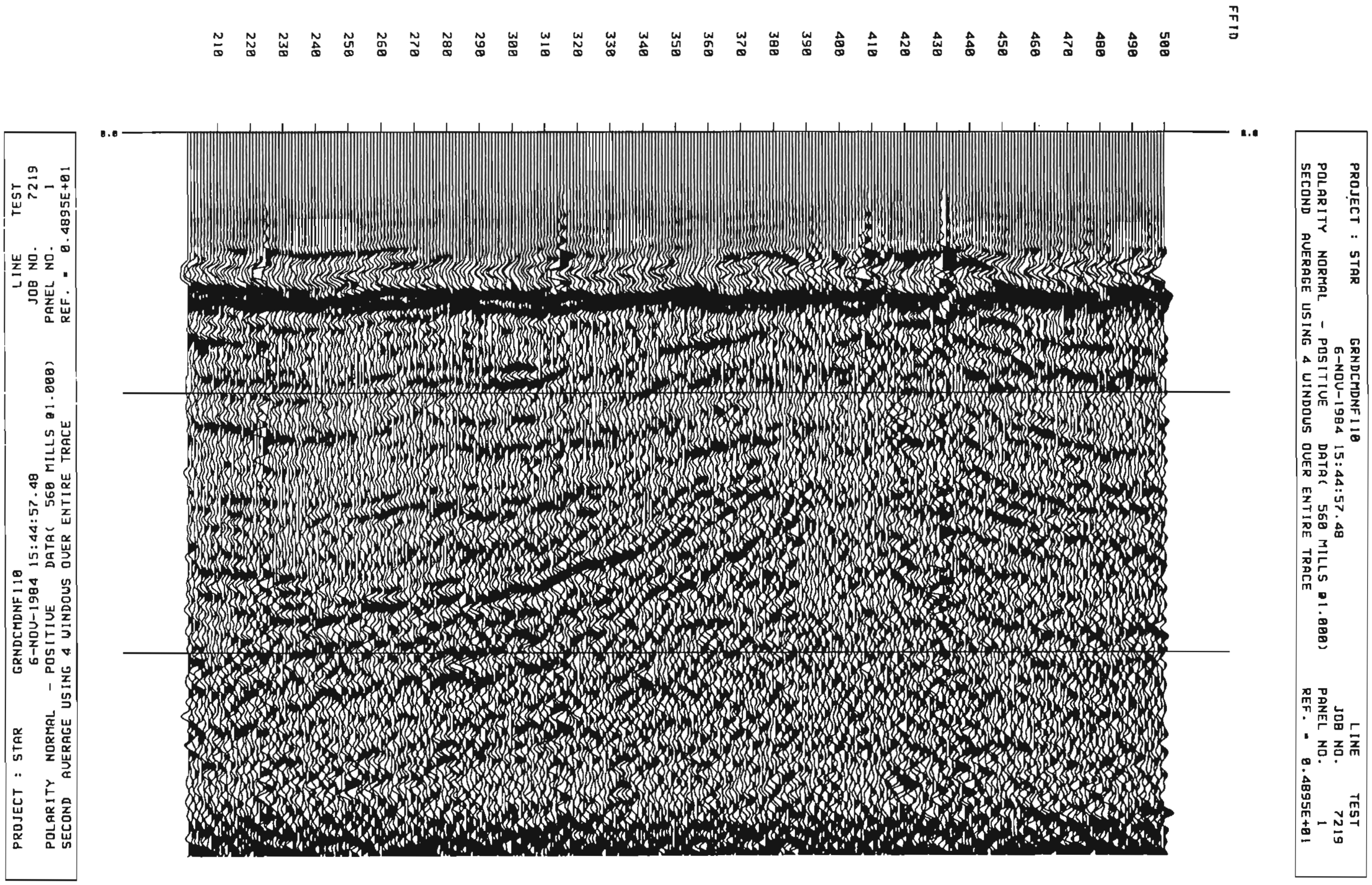

Figure 3. Data of Figure 1 processed using a spiking filter.

Minimum entropy deconvolution

The next process to be applied was minimum entropy deconvolution (MED). The MED process, described by Wiggins (1978), seeks to find "a linear operator that maximises the 'spike-like' character of a representative number of traces". The major attraction of this technique is that it requires neither any phase assumption of the source wavelet nor the reflection coefficient series to be a white series. In the application of the process, only one filter was used, which was designed from the entire record. The results are illustrated in Figure 4.

The outcome of MED processing is considered a success as reflection events have been enhanced and the low amplitude nature of the crevasse has been preserved.

Drift correction and matched filters

Although well established seismic processing techniques offer attractive methods to process the data, they may not necessarily offer a complete solution; vast improvements to the data can be gained through applying simpler processes, such as drift correction (Rees, unpublished report, 1988). Figure 5 illustrates the original field data presented in the grey-shade pixel format. The light and dark vertical bands on the lower part of the profile are caused by a DC drift superimposed on the signal. The drift correction process assumed that the data would normally have a zero mean value. The signal deviation from the mean is determined by estimating a function f(t) to fit the data, using the least squares criteria. Finally the function f(t) is subtracted from the trace to yield the drift corrected data.

Many types of function could be used to estimate the drift. A reasonable approximation has been achieved using functions of the type:

$$f(t) = \alpha n^{i}$$

where

n is sample index/number

α is constant, which differs for each trace

The power 'i' is determined by experimentation on a set of data taken from the entire record. The data of Figure 5 were corrected using a value i = 3, with α calculated for each trace.

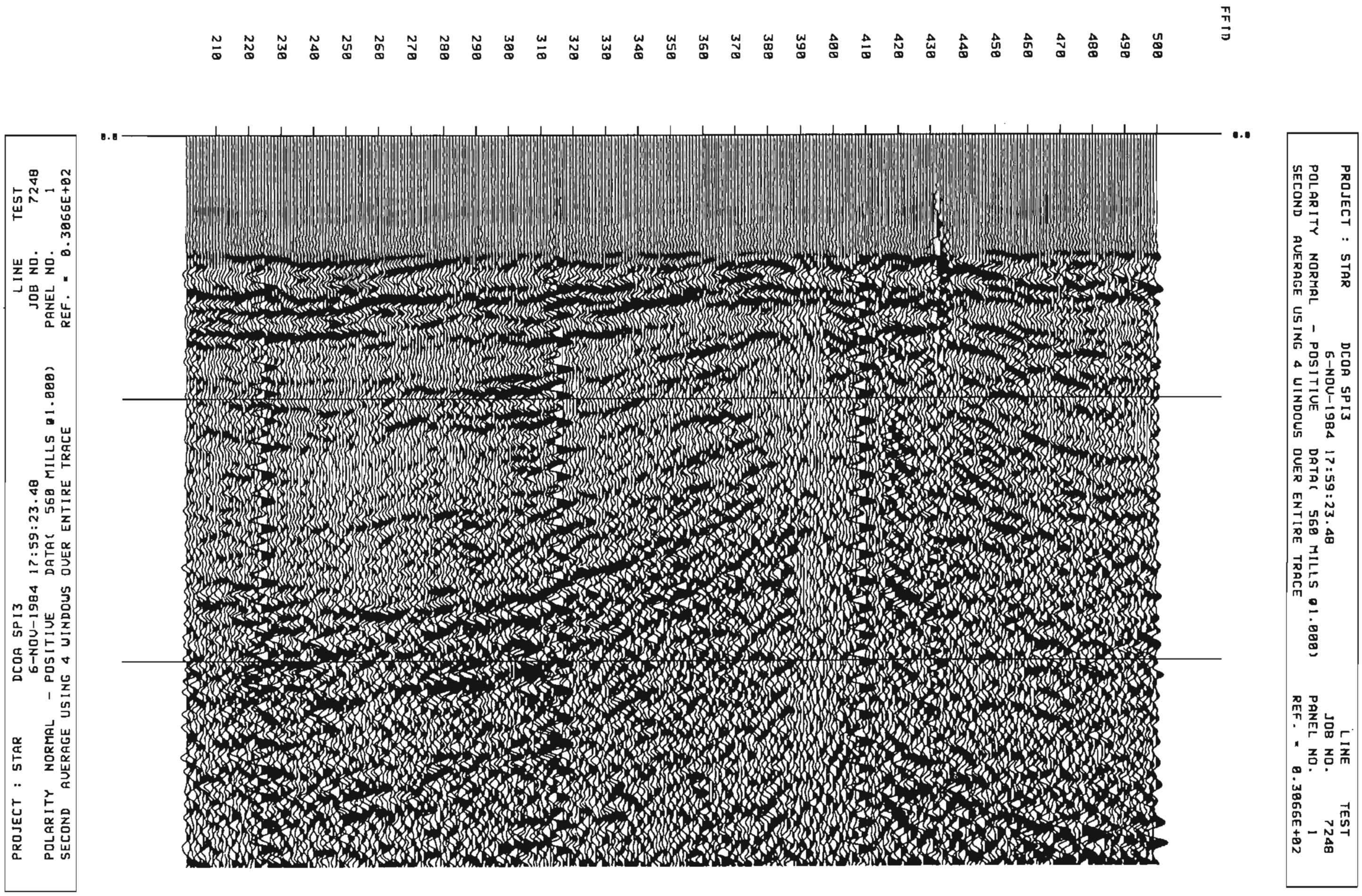

Figure 4. Data of Figure 1 processed using MED.

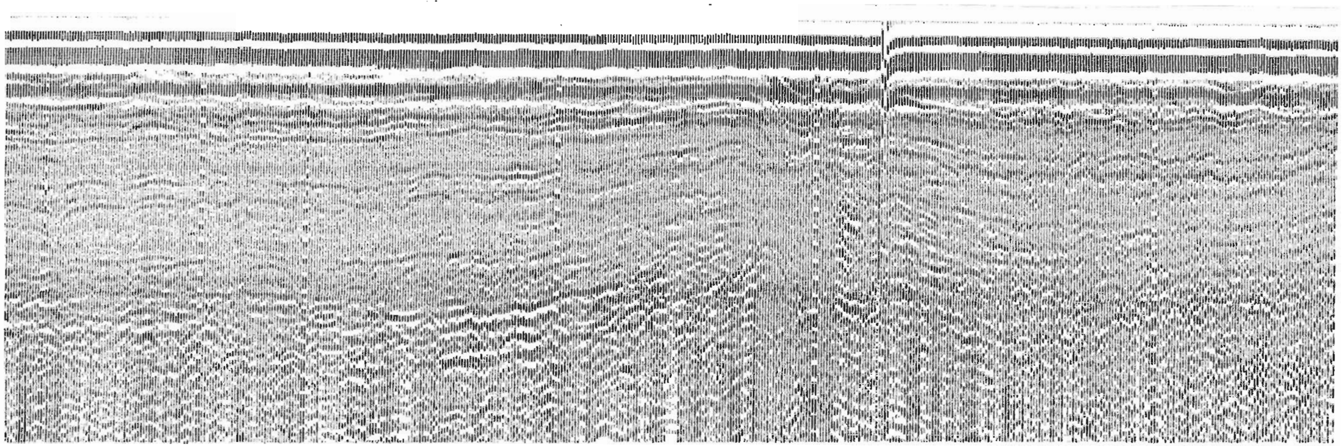

Figure 5. Unprocessed profile across a type 1 crevasse response presented using variable line format.

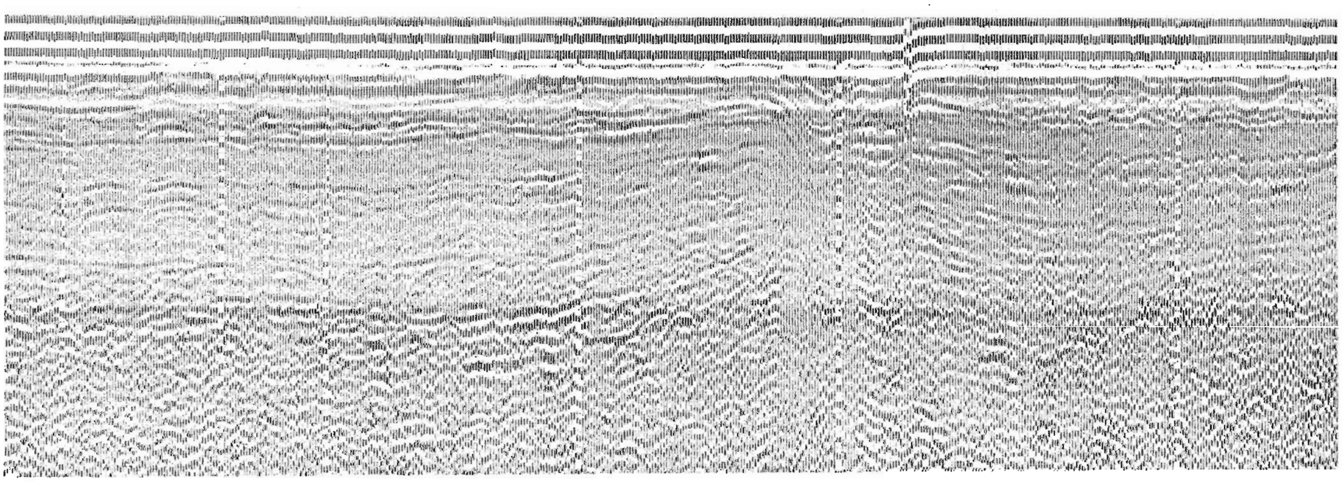

Figure 6. Data of Figure 5 processed using drift correction and matched filter processing.

The record illustrated in Figure 6 shows the drift corrected data. This record has also had a matched filter applied to it, which successfully increased the signal-to-noise ratio.

The wavelet estimate on which the matched filter was based was done by log spectral averaging (Otis and Smith, 1977). Log spectral averaging is a technique used to retrieve the source wavelet by averaging the complex cepstra as a set of traces. This assumes that the contribution of the source wavelet in each complex cepstrum will remain constant, where the contribution made by the reflection coefficient series will be different. Averaging the complex cepstra emphasises the contribution due to the wavelet and attenuates the reflection coefficient series. The inverse of the average complex cepstrum will yield the source wavelet. This technique requires no phase assumptions to be made.

CONCLUSIONS

This paper describes work that set out to enhance the quality of GPR data through the application of seismic processing techniques. The main problems with this approach were caused by the minimum phase wavelet and white noise reflection coefficient assumptions, inherent to certain of the seismic processing methods.

The results of MED appeared to enhance the reflection events produced by the ice layers within the firn, without removing the low amplitude characteristics of the crevasse. The MED process can only be applied once a suitable data set has been acquired, which could lead to storage problems in a real time system and, almost certainly, to delays in data acquisition. Perhaps the most interesting feature of the MED processing was that the same filter was applied across the entire record therefore maintaining uniformity. Such filters could be designed through wavelet estimation using cepstral analysis. However, such methods could only be practically implemented if the filter designs were based on smaller data sets acquired at the beginning of the survey (i.e., a pilot survey).

The drift correction process appears to significantly enhance reflection events in the lower part of the record. The correction applied to the data is proportional to the ith power of the sample index (in this case i=3). It may be possible to apply this process in real time to varying drift functions, by applying curve fitting algorithms that would allow both the values of i and the constant α to vary for each trace. This process combined with MED processing offers the potential for real time enhancement of GPR data.

ACKNOWLEDGMENTS

The authors are grateful to Professor D.J. Blundell, Royal Holloway and Bedford New College, University of London, for supervising this research project, which was funded by NERC CASE research grants. We also wish to thank Cominco Europe Ltd. for allowing these data to be used for research purposes. We also acknowledge the assistance of GSE Rentals Ltd., DPTS Ltd., and Mr. T. Woods for providing equipment and data processing facilities.

REFERENCES

Glover, J.M. and Rees, H.V.
1992: Radar investigations of firn structure and crevasses; in Ground penetrating radar, J.A. Pilon (ed.); Geological Survey of Canada, Paper 90-4.

McMechan, G.A.
1983: Application of image enhancement and pattern recognition algorithms to seismic reflection data; Bulletin, Seismology Society of America, v. 73, no. 1, p. 307-314.

Otis, R.M. and Smith, R.B.
1977: Homomorphic deconvolution by log spectral averaging; Geophysics, v. 42, no. 6, p. 1146-1157.

Wiggins, R.A.
1978: Minimum entropy deconvolution; Geoexploration v. 16, p. 21-35.

Cepstral analysis of subsurface data

Dennis Roddy[1]

Roddy, D., 1992: Cepstral analysis of subsurface data; in Ground penetrating radar, ed. J. Pilon; Geological Survey of Canada, Paper 90-4, p. 193-198.

Abstract

In an experimental setup using carrier free radar, overlapping echo signals were obtained using reflectors in a water tank. Deconvolution of the echoes was achieved using cepstral analysis. For two reflectors, for which the separation could be adjusted to 4.2, 8.2, and 12 cm, the complex cepstral analysis yielded corresponding values of 4.8, 7.7, and 10.3 cm. Noise introduced by oversampling was reduced to negligible levels by a decimation procedure, which effectively reduced the sampling rate.

Résumé

Dans un montage expérimental où l'on a utilisé un radar sans onde porteuse, on a obtenu un chevauchement d'échos par l'emploi de réflecteurs dans un réservoir d'eau. La déconvolution des échos a été réalisée en recourant à l'analyse cepstrale. Pour deux réflecteurs, pour lesquels la séparation pouvait être ajustée à 4,2, 8,2, et 12 cm, l'analyse cepstrale complexe a donné les valeurs correspondantes de 4,8, 7,7 et 10,3 cm. Le bruit introduit par le suréchantillonnage a été réduit à des niveaux négligeables par un procédé de sous-échantillonnage qui a en fait abaissé le taux d'échantillonnage.

INTRODUCTION

Previous experience with impulse-type radar used for a variety of surveys had highlighted the problem of separating overlapping echo returns. In particular, in surveying the roof of a mine stope for fractures (Roddy and Coolen, 1982), the reflections from a number of nearsurface fractures overlapped with the surface reflection making it difficult to visually separate these signals. Part of the problem originates from the bandwidth limitations of the transmission medium producing time spreading of the pulse.

Cepstral analysis, first introduced by Bogert et al. (1963) appeared to offer a means of deconvolving signals of this nature. To investigate the method, test results were obtained using known reflectors, and these were analyzed using the cepstral analysis programs contained in the IEEE Programs for digital signal processing (1979).

DEFINITION OF TERMS

The terminology used in cepstral analysis was introduced originally by Bogert et al. (1963). By taking the logarithm of the spectrum, multiplicative components of the spectrum are converted to additive terms, with the echo signal contributing a "harmonic" component in the frequency domain. This Bogert paraphrased as "rahmonic". He termed the method of analysis "cepstrum", as the nearest pronouncable paraphrase of spectrum. The paper by Bogert et al. provides an excellent introduction to the topic, and a more recent paper at the introductory level is that by Randall and Hee (1981). Although not all the terms associated with cepstral analysis are widely used, the main ones are listed here for convenience:

spectrum	→	cepstrum
frequency	→	quefrency

---

[1] Department of Electrical Engineering, Lakehead University, 955 Oliver Road, Thunder Bay, Ontario P7B 5E1

period → repoid
filter → lifter
harmonics → rahmonics
phase → saphe
magnitude → gamnitude

The original work on cepstral analysis was carried out on real signals in the time domain and the frequency domain and is now referred to in the literature as real cepstral analysis. Later work (Schafer, 1969; Tribolet, 1979) extended the method to the complex frequency domain and is referred to as complex cepstral analysis.

EXPERIMENTAL SET-UP

The experimental setup is shown in Figure 1. The radar equipment used in the tests is manufactured by Geophysical Survey Systems Inc. (GSSI). This equipment is capable of operating with any one of a number of transducers; model 101-C was used. This transducer contains separate dipoles for transmitting and receiving. The dipoles are stacked in parallel form in the normally horizontal plane. The transmitted pulse has a specified pulse width of 1 ns at a pulse repetition rate of 52 kHz. A sampling circuit in the transducer converts the received short- to long-duration pulses suitable for display on a low frequency oscilloscope and graphics recorder. The time expansion factor, which is controlled by the radar settings, was 1.183 X 10^6 for all the tests.

The low frequency output from the radar unit was recorded directly on a floppy disk, using an Apple II microcomputer in conjunction with an A/D converter. The sampling rate of the A/D converter was 12.6 kHz. In addition, a separate series of tests were conducted in which the data were first recorded on tape using a Hewlett Packard model 3963A tape recorder. A total of 1024 points were sampled in each test.

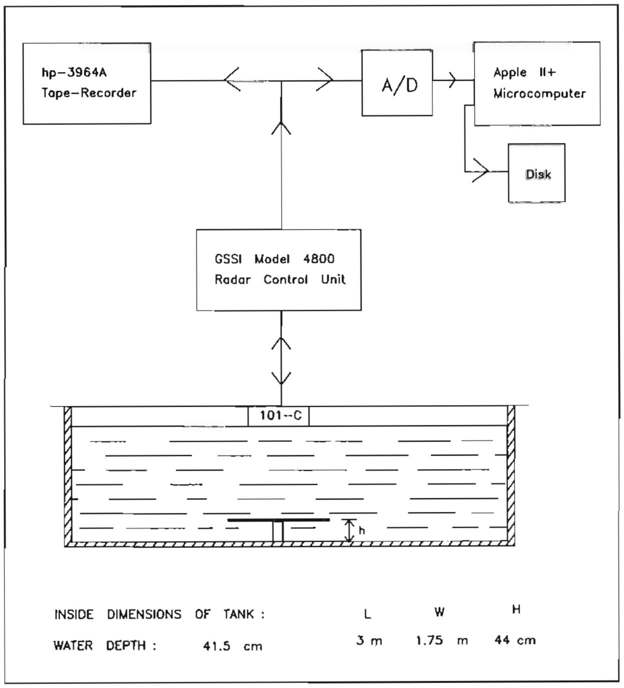

Figure 1. Experimental set-up.

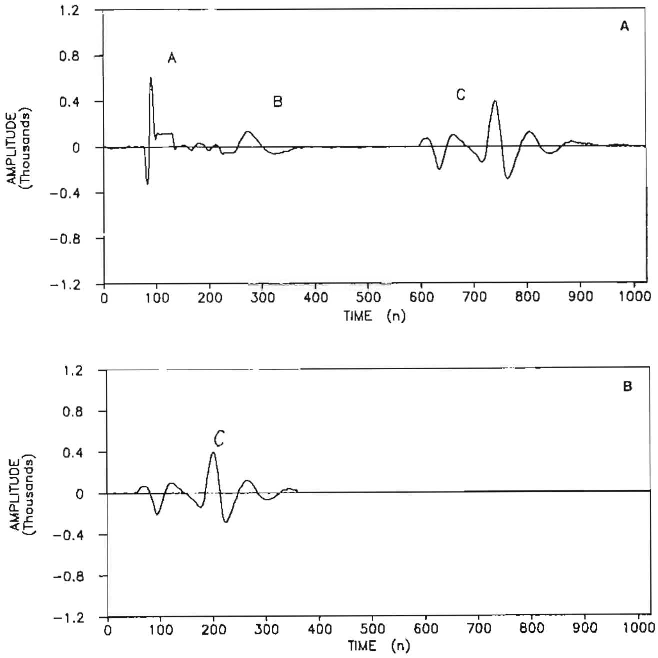

Figure 2A. Pulse waveforms A- start of scan; B- at air/water interface; C- double reflexion for reflector spaces 8.2 cm; **B.** Preprocessed data to eliminate the first two pulses and move the desired reflexions to the start of the record. Unit interval (n=1) on time scale represents 0.044 ns. Amplitude axes unscaled.

The digital signal processing programs (IEEE, 1979) were installed on a Sun 180 computer at Lakehead University. The experimental data were uploaded to the Sun through the Apple II microcomputer. Separate programs were written to preprocess the data, and to lifter the cepstra, as described in the next two sections.

To achieve reasonable echo delay times, while using a relatively short test range, the reflectors were submerged in water as shown in Figure 1. A metal rod was used as the first reflector and the tank bottom as the second. The interecho arrival time was altered by altering the height h of the rod above the bottom of the tank. Tests were conducted for values of h of 4.2, 8.2, and 12 cm, with corresponding interecho intervals of 2.52, 4.92, and 7.2 ns respectively. A dielectric constant (relative permittivity) of 81 was assumed for water.

Tests were conducted for different orientations of the metal rod relative to the dipole axes, and for the transducer at various heights above the water surface. The results presented here relate to the transducer just touching the water surface and the metal rod positioned parallel to the dipole axes.

TEST RESULTS

The data as recorded directly on disk are shown in Figure 2 for a reflector separation of 8.2 cm, with the base of the transducer casing submerged slightly into the water. In Figure 2A the pulse labelled A is the start-of-scan pulse; pulse B is a combination of the directly coupled incident pulse and the reflection from the air-water interface; and pulse C is the combined echo pulses from the metal rod and the tank bottom. Figure 2B shows how the data were preprocessed to eliminate the first two pulses and move the desired reflections to the start of the record. The recorded data were truncated at 350 points and padded with zeros out to 1024 points. Similar data were recorded for reflector separations of 4.2 and 12 cm.

The radar timebase was calibrated using a 10 ns pulse source provided with the equipment. The sampling interval for the 1024 record was found to be about T = 0.044 ns. The time variable for the discrete signal was t = nT, and the axes on the graphs was scaled in n where $0 \le n \le 1023$. Thus, to convert the n-values to real time, it was only necessary to multiply the n-value by 0.044 ns(for the basic sampling rate). In those tests where a reduced sampling rate was used, the sampling interval was increased by the sample-rate reduction factor as described later in the test results. The same variable n was used for quefrency, and the same comments apply.

In the frequency domain, the variable k was used where $0 \le k \le 511$. The frequency sampling interval was the reciprocal of the full-scale timebase of the radar, or what is termed the timerange. Denoting this by T_R, then to convert k to frequency, it was necessary to multiply the k-values by $1/T_R$. The measured value for T_R, which was constant for the radar settings used, was 44.5 ns, and thus the frequency multiplying factor was 1/(44.5 ns) or 22.5 MHz (for the basic sampling rate).In those tests where a reduced sampling rate was used, the frequency sampling interval was decreased by the sample-rate reduction factor as described later.

REAL CEPSTRAL ANALYSIS

Figure 3 shows the spectrum (A), the log magnitude of the spectrum (B), and the real cepstrum for the preprocessed data (C) for the reflectors spaced at 8.2 cm. In Figure 3A the signal is seen to have been severely oversampled. Noise in the

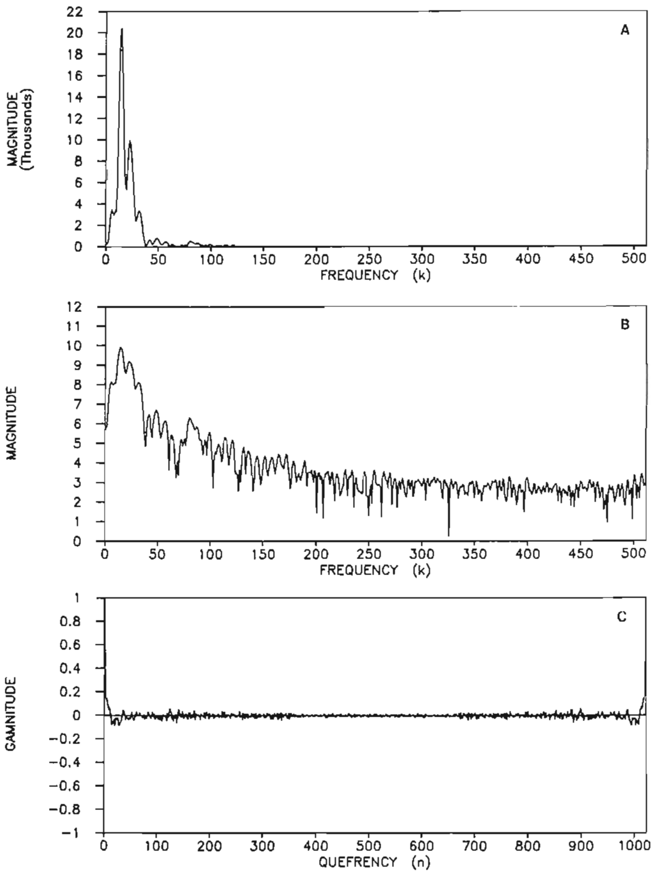

Figure 3A. Spectrum magnitude; **B.** Log magnitude; **C.** Real cepstrum for the waveform C in Figure 2 (reflectors spaced 8.2 cm). Unit interval (k=1) on frequency scales represents 22.5 MHz. Unit interval (n=1) on quefrency scale represents 0.044 ns. Vertical axes unscaled.

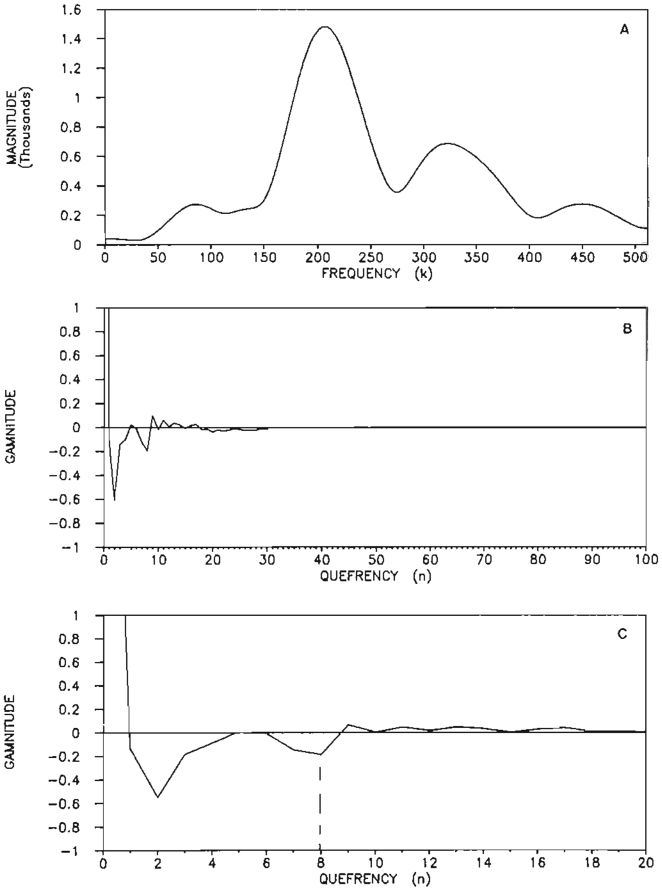

Figure 4A. Spectrum magnitude with the sampling rate reduced by a factor of 14:1; **B.** Log magnitude with the sampling rate reduced by a factor of 14:1; **C.** Real cepstrum with the sampling rate reduced by a factor of 14:1. Unit interval (k=1) on (a) represents 1.61 MHz. Unit interval (n=1) on (b) and (c) represents 0.616 ns. Vertical axes unscaled.

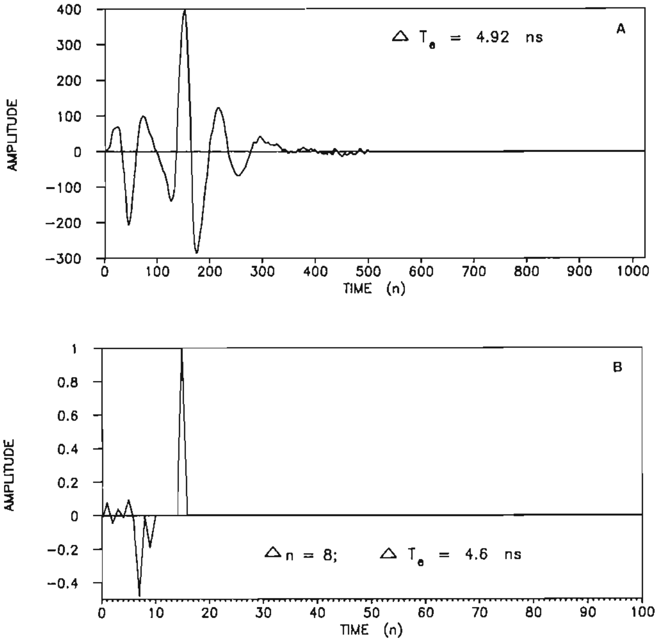

Figure 5. Reflector spacing 8.2 cm. **A.** Double reflection (n=1 represents 0.044 ns); **B.** Complex cepstrum (n=1 represents 0.572 ns). Vertical axes unscaled.

spectrum is very evident in the log magnitude graph (Fig. 3B), whereas the real cepstrum graph (Fig. 3C) yields little information.

From Figure 3, it was estimated that to have the major peak occupy the full bandwidth, the sampling rate would have to be reduced by a factor of about 14:1. This rate was achieved by taking every 14th sample from the data. The analysis was repeated for this reduced sampling rate, the results of which are shown in Figure 4A-C. The interecho interval is given by the first rahmonic, which on Figure 4C is seen to occur at n = 8. Referring this back to the original sampling rate gives an interval of 8 X 14 = 112. Using the value of T = 0.044 ns gives an interecho interval of 112 X 0.044 = 4.93 ns, which compares very favourably with the expected value of 4.92 ns.

From Figure 4A the spectrum is seen to peak at about k = 210. A pulse modulated sinewave will peak at the carrier frequency. In this case, assuming a pulse that is a single cycle sinusoid, the pulse width is equal to the periodic time of the carrier, and hence the spectral peak occurs at a frequency that is the reciprocal of the pulse width. As shown in the section on test results, the basic frequency sampling interval is 22.5 MHz, and with the sampling-rate reduction factor of 1/14, the peak frequency corresponds to 210 X 22.5/14 MHz = 337.5 MHz. The corresponding period is 1/(337.5 MHz) = 2.96 ns, which is considerably wider than the pulse width of 1 ns specified by the manufacturer.

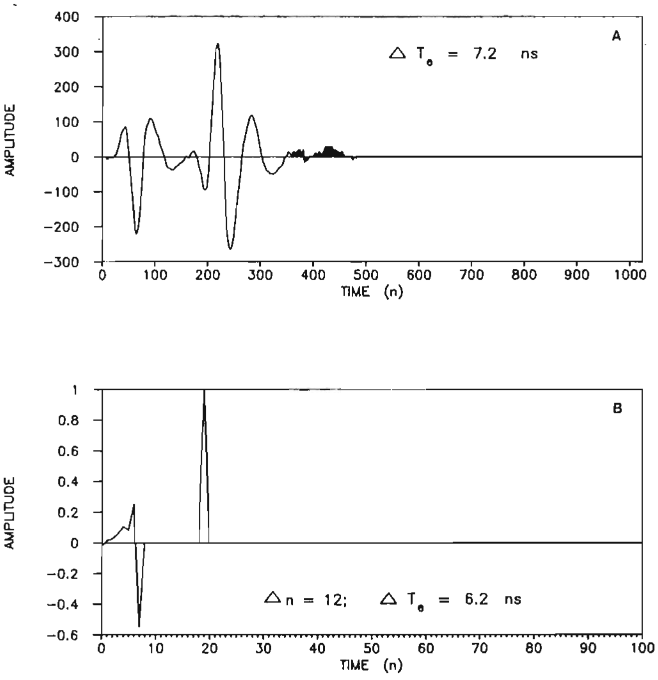

Figure 6. Reflector spacing 12cm. **A.** Double reflection (n=1 represents 0.044 ns); **B.** Complex cepstrum (n=1 represents 0.572 ns). Vertical axes unscaled.

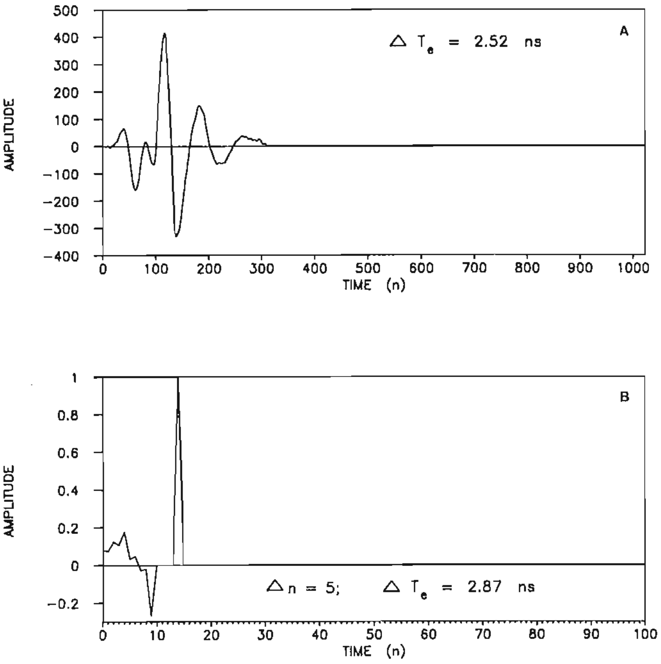

Figure 7. Reflector spacing 4.2 cm. **A.** Double reflection (n=1 represents 0.044 ns); **B.** Complex cepstrum (n=1 represents 0.572 ns). Vertical axes unscaled.

Table 1. Summary results for spacings of 4.2, 8.2 and 12 cm

Reflector spacing		Complex cepstrum results	
(cm)	(ns)	(ns)	(cm)
4.2	2.52	2.87	4.8
8.2	4.92	4.6	7.7
12	7.2	6.2	10.3

COMPLEX CEPSTRAL ANALYSIS

Complex cepstral analysis was performed on the same data as used for the real cepstral analysis. However, bandpass mapping, as described by Tribolet (1979), was used to convert the data to fullband. With the lower frequency limit being zero, the bandpass mapping procedure was considerably simplified, requiring only to be decimated by a ratio of 1/13 and low pass filtered. The necessary computations were made using the programs 5.1 and 8.3 (IEEE, 1979).

Bandpass liftering was applied to the complex cepstrum to remove the wavelet cepstrum and leave only the cepstrum for the echo series. Inverse transforming the liftered cepstrum resulted in the reflector series.

For the 8.2 cm reflector separation, a lifter passband extending from $n = 5$ to $n = 1020$ was tried initially, yielding good results. The liftering was refined by making use of the fact that the reflector series was known to be maximum phase, allowing the lower cutoff for the bandpass lifter to be increased to 512. (The significance of maximum phase in this context is that rahmonics appear in theory only for $n < 0$, which in practice means that they appear between N/2 and N on the positive n axis, where $N = 1024$.) The reflector series obtained were similar in each case, but with the lower cutoff at $n = 512$, the noise was much reduced. The results for this case are shown in Figure 5.

Figure 5A shows the data as recorded; Figure 5B shows the reflector series. From the reflector series, the interecho interval is $n = 8$, which for a decimation ratio of 1/13 and a sampling period of $T = 0.044$ ns gives a time interval of about 8 X 13 X 0.044 = 4.6 ns. Because a variation of 1 in n gives a tolerance of 1 X 13 X 0.044 = 0.572 ns, the result of 4.6 ns compares favourably with the expected value of 4.92 ns.

Similar processing was carried out for the reflector spacings of 12 and 4.2 cm, the results being shown in Figures 6 and 7, respectively. In each case, the interecho interval estimated from the reflector series was within the tolerance of 1 count in n. Table 1 summarizes these results.

The graphical data for the complex cepstrum show that the reflection coefficients have the correct relative signs, the metal rod being negative and the wooden tank bottom positive. No attempt was made to correlate the observed magnitudes of the reflection coefficients with theoretical values.

COMMENTS AND CONCLUSIONS

The method of cepstral analysis allowed the echo information to be successfully extracted from the data, information which was otherwise difficult or impossible to obtain directly from the time waveforms. As well, the relative magnitudes and signs of the reflection coefficients were obtained from the complex cepstral analysis.

To apply the method, however, it was necessary to have some estimate of the bandwidth of the spectrum and to apply bandpass mapping, thus reducing the noise introduced by oversampling. In comparing experimental data with simulated data it was observed that, whereas oversampling presented no problem with simulated data, it introduced noise, which was the major source of error with experimental data.

Knowing that the reflector series was maximum phase also helped greatly in applying liftering to the cepstrum. In more practical situations such information on the nature of the signal is unlikely to be available. A method of mapping the signal into minimum phase was proposed by Schafer (1969) and has been used by a number of workers (Ulrych, 1971; Childers et al., 1977). (With minimum phase signals, the theoretical cepstrum has rahmonics for $n > 0$ only, as distinct from maximum phase that requires $n > 0$.) This approach may have to be employed with subsurface radar signals.

No attempt was made in these tests to investigate in detail the tolerance on the results, but the following estimate can be made. Assuming that the n-values on the time scale can be read to within ±1, the tolerance on the time values will be $\pm T$, where T is the sampling interval. For the basic sampling rate, $T = 0.044$ ns, and for a sampling rate reduction factor of 1/13 $T = 0.044$ ' 13 = 0.572 ns.

ACKNOWLEDGMENTS

The author is pleased to acknowledge the major contributions made by the students who worked on this project; in particular Chris Stiletto who assisted in the experimental work and who organized the computational runs, also Julius Tichaczek, who so ably assisted in the computational work and in preparing the diagrams for this report. The author would also like to thank Mr. Len Collett of the Geological Survey of Canada, who was instrumental in making the radar equipment available on extended loan to Lakehead University. Finally, the author would like to thank Energy, Mines and Resources Canada for their financial assistance, and Lakehead University for making available laboratory and computing facilities.

REFERENCES

Bogert, B.P., Healy, M.J.R., and Tukey, J.W.

1963: The quefrency alanysis of time series for echoes: cepstrum, pseudo-autocovariance, cross-cepstrum and saphe cracking; in Proceedings, Symposium on Time Series Analysis, M. Rosenbblatt (ed.), Wiley, New York, N.Y., p. 209-243.

Childers, D.G., Skinner, D.P., and Kemerait, R.C.
1977: The cepstrum: a guide to processing; in Proceedings, IEEE. v. 65, no. 10, p. 1428-1441.

IEEE
1979: Programs for digital signal processing; Digital Signal Processing Committee (ed.), IEEE Press, New York, N.Y.
The following programs were used:
FIR linear phase filter design program; McClellan, J.H., Parks, T.W., and Rabiner, L.R. (IEEE program 5.1)
Computation of the complex cepstrum; Tribolet, J.M. and Quatieri T.F. (IEEE program 7.2)
Computation of the real cepstrum and minimum phase reconstruction; Quatieri, T.F. and Tribolet, J.M. (IEEE program 7.2)
A Program for Multistage Decimation, Interpolation and Narrow Band Filtering, by Crochiere, R.E. and Rabiner, L.R. (IEEE program 8.3)

Randall, R.B. and Jens Hee
1981: Cepstrum analysis; Bruel & Kjaer Technical Review, no. 3, p. 3-40.

Roddy, D. and Coolen, J.G.
1982: Detection of fractures in geological structures utilizing subsurface radar; Final Report (Contract No. 20SU.23440-0-9108), Energy Mines and Resources, Ottawa, p. 45-48.

Schafer, R.W.
1969: Echo removal by discrete generalized linear filtering; Technical Report 466, MIT Research Laboratories of Electronics, p. 8-11; p. 24-33.

Tribolet, J.M.
1979: Seismic applications of homomorphic signal processing. Prentice-Hall Inc., Englewood Cliffs, N.J., p. 24-34; p. 41-52.

Ulrych, T.J.
1971: Application of homomorphic deconvolution to seimology; Geophysics, v. 36, no. 4, August, p. 650-660.

Radar cross-section of fish at VHF

J.R. Rossiter[1], E.M. Reimer[2], L. Lalumiere[1] and D.R. Inkster[3]

Rossiter, J.R., Reimer, E.M., Lalumiere, L., and Inkster, D.R., 1992: Radar cross-section of fish at VHF; in Ground Penetrating radar, ed. J. Pilon; Geological Survey of Canada, Paper 90-4, p. 199-202.

Abstract

A proposed tool for assessing riverine fish stocks is a ground probing impulse radar with antennas placed on the water surface. The fish are targets moving through the relatively narrow (±20°) radar beam in a fresh water stream. This paper reports measurements of the radar cross-section of a member of the salmonid family, which vary from 1.8-3.4 x 10^{-3} m^2 for a 2.54 kg fish to 3.4-8.6 x 10^{-6} m^2 for a 39 g fish. The riverbed has a radar cross-section of 5.5 x 10^2 m^{-2}, but this stationary reverberation (clutter) echo can be reduced by about 20 dB through signal processing.

Résumé

Pour évaluer les stocks de poissons dans les cours d'eau, on a proposé d'utiliser un géoradar à impulsion dont les antennes sont placées sur la surface de l'eau. Les poissons sont des cibles se déplaçant à travers la faisceau radar relativement étroit (±20°) dans un cours d'eau douce. Le présent article contient les mesures de la coupe radar d'un membre de la famille des salmonidés qui varie de 1,8 - 3,4 x 10^{-3} m^2 pour un poisson de 2,54 kg à 3,4 - 8,6 x 10^{-6} m^2 pour un poisson de 39 g. Le lit du cours d'eau donne une coupe radar de 5,5 x $10^{-2}$$m^2$, mais cette réverbération stationnaire (fouillis d'échos) peut être réduite d'environ 20 dB en recourant au traitement des signaux.

INTRODUCTION

Assessing riverine fish stocks poses an important problem in many countries, especially for commercial species, such as the salmonid family. Traditional methods of stock assessment are visual counting and use of hydroacoustic technology. Visual counting is labour intensive and impossible in turbid waters. Acoustics is unreliable because of the relatively low acoustic backscatter of individual fish (Mitson, 1983). Recently, short pulse radar has been proposed as a counting tool (Canpolar, 1986, 1987). Fundamental to this approach is knowledge of the radar cross-section (rcs) of fish. To our knowledge this parameter has not been previously reported.

METHODOLOGY

Use of radar for detection of fish in freshwater is shown in Figure 1. The transmitted pulse travels through the water, is partially reflected by the target and detected at the receiver. Of special importance is the attenuation rate through water, which is strongly controlled by the water's conductivity (von Hippel, 1954). Attenuation through water is given (Fig. 2) as a function of radar frequency and water conductivity. Typical riverine salinities provide conductivities of 2 x 10^{-3} to 2 x 10^{-2} S/m (20-200 uS/cm) giving attenuation rates of about 2-6 dB/m at 200 MHz. Currently available short pulse radars have a performance figure (transmit power/minimum detectable signal) of about 100 dB.

---

[1] Canpolar Inc., 265 Rimrock Road, Unit 4, Toronto, Ontario M3J 3C6
[2] Canpolar East Inc., 1 Duffy Place, St. John's, Newfoundland A1B 3N7
[3] Intera Technologies Ltd., 2500, 101-6th Avenue S.W., Calgary, Alberta T2P 3P4 (now with Quester Tangent, Sidney, B.C.)

To detect individual fish, the transmit pulse should be less than about 10 ns. Commercially available impulse radars designed for ground penetrating and other applications can transmit pulses with 1-2 cycles of the centre frequency, giving a relative bandwidth of about ±50-70% of the centre frequency (Annan et al., 1975; Rossiter and Gustajtis, 1978).

We used a radar built by A-Cubed Inc. of Mississauga, Ontario (Davis et al., 1987) operating with a centre frequency of 200 MHz and a pulse length of 7 ns. The transmitter, receiver, and antennas were housed in a specifically designed water-proof container connected to the control unit by a fibre optic cable (Fig. 3). Pulses were transmitted at a maximum rate of 30 kHz. With sampling and then hardware stacking of eight scans, the resultant maximum output rate was 14 scans per second. The scans were passed to a portable computer for recording and display. Dynamic range of the system is 15 bits in voltage, or 90 dB.

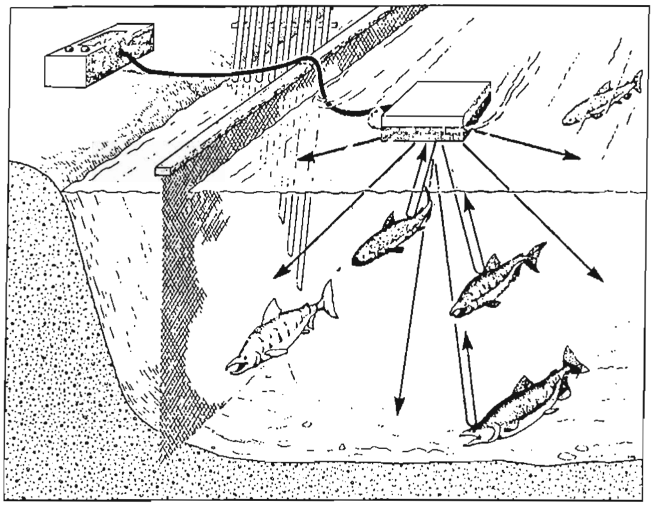

Figure 1. Sketch of radar fish counting system.

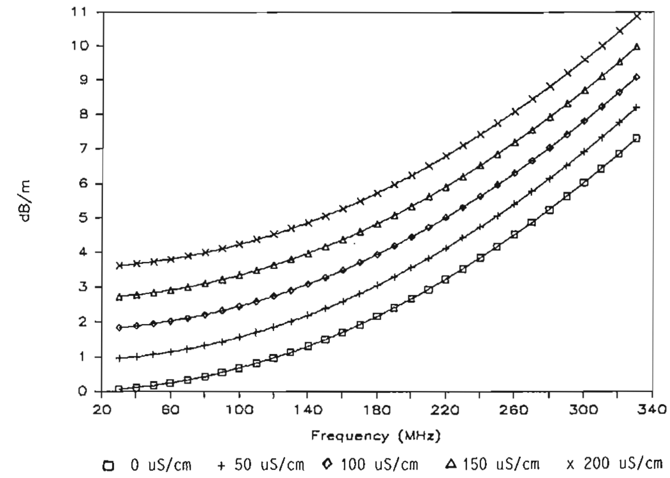

Figure 2. Attenuation of electromagnetic waves in freshwater as a function of frequency for various water conductivities.

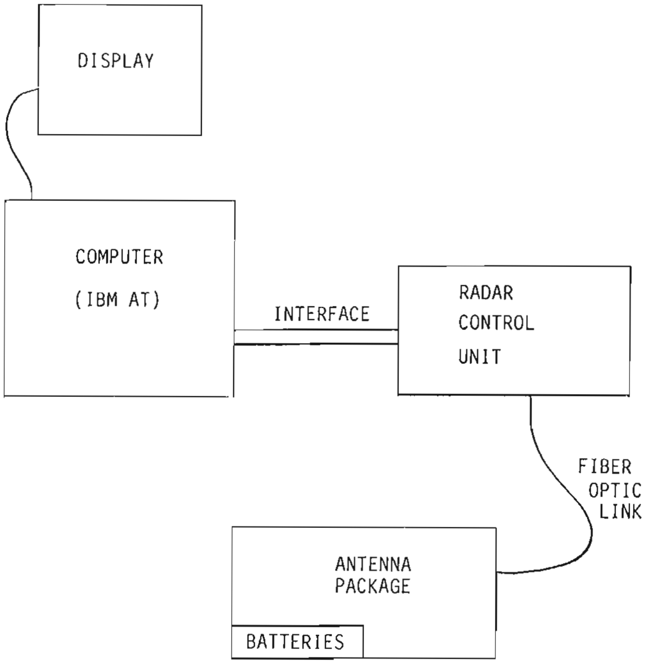

Figure 3. Schematic sketch of radar system.

Measurements were made with the antenna package floating on the water surface. The effective beam pattern was measured by recording the signal returned from a 5.0 cm diameter steel ball and a 7.0 cm diameter lead ball at a number of positions beneath the antenna. With the antennas on the air-water dielectric boundary, most of the energy was directed into the medium with the higher dielectric constant (Annan et al., 1975). Water has a relative dielectric constant of 81; air, 1. Therefore, the effective beam had a 3 dB half-angle of about 20° (Fig. 4), with slightly different patterns parallel and perpendicular to the electric field.

These experiments also gave an attenuation rate in the water of about 3 ± 2 dB/m after compensating for geometric spreading losses of $1/r^4$. This estimate is consistent with the predicted attenuation rate of about 2 dB/m (at 200 MHz) for the measured water conductivity of 25 ± 5 uS/cm (Fig. 2).

Using the resonance (or Mie) scattering curve in Figure 5 (Skolnik, 1970), the radar cross-section can be calculated. Because the radius of the ball is known, the received signal is known for a particular rcs of target at a given range. However, because a broadband signal is used and because the ball is in the resonance backscatter region, the rcs determined is approximate: for a 5 cm diameter ball it is 6.87×10^{-3} m^2; for a 7 cm diameter ball, 5.7×10^{-3} m^2.

The rcs of the background terrain (riverbed) was estimated by comparing the backscatter to the reflection from the 5 cm ball. The rcs of a boulder bottom was found to be 5.5×10^{-2} m^2.

Measurements of the rcs of fish were made by pulling a recently killed specimen through the beam at a constant range from the antennas. The voltage return was measured and

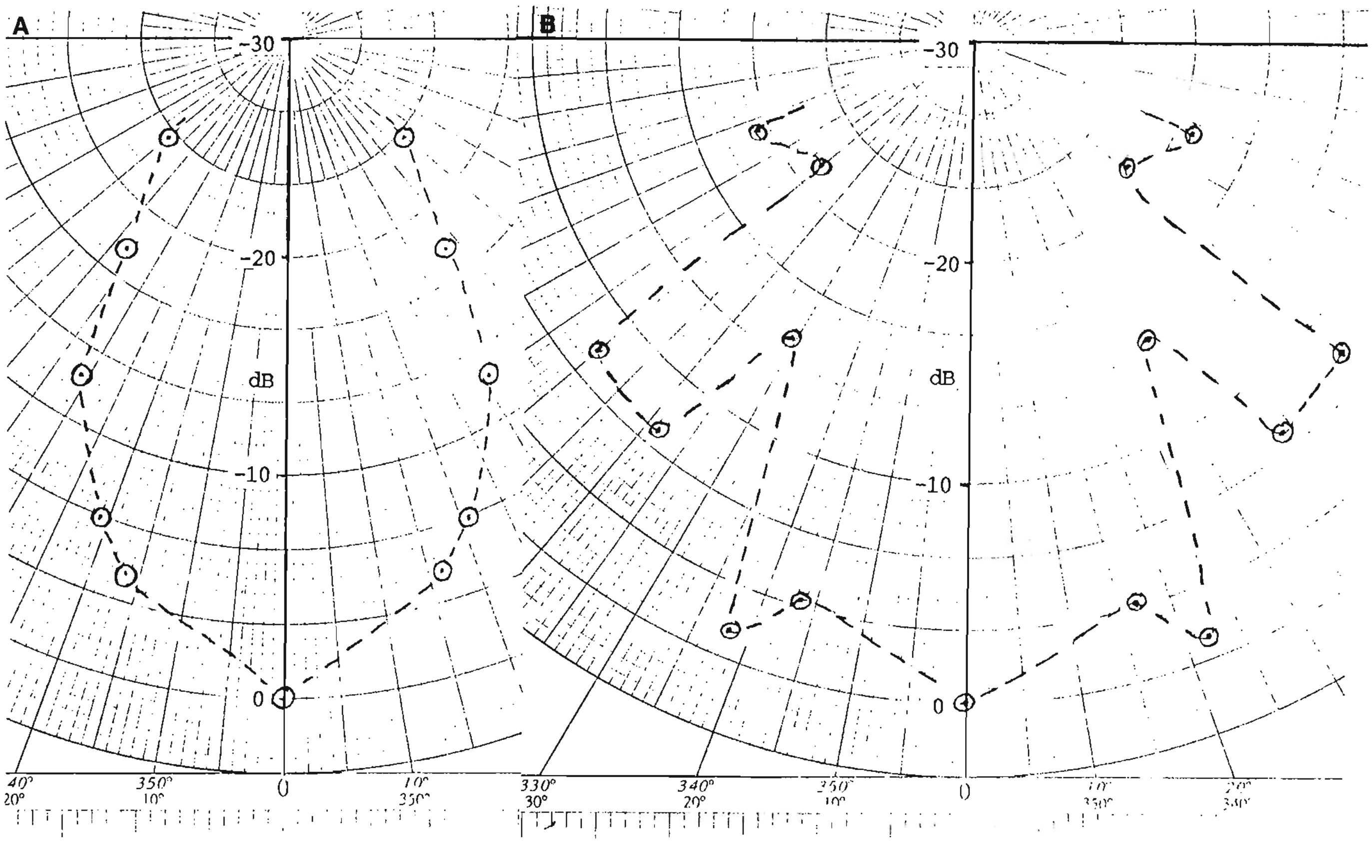

Figure 4. Radiated beam patterns into water calculated from 5 cm steel ball: **A.** parallel to electric field; **B.** perpendicular to electric field.

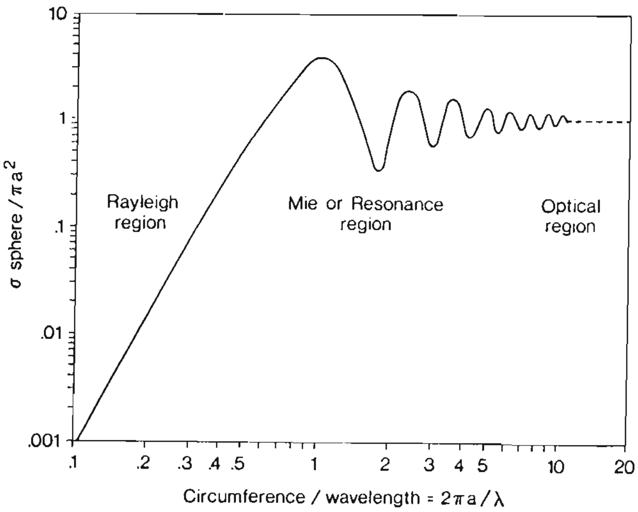

Figure 5. Mie scattering diagram (from Skolnik, 1970).

compared to the rcs of the spheres (after appropriate corrections for different ranges). Two steelhead trout (Salmo shirdneri) were studied: an adult female, weighing 2540 ± 40 g; and a 15 month old, weighing 38.7 ± 0.1 g. Approximate dimensions are given in Table 1, as well as the rcs of the two fish for orientations parallel and perpendicular to the electric field.As can be seen the rcs for the large fish is higher when it is parallel to the electric field.

DISCUSSION

A stationary reverberation echo is received from the environment around the antenna as well as the fish target echoes. For example, the bottom echo was found to be 12 dB higher than the return from the larger fish. With signal processing the background can usually be reduced by up to 20 dB. The rcs of fish is then in the same order of magnitude as that of the surrounding riverbed. This measurement compares favorably with the signal-to-background for acoustic detection of fish, and is only really a concern when the fish echo arrives simultaneously with a bottom or reverberation echo.

CONCLUSIONS

Short pulse radar operating in the VHF frequency band offers an attractive alternative for detecting and assessing riverine fish under some circumstances. Fundamental to development of this methodology is the radar cross-section of fish. Measurements reported have shown that the rcs is related to fish size and is substantial enough to allow for fish detection using radar. The advantages of radar detection are as follows:

- it is unaffected by turbidity, turbulence, and so on of the water;
- it has relatively high signal-reverberation levels compared to acoustics;

Table 1. Properties of steelhead trout

Specimen	Weight	Length	Width	Height	Radar cross-section	
					Parallel	Perpendicular
Adult female	2540 g	63.5 cm	5.1 cm	12.7 cm	3.44×10^{-3} m^2	1.83×10^{-3} m^2
Yearling	38.7 g	15.0 cm	1.5 cm	3.2 cm	3.37×10^{-6} m^2	8.56×10^{-6} m^2

- it can be measured within a few centimetres of the antennas;
- it has rapid travel speed of signals in water, which could allow signal processing.

Although we have not discussed it in this report, the ability to move the antenna out of the water may be possible, which would provide substantial flexibility of operation.

The major drawback of radar detection of fish is the relatively high attenuation of radar signals through water, limiting detection to several metres range in typical rivers. However, this factor is not necessarily a stringent limitation in shallow streams or in confined channels such as fish ladders.

ACKNOWLEDGEMENTS

This work was funded by the Canadian Department of Fisheries and Oceans under several research contracts. Dr. Brian Riddell was instrumental in obtaining support, and we were also assisted by Dr. Robert Keiser and Dr. Tim Mulligan. All are from the Pacific Biological Station, Nanaimo, British Columbia. We also gratefully acknowledge assistance from the staff at A-Cubed Inc., especially Dr. Peter Annan, Mr. Les Davis, and Mr. David Leggett.

REFERENCES

Annan, A.P. and Davis, J.L.
1976: Impulse radar sounding in permafrost; Radio Science, v. 11, p. 383-394.
Annan, A.P., Waller, W.M., Strangway, D.W., Rossiter, J.R., Redman, J.D., and Watts, R.D.
1975: The electromagnetic response of a low-loss, 2-layer, dielectric earth for horizontal electric dipole excitation; Geophysics, v. 40, p. 285-298.
Canpolar Consultants Ltd.
1986: Novel techniques for detection of riverine fish; Department of Fisheries and Oceans, Nanaimo, B.C., Canada.
Canpolar Inc.
1987: Continued development of radar-based riverine fish counting system – analysis of January 1987 field measurements; Department of Fisheries and Oceans, Nanaimo, B.C., Canada.
Davis, J.L., Annan, A.P., Vaughan, C.
1987: Placer exploration using radar and seismic methods; CIM Bulletin, v. 80, p. 67-72.
Mitson, R.B.
1983: Fisheries Sonar; Fishing News Books, Surrey.
Rossiter, J.R. and Gustajtis, K.A.
1978: Iceberg sounding by impulse radar; Nature, v. 271, p. 48-50.
Skolnik, M.I.
1970: Radar Handbook; McGraw-Hill, Toronto, Ont.
von Hippel, A.R.
1954: Dielectrics and Waves; MIT Press, Cambridge, Mass.

Forensic applications of ground penetrating radar

K.B. Strongman[1]

Strongman, K.B., 1992: Forensic applications of ground penetrating radar; in Ground penetrating radar, ed. J. Pilon; Geological Survey of Canada, Paper 90-4, p. 203-211.

Abstract

The Royal Canadian Mounted Police (R.C.M.P.) tested a ground penetrating radar (GPR) system in the province of British Columbia to determine the feasibility of using GPR technology for detecting buried or hidden evidence.

The test site, on the side of a mountain at Simon Fraser University in Burnaby, B.C., consisted of three animal carcasses that simulated both young children and adult cadavers. The animals had been buried 5 years prior to the test and the exact site was unknown to the evaluators of the equipment. Although the site was not originally designed for this particular test, it was appropriate because it was a controlled environment; thus the results were not biased by prior knowledge and could be accurately and scientifically compared with the prerecorded data.

The R.C.M.P. investigators successfully located all three buried animals. The methods and techniques used in this test have since been applied to other forensic scenes. The technology was determined to be widely applicable to crime scene analysis.

Résumé

La Gendarmerie royale du Canada (GRC) a mis à l'essai un géoradar en Colombie-Britannique afin de déterminer si l'appareil peut servir à détecter des indices enfouis ou cachés.

Le site d'essai, situé sur le flanc d'une montagne à l'université Simon Fraser à Burnaby (C.-B.), contenait trois carcasses d'animaux simulant des cadavres de jeunes enfants et d'adultes. Les animaux avaient été enfouis cinq ans avant l'essai, et l'endroit exact n'était pas connu des évaluateurs de l'équipement. Même si le site n'avait pas été spécifiquement conçu en fonction de cet essai particulier, il était approprié puisqu'il s'agissait d'un milieu contrôlé; par conséquent, les résultats n'ont pas été biaisés par des connaissances antérieures et ils pouvaient être comparés de façon précise et scientifique avec les données préenregistrées.

Les chercheurs de la GRC ont localisé avec succès les trois animaux enfouis. Les méthodes et les techniques utilisées dans cet essai ont été depuis appliquées à d'autres situations à caractère médico-légal. Cette technologie s'est avérée largement applicable à l'analyse des lieux de crime.

---

[1] "K" Division, Royal Canadian Mounted Police, Box 1320, Edmonton, Alberta T5J 2N1

INTRODUCTION

For many years the search for buried objects has stymied investigators, mainly because they lacked of an accurate means of remote sensing that would pinpoint valuable evidence. In most cases this crucial evidence would mean the difference between proving a case or having a lesser charge laid for lack of incriminating evidence. Without further corroborating evidence many homicide charges have been stayed for lack of a *corpus delicti.*

In all homicide cases to date, the investigator has relied on associated objects buried on or about the victim, which react to a metal detector or a magnetometer. Some investigators have had to rely on time consuming techniques such as the "soil examination stick" (Imaizumi, 1974) that is used like a probe and tests for high concentrations of alkalines. Others have used methane gas detectors (Boyd, 1979). Instruments such as metal detectors or magnetometers react to the electrical conductivity of the various forms of metals. Some, in the case of metal detectors, react to numerous metals but can be used selectively in the types of metals being sought. Unfortunately, their sensitivity is limited to a maximum depth of about 30 cm and is much dependent on the size of the object. Magnetometers on the other hand have been accurate to depths of 1 m. Unfortunately they only react to the magnetic fields of ferrous metals and their sensitivity can be severely hampered by outside interference such as 60 cycle electricity. For these reasons a more accurate and dependable form of remote sensing was sought and subsequently found in the form of ground penetrating radar (GPR).

This research was initiated in British Columbia by the "E" Division Royal Canadian Mounted Police (R.C.M.P.). It seeks to determine the applicability of GPR being used by the expert crime scene examiner as an investigational aid. The actual principles of the technology are not discussed; only a simplistic overview is given for basic methodology.

The idea of using radar technology to detect buried and hidden objects is not new. It has been used for geological surveys in the search for natural resources and for archaeological surveys (Vaughn, 1986). Recently it was used by the Japanese to detect cavities in the Pyramids (Chaigneau, 1987), which up until now were not known to exist. As in most cases the development of new and innovative technology is the result of necessity, natural disasters, or war. In the latter case, the British have further refined and improved the technology to detect buried objects such as plastic antipersonnel and antitank mines many of which were buried by the Argentinians during the Falklands War. Dr. Lambert T. Dolphin of the Geoscience and Engineering Centre in California in his recent paper (Dolphin and Vickers, 1987) added to the British research and indicated that GPR is suitable for finding buried nonmetallic objects. He also confirmed the theories presented in this report.

PURPOSE OF RESEARCH

The purpose of the research was to assess the feasibility of using GPR for examining crime scenes. The examination could take the form of finding buried human remains (murder investigations); locating buried and hidden objects, (drug caches, arms caches, avalanche victims, and so on); detecting voids; and determining the composition of walls when immediate entry is required for emergency situations.

BASIC PRINCIPLES OF GROUND PENETRATING RADAR

To determine the suitability of the GPR equipment and its applicability to forensic investigations, the basic principles of GPR should be highlighted.

The system uses the same principles as any radar system. An electromagnetic pulse is directed down through the ground and is partially reflected by any change in the bulk electrical properties of the ground. This change usually correlates with a change in volumetric water content and may indicate a change in bulk density. The reflected energy is detected by the receiving antenna, which measures the delay time (difference between transmitted and reflected returning signal). The signal or pulse is repeated many times a second

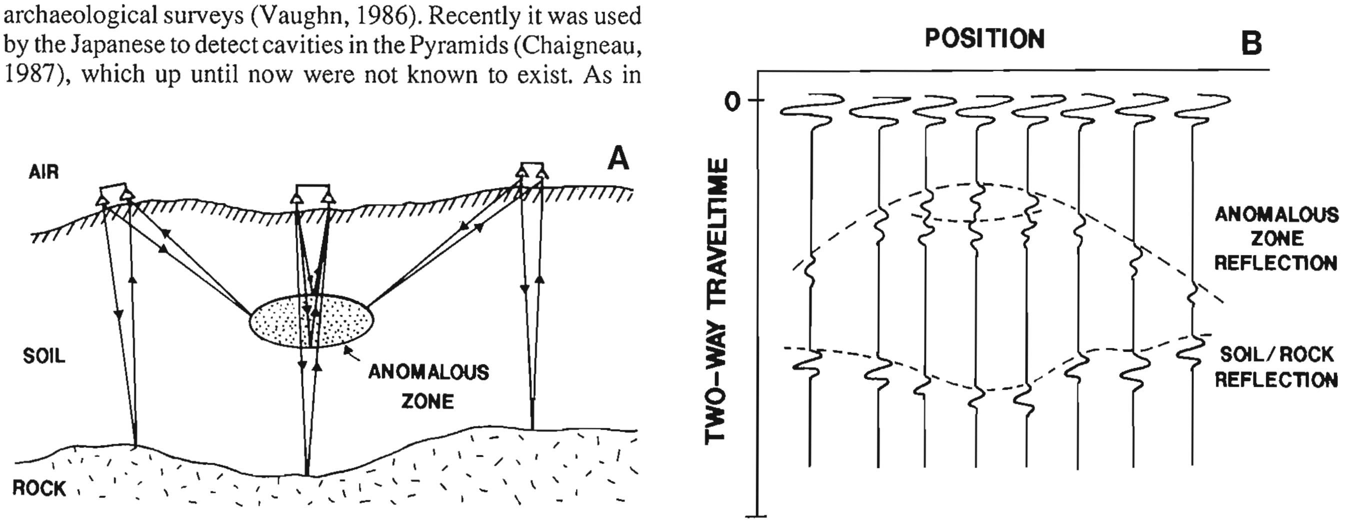

Figure 1A. Simplified section of test site. **B.** Simplified record of reflections on the printout from the test site.

as the transmitter-receiver is moved across the surface interpreting the transmitted-reflected signals. The result is a cross-sectional view of the subsurface recorded on a paper printout, which graphically displays the varying layers of soil (strata) as well as any other objects that may be buried. Figure 1A (Vaughn, 1986) is a simplistic view of the investigated subsurface; Figure 1B depicts the resulting signals and their record on the printout.

In Figure 1A the antenna on the surface is depicted in three positions. Each position records a different reflection from the object or anomaly. In Figure 1B, which is greatly simplified in comparison to the actual number of pulses actually transmitted, the signals are affected by the anomaly and the reflected signal indicates the anomaly. In actual fact, rather than a series of simple lines, the observer sees instead a continuous grey toned profile of the target.

The distance to an object below the surface cannot be accurately measured without knowing the composition of the soil and the water content. A simple test reading in the search area, using a known object buried at a known depth, can help to determine the sensitivity of the instrument in that particular soil. This information can then be used to accurately assess future readings in the search area.

EQUIPMENT USED FOR RESEARCH PROJECT

The equipment used for this project was manufactured by Geophysical Survey Systems Inc. of Hudson, New Hampshire; it consisted of the following items, collectively known as a subsurface interface radar system (SIRS)

- antenna – model 3102, 500 MHZ transducer
- control unit – model 4400A radar control unit
- recorder – model SR-8105H graphic recorder
- optional recorder – Adtek DT-6000 microprocessor digital tape recorder.

This particular equipment was used because it was owned by another department of the Canadian Government and was available, complete with a trained operator, at minimal cost during the time which we had to complete this research. There are other sources and other manufacturers but, because of the cost and availability, this was our most efficient and economical course of action.

FIELD TEST AND RESULTS

To accurately and fairly assess the suitability of GPR technology for examining forensic scenes we needed to deal with a real life situation that was manufactured under controlled circumstances. Briefly, more than 5 years ago, Dr. Mark Skinner, Professor of Anthropology, at Simon Fraser University (SFU) in Burnaby, British Columbia buried two goats and a bear separately in a wooded area on Burnaby Mountain. He originally intended these sites to be used as forensic sites for his forensic anthropology students to discover and recover. He generously volunteered them for our research as they were totally suited to a scientific evaluation of the GPR technique. Dr. Skinner also had accurate records of the exact location of each animal, which facilitated a quick and easy check of the GPR accuracy.

We treated the site as we would any forensic site once reliable information was received that a burial existed and the suspected area had been narrowed down to a reasonable search area. In this case we were dealing with an area of about 700 m^2 on the side of a mountain. The flora consisted of secondary growth of deciduous trees, which had grown after SFU was opened in 1965. The mostly older trees had a ground cover of blackberry bushes. The soil was sandy, interspersed with small rocks and some rotting cedar stumps.

We found the actual search area by determining new and old vegetation, based on the premise that the new growth indicated the disturbed area where the burial excavations had destroyed the symmetry of mature forest. We then tried unsuccessfully to pinpoint the graves by observing humps, hollows, or any variance in soil coloration. A methodical removal of the new growth narrowed our search site to about 42 m^2. Standard forensic procedures of scraping the entire surface area down to a depth of about 3 cm were tried to detect differences in soil colour, on the premise that the disturbed fill or matrix of the graves would differ in colour from the normal undisturbed soil. However, we detected no differences. Also, no hollows were evident, which are thought to form as the grave matrix settles and compacts with time.

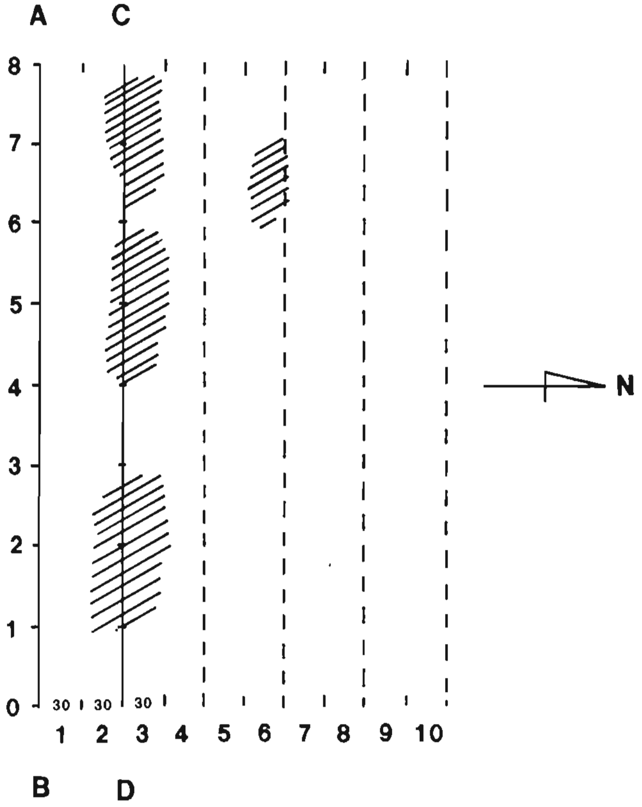

Figure 2. Rough sketch of search site.

Satisfied that we had used all the known latent grave site discovery techniques at our disposal, we began the second stage of the search using the SIRS equipment. First, the proposed search area was marked at 1 m intervals along a base line AB that formed the southern border of the search site (Fig. 2). Each 1 m position was marked with a stake. Then a chain equivalent in length to AB was marked at 1 m intervals with surveyors tape and aligned parallel to AB exactly 60 cm to the north (CD).

As the antenna was exactly 30 cm wide, a sweep search was conducted on the north side of AB, traversing the entire 8 m length. It was then moved to the south side of CD and a similar sweep was conducted. Once that was completed, the next sweep was made on the north side of CD. CD was then moved a further 60 cm to the north, and the search pattern was repeated. This process was repeated until the entire area was covered (Fig. 2). The anomalies that were identified by the SIRS equipment are indicated on the third and sixth sweeps.

To orient each metre interval on the paper printout an electrical impulse was triggered on the antenna and was recorded on the resulting paper display of the subsurface of the soil. Thus the operator could number the 1 m intervals and could narrow down the exact location of an anomaly when later viewing the printouts. Incidentally, each sweep printout was not identical in length to the others as the speed of the antenna being dragged across the surface is directly dependent on the stride of the operator and the roughness of the soil surface. This variation does not pose an accuracy problem because each indication is relative to each metre marker recorded on the printout.

A strong indication of recently disturbed strata would be the abrupt termination of the pattern of the strata followed by a void or clear area on the printout. This change, called a shear, marks the outer extremities of a grave. When each printout is viewed in conjunction with the surrounding printouts, size and patterns of anomalies are readily recognized by a trained interpreter. This interpretation helps

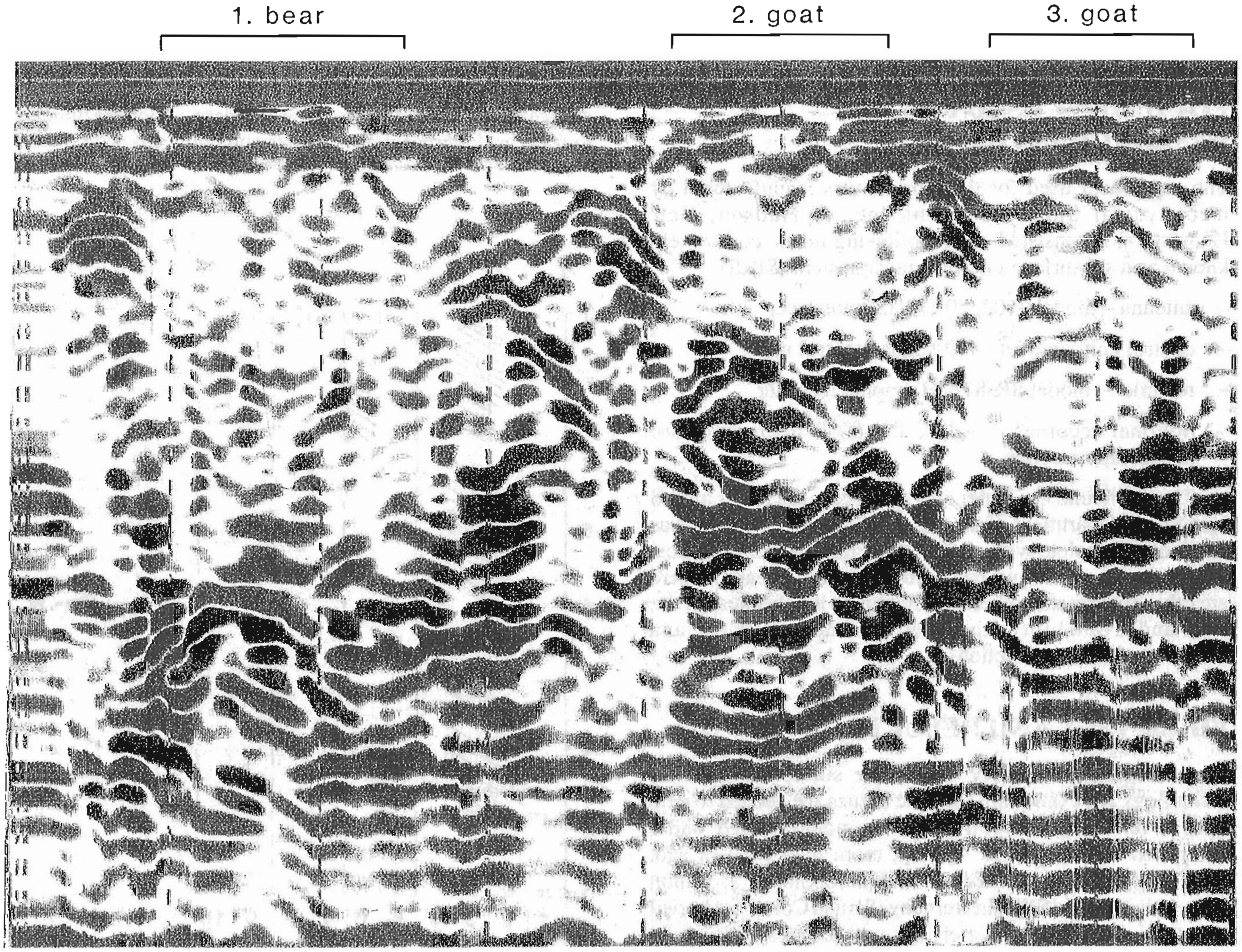

Figure 3. Real time GPR printout shows three anomalies.

to narrow down the search area. When a suspect area that did not conform to the regular strata was noted, several sweeps 2 m long were made across the grid lines. One was made 1 m east of the anomaly, one directly over top of it, and another 1 m to the west. These gave a cross-sectional dimension to the anomaly and, therefore, a more accurate picture of its location, size, and shape.

Our search indicated four such anomalies (Fig. 2, 3) as follows:

1. Sweep #3 – between the 1 m and 3 m marks
2. Sweep #3 – between the 4 m and 6 m marks
3. Sweep #3 – between the 6 m and 7 m marks
4. Sweep #6 – between the 6 m and 7 m marks.

The first three anomalies conformed exactly to Dr. Skinner's records and were later confirmed by exhumation to be

1. Bear
2. Goat
3. Goat.

Figure 3 is a reduced reproduction of the real time printout, which resulted from the GPR scene examination on the third sweep and is depicted in Figure 2. This reproduction illustrates what one has to work with at the scene and how one can use it for future record purposes. Voids are visible between about the 1 and 2.5 m marks (bear); the 4 and 5.75 m marks (goat); and the 6.25 and 8 m marks (goat). Unfortunately, the 8 m end of the printout is cropped out and not recorded. All these voids are about 0.5-1 m in depth. The shears are visible up to these depths at about the 1, 3, 4, 6, and 8 m marks.

The fourth anomaly (not shown in Fig. 3) was excavated and turned out to be a completely decomposed cedar stump. Being of a different density and not conforming to the strata, it was an obvious indicator and had to be investigated. No doubt, at actual forensic scenes, this type of anomaly will occur and will result in time consuming excavation.

A further test was conducted to determine the SIRS sensitivity to a firearm. Once the bear was located, a cross-sectional sweep was conducted of the known site with and without a Smith and Wesson 38 calibre snubnosed revolver buried and resting on the bear's skull (Fig. 4). In Figure 4A the metal of the gun is recorded by the numerous

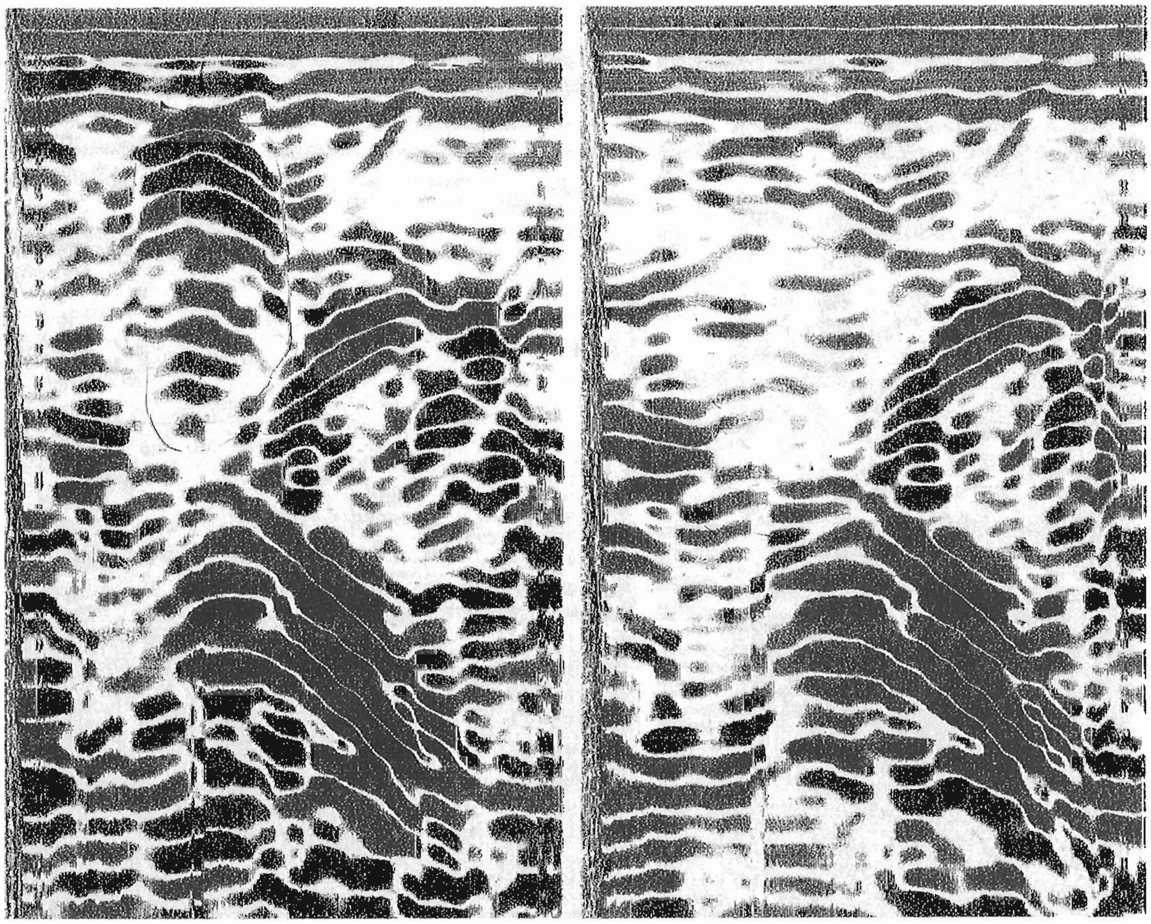

Figure 4. GPR printout shows **A.** the firearm 0.5 m below the surface, and resting on the buried bear; **B.** the buried bear only. Shear marks are visible in both A and B.

inverted reflections in the top left quadrant of the printout. No gun by contrast produced the lack of such reflections in the same quadrant in Figure 4B.

CRIME SCENE EXAMINATIONS

Scene #1

This scene was examined to determine if in fact a culprit had buried his victim. All his recovered victims had been found on the surface up until this time. In this case all areas suitable for burials, in the vicinity where the culprit said he had buried his victim, were searched using the SIRS equipment. Most of the terrain was bedrock. Those areas where the sediment had collected and were not covered with old vegetation (most trees were mature oak trees) were scanned.

No positive indications were received and the area was eliminated. Without more precise site information, further searches using the SIRS equipment was not recommended.

One positive piece of information was discovered to do with search techniques, which could be used when developing future remote sensing radar equipment for forensic scene examination.

To rectify the problem caused by the rough terrain, the antenna was held about 1 m above the surface and was carried in this position for the duration of the sweep. Although the signal would be weaker, we were not worried about reaching the maximum depth capable of the antenna, as this would not hinder our search. The results were to the contrary. Instead of a diminished signal, we appeared to receive an enhanced signal (Fig. 5A). The interface between the antenna, the air, and the surface did not obstruct the data below the surface. The printout was denser and more defined. When comparing the two readings predominant strata stand out, but the finer detail is lost in the dragged antenna data (Fig. 5B). The carried antenna, kept parallel to the surface, recorded more detail throughout, and the bedrock was not eliminated by interference created by the rough surface. Also the signal was still strong enough to overcome the 1 m added distance and still managed to record the bedrock accurately.

Although no remains were found it is felt, based on previous performance, the search was a success. An area was eliminated from consideration for future searches.

Scene #2

This scene was examined to find a victim buried in a large trunk. The area had been obliterated by the surface being covered by bark mulch. As the object was larger than a normal

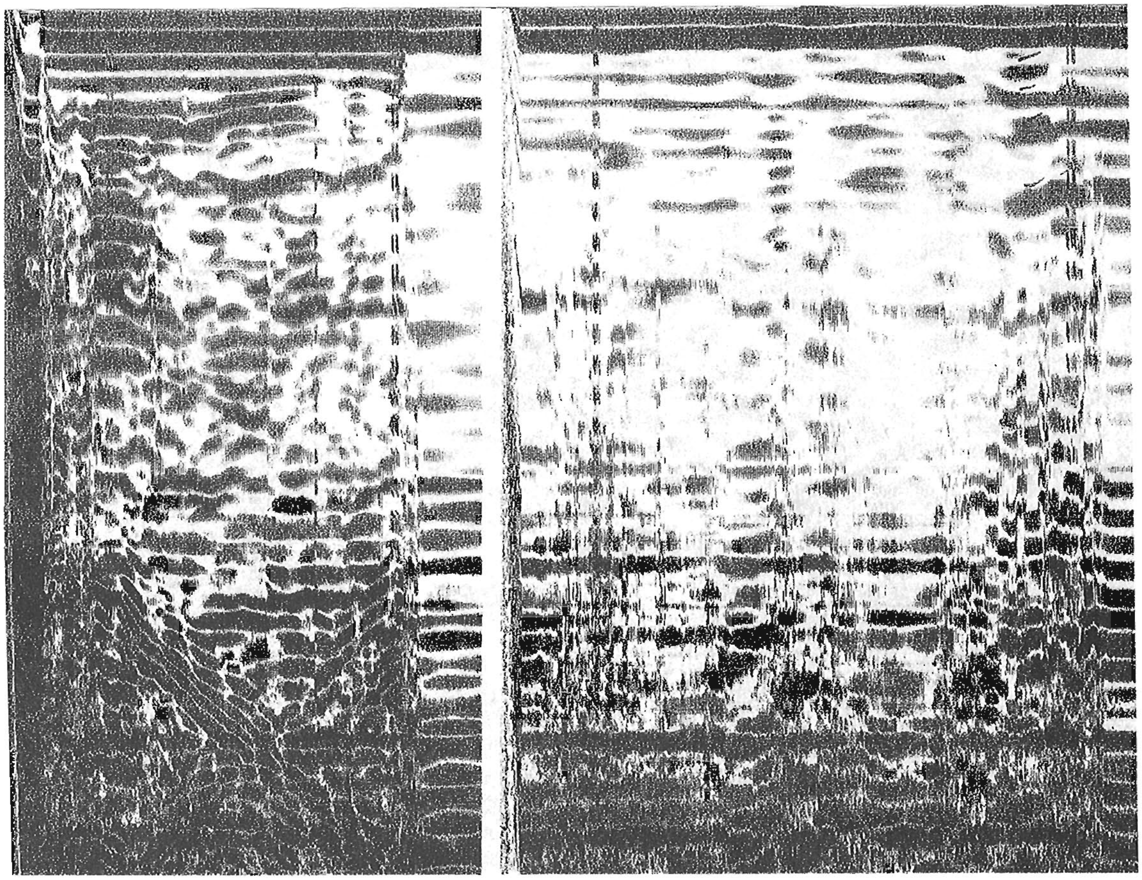

Figure 5. GPR printouts from using antenna **A** carried above the surface, and **B** dragged on the surface.

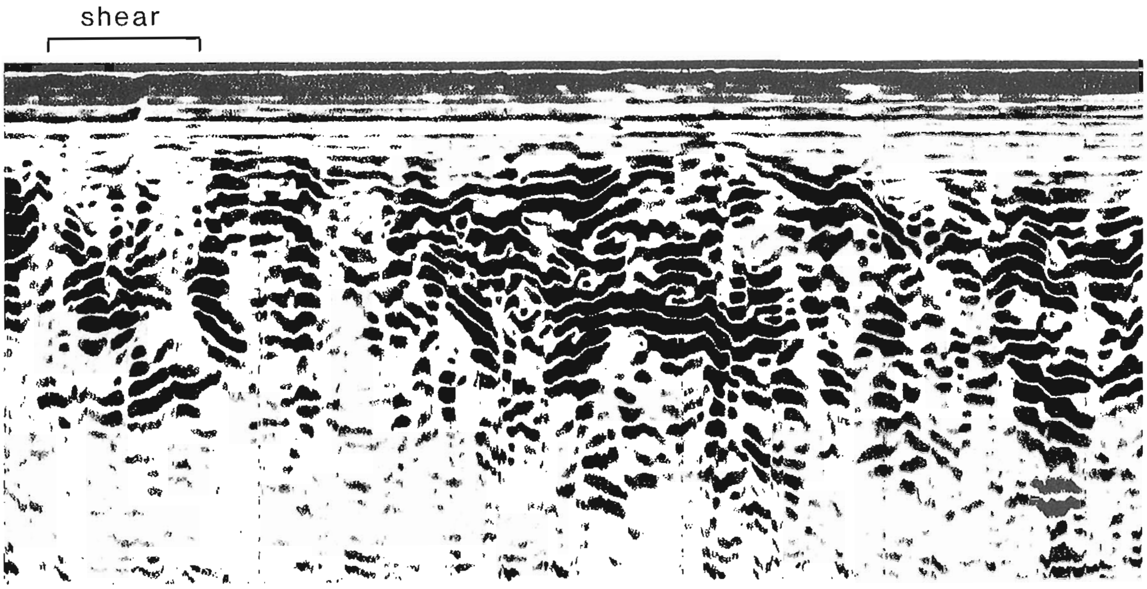

Figure 6. Printout shows clearly defined shear.

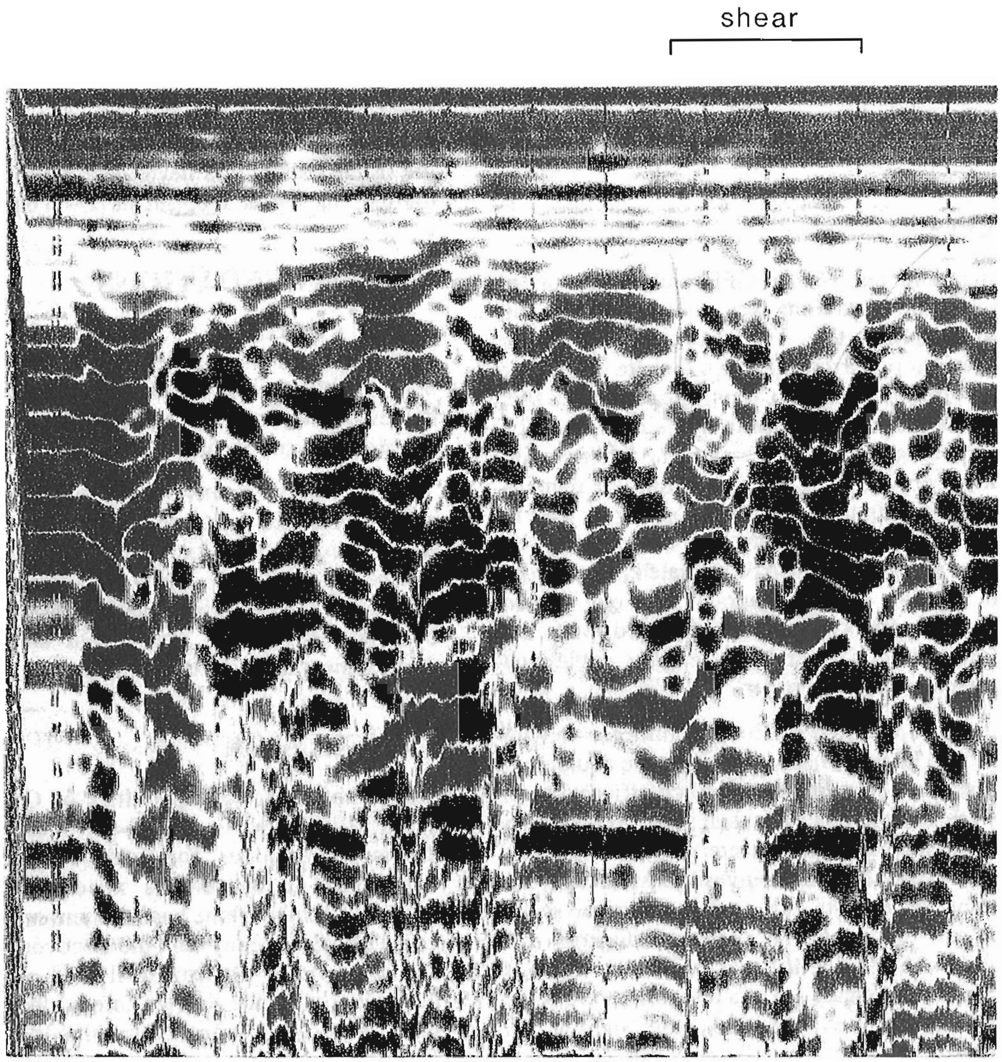

Figure 7. Cross-sectional readings confirm dimensions of shear in Figure 6.

body the search pattern was enlarged to accommodate the larger area yet still be able to cross the trunk on at least two sweeps. The SIRS equipment worked very well and gave a clear picture of the subsurface strata. Even though the bark mulch surface was flat, the irregular surface of the soil below was clearly defined.

On sweep #8 a clearly defined shear was recorded on the printout (Fig. 6). Its exact size and shape was confirmed by cross-sectional readings (Fig. 7) and the suspect area was marked for future excavation.

This example is yet another application of this technology. The searches can be made and the results interpreted for excavation at a later date when personnel and equipment are available.

Scene #3

This case is similar to the others in that an area was eliminated. It is different in that the terrain was heavily forested and the soil (humus) was impregnated with various forms of metal garbage and rocks. The same techniques were used and all anomalies were excavated. What was interesting to note was the sensitivity of the instrument to metals. In one case a 12 gauge shotgun shell was located several feet below the surface. The metal cap of the shell gave a very strong echo.

DISCUSSIONS

In essence, this field test of the GPR technology under simulated but realistic conditions was a total success. The entire search took no more than 4 h, starting from receiving the general information, narrowing down the site area using conventional environmental indicators, cleaning the site, setting out the measured site pattern, using the SIRS equipment, interpreting the data, confirming the findings with cross-sectional sweeps and partially excavating the remains to confirm the findings. In this test three people were used to conduct the search. Once the pattern was determined, one person moved the antenna, one person operated the recorder and correlated the data with a diagram, and one person recorded the proceedings on film and aided with the movement of the chain CD and the lengthy cable that connected the antenna to the recorder.

If need be, two people could conduct an entire search with no difficulty, as was later learned when using the equipment at actual crime scenes. We note that a police officer who is untrained in physics or the other physical sciences can, with a little expert instruction, learn to interpret the real time printout and use it at the scene as an investigative aid. On the spot field training by experts can produce a crime scene examiner who can recognize the various indicators and densities, which help to identify or point out various anomalies. Whether or not they are of a forensic nature bears further examination or excavation. Indicators such as the shear marks help to point out to the layman that excavation has destroyed the symmetry of the subsurface strata. They are key factors in determining a burial site. This type of indicator was plainly obvious in the simulated crime scene and was used to pinpoint the bear and two goats (Fig. 3).

Being able to pinpoint a burial, as was the case with the bear and goats, helps to reduce the actual search time and ultimately contributes to the accurate and safe recovery of the remains. Without this scientific aid, investigators in the past have had to rely on hit and miss, time consuming excavation techniques, which at times have proved to be destructive as well as costly. Now, a trained crime scene examiner can accurately identify or eliminate potential burial sites thus cutting the cost of lengthy investigations and guaranteeing the safe and complete recovery of crucial evidence.

SUMMATION

In addition to the simulated crime scene at Simon Fraser University, three types of actual crime scenes were examined with positive results. These results were based on the capabilities of GPR which was established under the controlled test. In two of these scenes (#1 and #3) the search areas were eliminated. In scene #2 a possible suspect area was identified for later excavation. In all cases the equipment was adaptable to the scenes. It may be noted that a simple car battery carried to the scene supplied enough power to operate the equipment for several hours. Power in these cases was never a problem and the life of the battery was never determined. In one instance the transporting vehicle supplied the power directly from its battery.

RECOMMENDATIONS

Beyond a doubt, remote sensing technology has a definite place in forensic scene examination. Although its cost may be prohibitive in most minor cases, the serious offence, where key evidence is not retrievable without this technology, will more than justify its acquisition.

Based on the positive results of the field tests, I strongly recommend that police forces purchase at least one set of these instruments and train a full time operator to apply GPR capabilities to forensic scene examinations. This technology can provide an expertise much in demand in this modern age of law enforcement and would also allow for future development in the forensic field.

CONCLUSION

The remote sensing capabilities of GPR has far-reaching capabilities, which would definitely enhance our law enforcement abilities. This field is only now being developed but already its capabilities are evident. The R.C.M.P. in British Columbia alone have numerous unsolved crimes that could be solved today with the discovery and recovery of the victims' remains. On a national scale, as this could be part of our National Police Service offered through the services of our Identification Branch, there should be more than enough justification to possess the investigational capabilities which such an aid would provide.

ACKNOWLEDGMENTS

I would like to thank the following people who have helped me to complete this research project. They are listed as they occur in this report, not necessarily prioritized as to importance of contributions. Everyone helped! Without them this particular application would not have been field tested and I would have been left with a sense of unfulfillment. C.O. "E" Division of the R.C.M.P. and Insp. M. Cassidy (OIC) Identification Services supported my research and obtained the approval and funds to complete the project. Mr. Raymond Fortin provided the equipment and the expertise, not to mention reams of background material. Without him I would still be proposing the feasibility of applying this technology to forensic scenes rather than actually having completed successful examinations. Dr. Peter Annan of A-Cubed Inc. confirmed that GPR was suited to forensic scene examination, provided much information, and is willing to develop a more portable instrument better suited to forensic scenes. Dr. Lambert T. Dolphin of Geoscience and Engineering Centre provided many examples of GPR applications. Mr. Tom Fenner of Geophysical Survey Systems Inc. represents manufacturer of the equipment that was used for the tests; he also provided a great deal of technical information. Dr. Mark Skinner and Simon Fraser University provided the controlled test site and aided me in past and present projects. C.O. "K" Division of the R.C.M.P. allowed me to complete this project after being transferred out of the Identification Branch and also provided the clerical assistance to produce the finished report. Detective Gary L. Hoving of the office of the Sheriff-Coroner, County of San Luis Obispo, San Luis Obispo, California, provided his research and put me on the trail of the manufacturers of the GPR equipment.

REFERENCES

Strongman, K. Brian
1987: Subsurface interface radar system. (Royal Canadian Mounted Police internal document), 28 p. + 3 append.
Imaizumi, Masataka
1974: Locating buried bodies; FBI Law Enforcement Bulletin, August 1974, p. 1-5.
Boyd, R.M.
1979 Buried buried buried body cases; FBI Law Enforcement Bulletin, February 1979, p. 1-7.
Vaughn, C.J.
1986: Ground penetrating radar surveys, used in archaeological investigations; Geophysics, v. 51, no. 3, p. 595-604.
Chaigneau, Jean-François
1987: In this pyramid un-touched rooms; Paris-Match.
Dolphin, L.T. and Vickers, R.S.
1987 New geophysical approaches to plastic mine detection; July 1987 (Stanford Research Institute Internation, p. 8).

SELECTED BIBLIOGRAPHY

This bibliography is compiled from the background information so generously provided by a vast field of experts. It is enclosed here for use by future investigators in the hope that many hours of research will be eliminated and, therefore, more time will be available for search and recovery of that elusive evidence, which we all strive to find to successfully conclude our investigations.

Alongi, A.V.
1970: A short-pulse high-resolution radar for cadaver detection; Calspan Corporation, Buffalo, New York 14221, 16 p.
Annan, A.P., Davis, J.L., and Vaughan, C.J.
1984: Radar mapping of buried pipes and cables; A-Cubed Inc., Technical Paper No. 5, Mississauga, Ontario L4W 1P4, Application Note, 8 p.
Boyd, R.M.
1979: Buried buried buried body cases; FBI Law Enforcement Bulletin, February, p. 1-7.
Chaigneau, J.F.
1987: In this Pyramid un-touched rooms; Paris-Match.
Dolphin, L.T.
1981: Geophysical methods for archaeological surveys in Israel; SRI International, 28 p.
Dolphin, L.T. and Vickers, R.S.
1987: New geophysical approaches to plastic mine detection; SRI international discussion paper, July, 8 p.
Dolphin, L.T. and Yetter, T.J.
1985: Geophysical survey at Neary-Rodriguez Adobe, Mission Santa Cruz; SRI International Project 7948, May, 42 p.
Fenner, T.J.
1988: Probing the past. . .non-destructively; Subsurface News, v. 1, no. 1, Winter.
Hoving, G.L.
1986: Buried body search technology; Identification News, February 3, 15.
Imaizumi, M.
1974: Locating buried bodies; FBI Law Enforcement Bulletin, August 2, 5 p.

Interpretation of short-pulse radar soundings from low latitude, high altitude glaciers of Peru and China

L.G. Thompson[1]

Thompson, L.G., 1992: Interpretation of short-pulse radar soundings from low latitude, high altitude glaciers of Peru and China; in Ground penetrating radar, ed. J. Pilon; Geological Survey of Canada, Paper 90-4, p. 213-225.

Abstract

From 1979 to 1987, short-pulse radar sounding experiments were conducted on six low latitude, high altitude glaciers in support of programs to assess the likelihood of recovery of long and useful ice core paleoclimatic and environmental records. Experiments were conducted on Quelccaya Ice Cap in southern Peru and on three ice fields in Cordillera Blanca of northern Peru; the col of Huascáran, Copap, and Pucahirca. Additionally, two sites in China were studied; Glacier No. 1 in Tian Shan of far western China and Dunde Ice Cap of Qilian Shan of central China. Ice thickness interpretations were used to determine the smoothness of the bedrock and maximum ice thicknesses. The maximum ice thicknesses measured were 165 m on Quelccaya Ice Cap, 190 m on the col of Huascáran, 201 m on Copap, 237 m on Pucahirca, 133 m on Glacier No. 1, and 157 m on Dunde Ice Cap.

The Quelccaya and Dunde Ice Cap data were used to produce bedrock topographic maps for selection of drilling sites. The short-pulse radar depths were compared to actual measured depths in boreholes drilled to bedrock on Quelccaya and Dunde ice caps. The average short-pulse radar ice thicknesses vary less than 5% from the actual measured values.

Résumé

De 1979 à 1987, des expériences de sondage par radar à impulsions courtes ont été faites sur six glaciers de haute latitude et de basse latitude à l'appui de programmes visant à évaluer la possibilité de recueillir de carottes de glace des données paléoclimatiques et environnementales utiles couvrant une vaste période. Les expériences ont été réalisées sur la calotte glaciaire Quelccaya dans le sud du Pérou et sur trois champs de glace de la Cordillera Blanca dans le nord du Pérou; le col du Huascáran, le Copap et le Pucahirca. De plus, deux sites situés en Chine ont été étudiés : le glacier n° 1 dans les Tian Shan de l'extrême ouest de la Chine et la calotte glaciaire Dunde dans les Qilian Shan de la Chine centrale. Les données d'interprétation de l'épaisseur de la glace ont été utilisées pour déterminer l'uniformité du socle et les épaisseurs maximales de la glace qui ont été de 165 m dans la calotte Quelccaya, de 190 m dans le col du Huascáran, de 201 m sur le Copap, de 237 m sur le Pucahirca, de 133 m dans le glacier n° 1 et de 157 m dans la calotte glaciaire Dunde.

Pour dresser les cartes topographiques du socle utilisées pour déterminer les sites de forage, on a eu recours aux données recueillies sur les calottes glaciaires Quelccaya et Dunde. Les profondeurs enregistrées sur le radar à impulsions courtes ont été comparées aux profondeurs réelles mesurées dans les trous de sondage forés jusqu'au socledans les calottes glaciaires Quelccaya et Dunde. Les épaisseurs moyennes de la glace enregistrées par le radar à impulsions courtes varie de moins de 5 % des valeurs réelles mesurées.

---

[1] Byrd Polar Research Centre, The Ohio State University, 125 South Oval Mall, Columbus, Ohio 43210-1308 U.S.A.

INTRODUCTION

A short-pulse ice radar sounder was used for ice thickness determinations on Quelccaya Ice Cap (13°56′S, 70°50′W; 5670 m asl) in Cordillera Oriental of southern Peru from 1979 to 1984, and at three sites in Cordillera Blanca of northern Peru (Fig. 1A): the col of Huascáran (9°07′S, 77°36′W; 6000 m asl) in 1980; Copap (9°19′S, 77°20′W; 5300 m asl) in 1983; and on Pucahirca (8°53′S, 77°35′W; 5200 m asl) in 1984. In addition, the sounder has been used to determine ice thicknesses on two glaciers in China; Glacier No. 1 in Tian Shan (43°07′N, 86°49′E; 4000 m) and Dunde Ice Cap, in Qilian Shan (38°06′N; 96°24′E; 5325 m asl) (Fig. 1B). Long ice core records of the past climate and environments were recovered from both Quelccaya Ice Cap (Thompson et al., 1985; Thompson et al., 1986; Thompson et al., 1988a) and Dunde Ice Cap (Thompson et al. 1988b, c). Preliminary ice thickness measurements from Quelccaya were presented by Thompson et al. (1982), and for Huascarán by Jezek and Thompson et al. (1982). This paper presents a complete set of thickness determinations for not only these two sites, but also four additional sites. Ice thickness determinations, coupled with current accumulation rates, are used to estimate the length of the climatic record available from ice cores drilled to bedrock. These measurements are important in these remote, high altitude sites not only in assessing the likely length and quality of the potential ice core record, but also in contributing to the design of drilling and field equipment to minimize the amount of research equipment needed.

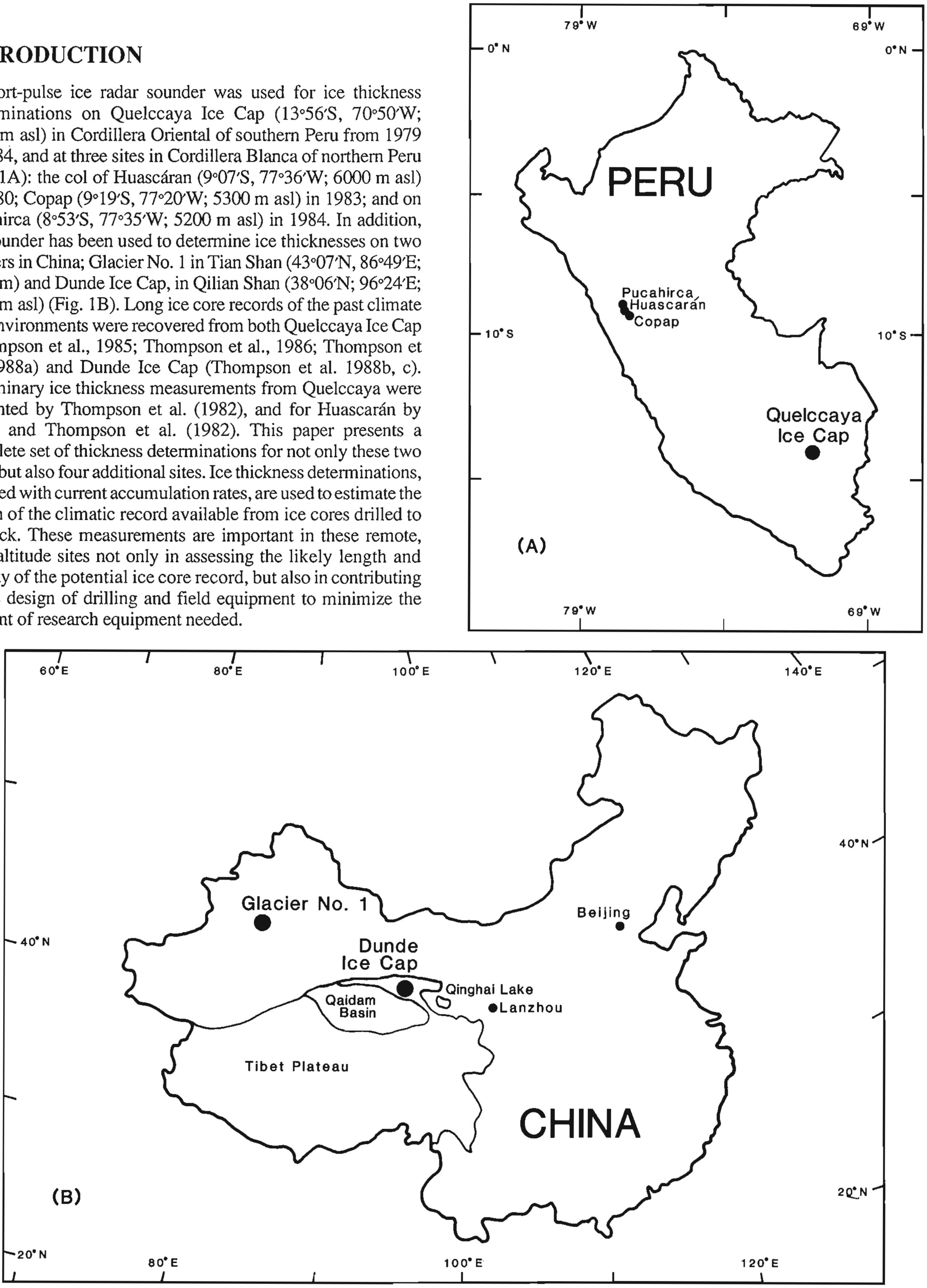

Figure 1. Locations of Huascarán, Copap, Pucahirca, and Quelccaya sites in Peru and of Dunde and Glacier No. 1 sites in China.

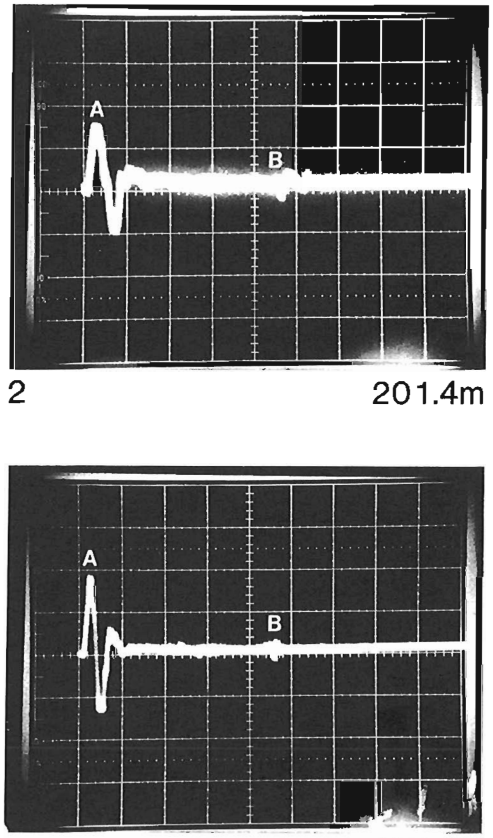

2 201.4m

1 197.4m

Figure 2. Typical echograms of short-pulse radar data obtained from Copap in Cordillera Blanca, Peru. In each echogram in this figure and in figures 3-6, A indicates the surface wave and B indicates the bottom reflection.

The recovery of detailed climatic and environmental records from a global array of glaciers constitutes an important aspect of the Global Change Initiative and will require selection of the very best sites for ice core recovery. Furthermore, on-site depth information can be used to reduce drilling cost by allowing recovery of maximum core without incurring the expense associated with the destruction of drill bits when bedrock is encountered. In northern Peru, which is located in an active earthquake zone, ice thickness determinations are important in calculating the volume of ice that might avalanche. In addition, potential flood areas can be identified by calculating the amount of water likely to be displaced by an avalanche proceeding into a glacial lake.

SHORT-PULSE RADAR SOUNDER

Radio echosounders have been used successfully for sounding cold polar ice since the early 1960s (Robin 1975a, b), but were not generally successful on warm temperate glaciers where the echo from the ice-bedrock surface could be obscured by echoes from water filled pockets in the ice (Smith and Evans, 1972; Watts and England, 1976). Appreciating this, Vickers and Bollen developed a temperate glacier sounder at the Stanford Research Institute under contract to the U.S. Geological Survey.

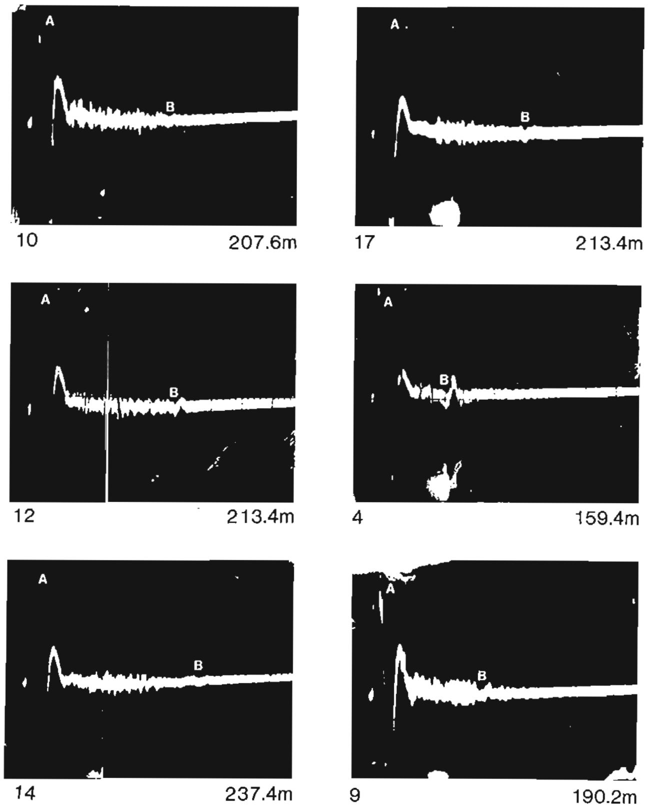

10 207.6m 17 213.4m

12 213.4m 4 159.4m

14 237.4m 9 190.2m

Figure 3. Typical echograms obtained from Pucahirca in Cordillera Blanca, Peru.

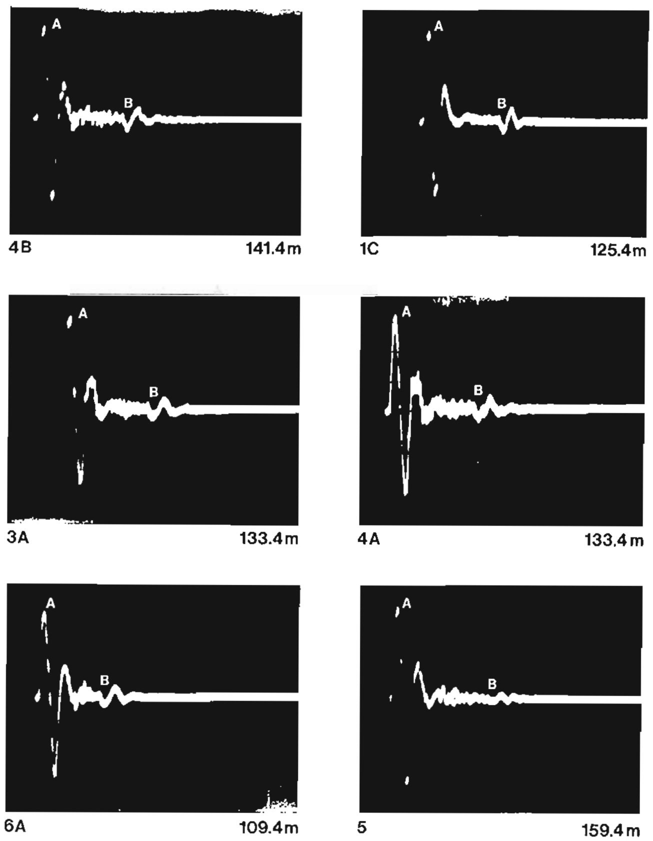

4B 141.4m 1C 125.4m

3A 133.4m 4A 133.4m

6A 109.4m 5 159.4m

Figure 4. Typical echograms obtained from Quelccaya Ice Cap in Southern Andes of Peru.

A glacier sounder was constructed in 1979 for temperate ice using designs furnished by S. Hodge (U.S. Geological Survey, Tacoma, personal communication). The equipment consists of a transmitter, used to generate voltage steps a few hundred volts in amplitude, and identical transmitting and receiving antennas. The antennas, resistively loaded dipoles tuned to radiate a single cycle at 15 MHz, were placed directly on the surface and separated by 50 m. Because signal levels were strong, the receiving antenna was coupled directly to an oscilloscope and the traces were photographed on Polaroid film. The oscilloscope time base, calibrated prior to going into the field and checked by pulse generator in the field, was used as the reference for all time measurements. Recording the signals in this manner permitted measurements of travel time, amplitude, and relative phase at many points on the glaciers.

Examples of radar data collected from Quelccaya Ice Cap, Copap, and Pucahirca, Peru and from Glacier No. 1 and Dunde Ice Cap, China, are presented in Figures 2-6. The complete wave train includes the surface wave (A) which travels along the upper surface of the air-snow interface, arrivals scattered from features within the ice, and a strong echo (B), which is interpreted as the reflections from the ice-rock boundary. Few of the waves interpreted as reflections from the ice-rock interface appear to be distorted, neither are there any strong arrivals later than the bedrock reflection, suggesting that the bedrock surfaces are relatively smooth in all cases except Glacier No. 1 in Tian Shan, which is a valley glacier.

Travel time measurements were made by correlating peaks and troughs on the transmitted and reflected pulses, taking into account the relative phase of the reflected pulse. Measurements were straightforward as in each case the entire wave train was recorded. The measuring error is estimated to be less than 0.05 s.

The oscilloscope receiver is triggered by the first arrival, which is the air wave (A) in Figures 2 to 6. The time lapse (T) between the air wave and the reflected wave arrival is

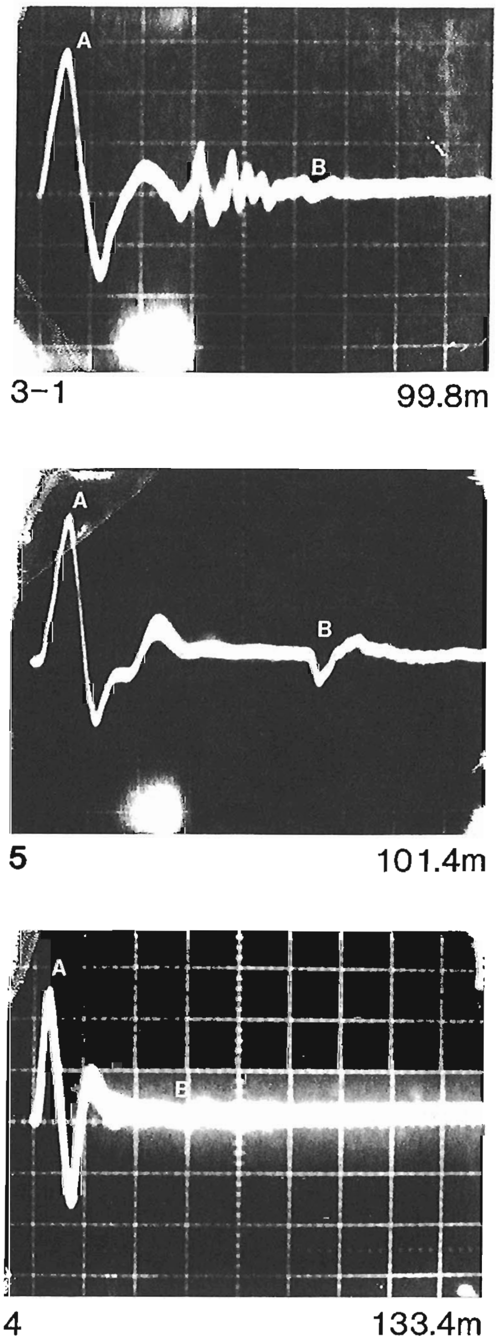

3-1 99.8m

5 101.4m

4 133.4m

Figure 5. Typical echograms obtained from Glacier No. 1 in Tian Shan of far western China.

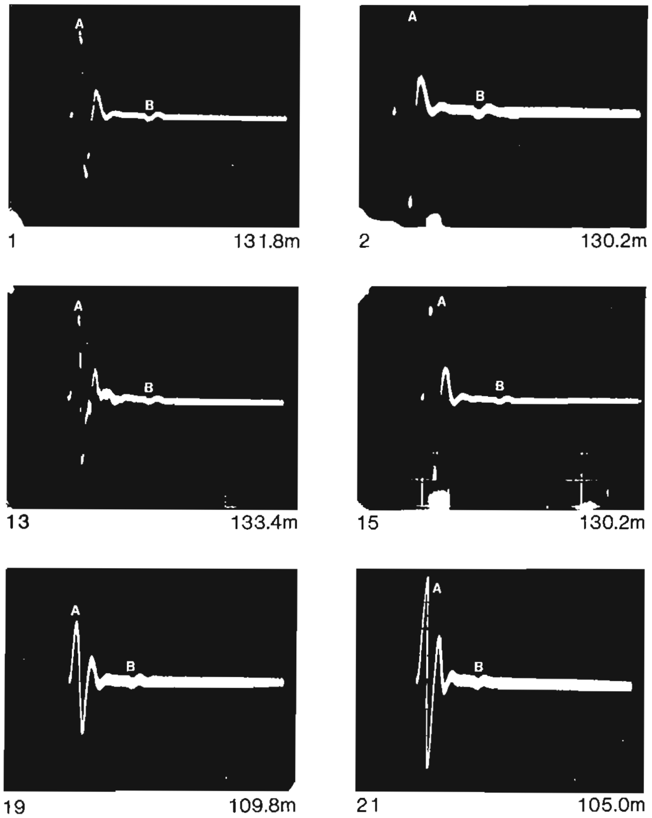

1 131.8m

2 130.2m

13 133.4m

15 130.2m

19 109.8m

21 105.0m

Figure 6. Typical echograms obtained from Dunde Ice Cap in Qilian Shan of central China.

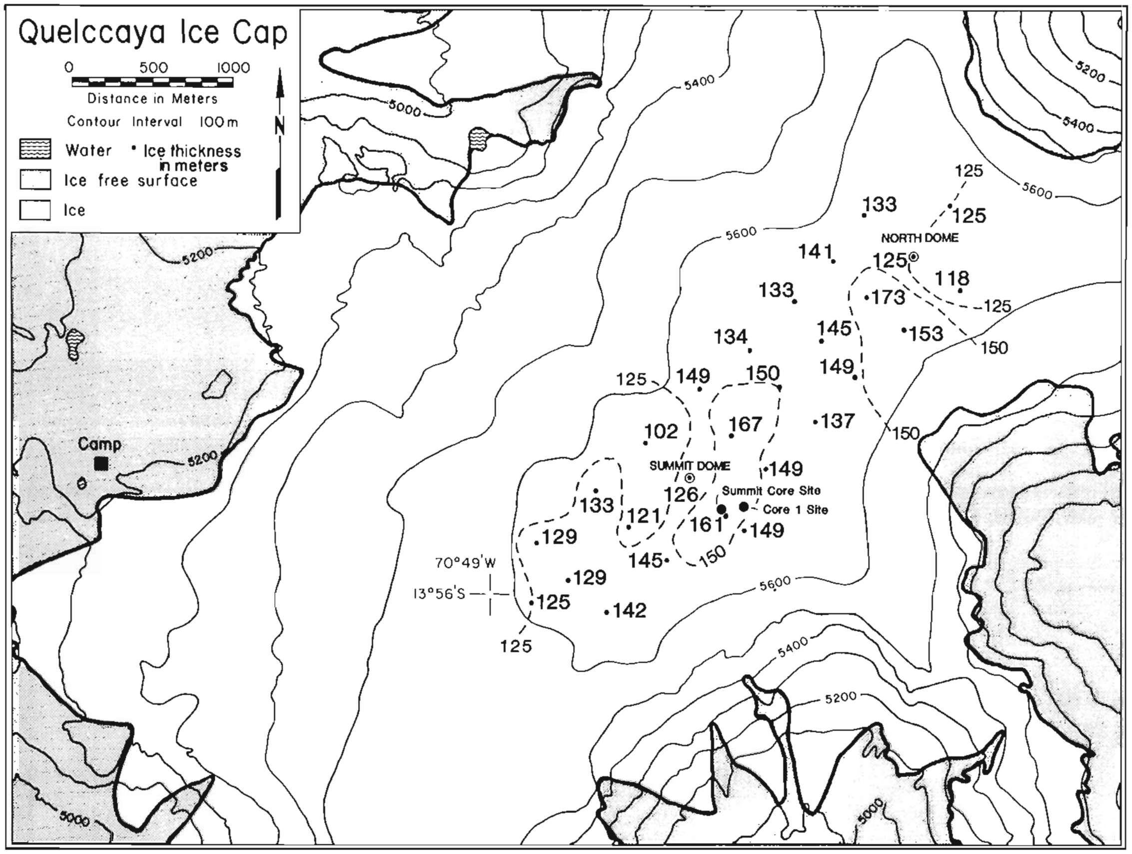

Figure 7. Isopach map of ice thickness on Quelccaya for sites above 5600 m contour. A distinct circular depression exists just east of the summit.

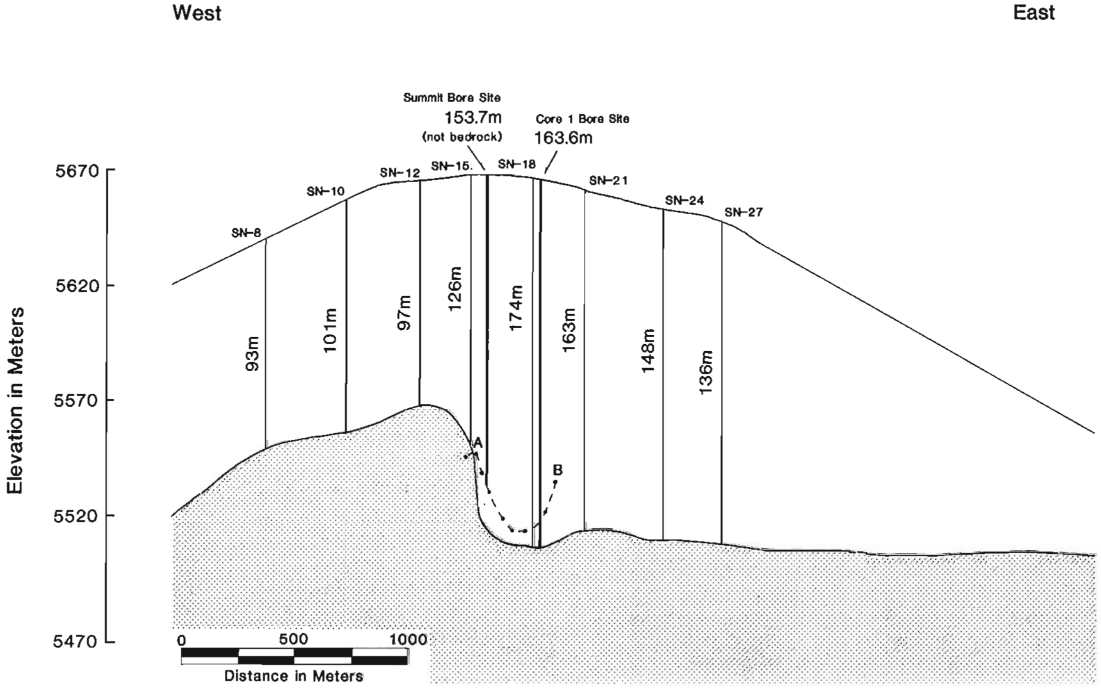

Figure 8. Ice cap thickness along an east-west traverse near the summit of Quelccaya calculated from short-pulse radar data and borehole depth measurements. The profile A-B represents detailed radar thickness determinations made at a horizontal spacing of 25 m distance, east-west across the depression.

measured. Using (S) antenna separation between the transmitter and receiver, the (I_t) ice thickness in a plane-layered situation is given as

$$I_t = (T + \frac{S}{c})^2 \frac{c^2}{4\varepsilon_i} - (\frac{S}{2})^2 \ {}^{1/2}$$

Where c = 300 m/µs and is the velocity of radar waves in air, and S equals the antenna separation distance in m. The relative dielectric constant of ice $_i$ is 3.2 (after Watts and Isherwood, 1978). Typical short-pulse echograms are presented in Figures 2 to 6, and a complete data set for four Peruvian sites is given in Table 1 and for two Chinese sites in Table 2.

Table 1. Ice thickness, Peru

	Site no.	Date	No. of echograms	Time µs/div	volt/ division	Antenna separation S (m)	Travel time T	Ice thick. It (m)
A. HUASCARÁN, PERU, 1980								
Huascarán	1	July 1980						164.0
Huascarán	2							123.0
Huascarán	3							192.0
Huascarán	4							144.0
Huascarâî	5							130.0
Huascarâî	6							139.0
B. COPAP, PERU, 1983 (Nevados Jacabamba-Cordillera Blanca)								
Copap	1	August 1983		0.5	0.2	50	2.30	197.4
Copap	2			0.5	0.2	50	2.35	201.4
Copap	3			0.5	0.2	50		-
Copap	4			0.5	0.2	50		-
Copap	5			0.5	0.2	50		-
Copap	6			0.5	0.2	50		-
C. PUCAHIRCA, PERU, 1984 (Cordillera Blanca)								
Puca	1	September	1	0.5	0.2	50	-	-
Puca	2	1984	1	-	-	-	-	-
Puca	3		1	0.5	0.2	50	1.80	187.8
Puca	4		3	0.5	0.2	50	1.25	159.4
Puca	5		1	0.5	0.2	50	1.60	178.0
Puca	6		1	0.5	0.1	50	1.75	185.4
Puca	7		1	0.5	0.2	50	2.00	197.1
Puca	8		1	0.5	0.5	50	1.85	190.2
Puca	9		1	0.5	0.2	50	1.85	190.2
Puca	10		1	0.5	0.5	50	2.10	207.6
Puca	11		1	0.5	0.5	50	1.85	190.2
Puca	11		2	0.5	0.2	50	2.10	207.6
Puca	12		1	0.5	0.2	50	2.50	213.4
Puca	12		2	0.5	0.2	50	2.50	213.4
Puca	13		1	0.5	0.2	50	2.50	213.4
Puca	14		1	0.5	0.2	50	2.80	237.4
Puca	17		1	0.5	0.2	50	2.50	213.4
D. QUELCCAYA, PERU, 1981 (Published: see Jezek & Thompsons, 1982)								
Quel	Summit Dome	July 1981	3	0.5	0.2	50	1.5	133.4
Quel	Summit Dome		1	0.2	0.2	50	1.54	136.6
Quel	North Dome 1		1	0.5	0.2	50	1.4	125.4
Quel	North Dome 1		1	0.5	0.2	50	1.4	125.4
Quel	North Dome 1a		1	0.5	0.2	50	1.5	133.4
Quel	North Dome 1b		1	0.5	0.2	50	1.31	118.2
Quel	2		1	0.5	0.2	50	2.0	173.4
Quel	2a		1	0.5	0.2	50	1.6	141.4
Quel	2b		1	0.5	0.2	50	1.75	153.4
Quel	3		1	0.5	0.2	50	1.64	144.6
Quel	3a		1	0.5	0.2	50	1.5	133.4
Quel	3b		1	0.5	0.2	50	1.7	149.4

RESULTS

The echograms from all the sites were easy to interpret and suggested that, with the exception of Glacier No. 1 in Tian Shan, the underlying bedrock was relatively smooth. The echograms showed striking differences. The echograms from Quelccaya and Pucahirca showed a great deal of structure between A and B in contrast to Dunde Ice Cap echograms. It is believed that the structure results from reflections caused by the distinct annual layering. The mean annual accumulation is 1.15 m of water equivalent, or 3 m of snow, for the Peruvian sites and only 0.4 m of water equivalent, or 0.65 m of snow for the Dunde Ice Cap. Layer separations of 1.25 m of ice near the surface on the Quelccaya Ice Cap thin to 1 cm at bedrock (Thompson et al., 1979, 1984, 1985). Field observations on the margins of Pucahirca also revealed a marked annual layering with annual accumulation of about 1 m of water equivalent. Summary maps of ice thickness and general bedrock topography are presented for the most extensively studied sites; the Quelccaya Ice Cap in Peru (Fig. 7, 8), and the Dunde Ice Cap in China (Fig. 9, 10). Of all

	Site no.	Date	No. of echograms	Time µs/div	volt/ division	Antenna separation S (m)	Travel time T	Ice thick. It (m)
D. QUELCCAYA, PERU, 1981 (cont.)								
Quel	4		1	0.5	0.2	50	?	-
Quel	4		1	0.5	0.2	50	1.8?	-
Quel	5a		1	0.5	0.2	50	1.7	149.4
Quel	5b		1	0.5	0.2	50	1.7	149.4
Quel	6		1	0.5	0.2	50	1.4	125.4
Quel	6b		1	0.5	0.2	50	1.85	161.4
Quel	6c		2	0.5	0.2	50	1.7	149.4
Quel	7		1	0.5	0.2	50	1.35	121.4
Quel	7a		2	0.5	0.2	50	1.5	133.4
Quel	7b		1	0.5	0.2	50	1.65	145.4
Quel	8		2	0.5	0.2	50	1.45	129.4
Quel	8a		1	0.5	0.2	50	1.45	129.4
Quel	8b		1	0.5	0.2	50	1.45	129.4
Quel	8c		2	0.5	0.2	50	1.61	142.2
Quel	1st Bore.	July 1983	1	1.0	0.2	50	1.8	157.4
Quel	1st Drill		1	1.0	0.2	50	1.85	157.4
E. QUELCCAYA, PERU, 1984								
Quel	1 E-W	August 1984	2	0.2	0.1	50	1.44	128.6
Quel	1 E-W		2	0.5	0.1	50	1.40	125.4
Quel	2 E-W		2	0.2	0.1	50	1.43	127.8
Quel	2 E-W		2	0.5	0.1	50	1.40	125.4
Quel	3 E-W Summit Core		2	0.2	0.1	50	1.52	135.0
Quel	3 E-W Summit Core		2	0.5	0.1	50	1.50	133.4
Quel	4 E-W		2	0.2	0.2	50	1.64	144.6
Quel	4 E-W		2	0.5	0.2	50	1.60	141.4
Quel	5 E-W		2	0.2	0.2	50	1.76	154.2
Quel	5 E-W		1	0.5	0.2	50	1.75	153.4
Quel	6 E-W		1	0.2	0.2	50	1.86	162.2
Quel	6 E-W		2	0.5	0.2	50	1.80	157.4
Quel	7 E-W		1	0.2	0.2	50	?out	-
Quel	7 E-W	August 1984	1	0.5	0.2	50	1.83	160.0
Quel	8 E-W Core 1		1	0.2	0.2	50	1.75	153.4
Quel	8 E-W Core 1		1	0.5	0.2	50	1.74	153.4
Quel	9 E-W		1	0.5	0.2	50	1.65	145.4
Quel	9 E-W		1	0.2	0.2	50	1.66	146.2
Quel	10 E-W		2	0.2	0.2	75	1.52	132.8
Quel	10 E-W		2	0.5	0.1	75	1.50	131.2
Quel	11 N-S		2	0.5	0.2	25	1.80	156.2
Quel	12 N-S		1	0.2	0.2	50	1.80	157.4
Quel	12 N-S		1	0.5	0.2	50	1.75	153.4
Quel	13 N-S		1	0.2	0.2	50	-	-
Quel	13 N-S		1	0.5	0.5	50	1.95	169.4
Quel	14 N-S		1	0.5	0.5	50	2.05	177.5
Quel	15 N-S		1	0.5	0.2	50	1.95	169.4
Quel	15 N-S		1	0.5	0.5	50	1.95	169.4
Quel	16 N-S		1	0.5	0.2	50	1.95	169.4

Table 2. Ice thickness, China

	Site no.	Date	No. of echograms	Time µs/div	volt/ division	Antenna separation S(m)	Travel time T	Ice thick. It (m)
A. DUNDE ICE CAP, CHINA, 1984								
Dunde	1	June 1984	2	0.5	0.1	50	1.7	149.4
Dunde	1		1	1.0	0.1	50	1.7	149.4
Dunde	2		2	0.5	0.2	50	1.45	129.4
Dunde	2		1	0.2	0.2	50	1.45	129.4
Dunde	3		3	0.5	0.2	50	1.50	133.4
Dunde	3		1	1.0	0.2	50	1.50	133.4
Dunde	3		1	0.2	0.2	50	1.51	134.2
Dunde	4		3	0.5	0.2	50	1.55	137.4
Dunde	4		1	0.2	0.2	50	1.56	138.2
Dunde	5		1	0.2	0.2	50	1.60	141.4
Dunde	5		1	0.5	0.2	50	1.58	139.8
Dunde	6		2	0.5	0.2	50	1.4	125.4
Dunde	6		1	0.2	0.2	50	1.4	125.4
Dunde	7		2	0.5	0.2	50	1.8	157.4
Dunde	8		1	0.5	0.5	50	1.49	132.6
Dunde	8		1	0.2	0.2	50	1.48	131.8
Dunde	8		1	0.5	0.2	50	1.45	129.4
Dunde	9		1	0.5	0.2	50	0.95	89.4
Dunde	9		1	0.5	0.1	50	?0.95	-
Dunde	10		2	0.5	0.2	50	1.0	93.4
Dunde	11		3	0.5	0.2	50	1.2	109.4
Dunde	12		2	0.5	0.2	50	0.75	73.4
B. DUNDE ICE CAP, CHINA, 1986								
Dunde	1 Summit Dome	August 1986	3	0.5	0.2	50	1.48	131.8
Dunde	1 Summit Dome		1	0.5	0.1	50	1.48	131.8
Dunde	1 Summit Dome		1	0.2	0.1	50	1.48	131.8
Dunde	2 P-10		2	0.5	0.2	50	1.46	130.2
Dunde	2 P-10		1	0.5	0.1	50	1.46	130.2
Dunde	2 P-10		1	0.2	0.2	50	1.48	131.8
Dunde	3 P-12		4	0.5	0.2	50	1.50	133.4
Dunde	3 P-12		1	0.5	0.1	50	1.50	133.4
Dunde	3 P-12		1	0.2	0.2	50	1.52	135.0
Dunde	4 P-16		1	0.5	0.2	50	1.46	130.2
Dunde	4 P-16		1	0.5	0.1	50	1.48	131.8
Dunde	4 P-16		1	0.2	0.2	50	1.48	131.8
Dunde	5 P-11		1	0.5	0.2	50	1.48	131.8
Dunde	5 P-11		1	0.2	0.2	50	1.49	132.6
Dunde	6 P-3	August 1986	6	0.5	0.2	50	1.46	130.2
Dunde	6 P-3		1	0.2	0.2	50	1.47	131.0
Dunde	6 P-3		1	0.5	0.1	50	1.46	130.2
Dunde	7 P-13		2	0.5	0.2	50	1.51	134.2
Dunde	7 P-13		1	0.5	0.1	50	1.53	135.8
Dunde	7 P-13		1	0.2	0.2	50	1.54	136.6
Dunde	8 P-14		1	0.5	0.2	50	1.50	133.4
Dunde	8 P-14		1	0.5	0.1	50	1.50	133.4
Dunde	8 P-14		1	0.2	0.2	50	1.52	135.0
Dunde	9 P-15		2	0.5	0.2	50	1.42	127.0
Dunde	9 P-15		1	0.5	0.1	50	1.43	127.8
Dunde	9 P-15		1	0.2	0.2	50	1.49	132.6
Dunde	10 P-7		3	0.5	0.2	50	1.44	128.6
Dunde	10 P-7		2	0.5	0.1	50	1.38	123.8
Dunde	10 P-7		2	0.2	0.2	50	1.44	128.6
Dunde	10 P-7		1	0.2	0.1	50	1.48	131.8
Dunde	11 P-2		3	0.5	0.2	50	1.39	124.6
Dunde	11 P-2		1	0.2	0.2	50	1.44	128.6
Dunde	12 P-9		3	0.5	0.2	50	1.43	127.8
Dunde	12 P-9		1	0.2	0.2	50	1.44	128.6
Dunde	13 P-4		2	0.5	0.2	50	1.50	133.4
Dunde	13 P-4		1	0.5	0.1	50	1.50	133.4
Dunde	13 P-4		1	0.2	0.2	50	1.52	135.0
Dunde	14 1/2 Sum. & SN8		2	0.5	0.2	50	1.48	131.8
Dunde	14		1	0.5	0.1	50	1.49	132.6

	Site no.	Date	No. of echograms	Time µs/div	volt/ division	Antenna separation S(m)	Travel time T	Ice thick. It (m)
B. DUNDE ICE CAP, CHINA, 1986 (cont.)								
Dunde	14		1	0.2	0.2	50	-	-
Dunde	15 SN-8		2	0.5	0.2	50	1.45	129.4
Dunde	15 SN-8		1	0.5	0.1	50	1.47	131.0
Dunde	15 SN-8		1	0.2	0.2	50	?	?
Dunde	16 SN-11		2	0.5	0.2	50	1.31	118.2
Dunde	16 SN-11		1	0.5	0.1	50	1.37	-
Dunde	16 SN-11		1	0.2	0.2	50	1.40	125.4
Dunde	17 SN-14		1	0.5	0.2	50	1.41	126.2
Dunde	17 SN-14		1	0.5	0.1	50	1.41	126.2
Dunde	17 SN-14		1	0.2	0.2	50	1.53	135.8
Dunde	18 Strain Net		2	0.5	0.2	50	1.46	130.2
Dunde	18 15 Om Beyond Str. Net		1	0.5	0.1	50	1.47	131.0
Dunde	18		1	0.2	0.2	50	1.52	135.0
Dunde	19 15 Om Beyond Pole 1		3	0.5	0.2	50	1.21	110.2
Dunde	19		1	0.5	0.1	50	1.20	109.4
Dunde	19		1	0.2	0.2	50	1.20	110.2
Dunde	20		2	0.5	0.2	50	1.06	98.2
Dunde	20 Site '84 16 m Borehole		1	0.5	0.1	50	1.06	98.2
Dunde	20		1	0.2	0.2	50	1.06	98.2
Dunde	21		2	0.5	0.2	50	1.14	104.6
Dunde	21 Site '84-1/3 to Summit		1	0.5	0.1	50	1.15	105.4
Dunde	21		1	0.2	0.2	50	1.12	103.0
C. DUNDE ICE CAP, CHINA, 1987								
Dunde	1 Tent Site	July/August 1987	2	0.5	0.2	50	1.6	141.4
Dunde	1 Drill Site 1		2	0.5	0.2	50	1.65	145.4
Dunde	3 Drill Site 1		1	0.5	0.2	50	1.60	141.4
Dunde	3 Drill Site 1		2	0.5	0.5	50	1.60	141.4
Dunde	Borehole 2		1	0.2	0.5	50	1.56	138.2
Dunde	Drillsite 2		1	0.5	0.2	20	1.60	141.4
Dunde	Drillsite 2		1	0.5	0.5	50	1.60	141.4
Dunde	Drillsite 2		1	0.2	0.2	50	1.54	136.6
Dunde	Drillsite 3		1	0.5	0.2	47	1.52	140.3
Dunde	Drillsite 3		1	0.5	0.2	47	1.52	140.3
Dunde	Drillsite 3		2	0.5	0.1	47	1.52	140.3
Dunde	Drillsite 3		2	0.5	0.2	50	-	-
Dunde	4 Middle Dome		2	0.5	0.2	50	0.95	89.4
Dunde	4 Middle Dome		1	0.5	0.1	50	0.95	89.4
Dunde	4 Middle Dome		1	0.2	0.2	50	0.95	89.4
Dunde	5 South Dome		2	0.5	0.2	50	0.78	77.9
Dunde	5 South Dome		1	0.2	0.2	50	0.78	77.9
Dunde	5 South Dome		1	0.5	0.1	50	0.78	77.9
Dunde	6 South Col.		1	0.5	0.5	50	0.65	77.3
Dunde	6 South Col.		1	0.2	0.2	50	0.60	70.1
Dunde	6 South Col.		1	0.5	0.2	50	0.60	70.1
Dunde	7 Eastside-Middle Dome		1	0.5	0.2	50	1.00	86.4
Dunde	7 Eastside-Middle Dome		1	0.2	0.2	50	0.90	85.4
Dunde	7 Eastside-Middle Dome		1	0.5	0.5	50	0.90	85.4
D. TIAN SHAN, CHINA, 1984								
Tian	1-2	1984	1	0.5	0.5	35	-	-
Tian	1-2		1	0.5	0.2	35	-	-
Tian	1-2		1	0.5	0.2	35	-	-
Tian	1-2		1	0.5	0.2	35	-	-
Tian	3-1		3	0.2	0.2	50	1.08	99.8
Tian	3-1		3	0.5	0.2	50	-	-
Tian	3-1		2	0.2	0.5	50	?1.10	-
Tian	3-2		4	0.2	0.5	50	?1.50	-
Tian	3-2		1	0.5	0.5	50	?1.45	-
Tian	4		3	0.5	0.2	50	1.50	133.4
Tian	4		1	0.2	0.2	50	1.10	101.4
Tian	5		2	0.2	0.2	50	1.08	99.8
Tian	5		1	0.5	0.2	50	1.10	101.4

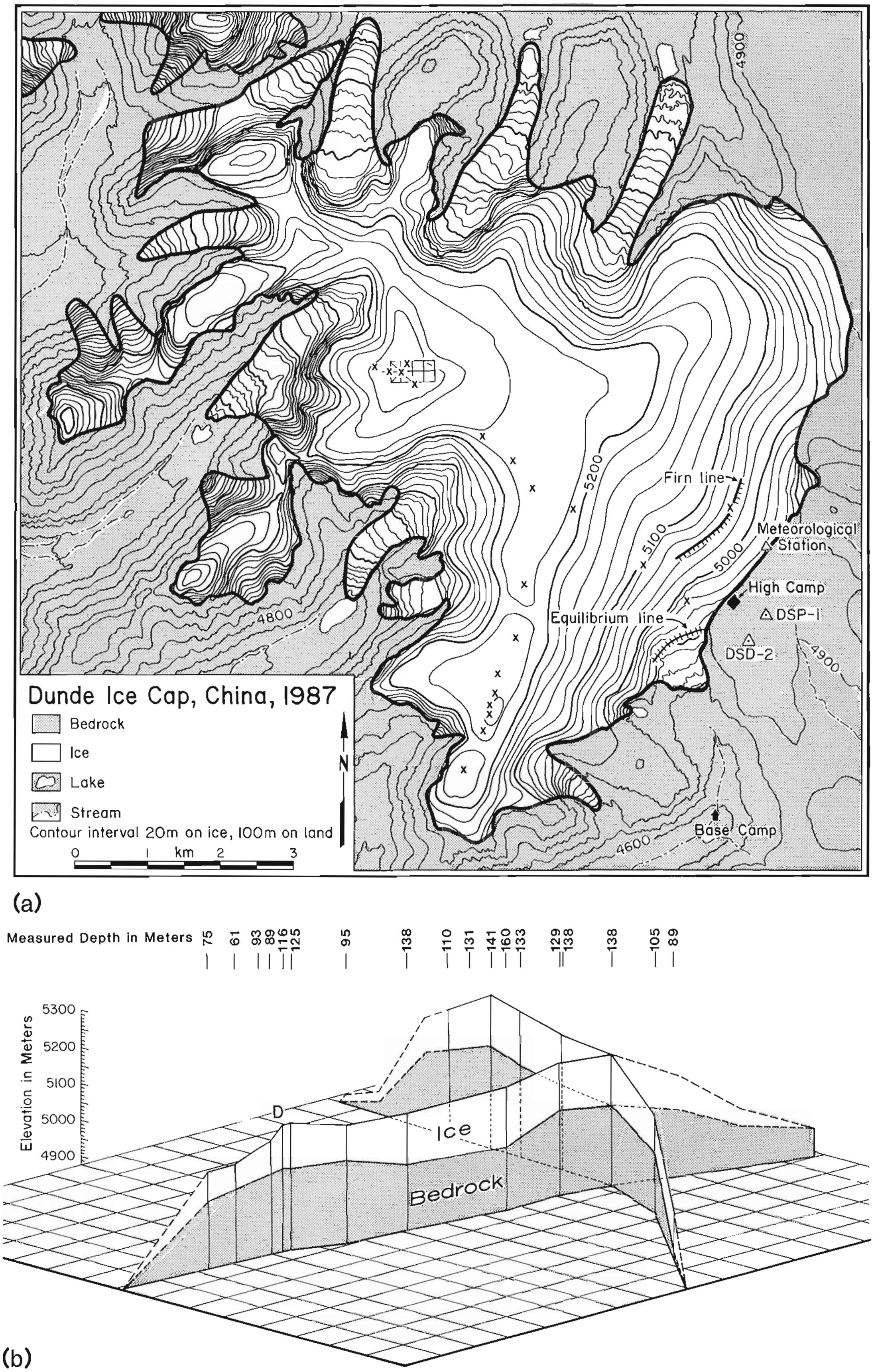

Figure 9a. Map of Dunde Ice Cap showing sites of radar sounding (x) and the location of the summit strain networks shown in Figure 10. (**b**) Ice cap thicknesses along the traverses calculated from short-pulse radar data collected at sites marked x in Figure 9(a).

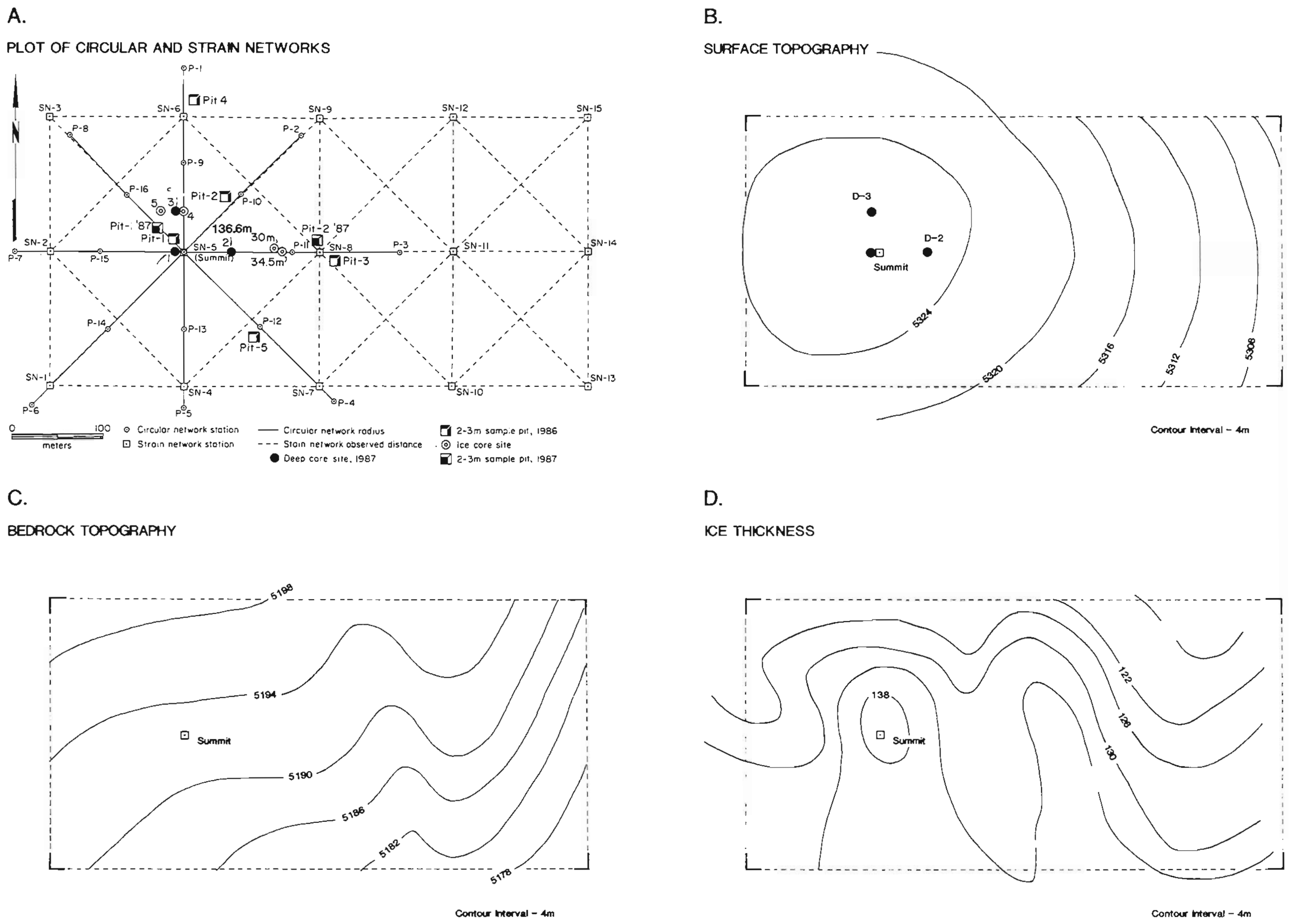

Figure 10. Summit area of Dunde Ice Cap: **A** circular and strain network; **B** contour map of surface topography; **C** contour map of bedrock topography, and D isopach map of ice thickness.

six sites studied, the greatest ice thickness of 237 m was found on Pucahirca Glacier in Cordillera Blanca. The short-pulse radar thickness determinations for both Quelccaya and Dunde ice caps were compared directly with depths measured in boreholes to bedrock at the summits. Two cores were recovered on the Quelccaya Ice Cap in 1983. One was 154.8 m long (summit core) and contained 1350 a of climatic information; the other was 163.6 m long (core 1) with a 1500 a record. Only core 1 reached bedrock. At the core 1 drill site, the radar indicated ice thicknesses that ranged from 153 to 157.4 m (average 155 m). Thus, the radar underestimated the borehole site depth by less than 9 m. The difference may result partially from the complicated bedrock topography in this area (Fig. 7, 8), and the possibility that the borehole itself deviated slightly from the vertical. The summit site is located on the edge of a bedrock depression just 30 m east of the summit, and 150 m west of core 1 (Fig. 8). Here, the radar consistently indicated a depth between 133 and 135 m and the measured borehole depth (not bedrock) was 153.7 m. The minimum 20 m difference was attributed to the abruptness of the slope into the bedrock depression.

A more detailed sounding was conducted in 1984 East-West across the Summit depression at 25 m intervals. In Figure 8, line A-B shows that the radar depths are generally less across the depression than the measured borehole depths indicate.

In 1987, three deep cores were recovered from the summit of Dunde Ice Cap, China. The ice cap summit topography has been extensively surveyed and radar soundings have been made (Fig. 9, 10A, B, C, D). The bedrock under Dunde Ice Cap is more uniform than that observed under Quelccaya Ice Cap. At drill sites 1 and 3 the measured depths between the surface and bedrock were 139.6 and 138.4 m, respectively, while the average shortpulse ice radar thicknesses were 142.4 and 140.3 m respectively. The differences of 3 and 2 m are considerably less than the differences obtained in the Quelccaya study. The more consistent results for Dunde result in part from the greater smoothness of the bedrock under the summit of Dunde Ice Cap. At drill site 2 (Fig. 10), the radar results were used to determine the ice thickness while in the field. With average thickness being 138.9 m, the actual drilling depth of 136.6 m allowed maximum recovery of ice core without destroying the drill bit. Clearly the depth determinations for both Quelccaya and Dunde Ice Caps by the short-pulse radar are quite accurate and provide essential information for planning for ice core recovery in future high altitude, low latitude sites.

CONCLUSIONS

The short-pulse ice radar proved to be an extremely useful tool for quick and accurate determination of ice thicknesses. Accuracy is essential for evaluating the potential length of ice cores and for planning the minimum size for the drill length to be used in these remote, high altitude, low latitude sites where logistics are always a challenge. The ice thickness determinations from the short-pulse radar system were important in northern Peru, for calculating the volume of ice that might avalanche as a result of an earthquake. By calculating the amount of water likely to be displaced by avalanches into high altitude glacial lakes, potential flood areas can be identified.

Comparison with measured depths from boreholes indicated the short-pulse radar determinations were within 5% of the actual depth near the summit of Quelccaya Ice Cap, and within 2% on Dunde Ice Cap. The accuracy of the radar depth was affected not only by the bedrock roughness, but also by changes in the dielectric constant of ice because of differences in ice temperature, rate of densification, and changes in the concentration of impurities within the ice. These parameters are seldom known prior to actual ice core recovery. However, as the Quelccaya and Dunde ice cap studies showed, they are not essential for initial ice thickness determinations.

ACKNOWLEDGMENTS

The Peruvian electric power company, ElectroPeru, and the Instituto Geologico Minero y Metalurgico in Peru and the Lanzhou Institute of Glaciology and Geocryology in China are gratefully acknowledged for field and logistical support. The Peru research was supported by NSF grants ATM 75-15513A02, ATM 7821609A01, ATM-8105079A02, and ATM 8213601A01. The NSF Division of Polar Programs supported 1974 field investigation (GV 41411) and development of the solar powered drill by the Polar Ice Coring Office, University of Nebraska, Lincoln, Nebraska. The work in China was supported by the Climate Dynamics Program and the Division of Polar Programs under NSF grant ATM-8519794 and by National Geographic Society grant 3323-86. The first year's support was provided by the National Academy of Sciences' Committee for Scholarly Communications with the People's Republic of China. Thanks to Raymond Watts and Steve Hodge of the USGS for many valuable discussions in the development of the short-pulse radar unit. Special thanks are extended to all members of the 10 Peruvian and 3 Chinese expeditions. This contribution is number C-624 of the Byrd Polar Research Center.

REFERENCES

Jezek, K.C. and Thompson, L.G.
1982: Interpretation of mono-pulse ice radar soundings on two Peruvian glaciers; IEEE Transactions on Geoscience and Remote Sensing, v. GE-20, no. 3, p. 243-249.

Robin, G. de Q.
1975a: Radioecho sounding: glaciological interpretations and applications; Journal of Glaciology, v. 15, no. 73, p. 49-64.
1975b: Velocity of radio waves in ice by means of bore-hole interferometric technique; Journal of Glaciology, v. 15, no. 73, p. 151-59.

Smith B.M. and Evans, S.
1972: Radio echo sounding: Absorption and scattering by water inclusions and ice lenses; Journal of Glaciology, v. 17, no. 75, p. 133-146.

Thompson, L.G., Hastenrath, S., and Arnao, B. Morales
1979: Climatic ice core records from the tropical Quelccaya ice cap; Science, v. 203, no. 4386, p. 1240-43.

Thompson, L.G., Bolzan, J.F., Brecher, H.H., Kruss, P.D., Mosley-Thompson, E., Jezek, K.C.
1982: Geophysical investigations of the tropical Quelccaya ice cap, Peru; Journal of Glaciology, v. 28, no. 98, p. 57-69.

Thompson, L.G., Mosley-Thompson, E., and Arnao, B.M.
1984: Major El Nino/Southern Oscillation events recorded in stratigraphy of tropical Quelccaya Ice Cap; Science, v. 226, no. 4670, p. 50-52.

Thompson, L.G., Mosley-Thompson, E., Bolzan, J.F., and Koci, B.R.
1985: A 1500-year record of tropical precipitation in ice cores from the Quelccaya ice cap, Peru; Science, v. 229, no. 4717, p. 971-973.

Thompson, L.G., Mosley-Thompson, E., Dansgaard, W., and Grootes, P.M.
1986: The 'Little Ice Age' as recorded in the stratigraphy of the tropical Quelccaya Ice Cap; Science, v. 234, no. 4774, p. 361-364.

Thompson, L.G., Davis, M., Mosley-Thompson, E., and Liu, K.
1988a: Pre-Incan agricultural activity recorded in dust layers in two tropical ice cores; Nature, v. 336, no. 6201, p. 763-765.

Thompson, L.G., Mosley-Thompson, E., Wu, X., and Xie, Z.
1988b: Wisconsin/Würm glacial stage ice in the subtropical Dunde Ice Cap, China; GeoJournal, v. 17, no. 4, p. 517-523.

Thompson, L.G., Wu, X., Mosley-Thompson, E., and Xie, Z.
1988c: Climatic records from the Dunde ice cap, China; Annals of Glaciology, v. 10, p. 178-182.

Watts, R.D. and England, A.W.
1976: Radio-echo sounding of temperate glaciers: ice properties and sounder design criteria; Journal of Glaciology, v. 17, no. 75, p. 39-48.

Watts R.D. and Isherwood, W.
1978: Gravity surveys in glacier-covered regions; Geophysics, v. 43, no. 4, p. 819-822.

Deconvolution of ground probing radar data

J.P. Todoeschuck[1], P.T. LaFlèche[2], O.G. Jensen[3], A.S. Judge[4], and J.A. Pilon[4]

Todoeschuck, J.P., LaFlèche, P.T., Jensen, O.G., Judge, A.S., and Pilon, J.A., 1992: Deconvolution of ground probing radar data; in Ground penetrating radar, ed. J. Pilon; Geological Survey of Canada, Paper 90-4, p. 227-230.

Abstract

The return signal received in the collection of ground probing radar (GPR) data in layered ground represents the convolution of the emitted wavelet and the reflection sequence for the local geology. Coupling between the transmit and receive antennas and the immediately underlying ground varies considerably from place to place. This variation leads to uncertainty in the precise form of the source wavelet making deterministic deconvolution of the signal impractical. Recent advances in GPR instrumentation have allowed the collection of large volumes of digital data. The close similarity between GPR and reflection seismic data suggests that deconvolution techniques that have been used in the seismic industry could be applied successfully to radar data. Predictive deconvolution allows estimation of the source wavelet from the observed time series. This method involves assuming a model for the reflection sequence. We derive a filter for the scaling noise model, where the power spectrum of the reflection sequence is proportional to some power of the spatial frequency. We show, using recent field data, that deconvolution can enhance the results and resolve additional near surface features.

Résumé

L'écho reçu, selon les données recueillies par géoradar dans un sol stratifié, représente la convolution du signal émis et la séquence de réflexion de la géologie locale. Le couplage des antennes de transmission et de réception avec le sol directement sous-jacent varie considérablement d'un endroit à l'autre. Cette variation crée une incertitude relativement à la forme précise du signal d'origine rendant impossible la déconvolution déterministe du signal. Les perfectionnements récents apportés au géoradar ont permis de recueillir une grande quantité de données numériques. L'étroite similarité entre les données radar et de sismique réflexion indique que les techniques de déconvolution utilisées dans l'industrie sismique pourraient être appliquées avec succès aux données radar. La déconvolution prédictive permet de déterminer le signal source des séries temporelles observées. Cette méthode fait intervenir un modèle de la séquence de réflexion. Un filtre est dérivé pour le modèle du bruit scalant où le spectre de puissance de la séquence de réflexion est proportionnel à une certaine puissance de la fréquence spatiale. À l'aide de données de terrain récentes, on montre que la déconvolution peut améliorer les résultats et permettre de résoudre d'autres éléments proches de la surface.

---

[1] Defence Research Establishment Pacific, FMO, Victoria, British Columbia V0S 1B0

[2] Targeted Research Directorate, NSERC, Ottawa, Ontario K1A 1H5

[3] Geophysical Research Laboratory, Department of Geology and Geophysics, McGill University, 3450 University Street, Montreal, Québec H3A 2A7

[4] Geological Survey of Canada, Terrain Sciences Division, 601 Booth Street, Ottawa, Ontario K1A 0E8

INTRODUCTION

Ground probing radar (GPR) has marked similarities to seismic reflection profiling, with electromagnetic replacing acoustic waves. Despite a shallower depth of penetration than seismic methods, GPR has enjoyed wide use in engineering and other applications because of the higher resolution offered by the shorter wavelengths used. The advent of digital data storage has increased the similarities to seismic practice and suggests the use of data processing schemes, which are common there. One of these techniques is deconvolution of the observations. Deconvolution has the effect of removing the character of the emitted pulse or wavelet from the observations, which can allow shaping the pulse for further display. This step is desirable before further processing, such as migration.

The return pulse from an interface is ideally a faithful echo of the transmitted pulse. Additional interfaces will produce additional returns which may very well overlap at the receiver. We can express the returned signal as the convolution of the wavelet with the reflection series representing the reflection coefficients and location of each interface.

If we discretize the wavelet as w_i and the reflection sequence in travel time as r_i then the observations x_i are given by equation (1)

$$x_k = \Sigma\, w_i\, r_{k-i} \tag{1}$$

or

$$x = w * r\,. \tag{2}$$

We want to use our observations to get the geophysically interesting part of the signal, the reflection sequence. Convolving the observations with a suitable filter which will remove the effects of the convolution with the wavelet. This process is referred to as deconvolution. An ideal filter would reproduce the reflection sequence exactly. In general our filter will produce an estimate of the reflection sequence, e_i. If the filter is a_i

$$e = x * a\,. \tag{3}$$

The filter is called the inverse of the wavelet. Now, if we know the wavelet, it is relatively straightforward to calculate its inverse. Use of this inverse can be called deterministic deconvolution. However, if the wavelet is not known, we can still calculate an inverse using the observations and an appropriate statistical model of the reflection sequence by the method of predictive decomposition.

Experience suggests that the waveform in GPR can vary from place to place in both shape and amplitude, perhaps because of the changing coupling with ground of differing electrical properties. This variation suggests the use of predictive decomposition on GPR traces. Note that this method assumes that the character of the wavelet does not change with depth, for example from dispersion. If dispersion is a problem, it will be necessary to break up the observations into shorter sequences over which the change is small.

PREDICTIVE DECOMPOSITION

The statistical measure that we focus on is the power spectrum of the reflection sequence, which we take to be known a priori. Knowing the power spectrum is equivalent to knowing the autocorrelation function (ACF). If the ACF of the observations is R_m then

$$m = E[x_k x_{k-m}] \tag{4}$$

where E denotes the expectation operator.

Assuming for a moment that we have an infinite amount of data, the output of our filter will be

$$e_k = \Sigma\, a_n x_{k-n} \tag{5}$$

and the ACF Y_j of the output is

$$Y_j = \Sigma\, a_m\, \Sigma\, a_n R_{m+j-n} \tag{6}$$

(Silvia and Robinson, 1979).

Suppose that the reflection sequence has only a few nonzero Y_j's, say for $0 \le j \le J$. (The reason for this will be explained below.) If

$$\Sigma\, a_n R_{p-n} = 0,\ p > J, \tag{7}$$

then from equation 6, the condition on the Y_j's for $j > J$ will be satisfied, i.e., they will equal zero. Now consider the last nonzero term, Y_J. We will normalize our filter so that $a_0 = 1$. Then, using equation 7, we see from equation 6

$$\Sigma\, a_n R_{J-n} = Y_J\,. \tag{8}$$

Likewise

$$Y_{J-1} = \Sigma\, a_n R_{J-1-n} + a_1\, \Sigma\, a_n R_{J-n} \tag{9}$$

so

$$\Sigma\, a_n R_{J-1-n} = Y_{J-1} - a_1 Y_J \tag{10}$$

and so on for the remaining nonzero terms. This process gives us a full set of equations, known as the normal equations, for the filter coefficients based on the ACFs of the observations and the model reflection sequence (Todoeschuck and Jensen, 1988).

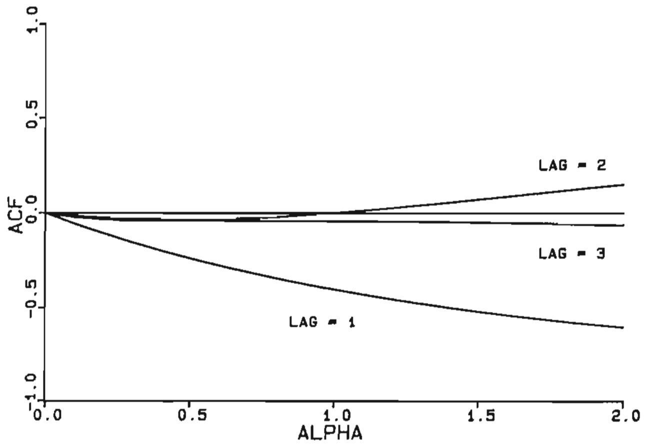

Figure 1. Variation with α of the lag = 1, 2, 3 terms of the autocorrelation function of an $f\alpha$ process.

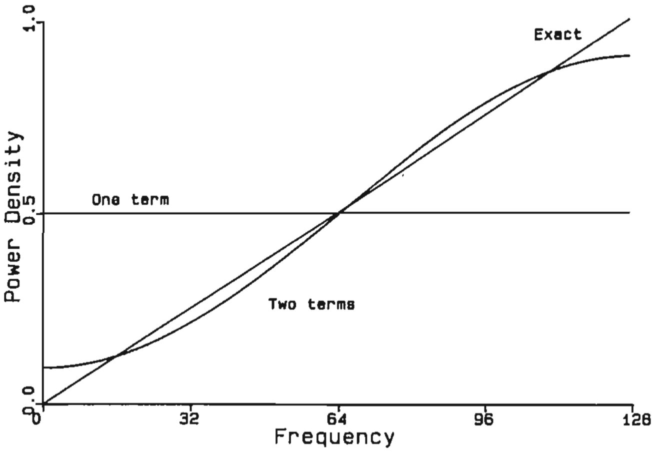

Figure 2. Power spectra obtained by keeping one term and two terms in the autocorrelation function of compared with the exact spectrum for $\alpha = 1$. (Frequency in arbitrary units).

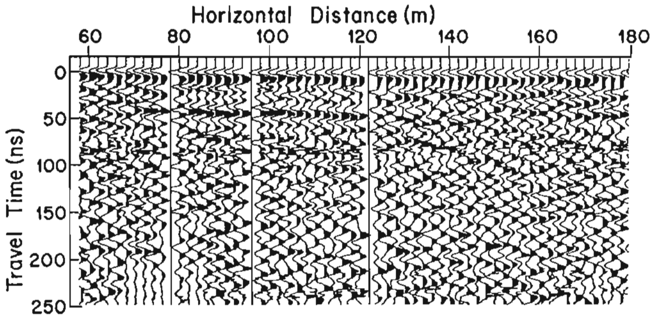

Figure 3. Portion of undeconvolved GPR profile of dam; near surface features are lost in the air and ground waves.

We must now select a model or at least a group of models for our reflection sequence. One class, which has been of great interest for seismic reflection sequences, is that of the scaling noises. A scaling noise is a random sequence with many interesting properties but the important one for us is that its power spectrum P is proportional to some power of frequency f, that is,

$$P \alpha f^{\alpha} \qquad (11)$$

where α is a real number. The power spectra of seismic reflection sequences have been found to be well characterized by equation 11 with $\alpha \cong 1$ (Walden and Hosken, 1985; Todoeschuck et al., 1989). When $0 \leq \alpha \leq 2$, the ACF dies away quickly for long lags. Figure 1 shows the magnitude of the ACF at the first few lags for this range of α. (Remember that the ACF at lag = 0 is unity.) As can be seen for $\alpha = 0$ (white noise) the ACF = 0 at all nonzero lags. The lag = 1 term grows much more quickly than the others, with the lag = 2 term becoming significant only for $\alpha > 1.5$, which suggests truncating the ACF at two terms. The result in terms of the power spectrum is shown (Fig. 2) for the case $\alpha = 1$. The exact spectrum is the result of Fourier transforming all the terms in the ACF. Taking one term in the ACF corresponds to a white spectrum, the horizontal line through the average. Taking one more term greatly improves the fit, which adding additional terms only slightly improves.

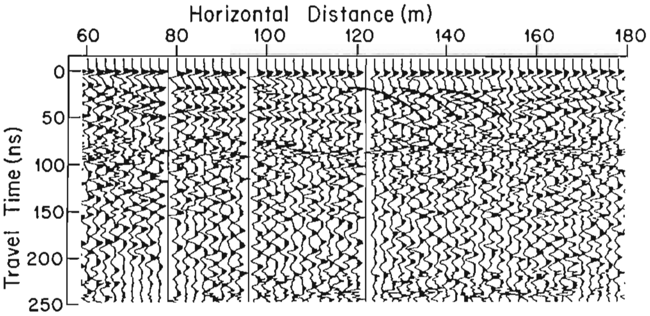

Figure 4. The profile of Figure 3 deconvolved with $\alpha = 0$ and then reconvolved with a half sine for direct comparison; note the near surface layering between 80 and 120 m and the three hyperbolic reflections discussed in the text.

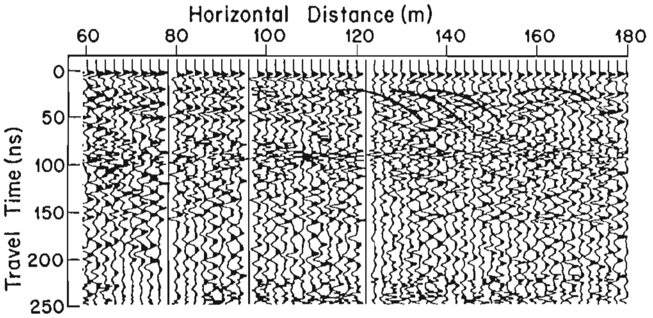

Figure 5. The profile of Figure 3 deconvolved with $\alpha = 1$ and then reconvolved with a half sine for direct comparison; an additional hyperbolic reflector is now discernable.

The normal equations for a two term ACF become

$$\Sigma\ a_n R_n = Y_0 - a_1 Y_1\ ,$$

$$\Sigma\ a_n R_{1-n} = Y_1\ ,$$

and

$$\Sigma\ a_n R_{p-n} = 0\ , p \geq 2\ . \qquad (12)$$

In all practical cases, we will be interested in obtaining a filter of finite length, L + 1, say, so we can write equation 12 in matrix form as

$$\begin{matrix} R_0 & R_1 & . & . & R_L \\ R_1 & R_0 & . & . & R_{L-1} \\ . & . & . & . & . \\ . & . & . & . & . \\ R_L & R_{L-1} & . & . & R_0 \end{matrix} \quad \begin{matrix} a_0 \\ a_1 \\ . \\ . \\ a_L \end{matrix} \quad = \quad \begin{matrix} Y_0 - a_1 Y_1 \\ Y_1 \\ 0 \\ . \\ 0 \end{matrix} \qquad (13)$$

The matrix is Toeplitz in form, which offers advantages in the solution. Our technique is to assume $Y_1 = 0$, solve for the filter coefficients, use these to calculate Y_0 which, for a given value of α gives us Y_1, and iterate. A small number of iterations is typically needed.

EXAMPLE

In 1986, a GPR survey was carried out over dam 1A at Lupin Mine near Contwoyto Lake, N.W.T., Canada (LaFlèche et al., 1987). The dam is 250 m long and 7 m high. It was constructed of a silty-sandy fill above graded overburden, with an added 2 m of gravelly sand. Bedrock outcrops at the ends of the dam but is 20 m below the top of the overburden near the centre. The dam leaks, probably because of the presence of unfrozen zones. The survey used an A-Cubed Inc. pulseEKKO III radar with 100 MHz centre frequency. The sampling interval was 800 ps. Figure 3 shows the undeconvolved results from a portion of the survey in a positive-shaded display. The data were filtered to remove any low frequency drift in the traces and automatic gain to a maximum multiplication of 300 was applied trace by trace.

For the deconvolution method outlined above to be fully exploited it is necessary to know the value of parameter α. In the case of seismograms, it was possible to use sonic logs to estimate α. Unfortunately the same has not been done for the variations in dielectric and conductivity properties causing the reflections in the radar case. It is hoped that core logs may indicate of the proper range of α. It may also be possible to determine α directly from the trace. We initially assume $\alpha = 0$ and produce a reflection sequence. We estimate a value of α from its power spectrum and deconvolve the observations using this new value, iterating as necessary. This technique has shown promising results with seismograms. Meanwhile, it is possible to proceed by taking the values $\alpha = 0$ and $\alpha = 1$. The first value gives the well known prediction error filter (Robinson, 1957) and corresponds to assuming a white power spectrum. There are two ways of looking at this. First, if you know nothing about a spectrum, drawing a horizontal line is the least damaging assumption (Fig. 2). Alternatively, it is equivalent to truncating the ACF at one term. The value $\alpha = 1$ has been found useful in the seismic case.

Figure 4 shows the data deconvolved with the prediction error filter (PEF) trace by trace. Now, the deconvolved reflection sequence consists of a series of numbers and can be transferred to, say, a migration algorithm in that form. They can also be displayed as a series of lines proportional to their value, but we have found this output to be hard to interpret. We have therefore reconvolved the sequence with a half-sine operator of known amplitude and wavelength. This display is comparable to the original. Several features, which were not clearly seen, are now evident in the near surface between 0 and 100 ns. In the interval from 65 to 100 m along the profile, several closely spaced reflecting horizons are now resolved. We interpret these horizons as layering in the uppermost gravelly sand fill. Three shallow hyperbolic reflectors can be seen from 100 to 150 m. They are obscured by the air and ground arrivals in the original data. We know that four culverts were buried 1 m deep between 100 and 168 m. Deconvolution of the data with $\alpha = 1$ yields somewhat improved results (Fig. 5). Four hyperbolic reflectors, which we interpret as the four culverts, can now be seen. It may be that better estimates of α would lead to even better results.

CONCLUSION

In the field of reflection seismology deconvolution has been an important, if not essential step in such things as migration, attenuation, or interpretation of reflection coefficients. The same will probably be true in the processing of digital GPR data. As the example shows, it is also useful for what is in effect shaping the radar pulse. Here we have shortened the pulse and removed any tail. The additional resolution obtained may well be useful, particularly for faint or closely spaced features such as may occur in the nearsurface region.

REFERENCES

LaFlèche, P.T., Judge, A.S. and Pilon, J.A.
1987: Ground probing radar investigation of the competency of frozen tailings pond dams; in Current Research, Part A, Geological Survey of Canada, Paper 87-1A, p. 191-197.

Robinson, E.A.
1957: Predictive decomposition of seismic traces; Geophysics, v. 22, p. 767-778.

Silvia, M.T. and Robinson, E.A.
1979: Deconvolution of Geophysical Time Series in the Exploration for Oil and Gas; Elsevier Scientific Publishing Co., Amsterdam, 251 pp.

Todoeschuck, J.P. and Jensen, O.G.
1988: Joseph geology and seismic deconvolution; Geophysics, v. 53, p. 1410-1414.

Todoeschuck, J.P., Jensen, O.G. and Labonte S.
1989: Gaussian scaling noise models of seismic reflection sequences: evidence from well logs; Geophysics, v. 55, p. 480-484.

Walden, A.T. and Hosken, J.W.J.
1985: An investigation of the spectral properties of primary reflection coefficients, Geophysical Prospecting, v. 33, p. 400-435.

A digital phase coded ground probing radar

Robert H. Wills[1]

Wills, R.H., 1992: A digital phase coded ground probing radar; in Ground penetrating radar, ed. J. Pilon; Geological Survey of Canada, Paper 90-4, p. 231-235.

Abstract

This paper describes a digital, phase coded radar, a new concept in ground probing radar. A complementary code is phase-modulated onto a transmitted carrier signal and propagated with conventional antennas. Upon reception, the signal is mixed to baseband to recover the code and then cross-correlated with the original code to find echo returns. The use of complementary codes eliminates the problems of time sidelobes associated with other coding techniques. First one code is sent, then another with exactly opposite autocorrelation sidelobes. The sum of these returns is a single spike. The design of, and preliminary results from, a prototype radar are presented.

Résumé

Dans le présent article est décrit un nouveau concept de géoradar, le radar numérique codé en phases. Un code complémentaire est modulé en phase sur un signal porteur transmis et propagé au moyen d'antennes classiques. Sur réception, le signal est mélangé à la bande de base pour récupérer le code avant d'être corrélé au code originel pour trouver les échos réfléchis. Le recours à des codes complémentaires permet d'éliminer les problèmes de formation de lobes latéraux associés à d'autres techniques de codage. Un code est d'abord envoyé, suivi d'un autre avec des lobes latéraux d'autocorrélation exactement opposés. La somme de ces échos donne une pointe d'impulsion unique. La conception d'un radar prototype et les résultats préliminaires obtenus à l'aide de cet appareil sont présentés.

INTRODUCTION

This paper describes a digital, phase coded radar, a new concept in ground probing radar (GPR). Preliminary results from a prototype radar are presented. Current commercial GPRs operate in the same manner as the first GPRs invented by Lerner (Lerner et al., 1967) and Morey (1974) nearly 20 years ago. In these "impulse"-type radars, the transmitting antenna is excited by a narrow pulse resulting in a short transmitted wavelet two to five half-cycles long. The received signal is generally sampled for display on an oscilloscope or graphic recorder, or is digitized for computer processing and display.

There are several problems with this technique: 1) The transmitted wavelet is not a true impulse, so single reflectors appear as multiple rather than single lines on the output record. 2) The transmitted waveform is dependent on antenna loading, and so, is ill defined. Poor definition makes deconvolution of the output signals (to yield the true subsurface reflection signal) difficult except in the most controlled situations (Payan and Kunt, 1982). 3) The need for a narrow transmitted pulse (for fine depth resolution) is opposed to the need for high average transmitted power (for range capability).

---

[1] Department of Physics and Astronomy, Dartmouth College, Hanover, New Hampshire, U.S.A. 03755, now at Skyline Engineering, Temple, New Hampshire, U.S.A. 03084

PULSE COMPRESSION

The contrary needs of short pulse length and high average power were recognized in atmospheric radars in the late 1940s. In the early 1950s, the problem was resolved by dispersing the transmitted impulse in time, producing a swept frequency (linear FM or "chirp") transmitted signal. The received signal is processed through an inverse delay line yielding impulse-like responses from reflectors.

Although it solves the problem for atmospheric radars, linear FM does not work well in GPR. The problem is that the radar output is in the form of a sinc (sin(x)/x) function, which has time sidelobes 32 dB below the main response. The sinc function time output is a direct result (i.e., a Fourier transform) of the rectangular frequency-domain function of the chirp. Even with additional filtering, the peak-to-sidelobe ratio seldom exceeds 40 dB in practical chirp radars.

Another approach to pulse compression was developed in the early 1960s. Using phase modulation, a digital code is modulated onto the transmitted waveform. The received signal is demodulated and cross-correlated with the original code yielding impulse-like responses for the reflectors. This method also suffers from unacceptably high sidelobe levels for geophysical work; the longest Barker code (codes with a maximum autocorrelation sidelobe amplitude of one) has a length of 13 and a peak-to-sidelobe ratio of 13 or 22 dB. Postfiltering and longer codes can achieve better results, but again, peak-to-sidelobe ratios of greater than 40 dB are difficult to achieve.

In the early 1969s, Golay (Golay, 1961) and Welti (Welti, 1960) discovered complementary codes. These pairs of digital codes have exactly opposite autocorrelation sidelobes (Fig. 1).

When used in a radar, both codes are phase modulated onto a carrier (Fig. 2), transmitted, received, and cross-correlated, one after another; then the resulting signals are added yielding a received signal essentially free from time sidelobes. (Small sidelobes are introduced by nonlinearities in the amplitude and phase response of the overall system, but these may be removed by appropriate filtering).

Complementary codes have been used in few practical radars (e.g., Rabiner and Gold, 1975; Woodman, 1980) because they rely on constant radar-target position between code transmissions and so are not suitable for tracking moving targets. Complementary coding is, however, ideal for geophysical radar as the antennas can remain stationary during transmissions, or at least be constrained to move slowly.

Complementary codes offer longer and better defined waveforms than existing GPRs. Correlation of the code sequence with the received signal achieves the same desired result as deconvolution; a single layer yields a single return. Longer pulses produce higher average powers and so increase range capability. The well defined waveshape and "automatic deconvolution" promise a cleaner, more representative map of the target medium.

Complementary coded radars have other benefits. Because the transmitted waveform is shaped by the transmit electronics, rather than the transmitting antenna alone, higher gain directional antennas such as yagis or log-periodics may be used. The antenna response still modifies the transmitted and received signals, but as the signal is mixed to baseband, it is the envelope of the antenna responses, rather than the antenna time response, that is superimposed upon a return echo. Antenna design, specifically a quickly decaying time response, is still a key factor in radar performance but not as crucial as for impulse radars. A single reflector will still return a single response even with antennas that have poor time responses.

Higher directivity antennas can produce better target profiles as their view is more focused (they have a smaller "footprint"). Higher gain also promises greater penetration. These two factors greatly increase the potential for airborne radar surveys. In addition, high power amplifiers can be used to boost the transmitted signal, whereas impulse type radars must use higher and higher pulse voltages to generate the transmitted impulse.

THE PROTOTYPE SYSTEM

A prototype digital phase coded (DPC) radar has been constructed with the following specification (Wills, 1987):

Carrier frequency	5-300 MHz
Modulating bit-rate	1-100 MHz
Code-length	16-128 000
Power output	100 mW
Receiver range	128 000 Time bins

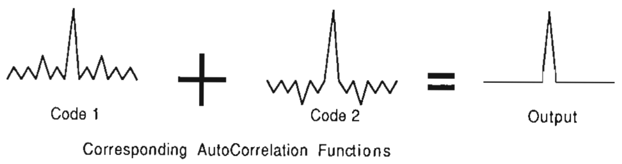

Figure 1. Autocorrelation functions of complementary codes.

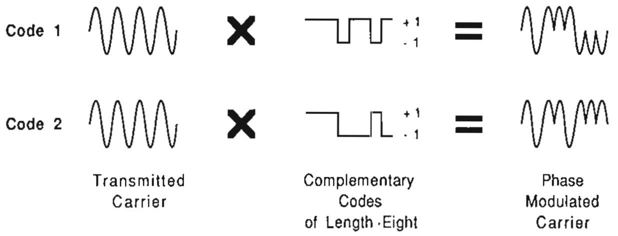

Figure 2. Complementary codes modulated onto a carrier signal.

The radar is based on an Ironics P32 68020 UNIX computer, which is used for control, signal processing, and data storage. The complete system consists of a digital code generator, carrier oscillator, modulator, amplifier, and transmit antenna in the transmitter, and a receive antenna, RF amplifier, mixer, IF amplifiers, and high speed analogue to digital converters in the receiver (Fig. 3).

The digital codes are generated in the computer and then loaded into the code generator memory. When transmission is initiated, codes are fed from the code generator memory to a shift register at rates of up to 100 million bits per second (Mbps). This signal feeds a biphase modulator, which produces signals similar to those in Figure 2. The modulated signals are gated to the code length, amplified, and fed to the transmit antenna.

Received signals are collected by a receiving antenna, amplified, and mixed down to two baseband IF channels by in-phase and quadrature signals at the carrier frequency. Logarithmic amplifiers with a dynamic range of 40 dB are used to increase the dynamic range of the receiver (the 6 bit analogue to digital converters have a dynamic range of only 36 dB). These are followed by 12 dB linear amplifiers to raise the signal to full range for the analogue to digital (A/D) converters.

The A/D converters are 6 bit 100 MHz flash converters whose output is stored using serial to parallel conversion to slow the data rate in computer memory.

Signal processing within the computer comprises cross-correlation with the transmitted code for both in-phase and quadrature channels, the summing of the received signals from each of the complementary codes and integration over several scans if desired.

The present display uses a graphics terminal to plot single or multiple waveforms. A grey-scale display similar to existing radar graphic recorders would greatly improve the output.

Antennas used to date have been impulse radar antennas fed with a balun from the transmitter amplifier. Preliminary tests between log-periodic antennas in air show reasonable results, but further testing is required to show their true practicality.

The DPC radar can operate in two different modes. For targets close to the surface, and when using very long codes, transmission and reception occur simultaneously, which can lead to dynamic range and overloading in the receiver as target range increases. For distant targets, the radar can be used in a pulse mode where the transmission of the coded signal is complete before reception begins. It is also possible to generate short codes for near surface exploration and longer ones for deeper penetration.

THEORETICAL PERFORMANCE

The prototype radar uses a 30 dB RF amplifier, 40 dB log IF amplifiers followed by 12 dB linear amplifiers feeding analogue to digital converters with a least significant bit

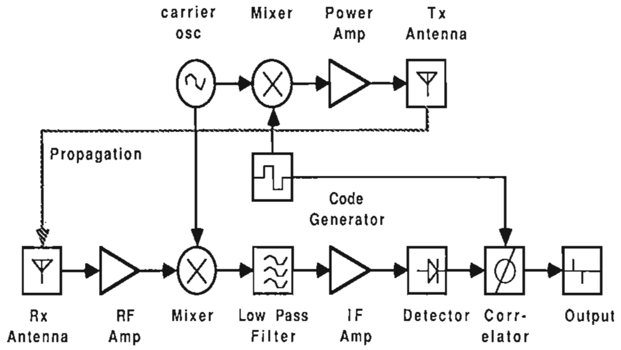

Figure 3. DPC radar block diagram.

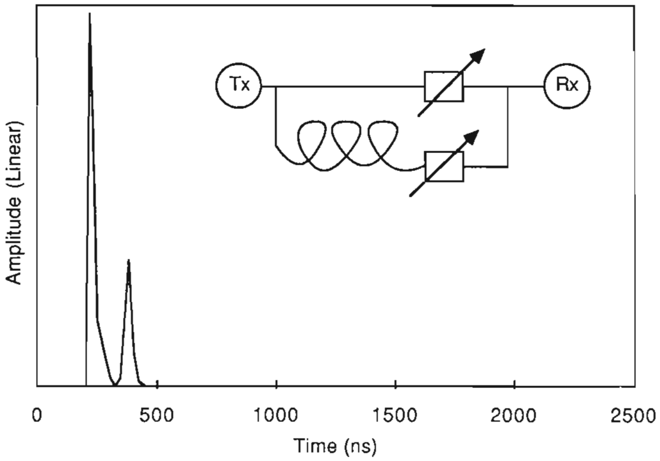

Figure 4. Response through coaxial cable and attenuators.

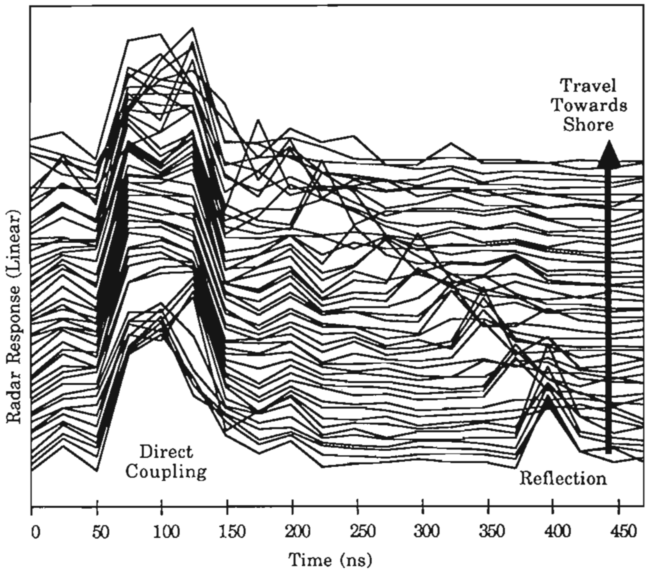

Figure 5. Reflections through water, Connecticut River, NH.

sensitivity of 23 dBm^{-1}. The receiver sensitivity, including losses is about 90 dBm^{-1}, or close to the thermal noise level at 100 MHz bandwidth. With a transmitted power of 0.1 W or +20 dBm^{-1}, the theoretical performance figure for the radar is 110 dBm. The actual performance figure measured using coaxial cable and attenuators from transmitter to receiver is more than 100 dB. The separate in-phase and quadrature outputs from the receiver allow the received signals to be coherently integrated reducing noise by the number of integrated scans rather than the square root of the number of scans if only the magnitude of the received signal is integrated. This reduction, and the equivalent action of increasing code length can result in processing gains of 20-30 dB at the cost of significantly increased processing time.

The resolution of a digitally coded radar is about a half cycle at the modulating frequency (and not a function of code length). This resolution is typically 0.75 m in air, 0.4 m in soil, and 8 cm in water for a 100 Mbps modulation rate. Higher modulation rates (and thus resolution) are possible using current technology. The modulating frequency must be less than, or equal to, the carrier frequency otherwise aliasing of the modulation information occurs. The minimum resolution is thus limited to a half cycle at the carrier frequency (i.e., the same as impulse radar resolution).

ACTUAL PERFORMANCE

Figure 4 shows the response of the radar through coaxial cable and attenuators. The first response is attenuated by 40 dB; the second is delayed through 30 m of cable and also attenuated by 40 dB. The carrier frequency is 160 MHz with a modulation rate of 40 MHz (25 ns per time bin). The second response is attenuated by cable loss, which is about 10 dB. The vertical scale is a linear output from the correlator, but the overall response is nonlinear because of the IF logarithmic amplifiers; the height of the delayed response represents about 35 dB.

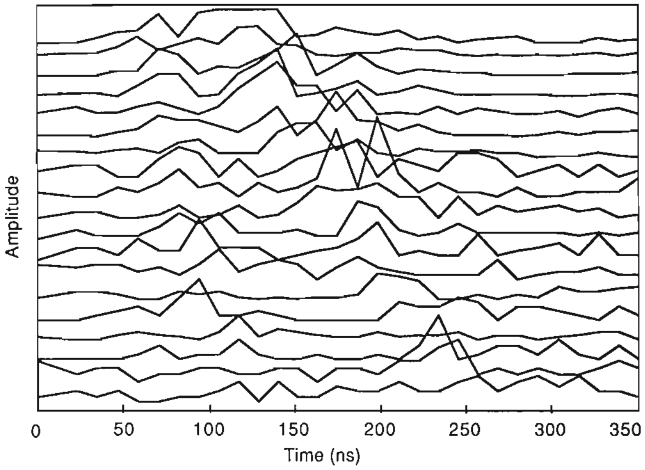

Figure 6. Wide angle refraction test in rock.

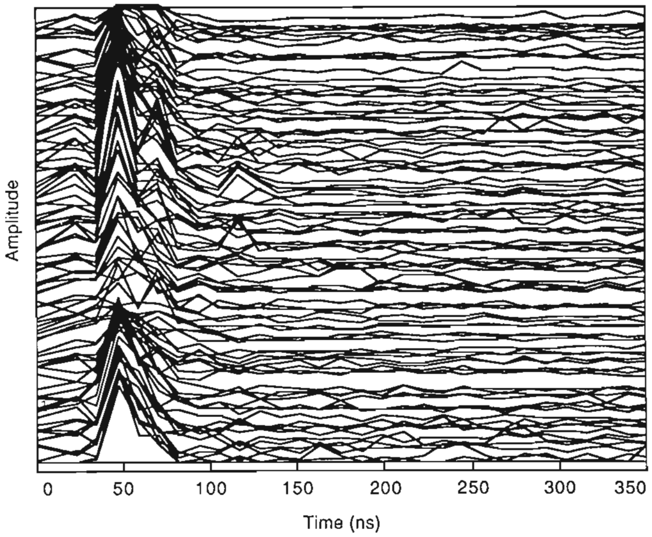

Figure 7. Traverse over rock (stations 32-18).

PROPAGATION THROUGH WATER

To prove the river depth sounding ability of the radar, tests were done at Wilson's Landing on the Connecticut River near Hanover, New Hampshire. Two GSSI 3107 antennas were mounted in the bottom of a canoe, end to end, about 0.6 m apart. The carrier frequency was 160 MHz with a modulating bit rate of 40 Mbps. Coaxial cables ran from the antennas to the radar unit on shore. Power was supplied by a portable generator. The length of the cables prohibited access to deeper water (future tests will use a small towing craft to carry the radar unit). The results, moving the boat from a measured depth of about 4.9 m of water to shore, are shown in Figure 5. Fifty scans are plotted here across the page, proceeding up the page as the boat moves closer to shore. The direct coupling between antennas is at 100 ns delay and shows strong limiting to the A/D converter maximum. The river bottom reflection moves in from 400 ns and merges with the direct coupled return. The time delay of 300 ns is as expected for two-way travel through 4.9 m of water.

The faint constant return at 200 ns delay is probably caused by ringing within the radar or reflections in the antenna cables.

SOUNDING THROUGH ROCK

Tests were done at an exposed granite site in Cannan, New Hampshire. Figure 6 shows the result of a wide angle refraction experiment with a carrier frequency and modulating bit-rate of 85 MHz. There is a significant increase in receiver noise, especially in the A/D converter stages at frequencies above 70 MHz. This noise along with inhomogeneity in the rock explain the rather noisy result. It is possible to see, however, air and ground wave coupling converging at the top of the figure.

Figure 7 shows a traverse over the rock surface with antennas spaced 1.5 m apart. The carrier frequency and modulation bit rate were again 85 MHz, yielding again a somewhat noisy response. Reflections can be seen at 25 and 100 ns from the direct signal. These reflections correspond quite well with impulse radar observations.

CONCLUSIONS

Digital phase coded radar using complementary codes is a viable alternative to impulse type radars for geophysical exploration. DPC radars offer high average power, well defined waveforms, a single response to a single reflector, and both magnitude and phase outputs. The ability to use directional antennas may significantly improve the airborne performance of GPR, but has yet to be tried.

The prototype radar has sounded successfully through water and rock with results similar to those achieved with impulse type radars but needs further development in the areas of data display, receiver noise levels, transmitter power, higher modulating frequencies (to improve resolution), and means to improve dynamic range.

Dynamic range is the biggest obstacle to successful implementation of pulse-compression type radars. The problems associated with amplifier and mixer dynamic range and intermodulation distortion, and sampling and digitization noise results in performance in typical cluttered ground probing applications that needs improvement.

ACKNOWLEDGMENTS

This work was done under contract 536115-DACA-89-81-K-004 with the U.S. Army Cold Regions Research and Engineering Laboratory. Thanks to Dr. Steven Arcone and Alan Delany of USACRREL for continual help with the project.

REFERENCES

Golay, M.J.E.
1961: Complementary series; IRE Transactions on Information Theory, IT-7, New York, Institute of Radio Engineers, p. 82-87.
Lerner, R., Enticknap, R.G., Guillette R.A., Nickoney, O.G., and Chick, R.W.
1967: Geodar. MIT Lincoln Laboratory Report AD-595823L EPS-1, 124 p.
Morey, R.M.
1974: Continuous subsurface profiling by impulse radar; in Proceedings, Engineering Foundation Conference on Subsurface Exploration for Underground Excavation and Heavy Construction, Henniker, New Hampshire. American Society of Civil Engineers, New York, p. 213-232.
Payan, I. and Kunt, M.
1982: Subsurface radar signal deconvolution; Signal Processing, v. 4, no. 4, p. 249-262.
Rabiner, L.R. and Gold, B.
1975: Theory and application of digital signal processing; Prentice Hall, New Jersey, p. 741-753.
Welti, G.R.
1960: Quaternary codes for pulsed radar; IRE Transactions on Information Theory, IT-6, New York, Institution of Radio Engineers, p. 400-408.
Wills, R.H.
1987: A digital phase coded ground probing radar; doctoral thesis, Thayer School of Engineering, Dartmouth College, Hanover, NH.
Woodman, R.F.
1980: High-altitude resolution stratospheric measurements with the Arecibo 430-MHz radar; Radio Science, v. 15, no. 2, p. 417-422.

LIST OF PARTICIPANTS

James W. Allen (303)242-8621
Technical Manager Ext. 215)
Geophysical Programs Dept.
UNC Geotech, P.O. Box 14000
2597 B 3/4 Road
Grand Junction, CO
81502-5504

Peter Annan (416)624-8878
Sensors & Software Inc.
5566 Tomken Road
Mississauga, Ontario
L4W 1P4

Steven Arcone (603)646-4368
USA CRREL
Lyme Road
Hanover, NH
03755

Doug Ballantyne (613)593-7609
OmniVision Systems
606 Kirkwood Ave.
Ottawa, Ontario
K1Z 5X6

William B. Barber (216)581-5975
BP America
4440 Warrensville Center Rd.
Cleveland, OH
44128

Simon Bate (416)365-0930
MPH Consulting Ltd.
2406 - 120 Adelaide St. W
Toronto, Ontario
M5H 1T1

Paul Bauman (519)746-1534
University of Waterloo
Waterloo, Ontario
N2L 3G1

Angelo Beano 040-62580/61286
Idrogeo S.R.L.
Via Mercato Vecchio 1
34124 Trieste
ITALY

Luc Beauchamp (705)472-4140
Mines Accident Prevention
Association of Ontario
P.O. Box 1468
North Bay, Ontario
P1B 8K6

Bill Bellens 32-13-335031
BLIS NV
Koning Albertstraat 74-76
3290 Diest
BELGIUM

Richard Benson (305)634-4507
TECHNOS
3333 Northwest 21st St.
Miami, FL
33142

M.J. Berry (613)995-5484
Director, Geophysics Division
Geological Survey of Canada
1 Observatory Cres.
Ottawa, Ontario
K1A 0Y3

Gary Black (416)624-8878
A-CUBED Inc.
5566 Tomken Road
Mississauga, Ontario
L4W 1P4

Stephen D. Booth (613)954-4761
Solicitor General of Canada
P.O. Box 9732
Ottawa Mail Terminal
Ottawa, Ontario
K1G 4G4

Quentin Bristow (613)992-9530
Geological Survey of Canada
601 Booth Street
Ottawa, Ontario
K1A 0E8

Margo Burgess (613)996-9317
Geological Survey of Canada
601 Booth Street
Ottawa, Ontario
K1A 0E8

Brian Byerley (416)487-1581
Canpolar Inc.
Ste 4 - 421 Eglinton Avenue W.
Toronto, Ontario
M5N 1A4

C.R. Carter (416)525-9140
Communications Research ext. 4964
Laboratory
McMaster University
Hamilton, Ontario
L8S 4K1

Glenn Chafe (514)399-7554
Project Engineer
Engineering Planning & Analysis
Canadian National
1060 University, Floor 2
P.O. Box 8100
Montreal, Quebec
H3C 3N4

David W. Cochrane (613)993-2927
R.C.M. Police
Central Forensic Lab.
P.O. Box 8885
Ottawa, Ontario
K1G 3M8

Len Collett (613)992-7955
Geological Survey of Canada
1 Observatory Cres.
Ottawa, Ontario
K1A 0Y3

L.M. Cumming (613)995-4003
Geological Survey of Canada
601 Booth Street
Ottawa, Ontario
K1A 0E8

Scott R. Dallimore (613)992-1658
Geological Survey of Canada
601 Booth Street
Ottawa, Ontario
K1A 0E8

Les Davis (416)624-8878
A-Cubed Inc.
5566 Tomken Road
Mississauga, Ontario
L4W 1P4

Debby De Bock 32-13-335031
BLIS NV
Koning Albertstraat 74-76
3290 Diest
BELGIUM

Allan Delaney (603)646-4252
USA CRREL
Lyme Road
Hanover, NH
03755

Claude Deschambeault (514)271-3150
SAGAX Geophysique Inc.
Suite 100, 6700 Ave. du Parc
Montreal, Quebec
H2V 4H9

Doug Doney (506)433-5371
Denison-Potacan Potash Co.
P.O. Box 5005
Sussex, N.B.
E0E 1P0

James A. Doolittle (215)499-3960
USDA - Soil Conservation Service
160 East 7th Street
Chester, PA
19013

Philip H. Duoos (201)735-9390
Delta Geophysical
116 West Main St.
Clinton, NJ
08809

Larry Dyke (613)545-6173
Dept. of Geology
Queen's University
Kingston, Ontario
K7L 3N6

Peter J. Dyne (613)992-3738
Director General
Office of Energy Research & Development
EMR, 580 Booth Street
Ottawa, Ontario
K1A 0E4

Paul A. Egginton (613)992-2451
Terrain Sciences Division
Geological Survey of Canada
601 Booth Street
Ottawa, Ontario
K1A 0E8

Robert Ehrnrooth 358-0-670036
Consultant
Tul, Lapin Piiri
Pl 194, 96101 Rovaniemi
FINLAND

Tony W. England (713)483-2787
NASA, Johnson Space Center
Houston, TX
77058

Peter Flavelle (613)995-3816
Atomic Energy Control Board
P.O. Box 1046
Ottawa, Ontario
K1P 5S9

Raymond Fortin (613)996-1622
Dept. des Affaires Exterieures
(MITI) 125 Rue Sussex
Ottawa, Ontario
K1A 0G2

Ed Freeborn (315)341-3044
State University of
New York at Oswego
Oswego, NY
13126

Guy Gilsoul 02/520-40-20
Les Entreprises SBBM
Blvd. Louis Mettewie 74-76, Bte 2
B-1080 Bruxelles
BELGIUM

Jonathan Glover 01-556-7433
Subsurface Geotechnical Services
35 Mornington Road
Leytonstone, London
E11 3BE, U.K.

Dr. R.H. Goodman (403)259-0296
Esso Resources Canada Limited
339 - 50 Avenue S.E.
Calgary, Alberta
T2G 2B3

Laurel Goodrich (613)993-3791
National Research Council
IRC M-20
Montreal Road
Ottawa, Ontario
K1A 0R6

Mr. Fred Graf (215)841-4873
Philadelphia Electric Co.
2301 Market Stree
Philadelphia, PA
19101

Mrs. Sandra Graf (215)841-4873
Philadelphia Electric Co.
2301 Market Stree
Philadelphia, PA
19101

Dr. James T. Gray
Dept. de Géographie
Université de Montréal
520 Cote Ste-Catherine
Montréal, Québec
H2V 2B8

John Greenhouse (519)885-1211 ext. 3791
Dept. of Earth Sciences
University of Waterloo
Waterloo, Ontario
N2L 3G1

R.A.F. Grieve (613)995-5372
Geophysics Division, GSC
3 Observatory Cres.
Ottawa, Ontario
K1A 0Y3

France Groupil (514)679-2400
Geophysique G.P.R. International Inc.
2545 rue Delorimier
Longueuil, Québec
J4K 3P7

David W. Hall (609)984-6587
DWR/New Jersey Geological Survey
CN-029, Trenton, NJ
08625

Jim Harkin (613)996-1622
Gov't of New Zealand
Box 12-424
Wellington
NEW ZEALAND

Andrew Harris (622)36967
Ground-Scan Ltd.
Cobham Manor, Water Lane
Thurnham, Maidstone, Kent
ENGLAND ME14 3LU

Martin Heroux (613)541-6071
Civil Engineering Dept.
Royal Military College
Kingston, Ontario
K7K 5L0

Art Holloway (204)753-2311
URL/Atomic Energy Local 3085
of Canada Ltd.
Pinawa, Manitoba
R0E 1L0

Peter Hood (613)995-4913
Geological Survey of Canada
601 Booth Street
Ottawa, Ontario
K1A 0E8

Jim Hunter (613)992-2560
Geological Survey of Canada
601 Booth Street
Ottawa, Ontario
K1A 0E8

Dr. Ronald M. Hutcheon (613)584-3311
Atomic Energy of Canada ext. 3963
Mail Stop 111
Chalk River, Ontario
K0J 1P0

Mr. James Hyatt (613)545-6368
Dept. of Geography
Queen's University
Kingston, Ontario
K7L 3N6

D.R. (Rob) Inkster (403)266-0900
Vice-President
INTERRA
2500, 101 6th Avenue S.W.
Calgary, Alta.
T2P 3P4

John Irvine (613)820-1525
Consulting Geophysicist
27 Brian Crescent
Nepean, Ontario
K2H 6X2

Dr. Robert W. Jacobel (507)646-3124
Dept. of Physics
St. Olaf College
Northfield, MN 55057

Higgin Jin (403)587-3145
Esso Resources Canada Ltd.
71 Edendale Cresc. N.W.
Calgary, Alta.
T3A 3W8

Rex Johnson (613)996-1622
Gov't of New Zealand
c/o Ray Fortin, MITI,
External Affairs
125 Sussex Street
Ottawa, Ontario
K1A 0G2

Francis M. Jones (604)261-5169
Univ. of British Columbia
3435 West 30th
Vancouver, B.C.
V6S 1W3

Clovis José 0195-34-62-49
UNESP - Rio Claro
Dep. de Fisica
Rua 10, No. 2527
13.500 - Rio Claro - S.P.
BRASIL

Alan Judge (613)996-9323
Terrain Science Div., GSC
601 Booth Street
Ottawa, Ontario
K1A 0E8

T.J. Katsube (613)995-5239
Geological Survey of Canada
601 Booth Street
Ottawa, Ontario
K1A 0E8

Frank G. Kiss (613)998-3518
Aeromag Contract Surveys Section
Geological Survey of Canada
1 Observatory Crescent
Ottawa, Ontario
K1A 0Y3

Doria Kutrubes (617)366-9191
Weston Geophysical
P.O. Box 550
Westboro, MA
01581

Leevi Koponen 358-0-357-959
Geo-Work Oy
Tul, Lapin Piiri
Pl 194, 96101 Rovaniemi
FINLAND

Austin Kovacs (603)646-4411
USA CRREL
72 Lyme Road
Hanover, NH
03755

K.V. Kunduri (705)672-3376
Haileybury School of Mines
Haileybury, Ontario
P0J 1K0

Pavel Kurfurst (613)992-1755
Geological Survey of Canada
Rm. 241, 401 Lebreton St.
Ottawa, Ontario
K1A 0E8

Branco Ladanyi (514)340-4804
Ecole Polytechnique
Dept. of Civil Engineering
Case Postale 6079 - Succursale "A"
Montréal, Québec
H3C 3A7

Paul LaFleche (613)996-5924
NSERC
244 Bayswater Ave.
Ottawa, Ontario
K1Y 2G8

Len LaFond (416)457-8120
General Manager
Graff Diamond Products
35 Hale Road
Brampton, Ontario
L5W 3J9

Louis Lalumiere (416)487-1581
Canpolar Inc.
421 Eglinton Ave. W.
Toronto, Ontario
M5N 1A4

Dominique Langlais (613)996-9315
Terrain Sciences, GSC
3 Observatory Cres.
Ottawa, Ontario
K1A 0Y3

Mr. Lauriol (613)764-6591
University of Ottawa
Ottawa, Ontario

Richard Levesque
Université Laval
Cité Universitaire
Pavillon F-A S
Sainte-Foy, Québec
G1K 7P4

David Leask (416)477-8400
Gartner Lee Limited
140 Renfrew Drive
Markham, Ont.
L3R 8B6

David Lieblich (203)240-3299
USGS, WRD, Hartford
United States Geological Survey
Rm 525 - 450 Main Street
Hartford, CT
06103

Lisanne Losier (613)992-6949
Geological Survey of Canada
244 Bayswater Ave.
Ottawa, Ontario
K1Y 2G8

James MacNae (416)596-1772
Lamontagne Geophysics Ltd.
Ste. 306, 49 Spadina Ave.
Toronto, Ontario
M5V 2J1

Glen McCrank (204)753-2311
Atomic Energy of Canada Ltd. ext. 3257
Pinawa, Manitoba
R0E 1L0

Richard G. McCreary (613)546-1012
Associate Professor
Engineering Seismology Lab.
Queen's University
Kingston, Ontario
K7L 3N6

Bill McFadden (519)681-4241
National Scientific & Marine
Research Ltd.
446 Three Valley's Cres.
London, Ontario

Willard McWilliams (519)681-4241
President
National Scientific & Marine
Research Ltd.
446 Three Valley's Cres.
London, Ontario

Yves Michaud
Geological Sciences
Queen's University
Kingston, Ontario

Peter S. Miller (808)438-1200
USA Central ID Laboratory
Fort Shafter, HI
96858-5480

Brian Moorman (613)828-3429
Terrain Science Div., GSC
601 Booth Street
Ottawa, Ontario K1A 0E8

Robert Morgan (416)671-3209
ROMOR Equipment Ltd.
1083 Britannia Rd. E.
Mississauga, Ont. L4W 3X1

Jamie Mugford (204)345-8625
URL/Atomic Energy of Canada Ltd.
Pinawa, Manitoba
R0E 1L0

Christine Neumiller (204)345-8625
U.S. Dept. of Energy, Chicago
URL/Atomic Energy of Canada Ltd.
Pinawa, Manitoba
R0E 1L0

Olle Olsson 46-1815-64-20
Engineering Geology
Swedish Geological Co.
Box 1424
S-751 44 Uppsala
Sweden

Gordon Oswald (223)358855
Cambridge Consultants Ltd.
Science Park, Milton Road
Cambridge CB4 4DW
ENGLAND

Neil Parry (403)451-2121
EBA Engineering Consultants Ltd.
14535 - 118th Avenue
Edmonton, Alberta
T5L 2M7

David L. Pasicznyk (609)984-6587
DWR/New Jersey Geological Survey
CN-029, Trenton, NJ
08625

Roger Pemberton (416)982-7255
Director of Geophysics
Noranda Exploration Ltd.
Ste 1300 - 4 King Street W
Toronto, Ontario
M5E 1J4

Jean Pilon (613)996-9315
Geological Survey of Canada
601 Booth Street
Ottawa, Ontario
K1A 0E8

Vladimir Poliscuk (613)995-5073
Project Officer
Atomic Energy Control Board
P.O. Box 1046
Ottawa, Ontario
K1P 5S9

Risto Pollari 358-60318808
Geo-Work Oy
Tul, Lapin Piiri
Pl 194, 96101 Rovaniemi
FINLAND

Jim Poplin (713)965-7660
EXXON Production Research
P.O. Box 2189
Houston, TX
77252-2189

Willard R. Pratt III (315)829-3388
PVE Research Inc.
P.O. Box 996
Snowden Hill Road
Clinton, NY 13323

Susan Pullan (613)992-3483
Geological Survey of Canada
601 Booth Street
Ottawa, Ontario K1A 0E8

John Race (514)399-7427
Industrial Engineer
Engineering Planning & Analysis
Canadian National
1060 University, Floor 2
P.O. Box 8100, Montreal, Quebec
H3C 3N4

David Redman (416)877-7021
McLennan Geophysics Labs
University of Toronto
60 St. George Street
Toronto, Ontario M5S 2E7

K.A. Richardson (613)992-4078
Mineral Resources Division
Geological Survey of Canada
601 Booth Street
Ottawa, Ontario K1A 0E8

J.E. Robinson (315)423-3626
Dept. of Geology
Syracuse University
Syracuse, NY
13244

Dennis Roddy (807)343-8110
Dept. of Electrical Engr.
Lakehead University
Thunder Bay, Ontario
P7B 5E1

Jamie Rossiter (416)487-1581
President, Canpolar Inc.
421 Eglinton Ave. W.
Toronto, Ontario
M5N 1A4

Brian Roulston (506)433-5445
Potash Co. of America
P.O. Box 1489
Sussex, N.B.
E0E 1P0

Timo Saarenketo 960-294 284
Roads & Waterways Administration
Tul, Lapin Piiri
Pl 194, 96101 Rovaniemi
FINLAND

Ron Salmons (613)998-1647
Identification Research
Field Ident. Resource Section
RCMP Ottawa
1200 Alta Vista Drive
Ottawa, Ontario K1A 0R2

Stewart K. Sandberg (609)984-6587
DWR/New Jersey Geological Survey
CN-029, Trenton, NJ
08625

Dr. Motoyuki Sato
Tohoku University, Japan
c/o Rudolf Thierbach
BGR, Hannover
Federal Republic of Germany

Jerry Schwartz (604)876-6409
c/o S. Schwartz
3137 Heather Street
Vancouver, B.C.

Saarelainen Seppo 358-0-4564895
MSC, Research Officer
Techn. Res. Centre of Finland
VTT, Geotechnical Lab
Betonimiehenkuja 1
SF-02150 Espod
FINLAND

Ken Shultz (613)995-3704
Atomic Energy Control Board
P.O. Box 1046
Ottawa, Ontario K1P 5S9

Vijay Singh (204)474-8863
Dept. of Geological Sciences
University of Manitoba
Winnipeg, Man.
R3T 2N2

Ajit K. Sinha (613)995-5489
Mineral Resources Division
Geological Survey of Canada
601 Booth Street
Ottawa, Ontario K1A 0E8

V.R. Slaney (613)998-6742
Geological Survey of Canada
Rm 598 - 601 Booth Street
Ottawa, Ontario K1A 0E8

Eero Slunga
Assoc. Professor
Technical University of Helsinki
Dept. of Civil Engineering
02150 Espoo 15
FINLAND

Stanley Smith (603)889-4841
Geophysical Survey Systems Inc.
15 Flagstone Drive
Hudson, NH
03051

K. Brian Strongman (403)471-9493
Assist. Staffing & Personnel Officer
Royal Canadian Mounted Police
11140 - 109 Street
Edmonton, Alberta
T5J 2N1

Raimo Sutienen (608)262-4983
Dept. of Geology & Geophysics
Weeks Hall, Univ. of Wisconsin
Madison, WI
53706

Jeff Sutton (613)728-6111
INTERA (Ottawa)
600 - 1525 Carling Ave.
Ottawa, Ontario
K1Z 8R9

Lonnie G. Thompson (614)292-6552
Byrd Polar Research Center
Ohio State University
125 S. Oval Mall
Columbus, OH
43210

Sylvie Tillard 42-59-53-11
DERS/SERE/LESS Bàt 153
CEA CEN CADARACHE
13108 St-Paul-les-Durance
FRANCE

John Todoeschuck (604)
Defence Research Establishment Pacific
FMO, Victoria, B.C.
V0S 1B0

G. Clarke Topp (613)995-5011
Land Resource Research Centre
Agriculture Canada
Ottawa, Ontario
K1A 0C6

Dr. Robert R. Unterberger (409)845-1366
Dept. of Geophysics
Texas A&M University
College Station, TX
77843

Noel Unwin (062)612 536
Director, Technical Services
Dept. of Foreign Affairs & Trade
Canberra, A.C.T.
AUSTRALIA

Paul Van Etten (315)330-4437
PVE Research Inc.
(315)737-8410
P.O. Box 996
Snowden Hill Road
Clinton, NY
13323

Jean Luc Walewijns 010/43-37-84
Université de Louvain 010/47-37-13
Faculté des Sciences Agronomiques
Unité de génie rural
1348 Louvain-La-Neuve
BELGIUM

Anne Wilkinson (613)996-9390
Geological Survey of Canada
Bldg. 3, 1 Observatory Cresc.
Ottawa, Ontario
K1A 0Y3

Thomas R. Williams (206)323-5995
Northland Geophysical Co.
Ste. 435, 2366 Eastlake Ave. E.
Seattle, WA
98102

Robert Wills (603)878-1600
Dept. of Physics
Dartmouth College
Hanover, NH
03755

Mr. Stephen Wolfe (613)547-6313
P.O. Box 134 fax (603)878-4643
Temple, NH, U.S.A.
03084

Hild Wood (622)36967
Ground-Scan Ltd.
Cobham Manor, Water Lane
Thurnham, Maidstone, Kent
ENGLAND ME14 3LU

Tony Wood (622)36967
Director
Ground-Scan Ltd.
Cobham Manor, Water Lane
Thurnham, Maidstone, Kent
ENGLAND ME14 3LU

Abdoulkhay Zhamaletdinov 37-208
Geological Institute
Kola Branch of the USSR
Acad. of Science
Apaity, Murmansk Region, 18420
U.S.S.R.

AUTHOR INDEX